T. Hikmet Karakoc · M. Baris Ozerdem
M. Ziya Sogut · Can Ozgur Colpan
Onder Altuntas · Emin Açıkkalp   *Editors*

Sustainable Aviation

Energy and Environmental Issues

Springer

Sustainable Aviation

T. Hikmet Karakoc · M. Baris Ozerdem
M. Ziya Sogut · Can Ozgur Colpan
Onder Altuntas · Emin Açıkkalp
Editors

Sustainable Aviation

Energy and Environmental Issues

Springer

Editors
T. Hikmet Karakoc
Anadolu University
Tepebaşı
Turkey

M. Baris Ozerdem
Bahçeşehir University
Beşiktaş, İstanbul
Turkey

M. Ziya Sogut
Anadolu University
Tepebaşı
Turkey

Can Ozgur Colpan
Dokuz Eylul University
Alsancak, İzmir
Turkey

Onder Altuntas
Faculty of Aeronautics and Astronautics
Anadolu University
Tepebaşı
Turkey

Emin Açıkkalp
Bilecik S.E. University
Gülümbe, Bilecik
Turkey

Preface

Environmental problems such as air pollution and global warming have started to be one of the main factors in the design and development of new vehicles. Using fossil fuels and inefficient power producing technologies have increased these problems. These fossil fuels will also be depleted in the near future. Therefore, there is a need to develop more efficient, environmentally friendly, and economical alternative technologies to be implemented in vehicles to create a sustainable future and meet the consumer demands for tomorrow. Among the different types of vehicles, aerial vehicles have a significant contribution in today's global problems. Not only aircrafts but also airports have serious effects on the pollution and other environmental impacts in aviation industry. The emissions released to the atmosphere from these vehicles and airports not only cause environmental problems but also threaten the human health as a result of the consequences of these problems. On the other hand, aviation is one of the biggest industries that consume a significant amount of energy. Improving the energy conversion efficiency using alternative technologies and renewable energy resources plays a key role for sustainability. The cost of the materials of the components used in the aerial vehicles and the fuel cost must also be decreased to increase the usage of these vehicles instead of other ways of transportation. Hence, aviation should be handled in detail with respect to new technologies and resources considering energy, environmental, economic, and sustainability effects.

This edited book entitled "Sustainable Aviation – Energy and Environmental Issues" focuses on alternative and sustainable energy solutions, modelling, planning and optimization in aviation, and aerodynamic features. This book contains 31 uniquely selected papers out of the conference papers presented in the International Symposium on Sustainable Aviation (ISSA-2015), which was held in Istanbul, Turkey on 31 May–3 June 2015. ISSA-2015 was an international, multidisciplinary symposium, aimed to address current issues in the field of aviation such as improving aircraft fuel efficiency, fostering use of biofuels, minimizing environmental impact, mitigating GHG emissions and reducing of engine and airframe noise.

This book provides different engineering solutions and methodologies for sustainable aviation. Policies of the environmental considerations in the aviation industry and ways for the solutions found to decrease environmental impacts are discussed. This book also focuses on modeling applications, biofuels for aerial vehicles, avionics and control systems, eco-design approaches, and several design, management, and planning aspects in the aviation industry. All of them are required tools to provide better energy efficiency and, of course, to decrease the negative impacts of environmental problems. Applications of alternative technologies such as fuel cells and renewable energy resources in aviation industry can also be found in this book.

We hope that this edited book will provide a unique source of sustainable aviation with a prime focus on energy and environmental issues. We sincerely appreciate the contribution of the authors and the assistance provided by the conference organizing committee members in the preparation of this book.

Turkey   T. Hikmet Karakoc
                                                                                   M. Baris Ozerdem
                                                                                    M. Ziya Sogut
                                                                                  Can Ozgur Colpan
                                                                                    Onder Altuntas
                                                                                   Emin Açıkkalp

Contents

Part I
Alternative and Sustainable Energy

Chapter 1
Power Flow Application on an Air Vehicle Electrical Power System

Gurkan Soykan and Eren Baharozu

Abstract Recently, aircraft power systems have started to change enabling more electric aircraft (MEA) concept which aims to replace pneumatic, hydraulic systems with electrical ones as much as possible. Based on this approach, required power generation and distribution amount inside a platform increase, where MW level power generation capacities are seen in current commercial aircraft. As a result of this amount of power, there are some key issues for MEA related with power such as quality, sustainability, and power flow. This paper focused on establishing an analyzing environment for studying these parameters. By using load flow analysis based on Newton–Raphson method, voltage magnitudes and angles at each bus, losses and the power flows at each branch were calculated under a given different sample load conditions on a generic commercial air vehicle. Matlab environment was used to analyze the system in this study. Some of the simulation results have been presented and obtained electrical power system values were evaluated.

1.1 Introduction

More electric aircraft concept has attracted more attention since the last two decades as a new trend in aviation industry. The main reasons of its popularity can be expressed as its performance, efficiency, and reliability (Emadi et al. 2000; Naayagi 2013). Although MEA has crucial advantages than traditional aircrafts, the sustainability and the efficiency of the system should be studied carefully (Purelku et al. 2011). To ensure the sustainability, system should be free from main faults such as overloaded lines and voltage values which exceed upper or lower limits. Line power flow capacities and bus voltages should be chosen reasonably to prevent these faults and provide sustainability. Also these reasonable parameters affect the general efficiency of the system positively. In order to analyze these, power flow method has been used for decades for general electrical power systems.

G. Soykan (✉) · E. Baharozu
Bahçeşehir Üniversitesi, Istanbul, Turkey
e-mail: gurkan.soykan@eng.bahcesehir.edu.tr

Power flow analysis also known as load flow analysis should be performed in the design phase of a system or during upgrade of a system such as changing consumers via modernizations. Also, different load conditions of the system should be tested in order to evaluate its effect to system (Dhar 1982). To obtain solution related with power flow analysis, iterative methods must be used owing to nonlinear equations of power flow studies (Saadat 2006; Acha et al. 2004). In the electrical power field, one of the most currently used methods is the Newton–Raphson method.

The origin of the solutions based on Newton–Rapshon method goes back to 1967 (Tinney et al. 1967). Since then it has become one of the most famous methods due to its reliability and its rapid convergence speed. That is why Newton–Rapshon method was also used in this study. Based on Newton–Raphson technique, results of two different loading conditions on a simplified power system of MEA are demonstrated in this study.

1.2 MEA Power System

A typical MEA power system consists of AC and DC subsystems. The DC subsystem is used mainly for both connecting the AC system and providing the necessary power to DC type loads. For simplicity, the DC subsystem is shown as AC load in this study. Figure 1.1 indicates a simplified portion of a generic commercial air vehicle electrical power system that is generated to study the effectiveness of the proposed method. There are two generators supplying power to the system without synchronization. Only during a generator fault, functioning generator takes the loads of other generator. Tables 1.1 and 1.2 indicates the electrical parameters of upper branch and during the simulation only this branch is considered in order to just show the applicability of the proposed method.

Fig. 1.1 A typical AC power system architecture for aircraft
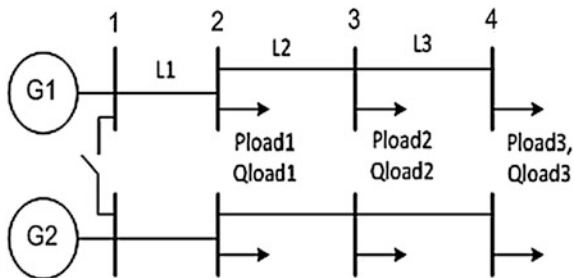
Table 1.1 Parameters of cables for the given power system of aircraft

Line no.	L1	L2	L3
Resistance, R (pu)	0.0025	0.007	0.014
Reactance, X (pu)	0.031	0.064	0.068

Table 1.2 Parameters of buses for the given power system of aircraft

Bus no.	Active power (pu)	Reactive power (pu)	Voltage mag. (pu)	Voltage angle (rad.)
1	–	–	1.0	0.0
2	0.24	0.18	–	–
3	1.17	0.56	–	–
4	0.38	0.24	–	–

Table 1.3 Base values of parameters for the given power system of aircraft

	Power (S)	Voltage (V)	Impedance (Z)
Base value	100 kVA	200 V	0.4 Ω

Differently from the conventional circuit analysis, oneline diagram and per-unit system are used in a load flow analysis (Dharamjit et al. 2012). Thus, the parameters such as power, voltage, reactance, and resistance values are converted into per-unit form using base values. Their base values are given in Table 1.3.

1.3 Bus Types

In a power system, a bus is a node at which is connection of lines, loads, and generators. Each bus has four main quantities: active power, reactive power, voltage magnitude, and phage angle of voltage. In load flow analysis, two of these four quantities are known and remaining two are obtained at the end of the analysis. Buses are categorized into three groups which are PQ bus (load bus), PV bus (Voltage controlled bus), and Slack bus (Swing bus). Their known and unknown quantities are indicated in Table 1.4.

- PQ Bus: There is not any connected generator in this bus. Thus, generated active power (P_g) and generated reactive power (Q_g) are zero for this type of buses. It only has active power (P_d) and reactive power (Q_d) which drawn from bus thanks to loads. Because of the fact that known terms are P and Q, such buses are called PQ bus.
- PV Bus: In such type buses, there is a generator connected to the bus. Thus, active power generation and the voltage magnitude of the bus are controlled in this type of buses. Q_g cannot be controlled or specified because it depends on the system configuration. Hence, known terms are P and $|V|$ in such buses, they are called PV bus.
- Slack Bus: Slack buses are used in order to provide required losses into the power system. The voltage angle of this bus is usually chosen as 0. The reason of this is to set the reference against to all other phase angles which are calculated. The voltage magnitude of this bus is also known. Generally it is taken as 1.0 pu in the load flow studies.

Table 1.4 Known and unknown information of four quantities for different bus types

Bus type	Active power (P)	Reactive power (Q)	Voltage mag. (|V|)	Voltage angle (δ)
PQ	Known	Known	–	–
PV	Known	–	Known	–
Slack	–	–	Known	Known

1.4 Newton–Raphson Load Flow Technique

Newton–Raphson load flow technique is used to solve the power flow equations. Active and reactive power equations for ith bus can be written by using general power flow equations given by Eqs. 1.1 and 1.2.

$$P_i = \sum_{j=1}^{n} |V_i||V_j||Y_{ij}|\cos(\delta_i - \delta_j - \theta_{ij}) \tag{1.1}$$

$$Q_i = \sum_{j=1}^{n} |V_i||V_j||Y_{ij}|\sin(\delta_i - \delta_j - \theta_{ij}) \tag{1.2}$$

Using Taylor series, first-order approximations in the matrix form can be obtained which is given by Eq. 1.3.

$$\begin{pmatrix} \Delta \mathbf{P} \\ \Delta \mathbf{Q} \end{pmatrix} = \mathbf{J}(\mathbf{x}) \begin{pmatrix} \Delta \boldsymbol{\delta} \\ \Delta \mathbf{V} \end{pmatrix} \tag{1.3}$$

Here $J(x)$ is the Jacobian matrix and formulated as follow Eq. 1.4.

$$\mathbf{J}(\mathbf{x}) = \begin{bmatrix} \frac{\partial f_1(x)}{\partial x_1} & \frac{\partial f_1(x)}{\partial x_2} & \cdots & \frac{\partial f_1(x)}{\partial x_n} \\ \frac{\partial f_2(x)}{\partial x_1} & \frac{\partial f_2(x)}{\partial x_2} & \cdots & \frac{\partial f_2(x)}{\partial x_n} \\ \vdots & \vdots & \ddots & \vdots \\ \frac{\partial f_n(x)}{\partial x_1} & \frac{\partial f_n(x)}{\partial x_2} & \cdots & \frac{\partial f_n(x)}{\partial x_n} \end{bmatrix} \tag{1.4}$$

where;

$$\mathbf{f}(\mathbf{x}) = \begin{bmatrix} P_2(x) \\ \vdots \\ P_n(x) \\ Q_2(x) \\ \vdots \\ Q_n(x) \end{bmatrix}; \quad \mathbf{x} = \begin{bmatrix} \delta_2 \\ \vdots \\ \delta_n \\ |V_2| \\ \vdots \\ |V_n| \end{bmatrix}$$

Also, the terms $\Delta P_i^{(k)}$ and $\Delta Q_i^{(k)}$ for Eq. 1.3 are the differences between the scheduled and calculated power values. Their formulas are given as Eqs. 1.5 and 1.6.

$$\Delta P_i^{(k)} = \mathrm{P}^{\mathrm{sch}} - P_i^{(k)} \tag{1.5}$$

$$\Delta Q_i^{(k)} = \mathrm{Q}^{\mathrm{sch}} - Q_i^{(k)} \tag{1.6}$$

In Newton–Raphson method, terms in the Jacobian matrix and the terms of ΔP and ΔQ must be recalculated at each iteration, and then $\Delta \delta$ and ΔV values must be resolved at each iteration. After finding $\Delta \delta$ and ΔV values, solved Δ value is added to old value of unknown terms to find new unknown terms which are the terms in the x-vector until the difference between unknown values of last two iterations is less than specific tolerance. Also, in the first iteration, the initial values for unknown variables are needed to start the solution. One of them is that unknown δ values must be equal to zero. Other one is that unknown $|V|$ values must be equal to 1. After all these calculations, voltage magnitude, and angle for each bus are found. Then active and reactive power values are calculated for each bus by using voltage magnitudes and phase angle.

1.5 Results and Discussion

The power flow analysis, for the given system in Fig. 1.1, was simulated on Matlab environment by considering full- and half-load conditions and results are given in Tables 1.5 and 1.6. These results can be used for performance enhancement of the system by comparing with available standards such as bus voltage limits, reactive power loading of the system. Depending on loading condition, the power loss on the line is different. When the load is decreased, the power loss also goes down.

Results of power flow analysis obtained in this study are very useful in terms of many aspects. Especially in design phase of air vehicle defining the related parameters such as bus voltages, active and reactive loading of buses and line loadings via power flow analysis will help to find optimum design parameters of subsystem components such as proper sizing of protection equipment, wire sizing,

Table 1.5 The results on full-load system

Bus no.	P_g (pu)	Q_g (pu)	P_d (pu)	Q_d (pu)	$|V|$ (pu)	θ (rad.)
1	1.83	1.43	–	–	1.0	0.0
2	–	–	0.24	0.18	0.95	−0.056
3	–	–	1.17	0.56	0.87	−0.17
4	–	–	0.38	0.24	0.85	−0.20

Table 1.6 The results on half-load system

Bus no.	P_g (pu)	Q_g (pu)	P_d (pu)	Q_d (pu)	$|V|$ (pu)	θ (rad.)
1	0.90	0.58	–	–	1.0	0.0
2	–	–	0.12	0.09	0.98	−0.027
3	–	–	0.58	0.28	0.94	−0.078
4	–	–	0.19	0.12	0.93	−0.091

and to define available further loading limits at each buses, which are all going to provide feedback for air vehicle power generation and distribution system design.

A fast algorithm with enough solution time cycle can provide online monitoring and maybe useful for active load management of system by sensing the line and bus capacities and switching the loads in order to enable more efficient operation. In addition to those, this study provides a base for stability analysis of the system.

1.6   Conclusions

In summary, the proposed power flow method on electrical power systems of air vehicles is able to provide results that can be useful for designing and verification of systems especially in terms of performance and their sustainability. This will also allow to study such as different loading condition, disturbance effects, stability of the system, and protection effects on the system parameters. The proposed solution also provides feedback for air vehicle power generation and distribution system design parameters. In this context, it seems that it is a useful scheme to guide system design.

References

Acha E, Claudio R, Hugo A, Cesar A (2004) Facts modelling and simulation in power network. Wiley, Southern Gate, Chichester, West Sussex, England

Dhar RN (1982) Computer aided power system operation and analysis. Tata McGraw-Hill Publishing Company Limited, New York

Dharamjit Tanti DK (2012) Load flow analysis on IEEE 30 bus system. Int J Sci Res Publ 2(11)

Emadi A, Ehsani M (2000) Aircraft power systems: technology, state of the art, and future trends. IEEE Aerosp Electron Syst Mag 15:28–32

Naayagi RT (2013) A review of more electric aircraft technology. International conference on energy efficient technologies for sustainability

Purellku I, Lücken A, Brombach J, Nya B, Schulz D (2011) Optimization of the energy-supply-structure of modern aircraft by using conventional power system technologies. International conference on electricity distribution, Frankfurt, Germany, 6–9 June 2011

Saadat H (2006) Power system analysis. McGraw-Hill, New York

Tinney WF, Hart CE (1967) Power flow solution by Newton's method. IEEE Trans Power Apparatus Syst 86(11)

Chapter 2
Investigation of Renewable Energy Sources for Airports

Süheyla Yerel Kandemir and Mustafa Özgür Yaylı

Abstract Renewable energy sources such as wind energy, solar energy, geothermal energy, and biomass energy are significant energy sources in the world. Some airports, using these sources will be less dependent on fossil fuels and less influenced in environmental pollution. In this study, important renewable energy sources including wind energy, solar energy, geothermal energy, and biomass energy were examined. After that renewable energy sources were investigated for the airport area. Finally, this study showed that the benefits of renewable energy sources for the airports.

2.1 Introduction

The global aviation community is continuously studying and increasingly adopting sustainable practices into their airport management plans (Giustozzi et al. 2012). Sustainability in global aviation has been enforced over last decades through various practices such as engine emissions reduction, low noise departing, recycling practices, waste management, and renewable energy sources utilization.

Energy consumption is one of the important problems for the world (Oktay 2009). The airport buildings present significant importance from the energy use point of view. This is due to the architectural and structural particularities (huge glass window and high ceilings) and also the kind of usage (continuous movement of large groups of people) (Koroneos et al. 2010).

While the world population today is four times more than that of the twentieth century, the primary energy consumption has grown about 10 times, up to 10,345

S. Yerel Kandemir (✉) · M.Ö. Yaylı
Faculty of Engineering, Department of Civil Engineering,
Bilecik Şeyh Edebali University, Gülümbe, Bilecik, Turkey
e-mail: suheyla.yerel@bilecik.edu.tr

M.Ö. Yaylı
e-mail: mozgur.yayli@bilecik.edu.tr

mtoe in 2002. At that time, the amount of energy was mainly achieved from fossil fuels (Ozgur 2008; Yerel and Ersen 2013).

Fossil fuel (i.e., coal, oil, and natural gas), led economic growth, through its releases carbon dioxide (CO_2) into the atmosphere, is considered to be the main driver behind global warming and climate change (IPCC 2007; Stern 2006). Increased concern over issues related to energy security and global warming suggests that in the future there will be a greater reliance on renewable energy sources (Salim and Rafiq 2012).

Renewable energy sources are clean technologies, as they generate very little waste and have a minimal environmental impact. Not only do they reduce the portfolio's CO_2 emissions, but also contribute to reducing other pollutant gas emissions, such as particulate matter, sulfur, nitrogen oxides, and volatile organic compounds (VOCs) (Johansson 2013; deLlano-Paz et al. 2015).

In this study, some of the renewable energy sources including wind energy, solar energy, geothermal energy, and biomass energy are examined for airports.

2.2 Energy Needs for Airport

One of the most important factors that take an active role in achieving such development level is energy. Energy, which is the requirement of sustainable development, can only be an impulsive force in industrialization and overall development of societies if it is supplied on time, with sufficient quantity and under reliable economic conditions, and considering the environmental impacts (Yilmaz 2008; Yerel 2014).

The extent to which different energy sources are available in a particular state or region conditions the way in which it produces electricity. All territories strive to access to energy resources safely, permanently, and at a reasonable cost, and to increase their energy efficiency, which also means less pollution (Omer 2008; Dincer 2000; Valentine 2011; deLlano-Paz et al. 2015).

The building sector is one of the world's largest energy consumers. It has been estimated that buildings consume 40 % of the world's energy and generate 33 % of the carbon dioxide emissions (Prez-Lombard et al. 2008).

Heating, ventilation, and air conditioning (HVAC) systems are one of the major building energy consumers, which account for almost one-half of the total building energy use (Huang et al. 2015).

Airports are high energy- and power-intensive investments both during their construction and operation (Kilkis 2014). And the energy needs of the airport in the areas of lighting, heating, and cooling (Koroneos et al. 2010).

Renewable energy source is one of the important clean, safe, and low-cost energy sources in the world. Wind energy, solar energy, geothermal energy, and

biomass energy are significant renewable energy sources. The energy sources have been used over last decades in the airports.

2.3 Renewable Energy Sources

Energy is an indispensable need in our everyday life. Man started to use energy in its primitive and basic forms (like burning straws, firewood, etc.) hundreds of years ago and he still uses energy nowadays in its modern and sophisticated forms (Khalfan and Imrek 2015).

Energy resources will play an important role in the world's future. Energy is a significant factor for economic development and social prosperity of countries. The World Energy Forum has predicted that fossil-based oil, coal, and gas reserves will be exhausted in less than another 10 decades. Fossil fuels account for over 79 % of the primary energy consumed in the world, and 57.7 % of that amount is used in the transport sector and are diminishing rapidly (Kumar et al. 2010). But with increasing air pollution, global warming concerns, diminishing fossil fuels, and their increasing cost have made it necessary to look towards renewable sources as a future energy solution (Chicco and Mancarella 2009; Grigoras and Scarlatache 2015).

There are many alternative new and renewable energy sources which can be used instead of fossil and conventional fuels. The energy resources have been split into three categories: fossil fuels, renewable resources, and nuclear resources (Demirbas 2000; Koua et al. 2015).

An efficient utilization of renewable resources has a significant potential in both stimulating the economy and reducing pollution. It could boost the economy with direct business benefits, increasing the overall capacity of regional players in enhancing science and technology based development. Despite the immense benefits from utilization of RES, their use is not exploited to the full potential due to technical, economic, and social constraints (Patlitzianas and Karagounis 2011; Colesca and Ciocoiu 2013). The renewable energy sources such as wind energy, solar energy, geothermal energy, and biomass energy can be used to overcome energy requirement in the airports.

2.3.1 Wind Energy

Wind is one of the fastest growing energy sources, and is regarded as an important alternative to traditional power-generating sources (Dursun and Alboyaci 2011). Wind energy is known as a renewable and environmental friendly energy source. The technology converting wind energy to other energy types is more economical compared to other conversions. It does not have transportation problem and does not require a high technology to utilize (Ilkilic and Nursoy 2010).

2.3.2 Solar Energy

Solar energy is the portion of the sun's energy available at the earth's surface for useful applications, such as exciting electrons in a photovoltaic cell and supplying energy to natural processes like photosynthesis. Solar energy consists of two parts: extraterrestrial solar, energy which is above the atmosphere, and global solar energy, which is under the atmosphere. This energy is free, clean, and abundant in most places throughout the year and is important especially at the time of high fossil fuel costs and degradation of the atmosphere by the use of these fossil fuels (Khatib et al. 2012).

2.3.3 Geothermal Energy

Geothermal is the energy generated from heat stored in the earth, or the collection of absorbed heat derived from underground. Immense amounts of thermal energy are generated and stored in the Earth's core, mantle, and crust (Kumar et al. 2010). Geothermal energy, a relatively benign energy source when compared with other energy sources due to reduction in greenhouse gas emissions, is used for electricity generation and direct utilization (Komurcu and Akpinar 2009).

2.3.4 Biomass Energy

Biomass is basically a stored source of solar energy initially collected by plants during the process of photosynthesis, whereby carbon dioxide is captured and converted to plant materials mainly in the form of cellulose, hemicelluloses, and lignin. Biomass includes crop residues, forest, and wood process residues; animal wastes including human sewage, municipal solid waste food processing wastes, purpose grown energy crops, and short rotation forests (Bilgili and Ozturk 2015).

2.4 Renewable Energy Sources in the Airports

Renewable energy sources like wind energy, solar energy, geothermal energy, and biomass energy is used in the airports.

The Makedonia airport of Thessaloniki, Greece could easily utilize the renewable energy sources that are available in the area. The renewable energy sources include solar energy, geothermal energy and biomass (Korones et al. 2010).

Nedaei (2012) is assessed 2 years study of wind data in Abadan Airport. The dataset has showed that this site is suitable for installation and development of large and commercial wind turbines.

Amsterdam Airport Schiphol with its 48 million passenger movements per year was taken as a challenging case. The Schiphol Group has the ambition to develop its properties and business park areas in a sustainable and socially responsible way. The results show that it is possible to create a multifunctional, sustainable and comfortable urban area in which the electric mobility is very well integrated. It can be stated that the sustainable urban development is becoming more feasible by the clever combination of renewable energy, electricity grid design, inductive Park and Charge and customized electric vehicle services (Silvester et al. 2013).

2.5 Conclusions

Renewable energy is one of the important energy sources in the world. An accurate investigation of energy consumption is a significant factor in the determination of energy issue. In this study, renewable energy sources like wind energy, solar energy, geothermal energy, and biomass energy were reviewed. The study presented that beneficial of renewable energy sources for the airports.

References

Bilgili F, Ozturk I (2015) Biomass energy and economic growth nexus in G7 countries: evidence from dynamic panel data. Renew Sustain Energy Rev 49:132–138

Chicco G, Mancarella P (2009) Distributed multi-generation: a comprehensive view. Renew Sustain Energy Rev 13:535–551

Colesca SE, Ciocoiu CN (2013) An overview of the Romanian renewable energy sector. Renew Sustain Energy Rev 24:149–158

deLlano-Paz F, Calvo-Silvosa A, Antelo SI, Soares I (2015) The European low-carbon mix for 2030: the role of renewable energy sources in an environmentally and socially efficient approach. Renew Sustain Energy Rev 48:49–61

Demirbas A (2000) Recent advances in biomass conversion technologies. Energy Educ Sci Technol 6:19–40

Dincer I (2000) Renewable energy and sustainable development: a crucial review. Renew Sustain Energy Rev 4(2):157–175

Dursun B, Alboyaci B (2011) An evaluation of wind energy characteristics for four different locations in Balikesir. Energy Sources, Part A: Recovery, Utilization, Environ Eff 33:1086–1103

Giustozzi F, Toraldo E, Crispino M (2012) Recycled airport pavements for achieving environmental sustainability: an Italian case study. Res Conser Recycl 68:67–75

Grigoras G, Scarlatache F (2015) An assessment of the renewable energy potential using a clustering based data mining method, Case study in Romania. Energy 81:416–429

Huang H, Chen L, Hu E (2015) A new model predictive control scheme for energy and cost savings in commercial buildings: an airport terminal building case study. Build Environ 89:203–216

Ilkilic C, Nursoy M (2010) The potential of wind energy as an alternative source in Turkey. Energy Sources, Part A: Recovery, Utilization, Environ Eff 32:450–459

Intergovernmental Panel on Climate Change (IPCC) (2007) Climate change 2007: mitigation of climate change. In: Metz ORDB

Johansson B (2013) Security aspects of future renewable energy systems: a short overview. Energy 61:598–605

Khalfan OM, Imrek H (2015) Energy generation from weights of moving vehicles: a case study at Alaeddin Keykubad Campus-Konya/Turkey. Energy 87:212–222

Khatib T, Mohamed A, Sopian K (2012) A review of solar energy modeling techniques. Renew Sustain Energy Rev 16:2864–2869

Kilkis B (2014) Energy consumption and CO_2 emission responsibilities of terminal buildings: a case study for the future Istanbul International Airport. Energy Build 76:109–118

Komurcu MI, Akpınar A (2009) Importance of geothermal energy and its environmental effects in Turkey. Renew Energy 34:1611–1615

Koroneos C, Xydis G, Polyzakis A (2010) The optimal use of renewable energy sources—The case of the new international "Makedonia" airport of Thessaloniki, Greece. Renew Sustain Energ Rev 14:1622–1628

Koua BK, Koffi PME, Gbaha P, Touré S (2015) Present status and overview of potential of renewable energy in Cote d'Ivoire. Renew Sustain Energy Rev 41:907–914

Kumar A, Kumar K, Kaushik N, Sharma S, Mishra S (2010) Renewable energy in India: current status and future potentials. Renew Sustain Energy Rev 14:2434–2442

Nedaei M (2012) Wind resource assessment in Abadan airport in Iran. Int J Renew Energy Dev 1 (3):87–97

Oktay Z (2009) Investigation of coal-fired power plants in Turkey and a case study: can plant. Appl Therm Eng 29:550–557

Omer AM (2008) Energy, environment and sustainable development. Renew Sustain Energy Rev 12(9):2265–2300

Ozgur MA (2008) Review of Turkey's renewable energy potential. Renew Energy 33:2345–2356

Patlitzianas K, Karagounis K (2011) The progress of RES environment in the most recent member states of the EU. Renewable Energy 36(2):429–436

Prez-Lombard L, Ortiz J, Pout C (2008) A review on buildings energy consumption information. Energy Build 40(3):394–398

Salim RA, Rafiq S (2012) Why do some emerging economies proactively accelerate the adoption of renewable energy? Energy Econ 34:1051–1057

Silvester S, Beella SK, Timmeren AV, Bauer P, Quist J, Dijk SV (2013) Exploring design scenarios for large-scale implementation of electric vehicles; the Amsterdam Airport Schiphol case. J Cleaner Prod 48:211–219

Stern N (2006) Stern review on the economics of climate change. Stern Review on the Economics of Climate Change, UK Treasury

Valentine SV (2011) Emerging symbiosis: renewable energy and energy security. Renew Sustain Energy Rev 15(9):4572–4578

Yerel S (2014) An investigation of cutoff calorific grade in a coal deposit: a case study. Energy Sources, Part A: Recovery, Utilization, Environ Eff 36:1383–1387

Yerel S, Ersen T (2013) Prediction of the Calorific value of coal deposit using linear regression analysis. Energy Sources, Part A: Recovery, Utilization, Environ Eff 35:976–980

Yilmaz AO (2008) Renewable energy and coal use in Turkey. Renew Energy 33:950–959

Chapter 3
Investigation of the Effect of Canola Methyl Ester on Cyclic Variation Using Wavelet Analysis Method

Şükran Efe and M.A. Ceviz

Abstract Diesel engines are the most commonly used internal combustion engine in transportation, power generation, and other industries. Combustion in the diesel engines takes place at high temperatures due to the high compression ratio, and therefore high energy is obtained when diesel fuel is used. But the most commonly used alternative fuel diesel engines is biodiesel today. The market share of biodiesel is on the rise because of the increasing damage of diesel and decreasing oil reserves to the environment. In this study, cyclic variation that occurred when canola biodiesel (canola methyl ester) that is produced by transesterification method was used as diesel fuel was investigated. Three different biodiesel ratios, B20, B50, and B100 were used in the study. In interpretation cyclic variations wavelet analysis method is used and all results are compared with diesel fuel. It is concluded that the use of biodiesel in diesel engines has positive effect on cyclic variation and this effect increases with the increasing ratio of biodiesel in the mixture.

3.1 Introduction

Use of fossil fuel due to the high energy potential is clearly bigger, when today's energy sources are examined. And the use of fossil fuels increases day by day due to the growing energy demands. This increase causes both reducing reserves and increasing harmful effects on the environment of the fossil fuel.

Diesel engines are the most commonly used internal combustion engine (ICE) in transportation, power generation, and other industries. Combustion in the diesel

Ş. Efe (✉)
Mechanical Engineering Department, Engineering Faculty,
Bayburt University, Bayburt, Turkey
e-mail: sefe@bayburt.edu.tr

M.A. Ceviz
Mechanical Engineering Department, Engineering Faculty,
Ataturk University, Erzurum, Turkey
e-mail: aceviz@atauni.edu.tr

engines takes place at high temperatures due to the high compression ratio, and therefore high energy is obtained when diesel fuel is used. Diesel engines have greater harm to the environment despite of high power generating capacity. NO_X emission occurs due to high combustion heat has the most important impact on the environment. NO_X emission reacts with hydrocarbons under ultraviolet sunlight and produce photochemical smog. The smog damages the ozone layer and the respiratory system of human and animals. NO_X emissions are known as the main source of acid rain (Lin and Lin 2007, 2008).

In order to reduce the harmful effect of diesel engines on the environment, it has become inevitable to use the alternative fuel in diesel engines. Geopolitical situation of the fossil fuel is one of the other important reasons for the alternative fuel research.

The first study related to the alternative fuels was carried out by Dr. Rudolf Diesel who is the inventor of the diesel engine. Dr. Diesel showed that diesel engine can run with 100 % nut oil at the World Exhibition in 1900. Although importance of Dr. Diesel's study was not fully understood in those years; his study is a leading milestone in alternative energy sector. Researchers who were inspired by the alternative fuel research of Dr. Diesel started their studies on vegetable oils. They determined that use of vegetable oil in diesel engines for long duration was not suitable due to the high viscosity of oils. However, we can see some studies that carried out on vegetable oils, particularly in emergency situations in the past years. For example, in China vegetable oils were used with pyrolysis process in World War I (Chang and Wan 1947), in Brazil cottonseed oil was used instead of diesel fuel, and in Japan soybean oil was used as replacement fuel in a warship in the World War II (Knothe 2009).

High viscosity of vegetable oils has been reduced by approximately ten times and was brought to close to the diesel fuel as a result of the studies on alternative fuels. The new low-viscosity alternative fuel that is known as biodiesel today was obtained by virtue of these efforts.

Rajasekar et al. (2010) stated that "*The American Society for Testing and Materials (ASTM) defines biodiesel fuel as mono alkyl esters of long-chain fatty acids derived from renewable lipid feed stocks, such as vegetable oils or animal fats, for use in diesel engines*".

Although the properties of biodiesel, like renewability and environmentally friendliness make it superior than diesel fuel, higher NO_X emissions and the difficulty of starting at low temperatures are the disadvantages of it. Therefore, many studies have been carried out to eliminate these negative features. Use and production of biodiesel is continuously increasing today all over the world. Global biodiesel potential is shown in Table 3.1 (Atabani et al. 2012).

Engine power is associated with the maximum pressure in the cylinder of an ICE. When the pressure values examined, it was seen that pressure vary from cycle-to-cycle or from cylinder-to-cylinder. This event is defined as cyclic variation that occurs both in diesel and gasoline engines which causes to reduce the engine output power, unstable operation, vibration, and noise. Therefore, the cyclic variation is not desired by the engine designers (Ceviz et al. 2012). There are three

Table 3.1 Global biodiesel potential (Atabani et al. 2012)

Rank	Country	Biodiesel potential (ML)	Production ($/L)
1	Malaysia	14.540	0.53
2	Indonesia	7.595	0.49
3	Argentina	5.255	0.62
4	USA	3.212	0.70
5	Brazil	2.567	0.62
6	Netherlands	2.496	0.75
7	Germany	2.024	0.79
8	Philippines	1234	0.53
9	Belgium	1213	0.78
10	Spain	1.073	1.71

reasons for cyclic variation which are: (1) the change in the movement of the mixture in the cylinder during ignition time, (2) the change in the quantity of the air-fuel mixture during the intake of each cylinder, and (3) the differences between the exhaust gas and charge mixtures inside each cylinder, especially during the ignition advance (Heywood 1988).

3.2 Wavelet Analysis Method

It is difficult to analyze a situation by examining a time series because of many periodic components. Therefore, the data must be moved to the frequency domain from the time domain. Frequency domain provides information about the signal and about the physical forces behind it. There are many mathematical methods that translate a signal from the time domain to the frequency domain such as Wigner distribution, Fourier transform, Hilbert transform, and radon Transform. Among them, Fourier transform is the most known and the most commonly used one (Oppenheim et al. 1997; Proakis and Manolakis 2010).

Fourier Transform converts the signal from the time domain to the frequency domain because it calculates the different frequency of a signal. However, when the signal is converted to the frequency domain many characteristics information in the time domain is lost. In other words, the moment of a special event cannot be detected. This disadvantage might be ignored if the time domain characteristics of a signal do not change over time. But, most of the signals may have important critical irregularities that can be the central focus of the analysis. Wavelet analysis method (WAM) is used due to this drawback of the Fourier transform. WAM determines the time of sudden changes such as broken time, edge detection, space, etc., in the signal (Valens 1999).

The basis of WAM was introduced in 1805 by Joseph Baptiste Fourier. Alfred Haar used the word Wavelet in his doctoral thesis in 1909. Details of the bases of this

theory were first put forward by a study group of Marseille Theoretical Physics Centre under the guidance of Alex Grossmann and Jean Morlet in 1985 (Abbak 2007).

The most important property of the WAM is that it can analyze the signal locally. In other words, it can analyze large variations in the signal that occurs in a short-time interval. For example, a discontinuity occurring in a signal can be lost in the Fourier transform, but the exact location of this discontinuity can be detected with the WAM.

What makes the WAM different from the Fourier method is that the WAM carries a signal from time-frequency domain to time-scale domain. The domain is defined by the window of observation but not by the signal lines. Signals with low frequency are analyzed in longer time intervals while shorter time intervals are sufficient for signals with higher frequency (Graps 2006).

Wavelet functions that are the basis of WAM are used to determine orthogonal or non-orthogonal functions, mostly orthogonal ones (Torrence and Compo 1998). A wavelet function $(\psi(t))$should have zero mean and finite energy at Eq. 3.1 (Sen et al. 2008).

$$\left(\int_{-\infty}^{+\infty} \psi(t)\mathrm{d}t = 0 \right), \left(\int_{-\infty}^{+\infty} \psi^2(t)\mathrm{d}t < \infty \right) \tag{3.1}$$

The wavelet functions used in the WAM process is a waveform that is effective in a limited time. A wavelet function is obtained by changing translation parameter (τ) and the scale parameter (s) from a mother wavelet (ψ). There are 15 different kinds of mother wavelet functions. They change according to the characteristics of the sequence to be analyzed. Haar, Mexican Hat, Meyer, Gaussian, and Morlet are the most popular ones among them. Properties of each function are different from each other (Torrence and Compo 1998).

There are two wavelet analysis methods: continuous wavelet analysis method (CWAM) and discrete wavelet analysis method (DWAM) (Valens 1999).

Wavelet Power Spectrum (WPS) represents the energy contained in a signal at a certain scale in a certain time interval and it is represented by $\left[\left(\mathrm{CWAM}_{(s,\tau)} \right)^2 \right]$. WPS represents the temporal variations. Fluctuations at various scale and frequency are better represented (Ceviz et al. 2012; Sen et al. 2008).

Global Wavelet Spectrum (GWS) provides additional information about the spectral properties of a time series. GWS is obtained as the average of the WPS on a given signal (Ceviz et al. 2012; Sen et al. 2008).

Cone Effect is used to eliminate the error in the time series that is panned. The values obtained other than by cone effect can be unreliable and should be interpreted carefully (Ceviz et al. 2012; Sen et al. 2008).

3.3   Experiments

3.3.1   Biodiesel Production

In the transesterification method, canola vegetable oil, methyl alcohol (CH_3OH), and potassium hydroxide (KOH) are used as oil, alcohol, and catalyser, respectively. The outcomes are the canola methyl ester and glycerol. In the reaction, 20 % alcohol in volume and 1 % catalysis in weight are used. The batch is kept at 56 °C and duration of the reaction was 60 min (Fig. 3.1a). The resulting mixture that consists of biodiesel, glycerol, and other substances, like tri-di glycerol, catalysis, methyl alcohol is then purified (Fig. 3.1b). The final product is biodiesel and it is ready to use in a diesel engine (Fig. 3.1c).

3.3.2   Engine Test

Engine tests are performed with a four-stroke two cylinders direct injection diesel engine (SuperStar, Motosan Motor Sanayi ve Ticaret A.Ş., Istanbul/TURKEY), with 1/17 compression ratio, 1.54 dm^3 cylinder volume, and power of 28 HP. The fuels, DF (diesel fuel), B100 (100 % biodiesel), B50 (50 % biodiesel and 50 % diesel), and B20 (20 % biodiesel and 80 % diesel) are tested with this engine. A quartz pressure transducer (KISTLER 6117BDF17) is attached to the combustion chamber of one of the cylinder and the pressure signals are transferred to a computer with a cable. The crank shaft angle is measured with optical devices. The pressure and the crank shaft angle data are stored in a personal computer with the help of a data acquisition card (National Instruments, M series, 6250 model, 1.25 MS/s DAQ). The cyclic variations are analysed with WAM using the recorded
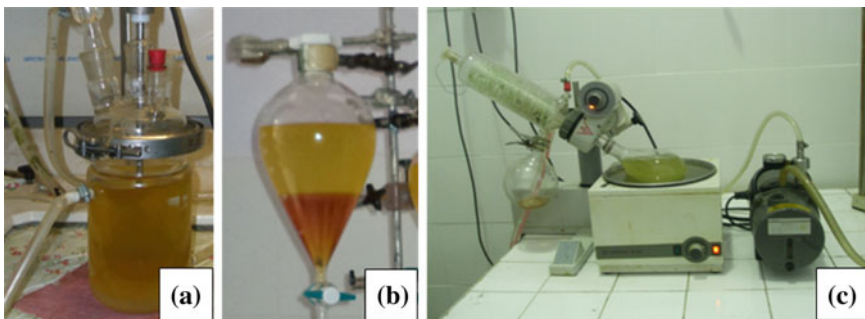

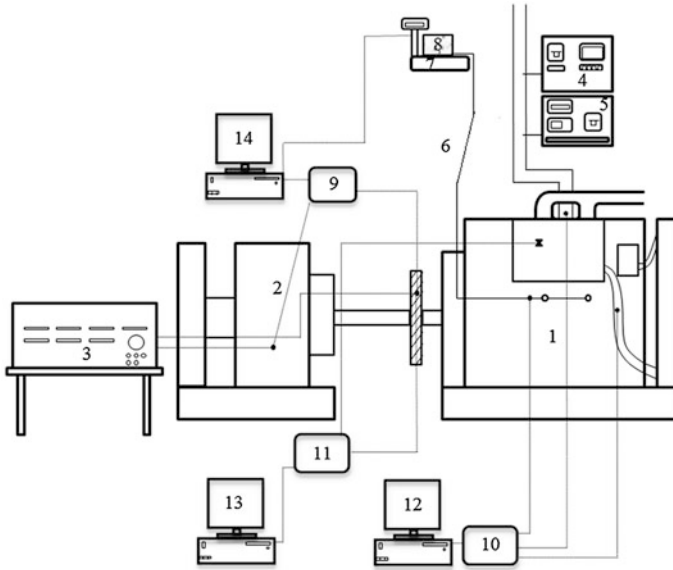**Fig. 3.1** Production of biodiesel

Fig. 3.2 Schematic of engine system. *1* Engine, *2* hydrolic brake, *3* control unit, *4* exhaust emiss. equ., *5* Soot metre equ., *6* fuel line, *7* scales, *8* fuel tank, *9* crank pos. sensor, *10* temperature sensor, *11* pressure sensor, *12–14* PC

pressure data. Pressure data was obtained at 1400 rev/min engine speed. The schematic experimental setup for engine test is shown in Fig. 3.2.

3.3.3   Wavelet Analysis Method

The pressure signals in a cylinder (Pmi) are processed with the wavelet software to analyze the cyclic variations. In WAM, the Morlet wavelet with central frequency of $\omega_0 = 6$ which provides a good compatibility between frequency and time is used.

Table 3.2 Properties of samples

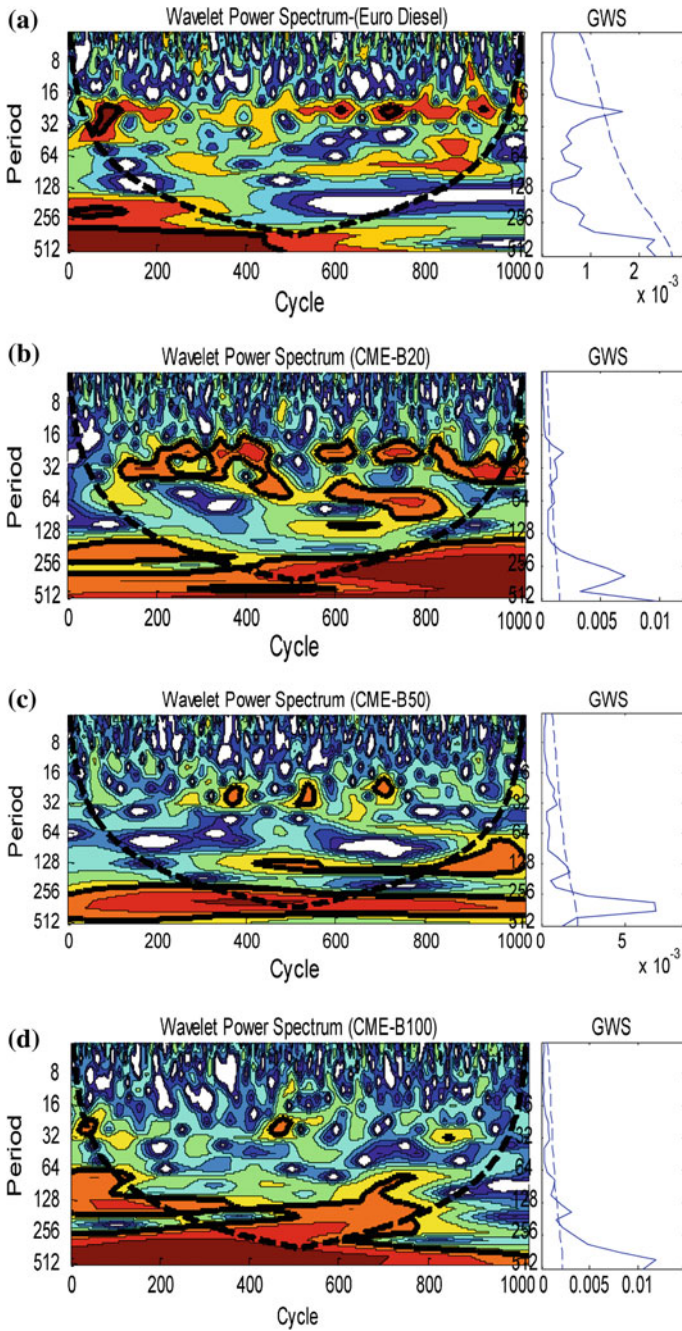| Properties	Canola oil	Canola methyl ester	Euro diesel
Heat value (kJ/kg)	39,583	39,986.5	45,951
Dyn. Visc. (40 °C) (mPa s)	28.954	3.8372	2.4257
Kin. Visc. (40 °C) (mm^2/s)	31.945	4.4339	2.9542
SFTN (°C)	11	−9	−6
Flash point (°C)	238	166	56
Density (g/cm^3)	0.9064	0.8654	0.8211
Cetane number	–	48.7	51

Fig. 3.3 Wavelet analysis of Pmi **a** euro diesel, **b** B20, **c** b50, **d** B100

3.4 Results

The physical and chemical properties of the canola oil, canola methyl esters, and Euro diesel are given in Table 3.2. The properties of the canola oil and the canola methyl esters are determined in Malaya University (Malaysia) and the properties of the Euro diesel is provided by Petrol Ofisi Company. The cetan number of the samples are determined by a formula that is developed with multilinear regression (MLR) with $R^2 = 0.9191$ (Eq. 3.2).

$$\begin{aligned} CN = {} & 56.16 + 0.07 * \text{La} + 0.1 * M + 0.15 * P - 0.05 * \text{Pt} + 0.23 * S \\ & - 0.03 * O - 0.19 * \text{Li} - 0.31 * \text{Ln} + 0.08 * \text{Ei} + 0.18 * \text{Er} - 0.1 * \text{Ot} \end{aligned} \tag{3.2}$$

The WAM results of the pressure data is shown in Fig. 3.3. It can be observed in Fig. 3.3 that there is a periodicity in 21–34 period interval for WPS and at 314 period for GWS for B20. The periodicity observed for B20 mixtures at low frequency disappears for B50 mixture and B100. However, this phenomenon is observed at higher frequencies for B50 and B100 fuels.

References

Abbak RA (2007) Jeodezide Zaman Dizilerinin Dalgacık (Wavelet) Analizi. PhD Semposium, Konya/Turkey. http://193.255.101.90/~aabbak/pubs/Phd_seminar.pdf

Atabani AE, Silitonga AS, Badruddin IA, Mahlia TMI, Masjuki HH, Mekhilef S (2012) A comprehensive review on biodiesel as an alternative energy resource and its characteristics. Renew Sustain Energy Rev 16:2070–2093

Ceviz MA, Sen AK, Küleri AK, Öner İV (2012) Engine performance, exhaust emissions, and cyclic variations in a lean-burn SI engine fueled by gasoline-hydrogen blends. Appl Thermal Eng. 36:314–324

Chang, C-C, Wan S-W (1947) China's motor fuels from tung oil. Ind Eng Chem 1543–1548

Graps A (2006) http://www.google.com.tr/url?sa=t&rct=j&q=&esrc=s&source=web&cd=1&ved=0CCAQFjAA&url=http%3A%2F%2Fwww.cis.udel.edu%2F~amer%2FCISC651%2FIEEEwavelet.pdf&ei=YmcxVY61A9PcaPPrgagG&usg=AFQjCNHyw_eZctNUgpEi5ScvTq7N3-py8A&bvm=bv.91071109,d.bGg&cad=rja

Heywood JB (1988) Internal combustion engine fundamentals. McGraw-Hill, Singapore

Knothe, G (2009, Dec) Historical perspectives on vegetable oil-based diesel fuels

Lin, CY, Lin HA (2007) Engine performance and mission characteristics of a three-phase emulsion of biodiesel produced by peroxidation. Fuel Process Technol 88:35–41

Lin CY, Lin HA (2008) Effects of NO_X-inhibitor agent on fuel properties of three-phase biodiesel emulsions. Fuel Process Technol 89:1237–1242

Oppenheim AV, Willsky AS, Nawab SH (1997) Signals and systems (vol 2). Prentice Hall

Proakis, JG, Manolakis DG (2010) Sayısal sinyal işleme ilkeler, algoritmalar ve uygulamalar. Çeviren Özgül Salor, Abdurrahman Karamancıoğlu, Nurhan Karabğa, Halis Altun, & Remzi Yıldırım. Nobel

Rajasekar E, Murugesan A, Subramanian R, Nedunchezhian N (2010) Review of NOx reduction technologies in CI engines fuelled with oxygenated biomass fuels. Renew Sustain Energy Rev 2113–2121

Sen AK, Litak G, Taccani R, Radu R (2008) Wavelet analysis of cycle-to-cycle pressure variations in an internal combustion engine. Chaos Solitons Fractals 38:886–893

Torrence C, Compo GP (1998, Jan) A practical guide to wavelet analysis. Bull Am Meteorol Soc 1

Valens C (1999) A really friendly guide to wavelets. https://www.google.com.tr/url?sa=t&rct=j&q=&esrc=s&source=web&cd=2&sqi=2&ved=0CCcQFjAB&url=https%3A%2F%2Fwww.cs.unm.edu%2F~williams%2Fc530%2Farfgtw.pdf&ei=gXIxVd-GHsS7swG9vIGYCw&usg=AFQjCNFXc0NMZhs9X2YgsxJtb8H-z2luTg&bvm=bv.91071109,d.bGg&cad=rja

Chapter 4
A Comprehensive Review: Ecodesign Approaches with the Use of Sustainable Textiles in Aviation Industry

Bukra Kalayci and Cevza Candan

Abstract Integration of sustainable textiles into aircraft design is promoted in order to increase sustainability goals of aviation industry. Textiles used for aircraft interior design not only pose threats to sustainable aims, but also create opportunities. This paper aims to draw the attention to utilize sustainable textiles for ecodesign of aircraft interiors. It also highlights the deficiency and opportunities regarding sustainable textile use for interior parts of the aircraft. The paper states that the environmental impact is created by both aviation and textile industries in a common perspective. The paper also provides examples from sustainable interior design initiatives of automotive industry. The compiled database provides general information about ecodesign approaches and integration of sustainable textiles into aircrafts. Flowingly, a brief summary of the environmental policies are referred.

4.1 Sustainability Issues in Aviation and Textile Industry

Governmental regulations and consumer awareness toward sustainable products and carbon neutral industry are increasing. Aeronautic industry which is stated as one of the most pollutant industries needs to be examined from every aspect, including textile materials, in order to achieve its ecological objectives (Moreira et al. 2014a, b). More explicitly, the entire supply chain of aviation industry needs to be considered in order to reach reduced carbon footprint target within aviation industry.

B. Kalayci (✉) · C. Candan
Istanbul Technical University, Istanbul, Turkey
e-mail: bukra.klyc@gmail.com

C. Candan
e-mail: c.candan@itu.edu.tr

27

4.1.1 Sustainability in Aviation Industry

According to the report released by A.T.A.G, aircraft transportation is responsible for 12 % of the CO_2 emissions from all transport vehicles in the world (A.T.A.G 2012). Another report released by the Intergovernmental Panel on Climate Change (IPCC 1999) clearly indicated that as a whole aviation industry accounts for nearly 2 % of global anthropogenic CO_2 emissions. Moreover, the report also leads our attention to the fact that aircraft emits gases and particles at a very close distance to or in the stratosphere where more significant and immediate impact on atmospheric environment is possible (Moreira et al. 2014a, b). As a supporting fact, the report published by the International Civil Aviation Organization (ICAO) indicates that, fossil fuel combustion in the atmospheric composition have the potential to affect our climate. The report by ICAO also explains that by the year 2030 air traffic is expected to double, which means that emissions will continuously increase (ICAO 2013).

4.1.2 Sustainability in Textile Industry

Textile industry is known for its highly hazardous manufacturing processes (Brigden et al. 2012a, b) and requires a comprehensive study of sustainability along its whole supply chain. There are social, environmental, and economic impacts at every stage of textile supply chain which need to be considered. As shown in the Fig. 4.1, Draper et al. (2007) summarized environmental impacts caused by textile supply chain.
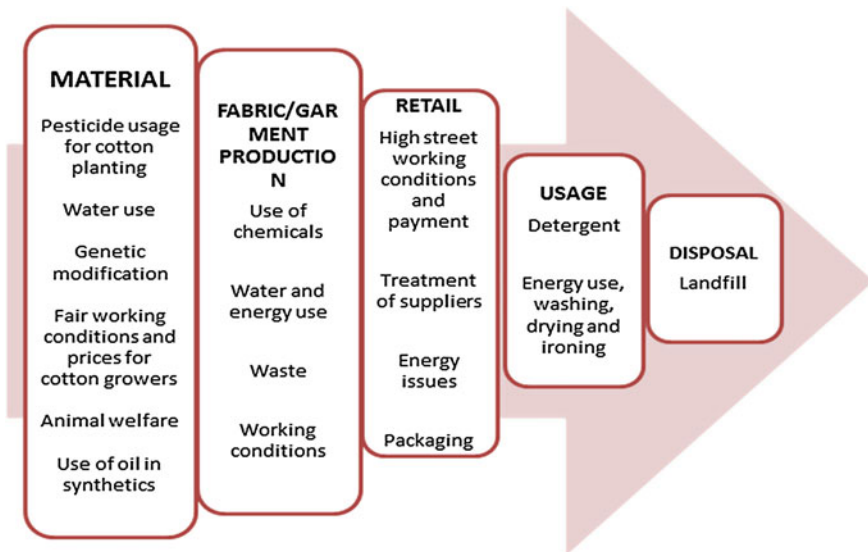

Fig. 4.1 Impact of textile supply chain (Draper et al. 2007)

As an overview, growing cotton requires high amount of water, petrochemical-based synthetic fibers, intense use of chemicals for dyeing and printing processes, logistics, and eventually use, and disposal phases cause significant environmental problems. Brigden et al. (2012a, b) indicated that the most visible impact of textile production is the discharged effluent into waterways. Moreira et al. (2014a, b) stated that combining these two highly polluting industries, textile, and aviation, together poses a serious threat to the environment. Due to the raising environmental concerns, green initiatives in the field of aeronautics are increasing. Aviation engineers and designers have been researching sustainable innovative technologies and materials in order to minimize aircrafts' negative effects (A.T.A.G 2014). Environmental impacts of aviation industry were assessed in detail by the IPCC (1999). However, at earlier times the main focus of aviation research papers was on supersonic technology and its effect, only a minor attention was given to green approaches such as future liquid hydrogen powered aircrafts. Eventually, within the last decade, studies on emission reduction and sustainability policies have gained speed (Lee et al. 2009a, b).

4.1.3 Research Gap: Design and Use of Sustainable Textiles within Aviation Industry

Ecodesign approaches in transportation sector are highly granted and widely studied (de Medina and Naveiro 2009). However, while there is much research on integration of sustainable textiles and ecodesign approaches in the automotive industry, similar studies are lacking in aviation industry. This lack of interest might be explained by the average life span of aircrafts which is much longer to compare to the cars. The average life of an aircraft is 30 years. Furnishings are replaced on a regular basis or when there is sign of wear (Anon 1999). The number of planes built in a year is considerably less than the number of cars built in a single day in the world (Laurent 1991). Moreira et al. also pointed out several reasons; as privacy issues, lack of interest in sustainable textile products, and underestimated perception of ecological textiles as being superfluous. Moreira et al.'s two research papers, (Moreira et al. 2014a, b) stand for the sole studies among visited sources that increase awareness and draw the attention to the integration of sustainably sound textiles into ecodesign activities of aviation industry.

4.1.4 Aircraft Textiles and Green Aviation Initiatives

Even though textiles only responsible for 1 % of the total aircraft's weight (excluding composites), however, from sustainable point of view, textiles play an important role since they are recyclable articles (Moreira et al. 2014a, b). As illustrated in Fig. 4.2, aircrafts include textile materials both in the structure and in

Fig. 4.2 Textiles used in commercial aircrafts (Horrocks 2013)

the interior parts. Light weight and high strength textile composites are commonly used for aircraft structure, namely in white parts. Interior textiles are used either for décor or furnishing purposes such as seating upholsteries, blankets, floor/wall/ceiling coverings and etc. Functional textiles such as tires, beltings, wiring harnesses, cargo liners and filters are some of the other textile products used in aircrafts (Horrocks 2013). Troitzsch noted that a modern aircraft includes 4000 kg of plastic materials, half of which presents within glass and carbon reinforced composites and the rest is within interior textiles (Troitzsch 2004). Horrocks listed the fiber composition and properties used in seating, curtain, floorcovering, cargo liner and wall panel textile products, with an emphasis on fire retardant (FR) wool or FR polyester (Horrocks 2013).

While sustainably sound textiles have not yet been considered as an important interior material for green aviation industry (Moreira et al. 2014a, b), due to their light weight and structural performances, a significant importance have been paid to textile composites for aircraft design. In fact, in 1989, NASA started a program which aimed to develop textile composite structures for commercial aircrafts at a competitive price to that of metallic structures (Dexter 1998). Beside textile composites, knitted, braided, and stitched textile fabrics were examined for a wing box by McDonough and Braungart (2002).

4.2 Ecodesign Approaches

Ecodesign contains a number of tools and approaches which facilitate the development of environmentally concerned sustainable products. Figure 4.3 chronologically shows several drivers, tools and legislation have been developed throughout ecodesign and sustainable development (SD) efforts (Sheldrick and Rahimifard 2013).

Sheldrick and Rahimifard (2013) noted that in order to get full benefit of SD tools and methods, they should be employed at every stage of design, rather than at
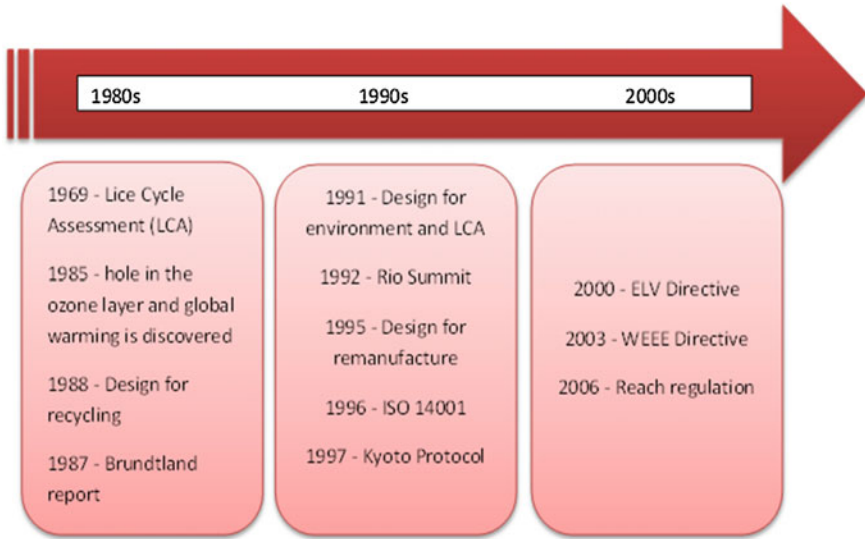
Fig. 4.3 Evolution of sustainable design by time (Sheldrick and Rahimifard 2013)

late "detail design" stage. The researchers also pointed out the drivers that force companies to implement SD activities into their policies so ecolabels, certificates, and standards can be shown as some of the drivers.

ISO/TR 4062 Standard, for example, supports companies who wish to insert environmental aspects into product design (ISO 14062). There are a number of regulatory frameworks of the European Union (EU) such as REACH, "waste electrical and electronic equipment directive", "end-of-life vehicle directive" which lead us to produce more ecologically sustainable products. Another governmental activity regarding sustainable activities is EU's "Horizon 2020" work which contains 'Clean Sky' program that aims to reduce environmental impact of aviation industry with a targeted entry into service in 2025 (EU) (de Medina and Naveiro 2009).

4.2.1 Life Cycle Assessment (LCA)

LCA is a management tool that quantifies environmental impact of a product, service or process. International Organization for Standardization (ISO) published its LCA methodology as 14000 series (ISO 14040 2006). ISO 14040:2006 describes the principles and framework for LCA including: definition of the goal and scope of the LCA, the life cycle inventory analysis (LCI) phase, the life cycle impact assessment (LCIA) phase, the life cycle interpretation phase reporting and critical review of the LCA, limitations of the LCA, the relationship between the LCA phases, and conditions for use of value choices and optional elements.

There are also a number of software programs which evaluate environmental impacts of products through their life cycles, as an illustration, Das (2011) utilized Simapro Software (PRé) for his studies in order to analyze environmental impacts generating by the use of light weight carbon fiber-reinforced composites within automobiles.

4.2.2 "Design for X" (DfX) Approach

DfX is one of the earliest design methods that consider environmental issues (Sheldrick and Rahimifard 2013). X stands for any sort of variable that affects design process (Moreira et al. 2014a, b). Okudan and Chiu (2010), summarized DfX concepts and tools. As shown in Fig. 4.4, researchers presented the DfX methods using two organizing themes: design for efficiency and green design. As a subclassification, researchers also define the DfX methods within three topics: (1) product scope, (2) system scope, and (3) ecosystem scope. Design for efficiency could be considered as a traditional approach whose main focus has been on reducing cost while improving quality. On the other hand, the main goal of the green design is to design a product which will cause minimum environmental
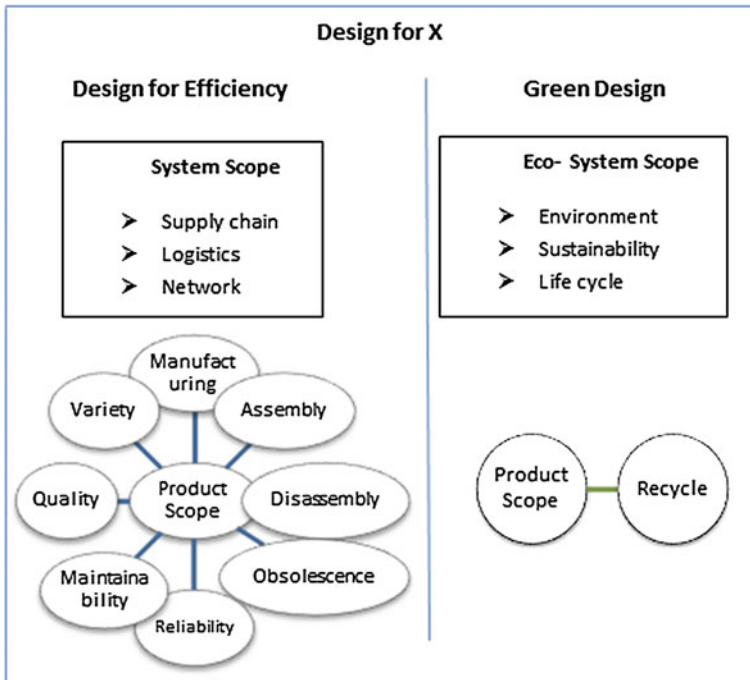
Fig. 4.4 Ecodesign challenges (Okudan and Chiu 2010)

impact along its life cycle. Overall design activity is classified into four steps: (1) problem definition and customer needs analysis, (2) conceptual design, (3) preliminary design, and (4) detailed design. The researchers also examined a number of DfX tools which are: (1) guidelines, (2) checklists, (3) metrics, (4) mathematical models, and (5) methods.

Considering ecodesign activities in aircraft industry, Moreira et al. (2014a, b) pointed out that the main focus has been on reducing the fuel consumption that is directly related to the weight of the aircraft, rather than the use of sustainable materials. However, interior design of aircrafts is gaining more importance for airline companies in order to welcome their passenger into a more comfortable, spacious and delightful environment (Garner 1996). At this point, textile industry contains sustainable challenges not only for green aviation industry, but also for the entire transportation sector. Light-weight composites for structural parts and light weight fabrics for internal parts are crucial aspects. Natural dye stuffs, recyclability, durability, easy-to-clean, and FR properties are some of the prominent requirements from transportation textiles for interior use. Since less weight means less fuel, use of light weight textiles will always play an important role for a green transportation system.

In addition, end-of-life management of transportation textiles poses great challenges such as textile recycling which offers great benefits but also difficulties. EU's end-of-life vehicle directive, for example, requires producers to collect all scrap and oversees their dismantling and recycling, without cost to the last owner (European Commission). Textile material faces are usually inseparably join to each other or to another material which are chemically different and which are difficult to separate, dispose, or recycle (Chen 2010). As an illustration, traditional seats in automobiles are composed of a three-layer composite structure which is formed by a polyester fabric; polyurethane foam, and a polyamide warp knit scrim (from outer layer to inner, respectively) (Ishtiaque et al. 2000). In seating systems, back coating, foam lamination, and use of different types of materials cause problems for recycling.

From environmental point of view, noncoated fabrics are lighter and can be recycled more easily (Fung and Hardcastle 2001). Krummheur (1993) suggested that using uniform composition for seats which is formed up with one type of material facilitates dismantling and recycling procedures. As an illustration to uniform composition, polyester face fabric, polyester nonwoven cover laminate, polyester seat squab, and cushion can be shown. Similarly, replacement of polyurethane foam with nonwoven polyester fabrics made from recycled fibers is suggested by Ostes (1993), Fuchs and Bottcher (1994). In addition, novel structures such as sandwich knitted fabrics and spacer fabrics (Ishtiaque et al. 2000) for example Kunit, Multiknit (Mayer), and Struto (Krema et al. 1997), are growing in practicality as an alternative structure for polyurethane replacement.

Powell (2008) indicated that the use of textile composites, made of natural fibers, will have a major role in developing sustainable products for all types of vehicles in the future (Powell 2004). Anon explained that composites or other textile materials which are consisted of natural fibers such as flax, hemp, coconut fibers, Ingeo™, and kenaf help decreasing aircraft weight thus resulting in less fuel consumption and emission (Anon 2007). Eason summarized the possible sustainable

opportunities such as using new generation yarns and fabrics which are biodegradable, made from recycled waste materials, and also fully recyclable at the end of their life (Eason 2012).

4.3 Conclusion

As a consequence, employing low weight—that is directly related to the fuel consumption, FR, and highly durable textiles—has been the prominent concerns of aircraft interior design. On the other hand, the usage of ecologically sustainable textiles within the aviation industry is disregarded. In order to fulfill a green design of aircraft interiors, a comprehensive ecodesign tool needs to be undertaken holistically, with a collaboration of aviation and textile industry.

References

Anon (2007) Nothing new about natural fibres in cars. Mobile-tex 2

Anon (1999) Boeing/Airbus on target for record shipment this year. Flight Int (14–20 July), 5

A.T.A.G. (2012) Facts and figures. Air Transport Action Group (ATAG), Geneva–Switzerland. http://www.atag.org/facts-and-figures.html

A.T.A.G. (2014) Aviation beyond borders. Air Transport Action Group (ATAG), Geneva, Switzerland. www.aviationbenefitsbeyondborders.org, www.atag.org

Brigden K et al (2012a) Toxic threads: putting pollution on parade: how textile manufacturers are hiding their toxic trial. Greenpeace International, Amsterdam

Brigden K et al (2012b) Toxic threads: the big fashion stitch up. Greenpeace International, The Netherlands

Chen JY (2010) Nonwoven textiles in automotive interiors. Woodhead Publishing Limited, Texas (Chapter 10)

Collins M, Aumônier S (2002) Streamlined life cycle assessment of two Marks & Spencer plc apparel products. Salvation Army, Oxford

Coll-Tortosa L (1998) Recyclable upholstery textiles for the automotive industry (BRITE-EURAM project). IMMF, Dornbirn

Das S (2011) Life cycle assessment of carbon fiber-reinforced polymer composites. Int J Life Cycle Assess 16:268–282

de Medina HV, Naveiro RM (2009) Eco-design practices in Europe fostering automotive vehicles recyclability in Brazil 7(1). Product: Management & Development

Dexter HB (1998) Development of textile reinforced composites for aircraft structures. In: 4th international symposium for textile composites. Kyoto Institute of Technology, Kyoto/Japan

Draper S, Murray V, Weissbrod I (2007) Fashioning sustainability: a review of the sustainability impacts of the clothing industry. Forum for the Future/Marks & Spencer, UK

Eason J (2012) New product development in automotive upholstery. In: New product development in textiles. North Carolina State University, North Carolina, USA, pp 80–108

EU (2015) Horizon 2020. http://ec.europa.eu/programmes/horizon2020/. Retrieved from 21 Apr 2015

European Commission (2015) Environment—end of life vehicles. http://ec.europa.eu/environment/waste/elv/. Retrieved from 23 Apr 2015

Fuchs H, Bottcher P (1994) Textile waste materials in motor cars—potential and limitations. Textil Praxis International

Fung W, Hardcastle M (2001) Textiles in automotive engineering. Woodhead Publishing Ltd, Cambridge, England

Garner R (1996) Aircraft interiors feel the pressure. Automot Transp Inter, 12–22

Hirschek H (1993) Recycling of automotive textiles. IMMF, Dornbirn

Horrocks A (2013) Flame resistant textiles for transport applications. Handbook of fire resistant textiles. Woodhead Publishing Limited, Bolton, UK, pp 603–622

ICAO (2013) ICAO environmental report: aviation and climate change. International Civil Aviation Organization (ICAO)

IPCC (1999) Aviation and the global atmosphere. IPCC, Cambridge

Ishtiaque SM et al (2000) A new approach to improve the performance of spacer fabrics. Man Made Textiles, pp 67–74

ISO 14062 (2002) Environmental management—integrating environmental aspects into product design and. Geneva, Switzerland

ISO 14040 (2006) Environmental management—life cycle assessment—principles and framework. http://www.iso.org/iso/home/store/catalogue_tc/catalogue_detail.htm?csnumber=37456

Krema R et al (1997) Whats new in high loft production. International Nonwovens

Krummheur W (1993) Recycling of used automotive seat belts. IMMFC, Dornbirn

Laurent H (1991) Fabrics used in transport vehicles. Techtextil, Frankfurt. 14–16 May 1991

Lee D, Fahey D, Forster P, Newton P, Wit R, Lim L et al (2009a) Aviation and global climate change in the 21st century

Lee D, Pitari G, Grewe V, Gierens K, Penner J, Petzold A et al (2009b) Transport impacts on atmosphere and climate: aviation. Atmos Environ 4678–4734

Mayer K (n.d.) Karl Mayer, solutions for the production of car interior linings, technical sheet. Retrieved from 14 Apr 2015. www.karlmayer.com, https://www.karlmayer.com/internet/en/anwendungen/713.jsp

McDonough W, Braungart M (2002) Cradle to cradle: remaking the way we make things. North Point Press. ISBN 0-86547-587-3

Moreira N, Santa-Eulalia L.A, Aït-Kadi D, Wood–Harper T, Trevor Wood–Harper, Wang Y (2014a) A conceptual framework to develop green textiles in the aeronautic completion industry: a case study in a large manufacturing company, J Cleaner Prod, 105:371–388

Moreira N, Aït-Kadi D, Rodrigues Vieira D, Romero A, Santa-Eulalia L.A, Wang Y (2014b) Integrating eco-design and PLM in the aviation. IFIP Adv Inf Commun Technol 442:169–180

Okudan G, Chiu M-C (2010) Evolution of design for X tools applicable to design stages: a literature review. In: Proceedings of international design engineering technical conferences and computers. ASME, Montreal, Quebec, Canada

Ostes M (1993) Use of textiles in vehicles and recycling; state of the art and outlook. IMMFC, Dornbirn

Poe CC Jr, Dexter H, Raju I (1997) A review of the NASA textile composites research. NASA Technical Reports Server, VA, United States

Powell N.B (2004) Design driven: the development of new materials in automotive textiles. J Text Apparel Technol Manage, Transp Text Issue 3(4). www.tx.ncsu.edu/jtatm

Powell N (2008) Design of automotive interior textiles. In: Textile advances in the automotive industry. Woodhead Publishing, Elsevier, North Carolina, USA, pp 113–139 (Chapter 6)

PRé (n.d.) Retrieved from 13 Apr 2015. www.pre-sustainability.com, http://www.pre-sustainability.com/

Sheldrick L, Rahimifard S (2013) Evolution in ecodesign and sustainable design methodologies. In: Re-engineering manufacturing for sustainability, pp 35–40

Troitzsch J (2004) Plastics flammability handbook. Hanser, Munich, pp 457–471

Chapter 5
Supportable, Sustainable, and Affordable Air Platforms

Sami Tarık Veske

Abstract The rule of thumb for a sustainable air platform is to apply the process of Integrated Logistics Support (ILS) thru Life Cycle of the System. Taking into consideration of all 12 (twelve) ILS Elements especially during the Preparation and Development and In Service phases, then you may have a System that is supportable, sustainable, and affordable.

5.1 Introduction

In our changing and demanding world, every day we need qualitatively and quantitatively better products. With the increase of airway transport demand nationally and internationally, airliners and air platform manufacturers are subject to the same demand and are in a position to supply what is demanded.

Thinking of the life cycle phases of the mentioned products, i.e. preparation, development, production, in Service, and disposal phase, some products (military) may live as long as almost 100 years in service. Thus, total life cycle of these products may exceed a century or at an average/minimum be 50 years for civil. On the other hand, acquisition cost of an average civil aircraft may be around $100 M which is around 30 % of Total Cost of Ownership (TCO), meaning that there is portion of TCO 70 % for "In Service", more than twice the cost of acquisition.

Life cycle and TCO footprints of air platforms are not negligible; therefore air platforms have to be designed such that they have features of;

- Supportability,
- Sustainability,
- Affordability

S.T. Veske (✉)
TAI—Turkish Aerospace Industries, Inc., Fethiye Mahallesi,
Havacılık Bulvarı No: 17, 06980 Kazan, Ankara, Turkey
e-mail: stveske@tai.com.tr; stveske@gmail.com

besides their "Performance" metrics. In other words, we have to pay attention to the subsurface portion of iceberg.

5.2   Supportability, Sustainability, and Affordability

Integrated logistics support (ILS) is an integrated and iterative process for developing materiel and a support strategy that optimizes functional support, leverages existing resources, and guides the systems engineering process to quantify and lower life cycle cost and decrease the logistics footprint (demand for logistics), making the system easier to support. Although originally developed for military purposes, it is also widely used in commercial product support or customer service organizations (Wikipedia-Integrated logistics support 2015).

One of the main ILS elements is supportability. Supportability engineering activities aim to measure the degree to which a system can be supported both in terms of its inherent design characteristics of reliability and maintainability and the efficacy of the various elements of ILS. Supportability is a prediction or measure of the characteristics of an item that facilitate the ability to support its mission capability within a predefined environment and usage profile (Jones 2007). By definition, set up of product support characteristics up to the delivery of the system is named and/or under responsibility of supportability, whereas after delivery thru in service up to disposal it is sustaining engineering.

Sustaining engineering aims to achieve a more reliable and sustainable product and support it in its operational environment. Sustaining engineering activities span below engineering and logistics task analyses to ensure continued operation and maintenance, known also as "Product Support", of a system with managed risks;

- Collection and triage of all service use and maintenance data,
- Analysis of safety hazards, failure causes and effects, reliability and maintainability trends, and operational usage profiles changes,
- Root cause analysis of in-service problems,
- The development of required design changes to resolve operational issues,
- Other activities necessary to ensure cost-effective support to achieve (peacetime and wartime) readiness and performance requirements over a system's life cycle.

Affordability is one of the sub elements of design interface which is one of the most important elements of ILS. Affordability assessments are both development and investment and O&S cots, hence continuously controlled by estimated or calculated Life cycle cost (LCC). Life cycle cost (LCC), whole life cost (WLC), cost of ownership (COO) and total ownership Cost (TOC) are also covered in any system regarding cost analysis.

Supportability, sustainability, and affordability issues are taken into consideration during product life cycle. In order to have air platforms or any kind of system with predefined customer support requirements, i.e., supportable and sustainable air

platforms/systems, with an affordable TCO, ILS with the systems engineering approach, have to be applied to the extent required.

5.3 Product Life Cycle

Product Life Cycle is the entire life cycle of a product from inception, through engineering design and manufacture, to service and disposal of manufactured products. Support activities are performed continuously through product life cycle phases.

During these phases supportability and sustainability activities aim to (Fig. 5.1);

- Influence design for support and sustainment,
- Identify and develop logistic support resources,
- Acquire necessary support,
- Provide required support for minimum cost.

5.4 Life Cycle Cost (LCC)

LCC represents all the costs that will be borne during the life of a system (Main System and Support System). The costs incurred over the life cycle of a product are acquisition costs, operation and support costs, and disposal costs.

Fig. 5.1 Product life cycle phases (Reproduced from EADS CASA. Supplementary training material 2003)
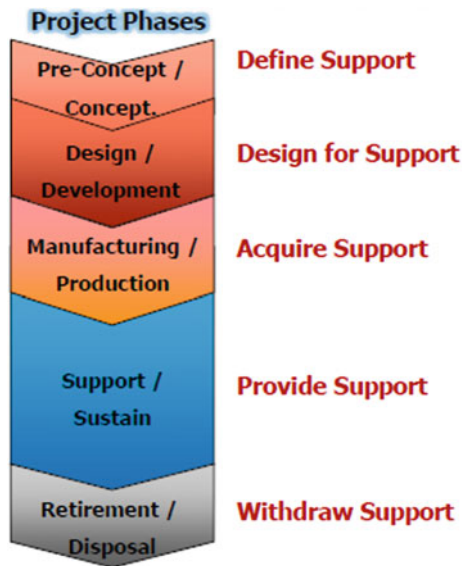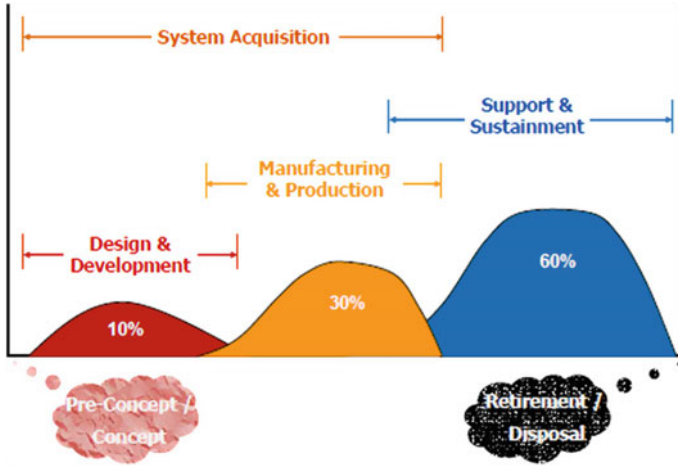
Fig. 5.2 Percent of the LCC (Reproduced from Turkish Aerospace Industries 2015)

Although acquisition cost is the most outstanding cost among the others, the largest percent of the LCC is incurred by operation and support of the product (Fig. 5.2).

To design product that establishes the technical performance requirements and also affordable, it is important to control especially operation and support cost by LCC. The decisions in very early phases of the projects affect LCC a lot more than the decisions thereafter. Therefore in these phases, it is critical to evaluate design alternatives through sensitivity analysis in terms of cost-effectiveness (Fig. 5.3).
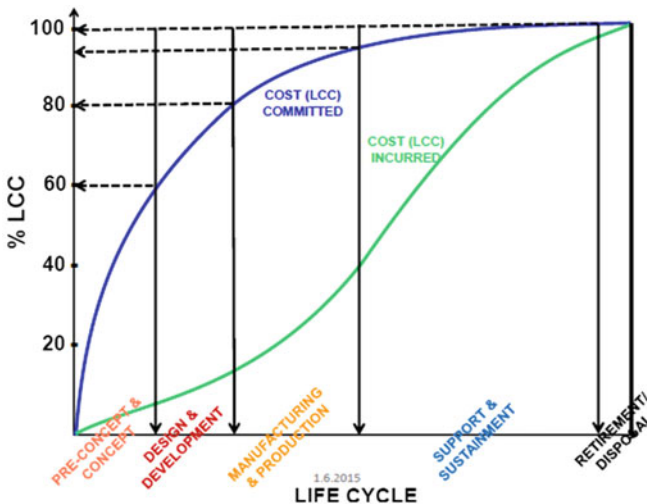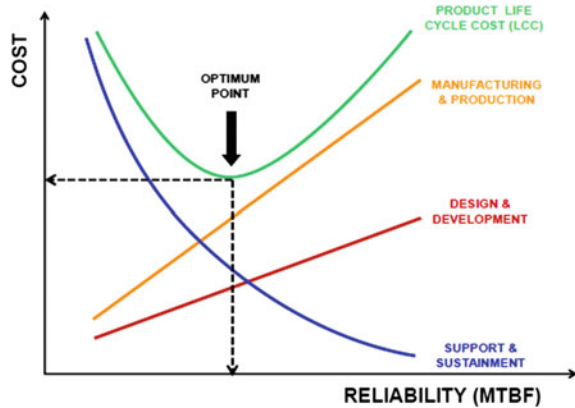

Fig. 5.3 LCC sensitivity analysis

Fig. 5.4 LCC optimization

One of the most important requirements that affect product availability and also LCC is reliability which is a supportability requirement. To establish a reliability requirement more than a system's operational need, increases LCC unnecessarily. While making decisions about product performance and supportability parameters, it is critical to consider LCC as a constraint and define an optimum point (Fig. 5.4).

Along with LCC optimization considering supportability parameters such as reliability, also decreases logistics footprint by decreasing maintenance activities and so resources needed.

5.5   Integrated Logistics Support (ILS)

ILS is the process and organization charged with the responsibility of managing the technical disciplines that plan and develop logistics support for the whole life cycle at minimum cost (Affordability) by influencing the design.

ILS activities are carried out to integrate all the functional components which are available to make up or define the required product support infrastructure. These functional components are grouped into twelve categories called the ILS Elements. These elements include:

- Product Support Management
- Supportability/Design Influence
- Sustaining Engineering
- Supply Support
- Maintenance
- Packaging, Handling, Storage, and Transportation (PHS&T)
- Technical Data
- Support Equipment
- Training and Training Support

- Manpower and Personnel
- Facilities and Infrastructure
- Computer Resources

In development phase of a program ILS activities are performed under three main topics:

- Design for Support
- Design the Support
- Support the Design

"Design for Support" and "Design the Support" activities prepares infrastructure and provide data for "Support the Design" activities.

5.6   ASD ILS Suite Map

ASD represents the civil aviation, space, security, and defense industries in Europe.

ASD-STAN (Product standards and Technical Specifications), since 1987, as an affiliated association of ASD, establishes, develops and maintains standards for products, quality systems and product support for the European aerospace industry (AeroSpace and Defense Industries 2015).

Some of the ASD specifications commonly used in aerospace industry are listed below.

- S1000D (International specification for technical publications)
- ASD-STE 100 (Simplified Technical English)
- S2000M (International specification for material management)
- S3000L (International procedure specification for Logistics Support Analysis LSA)
- S4000P (International specification for developing and continuously improving preventive maintenance)
- S5000F (International specification for operational and maintenance data feedback)

There is also a guide prepared for the use of these S-Series Integrated Logistics Support Specifications, named SX000i. SX000i explains how the S-Series ILS specifications interface with other standardization domains including project management, global supply chain Management, quality, data exchange and integration, and LCC.

S-Series ILS specifications aim to establish a common understanding for ILS processes. Main goal of these specifications is LCC and performance optimization by defining global ILS processes and also enabling costumer and industry collaborate easily.

According to SX000i value proposition of using S-Series ILS specifications are:

- Globally acceptance,
- Reduction in the set up costs of projects and associated IT tools,
- Reduction project complexity,
- Guarantee of being future-proof

5.7 Conclusion

To design a technically capable product which is also supportable and sustainable requires continuous integrated process through development and production phases. Technical effectiveness of a product is achieved by not only with technical performance capability, but also supportability and sustainability characteristics. However, to have a cost-effective operational effectiveness, affordability also has to be taken into account during technical performance and supportability/sustainability activities.

Thus, ILS activities provide increase in operational effectiveness by designing support sustainment of the product in its operational environment together with affordable TOC and hence smaller logistics footprint.

References

AeroSpace and Defence Industries Association European (2016). http://www.asd-europe.org/about-us/structure/asd-stan. Accessed 12 May 2015

EADS CASA. A-400M Integrated Logistic Support (ILS) (2003) Supplementary training material, Ankara. 6 Oct 2003

Jones JV (2007) Supportability engineering handbook. McGraw Hill, p 1

SX000i—International guide for the use of the S-Series Integrated Logistic Support (ILS) specifications. http://www.sx000i.org/docs/SX000i_Issue_1.0.pdf

Turkish Aerospace Industries Logistics Support Analysis (2015). https://www.tai.com.tr/en/programs/logistics/logistics-support-analysis-lsa. Accessed 13 May 2015

Wikipedia-Integrated logistic support (2015) https://en.wikipedia.org/wiki/Integrated_logistics_support. Accessed 10 May 2015

Chapter 6
Consumer Affect and Type of Water Recycling Projects: Implementation at Airports

Ismael Cremer, Stephen Rice, Sierra Gaenicke and Korhan Oyman

Abstract Previous studies have shown that the level of contact with recycled water has a significant impact on users' attitude and perceptions toward its use. Recycled water is an engineering process that allows water to be reused for various processes and can mitigate the consumption of freshwater resources used by the airport. The current study aims to determine whether affect mediates the relationship between the type of water recycling projects and a person's preference toward the use of that airport. Participants were presented with a scenario of an airport that uses recycled water for their sprinkler system or for their drinking fountains. This study found that affect was a significant mediator that mediated the relationship between the type of water recycling project and a person's preference towards using that airport. We discuss the theoretical and practical implications of this data.

6.1 Introduction

The purpose of this study is to investigate whether affect mediates consumer's perception of using recycled water at airports. Previous studies have investigated the public perceptions of water reuse to gain a better understanding of the acceptance of implementing projects in this area (Hurlimann 2007; Toze 2006). Water is a resource that is scarce in many parts of the world and with established technologies that is possible to mitigate the use of fresh water for such practices using recycled wastewater. The emotions of the public regarding this type of sustainability are important in the future development of reducing the use of valuable fresh water.

The term sustainability was derived in 1987 at the World Commission of Environment and Development. The idea of sustainability is important in today's

I. Cremer (✉) · S. Rice · S. Gaenicke · K. Oyman
Florida Institute of Technology, 150 W. Uni Blvd, Melbourne, FL 32901, USA
e-mail: ismaelcremer@gmail.com; icremer@fit.edu

market and relates the balance between three factors of the environmental, the societal, and the economic well-being of the companies.

According to the Water Security Risk Index, there are currently 18 countries that are considered to be at extreme risk with respect to their water security. In parts of the United States that have water scarcity, the population is growing more rapidly than the national rate. Europe also contains some of the same issues; however, there is water shortage and high consumption demand in the countries that have intensive irrigated river basins. Direct water reuse is considered to be the creation of new water supplies from recycled water to be used for various purposes, while indirect water reuse is considered to be the practice of recharging current water sources with reused water. There have been some countries and states that have high shortage of water that have already implemented indirect and direct water reuse.

In a previous study conducted by Hurlimann (2007), the differences in an individuals risk perception in regards to water reuse between two Australian counties were investigated. It was found that the higher level of contact with recycled water, the more unaccepting the participants were to the idea. However, level of water shortage did not affect the participant's acceptance of using recycled water. Cultural studies have also been conducted between Indians and Americans. The results of on of the previous cultural studies showed that Indians were accepting towards using recycled water for contact use, while Americans were less accepting. These results demonstrated the connection of the concept of collectivistic versus individualistic cultures.

This study investigates the relationship of human affect with respect to using recycled water at an airport. There are two types of affect, positive and negative, which are distinct and independent constructs regarding human emotions (Diener and Emmons 1984). Positive affect would be described as enthusiastic, energetic activity, and level of alertness, while negative affect would be described as distress, displeasure, anger, and contempt. An individual with positive affect will have a more positive view of the world (Jones and George 1998). It is therefore possible to state that an individual with positive affect toward a certain type of recycled water usage will more have a more positive sentiment toward the airport itself. Moreover, it has also been seen that positive and negative affects have an effect on cognitive judgments), and therefore relates to how an individual will connect their judgment based on their feeling toward the water reuse project.

Airports are large users of water, therefore, water reuse programs can be implemented in order to account for the 5 % forecasted annual growth within the air transportation system. It would be possible to reuse wastewater for activities such as flushing toilets, washing hands, drinking water, firefighting, and landscape applications if treated appropriately. While wastewater contains various types of contaminants (naturally occurring, anthropogenic inorganic chemicals, and unidentified chemicals), there have been some potable reuse studies that have shown that advanced wastewater treatment can produce water that meets the US drinking water

standards (Crook et al. 1999). Therefore, it can be noted that it is very possible to implement water reuse projects safely at airports.

6.2 Methodology

In this study, we investigated the relationship between affect and willingness to use an airport depending on the type of use the recycled water would be implemented for. The two types of water reuse that was used in this study were landscaping and for drinking. We hypothesized the following:

1. That affect ratings would be more negative for the airport identified as using recycled water for drinking fountains compared to the airport using recycled water for their sprinkler system.
2. That participants would be more likely to choose the airport using recycled water for their sprinkler system over a random airport, compared to the airport identified as using recycled water for drinking fountains.
3. That affect, in general, would mediate the relationship between the type of recycling project and airport preference.

Participants. Ninety-seven (41 females) participants from the United States were recruited via a convenience sample using Amazon's® Mechanical Turk® (MTurk). Although MTurk participants are compensated for their participation, studies have shown that the data is reliable for analysis (Buhrmester et al. 2011; Germine et al. 2012). The mean age of the participants was 31.18 (SD = 9.75).

Materials and Procedure. Participants first signed an electronic consent form. They were then given instructions about the study. Following this, they were presented with a scenario about an airport that uses recycled water. Specifically, they were told "Imagine an airport that is trying to be more environmentally conscious by using recycled water in the lawn sprinkler system." In a separate condition, they were told, "Imagine an airport that is trying to be more environmentally conscious by using recycled water in the drinking fountains."

Next, participants were asked to complete the affect scale created by Rice and Winter (2015). The affect scale measures the participant's emotional response to the scenario. Following this, participants gave responses to the following three statements: (a) I would be more comfortable using this airport than other airports who do not do this; (b) I would be more willing to use this airport than other airports who do not do this; and (c) I would be more likely to use this airport than other airports who do not do this. Participants responded on a 5-point bipolar Likert-type scale from −2 (strongly disagree) to +2 (strongly agree) with a neutral choice of zero. Lastly, participants were asked basic demographics questions, debriefed, and paid for their time.

6.3   Results and Discussion

Affect Measures. Prior to conducting analyses on the affect data, the results from the affect instrument were subjected to a Cronbach's Alpha test to measure internal consistency. The scores ranged from 0.93 to 0.96. Thus, all affect measures were combined for the following analyses.

Figure 6.1 shows the differences between the affect scores and willingness scores between the two conditions. A *t* test between the two conditions revealed that affect differed as a function of the condition, $t(192) = 7.383$, $p < 0.001$, $d = 1.01$, indicating that participants felt more negatively about the target airport that used recycled water for drinking fountains ($M = -0.04$, SD = 1.14) compared to the airport that used recycled water for the sprinkler system ($M = 0.98$, SD = 0.74).

Outcome Variable. The outcome variable refers to the variable that tests whether participants preferred the target airport or a random other airport that does not use the recycling method. In other words, the outcome variable was the consumer's preference to use the airport. Prior to conducting analyses on the outcome data, the three measures were subjected to a Cronbach's Alpha test to measure internal consistency. The scores ranged from 0.90 to 0.94. Thus, the three measures were combined for the following analyses. A *t* test between the two conditions revealed that the outcome variable differed as a function of the condition, $t(192) = 4.39$, $p < 0.001$, $d = 0.61$, indicating that participants were less likely to prefer the airport that used recycled water for drinking fountains ($M = -0.35$, SD = 1.00) over a random airport compared to the airport that used recycled water for the sprinkler system ($M = 0.26$, SD = 0.94).

Mediation Analyses. The standardized regression coefficient between Condition and Affect was statistically significant, as was the relationship between Affect and

Fig. 6.1 Differences between type of water reuse

	Affect	Willingness to use
Landscaping	0.98	0.26
Drinking	-0.04	-0.35
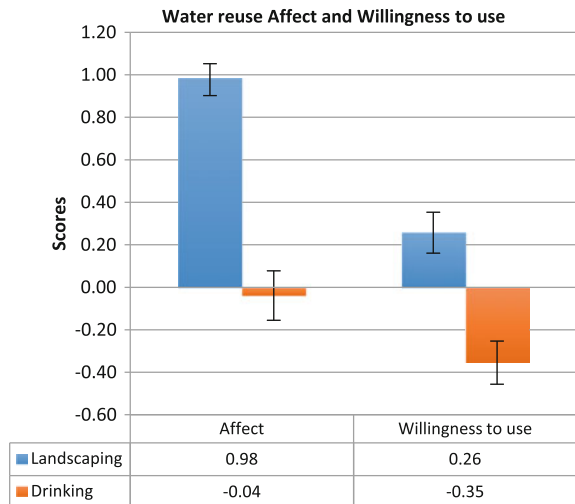
Preference. The standardized indirect effect was $(-1.02)(0.64) = -0.65$. The significance of this indirect effect was tested using bootstrapping procedures with 10,000 bootstrapped samples. The bootstrapped 95 % confidence interval ranged from -0.90 to -0.42. Thus, the indirect effect was statistically significant and there was mediation with an effect size of 0.65.

6.4   Discussion

The purpose of this study was to investigate whether emotions play a significant role in a passenger or consumer's perception of using recycled water for two different purposes. In this study, we first wanted to determine if the type of water recycling project (drinking fountain versus sprinkler system) had any effect on the affect ratings of participants. Second, we wanted to test whether the type of water recycling project had any effect on participants' preference for that airport over another airport that did not use that water recycling project. Third, we wanted to determine if affect mediated the relationship between type of water recycling project and participants' preference for using that airport.

The data provided strong evidence for all three hypotheses. Furthermore, it provided the same results of a previous similar study conducted by Cremer and Rice that investigated the effect of affect on type of water reuse and looked at which emotions in particular played significant roles. Ratings of affect differed significantly between conditions, as did preference for using that particular airport. Affect showed mediation over the relationship between the condition and outcome variable, indicating that a person's preference for using an airport based on the type of water recycling project is an emotion-driven decision rather than a cognitive one.

General Discussion. This study investigated the relationship of affect and perception of using recycled water for two different purposes. We hypothesized that: (1) affect ratings in would change for the airport that is identified as using recycled water for drinking; (2) preference ratings of the airport would decrease for the airport that uses recycled water for drinking; and (3) affect, in general, would mediate the relationship between the type of water reuse and preference for that particular airport.

Our first hypothesis was supported by the results. Affect ratings were different between using recycled water for drinking compared to landscaping. Consumers were more willing to use recycled water for landscaping purposes rather than for drinking. Furthermore, when asked about their attitude toward the airport as a whole if they used recycled water for drinking rather than for landscaping, consumers were less likely to want to use the airport that utilized recycled drinking water. Cremer and Rice also found similar results when investigating preference of water reuse with respect to various levels of contact. Consumer perceptions became more negative the higher the level of contact with the recycled water.

The third hypothesis was also supported. It was seen in the results that affect mediated the relationship between water reuse type and user preference toward the airport.

Theoretical Contributions. The current study contributes to the literature on airport sustainability, affect, and preference of an airport. Airports such as Chicago and Sydney airport have begun taking the sustainability initiative in their planning process. They are implementing new projects that will help mitigate the environmental impact of the airport itself, ranging from renewable energy initiatives to recycled water for various purposes. Research however has been limited with respect to investigating the end user response to this, the passenger. The current study adds to this branch of literature by examining how different passenger emotion can have differential effects on the relationship between airport sustainability and preference of the airport.

Practical Implications. There are practical implications in this research for airport managers and environmentalists. There have been a number of media articles that have branded the use of recycled water as unsanitary or unsafe. The engineering processes have been studied and proven to be successful and useful in places that have a limited resource of natural water. It is important for any airport or entity that wishes to begin using recycled water to understand that it is imperative to include the end user. The results from this study indicate that the response toward this type of sustainable practice is largely, if not completely, due to an emotional response. By understanding that this practice can in fact increase the sustainability of the airport, the passengers may be more willing to be involved with such practices. It has been suggested in previous research that individuals typically have a positive emotion associated with contributing to the welfare of the environment.

Delimitations and Limitations. There were several delimitations and limitations of the current study. First, we only chose two purposes that the recycled water could be used for. This was due to constraints in funding available to obtain participants. To include various types of use for recycled water would require a larger sum of resources to investigate the differences.

Second, we used a convenience sample from Amazon's® Mechanical Turk® (MTurk). MTurk provides participants who complete human intelligence tasks in exchange for monetary compensation. While prior research has shown that data from MTurk is as reliable as normal laboratory data (Buhrmester et al. 2011; Germine et al. 2012), we recognize that any convenience sample negatively affects external validity, thus preventing us from making universal generalizations about the data.

Another limitation is the use of only American participants. It would be prudent for future research to investigate if culture and background play a role with the acceptance of recycled water with respect to the level of physical contact.

6.5 Conclusion

The primary goal of the current study was to determine whether affect had a mediating effect on the relationship between the type of water reuse at airports and preference. In this study, we were able to conclude that affect and preference are both negatively affected by the stigmatization of the use of recycled water for drinking purposes. Furthermore, affect mediated the relationship between the type of water reuse at airports and preference. We hope that future research both replicates and expands upon these findings.

References

Buhrmester M, Kwang T, Gosling SD (2011) Amazon's Mechanical Turk: a new source of inexpensive, yet high-quality data? Perspect Psychol Sci 6(3):3–5

Cremer I, Rice S, Winter S (in press) Attitudes toward sustainability between Indians and Americans on water reuse for different purposes at airports. Int J Sustain Aviat

Crook J, MacDonald AJ, Trussell RR (1999) Potable use of reclaimed water. Am Water Works Assoc 91(8):40–49

Diener E, Emmons RA (1984) The independence of positive and negative affect. J Pers Soc Psychol 47(5):1105–1117

Germine L, Nakayama K, Duchaine BC, Chabris CF, Chatterjee G, Wilmer JB (2012) Is the web as good as the lab? Comparable performance from web and lab in cognitive/perceptual experiments. Psychon Bull Rev 19(5):847–857

Hurliman AC (2007) Recycled water risk perception—a comparison of two case studies. Water Pract Technol 2(4):1–11

Jones GR, George JM (1998) The experience and evolution of trust: implications for cooperation and teamwork. Acad Manag Rev 23:531–546

Rice S, Winter S (2015) A quick affect scale: providing evidence for validity and reliability. In: 10th international conference on interdisciplinary social sciences

Toze S (2006) Water reuse and health risks—real vs. perceived. Desalination 187:41–51

Chapter 7
Sustainable Aviation Applications in Turkey: Energy Efficiency at Airport Terminals

Mehmet Necdet Büyükbay, Gülsan Özdemir and Erhan Üstündağ

Abstract This paper gives an overview of what the airports and terminals at TAV Holding is doing as far as energy efficiency is concerned. The efforts at TAV consist of small incremental projects (addition of insulations, automatic door installation, performance improvements at cooling, heating, etc.) and big projects (Photovoltaic panels, Trigen, etc.). The building structure of the terminals is the main parameter in defining project outlines. Beside terminal structure, there are also other parameters that are affecting the energy performance of the building. By the cooperation with universities, thermal camera analyses had been carried out to detect the thermal insulation efficiency at the terminal shell. Customer satisfaction is the main parameter in terms of passenger comfort in terminal for aviation services. For this purpose, projects were carried out to decrease operational energy consumptions related to HVAC systems and thereby increase in passenger satisfaction. The most energy consuming system in terminals is the HVAC system with the percentage of 60 of the overall energy consumption. Thermal stratification system was implemented in a lounge area in one terminal. All projects had been analyzed for their payback period.

7.1   Introduction

Airports have a main role in transportation of people and goods at national and international boundary. Generally, airports are big areas with governmental and nongovernmental companies and entities including airlines, fuel supply units,

M.N. Büyükbay (✉) · G. Özdemir
TAV Airports Holding, Adnan Menderes Airport, Izmir, Turkey
e-mail: necdet.buyukbay@tav.aero

G. Özdemir
e-mail: gulsan.ozdemir@tav.aero

E. Üstündağ
TAV Airports Holding, Istanbul, Turkey
e-mail: erhan.ustundag@tav.aero

terminal operators, catering companies, etc. Airports are similar to small towns in which many environmental issues are concerned. In recent years, the most important environmental issues is carbon management at airports. Carbon footprint management is directly related with energy and natural resource consumption. Therefore, energy and resource management is a critical point that needs special strategies in terms of environmental sustainability. On the other hand, energy and resource management gives the opportunity to decrease OPEX (operational expenditure) values.

Airport terminals are consuming high amounts of energy for lighting, heating, ventilation, air conditioning, and operational systems such as conveyance systems. The breakdown of energy consumption at terminal results in the highest energy consumption comes from HVAC systems. Therefore, many airport operators have focused on reducing operating expenses by focusing on energy efficiency, considering both energy supply and energy consumption. Airport operators. There are also renewable energy system applications of airports. Research is necessary to solve common operating problems, to adapt appropriate new technologies from other Industries to introduce innovations in the airport industry. Focus should be on increasing customer comfort, energy efficiency, and reducing operating costs at airport terminals. The main and simplest way is calculating payback period (in years) to determine the feasibility of energy efficiency projects.

More than two decades ago, the Bruntland Report identified buildings and energy efficiency as major areas to save the energy resources. Today, reports continue to echo the benefits and potentials of efficiency, including what could be described as its minimal environmental impact and ability to displace costly and disagreeable energy supplies, enhance security and prosperity, speed global development, and protect Earth's climate not at cost but at a profit (ACRP Synthesis 21 2010).

As in Turkey's airports, energy cost is 10–15 % of the total operating budget. Therefore, energy efficiency is identified as a high priority by respondents in current long-range plans.

7.2 Results and Discussion

The important point is to have normalized benchmarking energy efficiency values among airports. Normalization will enable airports to benchmark themselves without any further discussion.

There are different factors that are effecting airport energy consumption:

(a) Airport size (area and volume of conditioned space, area of externally exposed building envelope)
(b) Shape factors

- Compact (one main building with bus transportation)
- Pier finger terminals

- Pier satellite terminals
- Remote satellite terminals

(c) Location-Climate (hot and cold degree days—HDD and CDD, solar radiation, and humidity levels)
(d) Hours of operation
(e) Building envelope
(f) HVAC Systems and controls
(g) Level of maintenance at the facility
(h) Occupant/user behavior and energy management (Costa et al. 2012)

Several projects have been carried out in one pilot airport terminal in Turkey that are given in detail below.

7.2.1   Thermal Camera Analyses

Thermal camera is a thermographic camera that forms an image using infrared radiation, infrared cameras operate in wavelengths as long as 14,000 nm (14 µm).

After construction of the airport, thermal camera analyses have given a big opportunity to identify heat leaking areas at different point of the terminal as shown in Fig. 7.1a–c (Ekonomi Gazetecileri Derneği (EGD), V. Küresel Isınma Kurultayı, 2013).

According to the thermal camera analyses of one terminal, all isolation that need had been determined. Approximately 2 tons of isolation material (glass wool) had been used. Payback period has been calculated and given in Table 7.1.

As seen from Table 7.1, the payback period is low than 1 year by simple isolation works.

7.2.2   Solar Reflective Material

After construction of the terminal glass domes and light houses created big problems as they let the sun light to get in the terminal and resulted with a temperature increase inside the terminal. That also increased passenger complaints especially in summer.

A solar UV resistant reflective material has been covered on top of the glasses and domes from outside the terminal during the summer season (Fig. 7.2). It is been taken out during the winter season. The material has 87 % UV resistance.

This material has given a comfortable environment for passengers in the terminal. As seen in Table 7.2, the payback period is lower than 1 year for this project by which seasonal changes brings advantages to terminal heating and cooling operations.

Fig. 7.1 a Thermal camera
analyses result of terminal
shell. **b** Thermal camera
analyses result of automatic
sliding door of the terminal
entrance. **c** Thermal camera
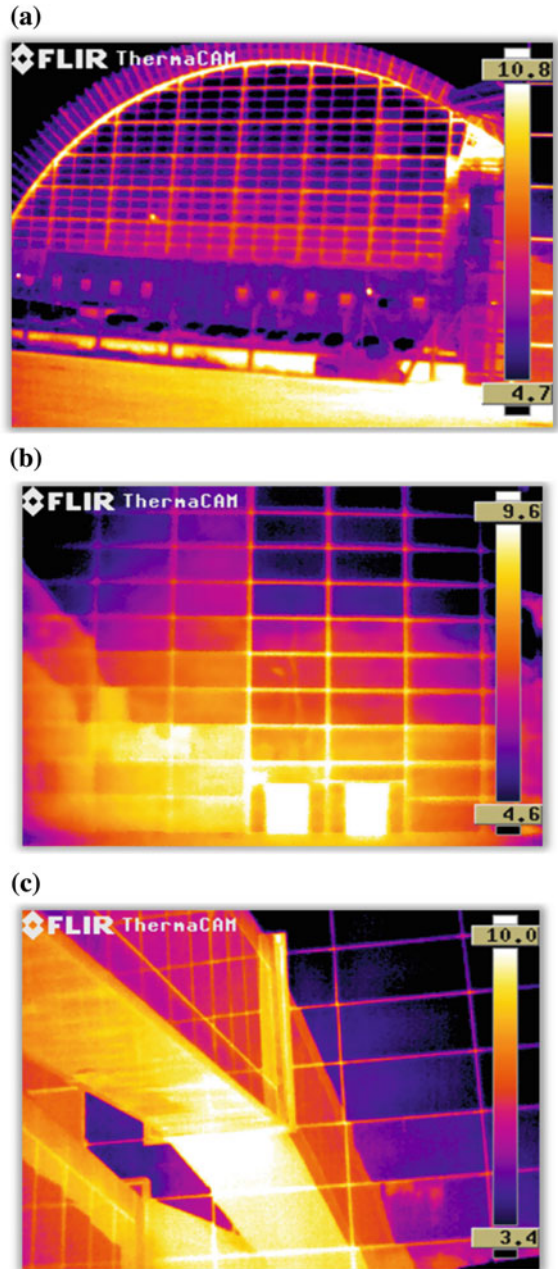analyses result of the
passenger boarding bridge

Table 7.1 Payback period calculation of investment according to thermal camera analyses

CO_2 emission decrease (tons CO_2)	Investment (TL)	Annual saving (TL)	Payback period (year)
480	80.000	277.000	<1

Fig. 7.2 Decorative solar reflective material application on light holes of the terminal

Table 7.2 Solar UV resistant reflective material application investment payback period calculation

CO_2 emission decrease (tons CO_2)	Investment (TL)	Annual saving (TL)	Payback period (year)
145	26.000	84.900	<1
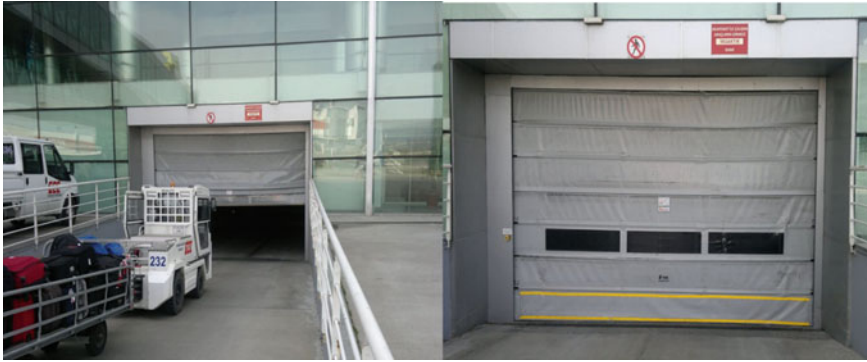
Fig. 7.3 Entrance door of Baggage Handling System (BHS) area

Table 7.3 High speed door application investment payback period calculation

CO_2 emission decrease (tons CO_2)	Investment (TL)	Annual saving (TL)	Payback period (year)
84	24.000	48.600	<1

7.2.3 Highspeed Doors

The gateway from the apron to the baggage handling system (BHS) area was being kept open previously. An automatic fast moving door has been installed to this entry (Fig. 7.3). Conventional automatic door linear speed was 0.5 m/s. The new type door that has been installed has a speed of 1.5 m/s. This resulted 6 °C temperature difference in baggage handling area.

These types of doors are now used at airports in Turkey. In Table 7.3, the payback period has been calculated for the high speed door usage. By this project, a comfortable environment has been obtained especially for staff working in BHS area.

7.2.4 Thermal Stratification

The use of ceiling (or floor) diffusers, (Fig. 7.4), that introduce air with some momentum alters the behavior in the lower zone by increasing the amount of mixing and changing the temperature profile. If the diffuser throw is close to the stratification height or already exceeds it, the throw will penetrate into the warm upper layer bringing warm air down into the lower region. The amount of air brought down influences the temperatures in the lower region. The amount of mixing in the lower layer influences the gradient. In the limit as throw and the

Fig. 7.4 Thermal stratification fan application

amount of mixing is reduced, thermal stratification systems tend to approach the operation of displacement ventilation systems. Higher throws that penetrate above the stratification height will result in warmer temperatures and less gradient in the lower region, all other conditions being constant (Webster et al. 2002).

Thermal stratification has been implemented recently in one terminal lounge area. The area is approximately 2000 m^3. In order to detect the expected homogen temperature profile, temperature sensors have been set at different heights in the area which are 1, 4, and 7 m. The most important issue is that temperature is a function of humidity and pressure. To obtain more detailed data, testing this system weather conditions (outdoor air temperature, relative humidity, pressure, solar radiation, wind speed, etc.) and inside conditions (temperature, humidity, pressure) should be tracked by inside and outside sensors.

While conventional HVAC systems cause drafts as a consequence of the high velocities of the incoming and outgoing air, distribution of air on the basis of the thermal stratification system basically ensures slow circulation of air at uniform air velocities of approx. 0.1 m/s throughout the entire room. The heating or cooling process is carried out by small ΔT increments. This uniform distribution also prevents local buildup of pollutants and reduces the levels of CO_2 and volatile organic compounds. For this purpose, the quality of the air is measured continuously and introduction of fresh air is adjusted on the basis of the measured values.

As seen in Fig. 7.5, airflow is more effective for thermal stratification system.

This project applied in the terminal has given a more comfortable environment in terms of heating and cooling. On the other hand approximately 30 % reduction in energy cost has been obtained. Payback period for this project is 2 years. Annual saving has been calculated as 19.000 TL with the investment of 38.000 TL for the lounge area in the terminal.
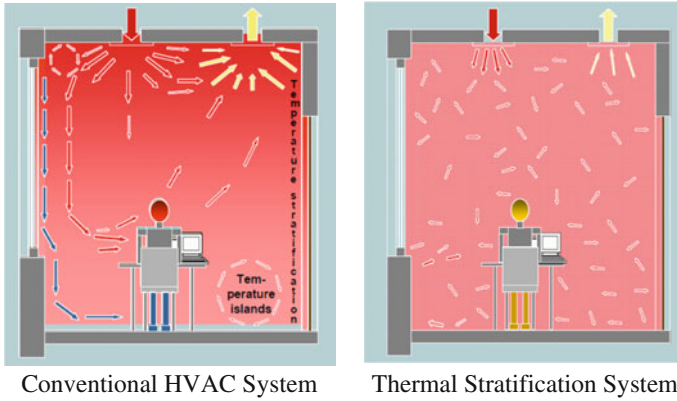
Conventional HVAC System   Thermal Stratification System

Fig. 7.5 Difference in airflow of conventional and thermal stratification systems

7.3   Conclusion

This paper gives a review of energy efficient applications at airports. Efficient energy management is an important concept in terms of carbon footprint and operational expenses. Carbon footprint is directly related with energy management strategies. By small efficient energy management projects approximately 30 % decrease can be obtained in energy consumption.

For airports, KPI, key performance index, normalization studies have to be carried out between energy consumption and operational data (flight numbers, passengers, baggage and freight movements, etc.). Normalization studies are very useful indicators for performance assessment and benchmarking.

References

ACRP Synthesis 21 (2010) Airport energy efficiency and cost reduction: a synthesis of airport practice. Transportation Research Board, Washington, D.C

Costa A, Blanes LM, Donnelly C, Keane MM (2012) Review of EU airport energy interests and priorities with respect to ICT, energy efficiency and enhanced building operation. In: Proceeding of the Twelfth International Conference for Enhanced Building Operations, Manchester, UK, 23–26 Oct 2012

Ekonomi Gazetecileri Derneği (EGD) (2013) V. Küresel Isınma Kurultayı, Enerjini Verimli Kullan, Geleceğine Sahip Çık p 61., May 2013, İstanbul, Turkey

Webster T, Bauman F, Reese J (2002) Underfloor air distribution: thermal stratification. ASHRAE J May 2002

Chapter 8
Investigation of the Vehicle Application of Fuel Cell-Battery Hybrid Systems

Ayse Elif Sanli and Goksel Gunlu

Abstract All electric vehicles (AEV) are developed using the new technology; they can be separated in two groups as battery-operated electric vehicles (EV) and fuel cell vehicles (FCV). The subject of this study, fuel cell-battery operated hybrid vehicles, is about full electric hybrid vehicles (FEHV). EV and FCV have different advantages and disadvantages, therefore it is necessary to develop the FEHV vehicles. The fuel cell-battery hybrid systems are under investigation. In the literature, some automotive applications are reported as examples for fuel cell-battery hybrid powered systems. The light hybrid vehicles have been tested in terms of the system design, power management, road tests, and efficiency. All of the presented systems consist of a proton exchange membrane fuel cell system, battery pack, powertrain system, and a connection strategy for powering the traction of an electrical car. However, these are not perfect vehicles, they require further work to address major drawbacks with the connection as well, to increase the efficiency and management of the hybrid components (fuel cell, battery, supercapacitors, motor drive, and electrical systems), motor drive and electrical systems. Their tests and the demonstration results are satisfactory.

8.1 Introduction

Using electric and fuel cell vehicles or hybrid vehicles will prevent the pollution caused by vehicles; in addition to that, they are the most suitable solution for the system efficiency with suitable power management strategies. Vehicles can be classified into three groups (Same et al. 2010): internal combustion engine vehicles (ICEV), hybrid electric vehicles (HEV), and all electric vehicles (AEV) (Fig. 8.1).

A.E. Sanli (✉) · G. Gunlu
Electrical and Electronic Engineering Department, Faculty of Engineering, Turgut Ozal University, Ankara, Turkey
e-mail: aecsanli@gmail.com; aecsanli@turgutozal.edu.tr

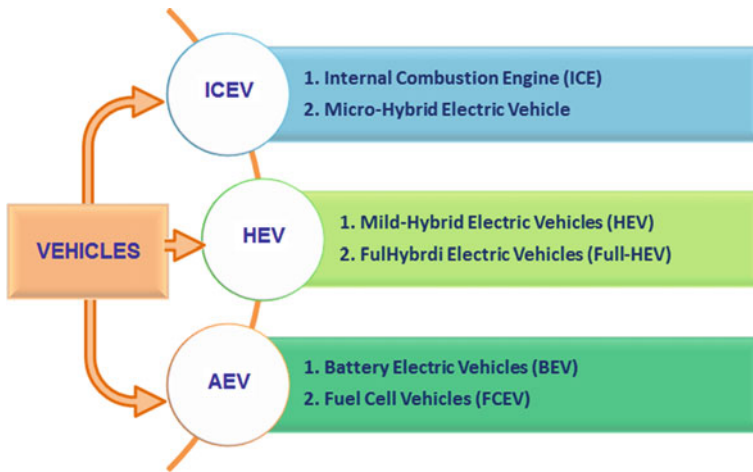G. Gunlu
e-mail: ggoksel@gmail.com; ggunlu@turgutozal.edu.tr

Fig. 8.1 Classifying vehicles

All electric vehicles (AEV) are developed using the new technology; they can be separated in two groups as battery-operated electric vehicles (EV) and fuel cell vehicles (FCV). The subject of this study, fuel cell-battery operated hybrid vehicles, could be called as full electric subject of the present study (FEHV). EA and FCV vehicles, classified in AEV, have different advantages and disadvantages; therefore, it is necessary to develop the FEHV vehicles (Tie and Tan 2013).

Electric vehicles work with zero emission and quietly. Regenerative breaking provides longer lifetime for breaks, and electricity generated from kinetic energy charges the batteries. Maintenance and fuel costs are lower comparing to that of the conventional vehicles. Since there are not any moving parts, there is no need for adjustments or oil change. Their high cost is their disadvantage and the battery weight in vehicles is also limiting. Conventional vehicles might cover distances of 500–600 km per one full fuel tank, while EAs can cover only 150 km distances with one charge. Also, charging time takes around 3–4 h, even using the high speed charging devices.

Fuel cell vehicles work with a 60–70 % higher efficiency comparing to conventional vehicles. Energy generation continues as long as fuel and oxidant are provided to the system. They can compute with EA on distance coverage. They can turn energy into electricity directly. Their emissions and maintenance costs are low. But it is necessary to decrease the costs of fuel cell system, process, and infrastructure (especially catalyzers). Electrical stability, fuel systems, reliability, hydrogen storage system, and safety technologies are suitable for development.

When comparing the electrical and fuel cell vehicles according to the cost of the electrical generation of electric vehicles based in kWh, it is seen that the fuel cell vehicles are the cost-effective systems (Veziroğlu 2011; Fadel and Zhou 2011; Marmara Araştırma Merkezi 2003). Fuel cells and electric vehicles systems are the

strongest candidates for alternating internal combustion engine vehicles in automobiles.

As a matter of fact, fuel cells and batteries have specifications to balance the disadvantages of each other, if they are used together. In fuel cells and hybrid electric (battery operated) vehicles; fuel cell systems increase the distance coverage by providing necessary power for stabile drive speed, they also provide the peak power for speeding on battery start time and storage the regenerative breaking energy. Fuel cell decreases high costs of the vehicles operated with battery which is their biggest disadvantage, and also increases the performance of power transfer and energy efficiency as well (Gao and Chris 2007; He et al. 2008; Neffati et al. 2013).

8.2 Hybrid Electric Vehicle Systems

Fuel cell-battery hybrid systems are consisted for the fuel cells as the power supply, the batteries as energy stores, and the electronic control unit for the power management. A fuel cell-battery hybrid system and the system units can be seen in Fig. 8.2.

There are important advantages of developing hybrid systems for FC-based vehicles: (1) To decrease the cost and weight of whole system, (2) to solve the FC's incapability problem of responding sudden power request, (3) to develop fuel economy, (4) to decrease heating time in order to work with a full capacity, (5) to decrease physical limitations that reduce FC system stability, (6) to provide safe working points by preventing to go up on higher voltage levels, and (7) to make FC work properly by providing necessary peak power through battery. On the other hand, the most important disadvantage of hybrid systems is that the vehicles and its control system are very complicated. Advantages and disadvantages of fuel cell-based hybrid systems can be understood by analyzing the role of energy storage systems (Bayındır et al. 2011; Arce et al. 2009; Bubna et al. 2010a, b; Bizon 2011a; Rodaz et al. 2005).
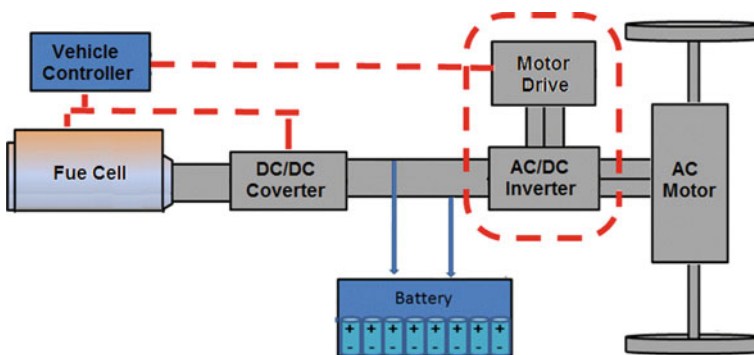

Fig. 8.2 Configuration of a hybrid system

8.3   Power Management Unit in the Hybrid Systems

It is essential to use power electronic technology in systems that use different energy sources especially like hybrid systems. In the hybrid systems, energy resources and component outages such as conversion, transfer, staging, resource selection, and control can be managed using power electronic.

In hybrid systems, it is required to optimize the performances of different energy units using power management systems. The voltage levels and dynamic characteristics of the energy generation and storage units are different. Power management systems of vehicles need to be combined with power converters. Size of the energy storages and controlling the energy flow are key parameters in order to maintain better fuel efficiency (Bizon 2011b, c).

Thereby, the energy management of hybrid system maintains more efficient working conditions for fuel converter, and it reduces the losses on discharging and energy storage processes, by doing that it increases the total fuel conversion efficiency of vehicle.

8.3.1   Drivetrain

In the vehicles, power is delivered to the wheels by the support of drivetrain. Some of the basic components of drivetrain are; clutch, gear box, shaft, rear axle, differential, transaxle, and brakes. If we include power sources such as engine, battery, or fuel cell, these systems would be called as powertrain. Simulation and design of the propulsion system of vehicles differ accordingly to their test drive (Ryu et al. 2010; Ogden et al. 1999; Doucette and McCulloch 2011). Two different types of driving cycle can be mentioned; highway driving cycle and city driving cycle. During highway driving cycle, idle time is very little or nonexisted and speed difference of the speed is not very large. During city driving cycle, idle time is constant and speed of the vehicle varies a lot. In the hybrid car tests, drive cycle recognition (DCR) as a vehicle control strategy more advanced is applied. The control strategy affects the performance of electrical vehicle more than that of the ICE vehicles.

Generally, it can be mentioned six different EV power flow configurations (Fig. 8.3). Fuel cells are used as primary or secondary energy generators depending on the power design of vehicle. As seen in Fig. 8.3a, EV configuration includes a gear box and clutch just same as ICE vehicles. In Fig. 8.3b, fixed gearing was used in order to reduce mechanical transmission weight and size. In Fig. 8.3c–d, use of the moving parts is shown as simplified with integrated gearing-clutch-differential. Figure 8.3e shows the system without a driveshaft that makes power transmission directly from the engine and gear. In Fig. 8.3f, traction motor is designed to be directly inside of wheels. Different configurations should be selected in order to
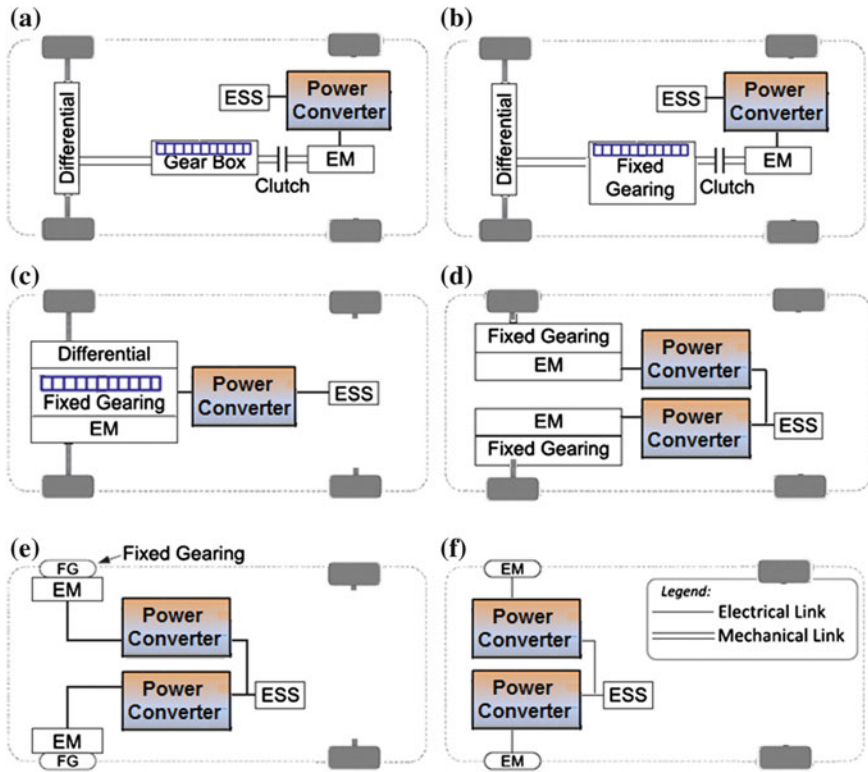
Fig. 8.3 The drive trains architectures on EV: **a** conventional drive line with clutch, **b** drive line with single-gear transmission without clutch, **c** drive line with integrated fixed gearing and differential, **d** drive line with two separate motor sand fixed gearing, **e** drive line with fixed gearing and motor, **f** in-wheel drive (Tie and Tan 2013)

provide different driving sets, as if the vehicle is being used in the city or on the highway (Tie and Tan 2013; Andaloro et al. 2013).

8.3.2 Converters

There are four different kinds of converters: DC–DC converter, AC–AC converter, inverter, and rectifier. Tie et al. defined five types of bidirectional DC–DC non-isolated converter topologies that are used in EV applications (Fig. 8.4). These converters are: stepped buck-boost, half bridge, Ćuk, SEPIC/Luo, and Split-pi (Tie and Tan 2013).

In HEV applications, it is desired to show low oscillation and have flexible tolerance in order to reach higher performance. For this purpose the interleaved converter, hybrid switched-capacitor, bidirectional DC–DC converter, power swap,
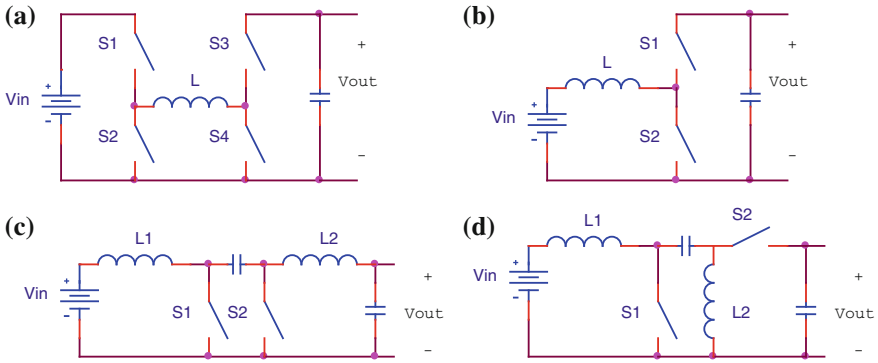
Fig. 8.4 The configuration of available bidirectional DC–DC converters: **a** cascade buck-boost, **b** half-bridge, **c** split-pi and **d** SEPIC/Luo
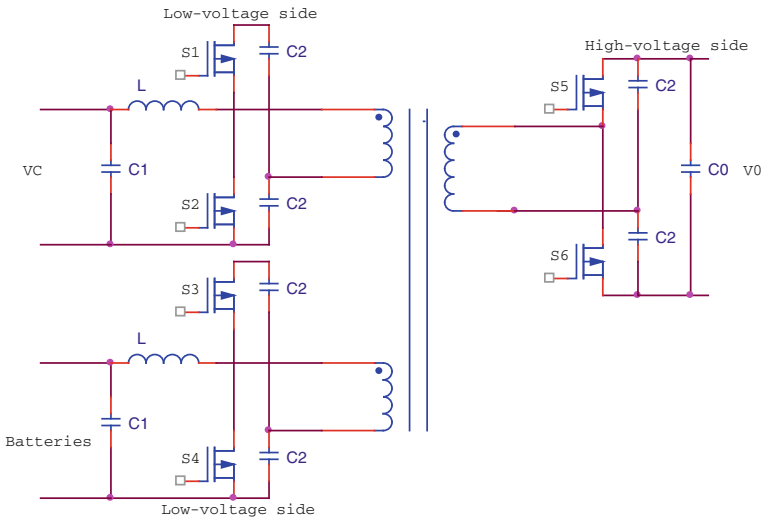
Fig. 8.5 Configuration of bidirectional DC–DC multiplier/divider converter (Tie and Tan 2013)

source selection on half bridge converter, Z-source network, bidirectional DC–DC multiplier/divider converter were developed (Fig. 8.5) (Tie and Tan 2013).

8.3.3 Power Management

In a hybrid vehicle design, it is expected to provide following criteria by controlling the energy conversion; maximum fuel economy, minimum emission, minimum system costs, and high drive performance. The purpose of the control of fuel

cell /battery hybrid vehicle control is to deliver the energy that transferred from the battery to the fuel cell with minimum lost possible. HEVs include the mores electrical components than EVs. In order to maximize the energy efficiency, to prevent the changes on the fuel cell conditions and to lengthen its lifetime, the fuel cell should be working steadily limited by the system. DC–DC converters provide the maximum power flow, nominal working for fuel cell, and setting the maximum power (Bayındır et al. 2011).

The power delivery of the vehicle can be designed by the simulation models. In order to make these models work, several parameters about the vehicle should be known. But it is impossible to model a complex design such as a vehicle with a fast and simple modification. Simulation models that are adjusted to system parameters, fast and repeatable are being developed in order to optimize the power delivery design of hybrid vehicle (Brown et al. 2008). Functions of such power-control modeling, the subsystems, and their functions are listed as: fuel cell subsystem, battery subsystem, load combiner subsystem, traction motor subsystem, hybrid controller, accessories subsystem, wheel/vehicle subsystem (Fig. 8.6) (Brown et al. 2008; Corbo et al. 2006).

Fuel efficiency in a vehicle is depended on this use or possible to use data. Total performance of the vehicle can be regulated using and analyzing these data. Accordingly that it is known that the controls include based on event-based or time-based conditions. Hybrid components can be controlled in two ways: rule-based (RB) and optimization-approached controls. Rule-based (RB) control is a control system that based on both mathematical model, predefinitions of driving circuits, loading level strategy of vehicle, and human experiences (engineer
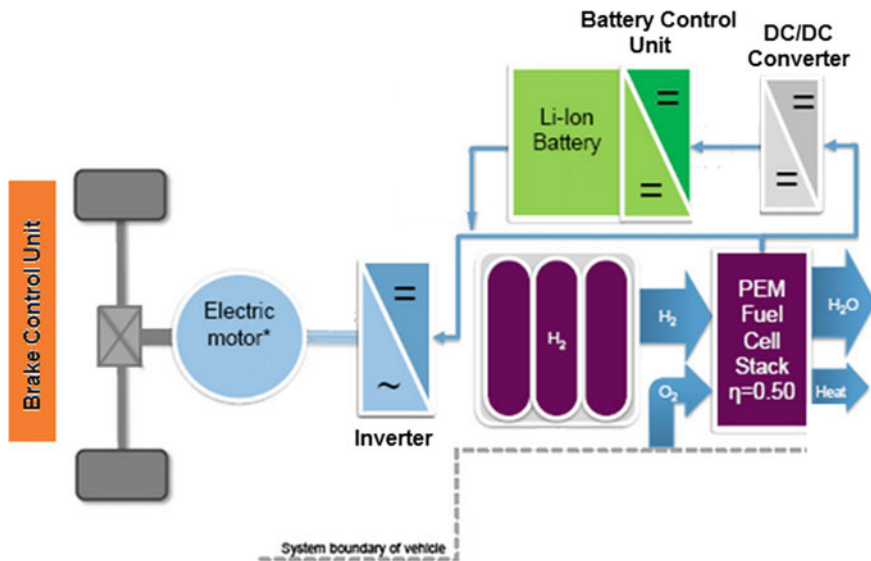

Fig. 8.6 Components of the hybrid system

knowledge) and skills. Optimization-approached control depends on analytic or numeric studies. In this way, it is clearly seen that is possible to minimize the cost function.

The most common method is the fuzzy logic control, RB type control (Kısacıklıoğlu et al. 2009). This method was developed based on the state of charge of battery (SoC). Another method depends on optimization of the vehicle's fuel consumption (Gao and Chris 2007). The power distribution optimization is made between fuel cell and battery by minimizing fuel consumption. In addition to that, there are new approaches where the fuel flow rate is used instead of the fuel consumption (Kim et al. 2010). The basic difference among the control methods is how to provide continuity of battery's charging level. Some control methods charge–discharge batteries more than others do. SoC is important for the lifetime of the battery, in addition to the charging battery, it will also decrease the total fuel efficiency. Over charging is caused by unqualified control schemes. Therefore, it is understood that power management strategies and control units developed for battery-fuel cell hybrid systems should be sensitive. Power management should provide a good balance between battery lifetime and fuel efficiency.

8.3.4   Source Selection

Hybrid energy storage systems (HESS) consist of batteries, ultracapacitors, supercapacitors, and likewise energy storage components. Because in a DC source most of the energy storage systems are used, DC-Bus system can be analyzed as a HESS example system. In DC-bus system, bidirectional DC–DC converter is being used to provide bidirectional energy transfer and stepping HESS. Source's and power outlet's peak power are considered. Power differences of converters cause a difference among the cost of power semiconductors, inductors, and total cost (Prakash et al. 2009; Kuperman and Aharon 2011; Burke 2007).

8.4   Fuel Cell-Battery Hybrid Systems

In the literature, it is seen that hybrid system studies are made for PEM fuel cells. But in upcoming years, usage of liquid fuel cell (Methanol, ethanol, hydrazine, Borohydride, etc.) will spread. In systems using sodium borohydride, methanol, etc., liquid fuels (DMFC and DBFC), the fuel cell can be used both as a active or passive type. In passive designed systems, it is simpler to maintain the system control, while active fuel cells need a strong system control. It is expected to minimize system control and to provide microprocessors working with higher performance. Otherwise, system efficiency will be unacceptable. In this kind of fuel cell-battery operated hybrid system, there should be control units such as fuel cell index, fuel booster pump, gas separators, fans, heat, concentration sensors, etc.

(Kim et al. 2010; Zhang and Zhou 2011; Lee et al. 2004; Saha 2011; Hwang et al. 2012). It is seen that control process is a hard and complicated procedure. In Fig. 8.7, control processes are shown for gas-fed and liquid-fed fuel systems (Kim et al. 2010).

8.4.1 Energy Management on Hybrid Vehicles

Renewable energy resources, storage units, and power management of power electronic which converters as interface units between the network usage are essential for the energy efficiency and the system reliability. It is known that the energy storage units in the fuel cell hybrid vehicles such as battery and super capacitor are going to be important factors on increasing the system dynamic performance and reducing the costs. Characteristics of the energy storage components and the voltage levels can differ according to the energy source, and the energy management systems are needed for the power cycle (Fig. 8.8). In order to achieve better fuel efficiency, sizing energy storage and controlling energy flow are essential (Lai and Nelson 2007; Zhang et al. 2012).

For now, the highest registered fuel cell efficiency is 98 %. But there are not any prestudies for bidirectional FC/EV applications. There are struggles of using high efficiency DC–DC converters on applications with wide voltage input distance and high power need. Silicon carbide (SiC), gallium nitride (GaN) magnetic components, and semiconductors are thought to be making a big difference (Zhang et al. 2012).

In many vehicles, including hybrids as well, the best way for energy efficiency is using the fuel directly for driving power. In the internal combustion engine vehicles, energy flows from the propulsion transmission line through tires. In fuel cell vehicles, best way for energy flowing is the same way, from fuel cell, conductor, or engine through the tires. Two essential futures in energy management are; "High power DC–DC converters" and "bidirectional flow" (Fig. 8.9).

(i) High power DC–DC converting is the nature of power converting energy management. In some fuel cell vehicle systems, power cycle is time adjusted for pairing bus tension and energy output of the fuel cell. Thus, high power cycle efficiency becomes essential, because it is related directly with fuel efficiency of the vehicles. High power DC–DC converters, designed and developed according to keying and passive components, are used for the hybrid vehicles.

(ii) Bidirectional power flow activates the power flow relatively during vehicles starting in order to regain breaking energy. Regained energy during breaking, as far as it is tempting, disperses and disappears because of heat on breaking. Saved energy during breaking is given to vehicle by fuel conversion system. Thus, energy management efficiency was maintained during power conversion (Lai and Nelson 2007).
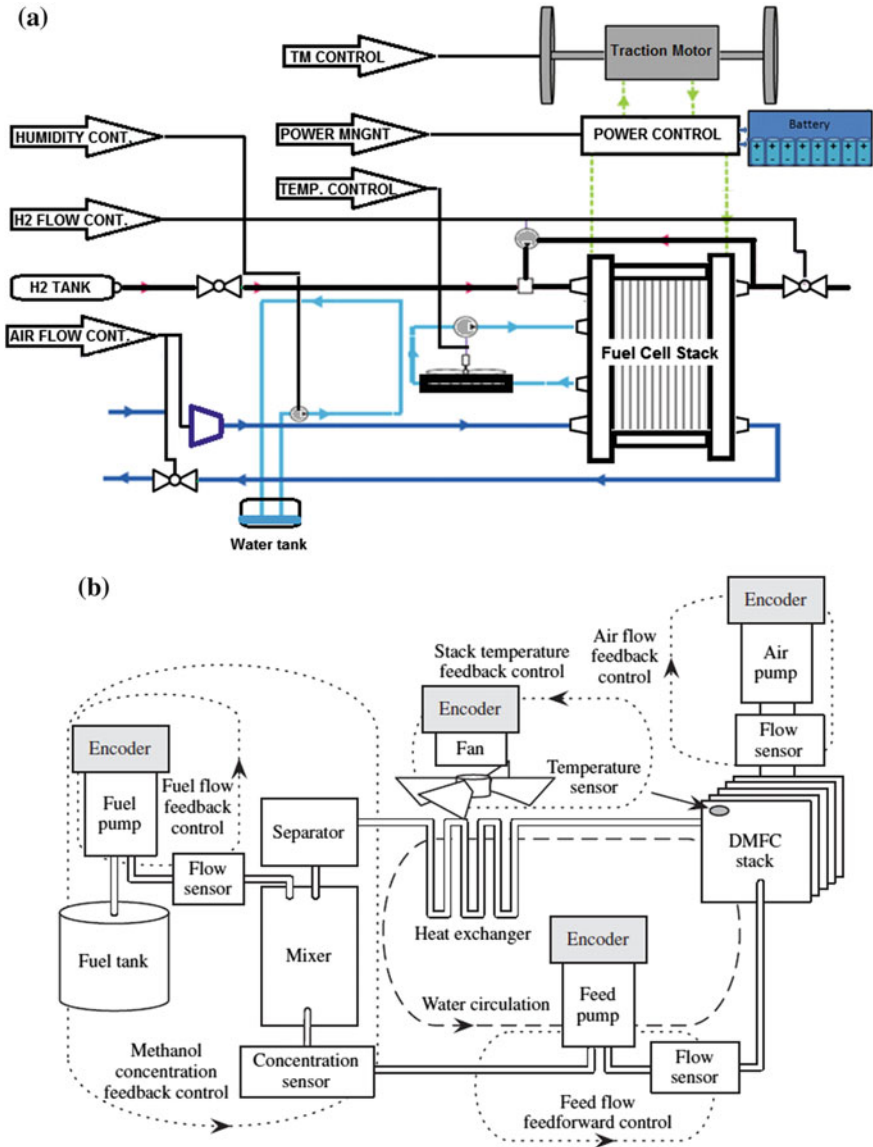
Fig. 8.7 a Schematic view for control units in PEM Fuel cell system. **b** Balance of Plant (BOP) system in liquid-fed fuel cells (Kim et al. 2010)

8.4.1.1 Energy System Configuration on FC-Based Hybrid Vehicles

Fuel cells have a large loading scale, but when it is slightly loaded, parasites occur in fuel cell system and efficiency decreases. For this reason, fuel cell vehicles'
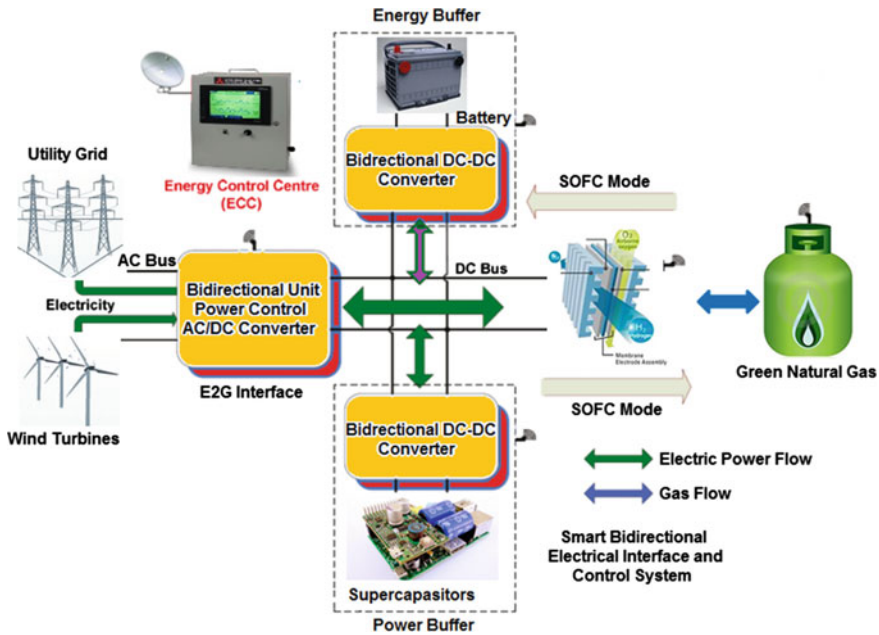
Fig. 8.8 Block diagram of a fuel cell-battery and supercapacitor powered line-interactive renewable generation system (Lai and Nelson 2007)

loading levels and loading during breaking become essential for efficiency. Fuel cell vehicles in low temperature environments are providing energy storage in addition to generate power when they are moved. Hybridization level differs according to vehicle's necessities; while using 70–90 % of saved energy, energy saved during breaking equals to 10–30 % (Lai and Nelson 2007). Energy management in FCHV can be made by bidirectional DC–DC converters or without any converters (Fig. 8.10).

Jhin-Sheng et al. developed energy management system for a 100 kWh system which can be seen in Fig. 8.11. In Fig. 8.8a, high voltage (HV) is provided by primer coiled low voltage (LV) accumulators. In Fig. 8.8b, it is provided by low voltage source and high voltage accumulators. In first design, it is necessary to have a 20 kW bidirectional DC–DC converter for accumulator management. In second situation, unidirectional boost converter unit would be enough for accumulator's charging. But accumulator will need 80 kW. Even just it has a more suitable converter; bidirectional DC–DC converter with 20 kW is more advantageous, because of its semiconductor power, coil value, and cost. **As a result, DC–DC converters are more useful on energy management units** (Lai and Nelson 2007).

Fig. 8.9 Energy managment
models for HEVs **a** high
power and **b** bidirectional
DC–DC converter
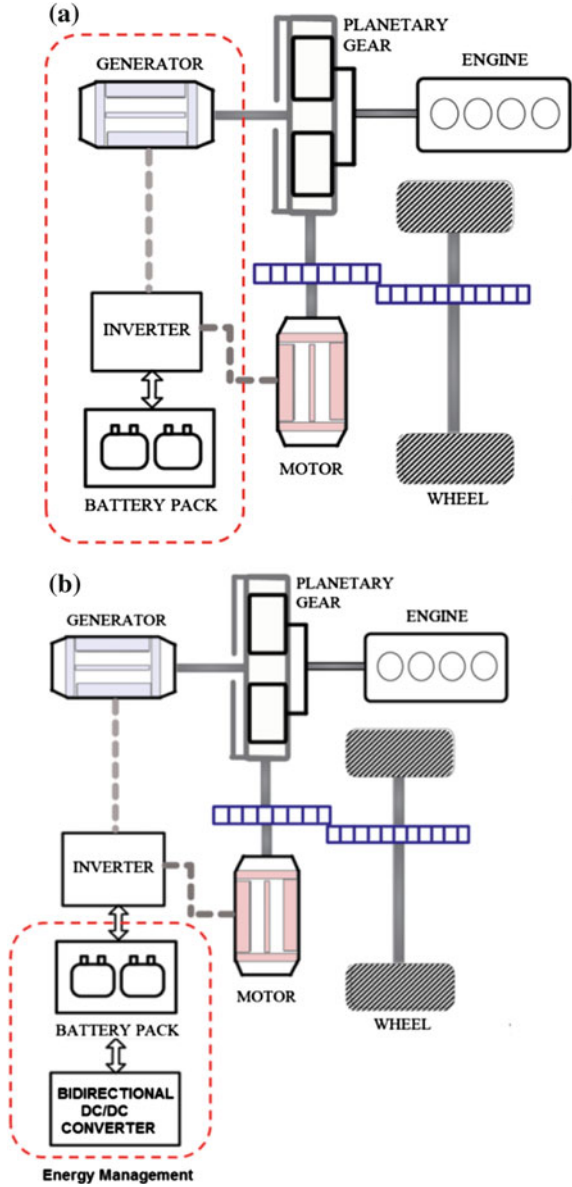
8.4.2 Bidirectional DC–DC Converters

Bidirectional DC–DC converters are classified as three types in according to energy
sources' placement; buck type, boost type, and buck-boost type. In Buck type,
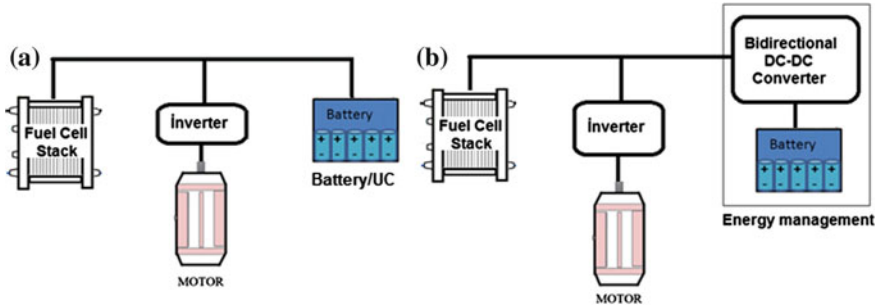energy storage placement is high voltage while boost units' is low voltage.

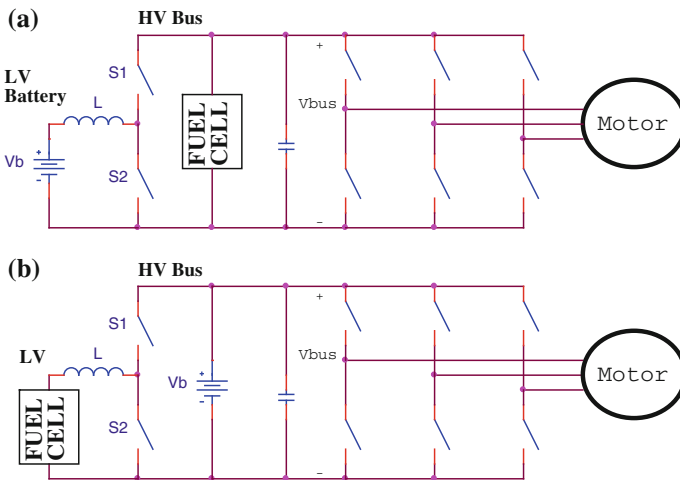Fig. 8.10 Energy management with and without converter

Fig. 8.11 DC–DC converter **a** high voltage fuel cell with low voltage battery and **b** low voltage fuel cell with high voltage battery

There are five types of HESS and converter regulation topologies. They are the passive parallel connection, one bidirectional DC–DC converter in series, two bidirectional DC–DC converter in series, two-input bidirectional DC–DC converter in parallel, and multiple-input ZVS bidirectional DC–DC converter. Passive parallel connection between the sources is the simplest and most inefficient energy management topology. Latest regulation suggested by researchers is multiple DC–DC converter topologies which has high power efficiency, high reliability and long lasting (Fig. 8.12). This converter topology provides optimum power share between the sources. But its total converter weight is bigger (Tie and Tan 2013).
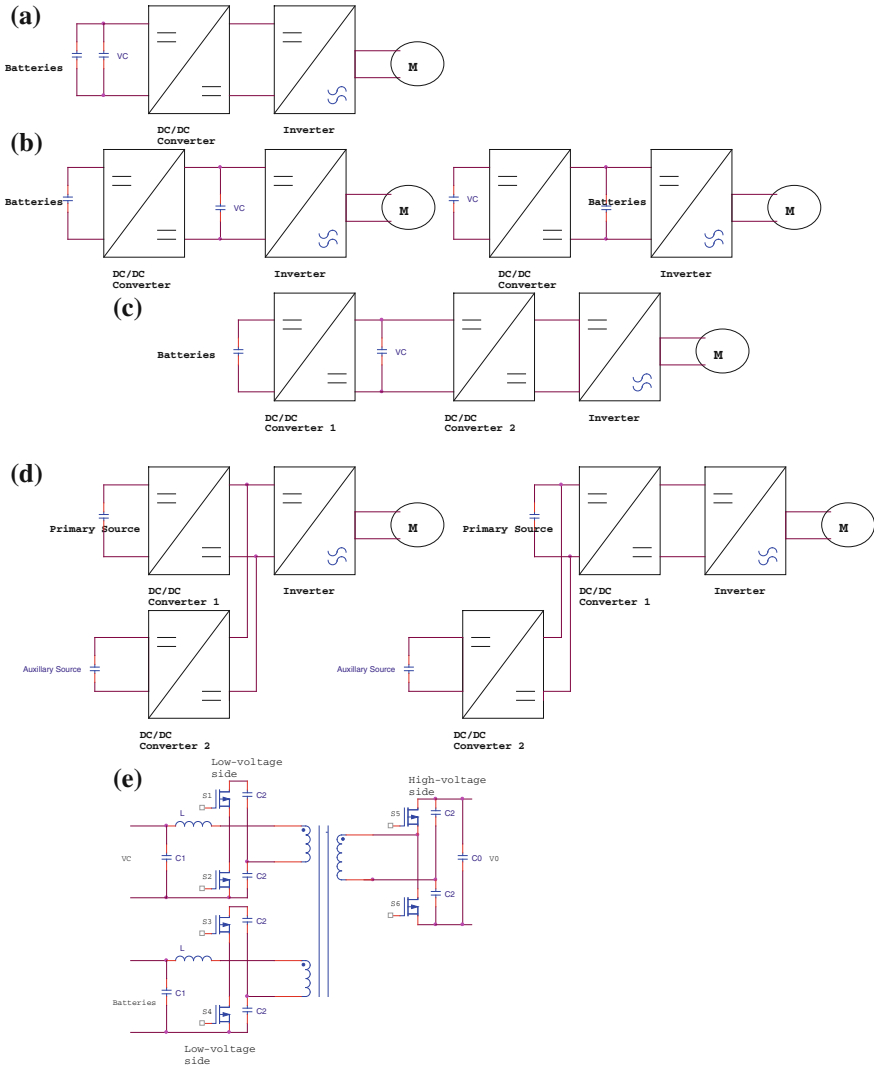
Fig. 8.12 The configuration of low component control systems: **a** passive parallel connection, **b** one bidirectional DC–DC converter in series, **c** two bidirectional DC–DC converter inseries, **d** two-input bidirectional DC–DC converter in parallel, **e** multiple-input ZVS bidirectional DC–DC converter (Tie and Tan 2013)

8.4.2.1 Nonisolated Converters

Bidirectional DC–DC converters can be isolated or nonisolated. In nonisolated units, the high voltage bus tension (Vdc) should be higher than low voltage tension (Vin). During high voltage low tension accumulator charging, switches and diodes

are serving for buck unit. During accumulator discharging, it distributes the energy in boost unit from low voltage (LV) to high voltage (HV) bus (Lai and Nelson 2007).

It is converted into buck type bidirectional DC–DC convertor for HEVs' and FCVs' driving motor systems by placing a battery on high voltage part of unit in Fig. 8.13. DC bus voltage rarely becomes lower than the input voltage if the driving motor needs higher voltage for high speed and high torque. But, if input voltage is on the same level with bus voltage, it needs a buck-boost type converter. In Fig. 8.14, there is a buck-boost type DC–DC converter that can be used in high power EV applications. Buck-boost type converters are more expensive and have lower efficiency since they use an extra key. But if battery voltage and DC bus voltage are on the same level, it is necessary to use a buck-boost type converter (Lai and Nelson 2007).

8.4.2.2 Isolated Converters

In isolated DC–DC converters, isolation protects the conversion. Bidirectional DC–DC converters should be isolated, there are several bidirectional isolated DC–DC converters. There are LV and HV corners on a voltage resource, therefore soft power transfer is made by defining these corners to voltage resource. There are two types of isolated bidirectional DC–DC converters (Fig. 8.15).

Power pack on low voltage or high voltage. When inductor works on high voltage corner, high voltage semiconductor is needed. In bidirectional DC–DC converters, inverter or rectifier might be used. On inverter mode, power transferred by switches, on rectifier mode it is transferred by diodes. If there is power mosfet being in use, in occurrence of a little voltage reduce, it is transferred through backflow direction under synchronized rectifier mode. There are also three main current sources converters (Fig. 8.16): Full bridge, half bridge, and push–pull (Lai and Nelson 2007).

8.4.3 Multi-Phased DC–DC Converters

8.4.3.1 Nonisolated Multi-Phased Converters

In high power applications, a simple converter should be able to process multiple devices in a parallel way. As shown in the previous design, since it is allowed to rectify every voltage and tension, there should be a lot of phase pins. In nonisolated case, high powered multi-phased bidirectional DC–DC converters for HEV energy management systems have based two- and three-phased configurations. In Fig. 8.17, Bidirectional three-phased DC–DC converter with a phase angel of 120° is given (Lai and Nelson 2007).
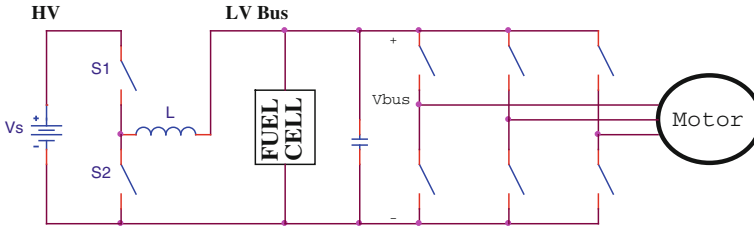
Fig. 8.13 Buck-type bidirectional converter for high power motor drive applications
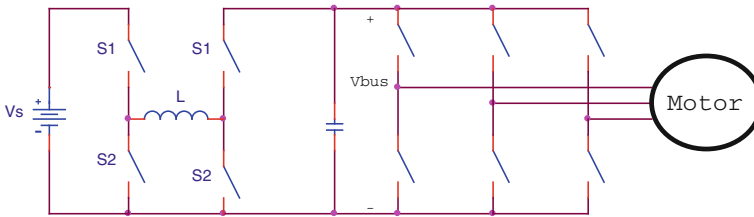

Fig. 8.14 Bidirectional buck-boost converter for EV applications
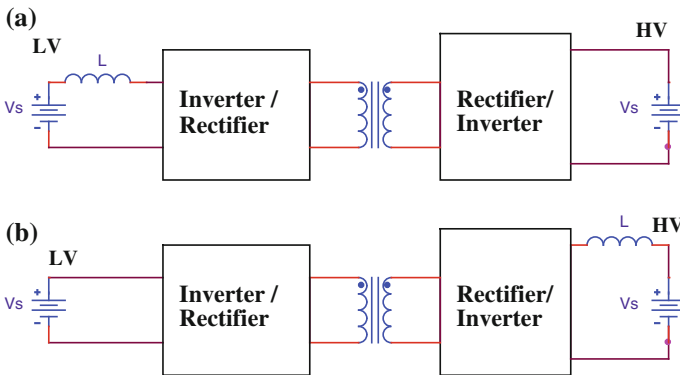

Fig. 8.15 Isolated bidirectional DC–DC converters **a** low voltage current and high voltage source **b** low voltage source and high voltage
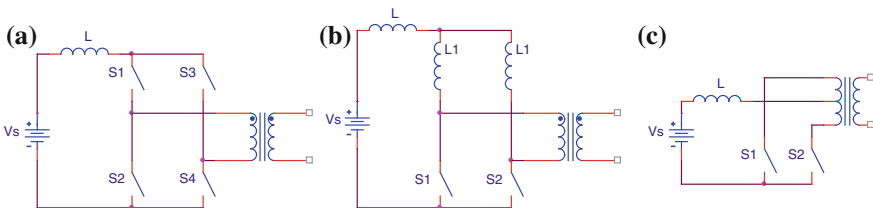

Fig. 8.16 Current source converters **a** full bridge, **b** half bridge and **c** push-pull

8.4.3.2 Isolated Multi-Phased DC–DC Converters

Three-phased converters were developed for high and low voltage (Lai and Nelson 2007). This three-phased converter receives voltage by low voltage, and tension by high voltage (Fig. 8.18). On higher power applications, three-phased systems can be widened to six-phased systems. Six pinned converters would be defined as V6 converters. Voltage regulating tension can be widened from 0° up to 120°. After 120° first voltage could be reset by other phase.

As a result; basic function of a vehicle's energy management power converter is providing bidirectional power flow between energy storage and inverter motor driver DC bus 1. Voltage level and battery size are the key factors for defining the converter unit. **The "High Power Bidirectional DC–DC Converter" is a basic component of energy management systems for HEVs and FCVs** (Lai and Nelson 2007).
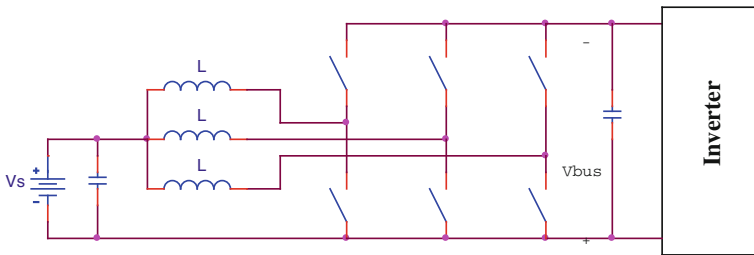

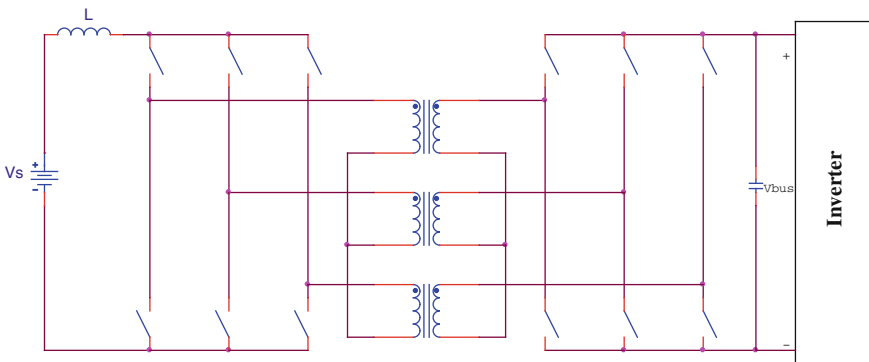**Fig. 8.17** Bidirectional 3-phase DC–DC converter

Fig. 8.18 Isolated 3-phase DC–DC converter

8.5 Liquid-Fed Fuel Cell-Battery Operated Hybrid Systems

PEM and direct liquid-fed (methanol, ethanol, borohydride) fuel cells work on the low temperature; therefore, they are really important especially for the portable applications. But storing hydrogen and struggles on refilling fuel makes it hard to use PEM fuel cells, even their advantages on costs, efficiency, and reliability. It is possible to generate hydrogen inside, but generating hydrogen from borohydride and likewise solid or liquid materials requires very sensitive temperature controls. Additionally, hydrogen flow, generated by this method, is not steady, and it is hard to receive changing charge or achieve sudden 'stop-start' process. Low temperature PEM fuel cell reformer unit is slow and inefficient. Therefore, it is not suitable for portable applications.

On the other hand, even stack control components of direct liquid fuel cells (DLFC) systems are more expensive than those of PEMFCs, DLFCs are more appealing because of their compactness, suitable sizes, and portability (Zhenith and Krewer 2010; Joh et al. 2008; Hwang et al. 2012; Sanlı et al. 2014). DLFC systems can be classified in three groups: active, passive, and semi-passive. A passive application field of DLFC, with no system balance (BOP) components, includes only systems with a few watts. An active DLFC is more powerful and efficient with a tight BOP control. But, BOP control is usually being left out, even it works safely and efficiently, and this study is out aim of the researchers. Even though BOP control should be an important part of the product development, there are not any significant published studies about it. In these systems, conditions below should be provided (Kim et al. 2010):

1. Working conditions of BOP systems, sources of the basic complications, and the control schemes to prevent those should be prepared
2. Voltage regulations and steady-flow working methods in DLFC stack and Li-ion battery hybridization should be prepared
3. BOP interface units and microprocessor interfaces should be defined
4. Real-time operating systems (RTOS) 32-bit RISC microprocessor and control software should be defined.

8.5.1 Active DLFC System

There is a complicated BOP system in Active DLFCs. An Active BLFC system developed in the Motorola's Laboratory is shown in Fig. 8.19. DLFC systems can be defined as below (Kim et al. 2010; Kamaruddin et al. 2013):
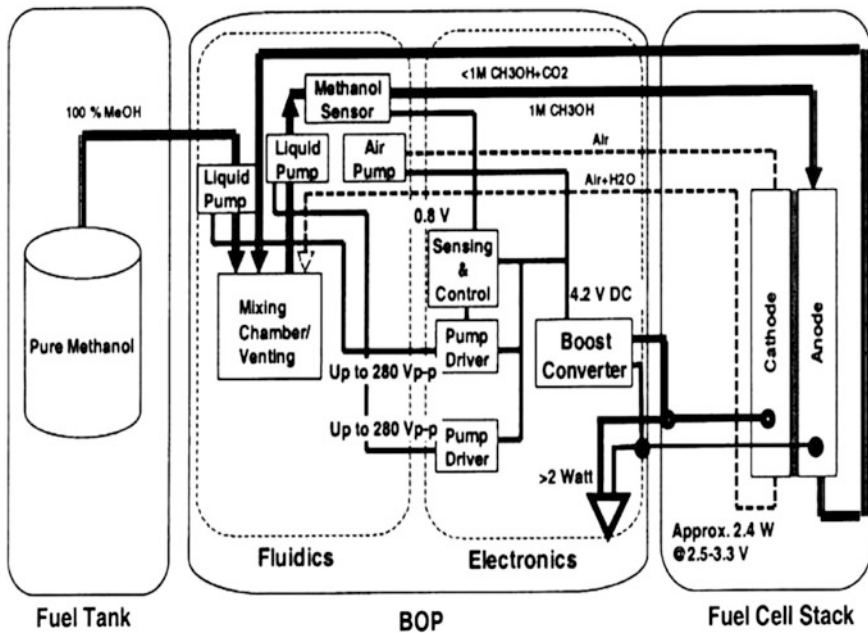
Fig. 8.19 Active DLFC system developed by Motorola Lab (Kamaruddin et al. 2013)

1. Fuel Management: In the active systems, fuel management is made by "Fuel Distribution Systems." Concentrations of the liquid fuels are the most essential parameter for the cell performance. Diluted fuels are used in DLFCs. Nevertheless fuel is consumed by chemical reactions, and water can produced as a byproduct. This results in more dilution of the fuel and it affects the performance. Therefore, system should include pure liquid, and concentration control should be made.

2. Water Management: Electric is generated by the chemical reactions in DLFCs, and water can produced as a byproduct. Water production dilutes the fuel in anode, and water produced in cathode should be taken away from the system. Also, the amount of the water is being reduced by the steam generation by heating in stack. Water management is as essential as the fuel management for cell performance.

3. BOP Control: BOP control and stack management are complicated for both the high power and the low power systems. Power consumption of the BOP components and control units should be little. Energy-efficient BOP systems will make it possible to add a few more components to the system. Otherwise, total efficiency of the system will be unacceptable.

4. BOP Side Control Components: Fuel and oxidant flow speeds in DLFCs affect both the performance and the stack temperature. Controls should be made using liquid and air pumps, flow meters, heat sensors, and barometers in BOP system. Heat control in the system is an important factor for the water and the fuel management. This control can be made by fluid flow as well as by a fan.
5. Efficiency of BOP Control: Cost of the BOP control is expensive. But the cost is effective for active DMFC high power production. Best working conditions should be set in the laboratory environment for the DMFC system. But, it should be kept in mind that there can be several environmental changes can occur.

8.5.2 Passive DLFC Systems

Passive systems can work without power consuming active sensors and processors. Two-phased mass and heat flowing models were developed for passive DLFC in order to find out thermal effects (Kamaruddin et al. 2013). Mass transferring models made for anode, cathode, and membrane are essential for designing system and understanding the processing. Fuel feeding and concentration distribution in the passive systems are made using the natural convection capillary force and the gravity theories.

Passive DLFCs seem like suitable systems, because of their low costs, reliability, and compactness. But, there are problems in the passive air breathing and fuel distributing systems, because they tend to work as a total and DLFC should be modified to the stack behavior carefully. Additionally, passive DLFCs need more catalyzers than active DLFCs in order to provide desired performance, and this makes them more costly.

Passive system storage fabrication is simple, light, and easy. It is safer for portable applications, because it does not have any moving parts. Fuel feed should be made again for passive systems depending on the system volume, after certain amount of electricity is generated. Since liquid fuels (methanol, hydrazine, ammonia, formic acid, and diborane) are harmful for human health upon contact, it is necessary to prevent fuel leak in these systems (Demirci 2009).

Passive DMFC system is different than active DMFC system. Differences between passive and active DMFCs cause different applications. The issues considered are followed below such as:

1. In the fuel providing system, designing of the anode current collectors, the anode diffusion layer, and the nondrifted fuel cell have an important role on mass transfer.
2. Increasing oxygen feeding on cathode and water removal management are important issues.
3. One of the most important issues is to reduce the heat dissipation.

8.6 Hybrid Vehicle Applications

In this section, some automotive applications have been selected from the literature and given as examples for the fuel cell-battery hybrid powered systems. They are the light vehicles applications; Buddy El-Jet Hybrid Vehicle developed by Hang and Chang (2012) in Taiwan, Microcab H2EV Hybrid Vehicle supported by the CABLET Project in England (Fisher et al. 2012), Norwegian Buddy El-Jet Hybrid Vehicle designed by Andreasen et al. (2008) in Denmark and Mini Train Hybrid System tested and demonstrated in Taiwan (Hsiao et al. 2012). The fuel cell-battery hybrid systems have been under investigation yet. In the next section, the hybrid vehicles have been investigated in terms of the system design, power management, road tests, and efficiency. All systems presented consist of a proton exchange membran fuel cell system, battery pack, powertrain system, and a connection strategy to power the traction of an electrical car. Although they are not being the perfect vehicles, requiring further work with major drawbacks such as connection and management of the hybrid components (fuel cell, battery, supercapacitors, motor drive, and electrical systems), reducing the size of fuel cell and the battery, the regenerative breaking, the heating strategy, their tests and the demonstration results are satisfactory. Four hybrid systems are given in the following section in detail.

8.6.1 Buddy El-Jet Hydrogen Fuel Cell Li-Ion Battery Operated Hybrid Vehicle

In this study, characterization study of a fuel cell/battery hybrid system created by Hwang et al. for an electrical vehicle is analyzed as an example. Fuel cell/battery hybrid system created by Hwang et al. Hwang is tested by using Toyota Autobody Coms's electric motor and transfer system together (Figs. 8.20 and 8.21) (Hwang and Chang 2012). Main components of this system are; one fuel cell stack, air ventilator, water pump, membrane moisturizer, Li-ion battery package, microcontroller, DC–DC convertor and H_2 storage tank. Microcontroller works with the highest efficiency by setting the optimum working conditions voltage. In the driving tests according with the driving conditions, the most suitable hybrid was implemented. System efficiency is calculated 46 % as a function of gross power output.

8.6.1.1 Power Management

(i) Microprocessors: It is necessary to use microprocessors in hybrid systems with the suitable algorithm. In this system, voltage, current, temperature, and pressure signals were recorded using Intel 8051 microprocessor. It can also control outer processors like air fan, solenoid valve, and cooling fans. In
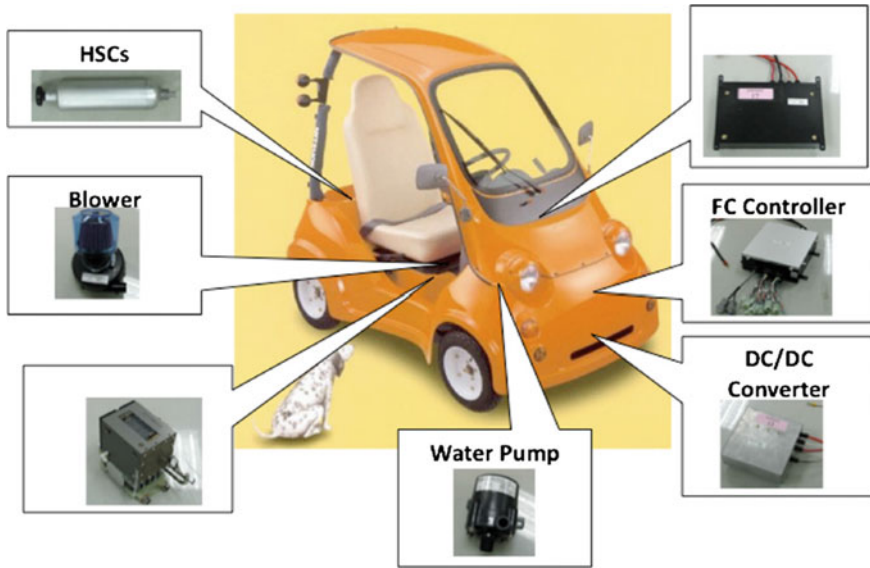
Fig. 8.20 Key components for a light electrical vehicle (Hwang and Chang 2012)

addition to that, it can save battery's SoC in order to control charging and discharging currents and preventing Li battery from over charging and discharging. Most importantly, microprocessor makes the fuel cell work on the voltage that it can provide power most efficiently.

(ii) DC–DC Converter: While electric motor's working voltage is 72 VDC, fuel cell's nominal voltage is 48 VDC. Therefore, there is need for boost or buck type voltage converter. DC–DC converters provide power transfer between different power sources and charges. Along with maintaining voltage stability, DC also has the futures as follows: (a) preventing fuel cell stack's damage because of concentration polarization by guarantying fuel cell's output voltage being higher than cut-off voltage (40 VDC), (b) protects Li-ion battery from over charging/discharging by regulating charge current on different SoCs, and (c) raises the voltage to 72 VDC in order to drive engine and charge Li-ion battery (Hwang and Chang 2012).

8.6.1.2 Road Drive Tests

Road drive tests were made on National University of Tainan. Hybrid power dynamic behavior under four different driving conditions is shown on Fig. 8.22 (Hwang and Chang 2012). A light vehicle was successfully driven by Li-ion battery and PEM fuel cell hybrid power. While battery was suppressing incapability of the fuel cell, it also saved extra energy occurred during breaking. Heat occurred inside
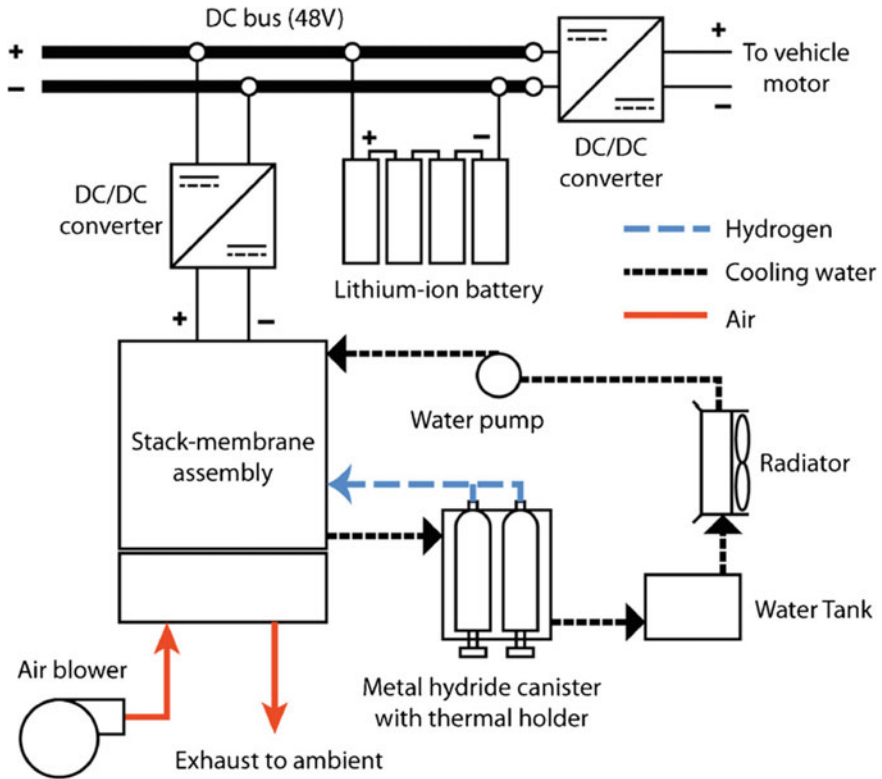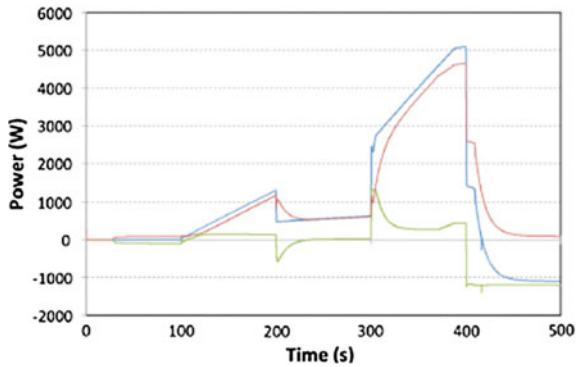
Fig. 8.21 Schematic drawing of the fuel cell/battery hybrid power system (Hwang and Chang 2012)

Fig. 8.22 Hybrid power dynamics during the road driving test (Hwang and Chang 2012)

the fuel cell was fed into metal hydride tank, and it provided hydrogen desorption, it also raised the efficiency up to 46 %.

8.6.2 Prototype Hydrogen—Electric Hybrid Microcab H2EV Vehicle

In this study, Microcab H2EV type hybrid vehicle tested under CABLED project that started in 2009 in England is analyzed (Fisher et al. 2012). This vehicle controlled by computer; therefore, performance, distance, driving behavior, and battery charging infrastructure information about hybrid vehicles was gathered. Microcab H2EV hybrid vehicle can be seen in Fig. 8.23. Light vehicle includes electrical driver (120 A nominal from Sigmadrive), a LiFePO$_4$ battery from Lifebatt.co.uk with 4×24 cell bank (nominal: 15 Ah 3.3 V/cell, 60 Ah 79.2 V/bank), a high temperature PEM fuel cell (HTPEM) providing 3.2 kWe, hot air at 150 °C and the hydrogen tank of 0.6 kg 350 bar with 95 % pure hydrogen and the permanent Magnet DC motor (12.56 kW, 220 A nominal) from Lynch Motor Company (Fisher et al. 2012). Fuel cell has to provide all the power for traveling, own by own. On the other side, battery has to provide necessary peak need in the system, not the total energy (Fig. 8.24).

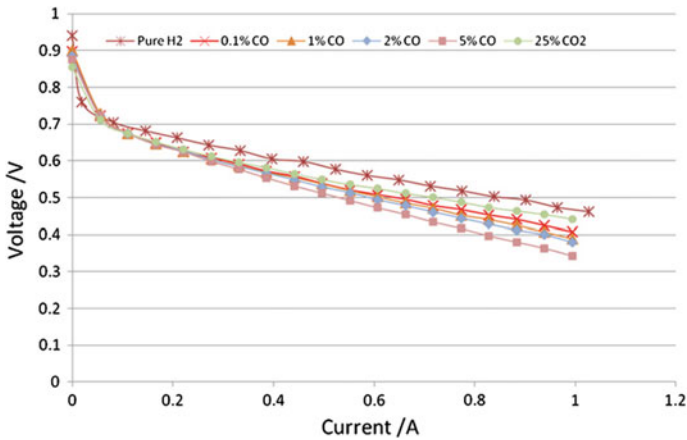**Fig. 8.23** Microcab H2EV hybrid lightweight vehicle (Fisher et al. 2012)

Fig. 8.24 The performance curves for the fuel cell stack (Fisher et al. 2012)

8.6.2.1 Power Management

(i) Electrical Interface System: An "I/O interface PCB (Printed Circuit Board) box" was designed to electrically integrate the fuel cell, battery, and motor systems and to allow operate the vehicle directly as an EV for testing purposes. A software-drive vehicle control unit (VCU) was added to the box in order to take charge of both the fuel cell and battery system. The complex electronic system was simplified using a CAN (controller area network) bus connection. The VAN can provide soma integration through CAN communication. It offers the finer controls and makes the system more manageable (Fig. 8.25).

(ii) Torque Monitoring Circuit: It is additional safety-related circuit. The vehicle system requires the independent monitoring of motor torque to check the torque output from the motor by two independent motor controller. The motor is isolated from the power should a fault be detected. Regenerative breaking cannot be used because of the current design of the circuit.

(iii) Testing of the system: The system can be checked visually by the diodes in the circuit by applying the 12 V power. It allows to find the faults occurred during the assembly, installation, and later. In the "I/O interface," the jumpers were used to force a relay function on the interface board echoed with LED indications. Therefore, the Microcab vehicle was tested for electrical performance after the road tests.
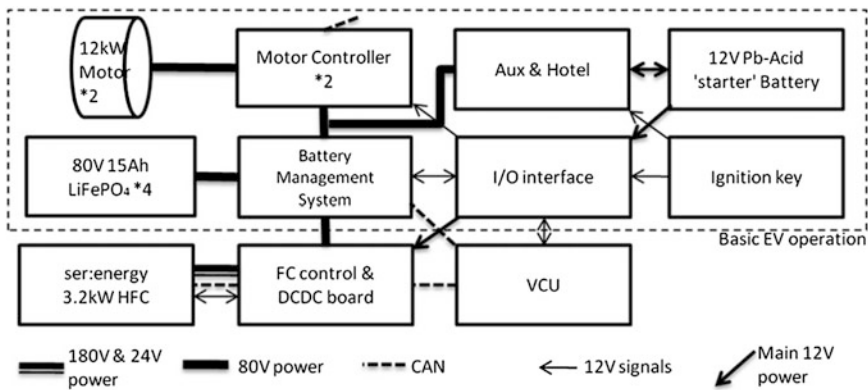
Fig. 8.25 Shematic illustration of the system detailing main power flows and lines of communication (Fisher et al. 2012)

8.6.2.2 Road Drive

System was tested on driving tires without moving or unnecessarily to be on the road. By this way, speeds up to 55 mph (88 kph) were simulated and driving screen was observed; by applying similar different torques break systems were tested. Later, Microcab vehicle tested for electrical performance before the road test. Before it was delivered to customers, nearly 600 miles (960 km) long road tests were made.

8.6.3 Norwegian Buddy El-Jet Hybrid System

In this study, high temperature PEM fuel cell was used to charge Li-ion battery (23 cells) package in an electric vehicle. 1 kW of serial connected fuel cell stack (37 V) was connected to six battery package (12 kWh) in parallel on the vehicle. Drive system of the vehicle was provided by Brushed DC engine with 13 kW, Curtis 1244 motor driver, controlled acceleration, breaking, speed, and general drive. Charge–discharge situation is controlled by the BMS (Battery Management System). Main components of the systems; Li-ion battery package, fuel cell system, metal hydride hydrogen storage tank, and air input manifolds can be seen on Fig. 8.26 (Andreasen et al. 2008). HTPEM fuel cell/Li-ion battery hybrid system's schematic view is given on Fig. 8.27.

Fig. 8.26 View of the vehicle's 3D model and basic systems (Andreasen et al. 2008)
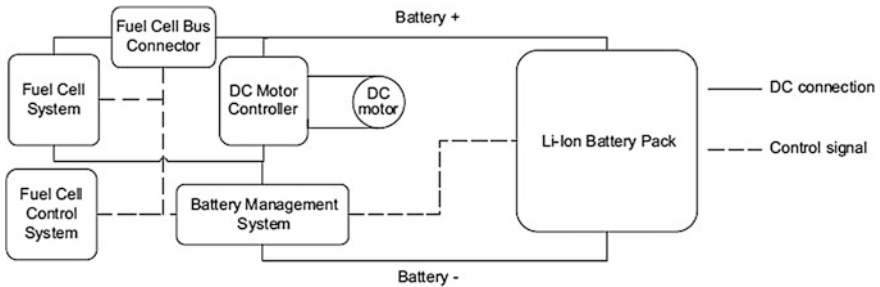

Fig. 8.27 Schematic view for hybrid electric system (Andreasen et al. 2008)

8.6.3.1   Power Management

When fuel cell was connected to battery, two keys were connected for each fuel cell. First one 0.2 Ω resistor is added for limiting the sudden current coming from fuel cell to batteries. Other one is connected to stacks directly and resistor is not attached. By this way, fuel stack voltage is limited at the beginning; connecting to the battery prevents large current peaks and low fuel cell voltages. Advantage of this kind of connection is preventing the loss caused by power electronics components like DC–DC converters. Fuel cell voltage is controlled by battery voltage and SoC.

Battery system is protected by battery management system (BMS), and this provides stable and reliable system processing as well as preventing thermal disperse during charging–discharging. Being BMS based, analog monitoring is made by fuel cell's galvanic separation, microcontrolling system, and protection of whole electrical system. Every single Li-ion cell is controlled by microprocessor and they are adjusted with fuel cell by being recorded by central controller. BMS decides for; fuel cell's connection time to system, deactivating fuel cell engine in presence of a problem. Fuel cell system's connection is cut by BSM when the battery is fully charged.

BMS fuel cell system works on these mods:

1. Starting and connecting fuel cell to the system (SoC = 80 %)
2. Stopping and disconnecting fuel cell (SoC = 95 %)
3. Disconnecting fuel cell (SoC = 99 %).

In an emergency situation, fuel cell system switches on to emergency mode and; stack connections are disconnected, hydrogen feeding is stopped, blowers provide high airflow, and stack hydrogen is cleaned out. When all the temperatures drops under 115 °C, fans are stopped, air input manifolds are closed, and air input to stack is blocked.

8.6.3.2 Drive Tests

Vehicle's charging tests are made. DC bus current is increasing on sudden acceleration and it decreases during slowing. During slowing, regenerative breaking of the vehicle is decreasing. Regenerative breaking increases battery voltage. Therefore, battery is charged from engine, and charging from fuel cell decreases.

Fig. 8.28 Fuel cell, voltage and DC vehicle current (Andreasen et al. 2008)
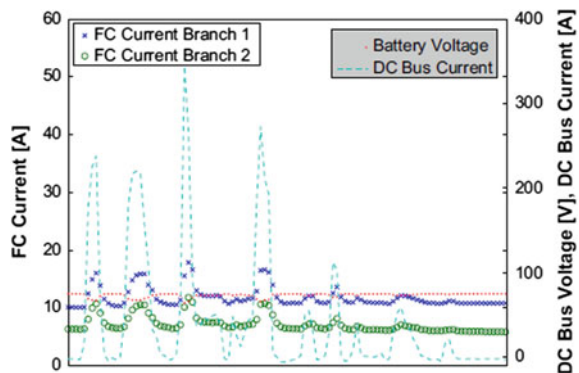
The fuel cell stack is restricted to deliver a current given by the voltage of the battery pack. The DC bus voltage and current provided fuel cell stack were plotted in Fig. 8.28 during the drive cycle.

8.6.4 Mini Train Hybrid System

In National Science and Technology Museum in Korea, a fuel cell-battery hybrid system-operated mini-train is developed for open air traveling purposes. This train is 18.4 cm width, 212 m length, and can work for 2000 h, and also can carry more than 70 passengers (Fig. 8.29). On this hybrid study by Hasio et al., fuel cell and lead-acid battery connected in parallel, and engine driver and all the electrical management units were coordinated for being able to carry passenger on daily basis.

System consist of: PEM fuel cell with air cooling, moisturizer, low pressure four metal hydrogen storage tanks, hydrogen generating module, and electronic control module. System's functional block diagram is shown in Figure. Fuel cell's total weight is 12 kg and electrical output is 22 V (200 W) (Hsiao et al. 2012).

8.6.4.1 Power Management

Current diagram of the electrical energy control system is shown in Fig. 8.30. After system started to work, battery voltage is determined. If the battery voltage is over 18 V, it provides power to charge. If it is lower than 18 V, fuel cell provides

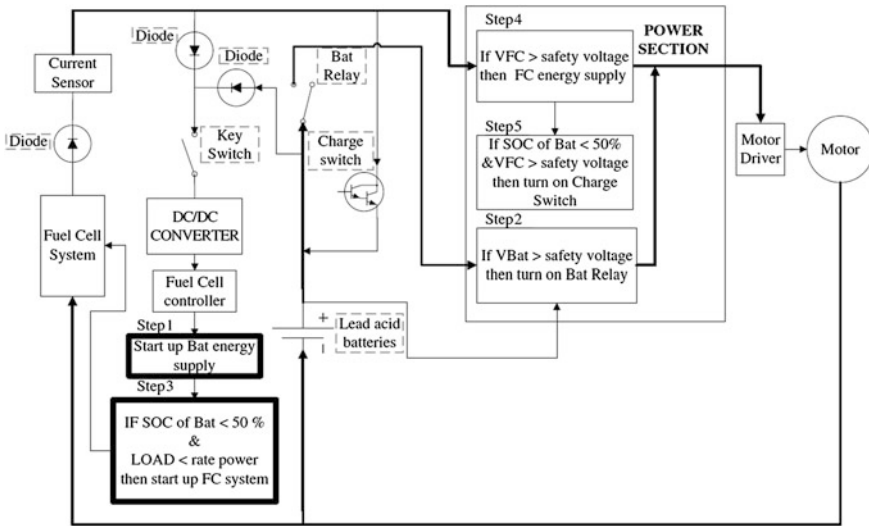**Fig. 8.29** Mini train during drive test (Hsiao et al. 2012)

Fig. 8.30 Current diagram of electric control system (Hsiao et al. 2012)

electrical charge and charges the battery at the same time. If the battery voltage is less than 50 % of SoC, it means it is lower than Rated Power and fuel cell starts to work.

If the Fuel cell goes over security voltage (18 V), fuel cell voltage provides electric charge and charge battery. When the battery voltage is full, fuel cell shutdown and charge is provided from battery (Hsiao et al. 2012).

8.6.4.2 Drive Test

While mini-train moving, system is controlled by lead-acid battery voltage. When battery is lower than 18 V, system switches to charging mode. Fuel cell's charge output power is 15–200 W. When mini-train is not working fuel cell voltage stays on 24.5–23 V. This can be seen in Fig. 8.31 A and B parts. When mini-train works the charge mode turns on. Both lead-acid battery and PEM fuel cell provide power to charge. Fuel cell's output power is around 275–315 W (B and C sections). Battery hybrid PEM fuel cell is affecting full system performance remarkably. If fuel cell stack output power is low, battery provides more power. System works 2000 h and provides 200 W power.
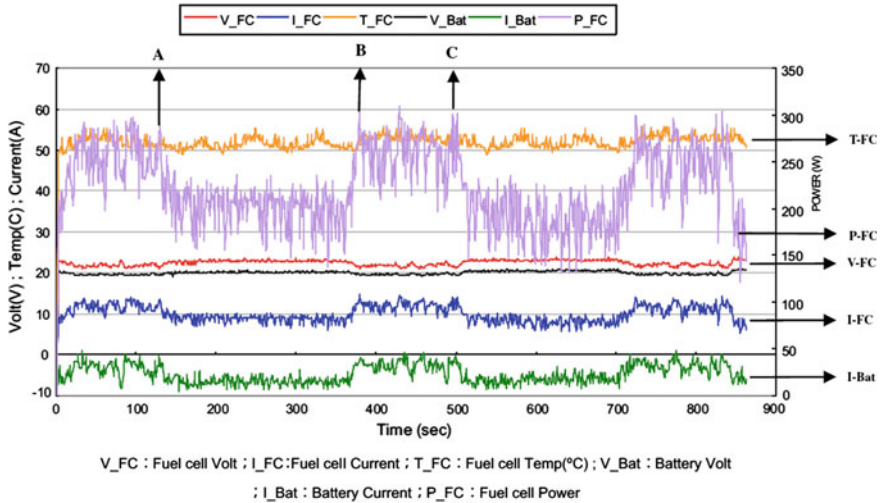
Fig. 8.31 Mini train drive test (Hsiao et al. 2012)

8.7 Conclusion

In the study, integration of fuel cell, battery, and electric engine have been investigated and three vehicle applications have been summarized. The most basic integration issue is the communication between; driver, VCU, lithium battery package, engine control unit, and fuel cell. Units are designed, configured, and communication between the transferring organs is tested. But in all studies, battery's performance on different SoCs and current charges should be determined. More advanced balance and optimization studies should be made between the battery and fuel cell. Fuel economy of the hybrid systems is rather low, yet. Efficiency needs to be optimized.

Fuel cells look promising for solving problems of the internal combustion engines. The unique characteristic of fuel cells creates other problems. Hybrid systems come front for solving these problems and increasing total efficiency. Hybrid systems consist of fuel cell with high energy density and battery with high power bring a strong solution for efficiency and distance problems on transportation. Right now, the biggest problem that prevent these systems from being tradable is the cost of fuel cells and batteries. It is obvious that hybrid systems will be used in wider range in the future by reducing material costs, making power management systems more efficient, improvements on battery technology and developing batteries with shorter charging time and higher charge circuit.

As seen in Fig. 8.32, in the next 30 years almost 50 % of the vehicles, and in the next half decade almost all the vehicles will transfer into hybrid system (Veziroğlu 2011).

Fig. 8.32 Transferring into hybrid technology for vehicles (Veziroğlu 2011)
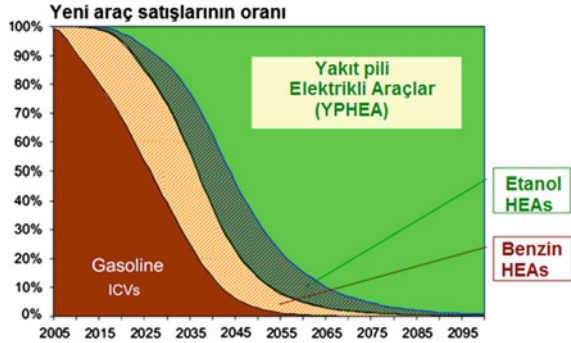
References

Andaloro L, Napoli G, Sergi F, Dispenza G, Antonucci V (2013) Design of a hybrid electric fuel cell powertrain for an urban bus. Int J Hydrogen Energy 38:7725–7732

Andreasen SJ, Ashworth L, Remón INM, Kær SK (2008) Directly connected series coupled HTPEM fuel cell stacks to a Li-ion battery DC bus for a fuel cell electrical vehicle. Int J Hydrogen Energy 33:7137–7145

Arce A, Real AJ, Bordons C (2009) MPC for battery/fuel cell hybrid vehicles including fuel cell Dynamics and performance improvement. J Process Control 19:1289–1304

Bayındır KÇ, Gözüküçük MA, Teke A (2011) A comprehensive overview of hybrid electric vehicle: powertrain configurations, powertrain control techniques and electronic control units. Energy Convers Manag 52:1305–1313

Bizon N (2011a) A new topology of fuel cell hybrid power sources for efficient operation and high reliability, J. Power Sources 196:3260–3270

Bizon N (2011b) Nonlinear control of fuel cell hybrid power sources: part I: voltage control. Appl Energy 88:2529–73

Bizon N (2011c) Nonlinear control of fuel cell hybrid power sources: part II-current control. Appl Energy 88:2574–91

Brown Darren, Alexander Marcus, Brunner Doug, Advani Suresh G, Prasad Ajay K (2008) Drive-train simulator for a fuel cell hybrid vehicle. J Power Sources 183:275–281

Bubna P, Brunner D, Gangloff J, Advani SG, Prasad AK (2010a) Analysis, operation and maintenance of a fuel cell/battery series-hybrid bus for urban transit applications, J. Power Sources 195:3939–3949

Bubna P, Brunner D, Advani SG, Prasad AK (2010b) Prediction-based optimal power management in a fuel cell/battery plug-in hybrid vehicle. J Power Sources 195:666–6708

Burke AF (2007) Batteries and ultracapacitors for electric, hybrid and fuel cell vehicles. IEEE 95:806–819

Corbo P, Corcione FE, Migliardini F, Veneri O (2006) Experimental assessment of energy-management strategies in fuel-cell propulsion systems. J Power Sources 157:799–808

Demirci UB (2009) How green are the chemicals used as liquid fuels in direct-feed fuel cells. Environ Int 35:626–631

Doucette RT, McCulloch MD (2011) A comparison of high-speed flywheels, batteries and ultracapasitors on the bases of cost and fuel economy as the energy storage system in a fuel cell based hybrid electric vehicle. J Power Sources 196:1163–1170

Fadel A, Zhou B (2011) An experimental and analytical comparison study of power management methodologies of fuel cell-battery hybrid vehicles. J Power Sources 196:3271–3279

Fisher P, Jostins J, Hilmansen S, Kendall K (2012) Electronic integration of fuel cell and battery system in novel hybrid vehicle. J Power Sources 220:114–121

Gao W, Chris M (2007) Hybrid vehicle design using global optimisation algorithms Int. J Electr Hybrid Veh 1:57–70

He J, CHoe SY, Hong CQ (2008) Analysis and control of a hybrid fuel delivery system for a polymer electrolyte membrane fuel cell. J Power Sources 185:973–984

Hsiao Der-Ren, Huang Bo-Wun, Shih Nai-Chien (2012) Development and dynamic characteristics of hybrid fuel cell-powered mini-train system. Int J Hydrogen Energy 37:1058–1066

Hwang JJ, Chang WR (2012) Characteristic study on fuel cell/battery hybrid power system on a light electric vehicle. J Power Sources 207:111–119

Hwang JJ, Chen YJ, Kuo JK (2012a) The study on the power management system in a fuel cell hybrid vehicle. Int J Hydrogen Energy 37:4476–4489

Hwang JJ, Chen YJ, Kuo JK (2012) The study on the power management system in a fuel cell hybrid vehicle. Int J Hydrogen Energy 37:4476–4489

Joh H-I, Hwang SY, Cho JH, Ha TJ, Kim SK, Moon SH, Ha HY (2008) Development and characteristics of a 400 W-class direct methanol fuel cell stack. Int J Hydrogen Energy 33:7153–7162

Kamaruddin MZF, Kamarudina SK, Dauda WRW, Masdar MS (2013) An overview of fuel management in direct methanol fuel cells. Renew Sustain Energy Rev 24:557–565

Kim Y, Shin D, Seo J, Chang N, Cho H, Kim Y, Yoon S (2010) System integration or a portable direct methanol fuel cell and a battery hybrid. Int J Hydrogen Energy 35:5621–5637

Kısacıklıoğu MC, Uzunuoğlu M, Alama MS (2009) Load sharing using fuzzy logic control in a fuel cell/ultracapacitor hybrid vehicle. Int J Hydrogen Energy 34:1497–1507

Kuperman A, Aharon I (2011) battery-ultracapacitor hybrids for pulsed current loads: a review. Renew Sustain Energy Rev 15:981–992

Lai JS, Nelson DJ (2007) Energy management power converters in hybrid electric and fuel cell vehicles. IEEE 95:766–777

Lee BD, Jung DH, Ko YH (2004) Analysis of DMFC/battery hybrid power system for portable applications. J Power Sources 131:207–212

Marmara Araştırma Merkezi (2003) Elektrikli Araçlar. Gebze

Neffati A, Guemri M, Caux S, Fadel M (2013) Energy management strategies for multi source system. Electr Power Syst Res 102:42–49

Ogden JM, Steinbugler MM, Kreutz TG (1999) A comparison of hydrogen, methanol and gasoline as fuels for fuel cell vehicles: implications for vehicle design and infrastructure development. J Power Sources 79:143–168

Prakash S, Mustain WE, Kohl PA (2009) Performance of Li-ion secondary batteries in low power, hybrid power supplies. J Power Sources 189:1184–1189

Rodaz P, Paganelli G, Sciarretta A, Guzzella L (2005) Optimal power management of an experimental fuel cell/supercapacitor-powered hybrid vehicle. Control Eng Pract 13:41–53

Ryu J, Park Y, Sunwoo M (2010) Electrical powertrain modelling of a fuel cell hybrid electric vehicle and development of a power distribution algorithm based on driving mode recognition. J Power Sources 195:5735–5748

Saha SS (2011) Efficient soft-switched boost converter for fuel cell applications. Int J Hydrogen Energy 36:1710–1719

Same A, Stipe A, Grosman D, Park JW (2010) A study optimization of hybrid drive train using Advanced Vehicle Simulator (ADVISOR). J Power Sources 195:6954–6963

Sanlı AE, Aytaç A, Mat MD (2014) Investigation of the electro-oxidation of artificial Black Sea water using cyclic voltammetry on molybdenum electrode (II). Int J Hydrogen Energy 39 (17):9221–9229

Tie SF, Tan CW (2013) A review of energy sources and energy management system in electric vehicles. Renew Sustain Energy Rev 20:82–102

Veziroğlu A (2011) Fuel cell vehicles: state of the art with economic and environmental concerns. Int J Hydrogen Energy 36:25–43

Zhang Y, Zhou B (2011) Modelling and control of a portable proton exchange membrane fuel cell-battery power system. J Power Sources 196:8413–8423

Zhang Z, Pittini R, Andersen MAE, Thomsen OC (2012) A review and design of power electronics converters for fuel cell hybrid system applications. Energy Proc 20:301–310

Zhenith F, Krewer U (2010) Modelling, dynamics and control of a portable DMFC system. J Process Control 20:630–642

Chapter 9
Design of Solid State High Power Amplifiers for Leo Satellite Communication Systems

Peiman Aliparast and Sevda Aliparast

Abstract The rapid development of the RF power electronics requires the introduction of wide band gap material due to its potential in high output power density. In this project, an X band (8.1 GHz) solid state power amplifier is designed with an output power of 25 W, bandwidth of 150 MHz as a part of an onboard transmitter. We report our result of an AlGaN/GaN HEMT power amplifier with the operating frequency in X band. There has been significant investment in the development of high performance microwave transistors and amplifiers based on GaN in a satellite communication system.

9.1 Introduction

Low Earth Orbit (LEO) satellites play an important role in Earth observation and communication fields. In a satellite communication system, main limitations are down link capabilities as well as sensing capabilities. A typical satellite communication system most of the time has been composed from Telemetry, Tracking and Control (TT&C) subsystems. TT&C subsystem of a satellite provides a connection between the satellite itself and the facilities on the ground (Pelton 2012). In this case the telemetry subsystems send voice, video, and data from satellite to ground stations. With considering of power limitation on satellites, the efficiency of the telemetry subsystem is very important. Recent Earth observations such as optical imaging, SAR imaging, and remote sensing by satellites require higher load power and power efficiency. Figure 9.1 shows typical radio frequency (RF) frontend of a transmitter for a telemetry subsystem. The RF signal has been amplified by power amplifiers (PA) just before antenna. As exhibited in Fig. 9.1 the final block before antenna which is a High Power Amplifier (HPA). In this block, the power of signal reach to maximum value. Because of high power consumption, the efficiency of this

P. Aliparast (✉) · S. Aliparast
Ministry of Science, Research and Technology, Aerospace Research Institute,
14665-834 Tehran, Iran
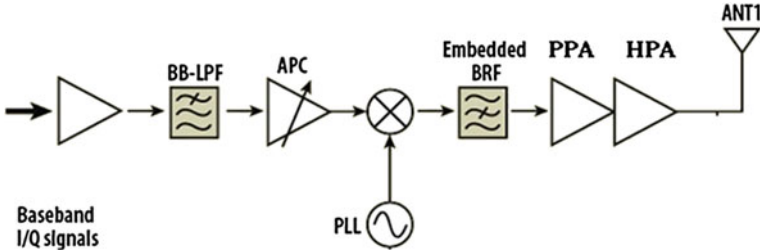e-mail: Aliparast@ari.ac.ir

Fig. 9.1 Typical RF frontend of a transmitter

stage is most important block in determining efficiency of the telemetry subsystem. On the other hand weight, band of frequency, bit rate, coding, encryption, sensitivity and occupied volume are very important parameters in designing of the telemetry subsystem for LEO satellites. All of these are primary requirements in designing of HPA. We know that the most of the telemetry subsystem of LEO satellites works in X Band. Also we know that they send a signal power about 10–100 W per each Antenna.

Thus high efficiency RF HPA is main requirement of a telemetry subsystem for LEO satellites as mentioned above. In the following we are discussing steps of designing high efficiency RF PA in X Band.

9.2 Process Selection

We need to determine process of active parts in the first step for designing a RF HPA. So, first we must decide between Traveling Wave Tube Amplifiers (TWTA) and Solid State Amplifiers (SSA). TWTA can produce more power in comparison with SSA but it has a larger dimensions and heavier weight. SSA can be better choice if we consider the other significant advantages of SSA in design, reuse, time to market, serviceability, maintainability, and reliability for microwave power amplifier applications. In SSA, the rapidly advancing Gallium Nitride Device industry offers the opportunity to upgrade the performance, reliability, serviceability, and robustness of systems currently using vacuum devices (Casto et al. 2011). Figure 9.2 shows technology adoption projections for power amplifiers (Aichele and Poulton 2009). A review of GaN on SiC High electron-mobility (HEM) power transistors is presented in Pengelly et al. (2012). This review is very helpful for designer of HPA. In Table 9.1 material properties of some famous solid state semiconductors are summarized. Baliga's figure of merit (BFOM) in Table 9.1 shows power transistor performance (Pengelly et al. 2012). GaN has largest BFOM in compare to other processes. So, it is best choice for designing HPA in X Band to meet the requirements of the telemetry subsystems of LEO satellites.
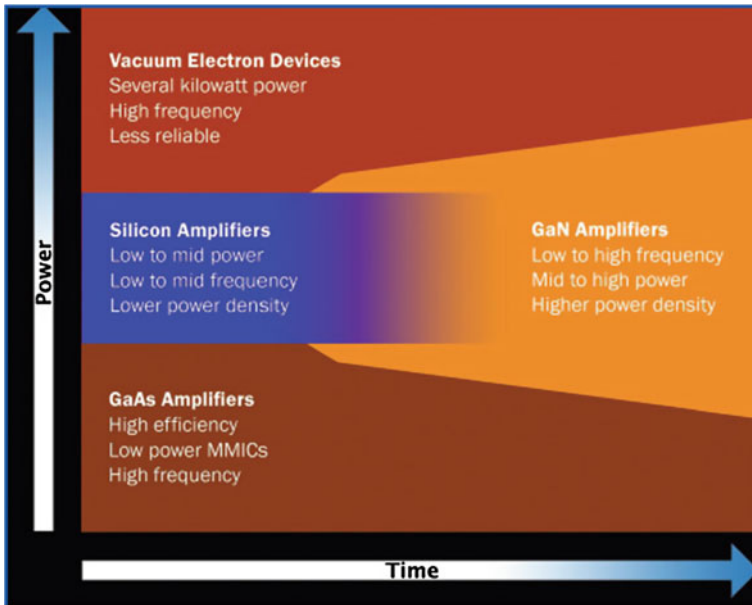
Fig. 9.2 PA technology adoption projections (Aichele and Poulton 2009)

Table 9.1 Material properties of solid state semiconductors (Pengelly et al. 2012)

Material	Mobility (cm²/V.s)	Die electric constant	Bandgap (eV)	Breakdown field (MV/cm)	BFOM ratio	T_{max} (°C)
i	1300	11.9	1.12	0.3	1.0	300
GaAs	5000	12.5	1.42	0.4	9.6	300
4H-SiC	260	10	3.2	3.5	3.1	600
GaN	1500	9.5	3.4	2	24.6	700

The proposed HPA in this project should be linear and covers the frequency band from 8.025 to 8.175 GHz and achieves 25 W output power. Besides the data sheet given by the manufacture which almost introduces the typical values regarding small signal as well as large-signal specifications, maximum stable gain (MSG) has to be considered. Based on the given specifications, a 25 W GaN HEMT die (CGHV1J025D) from Cree manufacture has been selected for the designing. Figure 9.3 shows layout of this transistor with its dimensions in μm. Figure 9.4 shows the I–V curves of the CGHV1J025D based on simulation results. We swept the gate-to-source voltage (V_{GS}) from +1 to −3 V to obtaining these curves. We never apply positive voltage to the gate-to-source in the real world. V_{GS} stay between −1 and −3 V most of the time. Also, Fig. 9.4 shows DC performance of this transistor and we can use it to find the best biasing point of the transistor.
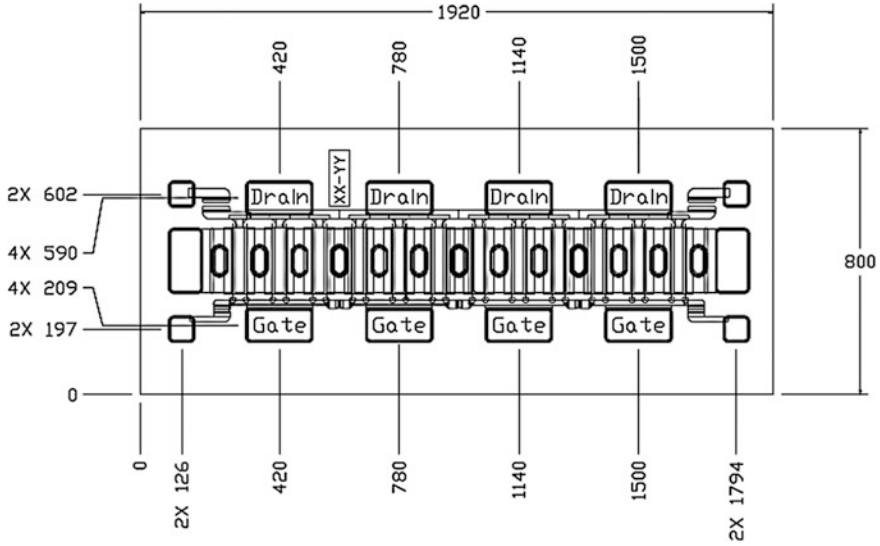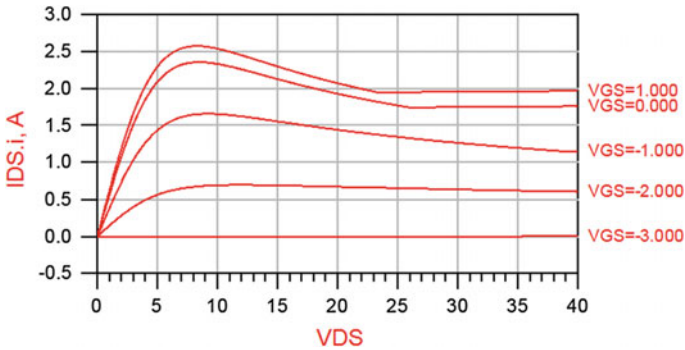
Fig. 9.3 Layout of CGHV1J025D

Fig. 9.4 I–V curves based on simulation results for CGHV1J025D

9.3 Architecture Selection

In the telemetry subsystems, HPA with high efficiency and linearity is required. There are some classes for power amplifiers which can be used regarding to the situations. In Mishra et al. (2008) many types of HPAs have been reported to improve efficiency, such as class E. A class E HPA is one of them which can theoretically obtain 100 % power efficiency but because of some non ideal elements such as non ideal transistor the efficiency would be lower than 100 %. Figure 9.5 shows the waveforms of the class E HPA that has been simulated by MATLAB. According to the reasons which have been mentioned, a class E power amplifier
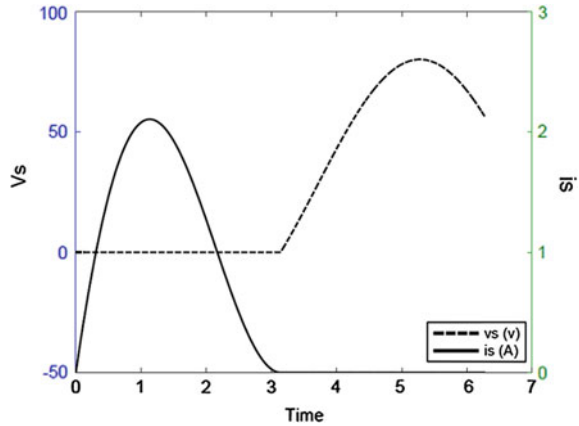
Fig. 9.5 Waveforms of a
class E HPA

Table 9.2 A list of the LEO satellite proposes X band HPA with them performance results

P_{load} (dBm)	G_p (dB)	PAE (%)	Frequency (GHz)	Transistor model	Class of power amplifier	Reference
37	14	20	0.35–8	CGH60015D	Class E	Sayed et al. (2009)
35.6	11	61	8.5–11.5	GaN HEMT	Class E	Moon et al. (2012)
41.3	16	–	10	AlGaN/GaN HEMT	Hybrid	van Raay et al. (2005a)
39.5	20	–	10	AlGaN/GaN HEMT	Two stage	van Raay et al. (2005b)
41.46	1.5	23.4	8–8.5	AlGaN/GaN HEMT	Wilkintson power amplifier	Chi et al. (2010)

was selected for high efficiency, it was attempted to use a matching network in
input and a filter network at the output. We had listed some of the LEO satellite
proposes X Band HPA with them performance results in Table 9.2.

9.4 Power and Linearity Performance

In the HPA, a high PAE is important in order to reduce the launch cost of the
satellite. The X band HPAs, in the frequency range of 8.025–8.175 GHz, are often
used for LEO satellite downlinks. Figure 9.6 shows schematic of deigned E class
HPA. The power performance of the proposed HPA at 8.1 GHz, $V_{DS} = 40$ V is
shown in Fig. 9.7. The output power measured 25.7 W where the input power is
1.54 W. The Gain of power (G_P) achieved 12.25 dB. The linearity of the HPAs is
the other important performance parameter. A single-tone AM to AM modulation
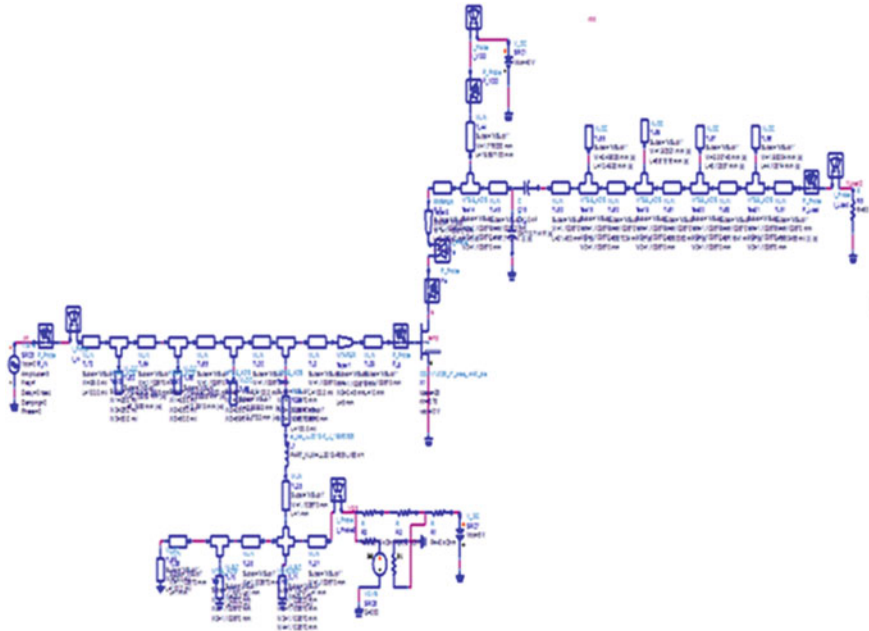
Fig. 9.6 Schematic of the proposed class E HPA

Fig. 9.7 P_{in} and P_{out} for the proposed class E HPA
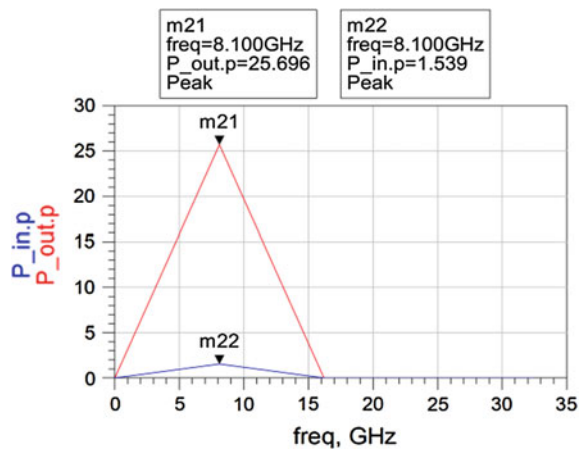
and AM to PM modulation test have been done for measured the linearity performance of the proposed HPA. Figure 9.8 shows the simulation results for distortion of the proposed class E HPA. Also the two-tone test has been done for measuring inter-modulation distortion 3 (ID_3). Figure 9.9 shows the power spectrum analyzer (PSA) results for the two-tone measurements at $f_c = 8.1$ GHz and

Fig. 9.8 Simulation results for distortion of the proposed class E HPA, **a** AM to PM distortion, **b** AM to AM distortion

Fig. 9.9 Results of two-tone test the proposed class E HPA

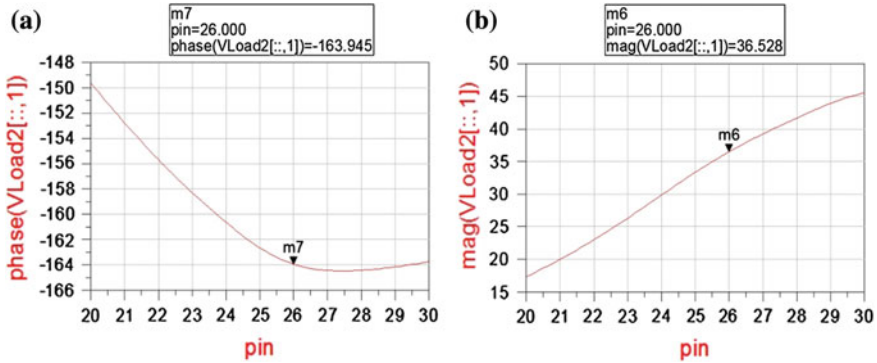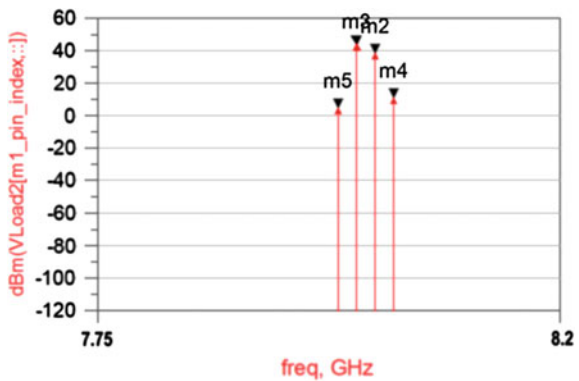P_{in} = 26dBm. As shown in Fig. 9.9, the proposed HPA in 8.1 GHz has 44.041 dBm and in 8.11 GHz has 38.388 dBm output power. Also, third harmonics at 8.115 and 8.095 GHz have 4.532 and 10.839 dBm output power, respectively. So, the ID_3 measured better than 27 dBc. Figure 9.10 shows stability of the proposed HPA based on its response to step input.

9.5 Matching Network

In ideal case, the concept that is being followed while designing the input and output matching network is that, small-signal simulations in ADS implemented to optimize for gain and return loss for input and output sides, on the other hand large-signal simulations in ADS is used for output power and efficiency optimization. These networks are designed for impedance transformation, typically

Fig. 9.10 Step response of the proposed class E HPA

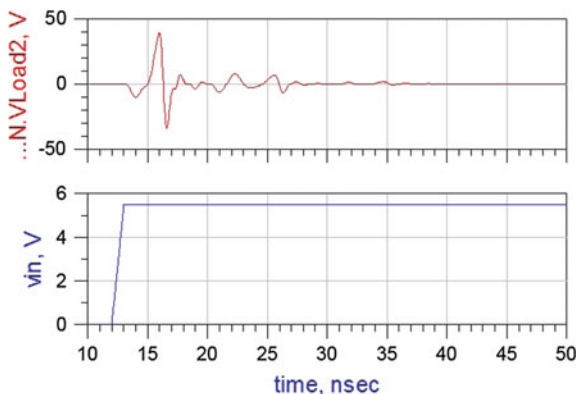**Table 9.3** A summaries of the performance results for the proposed HPA

P_{out} (dBm)	P_{in} (dBm)	G_p	Eff (%)	PAE (%)	Transistor model
44.098	31.872	16.697	49.419	46.459	CGHV1J025D

between the transistor and 50 Ω terminations on the input/output of amplifier. They might be designed with lumped elements, quarter wave transformers or micro strip stubs. Generally, input matching side provides for the maximum power transfer, which occurs according to complex conjugate theorem and gives low input return loss. On the other hand, output matching network is designed according to requirements and matching the device to the output side is not always the case. For instance, loss of half the power happens on maximum power transfer and high efficiency cannot be ensured.

9.6　Conclusions

In this research a simulations has been performed by the Process Design Kit (PDK) of CGHV1J025D GaN HEMT transistor, manufactured by CREE Company. Results show At 8.1 GHz, we achieved 48.521 % drain efficiency, 43.342 % PAE, 44.115 dBm load power and 12.25 dB power gain. The results show the developed 25 W AlGaN/GaN HEMT has high power capability covering practical frequency range for X band high power applications. Power performance of the implemented PA has been tested at 8.1 GHz for 40 V DC drain voltages and 450 mA DC drain current as presented before (Table 9.3).

References

Aichele D, Poulton M (2009) Next-generation, GaN-based power amplifiers for radar applications. http://www.mpdigest.com/issue/Articles/2009/Jan/rfmd/. Jan 2009

Casto M, Lampenfeld M, Jia P, Courtney P, Behan S, Daughenbaugh P, Worley R (2011) 100 W X-band GaN SSPA for medium power TWTA replacement. In: IEEE 12th annual wireless and microwave technology conference (WAMICON). Clearwater Beach, FL, 18–19 Apr 2011

Chi C, Yue H, Hui F, Linan Y, Xiaohua M, Huantao D, Shigang H (2010) An X-band GaN combined solid-state power amplifier. J Semiconductors 30(90), Jan 2010

Mishra UK, Shen L, Kazior TE, Wu Y-F (2008) GaN-Based RF power devices and amplifiers. In: Proceedings of the IEEE, vol 96, no 2, Feb 2008

Moon JS, Moyer H, Macdonald P, Wong D, Antcliffe M, Hu M, Willadsen P, Hashimoto P, McGuire C, Micovic M, Wetzel M, Chow D (2012) High efficiency X-band class-E GaN MMIC high-power amplifiers. In: 2012 IEEE Topical Conference on Power Amplifiers for Wireless and Radio Applications (PAWR). Santa Clara, CA

Pelton, JN, Madry S, S Camacho-Lara (eds) (2012) Handbook of satellite applications, chapter 41. Springer, New York. ISBN: 978-1-4419-7670-3 (Print) 978-1-4419-7671-0 (Online) (Arthur Norman Guest)

Pengelly RS, Wood SM, Milligan JW, Sheppard ST, Pribble WL (2012) A review of GaN on SiC high electron-mobility power transistors and MMICs. In: IEEE Transactions On Microwave Theory And Techniques, vol 60, no 6, June

Sayed A, Al Tanany A, Boeck G (2009) 5 W, 0.35—8 GHz linear power amplifier using GaN HEMT. Microwave Engineering Laboratory, Berlin University of Technology Einsteinufer. Berlin, Germany, 25, 10587

van Raay F, Quay R, Kiefer R, Walcher H, Kappeler O, Seelmann-Eggebert M, Müller S, Schlechtweg M, Weimann G (2005a) High power/high bandwidth GaN MMICs and hybrid amplifiers design and characterization. In: 13th GAAS. Gallium arsenide and other semiconductor application symposium, EGAAS 2005. European, Paris

van Raay F, Quay R, Kiefer R, Fehrenbach W, Bronner W, Kuri M, Benkhelifa F, Massler H, Müller S, Mikulla M, Schlechtweg M, Weimann G (2005b) A microstrip X-Band AlGaN/GaN power amplifier MMIC on s.i. SiC substrate. In: 13th GAAS. Gallium arsenide and other semiconductor application symposium, EGAAS 2005. European, Paris

Chapter 10
Different Efficiency Calculations of a Combined Cycle Power Plant

Ismail Ekmekci and Ahmet Coşkun Dundar

Abstract Brayton cycle has a great importance for aviation industry in gas turbines of aircrafts. The aim of this study is to obtain the different efficiency values of one of the combined thermal power plant in our country that its working principle mainly depends on gas turbine Brayton cycle. Ambarlı Combined Cycle Power Plant has been examined to make some comparisons with different efficiency approaches. This power plant is examined by using different efficiency definitions: Thermal, Carnot, Curzon-Ahlborn, Caputo Efficiency and Exergetic Efficiency.

Nomenclature

A	Area, m^2
T	Temperature (^{o}C)
CCPP	Combined cycle power plants (–)
HRSG	Heat recovery steam generator
ŋ	Efficiency
CA	Curzon-Ahlborn
CPT	Caputo
ACCPP	Ambarlı combined cycle power plant
Ex	Exergetic

I. Ekmekci (✉)
Engineering and Design Faculty, İstanbul Commerce University, İstanbul, Turkey
e-mail: iekmekci@ticaret.edu.tr

A.C. Dundar
Applied Science Faculty, İstanbul Commerce University, Istanbul, Turkey
e-mail: acdundar@ticaret.edu.tr

10.1 Introduction

Gas turbines is an engine designed to convert the energy of a fuel into some form of useful power, such as mechanical (shaft) power for power plants or high-speed thrust of a jet for aviation industry. A gas turbine is basically comprised of a compressed gas generator section and a power conversion section. The Brayton cycle (or Joule cycle) represents the operation of a gas turbine engine. It has a great importance for aviation industry in gas turbines of aircrafts. It is a thermodynamic cycle that describes the workings of the gas turbine engine, basis of the air breathing jet engine and others. It is named after George Brayton (1830–1892), the American engineer who developed it, although it was originally proposed and patented by Englishman John Barber in 1791 (Bathie 1984). It is also sometimes known as the Joule cycle. The Ericsson cycle is similar but uses external heat and incorporates the use of a regenerator. Today the term Brayton cycle is generally associated with the gas turbine, even though Brayton only built piston engines.

The Brayton cycle is a cycle which can be used in both internal combustion engines (such as jet engines) and for external combustion engines. Although the Brayton cycle is usually run as an open system (and indeed must be run as such if internal combustion is used), it is conventionally assumed for the purposes of thermodynamic analysis that the exhaust gases are reused in the intake, enabling analysis as a closed system. The cycle consists of four processes, as shown in Fig. 10.1 alongside a sketch of an engine:

a b: Adiabatic, quasistatic (or reversible) compression in the inlet and compressor;
b c: Constant pressure fuel combustion (idealized as constant pressure heat addition);
c d: Adiabatic, quasi-static (or reversible) expansion in the turbine and exhaust nozzle, with which we

1. Take some work out of the air and use it to drive the compressor, and
2. Take the remaining work out and use it to accelerate fluid for jet propulsion, or to turn a generator for electrical power generation;

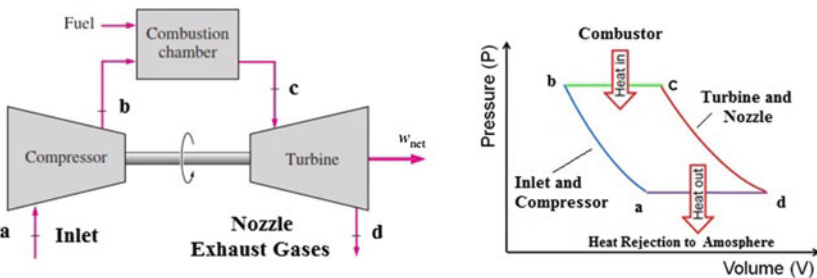d a: Cool the air at constant pressure back to its initial condition

Fig. 10.1 Sketch of the gas turbine engine components and corresponding thermodynamic states

A more popular modification involves a gas power cycle topping a vapour power cycle, which is called the Combined Gas-Vapour Cycle, or just the Combined Cycle. The Combined Cycle of greatest interest is the gas turbine (Brayton) cycle topping a steam turbine (Rankine) cycle, which has a higher thermal efficiency than either of the cycles executed individually. Gas turbine cycles typically operate at considerably higher temperatures than steam cycles.

As an engineering sense to take advantage of very desirable characteristics of the gas turbine cycle at high temperatures and to use the high-temperature exhaust gases as the energy source for the bottoming cycle such as a steam power cycle as Rankine cycle. The result is a Combined Gas–Steam Cycle and in this cycle, energy is recovered from the exhaust gases by transferring it into steam in a heat exchanger (HRSG—Heat Recovery Steam Generator) that serves as the boiler. In general, more than one gas turbine is needed to supply sufficient heat to the steam. Recent developments in gas turbine technology have made the combined gas–steam cycle economically very attractive. The combined cycle increases the efficiency without increasing the initial cost greatly. Consequently, many new power plants operate on combined cycles, and many more existing steam or gas turbine plants are being converted to combined cycle power plants. Thermal efficiencies well over 40 % are reported as a result of conversion. In Turkey, one of the important and successful example of conversion project of existing fuel oil-fired steam turbine plants is Ambarlı Units Rehabilitation Project involves the conversion of the existing Fuel Oil-fired boiler steam plant into Combined Cycle by addition of new Gas Turbine Generators and new Heat Recovery Steam Generators and rehabilitation and modification of existing Steam Turbines under new steam regime to achieve maximum performance. Thus, thermodynamic efficiency is increased from 36 % to 54 %, energy production costs are decreased, plant reliability is increased and excessive levels of atmospheric emissions are reduced significantly. Ambarlı Project is a "Full Repowering by CCPP Conversion" Project that is a "first of its kind" Project in Turkey and is equalled in magnitude and complexity by only a handful of worldwide examples.

The aim of this study is to obtain the different efficiency values of one of the successful CCPP conversion example in our country that its working principle mainly depends on gas turbine Brayton cycle and Rankine cycle, Ambarlı combined cycle power plant has been examined to make some comparisons with different efficiency approaches. This power plant is examined by using different efficiency definitions: Thermal efficiency, Carnot efficiency, Curzon-Ahlborn and Caputo efficiencies of Ambarlı combined cycle power plant (ACCPP).

10.2 Different Efficiency Definitions

10.2.1 Thermal Efficiency (η_T)

Thermal efficiency (η_T) is simply cycle efficiency, the ratio of the network output (W_{net}) to heat supplied (Q_s).

$$\eta_T = W_{\text{net}}/Q_s$$

Thermal efficiency tends to increase as the average temperature of heat addition increases and/or the temperature of heat rejection decreases.

10.2.2 Carnot Efficiency (η_C)

It is clear and well known that practical heat engines are not as efficient as the classical Carnot cycle. Due to the heat leaks or degradation of kinetic energy into heat by means of friction are the main causes of the inefficiencies.

"Carnot Efficiency (η_c)" is the upper bound of the efficiencies of all heat engines. It is formulated as

$$\eta_C = 1 - (T_L/T_H)$$

where T_H and T_L the temperature of the hot and cold thermal reservoirs, respectively.

10.2.3 Curzon-Ahlborn Efficiency (η_{CA})

"Curzon-Ahlborn Efficiency" was introduced by Curzon and Ahlborn in 1975. This efficiency basically considers the influence of finite rate heat transfer between the external heat reservoirs and the working fluid on the performance of a Carnot-like thermal engine in which there is no thermal equilibrium between the working fluid and the thermal reservoirs at the isothermal branches of the cycle. Curzon and Ahlborn indicated that such an engine produces nonzero positive power (contrary to the Carnot engine), and that the power output can be optimized by varying the temperature of the cycle's isothermal branches. They formulated their theory for the efficiency under these conditions as follows,

$$\eta_{CA} = 1 - \sqrt{\frac{T_L}{T_H}}$$

10.2.4 Caputo Efficiency (η_{CPT})

Because of the external and internal irreversibilities within the cycle, gas turbine cycles as well as heat engines do not achieve the Carnot efficiency. "Caputo" introduced a new efficiency equation by considering the measure of the irreversibilities.

According to Caputo, the efficiency of the real cycle is expressed in terms of τ (the ratio of minimum to maximum temperature) and μ which encompasses the overall effect of failures.

Caputo introduced a parameter σ which is a measure of the irreversibilities within the real cycle. He first defined:

$$\sigma_i = \frac{Q_i}{T_i}$$

where mean temperature can be defined as follows:

$$\overline{T}_i = \frac{Q_i}{\int \frac{dQ_i}{T}}$$

Then the parameter σ is then defined as:

$$\sigma = \frac{\sigma_H}{\sigma_L}$$

the ratio of entropy change in heat supply to entropy change in heat rejection. For the Carnot cycle σ is unity, but for other (irreversible) cycles, a value of σ less than unity indicates a 'widening' of the cycle on the T-s diagram due to irreversibilities (e.g. in compression and/or expansion in the gas turbine cycle) and a resulting loss in thermal efficiency.

Parameters ξ_H and ξ_L are then defined to measure the failures to achieve the maximum and minimum temperatures $T_{\max}$ and $T_{\min}$,

$$\xi_H = \frac{\overline{T}_H}{T_{\max}}, \quad \xi = \frac{\overline{T}_L}{T_{\min}}$$

Then combined parameter can be defined as:

$$\xi = \frac{\xi_H}{\xi_L} = \left(\frac{T_{\min}}{T_{\max}}\right)\left(\frac{\overline{T}_H}{\overline{T}_L}\right) = \tau\left(\frac{\overline{T}_H}{\overline{T}_L}\right)$$

where is the ratio of minimum temperature to maximum temperature.

ξ is then an overall measure of the failure of the real cycle to achieve the maximum and minimum temperatures and is always less than unity (except for the Carnot cycle, where ξ becomes unity).

The overall effect of these failures to achieve Carnot efficiency is then encompassed in a new parameter μ where,

$$\mu = \sigma\xi$$

Then Caputo efficiency can be obtained as follows:

$$\eta_{\text{Caputo}} = 1 - \left(\frac{Q_L}{Q_H}\right) = 1 - \frac{\sigma_L \overline{T}_L}{\sigma_H \overline{T}_H} = 1 - \frac{\sigma_L \xi_L T_{\min}}{\sigma_H \xi_H T_{\max}} = 1 - \frac{\tau}{\sigma\xi} = 1 - \frac{\tau}{\mu}$$

In equations above, T_A and T_B are the mean temperatures of heat supply and rejection; ξ is an overall measure of the real cycle to achieve the maximum and minimum temperatures. σ is the measure of the irreversibilities within the cycle.

10.2.5 Exergetic Efficiency (η_{Ex})

In thermodynamics, the exergy of a system is the maximum useful work possible during a process that brings the system into equilibrium with a heat reservoir (Bathie 1984). When the surroundings are the reservoir, exergy is the potential of a system to cause a change as it achieves equilibrium with its environment. Exergy is the energy that is available to be used. After the system and surroundings reach equilibrium, the exergy is zero. Determining exergy was also the first goal of thermodynamics.

Energy is never destroyed during a process; it changes from one form to another (see First Law of Thermodynamics). In contrast, exergy accounts for the irreversibility of a process due to increase in entropy (see Second Law of Thermodynamics). Exergy is always destroyed when a process involves a temperature change. This destruction is proportional to the entropy increase of the system together with its surroundings. The destroyed exergy has been called anergy (Bathie 1984). For an isothermal process, exergy and energy are interchangeable terms, and there is no anergy.

As a simple example of exergy, air at atmospheric conditions of temperature, pressure, and composition contains energy but no exergy when it is chosen as the thermodynamic reference state known as ambient. Individual processes on Earth like combustion in a power plant often eventually result in products that are incorporated into a large atmosphere, so defining this reference state for exergy is useful even though the atmosphere itself is not at equilibrium and is full of long- and short-term variations.

If standard ambient conditions are used for calculations during plant operation when the actual weather is very cold or hot, then certain parts of a chemical plant might seem to have an exergy efficiency of greater than 100 % and appear on paper to be a perpetual motion machine! Using actual conditions will give actual values, but standard ambient conditions are useful for initial design calculations.

One goal of energy and exergy methods in engineering is to compute what comes into and out of several possible designs before a factory is built. Energy input and output will always balance according to the First Law of Thermodynamics or the energy conservation principle. Exergy output will not balance the exergy input for real processes since a part of the exergy input is always

destroyed according to the Second Law of Thermodynamics for real processes. After the input and output are completed, the engineer will often want to select the most efficient process. An energy efficiency or first law efficiency will determine the most efficient process based on wasting as little energy as possible relative to energy inputs. An exergy efficiency or second-law efficiency will determine the most efficient process based on wasting and destroying as little available work as possible from a given input of available work. Second-Law efficiency or Exergetic Efficiency can be defined as follows:

$$\eta_{Ex} = (\text{Exergy Recovered})/(\text{Exergy Supplied})$$

and overall exergetic efficiency value for ACCPP has been calculated and compared with other efficiency values.

10.3 Required Data of Power Plant

Required technical data and obtained thermodynamical results of the Ambarlı combined cycle power plant are tabulated in Tables 10.1 and 10.2:

10.4 Results of Efficiency Calculations

In this study, Ambarlı combined cycle thermal power plants' performance is evaluated through energetic performance criteria based on "First Law of Thermodynamics", which is thermal efficiency. Also with respect to upper and lower temperatures, Carnot efficiency values for the Units of ACCPP have been calculated. Then Curzon-Ahlborn efficiency, Caputo efficiency and Exergetic efficiency values are also been calculated and summarized in Table 10.3.

Table 10.1 ACCPP technical data

Ambarli combined cycle power plant						
Total power	1350,9 MW					
Unit number	3					
	I. & II. Unit		III. Unit		IV. Unit	
Power of unit	450,3 (155,6–155,6–139) MW		450,3 (155,6–155,6–139) MW		450,3 (155,6–155,6–139) MW	
Age	18-18-16		18-18-15		17-17-15	
Unit structure	GT-GT-BT		GT-GT-BT		GT-GT-BT	
Turbine sequence	HP-LP		HP-LP		HP-LP	
High steam pressure	86.2 ata	17468.43 kPa	86.2 ata	17468.43 kPa	86.2 ata	17468.43 kPa
High steam temperature	526 °C	799.15 K	526 °C	799.15 K	526 °C	799.15 K
High steam mass flow	231.1 t/h		231.1 t/h		231.1 t/h	
Low steam pressure	6.4 ata	1296.96 kPa	6.4 ata	1296.96 kPa	6.4 ata	1296.96 kPa
Low steam temperature	199 °C	472.15 K	199 °C	472.15 K	199 °C	472.15 K
Low steam mass flow	45.2t/h		45.2t/h		45.2 t/h	
Low pressure pre-heaters	1		1		1	
High pressure pre-heaters	–		–		–	
Feedwater boiler inlet	106 °C	379.15 K	106 °C	379.15 K	106 t/h	379.15 K
GT exhaust temperature	558 °C	831.15 K	558 °C	831.15 K	558 °C	831.15 K
Compressor pressure	11 ata	2229.15 kPa	11 ata	2229.15 kPa	11 ata	2229.15
Fuel type	Natural gas		Natural gas		Natural gas	
Lower heating value	8050 kcal/kg		8050 hcal/kg		8050 kcal/kg	

Table 10.2 Thermodynamically Obtained Data for ACCPP

		Unit 1 and 2	Unit 3	Unit 4
Pump inlet	hpg	167.5 kJ/kg	104.71 kJ/kg	188.42 kJ/kg
	spg	0.4721 kJ/(kgK)	0.3858 kJ/(kgK)	0.6385 kJ/(kgK)
Condenser pressure	v1	0.001 m³/kg	0.001 m³/kg	0.00101 m³/kg
Pump power consuption [$Wp = v1*(P2 - P1)$]	Wp	17.608 kJ/kg-s	17.521 kJ/kg	17.6431 kJ/kg
Pump outlet (heater inlet)	hpç	185.11 kJ/kg	122.23 kJ/kg	206.063 kJ/kg
High pressure turbine inlet	hhi	3222.9 kJ/kg	3222.9 kJ/kg	3222.9 kJ/kg
(27,35 MPa and 535 C)	shi	5.9634 kJ/(kgK)	5.9634 kJ/(kgK)	5.9634 kJ/(kgK)
High pressure turbine outlet	hhi	2857.9 kJ/kg	2857.9 kJ/kg	2857.9 kJ/kg
(7,3 MPa and 535 C)	sho	5.9634 kJ/(kgK)	5.9634 kJ/(kgK)	5.9634 kJ/(kgK)
Low pressure turbine outlet	hli	3494.7 kJ/kg	3494.7 kJ/kg	3494.7 kJ/kg
(7,3 MPa and 535 C)	sli	6.9034 kJ/(kgK)	6.9034 kJ/(kgK)	6.90336 kJ/(kgK)
Low pressure turbine outlet	h_{lo}	2150.1 kJ/kg	2150.1 kJ/kg	2150.1 kJ/kg
	x	0.824	0.824	0.824
HP turbine power generation	Whpt	365 kJ/kg	365 kJ/kg	365 kJ/kg
LP turbine power generation	Wlpt	1344.6 kJ/kg	1344.6 kJ/kg	1344.6 kJ/kg
Carbon	C, %	20.81	20.81	20.81
Hydrogen	H, %	1.78	1.78	1.78
Oxygen	O, %	9.35	9.35	9.35
Nitrogen	N, %	1.15	1.15	1.15
Total power generation	Wt	1709.6 kJ/kg-s	1709.6 kJ/kg	1709.6 kJ/kg
Total heat supplied	qt	3037.8 kJ/kg	3100.7 kJ/kg	3016.84 kJ/kg
HP turbine efficiency	ηhpt%	0.1133	0.1133	0.11325
LP turbine efficiency	ηlpt%	0.3848	0.3848	0.38475
Exergy factor (based on LHV)	β	1.0894	1.0894	1.08944
Thermal efficiency	η_T%	0.557	0.5457	0.56084
Curzon-Ahlborn efficiency	η_{ca}%	0.4394	0.4154	0.41536
Carnot efficiency	η_c%	0.6582	0.6582	0.6582
Exergetic efficiency	η_{ex}%	0.5113	0.5009	0.5148

Table 10.3 Summary of the efficiency for ACCPP

	η_T (%)	η_C (%)	η_{CA} (%)	η_E (%)	η_{CPT} (%)
Unit 1 and 2	55.70	65.82	43.94	51.13	49.22
Unit 3	54.57	65.82	41.54	50.09	34.03
Unit 4	56.08	65.82	41.54	51.48	34.98

10.5   Conclusion

As seen in Table 10.3, Carnot efficiency values are hypothetical and very high values according to real states. Curzon-Ahlborn and Caputo efficiency values give more realistic values with respect to Carnot and Exergetic efficiencies.

References

Bathie WW (1984) Fundamentals of gas turbines. Wiley (1984)

Boehm RF (1987) Design analysis of thermal systems. Wiley (1987)

Çengel YA, Boles MA (2002) Thermodynamics: an engineering approach (4th edn). McGraw Hill

Dincer I, Cengel YA (2001) Energy, entropy, and exergy concepts and their roles in thermal engineering. Entropy 3:116–149

Ediger VS, Çamdali U (2007) Energy and exergy efficiencies in Turkish transportation sector. Energ Policy 35:1238–1244 1988–2004

Ehsan A, Yilmazoglu MZ (2007) Design and exergy analysis of a thermal power plant using different types of Turkish lignite. Int J Thermodyn 14(3)

Erdem HH, Akkaya AV, Cetin B, Dagdas A, Sevilgen SH, Sahin B, Teke I, Gungor G, Atas S (2009) Comparative energetic and exergetic performance analyses for coal-fired thermal power plants in Turkey. Int J Therm Sci 48:2179–2186

Erdem HH, Dagdas A, Sevilgen SH, Cetin B, Akkaya AV, Sahin B, Teke I, Gungor C, Atas S (2010) Thermodynamic analysis of an existing coal-fired power plant for district heating/cooling application. Appl Therm Eng 30:181–187

Perrot P (1998) A to Z of thermodynamics. Oxford University Press. ISBN 0-19-856552-6

Rant Z (1956) Exergie, ein neues Wort fur "Technische Arbeitsfahigkeit" (Exergy, a new word for "technical available work"). Forschung auf dem Gebiete des Ingenieurwesens 22:36–37

Wilson DG, Korakianitidis T (2014) The design of high-efficiency turbomachinery and gas turbines

Chapter 11
Sustainability Assessment in Piston-Prop Helicopter Engine

Elif Yildirim, Onder Altuntas, T. Hikmet Karakoc and Necati Mahir

Abstract About 75 % of the world's energy requirement is provided by fossil fuels, and there are various improvement efforts in all fields to ensure the effective use of available sources, taking into consideration the gradual decrease in fossil fuels. Several approaches are used against the decrease in energy sources including the concept of sustainability. Sustainability refers to the careful use of available sources by making advance plans to ensure that natural sources are not exhausted and are used in moderation so that the future generations can benefit from these sources. This study includes a sustainability assessment based on energy analyses for different engine power values varying between 150 and 600 SHP (Shaft Horse Power) in a spark-ignited, unsupercharged and air-cooled piston-prop helicopter engine. As a result of calculations, the highest exergetic sustainability index was found to be 0.15, and the lowest environmental impact factor value was found to be 6.86 at a power of 250 SHP. The lowest waste exergy ratio and the lowest exergy destruction factor were calculated to be 87.28 and 66.77 %, respectively. The power with the highest energy and exergy efficiency provided the highest exergetic sustainability index and thus the lowest waste exergy ratio, the lowest exergy destruction factor and the lowest environmental impact factor.

E. Yildirim · O. Altuntas (✉)
Civil Aviation Research and Application Center,
Anadolu University, Eskişehir, Turkey
e-mail: oaltuntas@anadolu.edu.tr

E. Yildirim
e-mail: e.yildirim@anadolu.edu.tr

T.H. Karakoc
Faculty of Aeronautics and Astronautics,
Anadolu University, Eskisehir, Turkey
e-mail: hkarakoc@anadolu.edu.tr

N. Mahir
Faculty of Engineering and Arhitecture, Department of Mechanical
Engineering, Eskişehir Osmangazi University, Eskisehir, Turkey
e-mail: nmahir@ogu.edu.tr

Nomenclature

$\dot{Ex}_{we}$	Waste exergy (kW)
$\dot{Ex}_{dest}$	Exergy destruction (kW)
$\dot{Ex}_{loss}$	Loss exergy (kW)
r_{we}	Waste exergy ratio (%)
$\dot{Ex}_{in}$	Exergy input (kW)
f_{exd}	Exergy destruction factor (–)
r_{eef}	Environmental impact factor (–)
ψ	Exergy efficiency (%)
Θ_{esi}	Exergetic sustainability index (–)

11.1   Introduction

Rapid increase in energy consumption causes rapid decrease in energy sources. It is a must to use the available energy sources in the most efficient manner and to find new energy sources to ensure that we can leave energy sources to future generations and to ensure sustainability. Effective use of energy would contribute to the reduction of environmental pollution that we face today. The exergy concept presents itself here. Exergy is expressed as maximum theoretical work that can be obtained from a system, and exergy calculations allow the calculation of maximum efficiency from a system and determination of improvement points in that system. When the system efficiency is increased, fuel consumption is reduced, and thus the fuel cost is reduced. Less energy is used to yield more work which increases both the lifetime of energy sources and their sustainability. In addition, the environment is less harmed. Exergy is an effective instrument to understand and to improve the sustainability of systems and processes (Aydın 2013). It is not possible to distinguish the concepts of exergy and sustainability. Like the exergy analysis, the sustainability analysis plays an important role in reducing the environmental impacts and costs of waste. The most economic and viable method to reduce greenhouse gas emissions and energy costs is to increase energy efficiency (Bakanlığı 2013; http://databank.worldbank.org 2014).

In recent years, the demand for aircrafts has increased and effective use of energy in aircrafts has become compulsory after the effective use of aircrafts in many different fields. There should be significant precautions in the field of aviation as well to prevent the growth of a negative impact of aviation emissions on local air quality and weather (Lee 2010). Helicopters, also known as rotating wing aircrafts, are one of the aircrafts with the most focused and technical development efforts. Helicopters use piston engines which are used in three fourths of all aircrafts in the world and which are classified as internal combustion engines. Turboshaft engines, which are included in the category of gas turbine engines, are also used in helicopters.

Open literature includes energy and exergy analyses and sustainability assessments to compare the engine performance for internal combustion engines and gas turbine engines with different fuels and at different speeds, phases and temperatures. Some of these assessments are mentioned below.

Çaliskan and Hepbasli (2011) conducted an exergetic cost analysis and sustainability assessment of an internal combustion engine by using diesel fuel and two different biodiesel fuels. As a result of their study, they demonstrated that the sustainability index decreases while the exergy destruction rate increases, that is, the sustainability index and exergy destruction are inversely proportional, and that the exergy efficiencies and sustainability indices of biodiesel fuels are higher than those of diesel fuel. Altuntaş (2011) applied the exergy-economic and exergo-environmental analysis method to a four-stroke, air-cooled, four-cylinder and unsupercharged piston-prop aircraft engine for the landing and take-off phases and for a cruise flight of 1 h. In another study, Altuntaş et al. (2012a) conducted exergy, exergy-economy and sustainability assessments of a four-stroke, air-cooled, four-cylinder and unsupercharged piston-prop engine at the landing and take-off phases. According to the results of the analysis, it was observed that the phase requiring the most work flow was the take-off phase while the fuel energy and exergy flows were the highest at this phase. The lowest energy and exergy losses were found at the taxi phase while the highest energy and exergy efficiencies were found at the climbing phase. They also studied the exergo-environmental analysis of a spark-ignited, four-stroke, unsupercharged and air-cooled piston-prop aircraft engine during the landing, take-off and cruise phases. The study included analyses including the exergy analysis application, exergo-environmental impacts and distributions of exergy and exergo-environmental impacts (Altuntaş et al. 2012b). Turgut (2007) conducted a detailed exergo-economic analysis for a CF6-80 type turbofan engine with a high bypass ratio used in wide-bodied, medium long-range passenger aircrafts. Turgut et al. (2009) studied the effects of various parameters like exergy destruction, system life, system annual working hours and costs, fuel costs on exergy destruction cost, relative cost difference and exergo-economic factors of a turbofan aircraft engine using kerosene as fuel. Tona et al. (2010) conducted exergy and thermoeconomic analysis of a turbofan engine during a typical commercial flight throughout all life cycles by taking exergy destruction into account. Turan et al. (2014) calculated some exergetic parameters of a JT8D turbofan engine at take-off thrust power. They analysed by calculating the fuel consumption ratio, efficiency decrease ratio, fuel exergy factors, potential improvement ratio and product exergy factors for the components of JT8D engine at the take-off phase (fan, high pressure compressor, combustion chamber, high pressure turbine and low pressure turbine). Aydın (2012) conducted an exergy analysis of a turbofan engine with high bypass ratio used in medium and long-range aircraft and a turboprop engine used in both regional aircrafts and in turboshaft model helicopters and obtained exergy parameters to calculate the exergetic sustainability indicators of these engines. The study included separate calculations and

evaluations for the fan, low pressure compressor, high pressure compressor, combustion room, high pressure turbine, low pressure turbine and turbofan engines, which are the main components of an engine. Aydın et al. (2012b) calculated the exergetic parameters, exergy costs and unit exergy costs for compressor, combustion room, gas generator, power turbine and outputs which are main components of the CT7-9C engine which is a turboprop engine (2012). Aydın et al. (2013a) conducted an energy and exergy analysis at full and partial loads of a turboprop engine in order to be able to support the design of propeller aircraft engines and to increase the efficiency of the current systems. These energy and exergy analyses are a supporting source to obtain an improved exergetic performance, low fuel consumption and high shaft horse power. In another study, Aydın et al. (2013b) calculated exergo-sustainability indicators by conducting exergetic analyses for a turboprop aircraft at the phases of taxi, landing, climbing, maximum cruise, normal take-off, automatic inverse power, maximum take-off and constant maximum power phases. The study showed that the maximum exergy efficiency for the concerned turboprop aircraft had a minimum exergy efficiency (20.6 %) and minimum exergo-sustainability index (0.26) during the phases of taxi and landing. Apart from that, it was found that the aircraft had a very good index of exergetic efficiency, waste exergy ratio and exergetic sustainability index at the phases of climbing, maximum cruise, normal take-off, automatic inverse power, maximum take-off and constant maximum power.

Ballı and Hepbaşlı conducted exergo-economic, sustainability and environmental damage cost analyses of the T56 turboprop engine. They assessed the effects of increasing fuel flow speed to the performance of the T56 turboprop engine and components in different power loadings in four different operation modes. They stated that the only way to increase the shaft power of the constant speed turboprop engine was to increase the fuel flow speed and that the generated shaft power and thrust increased with the increase of fuel flow speed and turbine input speed at different operation modes (Ballı and Hepbaşlı 2014). Atılgan et al. (2013) used the exergo-environmental analysis method to study the environmental impact of the engine of a turboprop aircraft that is generally used in regional transportation and generates a torque of 1948 SHP and 640 Nm. When the total environmental impact of the turboprop aircraft engine was examined as a result of the study, it was determined that 9 % took place in the compressor, 69 % in the combustion room, 13 % in the gas turbine generator, 72 % in the power turbine and 22 % in the exhaust nozzle and that the combustion room had the priority for improvement according to these results. The study also found that the exergo-environmental analysis could be used sued to estimate the environmental impact measurements of aircraft drive systems. Etele and Rosen (2001) conducted an exergy analysis at a certain altitude from sea level (up to 15.000 m high from sea level) to a turbojet engine. They observed as a result of this study that the majority of the exergy losses were caused by the exhaust emissions and that the rational efficiency with increasing height was reduced by nearly 2 %. In another study to increase efficiency

in aviation applications and to reduce losses by using exergy methods, Rosen and Etele (2004) assessed the exergy efficiency of a turbojet engine during a typical flight cycle. Ballo et al. (2008) conducted an exergy and exergo-economic analysis in a J69-T25 model used in T-37 B/C model training aircrafts. Numerical exergy and exergo-economic cost balance equations were found for each component of the engine (air compressor, combustion room, exhaust channel, mechanic shaft) and for a general J69-T25A engine. In addition, the exergy cost ratio and unit exergy cost ratio of the engine was calculated.

This study included a sustainability assessment by using the exergy analyses of a spark-ignited, unsupercharged and air-cooled piston-prop helicopter engine in the engine power range of 150-600 SHP. While making the calculation, the temperature and pressure values of the reference environment were measured as 25 °C (298 K) and 1 atm, the cooling air temperature as 330 K and system output temperature as 1200 K (Yıldırım 2014).

11.2 Method

Exergy can be simply defined as the maximum operation potential that can be obtained from an energy source (Moorhouse 2003). Exergy analyses are currently used in the fields of analysis, design and performance improvement areas as well as to evaluate the sustainability levels of systems. In exergy-based sustainability calculations, values calculated by exergy analysis are used.

Exergy efficiency, waste exergy ratio, exergy destruction factor, environmental impact factor and exergetic sustainability index parameters are the indicators of exergetic sustainability.

11.2.1 Waste Exergy Ratio

During the engine run time, some part of exergy is lost through the discharge of exhaust gas to the environment while some part is destructed in engine components. The waste exergy (Ex_{we}) in the system is equal to the total of exergy destruction ($\dot{Ex}_{dest}$) and loss exergy ($\dot{Ex}_{loss}$).

$$\sum \dot{Ex}_{we} = \sum \dot{Ex}_{dest} + \sum \dot{Ex}_{loss} \tag{11.1}$$

The waste exergy ratio (r_{we}) is the ratio of total waste exergy output to total exergy input ($\dot{Ex}_{in}$).

$$r_{we} = \frac{\sum \dot{E}x_{we}}{\sum \dot{E}x_{in}} = \frac{\sum \dot{E}x_{dest} + \sum \dot{E}x_{loss}}{\sum \dot{E}x_{in}} \qquad (11.2)$$

11.2.2 Exergy Destruction Factor

The exergy destruction factor (f_{exd}) is an important parameter indicating the reduction of the positive effect of the engine on exergy-based sustainability, and it is found by the ratio of the exergy destruction to total exergy input.

$$f_{exd} = \frac{\sum \dot{E}x_{dest}}{\sum \dot{E}x_{in}} \qquad (11.3)$$

11.2.3 Environmental Impact Factor

The environmental impact factor (r_{eef}) is a factor that is destructed in the system and is an important parameter indicating whether the exergy discharged to the environment, i.e. the waste exergy, damages the environment. It is the ratio of the waste exergy ratio to the exergy efficiency (ψ).

$$r_{eef} = \frac{r_{we}}{\psi} \qquad (11.4)$$

11.2.4 Exergetic Sustainability Index

The exergetic sustainability index (Θ_{esi}) is a very important parameter to be able to assess the sustainability level of the system. Very high efficiency refers to a high exergetic sustainability index and therefore to a low waste exergy ratio and low environmental impact factor. Exergy helps in determining how well efficiency can be improved, and it is associated with the reduction of thermodynamic losses in processes. Measures to increase the exergy efficiency reduce energy losses and negative effects on the environment. It contributes to the sustainability by increasing the exergy efficiency and reducing exergy losses and therefore by reducing both the internal exergy consumption and waste exergy emissions. The exergetic sustainability index is the ratio of the exergy efficiency to the waste exergy ratio.

$$\Theta_{esi} = \frac{1}{r_{eef}} = \frac{\psi}{r_{we}} \qquad (11.5)$$

11.3   Conclusion

A sustainability assessment was done for the relevant power values by using the energy and exergy analyses. Waste exergy ratios, exergy destruction factors, environmental impact factors and exergetic sustainability indices were calculated by using Eqs. (11.2), (11.3), (11.4) and (11.5), respectively. Table 11.1 includes the exergetic sustainability indicators calculated for the relevant power values.

Graphics based on the findings are given in Fig. 11.1 (Waste Exergy Ratios), Fig. 11.2 (Exergy Destruction Factors), Fig. 11.3 (Environmental Impact Factors), Fig. 11.4 (Exergetic Sustainability Indices).

When we study the graphics, we see that the waste exergy ratio, exergy destruction factor and environmental impact factor were reduced to 250 SHP and that the energy and exergy efficiencies took the minimum value at 250 SHP where they had the highest calculation and they increased again after 250 SHP and reached the maximum value at 650 SHP. The highest exergetic sustainability index was

Table 11.1 Exergetic sustainability indicators calculated for the relevant power values

Power (SHP)	r_{we} (%)	f_{exd} (%)	r_{eef}	Θ_{esi}
150	88.116	67.522	7.414	0.135
200	87.417	66.891	6.947	0.144
250	87.285	66.771	6.865	0.146
300	87.683	67.131	7.119	0.140
350	88.581	67.942	7.757	0.129
400	89.859	69.096	8.861	0.113
450	91.324	70.419	10.526	0.095
500	92.784	71.738	12.859	0.078
550	94.106	72.932	15.968	0.063
600	95.230	73.946	19.964	0.050
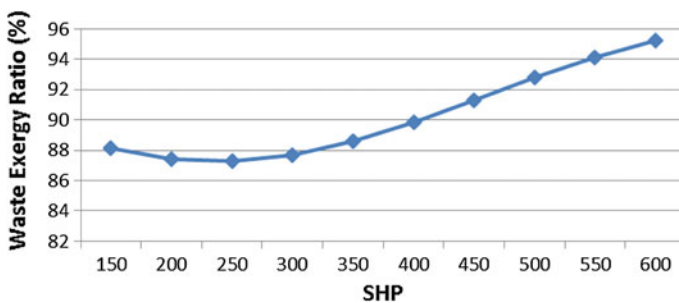
Fig. 11.1 Waste exergy ratios
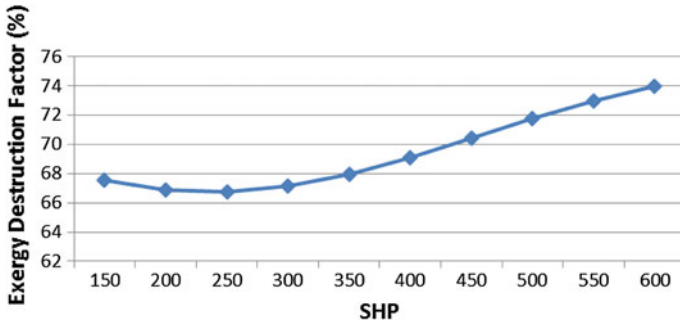
Fig. 11.2 Exergy destruction factors
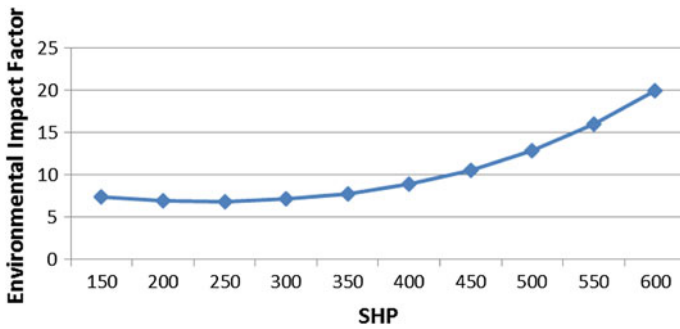
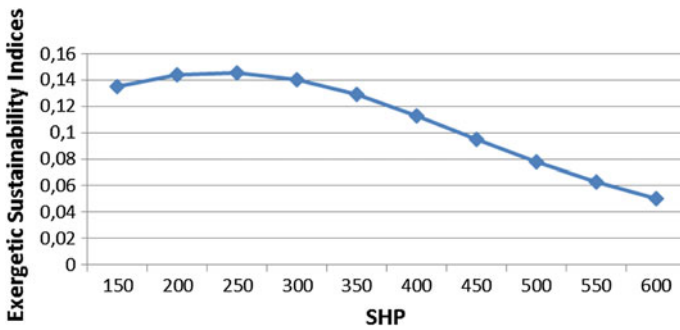**Fig. 11.3** Environmental impact factors

Fig. 11.4 Exergetic sustainability indices

calculated at 250 SHP where the energy and exergy efficiencies had the highest value, while the lowest exergetic sustainability index was calculated at 600 SHP where the energy and exergy efficiencies had the lowest value.

References

Altuntaş Ö (2011) Piston prop uçak motorlarında ekserjoekonomik çevresel optimizasyon, Doktora Tezi, Anadolu Üniversitesi, Fen Bilimleri Enstitüsü, Sivil Havacılık Anabilim Dalı, 99 s

Altuntaş Ö, Karakoç HT, Hepbaşlı A (2012a) Exergetic, exergoeconomic and sustainability assessments of piston-prop aircraft engines. J Therm Sci Technol 32(2):133–143

Altuntaş Ö, Karakoç HT, Hepbaşlı A (2012b) Exergoenvironmental analysis of piston-prop aircrafts. Int J Exergy 10(3):290–298

Atılgan R, Turan Ö, Altuntaş Ö, Aydın H, Synylo K (2013) Environmental impact assessment of a turboprop engine with the aid of exergy. Energy 58:664–671

Aydın H (20120 Ticari uçakların ekserjetik sürdürülebilirlik indikatörlerinin geliştirilmesi, Doktora Tezi, Anadolu Üniversitesi, Fen Bilimleri Enstitüsü, Sivil Havacılık Anabilim Dalı, 217 s

Aydın H (2013) Exergetic sustainability analysis of LM6000 gas turbine power plant with steam cycle. Energy 57:766–774

Aydın H, Turan Ö, Midilli A, Karakoç TH (2012) b, Exergetic and exergo-economic analysis of a turboprop engine: a case study for CT7-9C. Int J Exergy 11(1):69–88

Aydın H, Turan Ö, Midilli A, Karakoç TH (2013a) a, Energetic and exergetic performance assessment of a turboprop engine at various loads. Int J Exergy 13(4):543–564

Aydın H, Turan Ö, Karakoç TH, Midilli A (2013b) b, Exergo-sustainability indicators of a turboprop aircraft for the phases of a flight. Energy 58:550–560

Bakanlığı TCME (2013) Motor Çevrimleri ve Yakıtlar, Ankara, 129 s

Ballı Ö, Hepbaşlı A (2014) Exergoeconomic, sustainability and environmental damage cost analyses of T56 turboprop engine. Energy 64:582–600

Ballı Ö, Aras H, Aras N, Hepbaşlı A (2008) Exergetic and exergoeconomic analysis of an Aircraft Jet Engine (AJE). Int J Exergy 5(5/6):567–581

Çalışkan H, Hepbaşlı A (2011) Exergetic cost analysis and sustainability assessment of an internal combustion engine. Int J Exergy 8(3):310–324

Etele J, Rosen MA (2001) Sensivity of exergy efficiencies of aerospace engines to reference environment selection. Exergy Int J 1(2):91–99

http://databank.worldbank.org. Erişim Tarihi, 11 Feb 2014

Lee JJ (2010) Can we accelerate the improvement of energy efficiency in aircraft systems. Energy Convers Manag 51:189–196

Moorhouse DJ (2003) Proposed system-level multidisciplinary analysis technique based on exergy methods. J Aircr 40(1):11–15

Rosen MA, Etele J (2004) Aerospace systems and exergy analysis: applications and methodology development needs. Int J Exergy 1(4):411–425

Tona C, Paolo AR, Pellegrini LF, Junior SO (2010) Exergy and thermoeconomic analysis of a turbofan engine during a typical commercial flight. Elsevier Energy 35:952–959

Turan Ö, Aydın H, Karakoç TH, Midilli A (2014) Some exergetic measures of a JT8D turbofan engine. J Autom Control Eng 2(2):110–114

Turgut ET (2007) Uçaklarda Kullanılan Gaz Türbinli Motorların Ekserjoekonomik Analizi, Doktora Tezi, Anadolu Üniversitesi, Fen Bilimleri Enstitüsü, Sivil Havacılık Anabilim Dalı, 158 s

Turgut ET, Karakoç TH, Hepbaşlı A (2009) Exergoeconomic analysis of an aircraft turbofan engine. Int J Exergy 6(3):277–294

Yıldırım E (2014) Helikopter Motorunun Ekserjetik Analizi ve Sürdürülebilirlik Değerlendirmesi, Yüksek Lisans Tezi, Eskişehir Osmangazi Üniversitesi, Fen Bilimleri Enstitüsü, 62 s

Chapter 12
Energy Efficiency Study on Air-Cooled Condensers

Ismail Ekmekci and Kemal Ermis

Abstract Cooling systems for HVAC applications in aviation area have a great importance and due to the limited space in complex aviation systems and equipment, energy efficiency is becoming increasingly importance. Energy efficiency affects the design of chillers that account for a significant ratio of the energy consumption in plants. Legal legislations in the short-term limit, and in the long term prohibit the use of refrigerants that have high global warming potential, which are very harmful to the ozone layer. Since air-cooled condensers are among the essential components of cooling groups, efforts to improve their energy efficiency are made incessantly, the related national and international standards are upgraded and limitations on their energy consumptions are always increasing. In light of the latest applicable standards, detailed and comparative information on applications aimed at improving the energy efficiency in air-cooled condensers, highlighting the importance of energy efficiency in cooling installations.

Nomenclature

A   Area, m^2
T   Temperature (°C)
R   Energy Ratio (–)

I. Ekmekci (✉)
Engineering and Design Faculty, İstanbul Commerce University, İstanbul, Turkey
e-mail: iekmekci@ticaret.edu.tr

K. Ermis
Sakarya University, Esentepe, Sakarya, Turkey
e-mail: ermis@sakarya.edu.tr

12.1 Introduction

Becoming increasingly important in HVAC applications of aviation area, energy efficiency affects the design of chillers that account for a significant ratio of the energy consumption in HVAC. Legal legislations in the short-term limit and in the long term prohibit the use of fluids of high global warming potential, which are very detrimental to the ozone layer. Since air-cooled condensers are among the essential components of cooling groups, efforts to improve their energy efficiency are made incessantly, the related national and international standards are upgraded and the limitations on their energy consumptions are always increasing.

In light of the latest applicable standards, detailed and comparative information on applications aimed at improving the energy efficiency in air-cooled condensers, highlighting the importance of energy efficiency in cooling installations.

12.2 Design Data Pertaining to the Factors Affecting the Performance of Condensers

The parameters required for the design and selection of air-cooled condensers have been listed below:

- The condenser capacity required for the system
- The type of refrigerant that will be used
- The dry-bulb temperature of the ambient inlet air
- Design condensation and evaporation temperatures
- The permitted values for fluid side pressure drops
- Unit size limits
- The permitted maximum noise level
- The desired energy efficiency class: the isolation, heat resistance, and protection class properties of the fans.

By knowing the design data specified above and the additional optional features, manufacturing firms may design and manufacture condensers in line with their own manufacturing techniques. It is highly important for potential difficulties which would not be easily remedied; that the manufacturing firms possess a performance-approved design software and design the coils by the help of this software and program.

There are essential design data and criteria which need to be observed for achieving the required performance in a condenser in an efficient manner over the long run. In the following pages, the parameters and criteria affecting the energy efficiency of condensers have been explained.

12.2.1 The Effect of Condensation Temperature on Capacity

The condensation temperature of the refrigerant is considered to be 6–20 °C above air inlet temperature for general purposes. The condensation temperature varies according to the ambient temperature in which the system will operate. The condensation temperature for applications is commonly taken as 30–60 °C.

Factors taken into consideration for determining the condensation temperature:

- Ambient temperature,
- Thermophysical properties of the refrigerant
- Properties of the selected compressor
- And the dimensions of the condenser.

While providing the nominal condenser capacity in condensers as per the Eurovent Standard, the air inlet temperature and condensation temperature are taken as 25 and 40 °C, respectively. In other words, $\Delta T = 15$ °C.

A low value should be selected for the temperature differential ΔT, in places of high ambient temperature. For instance, while designing for the conditions of Antalya the ΔT value should be selected within the range of 7–10 °C. For systems that will operate in outdoor environments in conditions of Turkey, the temperature differential should be lowered as one goes from the north to the south and selections should be made accordingly. It must always be considered that high compression temperature creates a load on the compressor that reduces efficiency and shortens its useful life. It will be quite beneficial in the design for the condensation temperature to be specified as low as possible. However, in some conditions it is not possible to take a low value for the condensation temperature. For example in Middle East countries where the outdoor temperature is 50–55 °C, high condenser temperature is unavoidable.

The following example shows the compressor-absorbed power at various condensation temperatures and the achieved cooling capacities for a semi-hermetic type HGX4/555-4 model compressor manufactured by Bock, which uses R134a gas as shown Table 12.1 (Bock). The cooling gas selected for the example is R134a. As

Table 12.1 Variation in the power absorption by the compressor, the achieved cooling capacity, and the effectiveness value at fixed evaporation and varying condensation temperatures

Condensation temperature (°C)	Evaporation temperature (°C)	Cooling capacity (kW)	Power drawn by the compressor (kW)	Cooling capacity/power drawn by the compressor (COP)
30	−5	21,997	5.93	3.71
40	−5	19,665	6.49	3.03
50	−5	16,876	6.99	2.41
60	−5	13,545	7.43	1.82
70	−5	9586	7.82	1.23

BOCK technical catalogue (selected model HGX4/555-4 R134A)

Effect of the condensation temperature on the compressor absorbed power

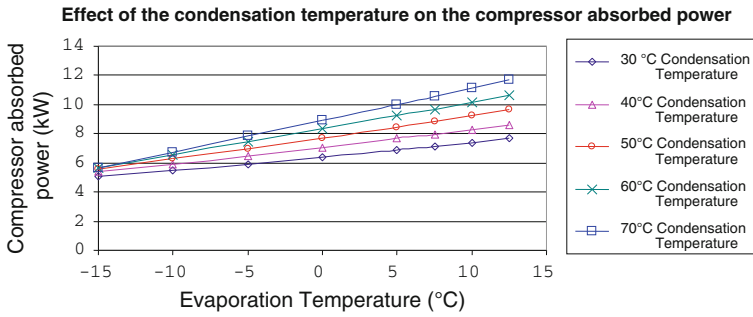**Fig. 12.1** Variation in cooling capacity in various condensation temperatures (BOCK Technical Catalogue; selected model HGX4/555-4 R134A)

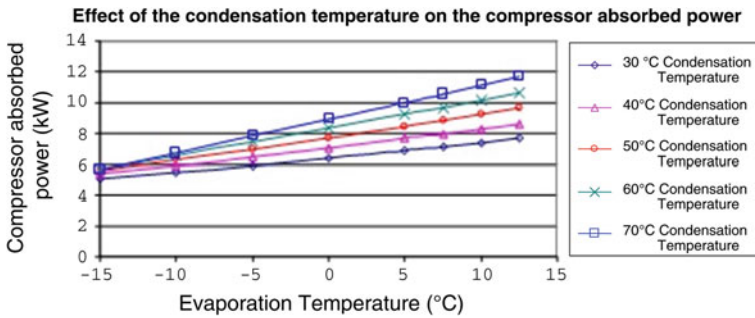**Effect of the condensation temperature on the compressor absorbed power**

Fig. 12.2 Variation in the power drawn by the compressor in various condensation temperatures (BOCK Technical Catalogue; selected model HGX4/555-4 R134A)

seen from the table, when the condensation temperature rises from 30 to 60 °C, the compressor draws 25 % more power while the cooling capacity drops by 38.5 %, the COP value (ratio of the cooling capacity to the power drawn by the compressor) decreases by 51 %, and the a unit that is 38.5 % larger must be used to achieve the cooling capacity declared in the design.

Variation in cooling capacity in various condensation temperatures is shown Fig. 12.1.

Variation in the power drawn by the compressor in various condensation temperatures is shown Fig. 12.2.

One of the systems used to improve energy efficiency in air-cooled condensers is the system of spraying water over a mesh. The mesh and spray system involves the spraying of the amount of water that is required by the system from nozzles placed on specific positions on the wide and fine mesh material located on the front of the air-cooled condenser, and lowering the inlet air temperature coming in

contact with the heat exchanger surface by the adiabatic vaporization of the sprayed water, thus increasing the efficiency of cooling (EPS Ltd. Ecomesh Technical Catalogue).

The sprayed water leads to adiabatic cooling of the inlet air flow. As the specified set values are exceeded, the control system initiates the water spraying system to lower the temperature of the air entering the heat exchanger. The period of operation and frequency setting of the water spray system is continuously maintained by the controlling unit in order to achieve optimization of system performance and minimization of water consumption. Since the water is not directly sprayed on the heat exchanger surface, but rather on the mesh surface, furring does not occur on the fins. In this way, drops in heat transfer efficiency are avoided. This system also renders any water softening process superfluous.

12.2.2   Effect of Fin Geometry on Capacity

In the design of air-cooled condensers, fin geometry which defines the diameter of the tube and distances between tubes influences capacity and pressure losses. The fin geometry is selected among its own standards by the manufacturer so as to provide the required cooling capacity within the appropriate pressure losses.

Geometries with intensive tubing can be said to yield more advantageous capacity/price ratios; however in this case, optimization is required since pressure losses will increase in tandem. Under practical conditions, it must be kept in mind that air-cooled condensers having the same heat transfer surface, yet different geometries will yield different cooling capacities and pressure losses under the same conditions (Fig. 12.3).

Fig. 12.3 Vertical and flatbed mesh and spray system air-cooled condensers (Friterm A.Ş. Technical Documents; EPS Ltd. Ecomesh Technical Catalogue)

12.2.3 Effect of Air Velocity on Capacity

Air velocity is an important criterion, since it affects the partial heat transfer coefficient on the air side. Since heat transfer increases with air speed, a smaller heat exchanger will be enough; however, in high speeds, the fan performance drops due to increased pressure loss in the air side. For this reason, the air velocity should be selected at optimum values. The air velocity recommended for air-cooled condenser design at standard noise levels is around 3.0–4.0 m/s. In environments where lower noise levels are desired, the air velocity will also be reduced. Air velocities below this figure require the selection of a large heat exchanger. Higher air velocities, on the other hand require stronger and costlier fans.

12.2.4 The Effect of Grooved Tubes on Capacity

The inner surface of tubes used in air-cooled condensers can vary with design and cost optimization. Smooth tubes and grooved tubes can be used in condenser coils. The properties of fluid and application to be used for grooved or smooth tubes should be evaluated. Figure 12.4 shows the measurements involved in the technical specifications of grooved tubes while Fig. 12.5 shows cross sections of grooved tubes.

An experimental study has been conducted by an international firm manufacturing copper tubes on the variation of capacity as a function of coil surface air speed
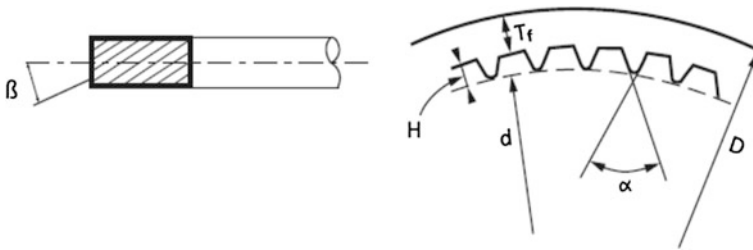
Fig. 12.4 The measurements involved in the technical specifications of grooved tubes (KME)
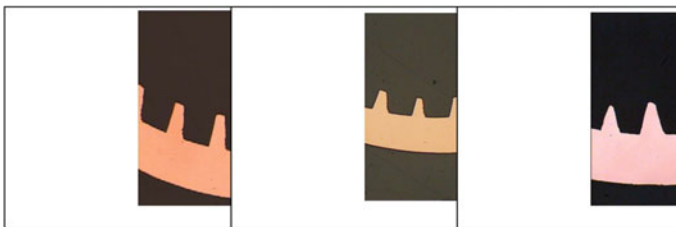
Fig. 12.5 Cross-sections of grooved tubes of different geometric forms (KME)

with the use of grooved tubes in air-cooled condensers. Prototype units of five different groove geometries have been used for the study. The working conditions of the tested prototypes and the fluid used have been the same. Table 12.2 and Fig. 12.6 give the data and results of the tests. In the comparison between smooth tubes and grooved tubes under conditions of 40 °C condensation, 25 °C air inlet temperature and the use of R404A gas, it has been observed that the use of grooved tubes yields 11.70 % higher capacity (KME Technical and Test Documents).

12.2.5 Effect of Fan Selection on Capacity and Noise Level and Control Options

Since cooling groups are used in cold storage facilities, air conditioner, process cooling systems etc. in some places, low noise level during the operation of the group is an important issue. Condenser fans and compressors are the two components that are sources of noise in cooling groups. The noise level which results primarily from the fan motor and the design of the fan blades is determined by evaluating manufacturer's data and checked in terms of conformance to the prescribed specifications. The sound level may be reduced by decreasing motor rotation, if need be; in this case the heat transfer area of the heat exchanger should be increased in order to provide the required cooling capacity.

Another point which requires consideration in condenser selection is the necessity to assure the adequacy of the design to provide the cooling capacity required in conditions of high ambient temperature. In periods where air temperatures are low, operating all fans at maximum rotation to achieve the desired capacity will be superfluous and costly. In systems monitored by condenser pressure—temperature, operating fans at low rotation or disabling them will provide an air supply of sufficient flow to the system.

12.2.5.1 Two Speed Fans

The most practical means of supplying air of varying flow is to use a two speed fan. Thanks to these fans that can operate at a secondary speed like three-fourths of the highest operating rotation, a substantial amount of energy can be saved in periods where the air inlet temperature falls far below design temperatures. For example, a condenser with four fans may be operated with lowered fan rotation when ambient temperature drops from 33 to 20 °C. In this case, 0.75 kW less of power will be consumed per fan, which means an energy consumption of nearly 40 %. This example pertains to four fans; systems of a much higher number of fans are being operated in most plants. The power consumed by the 800-mm diameter fan in both

Table 12.2 Sample comparison: difference in annual expenditure (Euros/year) for condensation temperatures of 50 and 35 °C (BOCK Technical Catalogue)

Condensation temperature (°C)	Cooling capacity (W)	Compressor absorbed Power (kW)	Coefficient of performance (C.O.P)	Consumed power due to 160 kW	Differences between the nominal condensation	Consumption price ($/kW)	Working hours of the unit (hour/year)	Compressor annual difference ($/year)	Difference in fan Power ($/year)	Total difference in unit ($/year)	Total difference in unit (EURO/year)	50–35 °C condensation difference (EURO/year)
30	186.202	45.47	4.10	39.05	−13.47	$0.13	6000	−$10,232	–	–	–	13,504 €
35	173.053	49.00	3.53	45.27	−7.25	$0.13	6000	−$5505	$607.63	−$4897	−3588.05 €	
40	159.904	52.52	3.04	52.52	–	–	–	–	–	–	–	
45	146.388	55.65	2.63	60.79	8.27	$0.13	6000	$6280	−$303.82	$5976	4378.48 €	
50	132.872	58.78	2.26	70.74	18.22	$0.13	6000	$13,838	−$303.82	$13,534	9915.61 €	

Selected condenser: Class A condenser—will be evaluated for 160 kW refrigeration load; The selected compressor: Semi-Hermetic (BOCK HGX7/2110-4 S) evaporation temperature: 5 °C
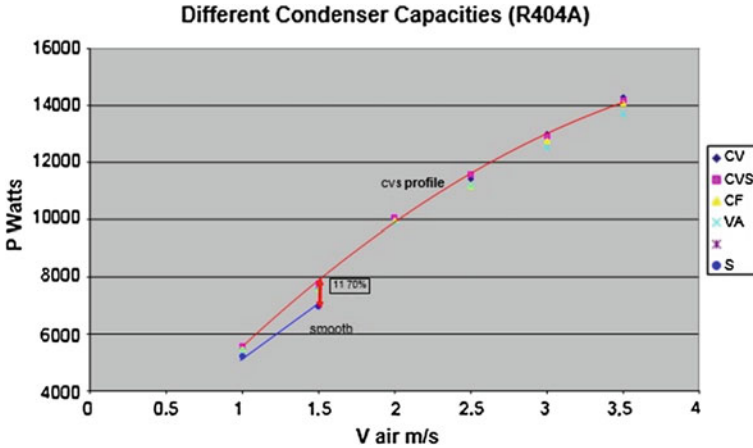
Fig. 12.6 Results of the experiment conducted for the R404A gas, graphical representation (KME Technical and Test Documents)

speed and data belonging to another fan which may be used in lower rotations has been given below (Ziehl Abegg Technical Catalogue).

880 d/d	2.00 kW
660 d/d	1.25 kW
440 d/d	0.37 kW
330 d/d	0.20 kW

12.2.5.2 Use of Frequency Inverters and Step Control Units

With control units used both in single- and two-speed fans, air flows can be adjusted to needs. In places where sensitive control over fan speed is not required, step control systems where fans are sequentially enabled and disabled are implemented. The working sequence of fans can be determined by the users, and alternatives where fan operating periods are evenly distributed are also available. Since step control units operate on the basis of the fans being enabled or disabled, they can be manufactured at a lower cost than systems monitoring fan rotation. For this reason, this method is widely preferred for systems including a great number of fans and which do not require sensitive control. The following graph shows the amount of energy saved in a step-controlled operation of a dry cooler with four fans. It has been assumed that all four fans operate at the hottest hours of the day and that a single fan is sufficient at the coolest hours (Fig. 12.7)

Fig. 12.7 Electricity
consumption of fans over a
period of one day, in a
condenser where fans are
enabled according to need by
way of step control. (The
filled area indicates the
amount of electricity
consumed by not using all
fans simultaneously, in terms
of kWh) (EBM-PAPST
Technical Brochure)
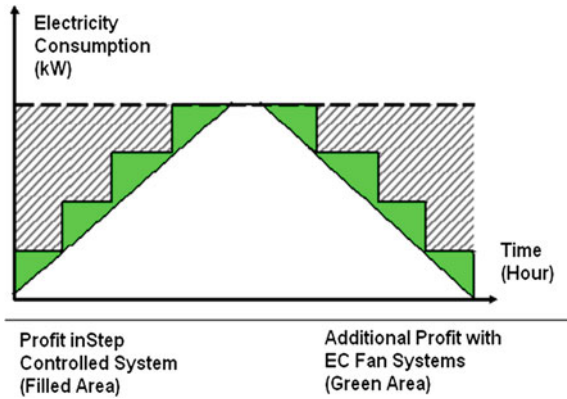
In cases where the number of fans used is low and where the temperature–pressure differences are sensitive, step control does not yield adequate results. In such cases, systems monitoring fan speed and which therefore offer much more sensitive control over air flow (frequency inverters/converters) are used. Frequency inverters/converters are more expensive than step control unit in terms of initial investment cost; therefore, the systems that are widely preferred are those where fans are controlled in groups and step control units and frequency inverters/converters are used together, as opposed to systems where all fans are controlled by separate frequency inverters/converters.

12.2.5.3 EC Fans

In addition to motor options of various speed ranges, the EC Motor technology whose areas of use have increased significantly over the last few years, are also used in condenser applications. EC fans facilitate controlling the fan motor at all speeds, independently of the number of poles. As seen in Graph 5.A, EC Motor systems save an average of 10 % energy at nominal speed as compared to conventional speed control systems such as frequency inverter-step control-transformer frequency. Due to the acoustically advantageous design of EC Motors, neither the unwanted resonances of frequency converter systems nor the buzzing of fan-controlled systems are observed in EC Motors. Thus, lower noise levels are achieved in EC Motor systems. As shown in Graph 5.B, while EC motor systems offer a minimum of 4 dBA advantage with respect to phase controlled and frequency converter systems, in low fan speeds and air flows in particular, this difference becomes as high as 15–30 dBA (Fig. 12.8).
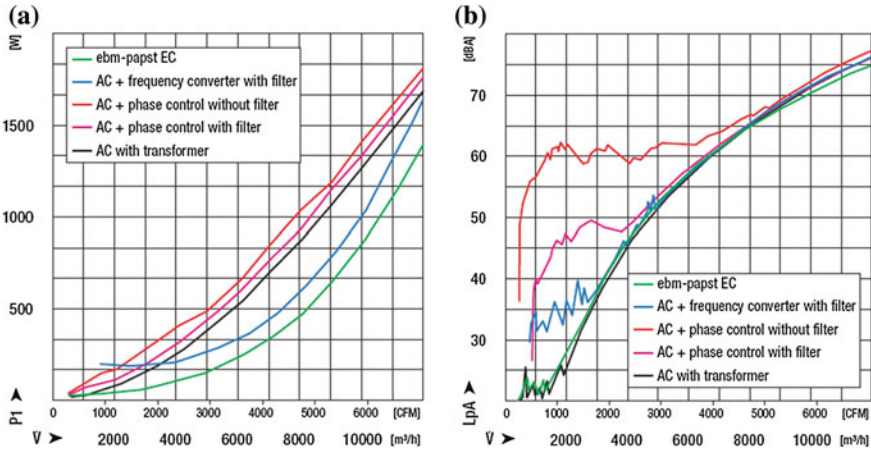
Fig. 12.8 a EC-Motor power consumption (EBM-PAPST GmbH "EC Fans" Technical Brochure). **b** EC motor noise level (EBM-PAPST GmbH "EC Fans" Technical Brochure)

12.3 Use of Free Cooling in Cooling Units with Air-Cooled Condensers

As opposed to conventional cooling units with air-cooled condensers, use of units with integrated free cooling coils has gained popularity of late. Free cooling is obtaining cooling water without operating or partially operating the chiller compressor of the group by taking advantage of the low ambient temperature (De Saulles 2004; ASHRAE 2000). For example in Great Britain, the use of integrated free cooling coil water cooling groups have a significant role in the fact that 62 % of the annual cooling demand is met through free cooling. In the country, only 38 % of the annual cooling requirement is obtained from mechanical cooling (De Saulles 2004; Oliver 2001).

Groups with integrated free cooling coils are alternative systems for cooling applications used in large computer and server rooms, Internet and telecommunication data centers. They have the capacity for both mechanical and free cooling (partial and complete) (De Saulles 2004). Figure 12.9a shows a view of the cased unit of the water cooling group with integrated free cooling coil, and Fig. 12.9b shows a simplified representation of the structure of this type of unit. The free cooling coil is placed in the front section—according to the air intake direction of the unit—of the air-cooled condenser coil. As the ambient temperature drops below that of the return water, the control valve sends the return water to the free cooling coil for precooling or for complete free cooling (De Saulles 2004) (Fig. 12.9).

The conclusions related to measurements taken in four European cities by a chiller manufacturing firm on cooling units with integrated free cooling coils in order to demonstrate the gain resulting from the use of free cooling in cooling systems have been given in Fig. 12.10.
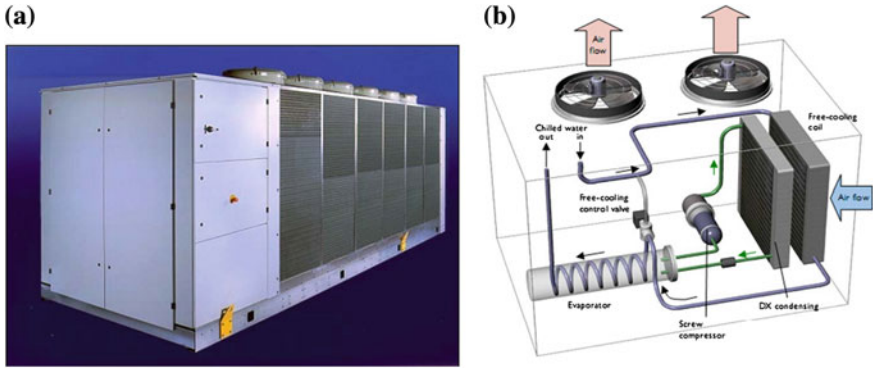
Fig. 12.9 a Air-cooled water cooling group with integrated free cooling coil (Airedale Technical Catalogue). **b** Schematic for air-cooled water cooling group with integrated free cooling coil (De Saulles 2004)
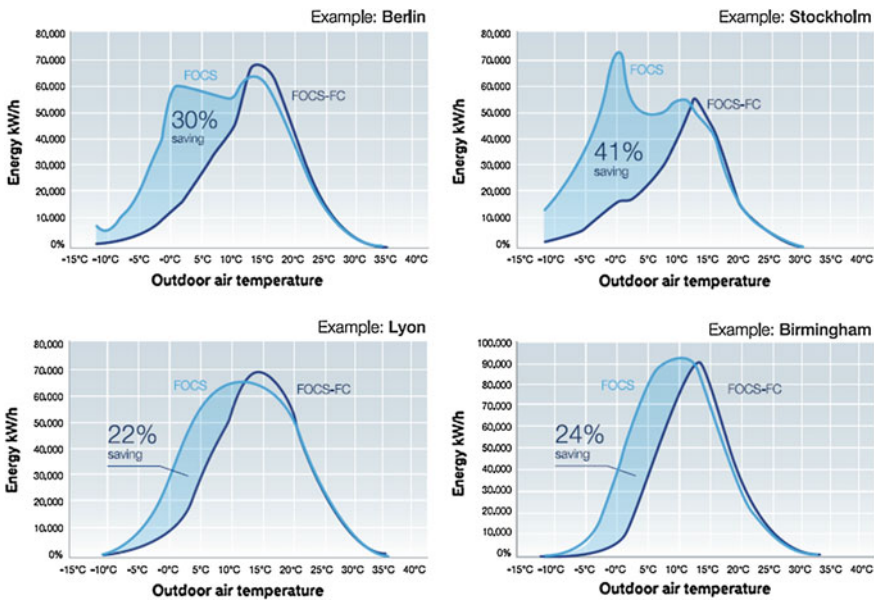

Fig. 12.10 Energy saving figures as a function of outdoor ambient temperature for groups with free cooling installed in air conditioning systems in four cities in Europe (Climaveneta, FOCS-FC/NG Technical Catalogue)

12.4 Standards and Energy Classification in Air-Cooled Condensers

Standard capacities in air-cooled condensers are defined in accordance with the conditions set forth in the TS EN 327 (Heat Exchangers-Test Procedure for Establishing the Performance of Forced Convection Air Cooled Condensers) (TS EN 327).

Condenser coils must be manufactured in conformance to the SEP (Sound Engineering Practice) defined under 97/23/EC PED (Pressure Equipment Directive) and the entire unit must meet CE requirements (97/23/EC The Pressure Equipment Directive).

Energy efficiency in products may be calculated for the value ranges given in Table 12.3, as per the EUROVENT Rating Standard for Forced Convection Air Cooled Condensers For Refrigeration "Air Cooled Condensers") 7/C/002—2007 (EUROVENT Rating Standard).

There is a significant correlation between increasing energy efficiency and initial investment costs. While the initial investment costs of products with high-energy efficiency is relatively high, they can be said to make up for the difference in costs in a short while.

Table 12.4 shows a sample comparison between two air-cooled condensers assumed to use the same type of cooling fluid have the same operating conditions and equal capacities. For the comparison, the condenser capacity requirement of the system has been assumed to be 160 kW and alternative condenser designs have been made accordingly. Basic differences between sample units:

- Heat transfer surfaces,
- Unit dimensions,
- Coil surface air speeds,
- Electrical powers,
- Energy efficiency classes,
- Noise levels and
- Costs.

The unit with a higher initial investment cost has a larger size and heat transfer area. This has a direct bearing on cost. However, low values for the air velocity and consequently for pressure loss on the air side has an impact on the electricity consumption value, which lowers costs of consumption. This increases the energy efficiency of the unit and places the unit in the A, B, C, and D energy Classes.

Table 12.5 shows the difference between the Class A product and the Class D product. It is seen that the Class A product which has a higher initial investment cost, self-finances within 1.7 years as compared to use of a Class D product (Table 12.6).

Table 12.3 Test results of prototypes with different groove geometries for R404A and R22 gases (KME)

Test conditions	Test 1	Test 2	Test 3	Test 4	Test 5	Test 6	Test 1	Test 2	Test 3
Fluid	R404A						R22		
Fin type	Wavy	Wavy	Wavy	Wavy	Wavy	Wavy	Wavy	Wavy	Wavy
Test conditions ENV327									
Condensation temperature (°C)	40	40	40	40	40	40	37,4	37,4	37,4
Air inlet temperature (°C)	25	25	25	25	25	25	26	26	26
dT	15	15	15	15	15	15	11,4	11,4	11,4
Supercooling (K)	2	2	2	2	2	2	4	4	4
Air flow (m^3/h)	1069.2	1603.8	2138.4	2673	3207.6	4347	1440	1728	1958
Air velocity (m/s)	1	1.5	2	2.5	3	3.5	2.5	3	3.4
Capacities—test results (Watt)									
CV type groove geometry	5492	7600	9967	11,422	12,998	14,288	4563	4802	4950
CVS type groove geometry	5577	7771	10,074	11,583	12,915	14,154	–	–	–
CF type groove geometry	5492	7571	9970	11,172	12,764	14,081	4,593	4,713	4,869
V or VA type groove geometry	–	7531	9894	11,172	12,518	13,696	–	–	–
Smooth type groove geometry	5219	6960	–	–	–	–	3644	3886	4089

Table 12.4 Energy efficiency class (Oliver P 2001)

Class	Energy consumption	Energy ratio (R)*
A	Extremely low	R > = 110
B	Very low	70 = < R < 110
C	Low	45 = < R < 70
D	Medium	30 = < R < 45
E	High	R < 30

*The energy ratio "R" is obtained by dividing the standard capacity of the product by the total energy consumption of fan motors

Table 12.5 Sample comparison of the four assumed condensers (Friterm, Technical Documents)

Specifications	Condenser 1		Condenser 2		Condenser 3		Condenser 4	
Model	FUH YK 80 23 C1 2,1 E		FUH YK 63 24 C1 2,1 Q		FUH YK 50 24 C3 2,1 L		FUH YK 63 23 A1 2,5 S	
Energy efficiency class	A	Class	B	Class	C	Class	D	Class
Q (condenser capacity)	161,396	KW	163,430	KW	162,250	KW	160,170	KW
Heat transfer surface	543.3	m^2	522.6	m^2	461.3	m^2	272.1	m^2
Coil length	3600	mm	4000	mm	3200	mm	3000	mm
Coil width	2150	mm	1800	mm	1500	mm	1800	mm
Air flow	39,150	m3/h	40,730	m3/h	39,530	m3/h	57,640	m3/h
Air velocity	1.4	m/s	1.6	m/s	2.3	m/s	3.0	m/s
Fan diameter	800	mm	630	mm	500	mm	630	mm
Fan devri	330	d/d	480	d/d	900	d/d	900	d/d
Number of fans	6		8		8		6	
Total fan power	1.2	kw/h	1.52	kw/h	2.56	kw/h	4.68	kw/h
Sound power level (LwA)	68	dBA	72	dBA	78	dBA	84	dBA
Sound pressure level (LpA)	36	dBA	40	dBA	46	dBA	52	dBA
Energy ratio (R)	134.5	–	107.5	–	63.4	–	34.2	–
Unit price	€8525	Euro	€6676	Euro	€5396	Euro	€4515	Euro

Friterm A.Ş Technical Documents and Applications

12.5 Conclusion

Becoming a matter of primary importance in air conditioning, industrial cooling, aviation applications, commercial cooling, blast freezing. and process cooling applications, etc., energy efficiency affects the design of chillers that account for a significant ratio of the energy consumption in applications. Legal legislations that

Table 12.6 Comparison of the assumed condensers and the calculation of the payback period of the initial investment cost

Calculations	Difference between the class A and class D products	
Difference between the electrical consumption of fan motors of units	kw/h	3.48
Difference between the annual electrical consumption of fan motors (20 h/day)	kw	25,404
Unit cost of electrical consumption	$/kW	0.13
Difference in unit electrical consumption (USD)	$	0.09
Difference in total annual electrical consumption (EURO)	€	2364.1
Difference in unit costs	€	4010.0
Pay back period of the difference in unit cost	Years	1.7

for the short-run limit, and in the long run prohibit the use of fluids of high global warming potential, that are detrimental to the ozone layer are also influential on designs. Since air-cooled condensers are among the essential components of cooling groups, efforts to improve their energy efficiency are made incessantly, the related national and international standards are upgraded and limitations on their energy consumptions are always increasing.

Investors, project and application engineers operating within the cooling sector, should be well versed in the issues described above. As the use of products with high energy efficiency spreads, efficiency will rise in our systems. It should also be kept in mind that these systems are environment friendly as well.

References

97/23/EC The Pressure Equipment Directive

Airedale Technical Catalogue (http://www.airedale.com)

ASHRAE (2000) Handbook 2000 systems and equipment, chapter 36, chapter 38

BOCK Technical Catalogue (Selected model HGX4/555-4 R134A) (http://www.bock.de)

Climaveneta, FOCS-FC/NG Technical Catalogue (http://www.climaveneta.it)

De Saulles T (2004) BSRIA guide: free cooling systems. BSRIA

EBM-PAPST GmbH "EC Fans" Technical Brochure (http://www.ebmpapst.com)

EPS (Environmental Process Systems Ltd) Ecomesh Technical Catalogue (http://www.epsltd.co.uk)

EUROVENT Rating Standard (for Forced Convection Air Cooled Condensers For Refrigeration) 7/C/002 – 2007

Friterm A.Ş Technical Documents and Applications (http://www.friterm.com)

KME Technical and Test Documents (http://www.kme.com)

Oliver P (2001) Making use of free cooling. Build Serv J, Nov 2001

TS EN 327 (Heat Exchangers-Test Procedure for Establishing the Performance of Forced Convection Air Cooled Condensers)

Ziehl Abegg Technical Catalogue (http://www.ziehl-abegg.com)

Part II
Modelling, Planning and Optimization in Aviation

Chapter 13
Multi-objective Optimization
of a Two-Stage Micro-turbine
for Combined Heat and Power Production

**Majid AmirAlipour, Shoaib Khanmohammadi, Kazem Atashkari
and Ramin KouhiKamali**

Abstract In recent years, reducing the cost of energy production and transmitting electricity in remote areas of the distribution network have attracted many researchers' attention. One of the methods to fulfill these objectives is using a gas micro-turbine cycle. In this paper, a two-stage micro-turbine with an intercooler was used to produce electricity and heat simultaneously. In this system, the impacts of the effective input parameters, such as compressor pressure ratio, bypass ratio, and re-cooperator yield on cycle performance were studied given that the values obtained from cycle modeling were not continuous, and using GMDH-type neural system (as one of the most widely used neural networks with high potential to model complex data), the desired objective functions were estimated and then simultaneous optimization of the objective functions were implemented. It was shown that the maximum electrical exergy efficiency is 58 % and maximum thermal exergy efficiency is 18 %.

13.1 Introduction

One of the extensive applications of gas micro-turbines is in the area of scattered power production for residential units with a limited energy demand. Numerous articles have been published in the field of gas cycle modeling, frequently on the modeling of gas micro-turbine cycles. There are a few articles to examine gas micro-turbine cycle parameters. Based on a test data, Labinov et al. (2002) proposed a similar commercial micro-turbine model. They considered the turbine, compressor, and re-cooperator efficiencies to be constant and assumed that the thermo-physical properties of air and fuel did not change. Also, they found a good consistency between the modeling and commercial mode results and analyzed the changes, given the constancy of air and fuel properties. Ehyaei and Bahadori (2007) modeled a single-shaft micro-turbine and assumed the shaft rotation speed as an

M. AmirAlipour (✉) · S. Khanmohammadi · K. Atashkari · R. KouhiKamali
Department of Mechanical Engineering, University of Guilan, Rasht, Iran
e-mail: Majid_amiralipour@yahoo.com

input variable to optimize the objective function. They inferred that the rotation speed in a micro-turbine plays a very important role in this type of scattered energy generator and thus the main distinguishing factor between micro-turbines and large gas turbines is the high speed of shaft rotation. Sadeghi et al. (2005) considered modeling and exergy analysis of a micro-turbine cycle along with a re-cooperator, compared the results with its industrial sample, and confirmed their modeling validity. In another study, Sadeghi performed a thermodynamic analysis of the different forms of a gas micro-turbine attached to are-cooperator using a cogeneration method and concluded that a micro-turbine with an intercooler is the best form in terms of efficiency and power generation. For a detailed analysis and evaluation of a potential energy-saving micro-turbine to be used in a cogeneration system, a simple but rather accurate model is desirable. Some of the general equations use mass-momentum and energy balance, thus to be nonlinear and highly complex requiring a great deal of time to be calculated. Jurado (2005) presented some of these models, by which they compared large and micro-gas turbines and concluded that the use of such models is desirable for large gas turbines. Hao et al. (2006) performed a thermodynamic modeling, numerical simulation of a single-shaft micro-turbine, and analysis of cycle performance with respect to the performance parameters of the cycle. By considering the modeled cycle performance parameters as variables, the authors obtained the study micro-turbine power and efficiency and compared their results with a commercial 100-kW micro-turbine. AmirAlipour and Khanmohammadi (2014) conducted an exergy-economic analysis of a 300-kW micro-turbine, and subsequently considered its simultaneous optimization by defining both the economic objective functions and efficiency. In other study, Khanmohammadi et al. (2015) conducted a multi-objective optimization of externally fired gas turbine CHP plant. They also, performed a sensitivity analysis to find the effect of design parameter on the system.

In this paper, the performance of a micro-turbine, including power, thermal efficiency, and exergy loss, associated with an intercooler and hot water generator were analyzed. Also, the effects of the input parameters, such as compressor pressure ratio and the ratio of bypass flow on the cycle performance were assessed. Finally, the micro-turbine optimization efficiency was determined by defining the objective functions.

13.2 Cycle Modeling

In this part, the cogeneration system was modeled as shown in Fig. 13.1.
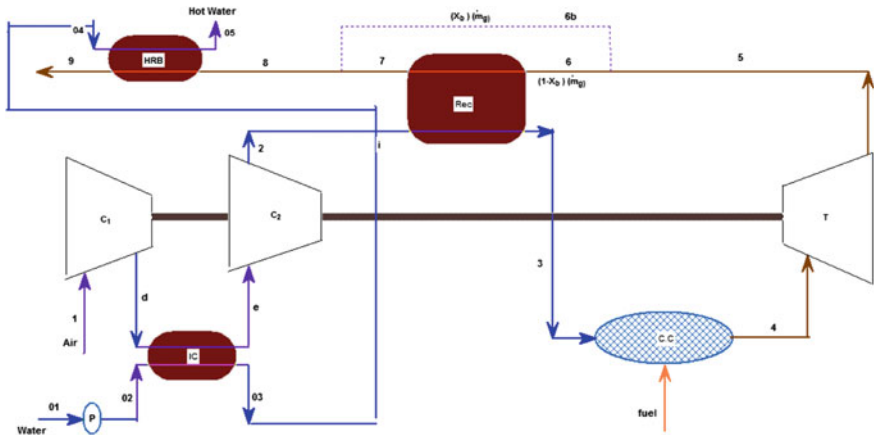
Fig. 13.1   Aschematic model of the cogeneration system

13.3   Thermodynamic Modeling

The equations governing the control capacities, including those of energy and mass balance for each component are presented as follows:

13.3.1   Compressor Modeling

13.3.1.1   First-Stage Compressor

The micro-turbine modeled had a two-stage compressor and an intercooler. The equations relevant to the first compressor analysis are as follows:

$$pd = p_1 \cdot \sqrt{\text{Cpr}} \tag{13.1}$$

$$\eta_c = \frac{h_{ds} - h_1}{h_d - h_1} \tag{13.2}$$

$$wc_1 = m_a \cdot (h_d - h_1) \tag{13.3}$$

where h_1 is air enthalpy in an ambient temperature and pressure; $\dot{m}_a$ is air mass current rate; Cpr is total cycle pressure ratio (3.5); and η_c is the compressor isentropic efficiency (88 %).

13.3.1.2 Second-Stage Compressor

The second-stage modeling is similar to the first compressor.

13.3.2 Intercooler

$$\eta_{ic} = \frac{h_d - h_e}{h_d - ha_{02}} \tag{13.4}$$

$$m_a \cdot (h_d - h_e) = m_w \cdot (h_{03} - h_{02}) \tag{13.5}$$

where $\dot{m}_w$ is mass flow rate of the input water; 2 kg/s h_{02} is the input water enthalpy; and η_{ic} is intercooler efficiency (0.85).

13.3.3 Pump Modeling

To increase intercooler water inlet a pump was utilized. The pump modeling equation is as follows:

$$h_{02} = h_{01} + \left(\frac{v_{01} * (p_{02} - p_{01})}{\eta_p} \right) \tag{13.6}$$

where p_{01} is inlet (city) water pressure before pump (101 kPa); and η_p is pump efficiency (0.85).

13.3.4 Re-cooperator

The purpose of using are-cooperator as a device for heat recovery was to reduce fuel consumption and improve the micro-turbine thermal efficiency. The hot gas energy emitted from the turbine was used for pre-heating the air entering the combustion chamber. Considering the air and fuel mass bypass, the related equations modeled are as follows:

$$m_g \cdot (1 - x_b) \cdot (h_6 - h_7) = m_a \cdot (h_3 - h_i) \tag{13.7}$$

$$\eta_{rec} = \frac{m_a \cdot (h_3 - h_i)}{m_g \cdot (1 - x_b) \cdot (h_6 - h_i)} \tag{13.8}$$

The percentages of the pressure losses from the gases emitted by air pre-heating ($\Delta P_{a,APH}$) and resulted from combustion in air pre-heating ($\Delta P_{g,APH}$) were 5 and 3 %, respectively.

13.3.5 Combustion Chamber Modeling

To analyze the combustion chamber, fuel to air molar ratio is written as follows:

$$\frac{\dot{n}_f}{\dot{n}_a} = \bar{\lambda} \tag{13.9}$$

$$\frac{\dot{n}_p}{\dot{n}_a} = \frac{\dot{n}_a + \dot{n}_f}{\dot{n}_a} = \bar{\lambda} + 1 \tag{13.10}$$

The fuel used in the present study was pure methane. The combustion equation performed in the combustion chamber is written as follows:

$$\bar{\lambda}CH_4 + [0.7748N_2 + 0.2059O_2 + 0.0003CO_2 + 0.019H_2O]$$
$$\to [\bar{\lambda} + 1][X_{N_2}N_2 + X_{O_2}O_2 + X_{CO_2}CO_2 + X_{H_2O}H_2O] \tag{13.11}$$
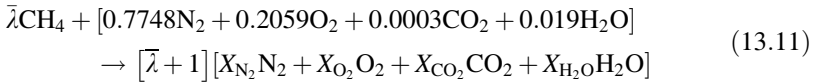
By balancing energy equations and considering the loss of heat in the combustion area equal to fuel thermal value, fuel to air ratio is written as follows:

$$\dot{Q}_{CV} - \dot{W}_{CV} + \dot{n}_f\bar{h}_f + \dot{n}_a\bar{h}_a - \dot{n}_p\bar{h}_p = 0 \tag{13.12}$$

$$\dot{Q}_{CV} = -0.02\dot{n}_f LHV = -\dot{n}_a(-0.02\bar{\lambda}LHV) \tag{13.13}$$

$$0.02\bar{\lambda}LHV + \bar{h}_a + \bar{\lambda}\bar{h}_f - (1 + \bar{\lambda})h_p0 = 0 \tag{13.14}$$

Using the basic concepts of an ideal gas mixture, air enthalpy and combustion products are expressed as follows:

$$\bar{h}_a = [0.7748\bar{h}_{N_2} + 0.2059\bar{h}_{O_2} + 0.0003\bar{h}_{CO_2} + 0.019\bar{h}_{H_2O}]_{a(T_3)}$$

$$\bar{h}_p = \frac{1}{\lambda + 1}[0.7748\bar{h}_{N_2} + (0.2059 - 2\bar{\lambda})\bar{h}_{O_2} + (0.0003 + \bar{\lambda})\bar{h}_{CO_2} + (0.019 + 2\bar{\lambda})\bar{h}_{H_2O}]_{at(T_4)}$$
$$\tag{13.15}$$

By combining Eqs. (13.14–13.16), fuel to air ratio is obtained as follows:

$$\bar{\lambda} = \frac{0.7748\Delta\bar{h}N_2 + 0.2059\Delta\bar{h}o_2 + 0.0003\Delta\bar{h}co_2 + 0.019\Delta\bar{h}H_2o}{\bar{h}F - 0.02LHV - (-2\bar{h}o_2 + \bar{h}co_2 + 2\bar{h}H_2o)_{T_4}} \tag{13.16}$$

13.3.6 Gas Turbine Modeling

The equations of adiabatic turbine analysis are expressed as follows (Khanmohammadi et al. 2016):

$$\eta_t = \frac{h_6 - h_4}{h_6s - h_4} \tag{13.17}$$

$$\dot{w}t = m_g \cdot (h_4 - h_6) \tag{13.18}$$

$$\dot{W}_{\text{net}} = wt - (wc_1 + wc_2) \tag{13.19}$$

wt is gas turbine and η_t is the isentropic efficiency of turbine equal to 89 %.

13.3.7 Generator (Hot Water)

To generate consumption water in a residential building in the cogeneration, energy T_{05} was used. The hot water outlet temperature was 330 K (Khanmohammadi et al. 2015).

$$\dot{m}_w \cdot (h_{05} - h_{03}) = m_g \cdot (h_8 - h_9) \tag{13.20}$$

13.4 Exergy Analysis

Exergy is composed of two parts: physical exergy and chemical exergy. In this paper, the terms kinetic and potential exergy were neglected. Physical exergy is the maximum vector work received from the amount of energy in a series of the ideal machines. Chemical exergy is the maximum amount of recoverable work when the material reaches a static state from its original state through the processes involving heat transfer and material exchange. Chemical exergy shows to be important in the chemical processes of combustion.

For exergy analysis, if each component of a cycle is considered as a control volume, by writing continuity law and the first and second thermodynamic laws, we will have

$$\sum_i \dot{m}_i = \sum_e \dot{m}_e \tag{13.21}$$

By considering the first and second thermodynamic laws, the exergy balance equation is used as follows

$$\dot{E}_Q + \sum_i \dot{m}_i e_i = \sum_e \dot{m}_e e_e + \dot{E}_W + \dot{I} \tag{13.22}$$

$$\dot{E}_Q = \left(1 - \frac{T_0}{T_1}\right)\dot{Q}_i \tag{13.23}$$

$$\dot{E}_W = \dot{W} \tag{13.24}$$

$$e_{\mathrm{ph}} = (h - h_0) - T_0(S - S_0) \tag{13.25}$$

It is equal to the temperature degree in terms of Kelvin. In the above relation, T is the mixed chemical energy that is defined as follows:

$$\mathrm{ex}_{\mathrm{mix}}^{\mathrm{ch}} = \left[\sum_{i=1}^{n} X_i \mathrm{ex}^{\mathrm{ch}_i} + RT_0 \sum_{i=1}^{n} X_i LnX + G^E\right] \tag{13.26}$$

In the equation, G^E is a term related to Gibbs energy that could be neglected at high pressures. To find the chemical exergy of fuels by the chemical formula of $C_\alpha H_\beta N_\gamma O_\delta$, the following equation is used (Khanmohammadi et al. 2013):

$$\mathrm{ex}_c^{\mathrm{ch}} = (\mu_{c,0} - \mu_c^e) \tag{13.27}$$

μ_c^e is the chemical potential of the different components at a static state

$$\mu_c^e = \alpha\bar{\mu}_{\mathrm{CO}_2}^e + \left(\frac{\beta}{2}\right)\bar{\mu}_{\mathrm{H}_2\mathrm{O}}^e + \left(\frac{\gamma}{2}\right)\bar{\mu}_{\mathrm{N}_2}^e + \left(-\alpha - \frac{\beta}{4} + \frac{\delta}{2}\right)\bar{\mu}_{\mathrm{O}_2}^e \tag{13.28}$$

$\mu_{c,0}$ represents the chemical potential of the various components in equilibrium by the standard environment state. However, to find the exergy of the fuels using the above equations would be so challenging since in the different references, a coefficient different for various fuels is defined as follows:

$$\xi = \mathrm{ex}_f / \mathrm{LHV}_f \tag{13.29}$$

For example, the coefficient for methane and hydrogen is as follows:

Fig. 13.2 The exergy
destruction rate in each
component of the modeled
micro-turbine cycle
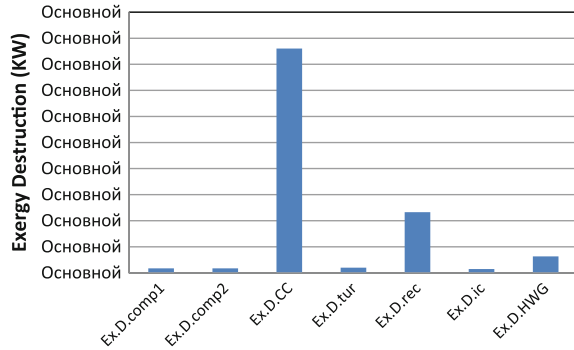
$$\xi_{\mathrm{CH_4}} = 1.06, \quad \xi_{\mathrm{H_2}} = 0.985 \tag{13.30}$$

Figure 13.2 shows the exergy deterioration rate in each component of the modeled micro-turbine cycle. As it is shown, the combustion chamber accounts for the maximum rate of the exergy destruction caused by the lack of recovery.

13.5 Definition of Objective Functions

Given the electrical and thermal requirements, the objective function in a cogenerator is divided into the parts including electrical and thermal efficiencies. In the present study, considering the modeled micro-turbine exergy, the objective function is defined as a combined function of the second law electrical efficiency and second law thermal efficiency.

The exergy of electrical efficiency is written as follows:

$$\text{Electrical exergy efficiency} = 100 \times \frac{(w_{\mathrm{net}})}{\dot{m}_{\mathrm{a^*}}(\mathrm{ex}\,[4] - \mathrm{ex}\,[3])} \tag{13.31}$$

And the exergy of thermal efficiency is written as follows:

$$\text{Thermal exergy efficiency} = 100 \times \frac{\left(E_{h\mathrm{wg}} + E_{\mathrm{ic}}\right)}{(m_*(\mathrm{ex}\,[4] - \mathrm{ex}\,[3])} \tag{13.32}$$

where

$$E_{hwg} = \dot{m}_{a^*}(ex\,[8] - ex\,[9]) \tag{13.33}$$

$$E_{ic} = \dot{m}_{a^*}(e_{xd} - e_{xe}) \tag{13.34}$$

Therefore, the objective function is written as follows:

$$\varepsilon_{tot} = 100 \times \frac{(w_{net} + E_{hwg} + E_{ic})}{(\dot{m}_{a^*}(ex[4] - ex[3]))} \tag{13.35}$$

13.6 Parametric Analysis

Figure 13.1 shows the effect of changes in the compressor pressure ratio relevant to the amount of bypass (0.5) on the two functions of the second law electrical and thermal efficiencies. As it is known, with an increase in the compression ratio, the direction of the above two functions are opposite each other.

Figure 13.4 represents the impact of changes in the mass bypass on the two characteristic functions. As indicated in the diagram, with an increase in the amount of the bypass, the efficiency of the second thermal law significantly increases. In contrast, the electrical efficiency reduces. This contrast is shown in Fig. 13.4 similar to Fig. 13.3.

Figure 13.5 displays the effect of the changes in the re-cooperator efficiency on the two characteristic functions. The results indicate that by an increase in the
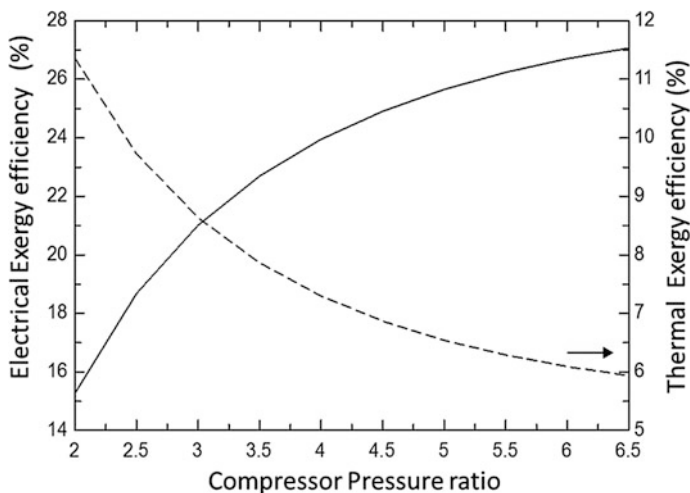
Fig. 13.3 Changes in the electrical and thermal functions in terms of the changes in the compressor pressure ratio
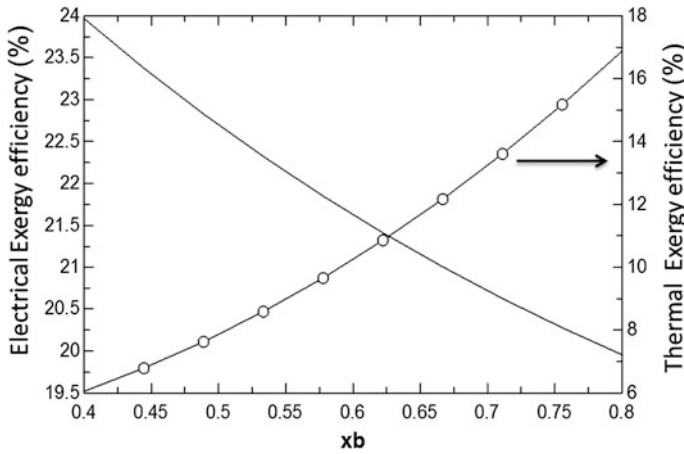
Fig. 13.4 Changes in the electrical and thermal functions in terms of the bypass changes
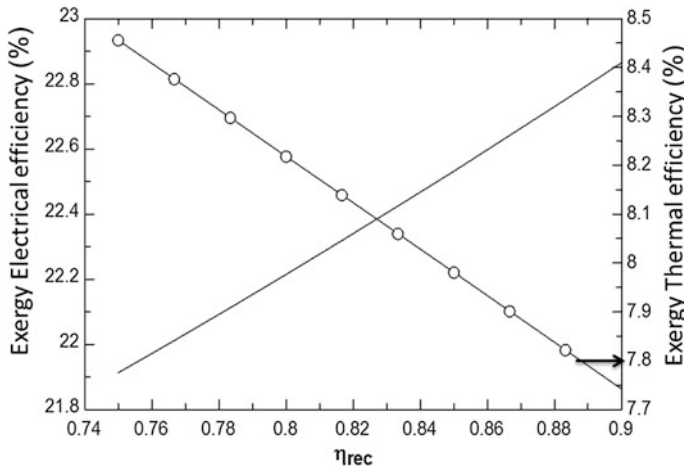
Fig. 13.5 Changes in the electrical and thermal functions in terms of changes in the re-cooperator efficiency

re-cooperator efficiency, the thermal second law reduces, while the efficiency of the electrical second law is enhances.

Figure 13.6 exhibits the impact of changes in the bypass on the total objective function at four different pressure ratios. An increase in the amount of bypass augments the total efficiency. The above efficiency further shows that by an increase in the pressure ratio, x_b has a less effect on the efficiency. Given that the amount of bypass in values less than 0.4 has reduced the total efficiency, the range of changes is selected between 0.4 and 0.8.

Figure 13.7 illustrates the effect of changes in the re-cooperator efficiency on the total objective function at bypass 0.5. As it is shown, with an increase in the

Fig. 13.6 Changes in the cycle second law in terms of the changes in the amount of the bypass
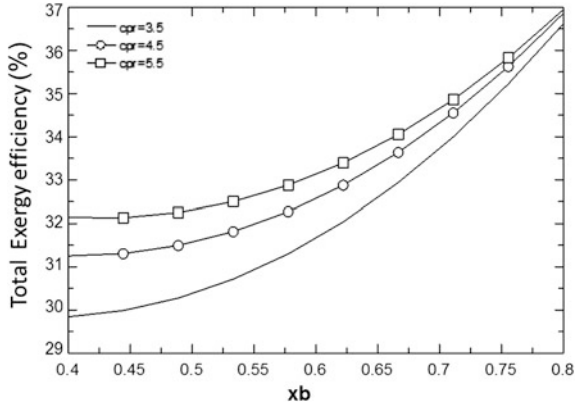
Fig. 13.7 Changes in the cycle second law in terms of changes in the re-cooperator Efficiency
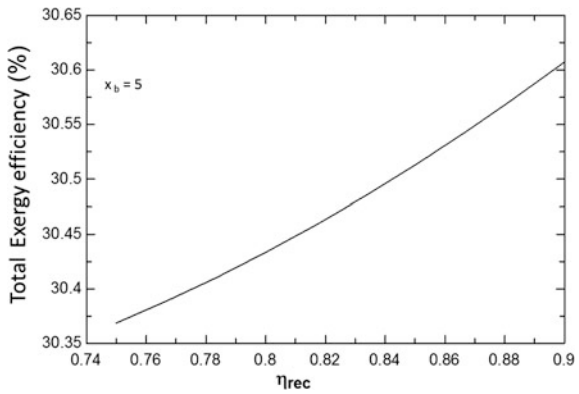
Fig. 13.8 Changes in the second efficiency of the cycle in terms of the changes in the compressor pressure ratio
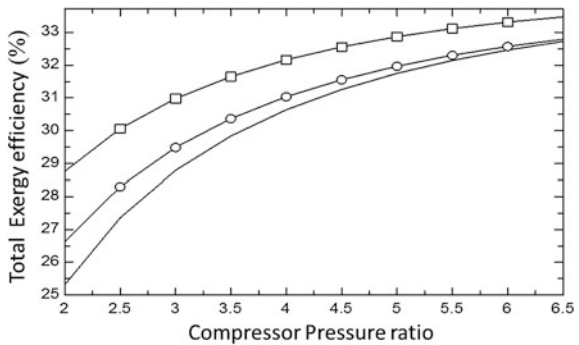
efficiency of the re-cooperator, the total efficiency enhances, but the rise is negligible with respect to the bypass.

Figure 13.8 depicts the changes in the total efficiency depending on the changes in the compressor pressure ratio in three different bypasses. As Fig. 13.8 shows, with an increase in the pressure ratio, the total efficiency enhances.

13.7   Optimization

The parametric study revealed that changes in the different parameters have different impacts on the modeled micro-turbine cycle. Given the type of modeling, the outputs obtained were not continuous. Therefore, in order to find the desired objective functions and optimization, GMDH neural network and evolutionary algorithm were utilized. The decision-making parameters and the relevant values are shown in Table 13.1. The range of changes is based on the permissible change of each parameter.

13.8   GMDH Neural Network

To find the desired functions in the present study, GMDH algorithm was employed. The above neural network is self-organizing and one-directional that is composed of several layers, each of which is composed of several neurons. All the neurons have a similar structure. All have two inputs and one output and each neuron with five weights and one bias performs processing among the input and output data. The conducting function is as follows:

$$yi = f\left(x_{ip}, x_{iq}\right) = a_0 + a_1 x_{ip} + a_2 x_{iq} + a_3 x_{ip}^2 + a_4 x_{iq}^2 + a_5 x_{ip} x_{iq} \qquad (13.36)$$

The above function has six passive coefficients, which must be arranged in a way that for each two-variable sample depending upon system (x_{ip}, x_{iq}), $i = 1, 2, 3, \ldots,$ the desirable output (y_i), $i = 1, 2, \ldots, N$ be established. Thus, the function is found on the least error squares and the differential square between the actual output and the model should be minimized.

$$\sum_{k=1}^{N} \left[\left(\hat{f}(xki, xkj) - yk \right)^2 \right] \to \text{Min} \qquad (13.37)$$

The composition method of the functions and neurons obtained for the two-objective functions, namely thermal and electrical exergy efficiency, are shown in Fig. 13.9.

Further information on the performance and efficiency of the GMDH-type neural system could be found in Namin-Zade et al. (2005), Toffolo and Benini (2003).

Table 13.1 The decision-making variables and range of changes	Decision-making variables	Unit	Range of changes
	Re-cooperator efficiency	%	$0.75 < \eta_{rec} < 0.9$
	Bypass ratio	%	$0.4 < x_b < 0.8$
	Compressor pressure patio	%	$2 < Cpr < 6.5$
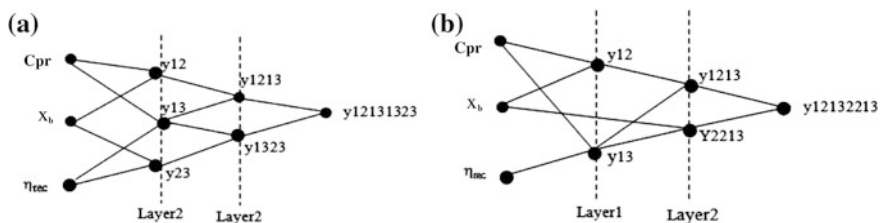
Fig. 13.9 The functions of the electrical and thermal second law efficiencies obtained by the neural network

Table 13.2 The optimal values of the decision-making variables in the single-objective optimization

	η_{rec}	x_b	Cpr
Designing values	0.75	0.5	3.5
Optimal values	0.8504	795.0	2.14

Table 13.3 The values obtained from single-objective optimization

	System's second law efficiency	Net Output (W_{net})	Transferred heat (kW)
Design values	27.37	117	107
Optimum values	36.08	91.55	250
Changes	8.71	−25.45	143

The results of the single-objective optimization targeted at achieving the total efficiency for the decision-making variables are presented in Table 13.2.

One can conclude that the maximum performance of the micro-turbine cycle can be obtained given the optimum values. In Table 13.3, the optimum point of the micro-turbine second law efficiency is shown to be increased by 8.71 compared to the designing mode. As Table 13.3 portrays, with an increase in the total efficiency, the network output as one a term of efficiency is reduced by 25.45 kW. In contrast, the transferred heat in the intercooler and hot water generator as another term of the total efficiency are increased by 143. Such a reduction and augmentation can be justified given the electrical and thermal requirements of a residential building.

At this part, using the mathematic functions obtained from the modeling and the evolutionary algorithm, the optimal amount for the two-objective functions was specified, i.e., the input variables were selected in such a manner that proper values could be found for the two conflicting functions.

Figure 13.10 depicts the diagram for the Pareto micro-turbine cycle. The horizontal axis accounts for the second law electrical efficiency and the vertical axis is the system thermal law efficiency. As it can be seen, maximum electrical and

Fig. 13.10 Pareto diagram of the electrical second law efficiency compared to the thermal second law efficiency
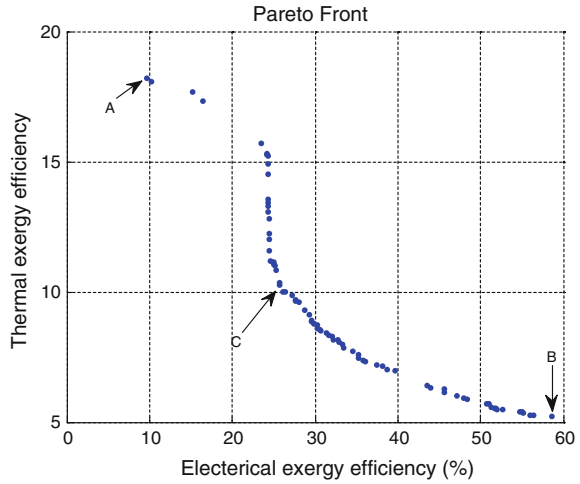
thermal efficiencies occurs at 58 and 18 %, respectively. By increasing the electrical efficiency, the thermal efficiency was reduced and vice versa. Therefore, the points around point (*c*) where exergetic electrical and thermal efficiencies achieved equilibrium could be selected as the design point. Therefore, these points have no superiority over each other and each can be regarded as the basis for the cycle performance according to the designer's view and electrical and thermal requirements.

13.9   Conclusion

In the current study, thermodynamic modeling, exergy analysis and single- and two-objective optimizations were examined based on neural network and evolutionary algorithm for a two-stage micro-turbine to perform cogeneration. The parametric study revealed changes in the design parameters have various effects on the cycle performance. To find the optimal values of the design parameters targeted at the second cycle efficiency, a single-objective algorithm was applied. The optimization results indicated that the optimal values of the design parameters can increase the total second law efficiency by 8.71 based on the net output, and further enhance the transferred heat in the convertors, so that the total efficiency rises from 27.37 to 36.08. In a two-objective optimization, two functions, including electrical exergy efficiency and thermal exergy efficiency were maximized simultaneously, and the optimal values of each function were obtained in terms of the types of electrical and thermal requirements. The maximum electrical and thermal efficiencies of the cycle were obtained 58 and 18 %, respectively.

References

AmirAlipour M, Khanmohammadi S (2014) Multi-objective exergy economic optimization of a 300kw micro-turbine using GMDH type neural network and evolutionary algorithm. A paper presented at international conferences of clean energy-Istanbul-Turkey, 8–12 May 2014

Ehyaei MA, Bahadori MN (2007) Selection of micro turbines to meet electrical and thermal energy needs of residential building in Iran. Int J Energy Build 39:1227–1234

Hao X, Zhang G, Chen Y, Zhou J (2006) Thermodynamic model and numerical simulation of single-shaft micro turbine performances. J HVAC Technol Energy Effi IV-10-1:1–7 (2006)

Jurado F (2005) Non-linear modeling of micro-turbines using NARX structures on the distribution feeder. Int Energy Convers Manage 46:385–401

Khanmohammadi S, Azimian AR, Khanmohammadi S (2013) Exergy and exergo-economic evaluation of Isfahan steam power plant. Int J Exergy 12(2):249–272

Khanmohammadi S, Atashkari K, Kouhikamali R (2015) Exergoeconomic multi-objective optimization of an externally fired gas turbine integrated with a biomass gasifier. Appl Therm Eng 91:848–859

Khanmohammadi S, Atashkari K, Kouhikamali R (2016) Modeling and assessment of a biomass gasification integrated system for multigeneration purpose. Int J Chem Eng 2016:11

Labinov SD, Zaltash A, Rizy DT, Fairchild PD, Devault RC, Vineyard EA (2002) Predictive Algorithms for microturbine performance for BCHP systems. J ASHRAE Trans 108:670–681

Nariman-Zadeh N, Atashkari K, Jamali A, Pilechi A (2005) Inverse modeling of multi objective Thermodynamically optimized turbojet engines using GMDH-type neural networks and evolutionary algorithms. Eng Optim 37:437

Sadeghi S, Ghofrani MH, Khaledi AF (2005) Analysis of micro-turbine cycle with heat recovery by energy and exergy method. PSC

Toffolo A, Benini E (2003) Genetic diversity as objective in multi-objective evolutionary algorithms. Evol Comput 11(2):151–167

Chapter 14
Buckling Analysis of a Column with Rotational Springs at Both Ends in Aircraft Column

Mustafa Özgür Yaylı and Süheyla Yerel Kandemir

Abstract In this work, a unified method is proposed for the buckling analysis of a simple supported column with rotational springs at both ends. The displacement is represented by a Fourier sine series. Stokes' transformation is applied to boundary conditions in order to construct the coefficient matrix of the corresponding systems of linear equations. The derived linear equations can be useful in theoretical investigation that leads to determinant calculation of a 2×2 matrix. The present 2×2 matrix is more efficient for calculating the buckling loads of the simple supported columns with rotational springs at both ends.

14.1 Introduction

Euler columns are important mechanical components in engineering applications, such as in the aircraft, aerospace, civil and mechanical engineering disciplines. Consequently, the stability properties of Euler columns have to be studied for buckling and safety reasons. There have been so many researches dedicated to the stability analysis of Euler columns. Pinarbasi (2012) investigated the stability of nonuniform rectangular beams using homotopy perturbation method. The elastic stability response of inclined beam column was explored by Sampaio and Hundhausen (1998). Elastic buckling behavior of axially compressed structures has attracted many investigators (Gere and Carter 1962; Eisenberger 1991; Zhou and Huang 2006; Kisa 2012).

In this study, a unified analytical method is presented for the buckling analysis of a simply supported Euler column with rotational springs at both ends. The lateral displacement function of the column under compression is represented by a Fourier

M.Ö. Yaylı (✉) · S. Yerel Kandemir
Faculty of Engineering Department of Civil Engineering, Bilecik Şeyh Edebali University, Gülümbe Kampüsü, 11210 Bilecik, Turkey
e-mail: mozgur.yayli@bilecik.edu.tr

S. Yerel Kandemir
e-mail: suheyla.yerel@bilecik.edu.tr

series. A coefficient matrix is derived by applying Stokes' transformation to the boundary conditions. This matrix can also be used to determine the buckling loads of a column with nondeformable boundary conditions such as clamped–clamped, clamped–simply supported. The reliability of the presented procedure is adequately validated through numerical examples.

14.2   Formulation of the Problem

The governing differential equation of the column in buckling is given by

$$EIv^{\mathrm{IV}} + Pv'' = 0 \tag{14.1}$$

where EI is the flexural rigidity of the column, E is Young's modulus, I is the moment of inertia of the cross section, P is the axial compressive force. In this work, a Fourier sine series is used to calculate the buckling response. The lateral deflection function $v(x, t)$ may be written in the form (Fig. 14.1)

Fig. 14.1 Sketch of a simple supported column with rotational springs at both ends
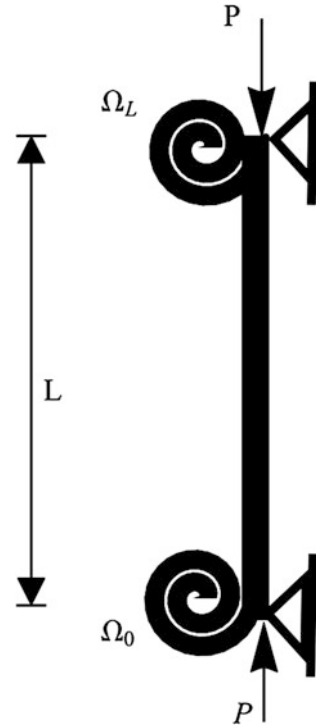
$$
v(x) = \left\{
\begin{array}{ll}
\mathbb{S}_0 & x = 0 \\
\mathbb{S}_L & x = L \\
\sum\limits_{k=1}^{\infty} \mathbb{Z}_k \sin(\beta_k x) & 0 < x < L
\end{array}
\right\}
\tag{14.2}
$$

where

$$
\beta_k = \frac{k\pi}{L},
\tag{14.3}
$$

L is the length of the column. The coefficient $(\mathbb{Z}_k)$ in the above equation can be written as

$$
\mathbb{Z}_k = \frac{2}{L} \int\limits_0^L v(x) \sin(\beta_k x)\, dx,
\tag{14.4}
$$

The first derivative of Eq. (14.2)

$$
v'(x) = \sum\limits_{k=1}^{\infty} \beta_k \mathbb{Z}_k \cos(\beta_k x).
\tag{14.5}
$$

Equation (14.5) may be written as a Fourier cosine series:

$$
v'(x) = \frac{\mathbb{N}_0}{L} + \sum\limits_{k=1}^{\infty} \mathbb{N}_k \cos(\beta_k x).
\tag{14.6}
$$

The above coefficients are given by

$$
\mathbb{N}_0 = \frac{2}{L} \int\limits_0^L v'(x)\, dx = \frac{2}{L}[v(L) - v(0)],
\tag{14.7}
$$

$$
\mathbb{N}_k = \frac{2}{L} \int\limits_0^L v'(x) \cos(\beta_k x)\, dx \quad (n = 1, 2 \ldots).
\tag{14.8}
$$

Integration by parts

$$\mathbb{N}_k = \frac{2}{L} [v(x) \cos(\beta_k x)]_0^L$$
$$+ \frac{2}{L} \left[\beta_k \int_0^L v(x) \sin(\beta_k x) \, dx \right] \qquad (14.9)$$

$$\mathbb{N}_k = \frac{2}{L} \left[(-1)^k v(L) - v(0) \right] + \beta_k \mathbb{Z}_k, \qquad (14.10)$$

then

$$\frac{dv(x)}{dx} = \frac{\mathbb{S}_L - \mathbb{S}_0}{L}$$
$$+ \sum_{k=1}^{\infty} \cos(\beta_k x) \left(\frac{2\left((-1)^k \mathbb{S}_L - \mathbb{S}_0\right)}{L} + \beta_k \mathbb{Z}_k \right). \qquad (14.11)$$

The second derivative of $v(x)$ can be calculated by using Stokes' transformation as follows:

$$\frac{d^2 v(x)}{dx^2} = -\sum_{k=1}^{\infty} \beta_k \sin(\beta_k x) \left(\frac{2\left((-1)^k \mathbb{S}_L - \mathbb{S}_0\right)}{L} + \beta_k \mathbb{Z}_k \right). \qquad (14.12)$$

Stokes' transformation can be adopted for evaluating all derivatives needed for satisfying Eq. (14.1).

$$\frac{d^3 v(x)}{dx^3} = \frac{\mathbb{S}_L'' - \mathbb{S}_0''}{L}$$
$$+ \sum_{k=1}^{\infty} \cos(\beta_k x) \left(\frac{2\left((-1)^k \mathbb{S}_L'' - \mathbb{S}_0''\right)}{L} \right.$$
$$\left. - \beta_k^2 \left(\frac{2((-1)^k \mathbb{S}_L - \mathbb{S}_0)}{L} + \beta_k \mathbb{Z}_k \right) \right) \qquad (14.13)$$

$$\frac{d^4 v(x)}{dx^4} = -\sum_{k=1}^{\infty} \beta_k \sin(\beta_k x) \left(\frac{2\left((-1)^k \mathbb{S}_L'' - \mathbb{S}_0''\right)}{L} \right.$$
$$\left. - \beta_k^2 \left(\frac{2\left((-1)^k \mathbb{S}_L - \mathbb{S}_0\right)}{L} + \beta_k \mathbb{Z}_k \right) \right) \qquad (14.14)$$

The boundary conditions are as follows:

$$\mathbb{S}_0 = 0, \quad x = 0, \tag{14.15}$$

$$\mathbb{S}_L = 0, \quad x = 0, \tag{14.16}$$

$$\Omega_0 \frac{\partial v}{\partial x} = EI \frac{\partial^2 v(x,t)}{\partial x^2}, \quad x = 0, \tag{14.17}$$

$$\Omega_L \frac{\partial v}{\partial x} = -EI \frac{\partial^2 v(x,t)}{\partial x^2}, \quad x = L \tag{14.18}$$

in which Ω_0 and Ω_L are rotational spring constants at $x = 0$ and $x = L$, respectively. After some mathematical manipulations, using Eqs. (14.1), (14.2), (14.11), and (14.12) leads to the two simultaneous homogeneous equations

$$
\begin{aligned}
&+ \left(-1 + \sum_{k=1}^{\infty} \frac{2\overline{\Omega_0}}{-\pi^2 k^2 + \overline{P}} \right) \mathbb{S}_0'' \\
&- \left(\sum_{k=1}^{\infty} \frac{2(-1)^k \overline{\Omega_0}}{-\pi^2 k^2 + \overline{P}} \right) \mathbb{S}_L'' = 0
\end{aligned}
\tag{14.19}
$$

$$
\left(\sum_{k=1}^{\infty} \frac{2(-1)^k \overline{\Omega_L}}{-\pi^2 k^2 + \overline{P}} \right) \mathbb{S}_0'' + \left(-1 + \sum_{k=1}^{\infty} \frac{2\overline{\Omega_L}}{-\pi^2 k^2 + \overline{P}} \right) \mathbb{S}_L'' = 0 \tag{14.20}
$$

where

$$\overline{P} = \frac{PL^2}{EI}, \tag{14.21}$$

$$\overline{\Omega_0} = \frac{\Omega_0 L}{EI}, \tag{14.22}$$

$$\overline{\Omega_L} = \frac{\Omega_L L}{EI}. \tag{14.23}$$

and the following system of equations can be obtained in matrix form to be solved for the constants ($\mathbb{S}_0''$ and $\mathbb{S}_L''$):

$$
\begin{bmatrix}
-1 + \sum_{k=1}^{\infty} \frac{2\overline{\Omega_0}}{-\pi^2 k^2 + \overline{P}} & -\sum_{k=1}^{\infty} \frac{2(-1)^k \overline{\Omega_0}}{-\pi^2 k^2 + \overline{P}} \\
\sum_{k=1}^{\infty} \frac{2(-1)^k \overline{\Omega_L}}{-\pi^2 k^2 + \overline{P}} & -1 + \sum_{k=1}^{\infty} \frac{2\overline{\Omega_L}}{-\pi^2 k^2 + \overline{P}}
\end{bmatrix}
\times
\begin{bmatrix}
\mathbb{S}_0'' \\
\mathbb{S}_L''
\end{bmatrix}
=
\begin{bmatrix}
0 \\
0
\end{bmatrix}
\tag{14.24}
$$

The characteristic equation of the coefficient matrix can be solved by assigning the proper values of $\overline{\Omega}_0$ and $\overline{\Omega}_L$ corresponding to any specified boundary conditions.

14.3 Results and Discussion

In this section, the buckling analysis of a Euler column with different boundary conditions is performed by the proposed method. For the purpose of verification, the present analytical method is used to find the first two critical buckling load of a column with classical boundary conditions; pinned–pinned (P–P), Clamped–Pinned (C–P), Clamped–Clamped (C–C) and compare the results with those available in the literature. The rotational spring parameter is taken as ($\overline{\Omega}_0 = \overline{\Omega}_L = 10,000$) for (C–C) boundaries. $\overline{\Omega}_0 = \overline{\Omega}_L = 0$ parameters are used for (P–P) ends. As seen from Table 14.1, the present results seem to be more acceptable.

The effect of the rotational restrained ends on the critical buckling loads is presented in Figs. 14.2 and 14.3. The analytical results in these two figures are

Table 14.1 Verification of the proposed method for different boundary conditions

Mode	P–P		C–P		C–C	
	Exact	Present	Exact	Present	Exact	Present
		$\sqrt{P}$		$\sqrt{P}$		$\sqrt{P}$
1	3.141	3.141	4.493	4.489	6.283	6.283
2	6.283	6.283	7.725	7.716	8.986	8.955

Fig. 14.2 Buckling loads for first three modes
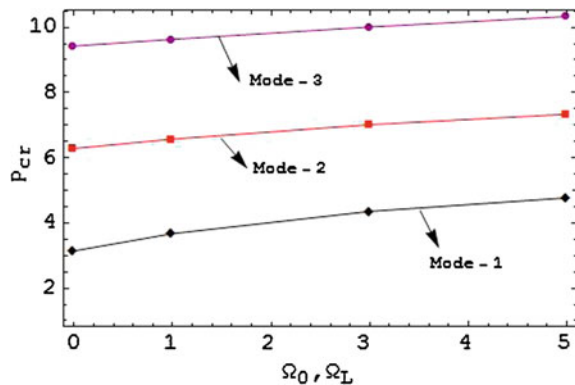
Fig. 14.3 Buckling loads for different boundary conditions
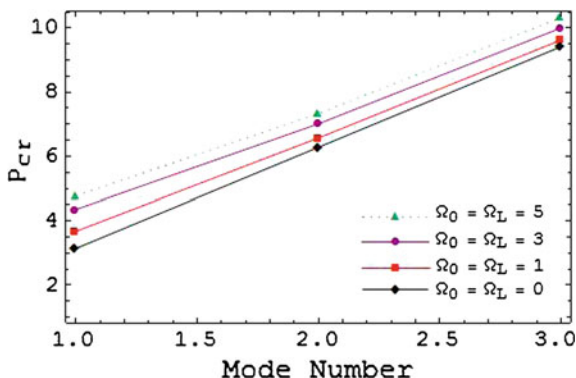
computed by using Eq. (14.24) for the values of $(\overline{\theta_0} = \theta_L = 0, 1, 3, 5)$. One can observe that the critical buckling loads are increased by considering the effects of rotational restraints.

14.4 Conclusions

A (2×2) coefficient matrix for buckling of column with deformable boundary conditions is presented. It is shown that the critical buckling load of column is shown to be dependent on the restrained boundary conditions. The critical buckling loads of column increases with an increase in rotational spring parameters.

References

Eisenberger M (1991) Buckling loads for variable cross-section members with variable axial forces. Int J Solids Struct 27(2):135–143

Gere JM, Carter WO (1962) Critical buckling loads for tapered columns. J Struct Eng ASCE 88 (1):111

Kisa M (2012) Vibration and stability of axially loaded cracked beams. Struct Eng Mech 44 (3):305–323

Pinarbasi S (2012) Stability analysis of nonuniform rectangular beams using homotopy perturbation method. Mathematical problems in engineering, Article ID 197483

Sampaio JHB Jr, Hundhausen JR (1998) A mathematical model and analytical solution for buckling of inclined beam columns. Appl Math Model 22:405–421

Zhou L, Huang Y (2006) Crack effect on the elastic buckling behaviour of axially and eccentrically loaded columns. Struct Eng Mech 22:169–184

Chapter 15
Emissions Prediction of a Reverse Flow Combustor Using Network Models

Gökhan Varol, Gürkan Sarıkaya, Onur Tunçer and Görkem Öztarlık

Abstract The purpose of this study is to predict the pollutant emissions generated within a 1000 hp turbo-shaft helicopter engine reverse flow combustor using two different approaches; a flow network-based one-dimensional network solver and a Chemical Reactor Network (CRN) model. The one-dimensional network solver is able to estimate mass flow distributions across holes, gas and liner temperatures, heat transfer and pressure drop across the combustion chamber. All are key parameters for a preliminary design. One-dimensional flow network model is also able to predict the emissions by utilizing a number of empirical and semi-empirical correlations. CRN model is based on the division the combustor flow field into a number of specific zones represented by simple chemical reactors such as Perfectly Stirred Reactors (PSR) and Plug Flow Reactors (PFR). CRN is created to estimate the emissions using CHEMKIN software and the reaction mechanism of n-heptane is provided to be used. CRN model receives mass flow rates from the one-dimensional network model. The results of two approaches are compared for three engine power settings for idle, cruise and take-off.

Nomencalture

A   Area, m^2
C_d Discharge coefficient
m Mass flow rate, kg/s
P Total pressure, Pa

G. Varol (✉) · G. Sarıkaya · O. Tunçer
Istanbul Technical University, ITU UUBF, Maslak, Istanbul 34469, Turkey
e-mail: varolgo@itu.edu.tr

G. Sarıkaya
e-mail: sarikayagu@itu.edu.tr

O. Tunçer
e-mail: tuncero@itu.edu.tr

G. Öztarlık
TUSAS Engine Industry Inc., Tepebaşı Eskişehir 356 26003, Turkey
e-mail: gorkem.oztarlik@tei.com.tr

S   Unmixedness degree
T   Temperature, K
V_c Combustion volume, m^3

Greek Letters

ρ Density, kg/m^3
Φ Equivalence ratio
σ Standard deviation of normal distribution

Subscripts

a   Airflow
g   Gas
h   Hole
st   Stoichiometric value
pz   Primary zone value
1   Flame side of liner wall
3   Combustor inlet

15.1   Introduction

As a core component of gas turbine, combustor design is a major challenge for designers because of the complexity of physics and chemistry of the flow within the combustor. Increasing global environmental concerns over the past decades has made the controlling of pollutant emissions important for gas turbine engines. Therefore, the prediction of pollutant emissions has become an important factor in the conceptual engine design phase.

Detailed investigation of reacting flow became possible with the development of advanced computational tools like CFD. Although CFD provides accurate description of the flow field, the prediction of the low concentration pollutants like NO$_x$ is limited by the high computation time necessity (Falcitelli et al. 2002).

On the other hand, a network approach is able to predict combustion performance efficiently and rapidly at the preliminary design stage. Stuttaford and Rubini (1997) described a network model which is compromised by elements that are linked together by nodes. This method make possible to predict mass flow distribution, overall pressure loss, combustion efficiency, temperature distribution through the liner and inside the flame tube and pollutant emissions.

Alternatively, the modelling combustor with CRN method was first described by Bragg (1953) and Novosselov (2006). They modelled a gas turbine combustor as an association of a perfectly stirred reactor (PSR) followed by a plug flow reactor (PFR).

The objective of this study is to investigate combustion performance and predict pollutant emission with using both of one-dimensional network model and CRN approaches for a reverse flow annular combustor.

A network code which is based on SIMPLE algorithm (Patankar 1980) was developed in conjunction with using the empirical and semi-empirical correlations. CRN model is created based on the zonal modelling (Swithenbank 1970) and physic-based emission model (Allarie 2006).

Finally, the results of both approaches were compared with each other for three different engine power settings.

15.2   Methodology

15.2.1   One-Dimensional Network Model

Figure 15.1 shows the network layout of reverse flow annular combustion chamber. This model consists of 100 nodes (circle) and 99 elements (square) that are linked together by nodes. Elements are classified according to their geometric features. DC elements represent flow within the annulus and flame tube and account for the duct area changes. RL elements represent the swirler, which account for the pressure drop through the feature contraction and RD elements represent the primary, secondary and dilution holes as well as film cooling devices.
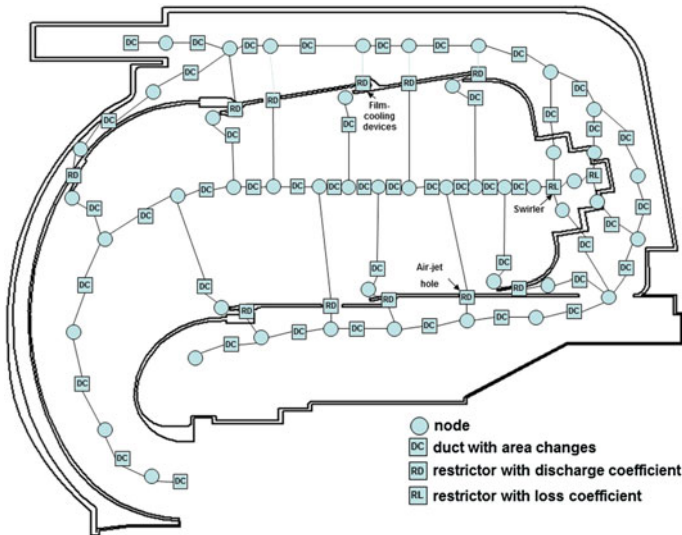
Fig. 15.1 Flow network layout for the reverse flow combustor

15.2.2 Mathematical Model

Pressure drop and mass flow distribution through the liner hole can be calculated using the basic empirical equations for incompressible flow which is derived from simple Bernoulli equation combined with continuity equation, which are expressed as follows:

$$m_h = C_d A_h \left(2\rho\left(P_1 - P_j\right)\right)^{0.5} \tag{15.1}$$

Discharge coefficient (C_d) through the various liner holes can be calculated using correlations which are presented by Norster (1980). In this study, machined ring type is used for film cooling hole.

Mass flow and gas temperature distribution within the combustor is followed by the adiabatic flame temperature calculation which is a function of local air/fuel ratio. To simplify the prediction of the airflow distribution in the combustor, combustion chamber is divided into four zones described as re-circulation, primary, secondary and dilution zones. The airflow mass fraction for each zones are calculated by the following assumptions. The flow in re-circulation zone is the sum of all the flow comes from swirler and half of the air comes from the first hole set. The flow in the primary zone is the sum of the remaining flow from the first hole set, half of the air comes from the second and third hole set. The secondary zone includes half of the air coming from second, third and fourth hole set plus one-third of the fifth hole set. The remaining air flow is used for dilution zone.

Using the total amount of air and stoichiometric air/fuel ratio of n-heptane, the equivalence ratio of each zone can be calculated. Olikara and Borman (1975) routine is utilized to predict the adiabatic flame temperatures.

During the prediction of gas temperature, combustion efficiency should be taken into account (Gosselin et al. 1999; Odgers and Kretschemer 1980a, b).

Both the gas temperature and the residence time have a strong effect on the NO_x production. Therefore, it is assumed that NO_x production is occurs up until the secondary zone since the highest flame temperature is located between primary and secondary zone.

A semi-empirical correlation suggested by Lefebvre (1988) is used to estimate NO_x production.

$$NO_x = 9 \times 10^{-8} P^{1.25} V_c \exp(0.01 T_{st}) / \dot{m}_a T_{pz} \tag{15.2}$$

Another correlation presented by Rizk and Mongia (1994) is used for the prediction of CO.

$$CO = 10^{(13.477 - 4.5276 \times \log 10(T_3))} \tag{15.3}$$

15.2.3 Chemical Reactor Network (CRN) Model

CRN model is created based on the location of combustion zones in the first approach and hole locations on the combustion liner are taken into account. The volumes of elementary reactors between each set of holes are modelled as a PSR for re-circulation, primary and secondary zones. The rest of the volume after the last hole described as dilution zone is modelled as PFR since there is no change in the radial direction along the flow path. Furthermore, to represent for non-uniformity and equivalence ratio dispersion (i.e., unmixedness degree) in the combustor, a set of nine parallel branches of reactor were specified. These branches represent the volume up to the first hole set.

The unmixedness degree, which is a function of combustor mean equivalence ratio, defines what fraction of the flow exists at a certain equivalence ratio (Heywood and Mikus 1973).

$$S = \frac{\sigma}{\phi} \tag{15.4}$$

Distribution of equivalence ratio is obtained using the value of unmixedness degree and mean equivalence ratio at the inlet. In this study, unmixedness degree was assumed 0.25 for each three engine power settings. Calculated equivalence ratio distributions are used for the inlets of the nine parallel branches.

Reactors are assumed as adiabatic and solved as steady-state condition. The layout of CRN model, which are created by a number of PSR and PFR reactors, is shown in Fig. 15.2.

Mass flow splits, which were obtained from the first approach (Table 15.3), are used as input for the inlets of the CRN model.

LLNL reduced reaction mechanism for n-heptane is used. For the prediction of thermal NO production, extended Zel'dovich et al. (1947) mechanism steps with the GRI 3.0 reaction rate coefficients were added into the mechanism.
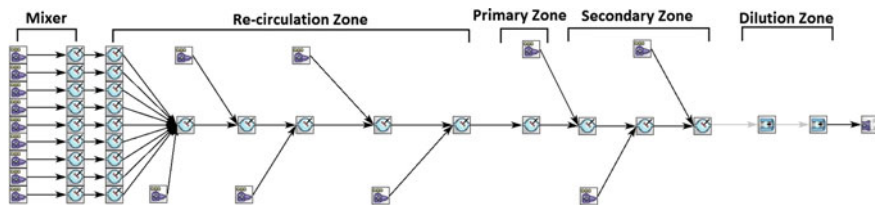
Fig. 15.2 Chemical reactor network

15.3 Results

Inputs are presented in Tables 15.1 and 15.2 for a particular combustor geometry operating at take-off condition.

Tables 15.3 and 15.4 present mass flow distribution and hole discharge coefficients through the cooling and dilution air holes on the inner and outer liners, respectively. To validate the results, 1-D network code results are compared with CFD simulations results for an isothermal case.

Figure 15.3 shows the prediction of the gas temperature distributions along the combustion chamber at the take-off regime for both approaches. The CRN predicted temperature results shows good agreement with the network code results in the secondary zone, dilution zone and combustor exit. However, CRN method gives over-predictions when compared to network code at the primary zone, because primary zone of the CRN model is constructed with PSR in which perfectly mixing and complete combustion is occurring while network code assumes some low combustion efficiency used in correlations.

Figure 15.4 shows the NO prediction for three different operation conditions of idle, cruise and take-off using the CRN model and comparison of the predicted results with the one-dimensional network code using empirical correlation (Eq. 15.3).

Predicted results of the NO emission show the reasonably good agreement with the 1-D network code. Both results show that NO emission is increasing when the

Table 15.1 Operating condition for take-off

Inlet temperature (K)	575.45
Inlet pressure (Pa)	802,494
Total mass flowrate (kg/s)	0.266
Overall air/fuel ratio	44.5

Table 15.2 Hole properties

Inner hole					
Hole position (mm) (Relative to swirler)	5.10	18.10	38.60	53.10	75.60
Hole type	MR	PH	MR	PH	MR
Number of hole	30	5	30	5	40
Hole diameter (mm)	1.34	3.58	1.39	5.60	1.00
Outer hole					
Hole position (mm) (relative to swirler)	14.30	35.20	44.80	70.40	78.90
Hole type	MR	PH	MR	PH	MR
Number of hole	30	5	40	5	40
Hole diameter (mm)	1.63	3.12	1.70	5.30	1.02

Hole Types: MR Machined Ring, PH Plain Hole

Table 15.3 Comparison of CFD and 1-D network code results for the isothermal case

		CFD		1-D network code		
	Hole types	Mass flow (kg/s)	Mass fraction (%)	Mass flow (kg/s)	Mass fraction (%)	Error (%)
	Swirler	0.0545	20.488	0.0434	15.915	20.4
Outer hole	1	0.0235	8.843	0.0224	8.234	4.7
	2	0.0127	4.771	0.0142	5.232	11.8
	1	0.0167	6.275	0.0325	11.925	94.6
	2	0.0384	14.438	0.0409	15.019	6.5
	1	0.0118	4.423	0.0116	4.266	1.7
Inner hole	1	0.0198	7.447	0.0151	5.564	23.7
	2	0.0182	6.856	0.0188	6.895	3.3
	1	0.0195	7.318	0.0163	5.984	16.4
	2	0.0370	13.916	0.0459	16.851	24.1
	1	0.0130	4.869	0.0112	4.116	13.8

Table 15.4 Comparison of discharge coefficients

Discharge coefficient				
	Hole types	CFD	1-D network code	Error (%)
	Swirler	0.528	0.625	18.4
Outer hole	MR	0.787	0.600	23.8
	PH	0.609	0.625	2.6
	MR	0.721	0.600	16.8
	PH	0.566	0.625	9.4
	MR	0.694	0.600	13.5
Inner hole	MR	0.633	0.600	5.2
	PH	0.559	0.625	10.6
	MR	0.579	0.600	3.6
	PH	0.608	0.625	2.8
	MR	0.587	0.600	2.2

operation condition changes from idle to take-off. On the other hand, CRN model gives relatively higher NO emission since its primary zone temperature is higher than first approach as represented in Fig. 15.4.

Figure 15.4 also shows the CO prediction and comparison for three different operation conditions of idle, cruise and take-off using both approaches. The results are quite different for both approaches. The reason of this difference is related with the subject of combustion efficiency in both approaches as described previously. For the CRN method, perfectly mixing is occurring in reactors and most of the CO is converted to CO_2 within the secondary and dilution zones, however, one-dimensional network code is using a correlation (Eq. 15.4).
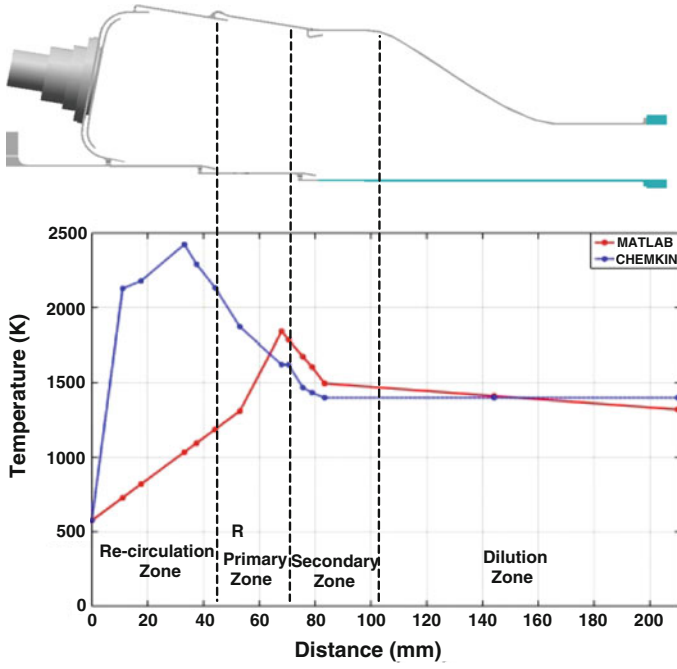
Fig. 15.3 Gas temperature distribution along the combustor axis
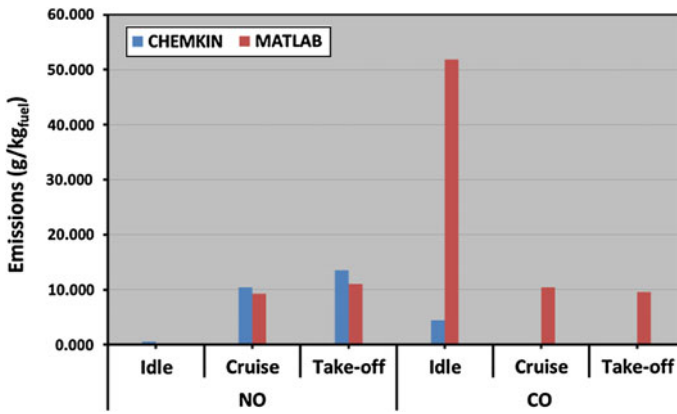
Fig. 15.4 Comparison of NO and CO emissions

15.4 Conclusion

This study demonstrates that the use of one-dimensional network code and CRN method provides similar results for exit temperature and NO emission at the preliminary design stage. However, the same cannot be said for the CO emission prediction.

CRN model has the ability to process most complex chemical mechanism so it can provide emissions results more accurately and can be coupled with CFD tools.

References

Allaire DL (2006) A physics-based emissions model for aircraft gas turbine combustors. Ms. thesis, Aerospace Engineering Department Massachusetts Institute of Technology, Boston, MA

Bragg SL (1953) "Application reaction rate theory to combustion chamber analysis" Aeronautical research council pub. ARC 16170, Ministry of Defense, London, England, pp 1629–1633

Falcitelli M, Pasini S, Rossi N, Tognotti L (2002) CFD+ reactor network analysis: an integrated methodology for the modelling and optimisation of industrial systems for energy saving and pollution reduction. Appl Therm Eng 22(8):971–979

Gosselin P, De Champlain A, Kretschmer D (1999) Prediction of wall heat transfer for gas turbine combustor. J Power Energy 213:169–180

Heywood JB, Mikus T (1973) Parameter controlling nitric oxide emissions from gas turbine combustors, in AGARD propulsion and energetic panel 41st meeting on atmospheric pollution by aircraft engines. London

Lefebvre AH (1988) Gas turbine combustion, 2 edn. Taylor and Franchis

LLNL (2003) website. https://www.llnl.gov/

Norster ER (1980) Combustor aerodynamics, in Northern Research and Engineering Corporation, the design and development of gas turbine combustors, vol 1. Woburn, Massachusetts

Novosselov IV, Malte PC, Yuan S, Srinivasan R, JCY Lee (2006) ASME, pp 1–10

Odgers J, Kretschmer D (1980a) "Performance evaluation and the prediction of pollutant formation, in Northern Research and Engineering Corporation, the design and development of gas turbine combustors, vol 2. Woburn, Massachusetts, USA

Odgers J, Kretschmer D (1980b) Basic design method—Can combustors, in Northern Research and Engineering Corporation, the design and development of gas turbine combustors, vol 2, Woburn, Massachusetts, USA

Olikara C, Borman GL (1975) Calculating properties of equilibrium combustion products with some applications to I.C. Engines, SAE Paper 750468

Patankar SV (1980) Numerical heat transfer and fluid flow. Hemisphere Publishing Corporation, USA

Rizk NK, Mongia HC (1994) Emmission prediction of different gas turbine combustors, AIAA Paper 94–0118

Stuttaford PJ, Rubini PA (1997) Preliminary gas turbine combustor design using a network approach. J Eng Gas Turbine Power 119:547–552

Swithenbank J (1970) Combustion fundamentals. AFOSR 70–2110 TR

Zel'dovich Y, Sadovnikov P, Frank-Kamenetskii D (1947) Oxydation of nitrogen in combustion. Academy of Sciences of the USSR, Tech. Rep. Moscow

Chapter 16
Performance Simulation of Serviceable Stratospheric Balloon Control Using MATLAB/Simulink

Öznur Kayhan, Özgün Yücel and M. Alaittin Hastaoğlu

Abstract The design of serviceable stratospheric balloon requires descent control mechanism to make it safe and reliable. On the basis of balloon dynamics, heat and mass transfer aspect, Gas-Compress-Release control model that is developed before used to describe the ascent, descent and flight processes for high altitude zero pressure balloons. The behavior of the balloon system during safe landing has been numerically investigated for the first time. The model was validated using NASA test flight. The effect of PID control on compress-release mechanism is discussed in detail. It was found that with the sacrificial flight Gas-Compress-Release model it is possible to place the balloon at its orbit, to extend flight time and to interfere with the balloon system whenever needed for technical service without using ballast. The results are helpful for the design and operation of safe and reliable serviceable high altitude stratospheric balloons.

Nomenclature

A_p	Projected area of the balloon, m^2
C_1, C_2	Surface concentrations of the Lift-Gas at the inside and outside surfaces of the balloon ($kmol/m^3$)
C_d	Drag coefficient
C_{ib}, C_{out}	Inside and outside concentrations of the Lift-Gas ($kmol/m^3$)
D_{ABre}	Real effective diffusion coefficient (m/s^2)
g	Gravitational acceleration (m/s^2)
h_{ci}, h_{co}	Convective heat transfer coefficients at the inside and outside surfaces of the balloon ($W/m^2 K$)
k_{ci}, k_{co}	Convective mass transfer coefficients at the inside and outside surfaces of the balloon (m/s)
k_f	Thermal conductivity of the balloon wall (W/mK)
M	Total weight of the balloon and auxiliary equipment (kg)
N_A	Lift-Gas flux ($kmol/m^2 s$)

Ö. Kayhan (✉) · Ö. Yücel · M.A. Hastaoğlu
Gebze Technical University, Kocaeli, Turkey
e-mail: okayhan@gtu.edu.tr

$q_{\text{inf ext}}$	External infrared radiation density (W/m^2)
$q_{\text{inf int}}$	Internal infrared radiation density (W/m^2)
$q_{\text{T}}, q_{\text{rad}}$	Total heat flux form the lift gas and solar radiation flux (W/m^2)
T_1, T_2	Temperatures of the Lift-Gas at the inside and outside surfaces of the balloon (K)
$T_{\text{a}}, T_{\text{ib}}$	Atmospheric temperature and bulk temperature of the Lift-Gas (K)
v	Velocity of the balloon relative to the air, (m/s)
α	Solar absorptivity of the balloon film
$\rho_{\text{air}}, \rho_{\text{b}}$	Density of the air and balloon system (kg/m^3)
Δt	Time step (s)
Δx	Balloon wall thickness (m)

16.1 Introduction

High altitude scientific balloons provide a cheaper way as an observation platform for atmospheric studies, research missions or data collection than is currently available. The preparation for the balloon mission requires an accurate and reliable flight performance prediction method in order to accomplish the job successfully (Dai et al. 2012).

The studies on balloon and airship systems have been continued for many years in areas of control, flight test, structure etc. (Xia et al. 2010). The high altitude airship is a thermal vehicle. It lives in a mostly radiant thermal balance considering many heat sources that influence it. When warm, the balloon gas expands and either pressurizes the gas envelope or is vented out.

If venting takes place with zero pressure balloons, night time cooling makes ballast dropping necessary (Farley 2005). However, up to now there was no balloon control model available that could carry large payloads at constant altitude without using ballast.

We have developed a model of stratospheric balloon using transport phenomena and Gas-Compress-Release system to keep balloon at constant altitude for a long time such as 485 days (Kayhan and Hastaoğlu 2014). In the past decades, some research has been published on high altitude balloons, but many of them have focused on the geometry, thermal designs, and selection of a suitable material to go to higher altitudes. To design a balloon system, not only temperature prediction is necessary but also the other transport mechanism and ascent and descent processes are necessary. Up to now, there is no study to interfere with the balloon if technical service is needed.

There has been no study about descent control and safe landing to the ground. Safe landing is important to keep the equipment from any damage and predict the balloon landing coordinates. The aim of this study is to combine heat, mass and momentum equations with a Gas-Compress-Release system for velocity control in

order to track the balloons and keep them at target altitudes for longer periods and interfere with it anytime needed.

16.2   Balloon Dynamics, Heat and Mass Transfer Model

For the stratospheric balloons, a model was developed based on balloon dynamics, heat and mass transfer aspects which had not been studied simultaneously before. It was combined with a velocity control mechanism (Kayhan and Hastaoğlu 2014). Summary of the model equations is given below.

Dynamic model for the balloon velocity:

$$\frac{d\boldsymbol{v}}{dt} = -\frac{\boldsymbol{v}}{\|\boldsymbol{v}\|} C_d \frac{1}{2M} \rho_{air} v^2 A_p + \frac{\rho_b - \rho_{air}}{\rho_b} \boldsymbol{g} \qquad (16.1)$$

Gas mass transfer model for calculating leakage of the Lift-Gas:

$$N_A = k_{ci}(C_{ib} - C_1) = D_{ABre}\left(\frac{C_1 - C_2}{\Delta x}\right) = k_{co}(C_2 - C_{out}) \qquad (16.2)$$

Heat transfer model equation to predict the temperature of the Lift-Gas:

$$\begin{aligned} q_T &= h_{ci}(T_1 - T_{ib}) + q_{\text{inf int}} = \frac{k_f}{\Delta x}(T_2 - T_1) \\ &= h_{co}(T_a - T_2) + \alpha q_{rad} + q_{\text{inf ext}} \end{aligned} \qquad (16.3)$$

16.3   Numerical and Control Method

In this study, the main program and subroutines for altitude control, heat, mass and momentum transfer models for the stratospheric balloons were written in MATLAB/Simulink software package. Gas-Compress-Release velocity control model was solved using an iterative equation solver program using MATLAB/Simulink. The balloon system consists of helium inside and Gas-Compress-Release control system. The storage unit of the control system has no mass transfer with the external environment. The mass transfer between the balloon inside and control system is conducted through valve. The sketch of the balloon system is presented in Fig. 16.1

Before the launch, on the ground, a certain amount of helium was pumped into the balloon until it started to rise from the ground. Balloon was controlled to reach the target altitude (30,000 m in this work) and made steady at its orbit. When the balloon ascends over the 30,000 m altitude, the Lift-Gas inside the balloon (helium

Fig. 16.1 Balloon control system
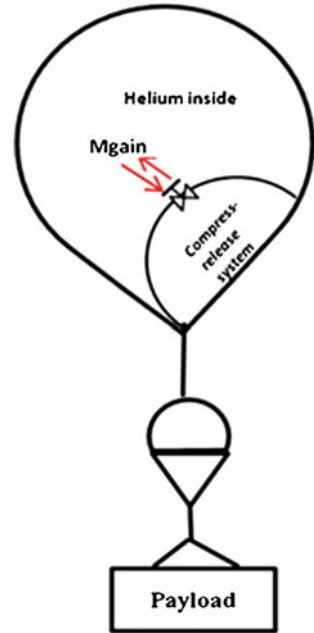
initially) is evacuated in a controlled manner (M_{gain}) by pumping it to the Lift-Gas-Storage. Thus the volume of the balloon decreases preventing its rise further. At altitudes higher than the target value, pumping is continued until the balloon started to descend below the target altitude. However for altitudes lower than the target value, Lift-Gas is released into the balloon from the storage tank. The Compress-Release cycle is continued until all available storage gas is consumed due to escape through the balloon wall. Naturally, then the descent starts. A certain amount of Lift-Gas is to be kept as landing gas to accommodate a soft landing. Anytime to start the balloon descent, certain amount of helium inside the balloon is compressed to the gas storage tank (M_{gain}). This amount is controlled by PID controller.

16.4 Results and Discussion

The accuracy of the zero pressure high altitude balloon model based on transport phenomena and Gas-Compress-Release system introduced in this work is considered by comparison with the experimental results of a NASA super pressure balloon Test Flight 586 NT (Cathey 2009). The test balloon flight took place at 07:18 AM on June 22, 2008 from Ft. Sumner, New Mexico. After the balloon reaching a steady float altitude of 30.5 km a total of 109 kg ballast was dropped to pressurize the balloon. In the present model ballast is not used. But a similar weight is stored

as Lift-Gas and used by Gas-Compress-Release control system. In the present model the same conditions and weight for NASA test flight were used.

Some simulation studies were made before (Dai et al. 2012; Liu et al. 2014) for flight at 30,000 m but only ascent process comparison with the measured data was validated; not all process was done. In the present model all ascent, flight and descent processes were compared with measured data without using ballast. Figure 16.2 compares the predicted altitudes with the measured data. The agreement is quite good.

Using the same conditions of NASA test flight in the present model, Lift-Gas Storage—helium inside the balloon and payload weights were increased to 1000 kg. Figure 16.3 plots the time-altitude variation. It can be seen that balloon system keeps its altitude for 330 days. Using this balloon with long flight performance, intervention to the balloon was studied.

Fig. 16.2 Altitude comparison of the predicted data with measured data
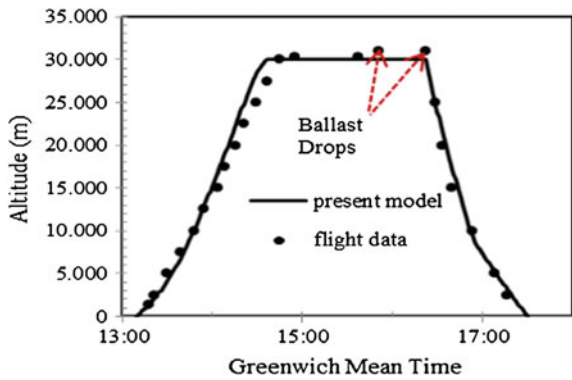
Fig. 16.3 Variation of flight time with altitude
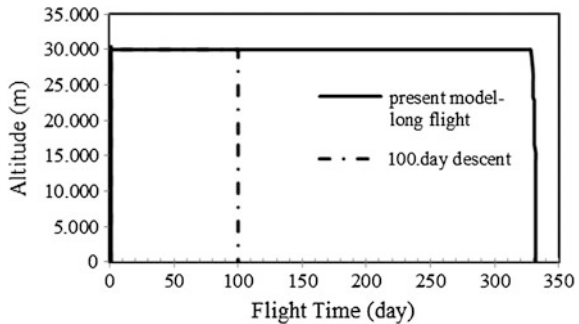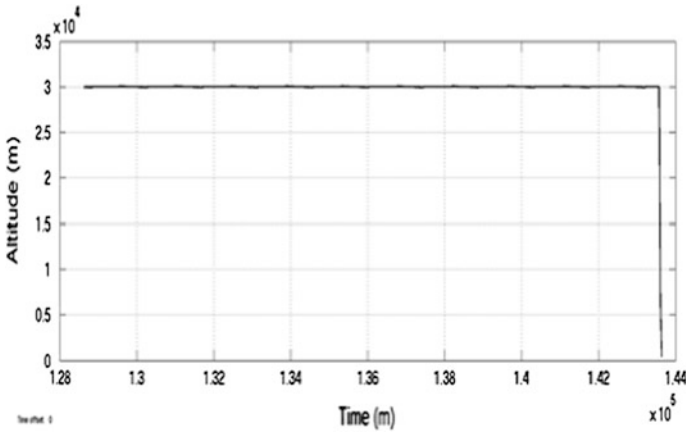
Fig. 16.4 100th day descent with PID control

Fig. 16.5 Variation of flight time with altitude with and without control
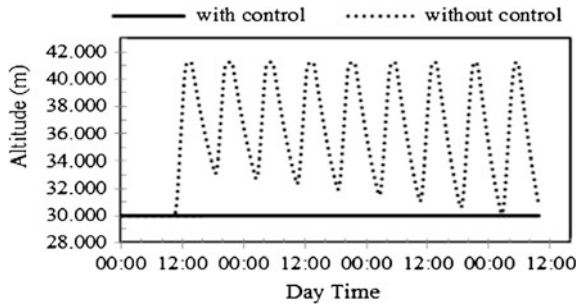
On the 100th day of the flight, command pulse was ordered to start the descent by Gas-Compress-Release System. From Fig. 16.3 it can be seen that it is possible to descend the balloon system any time when technical service is needed. Figure 16.4 shows PID descent control Simulink result for the 100th day. It can be seen that before descent Gas-Compress-Release mechanism with PID control keeps the balloon at 30,000 m altitude well and provides to reach to the ground.

Without control, the balloon system behavior is shown in Fig. 16.5 for eight days of long flight. It can be seen that without control the balloon rises 12,000 m over the desired altitude (30,000 m).

For the safe landing, descent velocity to the ground is a critical parameter of flight. From Fig. 16.6 it can be seen that balloon lands to the ground with 0.78 m/s and this velocity is very safe for the equipment which balloon carries. Also, landing time is recorded as 70 min.
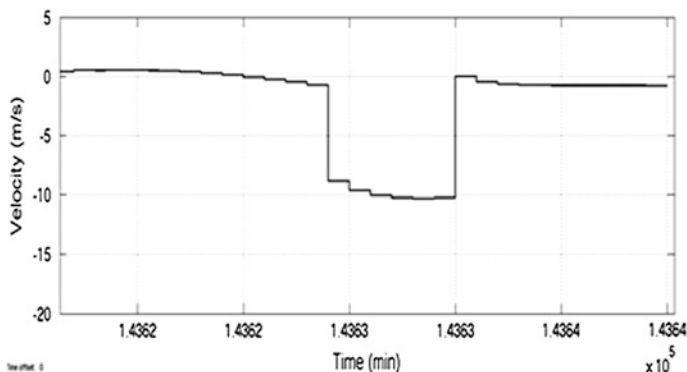
Fig. 16.6 100th day descent velocity variation to the ground

16.5   Conclusions

In this study, an algorithm for a balloon system has been written with MATLAB/ Simulink. The descent and flight behavior of a high altitude balloon with PID control has been numerically investigated and validated using field data. It is believed that the Gas-Compress-Release model with PID control permits a way to intervene the balloon any time for technical service. And this control also permits better prediction of not only the ascent but also the descent process and flights at constant altitude for longer periods. The following conclusions were made:

- Safe landing to the ground is a strong function of the helium mass inside the balloon and it can be controlled by PID controller.
- The PID Control of Compress-Release helps the balloon reach the target altitude keeping it there for a longer period and descent anytime of the flight with safe landing speed for the equipment without using ballast.
- It is found that when stored gas and content of the balloon lifting gas weights are 1000 kg, balloon could carry 1000 kg payload at 30 km for 330 days. Under these conditions, it is possible to descend the balloon to the ground with PID control for technical service. The landing velocity of 0.78 m/s is quite reliable and safe.
- Using the developed model and MATLAB/Simulink software package one can generate velocity, temperatures and all outputs of ascent, descent and flight continuously.

References

Cathey HM Jr (2009) The NASA super pressure balloon—a path to flight. Adv Space Res 44:23–38

Dai Q, Fang X, Li X, Tian L (2012) Performance simulation of high altitude scientific balloons. Adv Space Res 49:1045–1052

Farley RE (2005) Balloon ascent 3-D simulation tool for the ascent and float of high altitude balloons. Paper presented at AIAA 5th aviation technology integration and operation conference, Virginia, 26–28 Sept 2005

Kayhan Ö, Hastaoğlu MA (2014) Modeling of stratospheric balloon using transport phenomena and gas compress-release system. J Thermophys Heat Tr 28:534–541

Liu Q, Wu Z, Zhu M, Xu WQ (2014) A comprehensive numerical model investigating the thermal-dynamic performance of scientific balloon. Adv Space Res 53:325–328

Xia XL, Li DF, Sun C, Ruan LM (2010) Transient thermal behavior of stratospheric balloons at float conditions. Adv Space Res 46:1184–1190

Chapter 17
Multi-objective 4D Trajectory Optimization for Online Strategic and Tactical Air Traffic Management

Alessandro Gardi, Roberto Sabatini, Matthew Marino and Trevor Kistan

Abstract Significant evolutions of aircraft, airspace and airport systems design and operations are driven by the continuous increase of air transport demand worldwide and by the concurrent push for a more economically viable and environmentally sustainable aviation. In the operational context, novel avionics and air traffic management (ATM) systems are being developed to take full advantage of the available communication, navigation and surveillance (CNS) performance. In order to attain higher operational, economic and environmental efficiencies, the generation of 4-dimensional trajectories (4DT) shall integrate optimisation algorithms addressing multiple objectives and constraints in real-time. Although extensive research has been performed in the past on the optimisation of aircraft flight trajectories and very efficient algorithms were widely adopted for the optimisation of vertical flight profiles, it is only in the last few years that higher levels of integration were proposed for automated 4DT planning and rerouting functionalities. This chapter presents the algorithms conceived for integration in next generation avionics and ATM Decision Support Systems (DSS), to perform the multi-objective optimisation of 4DT intents. In particular, the algorithms are developed for 4DT planning, negotiation, and validation (4-PNV) in online strategic and tactical operational scenarios, and are conceived to assist the human flight crews and ATM operators in planning and reviewing optimal 4DT intents in high air traffic density contexts. The presented implementation of the multi-objective 4DT optimisation problem includes a number of environmental objectives and operational constraints, also accounting for economic and operational performances as well as weather forecast information from external sources. The current algorithm verification activities address the Arrival

A. Gardi · R. Sabatini (✉) · M. Marino · T. Kistan
School of Aerospace, Mechanical and Manufacturing Engineering,
RMIT University, Melbourne, Australia
e-mail: roberto.sabatini@rmit.edu.au

T. Kistan
THALES Australia, Melbourne, Australia

Manager (AMAN) scenario within a Terminal Manoeuvring Areas (TMA), featuring automated point-merge sequencing and spacing of multiple arrival traffic in quasi real-time.

17.1 Introduction

In order to achieve the ambitious objectives set by national and international organisations for capacity, efficiency, sustainability and safety of flight operations in the future, substantial technological and operational evolutions are required. A key area of improvement for attaining the higher capacities necessary to cope up with the steady growth of air transport demand and at the same time to enhance the levels of safety, efficiency and sustainability of flight operation consists in the adoption of 4-dimensional trajectory (4DT) functionalities in an intent-based operations (IBO) environment (The ATM Target Concept—D3 2007). The conventional operational paradigms involving the manual dispatch via voice communications of route clearances consisting of a limited set of flight path descriptors are in fact constraining the available capacity and affecting operational efficiencies in an ever-growing number of airspace regions. Furthermore, voice communication channels are quickly saturating the available aeronautical very high frequency (VHF) spectrum in high air traffic density areas. Data-link communications feature a more efficient exploitation of the available aeronautical radio spectrum, and enable a secure high-integrity and seamless networking and extensive information sharing. An automation-assisted planning and negotiation/validation of 4DT intents will permit the full exploitation of the enhanced navigation and surveillance performances provided by modern ground, avionics and satellite-based systems, as it will be natively capable of processing more complex route clearances and higher amounts of shared information supplied by data-link communications, presenting them to the human operators in user-friendly formats. In order to operationally deploy the 4DT-IBO functionalities, novel avionics and air traffic management (ATM) systems are required. These advanced airborne and ground-based decision support systems (DSS) will assist human operators in the generation, validation, execution and monitoring of optimised 4DT intents in real-time. Enhanced traffic separation and spacing standards will be made available in high performance communication, navigation and surveillance (CNS) airspace regions, thanks to the extensive deployment of 4DT capabilities. In particular, two DSS are being developed at present to implement 4DT-IBO: a Next Generation Flight Management Systems (NG-FMS) for manned and unmanned aircraft, and the 4DT planning, negotiation and validation (4-PNV) assisting ATM operators on the ground. (Sabatini et al. 2015; Gardi et al. 2015; Ramasamy et al. 2015). In order to promote a higher efficiency and environmental sustainability of flight operations, the generation and negotiation of 4DT shall integrate multi-objective trajectory optimisation (MOTO) software algorithms, addressing all environmental and

economic impacts of the generated trajectories. MOTO algorithms are thereby a key feature of avionics and ATM DSS in the future. This chapter reviews the state-of-the-art of trajectory optimization for aviation applications and presents the customised MOTO algorithm that was developed to meet the stringent requirements of online strategic and tactical ATM timeframes. The MOTO algorithm attempts the optimisation of the planned flight path with respect to multiple objectives and constraints and is based on the timeframe convention for offline and online air traffic operations previously adopted (Gardi et al. 2014). The adopted formulation of the multi-objective 4D trajectory optimisation (MOTO-4D) problem includes a number of environmental objectives and operational constraints such as flight time, fuel consumption, multiple engine emissions, noise and contrails. The novel avionics and ATM DSS are capable of generating multiple intents in real-time based on a set of environmental performance criteria, allowing more sustainable air traffic operations.

17.2   Statement of the Problem

A number of operational aspects and environmental impacts associated with the aircraft mission have significant dependencies on the flown trajectory (Gardi et al. 2016). On-board trajectory optimisation algorithms were investigated as early as the 1970s (Sorensen et al. 1979), and deployed in larger civil transport aircraft during the following two decades in the form of new automatic flight and flight director modes for most phases of flight, targeting in particular the vertical guidance and optimised standard turns. Although the savings derived from these measures were very significant with respect to the previous operational paradigms, it has been proposed that more substantial gains can be attained by adopting real-time optimisation algorithms for strategic and tactical replanning of 4D flight trajectories in an intent-based network-centric ATM scenario. Figure 17.1 represents the concept of MOTO to tackle multiple operational, economic and environmental criteria in the aviation context. In order to obtain optimal 4D intents with respect to the set optimality objectives, the MOTO suite comprises a number of essential aircraft, environmental and operational models. These models include local/global weather, operational costs, pollutant emissions, airspace structure, contrails and aircraft noise. As the emphasis is on the noise perceived by the population on the ground, the aircraft noise model must be complemented by suitable demographic distribution and digital terrain elevation databases.

   Significant research activities and outcomes on multi-objective 4DT optimisation algorithms are being achieved as part of the major research programmes worldwide. The progresses in optimal control theory and nonlinear programming for trajectory optimisation are leading to substantial improvements to the numerical solution methods for real-time applications. A considerable opportunity for direct
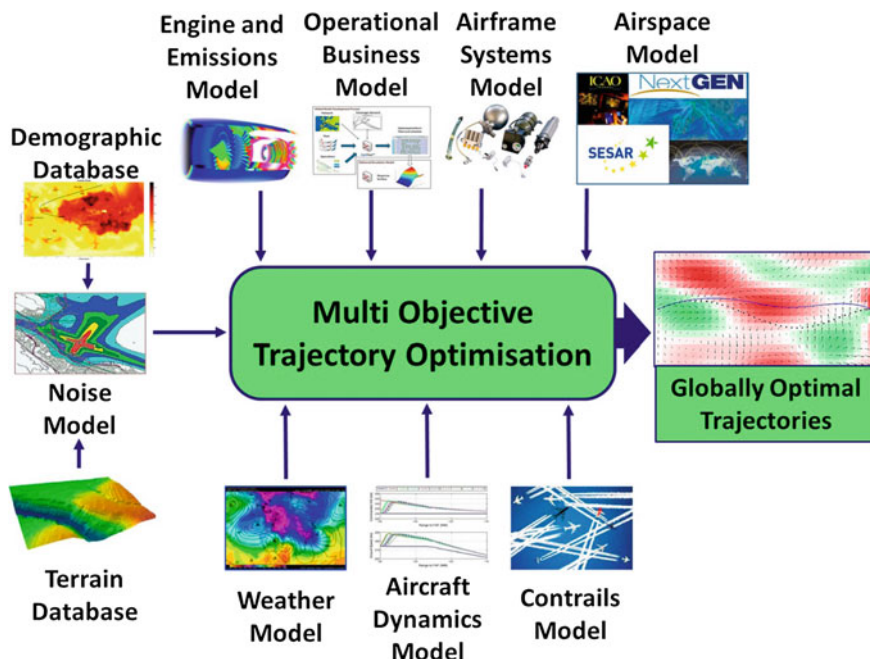
Fig. 17.1 Multi-objective trajectory optimisation concept (Sabatini et al. 2014)

exploitation of these research outcomes into the next generation avionics and ATM systems is emerging. The adoption of computational algorithms for optimal 4DT planning represents a substantial evolution from the conventional flight planning methodologies currently in place and their associated limitations. The conventional flight plan is, in fact, an essentially static entity, hence unforeseen weather and air traffic perturbations have the effect of progressively compromising its optimality. Furthermore, only fuel and time costs are normally considered in traditional optimisation methods. Reducing fuel consumption leads to reduced carbon dioxide (CO_2) emissions with current generation turbofan engines but, unfortunately, most of the noxious emission such as carbon monoxide (CO), nitrogen oxides (NO_X) and unburnt hydrocarbons (UHC) are not typically addressed. Growing R&D efforts are therefore addressing practical implementations of real-time trajectory optimisation algorithms as well as pollutant and noise emission models for the optimization of flight trajectories with respect to multiple objectives, while encompassing constraints that also entail strategic and tactical ATM and air traffic flow management (ATFM) directives in an evolving airspace (Visser and Wijnen 2001; Jardin 2003; Wijnen and Visser 2003; Hartjes et al. 2009; Torres et al. 2009; Soler et al. 2010; Sridhar et al. 2011; Vaddi et al. 2012).

17.3   Mathematical Formulation

Although different formulations of the trajectory optimisation problem (TOP) were adopted for aeronautical applications, partly due to the considerable dependence on geographic descriptors to characterise the flight path in three dimensions, in the mainstream literature a considerable emphasis is given to the optimal control problem (OCP) formulation. This is mainly due to the consideration of the aircraft as a dynamical system and to the conspicuous mathematical framework guaranteeing the optimality of theoretical optimal control results. The theoretical framework of optimal control and its application to aerospace vehicles and systems is extensively presented in Ben-Asher (2010) and Betts (2010). Adopting the formulation of Bolza, the TOP is analytically stated as (Rao 2010a):

"*Determine the states $\boldsymbol{x}(t) \in \mathbb{R}^n$, the controls $\boldsymbol{u}(t) \in \mathbb{R}^m$, the parameters $\boldsymbol{p} \in \mathbb{R}^q$, the initial time $t_0 \in \mathbb{R}$ and the final time $t_f \in \mathbb{R}\mid t_f > t_0$, that optimise the performance indexes*

$$\boldsymbol{J} = \boldsymbol{\Phi}\big[\boldsymbol{x}(t_f), \boldsymbol{u}(t_f), \boldsymbol{p}\big] + \int_{t_0}^{t_f} \mathcal{L}[\boldsymbol{x}(t), \boldsymbol{u}(t), \boldsymbol{p}]\mathrm{d}t \qquad (17.1)$$

subject to the dynamic constraints

$$\dot{\boldsymbol{x}}(t) = \boldsymbol{f}[\boldsymbol{x}(t), \boldsymbol{u}(t), t, \boldsymbol{p}] \qquad (17.2)$$

to the path constraints

$$\boldsymbol{C}_{\min} \le \boldsymbol{C}[\boldsymbol{x}(t), \boldsymbol{u}(t), t; \boldsymbol{p}] \le \boldsymbol{C}_{\max} \qquad (17.3)$$

and to the boundary constraints

$$\boldsymbol{\Phi}_{\min} \le \boldsymbol{\Phi}\big[\mathbf{x}(t_0), \mathbf{x}(t_f), \mathbf{u}(t_0), \mathbf{u}(t_f); \mathbf{p}\big] \le \boldsymbol{\Phi}_{\max}\mathit{"} \qquad (17.4)$$

For the solution of TOP, two mainstream strategies have been extensively investigated in the literature, namely *direct methods* and *indirect methods* (von Stryk and Bulirsch 1992; Visser 1994; Betts 1998; Rao 2010b). In the first class, also defined by the paradigm "*discretise then optimise*" the determination of the unknown control function is attempted directly, and this involves the discretisation of the infinite-dimensional TOP into a finite-dimensional nonlinear programming (NLP) problem. In the indirect methods, which historically emerged beforehand and are defined by the paradigm "*optimize then discretise*", analytical manipulations based on the theory of the calculus of variations are exploited to transform the OCP into a nonlinear boundary value problem (BVP).

17.3.1 Numerical Solution

Due to their higher versatility and to the recent emergence of very efficient computational implementations, direct solution methods are currently favoured in a considerable number of applications. The transcription into finite-dimensional NLP problem can be performed either by introducing a control parameterisation based on arbitrarily chosen analytical functions, as in *transcription* methods, or by adopting a generalised piecewise approximation of both control and state variables based on a polynomial sequence of arbitrary degree, as in *collocation* methods. In both cases, the transcribed dynamical system is integrated along the time interval $[t_0; t_f]$. The search of the optimal set of discretisation parameters is formulated as a NLP problem, which is solved computationally by exploiting the most efficient numerical NLP solution algorithms available. In direct transcription methods, a basis of known linearly independent functions $q_k(t)$ with unknown coefficients $\boldsymbol{a}_k$ is adopted as the parameterisation in the general form:

$$z(t) = \sum_{k=1}^{N} \boldsymbol{a}_k q_k(t) \tag{17.5}$$

Considerable research on computationally efficient TOP solution algorithms based on direct transcription and collocation was performed in the last two decades (Betts and Cramer 1995; Betts and Huffman 1998, 1999, 2004; Betts et al. 2000, 2002, 2007; Gherman et al. 2006; Engelsone et al. 2007; Benson et al. 2006; Huntington and Rao 2008; Garg et al. 2010, 2011; Rao et al. 2010; Darby et al. 2011a, b; Patterson and Rao 2012). Although most diverse implementations of direct solution methods are currently researched and developed, global orthogonal collocation methods are considered the state-of-the-art for the solution of large nonlinear OCP, particularly on longer timeframes, and show remarkable computational performances, provided the constraints are carefully defined and the initial guess supplied to the algorithm lies sufficiently close to the global convergence region. In global collocation methods, the direct solution of the OCP is attempted by enforcing the evaluation of the state and control vectors in discrete collocation points across the problem domain by means of orthogonal (spectral) polynomial basis functions. Since pseudo-spectral methods were developed from this very principle, global orthogonal collocation methods are also widely known as pseudo-spectral optimal control methods or simply pseudo-spectral methods (PSM). These methods consist in the following steps. The original time variable is replaced by the scaled and normalised $\tau \in [-1, 1]$ as in:

$$t = \frac{t_f - t_0}{2} \tau + \frac{t_f + t_0}{2} \tag{17.6}$$

The differential operator is consequently modified as follows:

$$\frac{\mathrm{d}}{\mathrm{d}t} = \frac{2}{t_f - t_0} \frac{\mathrm{d}}{\mathrm{d}\tau} \tag{17.7}$$

If the final time is not known a priori (i.e. it is either unconstrained or inequality-constrained in the boundary conditions), t_f will be an additional unknown variable to be determined by the NLP solver. The states and control variables of the OCP are approximated by a set of polynomials of order N, and the problem is thereby discretised in $N + 1$ nodes. These interpolation polynomials must be an orthogonal basis in the discretised space. Hence, they have to satisfy the null scalar product property:

$$P_i(x_j) * P_k(x_l) = 0 \quad \forall i \neq j, \ \forall k, l \in \{1, \dots N+1\} \tag{17.8}$$

Various families of interpolating polynomials can be successfully adopted and comprehensive dissertations may be found in Boyd (2000) and Funaro (1992). At present, the most computationally efficient implementations of PSM adopt simple interpolation polynomials in conjunction with a careful selection of the collocation nodes distribution. For such reasons, the basic Lagrange polynomials are most frequently adopted for the interpolation of states and controls. A Gaussian quadrature rule ensures the exact results of discrete integral evaluations. Adopting the interpolation polynomials $P_k(\tau)$ on the $N + 1$ nodes τ_k, the states are approximated as:

$$\tilde{x}_i(\tau) = \sum_{k=1}^{N} \tilde{x}_i(\tau_k) \cdot P_{i,k}(\tau) \tag{17.9}$$

and the controls are approximated as:

$$\tilde{u}_j(\tau) = \sum_{k=1}^{N} \tilde{u}_j(\tau_k) \cdot P_{j,k}(\tau) \tag{17.10}$$

The evaluation of the dynamic constraints (i.e. the state equations) is then performed in the nodes only, leading to a problem of finite dimensions. The dimension of the discrete problem is not the same in all cases, though. Lagrange polynomials of order N are expressed as:

$$P_k(\tau) = \prod_{j \neq k} \frac{\tau - \tau_j}{\tau_k - \tau_j}, \quad \forall j \in [0, N] \tag{17.11}$$

Chebyshev pseudo-spectral methods (CPM) adopt Chebyshev polynomials of order N. An application of the CPM to aircraft dynamics is discussed in Bousson and Machado (2010) and involves the evaluation of the Chebyshev trigonometric polynomials:

$$P_N(\tau) = \cos(N\cos^{-1}\tau) \qquad (17.12)$$

in the $N+1$ nodes:

$$\tau_k = \cos\frac{k\pi}{N}, \quad k \in [0,N]. \qquad (17.13)$$

Two recently adopted PSM variants are the Gauss PSM and the Legendre–Gauss–Lobatto (LGL) PSM (Basset et al. 2010). Gauss PSM are based on the Gauss–Legendre quadrature, whereas the LGL PSM are based on the LGL quadrature, also simply known as Lobatto quadrature. Gauss PSM are specifically conceived to ensure that the Karush-Kuhn-Tucker (KKT) conditions are identical to the discretised first-order optimality conditions. Legendre polynomials may be calculated by using the Rodrigues formula:

$$P_N(\tau) = \frac{1}{2^N k!} \frac{\mathrm{d}^{(N)}}{\mathrm{d}\tau^{(N)}}\left[\left(\tau^2 - 1\right)^N\right] \qquad (17.14)$$

The LGL nodes are the $N+1$ zeros of the polynomial:

$$L_N(\tau) = \left(1 - \tau^2\right)\dot{P}_N(\tau) \qquad (17.15)$$

where $\dot{P}_N(\tau)$ is the first derivative of the Legendre polynomial of degree N (Brix et al. 2013).

In Gauss PSM, the dynamic constraints are not collocated at the boundary nodes, whereas in the LGL PSM the evaluation of states and controls is performed also at the boundary nodes, thereby the dimension of the NLP problem is increased by two additional nodes. For further reference the reader may refer to Rao (2010b) and Rao et al. (2010).

17.3.2 MOTO-4D Algorithm Implementation

The real-time MOTO-4D algorithms implemented in the 4-PNV system adopt the same dynamic and path constraints implemented in the NG-FMS (Ramasamy et al. 2015). Aircraft dynamics data are shared between the NG-FMS and the 4-PNV through the Next Generation Aeronautical Data-Links (NG-ADL), along with the relevant aircraft and airspace information, to ensure synchronisation and, consequently, mathematical consistency. In order to characterise the flyable

envelope of the aircraft, a flight dynamics model is adopted as part of the dynamic constraints in the OCP formulation. The three degrees of freedom (3DOF) point-mass model with variable mass traditionally adopted as flight dynamics in NG-FMS and 4-PNV is:

$$
\dot{\boldsymbol{x}} = \begin{cases}
\dot{v} = \frac{\tau \cdot T_{\text{MAX}} - D}{m} - g \sin \gamma \\
\dot{\gamma} = \frac{g}{v} \cdot (N \cos \mu - \cos \gamma) \\
\dot{\chi} = \frac{g}{v} \cdot \frac{N \sin \mu}{\cos \gamma} \\
\dot{\phi} = \frac{v \cos \gamma \sin \chi + v_{w_\phi}}{R_E + z} \\
\dot{\lambda} = \frac{v \cos \gamma \cos \chi + v_{w_\lambda}}{(R_E + z) \cos \phi} \\
\dot{z} = v \sin \gamma + v_{w_z} \\
\dot{m} = -FF
\end{cases}
\tag{17.16}
$$

where v is the true airspeed, $\boldsymbol{v}_w$ is the wind velocity vector, γ is the flight path angle, χ is the track angle, m is the aircraft mass, ϕ λ and z are, respectively, the geodetic latitude, longitude and altitude, g is the gravity acceleration, R_E is the geodetic Earth radius, D is the aircraft drag, T_{CL} is the maximum climb thrust. The control variables are $\boldsymbol{u} = \{N, \tau, \mu\}$, which, respectively, represent the load factor, the throttle and the bank angle. The drag is calculated with the conventional parabolic approximation as:

$$
D = \frac{1}{2} \rho v^2 S C_{D0} + \frac{2 C_{D2} m^2 g^2}{\rho\, v^2 S}
\tag{17.17}
$$

where ρ is the local air density, and S, C_{D0}, C_{D2}, respectively, represent the aircraft reference area and the two parabolic drag coefficients. These parameters are typically available for the most commonly flown aircraft, and for instance may be obtained from the Eurocontrol's Base of Aircraft Data (BADA) database. The drag coefficient increases to account for flaps and landing gear are also available (BADA 2013). Adopting the formulation from BADA, the maximum climb thrust and the fuel flow of a turbofan engine are calculated as (BADA 2013):

$$
T_{\text{CL}} = C_{T1} \cdot \left(1 - \frac{H_P}{C_{T2}} + C_{T3} \cdot H_P^2\right) \cdot [1 - C_{T5} \cdot (\Delta T - C_{T4})]
\tag{17.18}
$$

$$
FF = \max\left[\tau\, C_{f1}\left(1 + \frac{v_{\text{TAS}}}{C_{f2}}\right), C_{f3}\left(1 - \frac{H_P}{C_{f4}}\right)\right]
\tag{17.19}
$$

where $C_{T1} \ldots C_{T5}, C_{f1} \ldots C_{f4}$ are the thrust and fuel flow coefficients from the BADA empirical models (BADA 2013). The emission of a generic gaseous pollutant (GP) is modelled as:

$$GP = \int\limits_{t_0}^{t_f} EI_{GP} \cdot FF \, dt \; [\text{Kg}] \tag{17.20}$$

The specific CO and UHC emission indexes are empirically modelled as:

$$EI_{CO/UHC} = c_1 + \exp(-c_2\tau + c_3) \; [\text{g/Kg}] \tag{17.21}$$

Similarly, the NO_X emission index is empirically modelled as:

$$EI_{NO_X} = c_1\tau^2 + c_2\tau + c_3 \; [\text{g/Kg}] \tag{17.22}$$

Equations (17.6) and (17.7) are accurate nonlinear fit of the ICAO Emissions Databank.[1] The fitting parameters $c_{1,2,3}$ accounting for the pollutant emissions of 165 currently operated civil turbofan engines which are $\boldsymbol{c} = \{0.556, 10.21, 4.068\}$ for CO, $\boldsymbol{c} = \{0.083, 13.2, 1.967\}$ for UHC and $\boldsymbol{c} = \{7.32, 17.07, 3.53\}$ for NO_X. Linearized models can be introduced to enhance computational performance when required.

17.3.3 Multi-objective Optimality

In line with the requirements for online tactical replanning, the weighted sum method, belonging to the category of a priori articulation of preferences, is adopted for the identification of a combined performance index $\boldsymbol{J}$ (Gardi et al. 2014; Marler and Arora 2004). The a priori multi-objective optimisation approach is conceptually represented in Fig. 17.2. The performance weightings can be dynamically modified along the flight and as part of an ongoing collaborative decision-making (CDM) process between the AOC and ANSP when required. multiple optimal 4DT are generated on-board each traffic, and then using a rule-based algorithm, a conflict free set of trajectories is found for all aircraft.

17.4 4DT Optimisation Algorithm

The numerical algorithm for the solution of the single (combined) objective optimal control problem is represented in Fig. 17.3. A mathematically optimal 4DT is generated by means of a numerical solver based on a direct method of the family of

---

[1]ICAO. ICAO Aircraft Engine Emissions Databank [Online]. Available http://easa.europa.eu/node/15672.

global orthogonal collocation (pseudo-spectral). This 4DT is a discretised version of a continuous/piecewise smooth (CPWS) curve, which in general may not be flyable by human pilots nor by conventional automatic flight control systems (AFCS), as it includes transition manoeuvres involving multiple simultaneous variations in the control inputs. Moreover, the discretised CPWS consists of a very high number of overfly 4D waypoints, which would have unacceptable impacts on the Next Generation Airborne Data-Link (NG-ADL) bandwidth usage. Therefore, an "operational smoothing" post-processing stage is introduced, which employs manoeuvre identification algorithms to segment the trajectory in conventional flight legs, including straight and level flight, straight climbs and descents, level turns, and climbing/descending turns. The final result is a concisely described 4DT consisting of operationally feasible flight segments.

17.5 Simulation and Results

The sequencing of dense arrival traffic towards a single approach procedure was extensively evaluated as a representative case study of online tactical Terminal Manoeuvring Area (TMA) management. The results of one representative simulation run are depicted in Fig. 17.4. The 4-PNV identifies the best arrival sequence among the available options. Longitudinal separation is enforced at the merge-point to ensure sufficient separation upon landing and to prevent separation infringements in the approach phase itself. The 4-PNV is capable of performing point-merge at
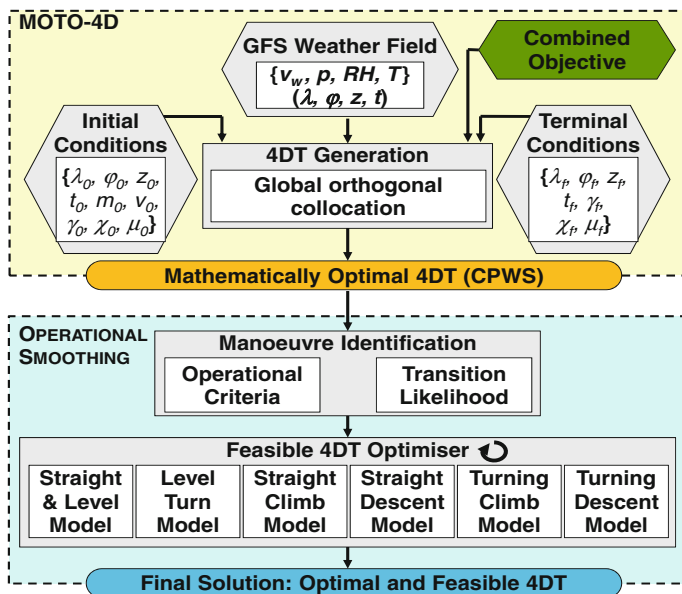
Fig. 17.3 Diagram of the MOTO-4D algorithm (Gardi et al. 2015)

any metering point. After the initial intents have been stored in the 4-PNV, the point-merge sequencing algorithm allocates the available time slots accordingly. The assumed minimum longitudinal separation is 4 nautical miles on the approach path for medium category aircraft approaching at 140 knots. Therefore, the generated time slots are characterised by a 90–160 s separation depending on the wake-turbulence categories of two consecutive traffics.

Figure 17.5 depicts the computed 4DT in the Arrival Manager (AMAN) schedule display format. Waypoints and lines depicted in magenta represent the flyable and concisely described 4DT consisting of a limited number of fly-by and overfly 4D waypoints, obtained through the smoothing algorithm.

Monte Carlo simulation was performed, resulting in an average of 41 s for single newly generated 4DT intents (and consistently less than 60 s). The 4DT post-processing allowed to reduce discretised CPWS trajectories of 150–450 points into a number of fly-by and overfly 4D waypoints consistently below 20. These results meet the set design requirements for tactical online data-link negotiation of the 4DT intents.
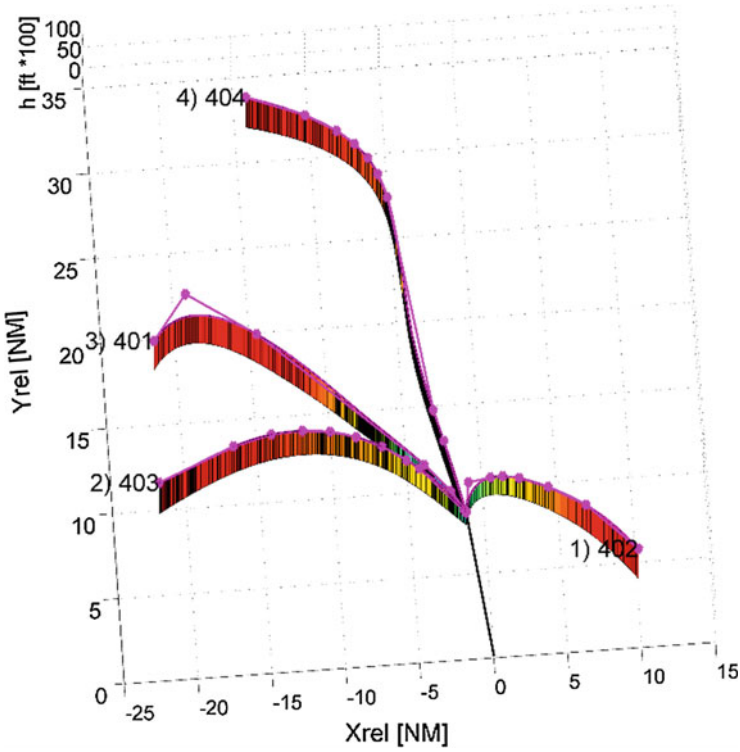
Fig. 17.4 Results of the 4-PNV exploiting the operational 4DT smoothing

Fig. 17.5 Traffic sequencing represented in an AMAN scheduler plot
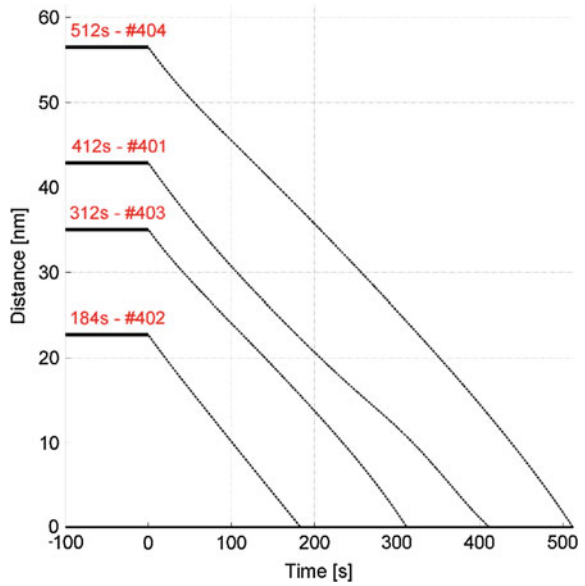
17.6 Conclusions

This chapter presented the key aspects of Multi-objective Trajectory Optimisation (MOTO) currently being developed for integration in future airborne avionics and ground-based air traffic management (ATM) decision support systems (DSS). The MOTO algorithms are specifically conceived to reproduce the dependency of various aircraft emissions on its particular 4-dimensional flight trajectory (4DT) in space and time, to ultimately improve the environmental sustainability of air traffic, while at the same time enhance the operational and economic performances. The presented MOTO algorithms are at the core of 4DT planning functionalities in the novel avionics and ATM systems, which are the Next Generation Flight Management System (NG-FMS) for manned and unmanned aircraft, and the 4DT Planning, Negotiation and Validation (4-PNV) system on the ground. The MOTO functionalities are designed to meet the stringent requirements for strategic and tactical online air traffic operations in the presence of dense air traffic, whenever airspace or air traffic reorganisation is required due to dynamically changing conditions. The chapter presented a number of MOTO algorithm design aspects and some algorithm verification activities involving sequencing and spacing of arrival traffic within a Terminal Manoeuvring Area (TMA). These simulation activities consistently meet the requirements set for online tactical routing/rerouting tasks, generating 4DT intents consisting of a limited number of overfly and fly-by waypoints. Future verification activities will address the en-route ATFM context, also implementing the Dynamic Airspace Management (DAM) functionalities currently being researched.

References

Basset G, Xu Y, Yakimenko OA (2010) Computing short-time aircraft maneuvers using direct methods. J Comput Syst Sci Int 49:481–513. doi:10.1134/S1064230710030159

Ben-Asher JZ (2010) Optimal control theory with aerospace applications. American Institute of Aeronautics and Astronautics (AIAA), Reston

Benson DA, Huntington GT, Thorvaldsen TP, Rao AV (2006) Direct trajectory optimization and costate estimation via an orthogonal collocation method. J Guid Control Dyn 29:1435–1440. doi:10.2514/1.20478

Betts JT (1998) Survey of numerical methods for trajectory optimization. J Guid Control Dyn 21:193–207

Betts JT (2010) Practical methods for optimal control and estimation using nonlinear programming, 2nd edn, vol 19. SIAM

Betts JT, Cramer EJ (1995) Application of direct transcription to commercial aircraft trajectory optimization. J Guid Control Dyn 18:151–159

Betts JT, Huffman WP (1998) Mesh refinement in direct transcription methods for optimal control. Optimal Control Appl Methods 19:1–21

Betts JT, Huffman WP (1999) Exploiting sparsity in the direct transcription method for optimal control. Comput Optim Appl 14:179–201. doi:10.1023/A:1008739131724

Betts JT, Huffman WP (2004) Large scale parameter estimation using sparse nonlinear programming methods. SIAM J Optim 14:223–244. doi:10.1137/S1052623401399216

Betts JT, Biehn N, Campbell SL, Huffman WP (2000) Compensating for order variation in mesh refinement for direct transcription methods. J Comput Appl Math 125:147–158. doi:10.1016/S0377-0427(00)00465-9

Betts JT, Biehn N, Campbell SL, Huffman WP (2002) Compensating for order variation in mesh refinement for direct transcription methods II: computational experience. J Comput Appl Math 143:237–261. doi:10.1016/S0377-0427(01)00509-X

Betts JT, Campbell SL, Engelsone A (2007) Direct transcription solution of optimal control problems with higher order state constraints: theory vs practice. Optim Eng 8:1–19. doi:10.1007/s11081-007-9000-8

Bousson K, Machado P (2010) 4D flight trajectory optimization based on pseudospectral methods. World Acad Sci Eng Technol 70:551–557

Boyd JP (2000) Chebyshev and Fourier spectral methods, 2nd edn. Dover publications, Mineola

Brix K, Canuto C, Dahmen W (2013) Legendre-Gauss-Lobatto grids and associated nested dyadic grids. Aachen Inst Adv Study Comput Eng Sci (arXiv:1311.0028)

Darby CL, Hager WW, Rao AV (2011a) An hp-adaptive pseudospectral method for solving optimal control problems. Optimal Control Appl Methods 32:476–502. doi:10.1002/oca.957

Darby CL, Hager WW, Rao AV (2011b) Direct trajectory optimization using a variable low-order adaptive pseudospectral method. J Spacecraft Rockets 48:433–445. doi:10.2514/1.52136

Engelsone A, Campbell SL, Betts JT (2007) Direct transcription solution of higher-index optimal control problems and the virtual index. Appl Numer Math 57:281–296. doi:10.1016/j.apnum.2006.03.012

Funaro D (1992) Polynomial approximation of differential equations. Springer, Berlin

Gardi A, Sabatini R, Ramasamy S, Kistan T (2014) Real-time trajectory optimisation models for next generation air traffic management systems. Appl Mech Mater 629:327–332. doi:10.4028/www.scientific.net/AMM.629.327

Gardi A, Sabatini R, Ramasamy S (2016) Multi-objective optimisation of aircraft flight trajectories in the ATM and avionics context. Prog Aerosp Sci 83:1–36. doi:10.1016/j.paerosci.2015.11.006

Gardi A, Sabatini R, Kistan T, Lim Y, Ramasamy S (2015) 4-Dimensional trajectory functionalities for air traffic management systems. In: Proceedings: integrated communication, navigation and surveillance conference (ICNS 2015), Herndon, VA, USA

Garg D, Patterson M, Hager WW, Rao AV, Benson DA, Huntington GT (2010) A unified framework for the numerical solution of optimal control problems using pseudospectral methods. Automatica 46:1843–1851. doi:10.1016/j.automatica.2010.06.048

Garg D, Hager WW, Rao AV (2011) Pseudospectral methods for solving infinite-horizon optimal control problems. Automatica 47:829–837. doi:10.1016/j.automatica.2011.01.085

Gherman I, Schulz V, Betts JT (2006) Optimal flight trajectories for the validation of aerodynamic models. Optimization Methods and Software 21:889–900. doi:10.1080/10556780600872281

Hartjes S, Visser HG, Hebly SJ (2009) Optimization of RNAV noise and emission abatement departure procedures. In: Proceedings: AIAA aviation technology, integration, and operations conference 2009 (ATIO 2009), Hilton Head, SC, USA. doi:10.2514/6.2009-6953

Huntington GT, Rao AV (2008) Comparison of global and local collocation methods for optimal control. J Guid Control Dyn 31:432–436. doi:10.2514/1.30915

Jardin MR (2003) Real-time conflict-free trajectory optimization. In: Proceedings: 5th USA/Europe air traffic management research and development seminar (ATM 2003), Budapest, Hungary

Marler RT, Arora JS (2004) Survey of multi-objective optimization methods for engineering. Struct Multi Optim 26:369–395. doi:10.1007/s00158-003-0368

Patterson MA, Rao AV (2012) Exploiting sparsity in direct collocation pseudospectral methods for solving optimal control problems. J Spacecraft Rockets 49:364–377. doi:10.2514/1.A32071

Ramasamy S, Sabatini R, Gardi A (2015) Novel flight management systems for improved safety and sustainability in the CNS+A context. In: Proceedings: integrated communication, navigation and surveillance conference (ICNS 2015), Herndon, VA, USA. doi:10.1109/ICNSURV.2015.7121225

Rao AV (2010a) Trajectory optimization. In: Encyclopedia of aerospace engineering. Wiley

Rao AV (2010b) Survey of numerical methods for optimal control. Adv Astronaut Sci 135:497–528

Rao AV, Benson DA, Darby C, Patterson MA, Francolin C, Sanders I et al (2010) Algorithm 902: GPOPS, a MATLAB software for solving multiple-phase optimal control problems using the gauss pseudospectral method. ACM Transact Math Softw 37. doi:10.1145/1731022.1731032

Sabatini R, Gardi A, Ramasamy S, Kistan T, Marino M (2014) Novel ATM and avionic systems for environmentally sustainable aviation. In: Proceedings: practical responses to climate change. Engineers Australia convention 2014 (PRCC 2014), Melbourne, Australia. doi:10.13140/2.1.1938.0808

Sabatini R, Gardi A, Ramasamy S, Kistan T, Marino M (2015) Modern avionics and ATM systems for green operations. In: Blockley R, Shyy W (eds) Encyclopedia of aerospace engineering. Wiley

Soler M, Olivares A, Staffetti E (2010) Hybrid optimal control approach to commercial aircraft trajectory planning. J Guid Control Dyn 33:985–991. doi:10.2514/1.47458

Sorensen JA, Morello SA, Erzberger H (1979) Application of trajectory optimization principles to minimize aircraft operating costs. In: 18th IEEE conference on decision and control, vol 1, pp 415–421

Sridhar B, Ng H, Chen N (2011) Aircraft trajectory optimization and contrails avoidance in the presence of winds. J Guid Control Dyn 34:1577–1584. doi:10.2514/1.53378

The ATM target concept—D3. SESAR definition phase DLM-0612-001-02-00, 2007

Torres R, Chaptal J, Bes C, Hiriart-Urruty J-B (2009) Multi-objective clean take-off flight paths for civil aircraft. In: Proceedings: AIAA aviation technology, integration, and operations conference 2009 (ATIO 2009), Hilton Head, SC, USA. doi:10.2514/6.2009-6931

User Manual for the Base of Aircraft Data (BADA) Revision 3.11. Eurocontrol experimental centre (EEC) technical/scientific report no. 13/04/16-01, Brétigny-sur-Orge, France, 2013

Vaddi S, Sweriduk G, Tandale M (2012) 4D green trajectory design for terminal area operations using nonlinear optimization techniques. In: Proceedings: AIAA guidance, navigation, and control conference (GNC 2012), Minneapolis, MN, USA. doi:10.2514/6.2012-4755

Visser HG (1994) A 4D trajectory optimization and guidance technique for terminal area traffic management. Delft University of Technology

Visser H, Wijnen R (2001) Optimization of noise abatement arrival trajectories. In: Proceedings: AIAA guidance, navigation and control conference 2001 (GNC 2001), Montreal, Canada. doi:10.2514/6.2001-4222

von Stryk O, Bulirsch R (1992) Direct and indirect methods for trajectory optimization. Ann Oper Res 37:357–373. doi:10.1007/BF02071065

Wijnen RAA, Visser HG (2003) Optimal departure trajectories with respect to sleep disturbance. Aerosp Sci Technol 7:81–91. doi:10.1016/s1270-9638(02)01183-5

Chapter 18
Physical-Based Simulation of a GaN High Electron Mobility Transistor Devices

Sevda Aliparast and Peiman Aliparast

Abstract Silicon-based semiconductor devices are rapidly approaching the theoretical limit of operation, making them unsuitable for future military and industrial applications. In a high electron mobility transistor (HEMT), two-dimensional electron gas (2DEG) which is formed at AlGaN/GaN interface is a critical part to tune the performance of HEMT devices. Inserting high bandgap layers, especially AlN spacer layer between AlGaN and GaN layer improves 2DEG density, mobility, and effects on quantum well. ATLAS toolbox of Silvaco results shows ID-VDS characteristics of the 1 μm gate length. Simulation results show both piezoelectric and spontaneous polarization effects at the interfaces of Al0.30Ga0.70N/AlN/GaN structure, contrary to the conventional HEMTs. The insertion of the very thin AlN interfacial layer (1 nm) supports high mobility at high sheet charge densities by increasing the effectiveness and decreasing alloy scattering. Devices based on this structure exhibit good DC and RF performance.

18.1 Introduction

GaN-based material systems are very interesting for electronic reason is their wide bandgap, excellent transport properties, high critical field, and high thermal stability. Gallium nitride (GaN) is a wide bandgap semiconductor which has been the core of many research investigations including the current study. In 1990s, GaN has attracted attention because of high material performance in systems for both optical and electronic applications. Fast development and performance demonstrations of GaN-based microwave and power devices in the last decade caused researchers to prefer GaN to its alternative, Si-based power. GaN-based transistors have brought a

S. Aliparast · P. Aliparast (✉)
Department of Electrical Engineering, Azad University, Tabriz, Iran
e-mail: Aliparast@ari.ac.ir

S. Aliparast
e-mail: aliparast.s@gmail.com

revolution in power amplifier circuits for mobile phone base stations, and power supply, motor drive, and other related circuits. These also include industrial equipment, white goods, automobiles, and other related industries. If we want to compare existing Si devices with HEMTs, they combine lower power losses with output up to ten times more, yielding circuits that are smaller and less power requirement than ever. For power switching, normally-on characteristics versus normally-off performance play a significant role. GaN-based semiconductor devices have five main characteristics including high dielectric strength, high operating temperature, high current density, high-speed switching, and low ON-resistance. As mentioned, GaN devices act on electrical breakdown characteristics ten times higher than that of Si, carrier mobility as good or better than that of Si, and a bandgap three times or more than that for Si. Choosing SiC with wide bandgap for the substrate off GaN HEMT make results in very low intrinsic carrier concentration that gives negligible junction leakage current up to 500. High-temperature operation is allowable without excessive leakage or thermal runaway and decrease in cooling requirements. The high breakdown strength requires thinner drift layers for a given blocking voltage, as compared to silicon, so it can reduce the specific on-resistance and storage of minority carriers. The associated switching loss is then reduced, which improves higher switching frequency of the devices and significantly decreases the size and weight of the magnetic components in power switches. Ultimately, the high thermal conductivity of the materials drains out dissipated power, with ultra-high-power operation. Recently, these advantages are becoming reality because of significant progresses in development and processing technology for SiC and GaN. One of the main advantages of SiC switches is blocking voltage of a few kilo volts and devices operating at a forward current density of up to 1 KA. The objective of this chapter is to study the possibility of GaN HEMTs with high voltage and low loss switching applications. At the same time, wide bandgap semiconductors, specially SiC and GaN, are more pronounced because they offer main advantages over silicon devices in the areas of switching (faster with lower losses), operating temperature, and blocking voltage. Table 18.1 compares specific electronic parameters of GaN, AlN, Si, and SiC among other major semiconductors such as wide bandgap, high saturated electron velocity, thermal conductivity, electron mobility, and relative dielectric constant. Thus, high-efficiency RF HPA is the main requirement of a telemetry subsystem for LEO satellites as mentioned

Table 18.1 Comparing some electronic properties of semiconductor materials

Parameter	Unit	GaN (AlGaN/GaN)	AlN	4H-SiC	Si
Bandgap	eV	3.39	6.1	3.26	1.1
Electron mobility	cm^2/V_s	900	1100	700	1350
Saturated electron velocity	$10^7 \times cm/s$	2.5	1.8	2.0	1.0
Thermal conductivity	W/cm K	2.5	1.8	4.5	1.5
Relative dielectric constant	ε_r	9.0	8.4	10	11.8

above. In the following we are discussing steps of designing high efficiency RF PA in X Band.

The result of wide bandgap in SiC and GaN give very low carrier concentration that can support junction leakage current up to 500. Cooling issue can be solved and prove high-temperature operation without excessive leakage or thermal runaway. Reducing the specific on-resistance and storage of minority carriers needs high breakdown strength and thinner drift layers for a given blocking voltage, as compared to silicon. In power switches, switching loss is reduced, so higher switching frequency of the devices and significantly reduces the size and weight of the magnetic components appear. For example, the electron affinity a conduction band offset of 65 %. $3.5 \leq 0.1$ eV and $1.9 \leq 0.2$ eV are the measured electron affinity values for GaN and AlN, 65 % is within experimental error for the conduction and valence bands the effective masses for electron and holes is 0.20 and 0.80. They are also used to compute the effective density of states. Al composition of 30 % is performing for material values of AlGaN/GaN HEMT for the optimization understanding and controlling the formation of the 2DEG in AlGaN/GaN HEMTs the source of the electrons in the channel are surface donor-like traps, and the strong polarization field push the electrons into the channel.

18.2 AlGaN/GaN HEMT Fundamentals

High-power millimeter wave radar and electronic warfare systems employee vacuum tubes. For future systems, GaN HEMTs have the potential to be replaced. GaN devices have potential to deliver high power at high voltage, the wide bandgap breakdown field of GaN is five times much more than vacuum tube and the power density of GaN is 10–20 times higher than GaAs-based devices.

As mentioned before, AlGaN/GaN high electron mobility transistors (HEMTs) grown on sapphire substrates have a low reliability due to thermal effects. If the reliable high-frequency, high-power HEMT device are to be responsed, it is necessary for future naval communication and radar needs that use specific other types of materials. The producing model developed is created with the available Silvaco software. The ATLAS™ model was created based on the parameters extracted from an actual AlGaN/GaN HEMT grown on a sic substrate. For the model development, the parameters extracted from the device were utilized as baseline. One of the critical parameters for heterojunction devices is polarization. The polarization effects in heterojunction devices are spontaneous polarization and the piezoelectric effect and they are crucial in the formation of the unique two-dimensional electron gas (2DEG) channel present in heterojunction devices.

Other name of The AlGaN/GaN HEMT is the modulation doped field effect transistor (MODFET) that has similar DC characteristics to the MESFET. The specification of the HEMT is channel formation that has grossly asymmetric heterojunction which is produced between a heavily doped high bandgap material and a lightly doped low bandgap region. There is not any channel being formed as

in a standard homojunction device. This layer is called two-dimensional electron gases (2DEG) which is formed at the heterointerface. For high conductive band of the GaN channel layer and operation of the device, the barrier layer $Al_xGa_{1-x}N$ must be at a higher energy level. The conduction band offset can cause moving electrons from the barrier layer to the channel layer. 2DEG layer is the surface that electrons are transferred and confined to a small region in the channel. This layer is called the 2DEG and a characteristic of the HEMT is as we mentioned. There are many factors that determine the quality of the 2DEG, the factors involved in the development of the 2DEG are type of substrate, growing method, and level of doping of the carrier supply layer the electron density and mobility are important factors when a 2DEG and a more detailed discussion of the 2DEG will be presented later in this chapter.

HEMT device is normally confined to the 2DEG and changed by the gate voltage like MOS devices, the charge flowing in a HEMT When a gate voltage is applied to the device, the sheet charge concentration (ns) is changed to gate voltage and is given by Eq. (18.1) (Sze 1998):

$$n_s = \frac{\varepsilon_i}{q(d_i + \Delta d)}(V_g - V_T)$$ (18.1)

where ε_i and d_i are the dielectric permeability and the thickness of the wide bandgap semiconductor, Äd can be interpreted as the effective thickness of the 2DEG A typical ns value for an AlGaN/GaN heterojunction is $\sim 10^{13}$ cm^{-2}. One of the important parameter is the threshold voltage, because it is a measure of the HEMT device conducting state. V threshold can be expressed as

$$V_T = \phi_B - \Delta E_C - \frac{qN_D}{2\varepsilon_i}d^2$$ (18.2)

where ϕ_B is the gate Schottky-barrier height, and ÄEC is the change in the conduction band for the heterojunction, and ND is the background doping of the GaN layer. In power amplifiers, saturation current and trans conductance are important measures and it can be develop by HEMT device. For long channel devices (Lg > 0.25im), the I_{DSat} can be expressed the same as a standard MOSFET (Tzeng 2004):

$$I_{DSat} = \frac{\mu CW}{2L}(V_g - V_T)^2$$ (18.3)

Here, i is the carrier mobility, C is the gate capacitance, W is the gate width, and L is the gate length. As mentioned quality for a HEMT device is depending on trans conductance. Drain current can change to trans conductance as defined (Pierret 1996):

$$g_M = \left.\frac{\partial I_D}{\partial V_G}\right|_{V_D=\text{Constant}} = \frac{\mu CW}{L}(V_g - V_t) \tag{18.4}$$

Conductance is the drain or channel conductance that is an important measure in the HEMT device

$$g_d = \left.\frac{\partial I_D}{\partial V_d}\right|_{V_g=\text{Constant}} \tag{18.5}$$

For the output impedance matching properties of different stages of an amplifier, the output conductance has very important role. In the modeling of the GaN HEMT device, there are many variables that should be modified to proper model of the device. The models in the Silvaco package can be incorporated into the device.

HEMTs have three terminals so the conduction could be controlled by the gate voltage. Therefore, one of the big differences between a HEMT and a MOS device is that instead of creating a channel between the source and drain with a doped material, a wider bandgap material barrier layer $(Al_xGa_{1-x}N)$ is grown on top of the channel and serves as a carrier supply layer. Therefore, the channel is formed as a 2DEG below the doped layer where the mobility enhancement depends on a reduction in impurity scattering. A technique utilized to increase the electron density in the channel is to increase the Al mole fraction (x) in the $Al_xGa_{1-x}N$ layer. An increase in the Al mole fraction results in a higher bandgap and a larger conduction band discontinuity ÄEC relative to the GaN. The effects of increasing the Al mole concentration are attractive, but there are limitations that have observed to benefit gained. Figure 18.1 illustrates the electron density as a function of Al composition.

For reducing carrier mobility due to different effects, the Al mole fraction also results in a including, intersubband scattering, increased disordering in AlGaN, it is important to make increasing density of interface charges and larger potential
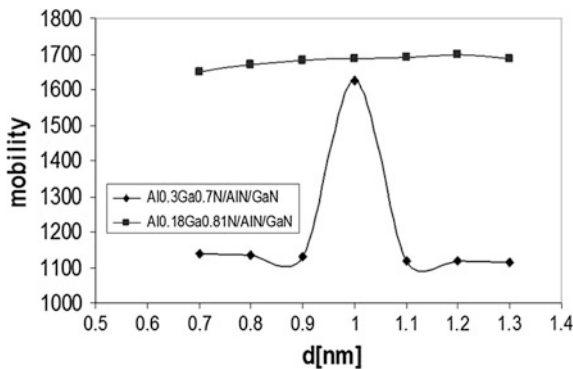
Fig. 18.1 Mobility of 2DEG as a function of AlN spacer thickness in Al0.18Ga0.82N/AlN/GaN and Al0.3Ga0.7N/AlN/GaN heterostructures
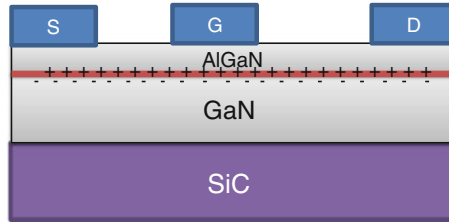
Fig. 18.2 2-D cross section of AlGaN/GaN HEMT

fluctuations at the surface of interface but the surface roughness should be emphasized. The Al composition for the device tested is considered to be 30 %, which roughly correlates to an electron density of $8e^{19}\,cm^{-3}$.

Because operational characteristics are based on the MESFET, then it is easy to provide an overview of the device structure. As mentioned before the 2DEG and the energy bandgap diagrams of an AlGaN/GaN HEMT device easily can be defined. The 2DEG is formed just below the heterojunction where the lower and higher electron mobility is possible. Figure 18.2 shows estimate of where the 2DEG will be within the structure. The conductivity of the two-dimensional channel is defined by Javorka (2004):

$$\sigma = qn_s\mu \tag{18.6}$$

where q is the electron charge, n_s is the sheet carrier concentration given by Eq. 18.6, and i is electron mobility.

The main reason for performing characteristic of a heterojunction device is the abrupt bandgap shift in the layer which meets the GaN Layer in conventional GaN HEMTs. Figure 18.2 shows that a small current began to flow in the 2DEG channel with no gate voltage. As soon as a positive voltage is applied to the drain, current will flow due to the potential difference between the source and drain, but the magnitude of the current flow can be controlled by the gate. The value of I_{Dsat} is dependent on the ns concentration, so increasing the concentration of ns, causes the 2DEG to transfer more charge from source to drain.

18.3 Two-Dimensional Electron Gas (2DEG)

The 2DEG in $Al_xGa_{1-x}N/AlN/GaN$-based HEMT is induced by strong polarization effects Javorka (2004). Ambacher et al., perform piezoelectric constants calculated the induced sheet charge at the heterojunction interface. The formation of the 2DEG in AlGaN/AlN/GaN structures was the result of both spontaneous polarization (PSP) and the strain piezoelectric effects (PPE). Making more realistic HEMT device model, the Silvaco software package includes different modeling parameters. Polarization effects of a GaN HEMT will provide some of the variables that affect the 2DEG.

18.3.1   Spontaneous Polarization

GaN HEMTs have two distinct polarization mechanisms that enable a high carrier concentration even though there may be no intentional doping. Spontaneous polarization is the effect that is at the heterojunction even though there is no strain present. The spontaneous polarization (PSP) is developed due to the Wurtzite group III-nitrides being tetrahedrally coordinated with a lack of symmetry along the [0001] axis or *c*-direction. The polarization effects vary according to formation of the structure. The structure will have either N-face or Ga-face surfaces. The suggested HEMT device provided was grown on SiC by MOCVD which results in Ga-faced structures only. Figure 18.3 shows the crystal structure of a wurtzite Ga-face.

   GaN-based and other group III-N based semiconductors exist under different crystal structures, Wurtzite, Zinkblende, and rock salt. Majority of AlGaN/AlN/GaN HEMTs could be grown on the Wurtzite formation. The Wurtzite structure has a known hexagonal unit cell and consists of two intercepting hexagonal closed packed (HCP) sub-lattice (Ambacher et al. 2000). We can define two lattice parameters, a_0 and c_0, in ideal ratio $c_0/a_0 = \sqrt{8/3} \approx 1.633$. As shown in Fig. 18.3 each atoms includes sub-lattice that constituted by one type of which are shifted with respect to each other along the *c*-axis by the amount $u_0 = 3/8$ in fractional coordinates. As the lattice nonideality increases, c_0/a_0 ratio moves away from 1.633 of the ideal lattice Wurtzite GaN-based semiconductors and a lack of inversion symmetry in the $\langle 0001 \rangle$ direction can cause other group III-N based semiconductors a polar axis. Owning to the difference in electron negativity (here given in Pauling's scale) between the gallium (1.81) and/or aluminum (1.61) and/or indium (1.78), atoms and the nitrogen (3.04) atom, the group III-N's are characterized with high ionicity of the metal-nitrogen covalent bond (Ambacher et al. 2000). Therefore, group III-N semiconductors exhibit exceptionally strong
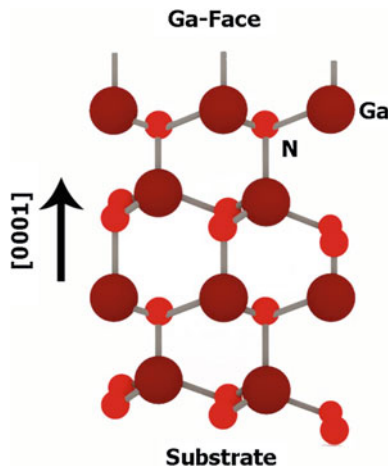
Fig. 18.3 Schematic drawing of the crystal structure of Wurtzite Ga-face (Ambacher et al. 2000)

Table 18.2 Spontaneous polarization, piezoelectric, and dielectric constants of AlN, GaN (Ambacher et al. 2000)

Wurtzite	AlN	GaN
P_{SP}	−0.081	−0.029
	1.46	0.73
e_{33}	1.55	1
		0.65
		0.44
e_{31}	−0.60	−0.49
	−0.58	−0.36
		0.33
		−0.22
e_{15}	−0.48	−0.3
		−0.33
		−0.22
e_{11}	9.0	9.5
e_{33}	10.7	10.4

polarization because of electronic charge redistribution inherent to the crystal structure. This polarization refers to spontaneous polarization, PSP. Because of their Wurtzite structure, GaN-based and group III-N based semiconductors can have different polarities, this reason causes uneven charge distribution between neighboring atoms in the lattice. The polarity of the crystal is related to the direction of the group III-N dipole along the $\langle 0001 \rangle$ direction. In Fig. 18.3, it is shown that two possible polarities are available. In cation-face, i.e., Ga-face, the polarization field points away from the surface to the substrate, while in anion-face, i.e., N-face, the direction of the polarization field is inverted. The Wurtzite crystal, as grown previously discussed, the PSP is the issue for a constant determined by the method of growth. Table 18.2 provides the spontaneous polarization, piezoelectric, and dielectric constants of AlN and GaN. Ambacher et al. (2000) developed this table from many sources and utilized the constants to determine the PSP and PPE for an structure.

To obtain a high carrier concentration at the 2DEG, the ability of the structure to confine carriers through the polarization effects should be noticed. Furthermore, to achieve a high carrier confinement, the polarization should be at the same directions. The polarization-induced sheet charge density (ó) should be positive. 2DEG is formed by positive sheet charge that attracts electrons. Figure 18.4 illustrates the polarization charge effects for different types of strain. The first figure (a) shows AlGaN (relaxed) which is grown on top of GaN (relaxed), a positive sheet charge (+ó) is developed at the surface and a 2DEG forms easily. In order to enhance the polarization effects, example (b) grew tensile strained AlGaN over GaN which resulted in all polarization effects acting in the same direction. This also results in a positive sheet charge at the interface.

Fig. 18.4 Ga-Faced polarization-induced sheet charge density and directions for the spontaneous and piezoelectric polarization effects
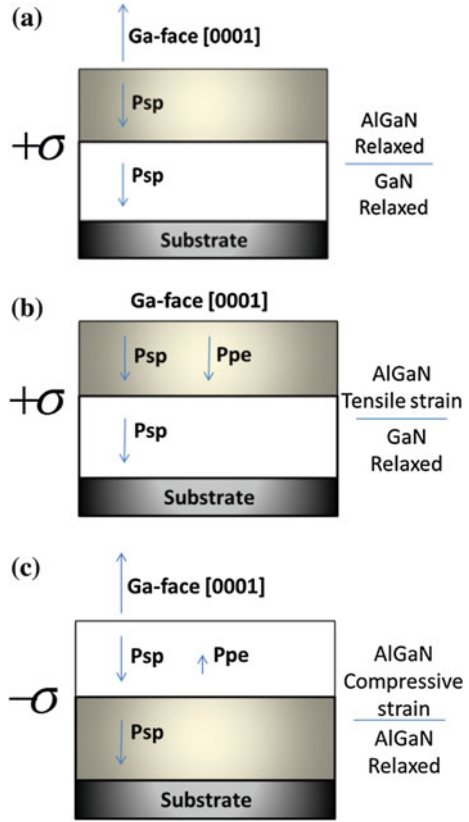
18.3.2   Piezoelectric Polarization

The total polarization in the structure for HEMTs is defined by PSP + PPE = PTOTAL. Table 18.2, shows the piezoelectric polarization that can be followed by equation given here (Ambacher et al. 2000):

$$P_{PE} = e_{33}\varepsilon_z + e_{31}(\varepsilon_x + \varepsilon_y) \tag{18.7}$$

where a_0 and c_0 are the equilibrium values of the lattice parameters $\varepsilon_z = \left(\frac{c-c_0}{c_0}\right)$ is the strain along the c-axis, and the in-plane strain $\varepsilon_x = \varepsilon_y = \left(\frac{a-a_0}{a_0}\right)$ is assumed to be isotropic.

The third independent component of the piezoelectric tensor e_{15} is related to the polarization induced by shear strain, which is not applicable in this device. The relation between the lattice constants of the hexagonal GaN is given by Ambacher et al. (2000) as

$$\left(\frac{c - c_0}{c_0}\right) = -2\left(\frac{C_{13}}{C_{33}}\right)\left(\frac{a - a_0}{a_0}\right) \tag{18.8}$$

where C_{13} and C_{33} are elastic constants provided in previous literature. The total piezoelectric polarization in the direction of the c-axis can be determined by Eqs. (18.7) and (18.8) (Ambacher et al. 2000)

$$P_{PE} = 2\left(\frac{a - a0}{a0}\right)\left(e_{31} - e_{33}\left(\frac{C_{13}}{C_{33}}\right)\right) \tag{18.9}$$

Since the value of $\left[e_{31} - e_{33}\left(\frac{C_{13}}{C_{33}}\right)\right] < 0$. For AlGaN over the entire range of compositions, the piezoelectric polarization is negative for tensile and positive for compressive strained barriers, respectively (Ambacher et al. 2000). The reason that GaN-based semiconductors are attractive in HEMT designs is their high piezo-electric constants. The piezoelectric fields in GaN devices can create a vertical electric field in the MV/cm range which can make the channel conductivity be increased. ATLAS™ as an upgrade to heterojunction modeling is supporting many of the polarization effects.

18.3.3 Device Structure and Simulation Model

This work investigates the methodology of modeling and model calibration of the AlGaN/GaN HEMTs with the AlN spacer against transfer characteristics of the device. Figures 18.1 and 18.6 shows the $Al_xGa_{1-x}N$ thickness as a function of the percent of the effect of Al layer on the operational behavior of the suggested HEMT that the best layer thickness of AlN layer is 1 nm and it can support mobility in amount of 1626 cm^2/v_s (see Fig. 18.5).

Fig. 18.5 Cross-section of the simulated Al0.185Ga0.815N/AlN/GaN and Al0.3Ga0.7N/AlN/GaN HEMTs
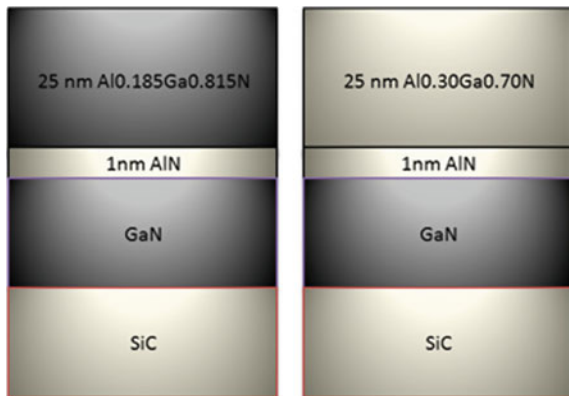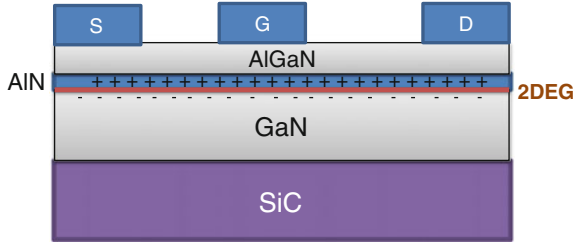
Fig. 18.6 2-D cross-section of suggested AlGaN/AlN/GaN HEMT

In order to simulate and calibrate simulations with respect to two models of HEMTs, The commercial simulation tool ATLAS by Silvaco Clara was employed. The results are presented in Fig. 18.6 higher sheet charge density is generated at the AlN/GaN interface compared to the AlGaN/GaNAlGaN/GaN interface. This is because of both the larger strain-induced (piezoelectric) and the built-in (spontaneous) polarization fields. The following equation expresses the polarization sheet charge density at the AlN/GaN interface

$$\sigma = -\left(P_{\text{AlN}}^{\text{total}} - P_{\text{GaN}}^{\text{total}}\right) \text{C}/m^2 \tag{18.10}$$

High carrier concentration at the 2DEG can be obtained through the ability of the structure to confine carriers through the polarization effects, the polarization directions should be the same for this purpose. The polarization-induced sheet charge density (σ) in (18.10) should be positive.

$$n_s = \frac{\sigma_{\text{AlGaN}} t_{\text{AlGaN}} - \frac{\varepsilon\varepsilon_0}{q}\phi_B + \frac{\varepsilon\varepsilon}{q^2}\Delta E_{\text{C,AlGaN}}}{t_{\text{AlGaN}} + d_0} \tag{18.11}$$

$$n_s = \frac{\sigma_{\text{AlGaN}} t_{\text{AlGaN}} - \frac{\varepsilon\varepsilon_0}{q}\phi_B + \frac{\varepsilon\varepsilon}{q^2}\left(\Delta E_{\text{C,AlGaN}} + \frac{q^2}{\varepsilon\varepsilon_0}\sigma_{\text{AlN}} t_{\text{AlN}}\right)}{t_{\text{AlGaN}} + t_{\text{AlN}} + d_0} \tag{18.12}$$

Definition of (18.11) and (18.12) show the conventional HEMT and HEMT variations with AlN spacer layer with respect to making differences between AlGaN/GaNAlGaN/GaN and AlGaN/AlN/GaN amount of sheet carrier concentration. Here, t stands for the layer thicknesses, ε the dielectric constant, d the distance, ϕ_B the gate Schottky-barrier height, q charge of an electron.

Applying SiN layer to the gate dielectric of high voltage GaN HEMTs will reduce the dispersion, while increases the leakage according to low breakdown voltage (Fig. 18.6). Double-layer of gate dielectric structure was implemented in insulated-gate of GaN HEMTs to combine the advantage of passivation from SiN and low leakage from. Therefore, both low dispersion and over 1000 V breakdown voltage are displayed. The passivation layer of SiN, AlGaN barrier, AlN spacer, and GaN layer thicknesses are 2, 25, 1, and 3 μm, respectively. Gate-to-source and gate-to-drain separations are 2 and 3 μm as shown in Fig. 18.2 quantitative
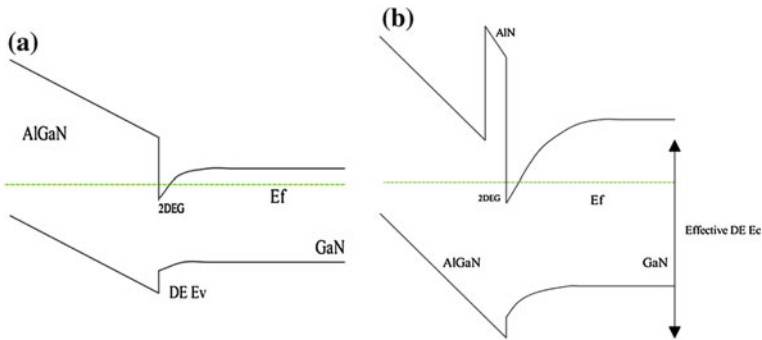
Fig. 18.7 Schematic diagram for energy band diagram of conventional AlGaN/GaN HEMT (**a**) and novel AlGaN/AlN/GaN HEMT (**b**)

prediction of the on-resistance of AlGaN HEMTs is estimated to be 50–200 times lower than that of SiC FETs through theoretical analysis. This depends on the aluminum composition Fig. 18.1. Noticeable amount of research is being carried out for gallium nitride HEMTs s for high power and radio frequency (RF) applications. Unique performance capabilities of III-V materials such as large energy bandgap are among the main reasons for this attention (Kim et al. 2010).

Figure 18.7 shows schematic energy band diagram of conventional AlGaN/GaN HEMT and novel AlGaN/AlN/GaN HEMT and a very high breakdown field (3500 kV/cm). This ensures the under high drain-source biases operation (Sze 1998). Therefore, conduction band diagram of AlGaN/GaN HEMT and AlGaN/AlN/GaN can be obtained, as shown in Fig. 18.7. It should be noticed that low breakdown voltages can be achieved, without design optimization such as field plates (Chen et al. 2015) and recessed-gate technologies. In this way, reliability of the device will be affected. The large gate leakage current at high input RF signal problem is another limiting issue for RF applications of a device. Recent AlGaN/GaN HEMT technologies address this problem. In order to deal with problem, dielectric layers such as SiN and FP to insulate the gate and hence the names MIS-HFET and MIS-HEMT are used. Transconductance, gain will be improved in this way which helps to reduce the leakage current. In order to suppress the current collapse at high drain voltages, channel, and surface effective separation has a key role. Recessed-gate is claimed to be main reason. In order to prevent the channel charge to be effectively modulated by surface potential fluctuations, a thick GaN cap layer is employed to increase the surface-channel distance. To avoid current collapse, "leaky" dielectric under the field-plate can be used as another technique. A semiconducting dielectric under the FP facilitates trapped charge discharge via the field-plate (Chen et al. 2015).

The result of conduction band diagram of conventional AlGaN/GaN HEMT and novel AlGaN/AlN/GaN HEMT is shown in Fig. 18.8 where there is a very high breakdown field ensuring operation under high drain-source biases Figs. 18.9, 18.10, 18.12 and 18.13 have specific differences of AlGaN/AlN/GaN and AlGaN/GaN and Id-Vd calculation of AlGaN/AlN/GaN and AlGaN/GaN are not
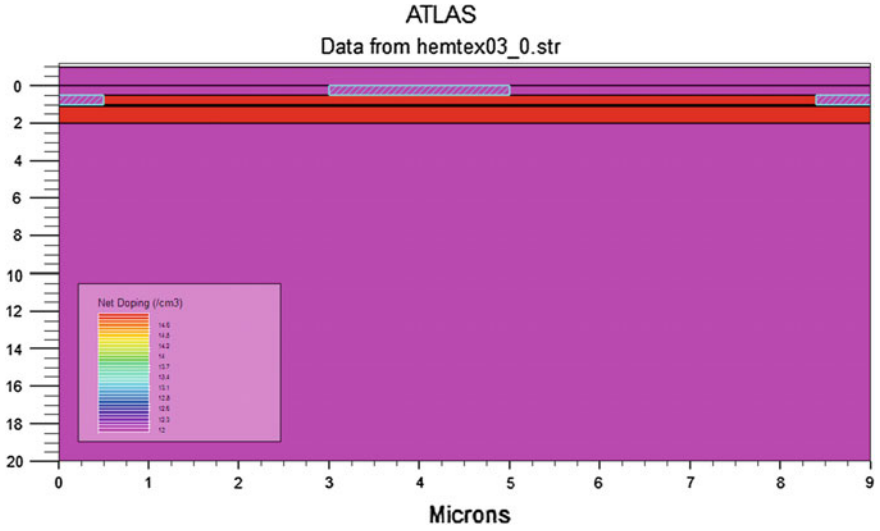
Fig. 18.8 2-D representation of the modeled AlGaN/AlN/GaN HEMT
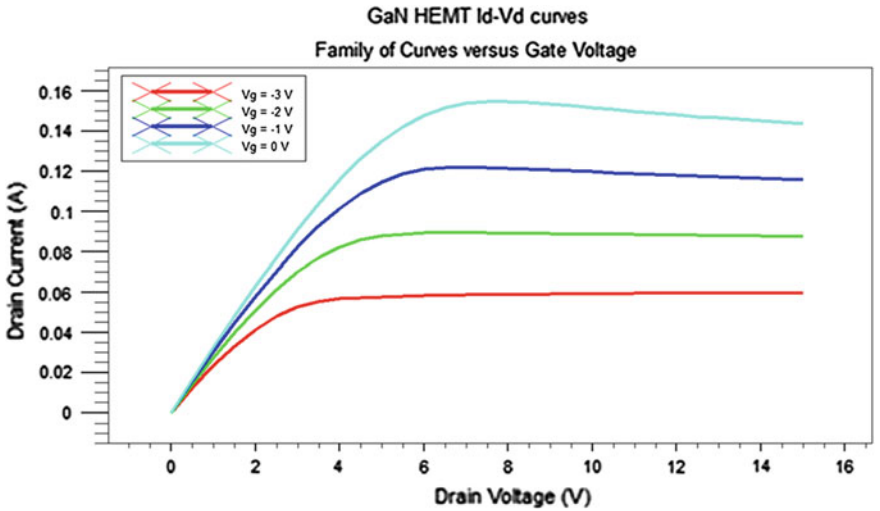
Fig. 18.9 AlGaN/AlN/GaN HEMT Id-Vd curves

exactly the same. The density of 2DEG is based on polarization and the mobility of μ is mainly dependent upon the lattice temperature and the ionized impurity concentration for undoped AlGaN/AlN/GaN := 1.22×10^{13} cm^{-2}, $\mu = 1520$ and for conventional undoped AlGaN/GaN = 1.1×10^{13} cm^{-2} and $\mu = 1200$. The AlN spacer has the advantage of reducing the alloy disorder scattering at the interface of
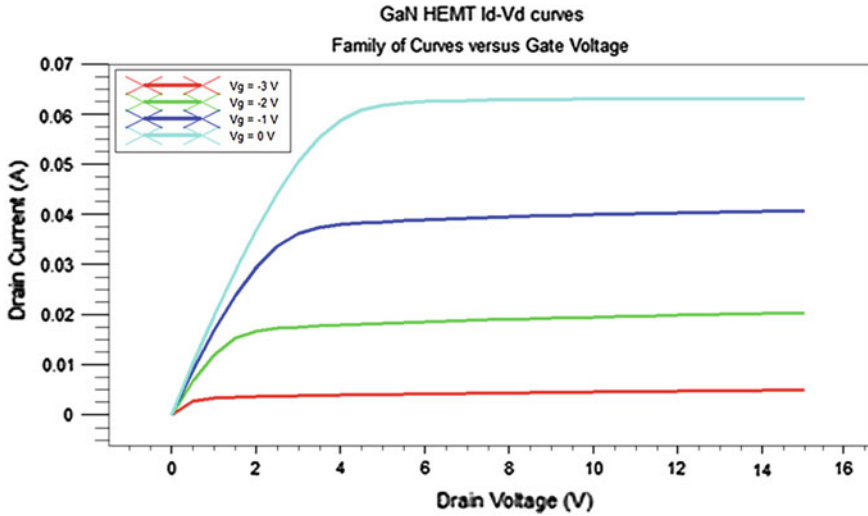
Fig. 18.10 AlGaN/GaN HEMT Id-Vd curves
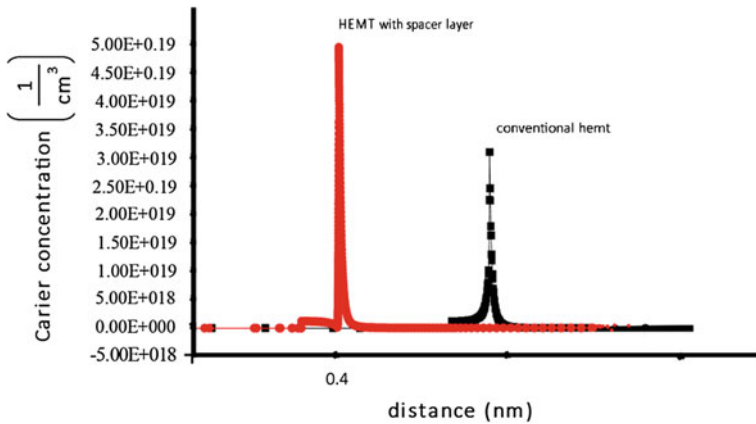
Fig. 18.11 The electron concentration for the device with and without AlN spacer layers

AlN/GaN. This leads to an increase in mobility by 20 %, mainly because of the Coulomb scattering between 2DEG carriers, using very thick spacer layer. AlN spacer thickness being up to 0.5 nm caused Coulomb force between ions and with lattice to have a lower value which reduces the scattering and mobility. By exceeding the thickness beyond 0.5 nm width of quantum well is small enough and coulomb scattering between carriers become dominant (see Fig. 18.11).

The spacer-based AlGaN/AlN/GaN device's exhibit improvement in electrical properties over Al GaN/GaN devices. Adding spacer layer AlN enhances the without degrading the radiation tolerance. For the sample with the 1.2 nm thick
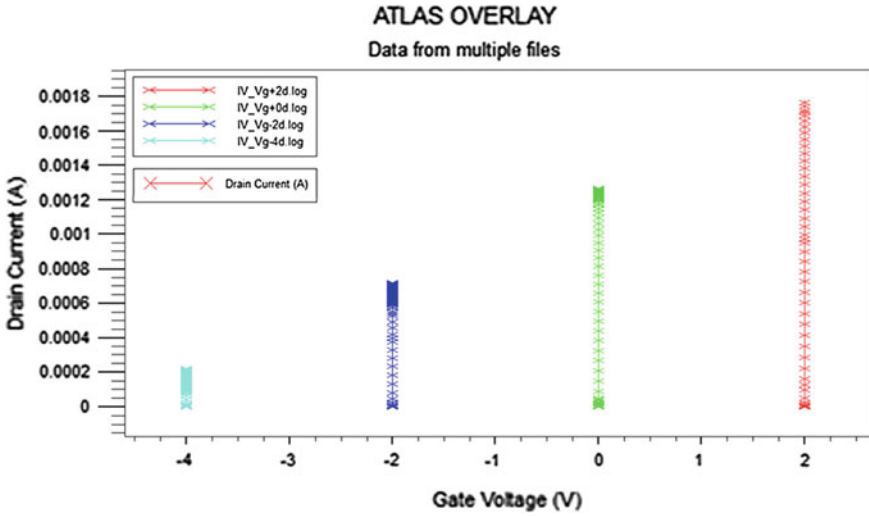
Fig. 18.12 AlGaN/GaN HEMT transconductance
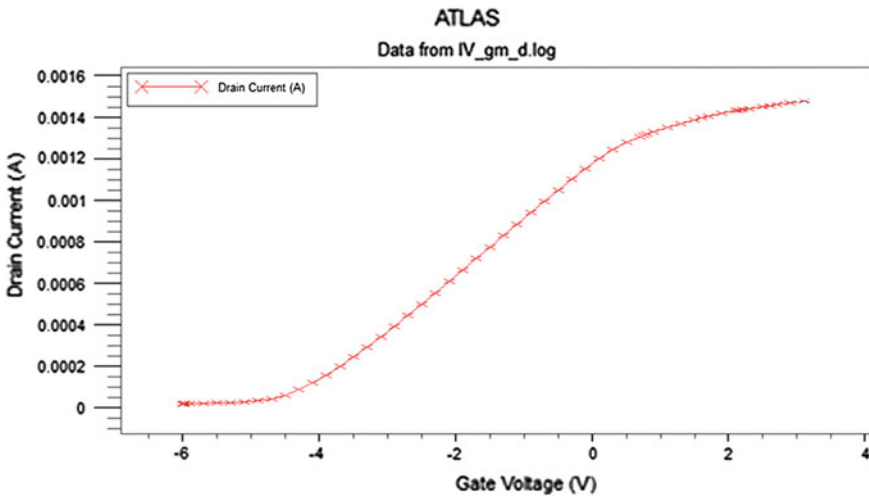
Fig. 18.13 AlGaN/GaN HEMT Id-Vg *curves*

AlN spacer in Al0.185Ga0.815N/AlN/GaN, the highest mobility (1700 cm^2 V$_s$) was observed. Also, 1625 cm^2 V$_s$ was observed for Al0.3Ga0.7N/AlN/GaN with the 1 nm thick AlN spacer Fig. 18.1. This states importance and effectiveness of Al mole fraction in AlGaN barrier. However, when the thickness of the AlN spacer exceeds a critical value, it may cause an increase in dipole scattering due to strong polarization effect (Javorka 2004) and therefore deteriorate 2DEG's mobility. The

AlN spacer enhances the conduction band offset for a thickness below the mentioned critical value. The reduction of penetration of the wave-function into AlGaN barrier effectively, in turn, reduces the effect of alloy disorder scattering. This is consistent with theoretical calculations.

18.4 Conclusions

The effect of AlN spacer layer thickness on the properties of $Al_{0.185}Ga_{0.815}N/AlN/GaN$ and $Al_{0.3}Ga_{0.7}N/AlN/GaN$ heterostructures has been investigated in the present study by employing theoretical methods. The increase in 2DEG Hall mobility in the samples with AlN spacer is assumed to be associated with alloy disorder scattering suppression. This, in turn, is mainly due to a decrease in the penetration of electron wave-function into AlGaN barrier. AlN spacer thicknesses and the percent of the Al in AlGaN layer determine the mobility can cause an increase in the polarization-induced dipole scattering mechanism. Alloy disorder scattering suppression by the AlN spacer layer is strongly dependent on the sharpness of AlN/GaN interfaces.

References

Ambacher O, Foutz B, Smart J, Shealy JR, Weimann NG, Chu K, Murphy M, Sierakowski AJ, Schaff WJ, Eastman LF, Dimitrov R, Mitchell A, Stutzmann M (2000) Two dimensional electron gases induced by spontaneous and piezoelectric polarization in undoped and doped AlGaN/GaN heterostructures. J Appl Phys 87:334–344 (1 Jan 2000)

Chen Tai, Hsu Chih-Wei Jr, Forsberg Urban, Janzén Erik (2015) Metal organic chemical vapor deposition growth of high-mobility AlGaN/AlN/GaN heterostructures on GaN templates and native GaN substrates. J Appl Phys 117(8):085301

Javorka P (2004) Fabrication and characterization of AlGaN/GaN high electron mobility transistors

Kim J, Stokes EB, Hunter GW, Sarkozy S (2010) Wide bandgap Semiconductor materials and devices 11-and-state-of-the-art program on compound semi-conductors, 52(sotapocs52) 28(4)

Pierret RF (1996) Semiconductor device fundamentals. Addison Wesley Long-man, Massachusetts, p 792

Sze SM (1998) Modern semiconductor device physics. Wiley, New York, p 556

Tzeng S (2004) Low-frequency noise sources in III-V semiconductor heterostructures

Chapter 19
Fault Detection, Isolation and Accommodation in Flight Control System of A340-Airbus Aircraft

Guillem Terre Balague and Chingiz Hajiyev

Abstract Optimal linear Kalman filter (OLKF), fault detection, fault isolation, Robust Kalman filter (RKF) and reconfigurable Kalman filter algorithms have been applied on the control system of an Airbus-340 aircraft this study. The discrete flight dynamic model of the Airbus A-340 aircraft is presented and discussed. Sensor faults have been implemented in two scenarios: continuous bias fault and noise increment fault. The fault isolation proposed algorithm involves the computation of the statics which is a rate of sample and theoretical variances. The algorithms for fault-tolerant estimation of aircraft states are discussed. Two types of fault accommodation algorithms: RKF and reconfigurable Kalman filter are investigated. Two different approaches of RKF have been tested applied to the Airbus A-340 aircraft model of dynamics: single measurement noise scale factor (SMNSF) and multiple measurement noise scale factor (MMNSF).

19.1 Introduction

Sensor fault detection and isolation by means of Kalman filtering technique are addressed in several studies. In Hajiyev and Caliskan (2005), the detection and isolation of aircraft sensor and control surfaces failures are approached by using the mean of the Kalman filter innovation sequence. The nonlinear dynamic system of the aircraft is stabilized with a linear quadratic optimal controller, and extended Kalman filter (EKF) and Robust Kalman filter (RKF) are applied. It is concluded

G.T. Balague (✉)
Industrial and Aeronautics Engineering Faculty, Politechnical University of Catalonia, Colom 11, 08222 Terrassa, Spain
e-mail: guillemterre@gmail.com

C. Hajiyev
Aeronautics and Astronautics Faculty, Istanbul Technical University, 34469 Maslak, Istanbul, Turkey
e-mail: cingiz@itu.edu.tr

that EKF does not allow distinguishing whether the failures are of an actuator or sensor, whereas RKF allows doing so.

A fast converging Kalman filter for sensor fault detection and isolation is proposed in Jayaram (2010). Thanks to an innovative initialization of the covariance matrix, and the implementation of an EKF, faults are detected and isolated faster than with classical Kalman Filter schemes. The obtained results are satisfactory.

Wei et al. (2010) study bias and multiplicative faults scenarios with the purpose of detecting and isolating sensor faults for wind turbines. It is concluded that both types of faults can be isolated and detected by implementing the proposed approach.

In Lim and Park (2014), a modified adaptive fading extended Kalman filter (AFEKF) is proposed for sensor fault detection and isolation in a satellite. The detection and isolation scheme are developed in three phases. The proposed scheme classifies fault detection and isolation as well as fault type identification.

In Van Eykeren and Chu (2014), the knowledge of the kinematic relations between the sensed variables is used to add analytical redundancy to the already existing hardware redundancy on modern aircrafts. To do so, a FDI scheme by means of an EKF is applied. Moreover, Jesussek and Ellermann (2013) and Kobayashi and Simon (2007) obtained good results when tackling the sensor fault detection by means of a hybrid Kalman filter. In the first case, the hybrid approach is taken to capture the nonlinear characteristics of desired sensors, whereas in the second the hybrid approach is taken to avoid the effect of the engine degradation over the time is set up. Those approaches do not have much in common with that of this thesis.

Du et al. (2013) address the problem of isolating actuator and sensor faults in nonlinear systems. The proposed method exploits the analytical redundancy in the system through state observers design. The faults are detected if the corresponding residual (computed by means of the proposed method) breaches its threshold. The isolation is performed by using a bank of residuals and a logic rule.

Fault accommodation by means of Kalman filtering technique is also extensively analysed in the literature. The fault detection, isolation and accommodation for attitude control system of a three-axis satellite are investigated in Bolandi et al. (2013). Adaptive thresholds are generated for evaluating residuals and detect the faults. Moreover, an accommodation system is designed based on reconfiguration of available actuators. The obtained results show that attitude control error is kept limited.

Reference Kiyak et al. (2008) proposes an approach to detect, isolate and accommodate the faults of the aircraft sensors and actuators using unknown input observers (UIOs). Sensor and actuator faults are detected using residuals, and fault isolation is done by considering the sensitiveness of the residuals to the other faults. Redundant sensor existence is assumed to perform the sensor accommodation via switching, whereas actuator accommodation is provided by gain scheduling. This technique is applied to a very large, four-engine, cargo jet.

In Hajiyev and Soken (2012), a RKF with filter-gain correlation for cases of measurement malfunction is introduced. The problem is addressed by using

measurement-noise scale factors. RKF algorithms are proposed with single and multiple scale factors for estimating the state vector of an UAV.

The purpose of this study is to investigate sensor fault detection, isolation and accommodation applied to the flight control system of A340 Airbus aircraft. Statistics based on innovation sequence of Kalman filter will be used to detect and isolate the faults. Reconfigurable Kalman filter approach and Robust Kalman filter approach will be investigated for fault accommodation purposes.

19.2 Airbus A-340 Aircraft Model

Airbus A-340 is a four-engine long-range wide-body commercial passenger jet airliner. It is suitable for long-haul trans-oceanic routes. The aircraft mathematical model is a set of parameters inside which the aircraft characteristics (weight, geometry, manoeuvrability, performance, controllability and stability) are represented. The Airbus A-340 aircraft model is as follows (Aykan et al. 2011):

$$x(k+1) = Ax(k) + Bu(k) + Gw(k) \tag{19.1}$$

$$y(k) = H(k)x(k) + v(k) \tag{19.2}$$

where x is the state vector, A is the system matrix, B is the control distribution matrix, G is the process noise transition matrix, $u(k)$ is the control input vector, y the vector of measurements, H is the measurement matrix, $w(k)$ is the process noise and $v(k)$ is the sensor noise.

The aircraft state variables are:

$$\boldsymbol{x}(k) = [v(k)\alpha(k)q(k)\theta(k)\beta(k)p(k)r(k)\varphi(k)(k)]^{\mathrm{T}} \tag{19.3}$$

where v is the forward velocity, α is the angle of attack, q is the pitch rate, θ is the pitch angle, β is the sideslip angle, p is the roll rate, r is the yaw rate, φ is the roll angle and ψ is the yaw angle. The units of the angles ($\alpha, \theta, \beta, \varphi, \psi$) in degrees. The units of the angle rates (q, p, β, r) are $°/s$. Finally, the unit of the forward velocity v is km/s.

The control input vector is:

$$u(k) = [\delta_{\mathrm{H}}(k)\delta_{\mathrm{E}}(k)\delta_{\mathrm{F}}(k)\delta_{\mathrm{A}}(k)\delta_{\mathrm{R}}(k)] \tag{19.4}$$

where δ_{H}, δ_{E}, δ_{F}, δ_{A} and δ_{R} are the deflections of stabilizer, elevator, flap, aileron and rudder, respectively.

The following mechanical limits may be taken on the deflections of the A340 control surfaces: $-0.26 \leq \delta_{\mathrm{H}} \leq 0.04$; $-0.54 \leq \delta_{\mathrm{E}} \leq 0.26$; $0.02 \leq \delta_{\mathrm{F}} \leq 0.44$; $\delta_{\mathrm{A}} \geq 0$; $-0.54 \leq \delta_{\mathrm{R}} \leq 0.54$. The units are radians.

$$A = \begin{bmatrix} 1.0004 & -0.0013 & 0.0008 & 0.0001 & -0.4597 & -0.1378 & -0.0004 & -0.9558 & 0 \\ 0 & 0.8095 & 0 & 0.438 & 0 & -19.5423 & 0.894 & 0.0003 & 0 \\ -0.0035 & 0.0001 & 0.98 & 0.1421 & 20.2723 & 0.0009 & 0.0164 & -0.0163 & 0 \\ 0 & 0.0008 & 0 & 0.9612 & 0 & 0.0066 & 0.0004 & 0 & 0 \\ 0 & 0 & 0 & 0 & 0 & 0.9723 & 0 & 0 & 0 \\ 0 & 0.0174 & 0 & 0.0012 & 0 & 0.8061 & 0.0086 & 0 & 0 \\ 0 & 0 & 0 & 0.0294 & 0 & 0.0007 & 1 & 0 & 0 \\ 0 & 0 & 0 & 0 & 0.0296 & 0.0005 & 0 & 1 & 0 \\ 0 & 0.0003 & 0 & 0 & 0.0005 & 0.028 & 0.0001 & 0 & 1 \end{bmatrix}$$

$$(19.5)$$

$$B = \begin{bmatrix} -0.0337 & -0.0144 & 0 & 0 & 0.0007 \\ 0 & 0 & 0 & 0.201 & 0.4502 \\ -3.5858 & -0.9127 & 0 & 0.0051 & 0.0004 \\ 0 & 0 & 0 & 0.0701 & 0.0054 \\ -0.1335 & -0.0367 & 0 & 0 & 0 \\ 0 & 0 & 0 & -0.0004 & -0.0081 \\ 0 & 0 & 0 & 0.0011 & 0.0001 \\ -0.002 & -0.0006 & 0 & 0 & 0 \\ 0 & 0 & 0 & 0 & -0.0001 \end{bmatrix}$$

$$(19.6)$$

To avoid aircraft model being unstable, a linear quadratic controller is added to the aircraft dynamic model.

19.3 Kalman Filter Algorithms

Mathematically, the Kalman filter is a system of first order ordinary differential equations with quadratic nonlinearity which are solved on digital computers. Kalman filter algorithms, or one of the many extensions and variations of them, have been applied in numerous practical situations, including navigation, space guidance and orbit determination. The optimal linear Kalman filter (OLKF) is the Kalman filter applied to linear systems, and its main purpose is to find the value of the state vector according to the sequence of the $y(k)$ measurements vectors. The equations of the OLKF algorithm are:

$$\hat{x}(k/k-1) = A(k, k-1)\hat{x}(k-1/k-1) \\ + B(k-1)u(k-1)$$

$$(19.7)$$

$$P(k/k-1) = A(k, k-1)P(k-1/k-1)A^{\mathrm{T}}(k, k-1) \\ + B(k-1)DuB(k-1)^{\mathrm{T}}G(k-1) + G(k, k-1)Q(k-1)G^{\mathrm{T}}(k, k-1)$$

$$(19.8)$$

$$K(k) = P(k/k - 1)H^{\mathrm{T}}(k)$$
$$\times \left[H(k)P(k/k - 1)H^{\mathrm{T}} + R(k)\right]^{-1} \tag{19.9}$$

$$\hat{x}(k/k) = \hat{x}(k/k - 1) + K(k)$$
$$x[y(k) - H(k)\hat{x}(k/k - 1)] \tag{19.10}$$

$$P(k/k) = P(k/k - 1) - K(k)H(k)P(k/k - 1) \tag{19.11}$$

The index $k/k - 1$ denotes one step predicted values, whereas index k/k denotes the estimate at time k using all measurements including $y(k)$. $\hat{x}(k - 1/k - 1)$ is $\hat{x}$ for the first estimation and $\hat{x}(k/k - 1)$ is the extrapolation variable. $K(k)$ is the gain matrix of the filter, $P(k/k - 1)$ is the correlation matrix of the extrapolation error, $P(k/k)$ is the correlation matrix of the estimation error. The innovation sequence is the difference between the actual system output and the predicted output based on the predicted state. The innovation sequence of Kalman filter is defined as:

$$\Delta(k) = [y(k) - H(k)\hat{x}(k/k - 1)] \tag{19.12}$$

The normalized innovation sequence is defined as:

$$\tilde{\Delta}(k) = [H(k)P(k/k - 1)H^T(k) + R(k)]^{-1/2}\Delta(k) \tag{19.13}$$

It is appropriate to use normalized innovation sequence to detect the faults (Hajiyev and Caliskan 2003). The faults, which change the system dynamic, also change the characteristic of $\tilde{\Delta}(k)$ sequence and make it different from white noise. The faults shift the average of $\tilde{\Delta}(k)$ sequence, which is also zero and changes its unit covariance matrix.

19.4 Fault-Tolerant Estimation of Aircraft States

Fault-tolerant estimation of aircraft states comprises all the techniques that have as its main goal to allow the control system to deal with possible errors. After a sensor fault is produced, several actions may be carried out to ensure that the system keeps estimating the state parameters: first of all, the fault must be detected. Moreover, the faulty sensor may be identified. This process is called fault isolation. Furthermore, if a sensor fault is detected and isolated, the system is able to adapt to that scenario and correct itself the faulty measurement that is receiving, by means of the RKF approach. Finally, another option to deal with a sensor fault is to discard completely the measurements from the faulty sensor and estimating the corresponding state parameter without any measurement input, which can be done by using the reconfigurable Kalman filter technique.

19.4.1 Fault Detection

Using innovation approach is suitable for detecting sensor faults (Caliskan and Hajiyev 2014). Let us consider the following two hypotheses: H_0: the system operates normally; H_1: sensor fault occurs.

To detect failures changing the mean of the innovation sequence $y_k - H\hat{x}_{k/k-1}$, the following statistical function can be used.

$$\beta(k) = \sum_{j=k-M+1}^{k} \tilde{\Delta}^T(j)\tilde{\Delta}(j) \tag{19.14}$$

where M is the width of the sliding window. This statistical function has χ^2 distribution. If the level of significance, α, is selected as,

$$P\left\{\chi^2 > \chi^2_{\alpha,Ms}\right\} = \alpha; \quad 0 < \alpha < 1 \tag{19.15}$$

where s is the dimension of the innovation vector, the threshold value, $\chi^2_{\alpha,Ms}$ can be found. Hence, when the hypothesis H_1 is true, the statistical value of the function β_k will be greater than the threshold value from $\chi^2_{\alpha,Ms}$.

19.4.2 Sensor Fault Isolation Algorithm

Once a fault is detected, the next thing one may need is to determine which sensor is the faulty one. That is the purpose of the fault detection algorithms. Sensor fault isolation algorithm is based on the rate of sample and theoretical innovation variances.

Let the statistics, which is a rate of sample and theoretical variances, $\hat{\sigma}_i^2/\sigma_i^2$ be used to verify the variances of one dimensional innovation sequences $\tilde{\Delta}_i(k), i = 1, 2, \ldots, s$. When $\tilde{\Delta}_i \sim N(0, \sigma_i)$ it is known that,

$$\frac{v_i}{\sigma_i^2} \sim \chi^2_{\beta,M-1} \quad \forall i, \quad i = 1, 2, \ldots, s \tag{19.16}$$

where $v_i = (M-1)\hat{\sigma}_i^2$. As $\sigma_i^2 = 1$ for normalized innovation sequence, it follows that:

$$v_i \sim \chi^2_{\beta,M-1}, \quad \forall i, \quad i = 1, 2, \ldots, s \tag{19.17}$$

According to the theory in Hajiyev and Caliskan (2005), the statics of the faulty sensor is assumed to be affected much more than those of the other sensors. When a fault affecting the variance of the innovation sequence occurs in the system, the

related statistic v_i exceeds the threshold value $\chi^2_{\beta,M-1}$ depending on the confidence probability β, and degree of freedom $(M - 1)$ (Hajiyev and Caliskan 2005).

v_i is the i diagonal element of the $S*(k) = (M - 1)\ S_{\tilde{\Delta}}(k)$ matrix, which is defined below

$$\bar{\tilde{\Delta}}(k) = \frac{1}{M} \sum_{j=k-M+1}^{k} \tilde{\Delta}(j) \tag{19.18}$$

$$S_{\tilde{\Delta}}(k) = \frac{1}{M-1} \sum_{j=k-M+1}^{k} \left[\tilde{\Delta}(j) - \bar{\tilde{\Delta}}(k)\right]\left[\tilde{\Delta}(j) - \bar{\tilde{\Delta}}(k)\right]^{\mathrm{T}} \tag{19.19}$$

$$S^*(k) = \sum_{j=k-M+1}^{k} \left[\tilde{\Delta}(j) - \bar{\tilde{\Delta}}(k)\right]\left[\tilde{\Delta}(j) - \bar{\tilde{\Delta}}(k)\right]^{\mathrm{T}} \tag{19.20}$$

Here M denotes the size of the moving window, $\tilde{\Delta}(k)$ is the normalized innovation at iteration k, and $\bar{\tilde{\Delta}}(k)(k)$ is the mean normalized innovation, averaged over the last M iterations. $S_{\tilde{\Delta}}$ is the selection covariance matrix. The dimensions of $S(k)*$ are $s \times s$, where s is the dimension of the innovation vector. In the case of A340 dynamic model, there are nine innovation parameters and therefore the dimension of $S*(k)$ is (9×9).

The decision-making process is the following:

$$\text{if} \quad S(k)^*_{z,z} > X^2_{\alpha,Ms} \rightarrow z\text{th sensor is faulty} \quad z = 1, 2, \ldots, 9 \tag{19.21}$$

In each iteration, the nine diagonal elements are compared with $X^2_{\alpha,Ms}$. If $S*(k)_{z,z}$ exceeds $X^2_{\alpha,Ms}$, the zth sensor is judged as faulty in the kth iteration. Like this, one can identify the faulty sensor, and therefore fault isolation is possible.

19.4.3 Robust Kalman Filter

With a scheme, one can determine if the system is faulty, and with a fault isolation scheme, one can determine which sensor is faulty. Nevertheless, with both of these schemes the estimation that provides the filter is not accurate because of the faults, and nothing is done to solve that. Fault accommodation is an approach that goes further than fault detection and fault isolation.

RKF is the fault accommodation approach used for the investigations. The principle of the RKF is the comparison of real and theoretical values of the covariance of the innovation sequence (Hajiyev 2007). An RKF algorithm brings the fault tolerance to the filter and secures accurate estimation results in cases of

faulty measurements without affecting the remaining good estimation characteristics. That is done by reducing the weight of the faulty channels in the final estimation. The KF gain is updated according to the differentiation in the covariance matrix of the innovation sequence when the operational condition of the measurement system mismatches the models used in the synthesis of the filter.

19.4.3.1 RKF with SMNSF

In the case of a fault in the measurement system, the adaptation of KF is performed by automatically increasing S_k to reduce the Kalman gain K_k (Hajiyev and Soken 2012). Specifically, the Kalman gain is re-evaluated when the prediction of the measurement $[(H(k)\hat{x}(k/k-1)]$ is considerably different from the actual measurement $y(k)$. In this situation the Kalman gain becomes:

$$K(k) = P(k/k-1)H^{\mathrm{T}}(k)x\big[H(k)P(k/k-1)H^{\mathrm{T}} + S(k)R(k)\big]^{-1} \qquad (19.22)$$

where S_k is the single measurement-noise scale factor (SMNSF). S_k is obtained from the expression below:

$$S(k) = \frac{\Delta^{\mathrm{T}}(k)\Delta(k) - \mathrm{tr}\Big\{H(k)P(k/k-1)H(k)^{\mathrm{T}}\Big\}}{\mathrm{tr}\{R(k)\}} \qquad (19.23)$$

To detect failures, the statistical function named quadratic innovation function is defined as

$$\beta^*(k) = \Delta(k)^{\mathrm{T}}[H(k)P(k/k-1)H(k)^{\mathrm{T}} + R(k)]^{-1}\Delta(k) \qquad (19.24)$$

This statistical function has X^2 distribution with s degrees of freedom, in which s is the dimension of the innovation vector. If the level of significance, α, is selected as:

$$P\Big\{X^2 > X^2_{\alpha,s}\Big\} = \alpha; \quad 0 < \alpha < 1 \qquad (19.25)$$

Then the threshold value, $X^2_{\alpha,s}$, can be determined. Hence, when the hypotheses H_1 is correct, the value of $\beta(k)$ will be greater than the threshold value, $X^2_{\alpha,s}$. In example:

$$H_1: \beta^*(k) \le X^2_{\alpha,s} \; \forall k \quad H_0: \beta^*(k) > X^2_{\alpha,s} \; \exists k \qquad (19.26)$$

Therefore, the adaptive algorithm is operated only when the measurements are faulty, in all other cases the procedure runs optimally with a regular OLKF.

19.4.3.2 RKF with MMNSF

The RKF with SMNSF algorithm may not be the best option for complex multi-variable systems, as the filter performance differs a lot for each state depending on if the state is faulty or not. In other words, when SMNSF is operated, all the states are affected, including those who are not faulty. With the multiple measurement-noise scale factor (MMNSF) approach, the goal is to fix only the relevant terms of the measurement noise-covariance and consequently, the Kalman gain.

RKF with the MMNSF approach, the goal is to fix only the relevant terms of the measurement noise-covariance and consequently, the Kalman gain. The MMNSF S_k can be determined via the formula (Hajiyev and Soken 2012):

$$S(k) = \left(\frac{1}{\mu} \sum_{j=k-\mu+1}^{k} \Delta(k)\Delta(k)^{\mathrm{T}} - H(k)P(k/k-1)H(k)^{\mathrm{T}} \right) R(k)^{-1} \qquad (19.27)$$

Here μ denotes the width of the moving window. In this case, instead of using the scale factor $S(k)$, a matrix $S^*(k)$ has been used. To compose the scale matrix S_k^*, using the following rule is suggested in Hajiyev and Soken (2012):

$$S^* = \mathrm{diag}\left(s_1^*, s_2^*, \ldots, s_n^* \right)$$

in which

$$s_i^* = \max\{1, S_{ii}\} \quad i = 1, n$$

Here S_{ii} represents the ith diagonal element of the matrix S_k.

At that point, the re-evaluation of the Kalman gain should be performed according to equation:

$$K(k) = P(k/k-1)H^{\mathrm{T}}(k)\left[H(k)P(k/k-1)H^{\mathrm{T}} + S^*(k)R(k) \right]^{-1} \qquad (19.28)$$

In the case of any kind of malfunction, the related element of the scale matrix increases. This brings out a smaller Kalman gain, which reduces the effect of the innovation on the state estimation process. As a result, more accurate estimation results are obtained. A MMNSF is more selective than SMNSF, given the fact that only the diagonal elements belonging to the faulty states are modified.

19.4.4 Reconfigurable Kalman Filter

The last analysed fault-tolerant approach is the reconfigurable Kalman filter. A reconfigurable Kalman filter is an active fault-tolerant control system which main idea is the following: In a reconfigurable control system, the faulty measurement

channel can be disabled and its data may no longer be used by the filter algorithm. In that case, the filter should estimate N states but incoming data from only $N - 1$ measurement channels. For the simulations carried out in this study, a simplest scenario, which is also useful to investigate the reconfigurable Kalman filter, has been implemented. From the first step of the algorithm, the measurement channel is removed from the algorithm. That way, during the whole simulation the algorithm is estimating N states with only $N - 1$ measurement channels.

Modifications have to be implemented in the OLKFL algorithm to investigate the reconfigurable technique. If one channel is disabled, that means that the row corresponding to the faulty channel has to be removed from the $H(k)$ $s \times n$ dimensional measurement matrix of the system. Hence, the new dimensions of $H(k)$ are $(s - 1) \times n$. Moreover, the component corresponding to the faulty state has to be removed from the $v(k)$ s-dimensional measurement noise vector. $v(k)$ becomes then $(s - 1)$-dimensional. As a consequence of these changes, the normalized innovation also changes its dimensions from 9 to 8 elements.

19.5 Simulations Results

Simulations have been done with 1000 iterations for a hypothetical period of 100 s. In each scenario, the fault is assumed to occur between $t = 30$ s and $t = 40$ s.

19.5.1 Fault Detection Algorithm Results

The techniques for fault detection, isolation and accommodation discussed above have been applied to the stabilized A-340 aircraft model. The simulations are carried during 1000 steps. In all the simulations, $s = 9$ and the reliability parameter $\alpha = 0.95$ is taken. For fault detection simulations, $M = 20$, and therefore the threshold value $X^2_{\alpha,Ms}$ is found as 212. A continuous bias fault (Fig. 19.1) and noise increment fault (Fig. 19.2) in the pitch rate gyroscope channel (third measurement channel) are introduced separately from the iteration 300 to 400.

As seen from Figs. 19.1 and 19.2, the introduced faults are detected immediately.

19.5.2 Sensor Fault Isolation Algorithm Results

Simulation results for the fault isolation based on rate of sample and theoretical innovation variances are shown in Fig. 19.3. For the noise increment case, when a
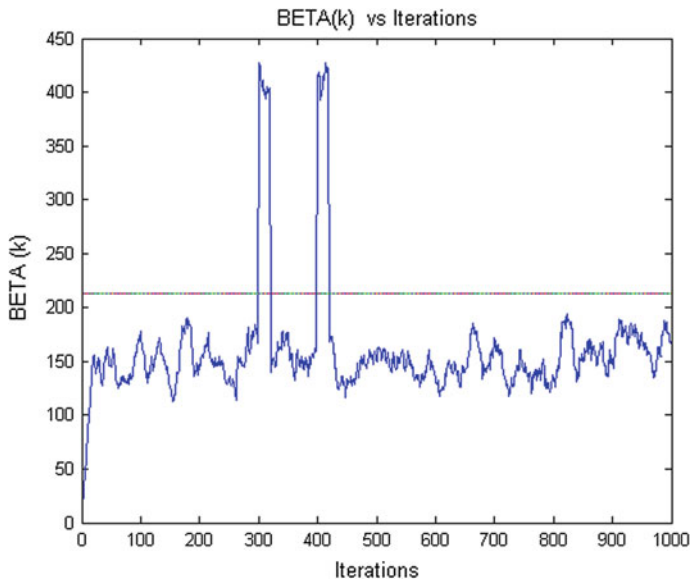
Fig. 19.1 $\beta(k)$ evolution for the case of continuous bias fault at q measurements
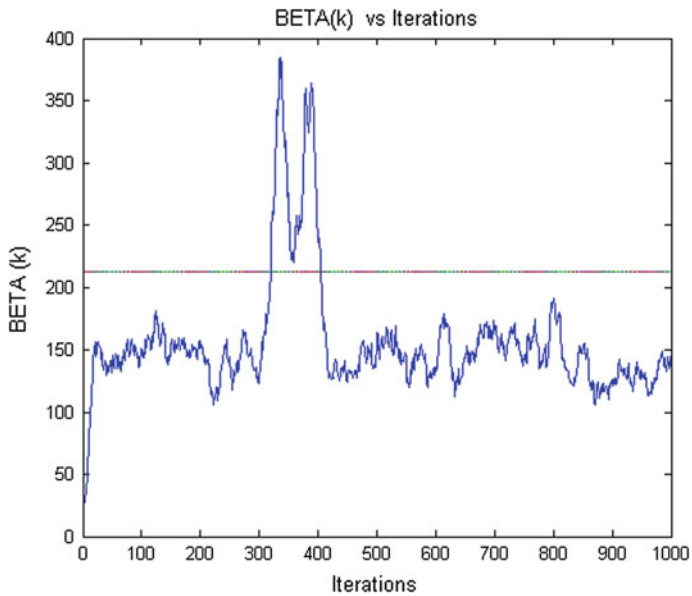
Fig. 19.2 $\beta(k)$ evolution for the case of noise increment fault at q measurements
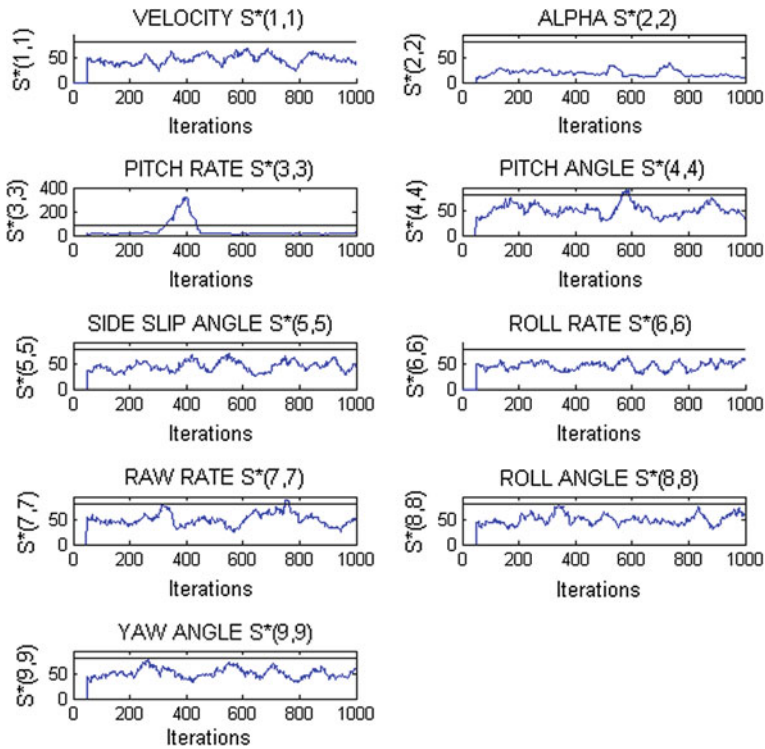
Fig. 19.3 Sensor fault isolation with noise increment at q measurements

fault in the pitch rate gyro occurs, only the appropriate v_i exceeds the threshold (see Fig. 19.3).

19.5.3 RKF Algorithm Results

19.5.3.1 RKF with SMNSF

The simulations of RKF have been carried out only with measurement noise increment faults. As it can be seen in Fig. 19.4, RKF with SMNSF algorithm allows smoothing the estimated value and making it closer to the real value.

19.5.3.2 RKF with MMNSF

Figure 19.5 shows that MMNSF approach allows to obtain estimation values with fewer oscillations than the measurements, and closer to the real value. By
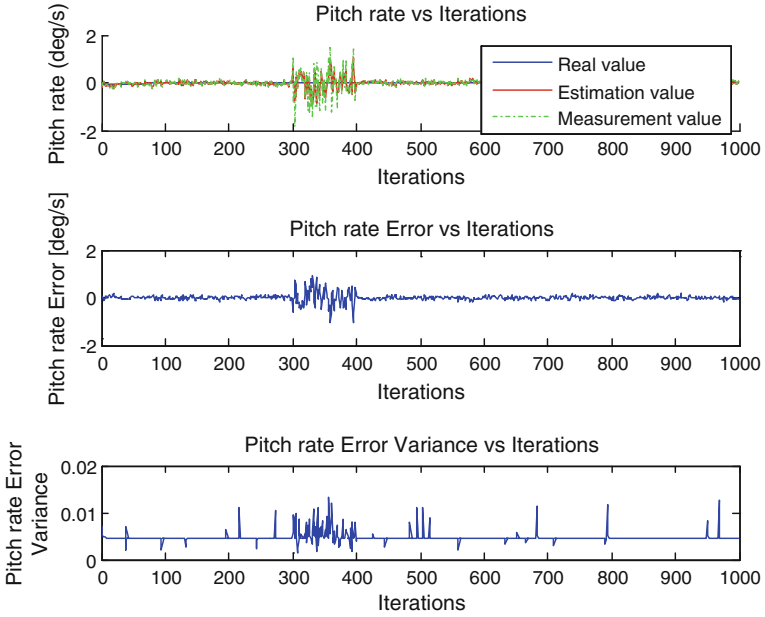
Fig. 19.4 Pitch rate estimation, error and error variance with SMNSF implemented
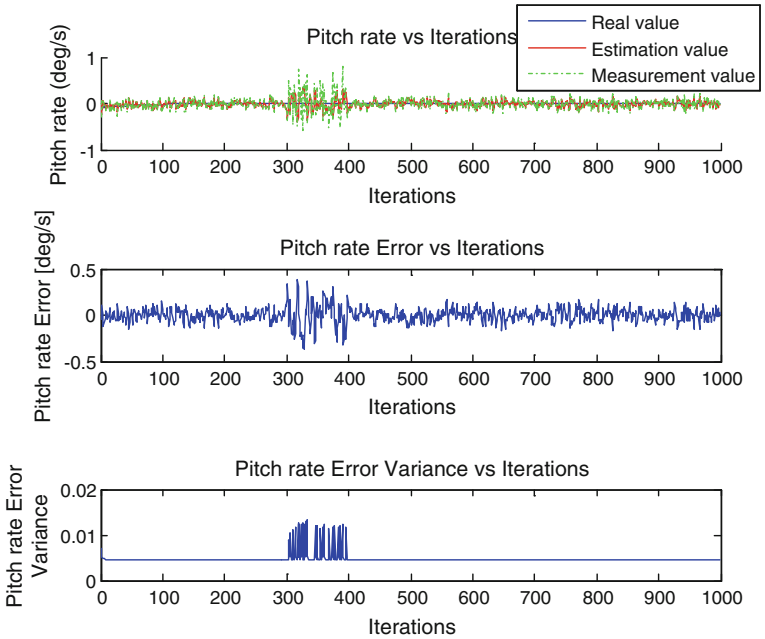
Fig. 19.5 Pitch rate estimation, error and error variance with MMNSF implemented

comparing the performance of RKF with SMNSF and RKF with MMNSF in the case of measurement-noise increment errors, it can be concluded that the RKF with MMNSF obtains slightly better results, with less oscillations and the estimations closer to the real values.

19.5.3.3   Reconfigurable KF

The technique has been implemented for the cases of 1 state parameter faulty (pitch rate, q) and two state parameters faulty (pitch rate q and roll angle φ). It is assumed that the fault occurs since the first iterations and therefore faulty channels are disabled during the whole simulations. Figure below contains the real, estimated and measured value evolution of the pitch rate, as well as its error and variance, for the case of only one parameter disabled.

As it can be seen in Fig. 19.6, the reconfigurable Kalman filter with one parameter disabled allows estimating with an insignificant error the value of the pitch rate, without any input measurement data. The main parameters to judge the performance of the estimation are: the velocity of the convergence, the evolution of the error absolute value and the error variance with the number of iterations, and the absolute value of the stationary error. In Fig. 19.6 it is seen that it is not until iteration 100 that the estimation achieves the stationary value. The first 100
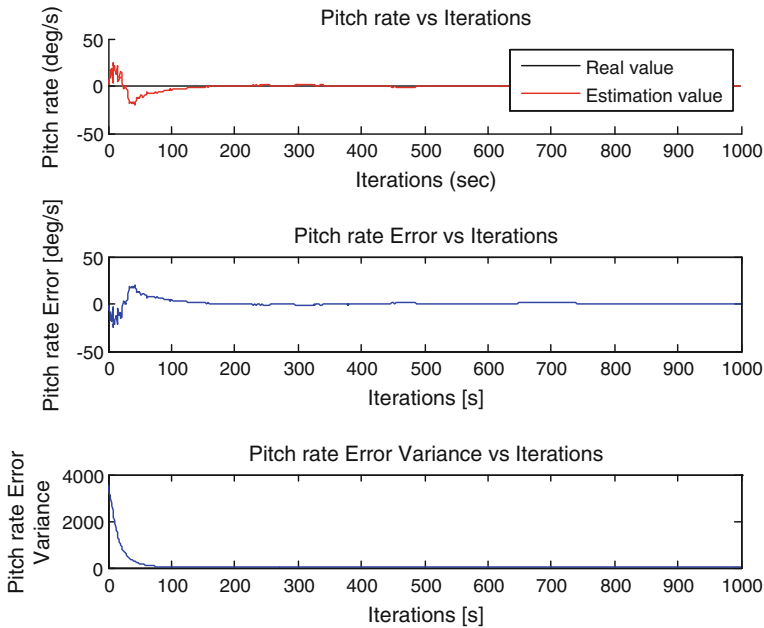
Fig. 19.6 Pitch rate evolution, error and error variance in reconfigurable Kalman filter (1 parameter faulty)
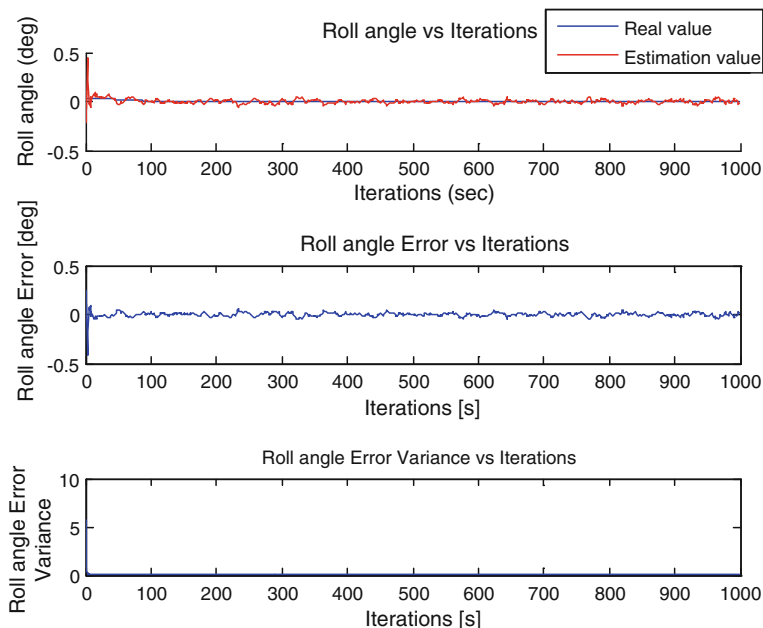
Fig. 19.7 Roll angle evolution, error and error variance in reconfigurable Kalman filter (2 parameters faulty)

iterations constitute a transitory state where fluctuations of the estimated value occur until the stationary value is achieved. The evolution of the absolute value of the error, which is defined as the difference between the real value and the estimated value, is consequent with this behaviour. The error variance is very large during the initial iterations (values over 3000), but it decreases and after iteration 100 it takes very small values.

Two state parameters faulty case (pitch rate q and roll angle φ) simulation results are shown in Fig. 19.7.

As seen from presented results, the reconfigurable Kalman filter gives sufficiently good results for the case of two faulty parameters.

19.6 Conclusions

Optimal linear Kalman filter, fault detection, fault isolation, Robust Kalman filter and reconfigurable Kalman filter algorithms have been applied on the control system of an Airbus-340 aircraft. The fault detection proposed algorithm allows to properly detect the faults in both bias and measurement-noise increment fault scenarios. Regarding the fault isolation proposed algorithm, the main conclusions to be drawn are that smaller moving window provides faster detections, but with

highest possibilities of false alarms. The RKF technique simulations show that SMNSF and MMNSF allow improving the estimation in the case of measurement-noise increment faults. MMNSF is slightly better, reducing more the oscillations of the estimation and getting it closer to the real value. Finally, from the reconfigurable Kalman filter analysis it can be concluded that no significant differences in the performance of the pitch rate estimation arise between when it is the only parameter missing and when also the roll rate must be estimated. The only difference is that the error variance is larger and converges slower in the case of two parameters missing.

Globally, the simulation results show that the fault detection, isolation and accommodation algorithms operate properly and can be used in Airbus A340 flight control system.

References

Bolandi H, Abedi M, Haghaparast M (2013) Fault detection, isolation and accommodation for attitude control system of a three-axis satellite using interval linear parametric varying observers and fault tree analysis. Proc Inst Mech Eng Part G: J Aerosp Eng 228 (8):1403–1424

Du M, Scott J, Mhaskar P (2013) Actuator and sensor fault isolation of nonlinear process systems. Chem Eng Sci 104:294–303

Hajiyev C, Caliksan F (2003) Fault diagnosis and reconfiguration in flight control systems. Kluwer Academic Publishers, Springer Science+Business Media. ISBN 978-1-4613-4818-4

Hajiyev C, Caliksan F (2005) Sensor and control surface/actuator failure detection and isolation applied to F-16 flight dynamic. Aircr Eng Aerosp Technol 7 (2):152–160

Hajiyev C, Soken HE (2012) Robust estimation of UAV dynamics in the presence of measurement faults. J Aerosp Eng 25(1):80–89

Jayram S (2010) A new fast converging Kalman filter for sensor fault detection and isolation. Sens Rev 30(3):219–224

Jesussek M, Ellerman K (2013) Fault detection and isolation for a nonlinear railway vehicle suspension with a Hybrid Extended Kalman filter. Veh Syst Dyn 51(10):1489–1501

Kiyak E, Çetin Ö, Kahvecioğlu A (2008) Aircraft sensor fault detection based on unknown input observers. Aircr Eng Aerosp Technol 80(5):545–548

Kobayashi S, Simon D (2007) Hybrid Kalman filter approach for aircraft engine in-flight diagnostics: sensor fault detection case. J Eng Gas Turbines Power 129(3):746–754

Lim JK, Park C (2014) Satellite fault detection and isolation scheme with modified adaptive fading EKF. J Electr Eng Technol 9 (4):1401–1410

Van Eykeren L, Chu QP (2014) Sensor fault detection and isolation for aircraft control systems by kinematic relations. Control Eng Pract 31:200–210

Wei X, Verhaegen M, Engelen TV (2010) Sensor fault detection and isolation for wind turbines based on subspace identification and Kalman filter techniques. Int J Adapt Control Signal Process 4(8):687–707

Chapter 20
Mathematical Modelling of a Tilt-Rotor by an Integral Method and CFX Modelling by ANSYS Fluent

Ilham Chaybi

Abstract In order to calculate the aerodynamic forces of a tilt-rotor, a calculation of the velocity induced was important. For this, the integral method is used for solving the Laplace equation, and discretization is used to find the velocity induced in all point of the blade surface and wake surface.

Notations

φ	Le Potentiel de Vitesse
$\vec{U}_i$	La vitesse induite
n	Le vecteur normal
ϑ	La vitesse de la surface
S_∞	La surface su sphère
S_W	Le sillage
S_B	La surface de la pale

20.1 Introduction

The term "tilt-rotor" indicates an aircraft provided with tip-up rotors, which so combines the vertical ascent of a helicopter at the speed of cruise and in the payload of a plane. It is one of types of plane with take-off and vertical landing.

Thus, in the conception of a convertible plane, the rotor is certainly one of the most essential elements.

That led us to focus on the rotor and make an aerodynamic complete study.

I. Chaybi (✉)
Research and Development Team: Mechanical Modelling and Multimedia,
Mohammadia School of Engineers, Rabat, Morocco
e-mail: Ilham.chaybi@gmail.com

20.2 Theoretical Background

20.2.1 Choice of Coordinates

Primarily, a Cartesian coordinate system will be used

$(O_0X_0Y_0Z_0)$ is taken as absolute system
$(OXYZ)$ is the reference linked to the rotor
$(O_0X_0Y_0Z_0)$ is the reference linked to the blade.

The fluid around the blade is an incompressible and irrotational fluid, we can then represent the velocity induced U_i by a scalar function called "potential φ

$$\vec{U}_i = \mathrm{grad}\varphi \qquad (20.1)$$

The Laplace equation is written as:

$$\Delta\varphi = 0 \qquad (20.2)$$

20.2.2 Boundary Condition

The first boundary condition is:

$$(\nabla\varphi + \vartheta) \cdot n = 0 \qquad (20.3)$$

$(-\vartheta)$: The surface velocity
$n = n(X_0, Y_0, Z_0, t)$: The normal vector.

The second boundary condition is

$$\lim_{|R_0 - R_1| \to \infty} \nabla\varphi = 0 \qquad (20.4)$$

$R_0 = (X_0, Y_0, Z_0)$ when $t = 0$
$R_1 = (X_1, Y_1, Z_1)$ when $t > 0$.

20.3 Resolution Method

The solution of Eq. (20.2) is given by Green identity
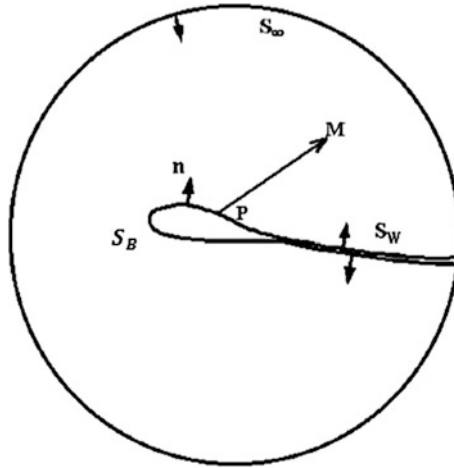
Fig. 20.1 Sketch of the integration surface

$$\varphi(M) = \frac{-1}{4\pi} \iint_S \frac{n.\mathrm{grad}\varphi}{r} \, ds + \frac{1}{4\pi} \iint_S \frac{\varphi n.r}{r^3} \, ds \tag{20.5}$$

For the blade of a Tilt-rotor, the surface S is the sphere surface S_∞.
The wake is represented by S_W.
The blade's surface is represented by S_B (Fig. 20.1).
Equation (20.5) becomes

$$\varphi(M) = \frac{1}{4\pi} \iint_{S_B} \frac{\varphi n.r}{r^3} \, ds + \frac{1}{4\pi} \iint_{S_W} \frac{[\varphi]n.r}{r^3} \, ds - \frac{1}{4\pi} \iint_{S_B} \frac{n.V_s}{r^3} \, ds \tag{20.6}$$

Induced velocity given by the source/doublet combination is

$$\nabla \varphi = \frac{1}{4\pi} \int_{S+w} \mu \nabla \left[\frac{\partial}{\partial n} \left(\frac{1}{r} \right) \right] ds - \frac{1}{4\pi} \int_S \sigma \nabla \left(\frac{1}{r} \right) ds \tag{20.7}$$

To establish the shape of the Neumann local velocity of each point must satisfy the zero-flow condition.
The final form of the integral equation is

$$\left\{ \frac{1}{4\pi} \int_{S+w} \mu \nabla \left[\frac{\partial}{\partial n} \left(\frac{1}{r} \right) \right] ds - \frac{1}{4\pi} \int_S \sigma \nabla \left(\frac{1}{r} \right) ds - V_0 - V_{\mathrm{rel}} - \Omega \wedge r \right\} \cdot n = 0 \tag{20.8}$$

20.4 Application to the Tilt-Rotor

We consider the rotation of the tilt-rotor's blade.
We have

$$V_0 = (0, 0, 0)$$
$$\Omega \wedge r = \left(-\dot{\Psi} y \quad \dot{\Psi} x - \dot{\varnothing} z \quad \dot{\varnothing} z \right)$$
$$n = (\sin \propto, 0, \cos \propto)$$

We replace in this equation

$$(\nabla \varphi - V_0 - \Omega \wedge r) \cdot n = 0 \tag{20.9}$$

We have

$$\frac{\partial \varphi}{\partial z} = - \left(\frac{\partial \varphi}{\partial y} + \dot{\Psi} y \right) \tan \propto - \dot{\varnothing} y \tag{20.10}$$

To solve this equation we will discretize surface S_W and surface S_B to many facets.

20.5 Discretization

At the end of the discretization we get (Fig. 20.2).

Fig. 20.2 Sketch of blade's discretization
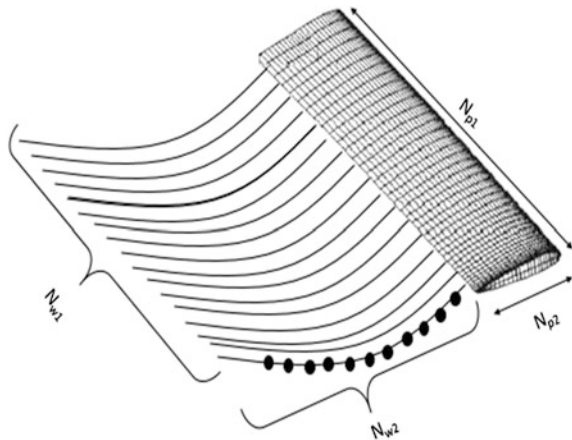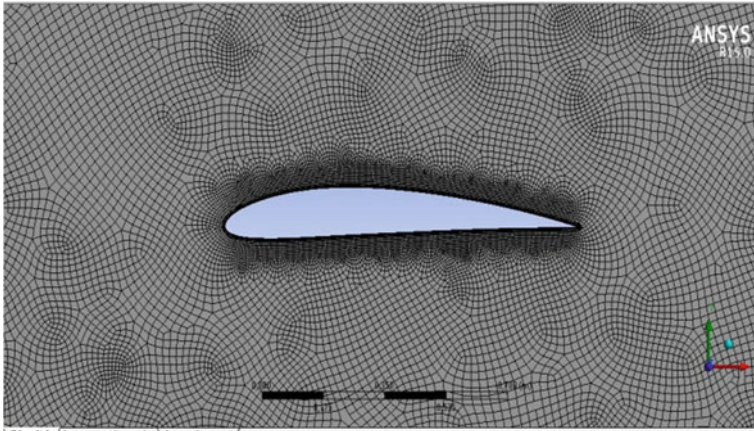
Fig. 20.3 Mesh of NACA 4412

$$4\pi\varphi = \sum_{i=1}^{N_{p1}} \sum_{j=1}^{N_{p2}} \varphi_{(i,j)} \cdot A_{(i,j)}$$

$$+ \sum_{i=1}^{N_{w1}} \sum_{j=1}^{N_{w2}} \varphi_{(i,j)} \cdot B_{(i,j)} - \sum_{i=1}^{N_{p1}} \sum_{j=1}^{N_{p2}} C_{(i,j)} \qquad (20.11)$$

20.6 Resolution CFX

The mesh of a NACA profile was done by ANSYS (Fig. 20.3).

20.7 Results

See Figs. 20.4, 20.5, 20.6, 20.7, 20.8 and 20.9.

20.8 Discussion

The velocity in the upper surface (extrados) is more than the lower surface (intrados).

The pressure is maximal at the leading edge.
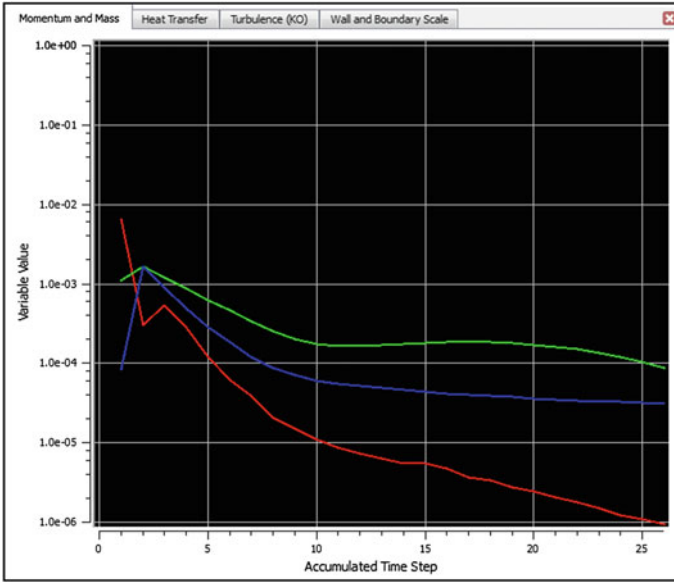
Fig. 20.4 Momentum and mass
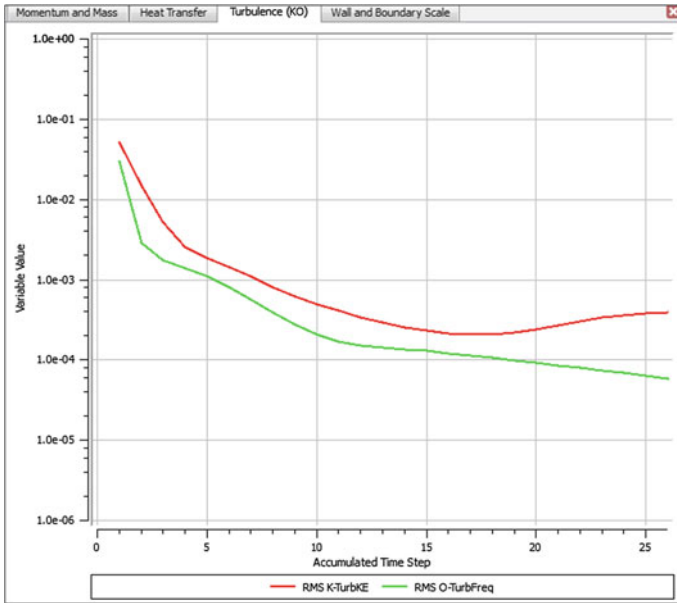
Fig. 20.5 Turbulence
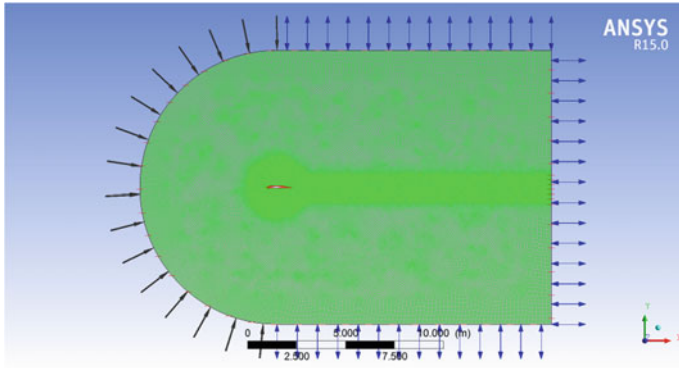
Fig. 20.6 Forces applied to boundary
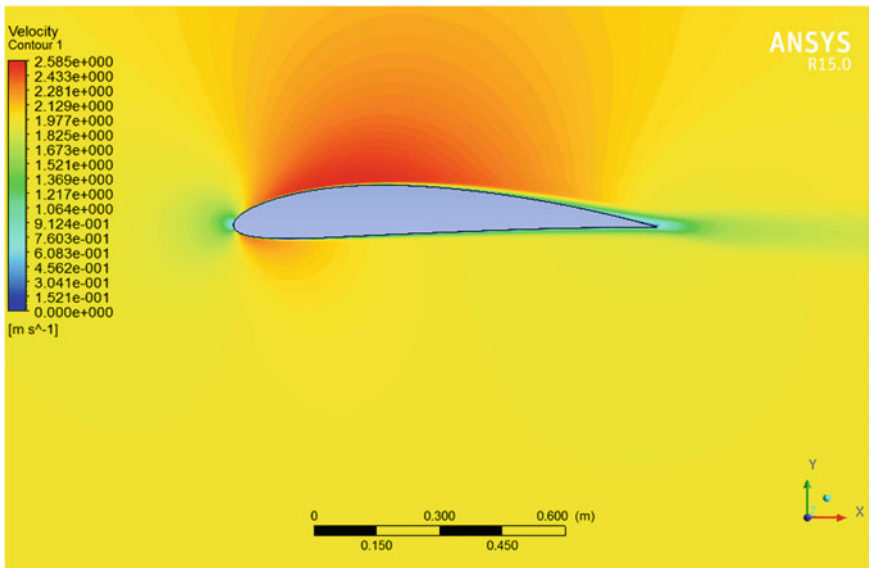
Fig. 20.7 Velocity

The temperature is higher at the leading and trailing edges.

The results obtained in theory are almost the same obtained by the software ANSYS-Fluent.

Fig. 20.8 Pressure

Fig. 20.9 Temperature

20.9   Conclusion

Integral method and the ANSYS CFX gave us a calculation of the velocity induced, pressure and temperature.

The integral method is used for solving the Laplace equation.

ANSYS CFX is used for discretization to find the velocity induced in all point of the blade surface and wake surface.

References

Barenes R (1999) Analyse expérimentale et modélisation du fonctionnement d'hélice de drones

Haertig J (2004) général 3D, Théorie générale des écoulements à potential de vitesse, A3F

Hoinville E (2007) Etude du sillage de rotors d'hélicoptère en configuration de vortex ring state

Joncheray P (1997) Aerodynamics of helicopter rotor in hover: the lifting-vortex line method applied to dihedral tip blades

Katz J, Plotkin A (1991) Low speed aerodynamics

Mahri ZL, Rouabah MS, Zid S (2007) Calcul des efforts aérodynamiques agissant sur les pales d'une petite éolienne

Muzard P (1994) Etude du comportement dynamique linéaire et non-linéaire d'un rotor d'hélicoptère

ONERA (2004) Aerodynamic and aero-acoustic optimization of modern tilt-rotor blades within the ADYN project

Paraschivoiu I (1998) Arodynamique subsonique, edition de l'école polytechnique de montréal

Peters DA (1988) Modeling of unsteady aerodynamics for rotary-wing aeroelasticity

Pflimlin JM (2006) Commande d'un mini drone à hélice carénée: de la stabilisation dans le vent à la navigation autonome

Phillips WF, Snyder DO (2000) Modern adaptation of Prandtl's classic lifting-line theory

Raletz R (1995) Théorie élémentaire de l'hélicoptère

Chapter 21
Modelling and Evaluation of Persistent Contrail Formation Regions for Offline and Online Strategic Flight Trajectory Planning

Yixiang Lim, Alessandro Gardi, Matthew Marino and Roberto Sabatini

Abstract This chapter presents a contrail mapping algorithm developed for integration into a Multi-objective Trajectory Optimisation (MOTO) software framework, targeting the mitigation of environmental impacts associated with aviation-induced cloudiness. The presented linear contrail mapping algorithm exploits analytical and empirical models to determine the formation, persistence and radiative properties of contrails along a defined flight trajectory. In order to determine the contrail formation and persistence, the algorithm takes into account aircraft characteristics as well as relative humidity, temperature, pressure as well as the speed and shear of winds aloft, derived from suitable weather forecast data inputs. The linear contrail mapping algorithm generates an accurate mapping of the contrail persistence and associated Radiative Forcing (RF) along a flight trajectory based on inputs of weather data and aircraft state. A 3D contrail mapping algorithm is developed by executing the linear contrail mapping algorithm along an arbitrary number of virtual sounding trajectories. These virtual trajectories are constructed radially around a centre position, at individual flight levels. Multiple 3D mappings are exploited to characterise time variations, ultimately leading to a 4-dimensional (4D) mapping in space and time of contrail formation, persistence and RF properties. These 4D contrail mappings can be exploited in a MOTO software framework to assess and minimise the environmental impacts associated with contrails.

21.1 Introduction

Increasing safety, capacity, cost-effectiveness, efficiency and environmental sustainability of air transportation worldwide are prime objectives of the aviation governance at present. Novel Communication, Navigation and Surveillance/Air

Y. Lim · A. Gardi · M. Marino · R. Sabatini (✉)
RMIT University, Melbourne, VIC 3001, Australia
e-mail: roberto.sabatini@rmit.edu.au

243

Traffic Management (CNS/ATM) and Avionics (CNS+A) operational concepts and systems are being developed as part of the Single European Sky ATM Research (SESAR) and Clean Sky programmes in Europe, specifically tackling the ambitious objective sets by the Advisory Council for Aeronautics Research in Europe (ACARE) in the Flightplan 2050 agenda, and in parallel in the US by NextGen and Environmentally Responsible Aviation (ERA) programmes as well as under various other R&D initiatives undertaken by governments and industrial organisations in the Asia Pacific and Latin America/Caribbean Regions (European ATM Master Plan 2012; Flightpath 2050; SESAR and the Environment 2010; Galindo and Candelario 2011; Oberthür 2003). The main objective with respect to the environmental sustainability of aviation is to reduce the amount of greenhouse emissions compared to the current levels. Other important areas of improvements are targeting pollutant emissions such as nitrogen oxides (NO_X) and Unburned Hydro Carbons (UHC), as well as aircraft noise. Aircraft emissions contribute to the global warming, either directly, such as in the case of carbon dioxide (CO_2), or by triggering chemical processes that alter the atmospheric composition and ultimately induce warming effects, such as in the case of stratospheric NO_X (Lee et al. 2009). Condensation trails (contrails) produced by aircraft at high altitude are considered to be a very significant contribution to global warming, as their Radiative Forcing (RF) is positive in various instances (Burkhardt and Kärcher 2011). In particular, contrails contribute positively to RF by the trapping of longwave thermal radiation emitted by the Earth's surface, while at the same time a negative contribution to RF is due to reflecting the shortwave radiation from the Sun (Minnis 2003). The exact balance between these opposite contributions is subject to a number of aspects and must be carefully assessed (Lim et al. 2015). Notwithstanding, irrespective of the exact balance between positive and negative RF contributions, it is alleged that an overall reduction in the amount of persistent contrails formed by aircraft daily will enhance the environmental sustainability of aviation.

This chapter reviews the current theoretical understanding of the contrail lifecycle and the associated radiative properties, upon which a linear and a 4-dimensional (4D) contrail mapping algorithms are developed for integration in Multi-objective Trajectory Optimization (MOTO) software frameworks. The contrail mapping algorithms evaluate the formation, persistence and radiative forcing properties across defined geographic extents and time periods, generating 4D fields that can be exploited by real-time MOTO implementations in CNS+A systems to promote the mitigation of environmental impacts associated with aircraft contrails.

21.2 Contrail Lifecycle

Contrails are thermodynamically formed as the water vapour in the plume of a jet engine cools to ambient conditions. In the case of persistent contrails, they have been observed to be a precursor to ice clouds such as cirrus, found at higher altitudes where ice super-saturation occurs.

Wingtip contrails, which are usually short-lived and are not the focus of this chapter, are triggered aerodynamically in the wake vortexes released from the wingtips, when the local drop in pressure and temperature on the upper surface of the wing causes condensation of ambient air. In contrast to short-lived wingtip contrails, exhaust-triggered contrails may persist for considerably longer periods of time and affect the radiative forcing balance of the Earth. Research done on the evolution of this type of contrails has discerned three distinct phases in their life-cycle: jet, vortex and dispersion phase. These phases occur at different timescales and are each governed by specific physical processes.

The jet phase occurs approximately in the first 20 s of the contrail lifecycle and involves the initial formation of the contrail from the jet exhaust. The cooling of the hot and humid exhaust plume triggers the condensation of a trail of water vapour, hence the term 'contrail'. The state of the exhaust plume can be characterised by the mixing diagram, as seen in Fig. 21.1. The y-axis denotes the vapour partial pressure as a function of ambient temperature, with the solid and dashed curves representing the saturation limits of water and ice, respectively. The region above these curves represents super-saturated states while the region below the curves represents sub-saturated states.

The dot-dashed mixing line describes the dynamics of the exhaust plume. Initially starting from a state of high temperature and moisture, the plume mixes in ambient conditions and moves right-to-left along the mixing line, to a state of lower temperature and partial pressure. The exhaust plume eventually reaches ambient conditions, denoted by Point C in Fig. 21.1, which at typical cruise altitudes of 33,000 ft are characterised by ambient temperatures of approximately −50 °C and water sub-saturation. The mixing line is characterised by its slope, which depends on aircraft properties, and also by its initial and terminal points, which, respectively, depend on the engine exhaust thermodynamic state at the nozzle and on ambient temperature and humidity.

Fig. 21.1 Mixing diagram
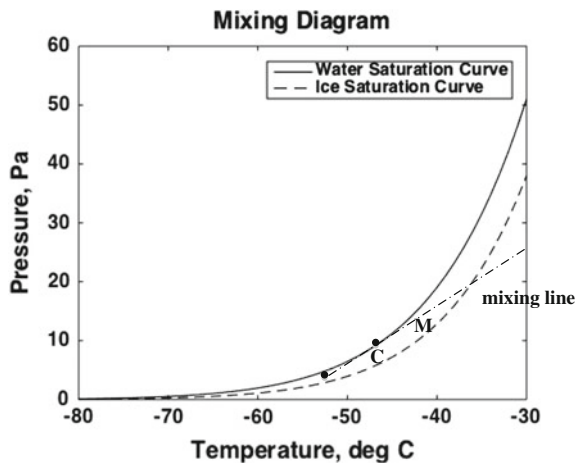
It can be seen from Fig. 21.1 that at a fixed temperature, there is a lower saturation limit for ice than for water. However, sublimation does not occur readily in the absence of nuclei. Nuclei forms when the water vapour in the exhaust first condenses at a higher saturation limit, and then undergoes freezing. Alternatively, frozen sulphur droplets or soot particles can also act as sublimation nuclei. Therefore, the formation of contrails usually requires the exhaust plume to undergo water saturation. This means that the mixing line has to cross the water saturation curve. The point where this occurs is given as Point M in Fig. 21.1. If the terminal state, represented by Point C, lies below the ice saturation curve, the contrails formed will quickly dissipate once the plume reaches ice sub-saturated conditions. However, if point C lies above the ice saturation curve, contrails will persist because additional water vapour will continue to sublimate around the ice crystals within these contrails. Given a large enough region of ice super-saturation, ambient water vapour can sublimate on the ice nucleation sites produced by the contrails in the initial plume, allowing the contrail to grow in time.

Following the jet phase, the contrail undergoes the vortex phase. This phase is characterised the exhaust plume being caught in the downwash vortex generated by the aircraft and is depicted in Fig. 21.2. Large Eddy Simulations (LES) by Lewellen and Lewellen (2001) suggest that the vortex phase occurs in the first 3 min of existence, and consists in a sinking of the plume (about 250 m for a Boeing 747 aircraft). As the plume sinks to a lower altitude, ambient pressure increases. The plume undergoes compression, which leads to adiabatic warming. Sublimation might occur, and the ice number (number of ice particles) of the plume will decrease.

The fraction of ice particles remaining after the vortex phase is defined *survival factor* $0 < f < 1$, and is dependent on the wake size, temperature and relative humidity. Schumann (2012) reports values of f that lie between 0.7 and 1. Notwithstanding, lower values corresponding to around 0.25, were found to be more common for most flight conditions of large aircraft. These are in good agreement with results by Unterstrasser et al. (2008). As the strength of the vortex (and subsequently the extent of adiabatic heating) is related to the aircraft mass, larger aircraft will have lower survival factors for similar ambient conditions. Lewellen and Lewellen (2001) concluded that the higher fuel flow of large aircraft (hence larger soot emissions and higher number of ice particles in the jet phase) could be offset by the smaller survival factor, and that a Boeing 737 aircraft could give rise to contrails with similar persistence as a Boeing 747 aircraft.

Contrails that survive the vortex phase consequently undergo a dispersion phase, in which they are advected and spread by wind. In particular, advection is associated with the average wind stream direction and magnitude, while spread is promoted by wind shear, which is the vertical derivative of the wind field. If contrails form in ice super-saturated regions, they will continue to grow as ambient water vapour is entrained within the contrail as it spreads. As the contrail evolves, its particle concentration decreases while its particle size increases, so that the ice crystals get larger and more spread out in the contrail, eventually approaching the properties of cirrus clouds, with typical concentrations of around $10^1 \, \text{cm}^{-3}$ and
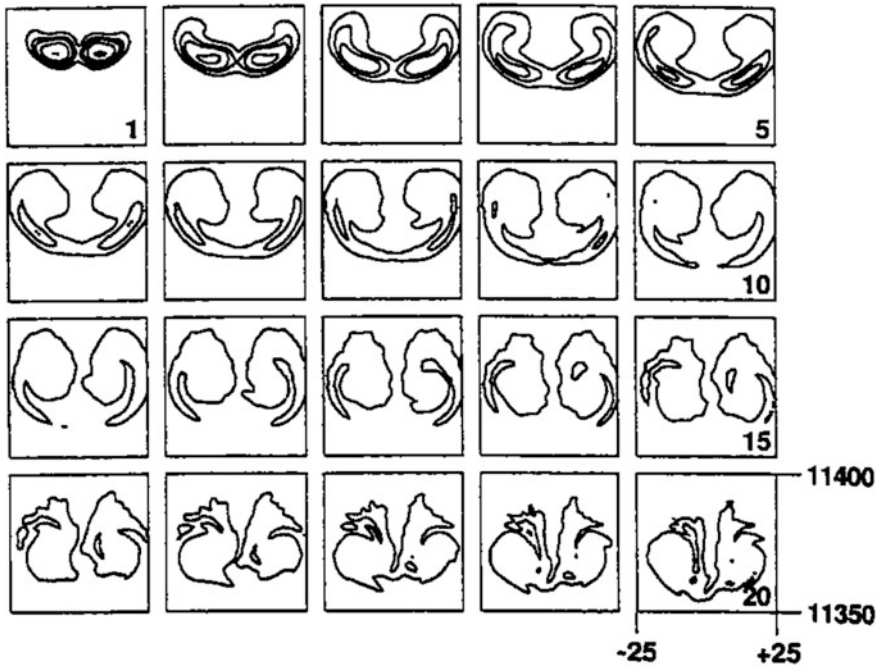
Fig. 21.2 LES results performed by Sussmann and Gierens (2001), represented by a time series of the contrail cross section in the first 20 s. Contours of ice mass concentrations are plotted at 1, 3, 5, 10 and 20 mg/m3. Reproduced with permission.

effective radii of around 10^1 μm. This is clearly described in Fig. 21.3, which shows the typical particle sizes and concentrations of a contrail at different stages in its growth.

Contrails disperse via sublimation of their ice particles, which can occur when the contrail drifts into an ice sub-saturated region. This can be caused either by wind advection (laterally), by sedimentation (vertically). The latter occurs when larger and heavier particles sink to the bottom of the contrail-cirrus. Over sufficient time, the entire contrail will sink, but sufficiently large ice particles will form fallstreaks; these have been observed and recorded via lidar by Atlas et al. (2006). The fallstreak/contrail then dissipates in the warm temperatures found at lower altitudes.

21.2.1   Radiative Properties

A key factor in determining the radiative properties of clouds is the *optical depth*, which is a measure of optical absorptivity. The optical depth of contrail-cirrus, an ice cloud, is much lower than the one characterising water (stratus) clouds found at
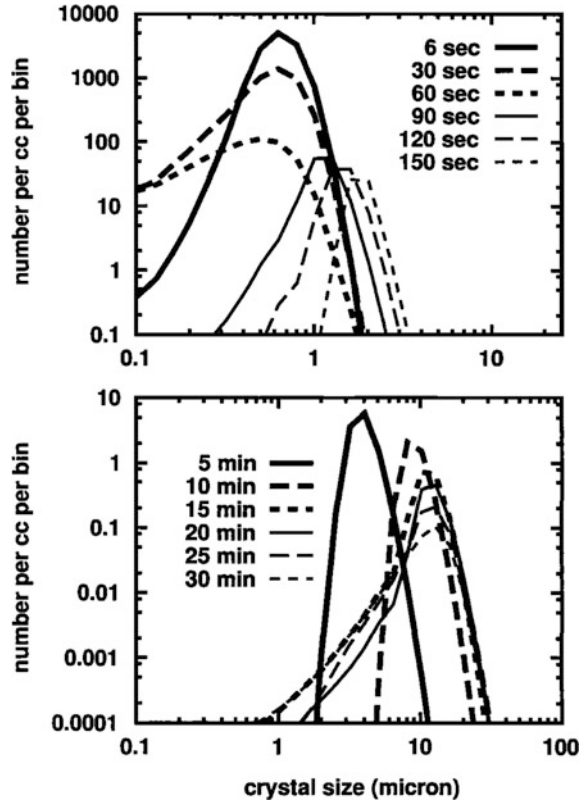
lower altitudes because of the differences in particle type and cloud thicknesses. Contrail-cirrus contains ice particles that are less tightly packed than water molecules found in stratus, and are also much thinner in depth than water clouds. Contrail optical depth typically ranges from $10^{-3} < \tau < 1$ (Kärcher et al. 2009), whereas those of water clouds can reach up to $\tau > 10^2$.

The net cloud radiative forcing depends on a combination of cooling and warming contributions. Cooling is caused by the reflection of incoming shortwave radiation from the sun and therefore is largely determined by the cloud *albedo*, which is a measure of its reflectivity. Warming is caused by the trapping of outgoing longwave radiation from the earth and is largely determined by the difference between the cloud temperature and the temperature of the surface of the earth. The cooling effect only occurs during daylight hours and therefore varies considerably with the time-of-day. On the other hand, the warming effect can be assumed to occur constantly and independent of time.

Lower clouds are characterised by a higher albedo and a temperature more similar to the surface of the Earth. As a result, they reflect shortwave radiation and emit longwave radiation at a higher intensity than upper clouds. Hence, while low

Fig. 21.4 Estimated contrail-cirrus induced radiative forcing (Burkhardt and Kärcher 2011). Reproduced with permission.
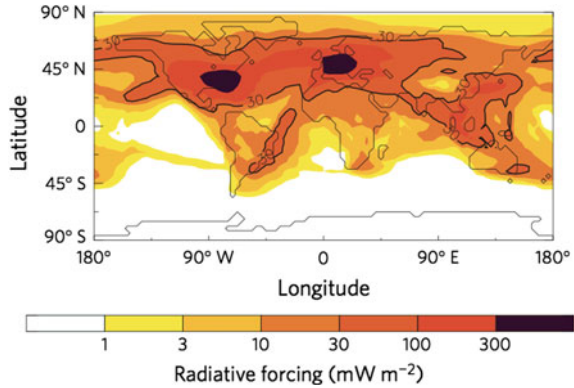
clouds generally induce a net cooling effect, higher clouds comprehensively induce a net warming effect.

The RF due to contrails is also correlated to air traffic density and has been shown to be larger over the northern hemisphere, where air routes are more congested, The higher occurrence localised in such areas causes an uneven warming effect by contrail-cirrus on the global scale. This is depicted in Fig. 21.4, where the majority of contrail-induced RF is shown to occur over the east coast of North America and over Western Europe.

21.3 Contrail Mapping Algorithm

A considerable emphasis was given to numerical implementations of contrail models in recent research. As an example, the Contrail-Cirrus Prediction (CoiCiP) tool by Schumann (2012) simulates contrails along the flight paths of a fleet of aircraft using weather and aircraft inputs. Capitalising on these models, we propose a contrail mappingContrail mapping algorithm specifically conceived for integration in a MOTO framework. The contrail mapping algorithm generates 4-dimensional (4D) fields (maps) of contrail iso-persistence and iso-RF over a region surrounding the reference aircraft trajectory. These iso-persistence and iso-RF maps can be graphically represented by contour maps similarly to isobaric or isothermal fields in weather studies. A novel method based on virtual sounding trajectories is employed to generate the 4D iso-contrail fields. Similar in principle to the technique of depth sounding, which makes use of sonar pulses to map the depth of the ocean floor, trajectory pulses are used to map the contrail formation, persistence and radiative properties over a defined region and time period. Within the contrail mapping algorithm, an arbitrary number of virtual sounding trajectories are generated at a specific time interval to span the defined region with adequate spatial resolution, allowing the retrieval of instantaneous contrail formation, persistence and radiative data at various spatial locations. A seamless 3-dimensional (3D) map of the region is

obtained by performing a numerical extrapolation of the contrail data across all the virtual sounding trajectories simulated at each *sounding pulse*. 4D fields are finally obtained by performing a series of 3D sounding pulses at different time instants and again numerically extrapolating the contrail persistence and RF values across the discrete pulses.

In our implementation of the contrail mapping algorithm, each sounding pulse comprises an arbitrary number of virtual sounding trajectories that are generated in a radial manner around an arbitrary centre position. For flight planning and rerouting purposes, such centre position can either consist of the intermediate point along the entire reference flight trajectory, or can consist of the centroid of a region of potential contrail formation, identified by comparing the local temperature and relative humidity conditions against accurately selected thresholds. In the first case, the radius of the mapping region will always consist of slightly more than half the total length of the reference trajectory. The second case may sometimes enable the adoption of smaller radii, enhancing the computational performances of the contrail mapping algorithm. An instantaneous flight is simulated along each sounding trajectory, permitting the retrieval of contrail formation, persistence and radiative properties along it. The contrail lifecycle is simulated along each sounding trajectory until dissipation conditions are detected or until a maximum time limit is reached, and the contrail formation, persistence and radiative values are stored. Upon interpolation in space, each pulse provides an instantaneous snapshot of the iso-contrail fields. By performing multiple pulses at different times, the snapshots can be combined to produce 4D fields, also considering dynamically varying weather conditions.

21.3.1   Contrail Model

The contrail model adopted in the mapping algorithm is based on CoCiP (Schumann 2012), and therefore consists of a parametric model that determines the contrail lifetime and associated RF along a single flight trajectory. The parametric model checks for contrail formation along trajectory segments with the Schmidt-Appleman criterion. It then computes the initial plume properties based on the downwash vortex and models the advection, spread, ice and radiative properties over time with a linear integration scheme. A radiation model based on Schumann (2012) then estimates the contrail-related RF based on the solar zenith angle and on the spread and lifetime of the contrail. The lifetime of a contrail segment is defined as the time elapsed since the sounding pulse up to the instant when ice concentration along the contrail segment falls below a set threshold.

Additional weather and solar models are also used in the contrail model. The weather model supplies the ambient input required for modelling the contrail lifecycle, whereas the solar model supplies the solar zenith angle required for computing the contrail radiative forcing balance.

21.3.1.1 Jet Phase

In the jet phase, the Schmidt-Appleman Criterion is used to determine the onset of contrail formation. This computes the slope of the mixing line according to Eq. (21.1):

$$G = \frac{EI_{H_2O} \cdot c_p \cdot p}{\varepsilon \cdot Q \cdot (1 - \eta)} \tag{21.1}$$

where G is the slope of the mixing line, in Pa K^{-1}, and describes the mixing of the exhaust plume with ambient air. EI_{H_2O}, Q and η are the emission index of water vapour, heat per mass of fuel and propulsive efficiency, respectively, and are engine characteristics, p is the ambient pressure, and c_p and ε are the specific heat capacity of air and the ratio of the molecular masses of water and air, respectively. The following approximation for the temperature in degrees Celsius at the threshold point is used (Schumann 2012):

$$T_{LM} = -46.46 + 9.43 \ln(G - 0.053) + 0.72[\ln(G - 0.053)]^2 \tag{21.2}$$

where the subscript 'L' denotes the threshold temperature for liquid saturation.

The critical temperature at ambient conditions (Point C) can then be found using the criterion given by Schumann (2012) based on curve fitting where T and T_{LM} are given in degrees Celsius:

$$T_{LC} = T_{LM} - (1 - RH_w)\frac{p_{liq}(T_{LM})}{G} - \Delta T_C \tag{21.3}$$

$$\Delta T_C = F_1 RH_w [W - F_2(1 - W)] \tag{21.4}$$

$$W = \left(1 - RH_w^2\right)^{x_2} \tag{21.5}$$

$$F_1 = x_1 + x_3 \ln(G), \quad F_2 = \left[\frac{1}{4} - \left(RH_w - \frac{1}{2}\right)^2\right]^4 \tag{21.6}$$

where $x_1 = 5.686$, $x_2 = 0.3840$, $x_3 = 0.6594$. The criterion for contrail formation is thus:

$$dT = T - T_{LC} < 0 \tag{21.7}$$

21.3.1.2 Vortex Phase

In the vortex phase, the initial geometric properties of the contrail plume are determined beforehand. This is done by first computing the maximum downward

displacement Δz_w and then scaling it to obtain the initial depth. The initial width is then parameterized from the depth, dilution and fuel flow. The parameters that determine the initial size of the contrail are

Wake vortex separation $b_0 = \pi S_a/4$,
Initial circulation $\Gamma_0 = 4M_a g/(\pi S_a \rho_{\text{air}} V_a)$,
Effective time scale $t_0 = 2\pi b_0^2/\Gamma_0$,
Initial velocity scale $w_0 = \Gamma_0/(2\pi b_0)$,
Normalised dissipation rate $\epsilon* = (\epsilon b_0)^{1/3}/w_0$.
These are dependent on the inputs
Wing span S_a,
Aircraft mass V_a,
True air speed M_a,
Air density ρ_{air},
Brunt-Vaisaila frequency N_{BV},
Turbulent kinetic energy dissipation rate ϵ.

Schumann's parameterization distinguishes between strongly and weakly stably stratified conditions. If $N_{\text{BV}}t_0 \geq 0.8$:

$$\Delta z_w = 1.49 \frac{w_0}{N_{\text{BV}}} \tag{21.8}$$

else, with $\epsilon* \leq 0.36$:

$$\frac{\Delta z_w}{b_0} = 7.68\left(1 - 4.07\epsilon* + 5.67\epsilon*^2\right)(0.79 - N_{\text{BV}}t_0) + 1.88 \tag{21.9}$$

with Δz_w as the maximum sinking.

The initial downward displacement is set to

$$\Delta z_1 = C_{z1}\Delta z_w, \quad C_{z1} = 0.25 \tag{21.10}$$

where the subscript '1' denotes the end of the vortex phase. The initial depth is set to

$$D_1 = C_{D0}\Delta z_w, \quad C_{D0} = 0.5 \tag{21.11}$$

and the initial width is:

$$B_1 = N_{\text{dil}}(t_0)m_F/[(\pi/4)\rho D_1] \tag{21.12}$$

with the m_F being the fuel flow in kg m^{-1} and the dilution N_{dil} of the wake vortex formation being

$$N_{\text{dil}}(t) \approx 7000(t/t_s)^{0.8} \tag{21.13}$$

with $t_s = 1$ s. The initial mass mixing ratio of ice I and the ice particle number N are also prescribed for the vortex phase:

$$I_1 = I_0 - \Delta I_{ad} \tag{21.14}$$

$$I_0 = \frac{EI_{\text{H}_2\text{O}}m_F}{(\pi/4)\rho D_1 B_1} + q_0 - q_s(p_0, T_0) \tag{21.15}$$

$$\Delta I_{ad} = \frac{R_0}{R_1}\left[\frac{p_{\text{ice}}(T_0 + \Delta T_{ad})}{p_1} - \frac{p_{\text{ice}}(T_0)}{p_0}\right] \tag{21.16}$$

Here, q_0 is the specific humidity of ambient conditions at stage "0" (the start of the vortex phase) and q_s is the specific humidity at saturation point. p_1 is the ambient pressure at stage "1", R_0 and R_1 are the specific heat capacities of air and water, respectively, and:

$$\Delta T_{ad} = T_0(R_0/c_p)(p_1 - p_0)/p_0 \tag{21.17}$$

The ice number N_1 at the end of the vortex phase is determined by the soot index and a survival factor based on the ice mass ratio

$$N_0 = EI_{\text{Soot}}m_F \tag{21.18}$$

$$N_1 = f_{\text{surv}}N_0, \quad f_{\text{surv}} = \frac{I_1}{I_0} \tag{21.19}$$

21.3.1.3 Dispersion Phase

The state of each contrail segment along the flight path evolves with time and is described by the state vector X, denoted as $X(\text{Position}, \text{Ambient}, \text{Plume}, \text{Particle})$, including its position in space and time, the relevant ambient conditions, and its plume and ice particle properties. The position at time t is given as

$$X.\text{Position} = (x(t), y(t), z(t), t) \tag{21.20}$$

where x, y and z gives the longitude, latitude and altitude of the contrail. The advection of the contrail with time is described by

$$x(t + \Delta t) = x(t) + U(t)\Delta t \tag{21.21}$$

$$y(t + \Delta t) = y(t) + V(t)\Delta t \tag{21.22}$$

$$z(t + \Delta t) = z(t) + W(t)\Delta t \tag{21.23}$$

with the absolute distances converted to geodetic coordinates based on approximations provided by Veness (2015). The ambient conditions include the parameters:

$$X.\text{Ambient} = (p, T, \rho_{\text{air}}, q_a, q_s) \tag{21.24}$$

which are pressure, temperature, density, and ambient and saturation specific humidity, respectively, obtained from the GFS, and are functions of X.Position. The plume parameters consist of:

$$X.\text{Plume} = (\sigma, B, D, D_{\text{eff}}, A, L, M, I, N, n, M_{\text{H}_2\text{O}}, D_{\text{H}}, D_{\text{V}}) \tag{21.25}$$

Respectively, these are the:

Covariance matrix σ,
Contrail width B,
Contrail depth D,
Effective depth D_{eff},
Contrail area A,
Contrail length L,
Air mass M,
Ice mass mixing ratio I,
Ice particle number N,
Ice concentration n,
Water mass $M_{\text{H}_2\text{O}}$,
Horizontal diffusivity D_{H},
Vertical diffusivity D_{V}.

The terms of the covariance matrix $\sigma = \begin{bmatrix} \sigma_{yy} & \sigma_{yz} \\ \sigma_{yz} & \sigma_{zz} \end{bmatrix}$ are initially given as:

$$\sigma_{yy}(t = t_0) = B_1^2/8 \tag{21.26}$$

$$\sigma_{zz}(t = t_0) = D_1^2/8 \tag{21.27}$$

$$\sigma_{yz}(t = t_0) = 0 \tag{21.28}$$

and evolve with time as

$$
\sigma_{yy}(t + \Delta t) = \left[\frac{2}{3} S^2 D_V \Delta t^3 + \left(S^2 \sigma_{zz}(t) + 2 D_S S \right) \Delta t^2 + 2 \left(D_H + S \sigma_{yz}(t) \right) \Delta t + \sigma_{yy}(t) \right]
$$
$$
\cdot \left[\frac{L(t)}{L(t + \Delta t)} \right]^2
$$

(21.29)

$$
\sigma_{zz}(t + \Delta t) = 2 D_V \Delta t + \sigma_{zz}(t)
$$

(21.30)

$$
\sigma_{yz}(t + \Delta t) = \left[S D_V \Delta t^2 + \left(2 D_S + S \sigma_{zz}(t) \right) \Delta t + \sigma_{yz}(t) \right] \cdot \left[\frac{L(t)}{L(t + \Delta t)} \right]
$$

(21.31)

with the shear diffusivity D_S set to 0 and the vertical shear of the plume normal velocity S is taken to be the total shear $S_T = \sqrt{ \left(\frac{\partial U}{\partial z} \right)^2 + \left(\frac{\partial V}{\partial z} \right)^2 }$. The shape and size of the contrail are based on the covariance matrix

$$
B(t + \Delta t) = \sqrt{8 \sigma_{yy}(t + \Delta t)}
$$

(21.32)

$$
D(t + \Delta t) = \sqrt{8 \sigma_{zz}(t + \Delta t)}
$$

(21.33)

$$
A(t + \Delta t) = 2\pi \left\{ \frac{1}{3} S^2 D_V^2 (\Delta t)^4 + \frac{2}{3} S^2 D_V \sigma_{zz}(t) (\Delta t)^3 \right.
$$
$$
+ \left[2 S \sigma_{zz}(t) (D_V - D_S) - 4 \left(D_H D_V - D_S^2 \right) \right] (\Delta t)^2
$$
$$
\left. + \left[2 \sigma_{zz}(t) (D_V + D_H) - 4 D_S \sigma_{yz}(t) \right] \Delta t + \sigma_{yy}(t) \sigma_{zz}(t) - \sigma_{yz}^2(t)^{1/2} \right\}
$$

(21.34)

$$
D_{\text{eff}}(t + \Delta t) = \frac{A(t + \Delta t)}{B(t + \Delta t)}
$$

(21.35)

and the length $L(t + \Delta t)$ is computed from the positions of the end-points of the contrail $x(t + \Delta t)$ and $y(t + \Delta t)$ in its position vector. The mass properties of the plume can then be calculated

$$
M(t + \Delta t) = \rho A L |_{t + \Delta t}
$$

(21.36)

$$
I(t + \Delta t) = \frac{M(t) \cdot [I(t) + q_s(t) + \Delta M \cdot q_a]}{M(t + \Delta t)} - q_s(t + \Delta t)
$$

(21.37)

$$
M_{H_2O}(t + \Delta t) = M(t + \Delta t) \cdot (I + q) |_{t + \Delta t}
$$

(21.38)

where $\Delta M = M(t + \Delta t) - M(t)$ and $q_a = \frac{q_a(t + \Delta t) + q_a(t)}{2}$.

Particle loss due to turbulence and aggregation are modelled to determine the evolution of the ice number and concentration, with the adjustable parameters E_A and E_T set to 2:

$$(dN/dt)_{agg} = -E_A 8\pi r_{eff}^2 V_T N^2 / A \tag{21.39}$$

$$(dN/dt)_{turb} = -E_T \left(\frac{D_H}{\max(B,D)^2} + \frac{D_V}{D_{eff}^2} \right) N \tag{21.40}$$

$$\alpha = -\frac{1}{N^2} (\partial N/\partial t)_{agg}, \quad \beta = -\frac{1}{N} (\partial N/\partial t)_{turb} \tag{21.41}$$

$$N(t+\Delta t) = \frac{N(t)\beta \exp(-\beta\Delta t)}{\beta + N(t)\alpha[1-\exp(-\beta\Delta t)]} \frac{L(t)}{L(t+\Delta t)} \tag{21.42}$$

$$n = N/A \tag{21.43}$$

where V_T, following (Rogers 1976), is stored in the particle properties:

$$X.\text{Particle} = (V_T, r_{eff}) \tag{21.44}$$

$$V_T = \begin{cases} k_1 r_{eff}^2, & r < 40\,\mu m \\ k_2 r_{eff}, & 40\,\mu m < r < 600\,\mu m \\ k_3 \sqrt{r_{eff}}, & r > 600\,\mu m \end{cases} \tag{21.45}$$

$$k_1 = 1.9e^8, \quad k_2 = 8e^3, \quad k_3 = 2.2e^2 \sqrt{\frac{\rho_0}{\rho}} \tag{21.46}$$

and r_{eff} is taken to be the effective particle radius

$$r_{eff} = \left(\frac{\rho_{air} I}{n \rho_{ice} 4\pi/3} \right)^{1/3} \tag{21.47}$$

Finally, the diffusivities are given in (Schumann 2012):

$$D_H = C_H(D^2 S_T), \quad C_H = 0.1 \tag{21.48}$$

$$D_V = \frac{C_V}{N_{BV}} w_n' + f_t(V_T D_{eff}), \quad C_V = 0.2, \quad w_n' = 0.1, \quad f_t = 0.1 \tag{21.49}$$

The time integration ends when the ice concentration n falls below 10^3 m^{-3} (or $1\,l^{-1}$), the ice mass ratio I falls below 10^{-8} (or 10^{-2} mg/kg), or when the time exceeds a given threshold, set to 5 h in this case.

21.3.1.4   Radiative Forcing

The RF model is based upon (Schumann et al. 2012). The parameterization scheme is based on a number of parameters that model the particle type (i.e. spherical, hollow, rosette, and plate) as well as a number of independent properties. The model parameters can be found in Schumann et al. (2012) and a fully droxtal habit is assumed for our verification case studies. The longwave radiation is positive and dependent on the following independent variables: the outgoing longwave radiation (OLR, W m^{-2}), the atmospheric temperature (T, K), the optical depths of the contrail and its overhead cirrus at 550 nm (τ and τ_c) and the effective particle radius (r_{eff}, μm). The contrail optical depth is computed from Schumann (2012) as follows:

$$\tau = \beta D_{\text{eff}} \tag{21.50}$$

$$\beta = 3Q_{\text{ext}}\rho I / (4\rho_{\text{ice}} r_{\text{eff}}) \tag{21.51}$$

$$D_{\text{eff}} = A/B \tag{21.52}$$

$$Q_{\text{ext}} = 2 - (4/\rho_\lambda) \frac{\sin(\rho_\lambda) - [1 - \cos(\rho_\lambda)]}{\rho_\lambda} \tag{21.53}$$

$$\rho_\lambda = 4\pi r_{\text{eff}}(\kappa - 1)/\lambda, \quad \kappa = 1.31, \quad \lambda = 550\,\text{nm} \tag{21.54}$$

The optical depth of overhead cirrus is assumed to be $\tau_c = 0$—the assumption of zero cloud cover. The long and shortwave RF can then be computed as

$$\text{RF}_{LW} = [\text{OLR} - k_{\text{T}}(T - T_0)] \cdot \{1 - \exp[-\delta_\tau F_{LW}(r_{\text{eff}})\tau]\} E_{LW}(\tau_c) \tag{21.55}$$

$$F_{LW}(r_{\text{eff}}) = 1 - \exp(-\delta_{lr} r_{\text{eff}}) \tag{21.56}$$

$$E_{LW}(\tau_c) = \exp(-\delta_{lc} \tau_c) \tag{21.57}$$

The shortwave radiation is negative and depends on the following independent properties: τ, τ_c, r_{eff}, the cosine of the solar zenith angle $\mu = \cos(\theta)$, and the effective albedo (A_{eff}), leading to:

$$\text{RF}_{SW} = -\text{SDR}(t_A - A_{\text{eff}})^2 \alpha_c(\mu, \tau, r_{\text{eff}}) E_{SW}(\mu, \tau_c) \tag{21.58}$$

$$\alpha_c(\mu, \tau, r_{\text{eff}}) = R_C(\tau_{\text{eff}}) [C_\mu + A_\mu R'_c(\tau') F_\mu(\mu)] \tag{21.59}$$

$$\tau' = \tau F_{SW}(r_{\text{eff}}), \quad \tau_{\text{eff}} = \tau'/\mu \tag{21.60}$$

$$F_{SW}(r_{\text{eff}}) = 1 - F_r[1 - \exp(-\delta_{sr} r_{\text{eff}})] \tag{21.61}$$

$$R_C(\tau_{\text{eff}}) = 1 - \exp(-\Gamma\tau_{\text{eff}}), \quad R_C(\tau_{\text{eff}}) = 1 - \exp(-\gamma\tau_{\text{eff}}) \tag{21.62}$$

$$F_\mu(\mu) = \frac{(1-\mu)^{B_\mu}}{(1/2)^{B_\mu}} - 1 \tag{21.63}$$

$$E_{SW}(\mu, \tau_c) = \exp\left(-\delta_{sc}\tau_c - \delta'_{sc}\tau_{c,\text{eff}}\right) \tag{21.64}$$

$$\tau_{c,\text{eff}} = \tau_c/\mu \tag{21.65}$$

The net instantaneous RF is simply the sum of the long and shortwave components:

$$\text{RF}_{\text{net}}(t) = \text{RF}_{LW}(t) + \text{RF}_{SW}(t) \tag{21.66}$$

The RF for the contrail segment is computed as the time-weighted average of the instantaneous RF

$$\text{RF}_{\text{seg}} = \frac{\sum_{t=0}^{t=t_{\text{seg}}} \text{RF}_{\text{net}}(t) \cdot \Delta t}{t_{\text{seg}}} \tag{21.67}$$

21.3.2 Weather

Weather data can be obtained from a variety of sources in the public domain and from commercial weather service providers. For the verification case studies conducted in this research, data is obtained from the Global Forecasting System (GFS), made freely available by the National Oceanic and Atmospheric Administration (NOAA) (2015). Forecast data is given in a 0.25° resolution, updated 4 times daily (every 6 h), and provides a projection of up to 180 h in 3 h intervals. In our algorithms, data is further interpolated to attain the desired resolution in space and time.

The data is accessed via nctoolbox (2015), a Matlab toolbox for processing geographic datasets. The toolbox allows atmospheric variables such as pressure, temperature, and wind to be extracted as 4-dimensional (3-dimensional space plus time) matrices for further analysis.

The relative humidity with respect to ice (RH_i) is not provided in the weather data. Instead, it is obtained in Eq. (21.68) as a function of the relative humidity with respect to water RH_w, and temperature T, both obtained from GFS data. The saturation pressures for water and ice, p_{liq} and p_{ice}, are based on empirical relations by Sonntag (1994) given in Eqs. (21.69) and (21.70):

$$\mathrm{RH}_i = \mathrm{RH}_w \frac{p_{\mathrm{liq}}(T)}{p_{\mathrm{ice}}(T)} \tag{21.68}$$

$$p_{\mathrm{liq}}(T) = 100 \exp\left[\frac{-6096.9385}{T} + 16.635794 - 0.02711193T + 1.673952\mathrm{e}^{-5}T^2\right.$$
$$\left. + 2.433502 \ln(T)\right] \tag{21.69}$$

$$p_{\mathrm{ice}}(T) = 100 \exp\left[\frac{-6024.5282}{T} + 24.7219 + 0.10613868T - 1.3198825\mathrm{e}^{-5}T^2\right.$$
$$\left. - 0.49382577 \ln(T)\right] \tag{21.70}$$

with T in Kelvin.

21.3.3 Solar Properties

The shortwave radiation is affected by the effective albedo, with changes with the solar zenith angle. There are varying degrees of complexity in estimating the solar zenith angle, taking into account the latitude and longitude, time of day and day of the year. A simple solar model is employed in our case and is based on NOAA's Earth System Research Laboratory (ESRL) equations (E Team 2015). More complex models can factor in other variables such as the position of the sun in the celestial coordinate system, or the effects of atmospheric refraction. One such model can be found in Reda and Andreas (2008), along with the associated links for the source code. ESRL's model first computes the fractional year in radians, as given in Eq. (21.71):

$$\gamma = \frac{2\pi}{365} * \left(\text{day of year} - 1 + \frac{\text{hour} - 12}{24}\right) \tag{21.71}$$

Empirical equations are used to estimate the equation of time in minutes and the solar declination angle in radians in Eqs. (21.72) and (21.73):

$$\mathrm{eqtime} = 299.18\left[7.5\mathrm{e}^{-5} + 1.868\mathrm{e}^{-3}\cos(\gamma) - 3.2077\mathrm{e}^{-2}\sin(\gamma)\right.$$
$$\left. - 1.4615\mathrm{e}^{-2}\cos(2\gamma) - 0.40849\mathrm{e}^{-2}\sin(2\gamma)\right] \tag{21.72}$$

$$\mathrm{decl} = \left[6.918\mathrm{e}^{-3} - 3.99912\mathrm{e}^{-1}\cos(\gamma) + 7.026\mathrm{e}^{-2}\sin(\gamma) - 6.758\mathrm{e}^{-3}\cos(2\gamma)\right.$$
$$\left. + 9.07\mathrm{e}^{-4}\sin(2\gamma) - 2.70\mathrm{e}^{-3}\cos(3\gamma) + 1.48\mathrm{e}^{-3}\sin(3\gamma)\right] \tag{21.73}$$

The timezone is computed based on the given longitude, with hourly increments every 15°. In Eq. (21.74), it is rounded down to the nearest whole number:

$$\text{timezone} = \frac{\text{long} + 7.5}{15}, \quad -180° < \text{long} < 180° \quad (21.74)$$

Next, the time offset is found in minutes in Eq. (21.75). Longitude is given in degrees and the timezone is given in hours from UTC. The time offset is added onto the current time to get the true solar time, in minutes, in Eq. (21.76). Here, hour, minute and sec represent the current time in hours (0–23), minutes (0–60) and seconds (0–60):

$$\text{time offset} = \text{eqtime} - 4 * \text{long} + 60 * \text{timezone} \quad (21.75)$$

$$\text{tst} = \text{hour} * 60 + \text{min} + \frac{\text{sec}}{60} + \text{time offset} \quad (21.76)$$

Finally, the solar hour angle is found, in degrees, in Eq. (21.77) and the solar zenith angle can be found from Eq. (21.78):

$$\text{ha} = \left(\frac{\text{tst}}{4}\right) - 180 \quad (21.77)$$

$$\mu = \cos(\theta) = \sin(\text{lat})\sin(\text{decl}) + \cos(\text{lat})\cos(\text{decl})\cos(\text{ha}) \quad (21.78)$$

21.3.4 Contrail Mapping Algorithm Architecture

The contrail model presented in Sect. 21.3.1 is implemented as part of an algorithm, currently developed in MATLAB. In the algorithm, the weather, aircraft type and trajectory are supplied as inputs. The weather input is a structure which contains the 4-dimensional matrices of ambient temperatures, relative humidities with respect to water and ice saturations, longitudinal, lateral and vertical winds, and pressures, along with the grid space-time coordinates. The aircraft input parameters consist of a structure containing aircraft-specific parameters required for simulating the vortex phase as discussed in Sect. 21.3.1.1. The basic verification case study assumes these aircraft parameters to be constant but they can also be made variable along the trajectory depending on the phase of flight, or in an optimal control implementation such as within the MOTO framework (Gardi et al. 2014, 2015; Sabatini et al. 2015). For instance, the airspeed and the fuel flow depend upon the throttle command, and the aircraft mass decreases in time. The trajectory is also a structure consisting of a series of 4D points in latitude, longitude, altitude, and time.

21.3.4.1 Linear Contrail Mapping Algorithm

In the linear model, a 4D trajectory based on the aircraft's flight dynamics is adopted as reference. For such trajectory, the algorithm first interpolates the 4D weather field to obtain the local ambient conditions at each point along the trajectory. The jet phase is modelled based on the Schmidt-Appleman criterion and serves as a quick check for contrail formation. For all the trajectory points satisfying the Schmidt-Appleman contrail formation criterion, the initial plume properties of the vortex phase are also computed.

Contrail segments are discretized using a backward rule; they are represented by a straight line joining the current point and the point preceding it. The dispersion of each segment is then modelled, with plume properties evolving according to Sect. 21.3.1.3. A forward Euler scheme is used to simulate the advection of each segment due to wind, and new ambient conditions are interpolated from the weather field. At the end of each time step, the plume state is updated in a structure and a check is conducted to determine if the contrail has dissipated. The iterative scheme ends if the ice concentration falls below a specified limit or if a time limit has been reached. Finally, the relevant properties, such as the contrail-induced radiative forcing and persistence, are stored for each segment.

The pseudocode of the linear contrail mapping algorithm is presented below.

```
1    function ContrailProperties
2          for all waypoints,
3          interpolate to obtain ambient conditions
4                if Schmidt-Appleman Criterion satisfied, then
5                      initialize starting plume properties
6                      while contrail segment not dissipated,
7                            determine intermediate plume properties
8                            advect contrail
9                            find ambient conditions at advected location
10                           store intermediate state
11                           advance timestep
12                      end
13                      store final contrail properties
14                end
15          end
16    end
```
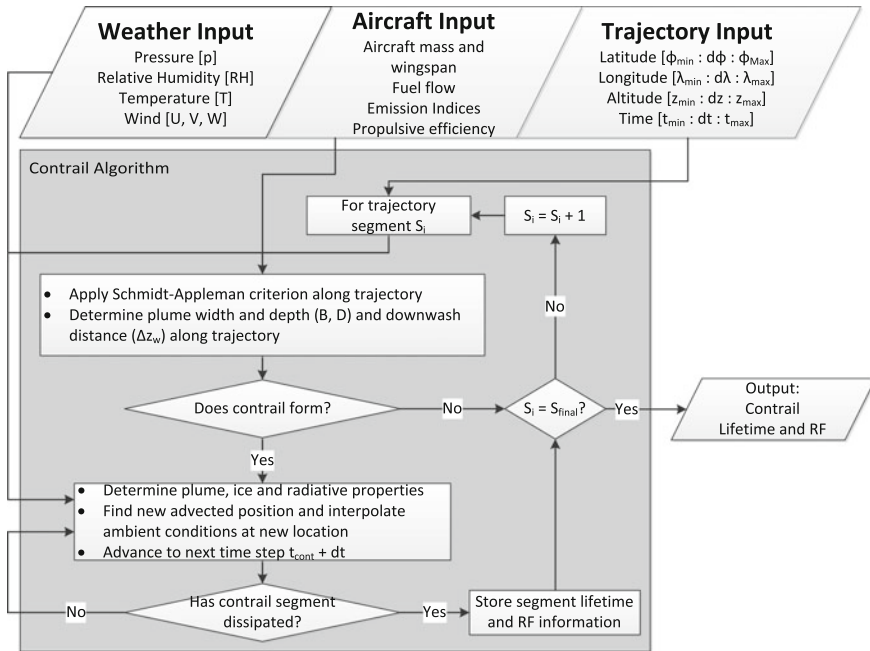
Fig. 21.5 Block diagram of the linear contrail mapping algorithm

The pseudocode can also be represented as a block diagram, depicted in Fig. 21.5.

21.3.4.2   4D Contrail Mapping Algorithm

The linear contrail mapping algorithm presented in Sect. 21.3.4.1 determines the contrail properties along an individual 4D trajectory flown in finite time. The 4D contrail mapping algorithm builds upon the linear contrail mapping algorithm, using it as a core function to perform virtual soundings to generate the 4D mappings. Contrail sounding essentially interpolates between multiple virtual trajectories to extrapolate the contrail properties over a defined region at specific time intervals.

In the 4D version of the contrail mapping algorithm, the weather input is unchanged with respect to the linear mapping algorithm, whereas aircraft and trajectory inputs are modified slightly. The aircraft inputs, like throttle, aircraft mass, and true airspeed, are assumed to be constant and should not be allowed to vary along a virtual sounding trajectory. The trajectory input is replaced with a region input, so instead of describing a line in space, this input now describes a 4D volume in space and time.

The algorithm first sets up sounding trajectories based on the region. In the case study, the sounding trajectories extend in a radial manner from the centroid of the region to map a 2-dimensional circular area. The linear contrail algorithm is applied to each trajectory to evaluate the contrail properties at constant time and altitude. An interpolation between the trajectories then produces a 2-dimensional "pulse". A similar sounding is conducted at different altitudes to obtain a 3-dimensional pulse. The pulses are then evaluated at different time steps to map out a 4-dimensional field. The pseudocode for the algorithm is presented below.

```
1    function ContrailSounding
2         set up sounding trajectories
3         for given time
4              for given altitude
5                   for each sounding trajectory
6                        do ContrailProperties
7                        end
8                        store contrail properties along trajectory
9                   end
10                  interpolate between trajectories to obtain 2D field
11             end
12             interpolate between pulses to obtain 3D field
13             store 3D field
14        end
15        store 4D field
15   end
```

The pseudocode can also be represented as a block diagram, depicted in Fig. 21.6.

21.3.4.3 Algorithm Verification

Refinement tests were conducted on the linear algorithm to investigate the impact of varying time steps and grid resolutions. The differences in contrail lifetime for a given flight are presented in Fig. 21.7 and the algorithm run times are listed in Table 21.1.
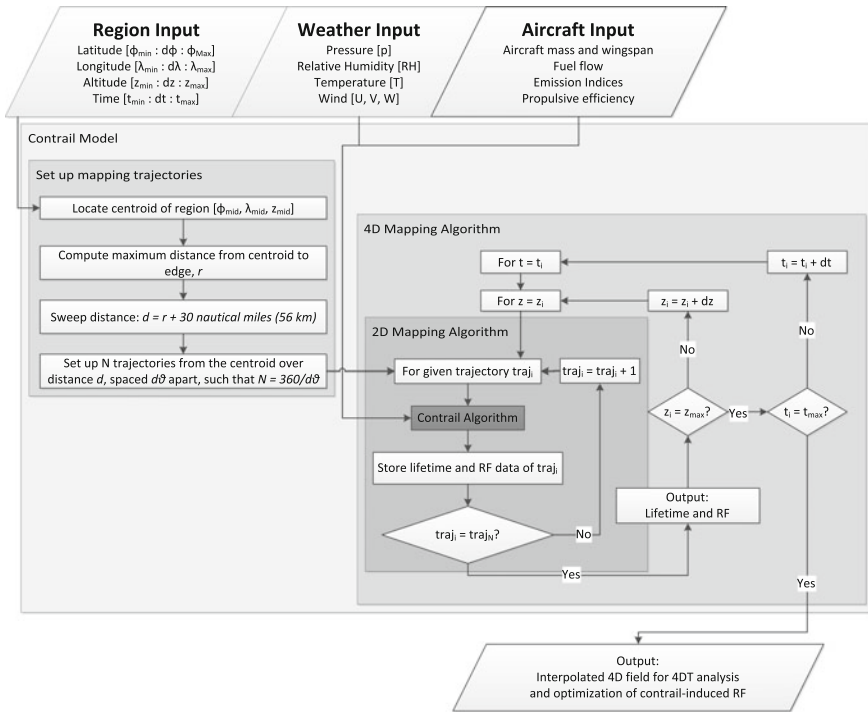
Fig. 21.6 Block diagram of the contrail model used for generating the 4-dimensional iso-contrail field

In addition, results from the contrail model were validated against Schumann (2012), which modelled an artificial, long lived contrail (up to 10 h age) in uniform atmospheric conditions. For the purposes of comparison, a uniform RH_i and temperature field of 120 % and 217 K was artificially created. The properties of a few contrail segments are displayed in Fig. 21.8 and show good agreement with the data presented in Schumann (2012).

Numerical validation of the 4-dimensional contrail mapping algorithm was performed using weather data from the Europe case study, for the region over Central Europe on 11 Apr 2015. The linear contrail mapping identifies persistent contrail formation regions along a large portion of the flight path from Stockholm to Venice. This persistent contrail formation region is closely correlated to ambient temperature and RH_i variations, and therefore roughly follows the ice super-saturation contour in Fig. 21.9.

To check the robustness of the interpolation method, contour maps interpolated with only the 'odd' and 'even' trajectories were compared with the contour map generated by interpolating all trajectories. The comparison showed good agreement. As the input weather data was limited to $45°N < lat < 60°N$, $-10°E < lon < 25°E$ due to bandwidth and storage limitations, the contour plots in Figs. 21.10 and 21.11
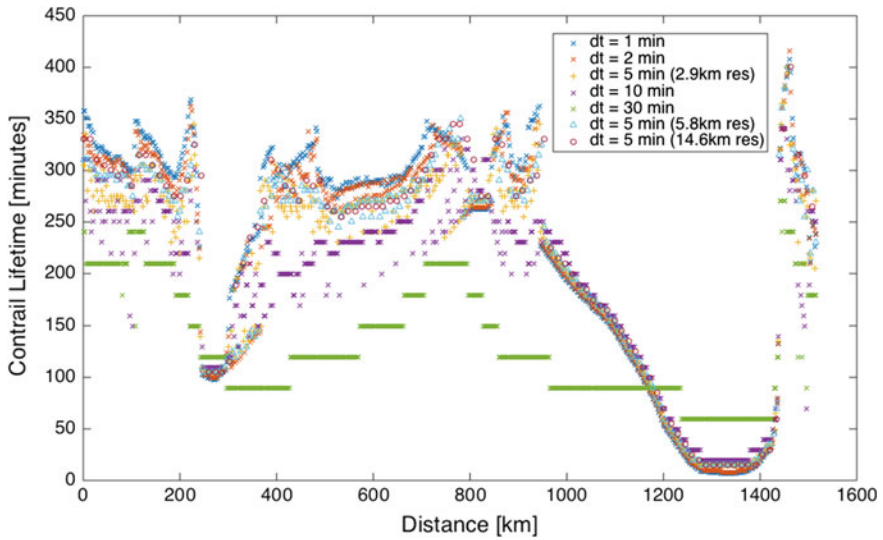
Fig. 21.7 Refinement tests, based on the contrail lifetime for the same trajectory and ambient conditions, at different time steps of 1 min (*blue* ×'s), 2 min (*red* ×'s), 5 min (*orange* +'s), 10 min (*purple* ×'s) and 30 min (*green* ×'s), and different grid resolutions of 5.8 km (*blue triangles*) and 14.6 km (*purple circles*) at a time-step of 5 min

Table 21.1 Timed results of refinement test

Time-step (min)	Mean resolution (km)	Algorithm run-time (s)
1	2.9	1142.9
2	2.9	525.7
5	2.9	194.3
10	2.9	89.1
30	2.9	21.7
5	5.8	100.6
5	14.6	41.8

show contrail lifetimes of 0 min outside the aforementioned geographical range. A drawback of the radial sounding is the varying spatial resolution at increasing ranges from the centre of the mapping. In particular, a high spatial resolution is attained in proximity of the centre, whereas at greater ranges the trajectories are spaced further apart so the spatial resolution is degraded. Issues such as spurious peaks and oscillations could arise when performing numerical extrapolation upon input data available at coarse resolutions, as noticed in Fig. 21.11. Further testing and validation could be conducted using different 2D/3D/4D contrail mapping patterns, like parallel horizontally or vertically spaced virtual sounding trajectories. It is important to verify whether different patterns produce a consistent mapping of the iso-contrail 2D/3D/4D region, as the orientation of the virtual sounding
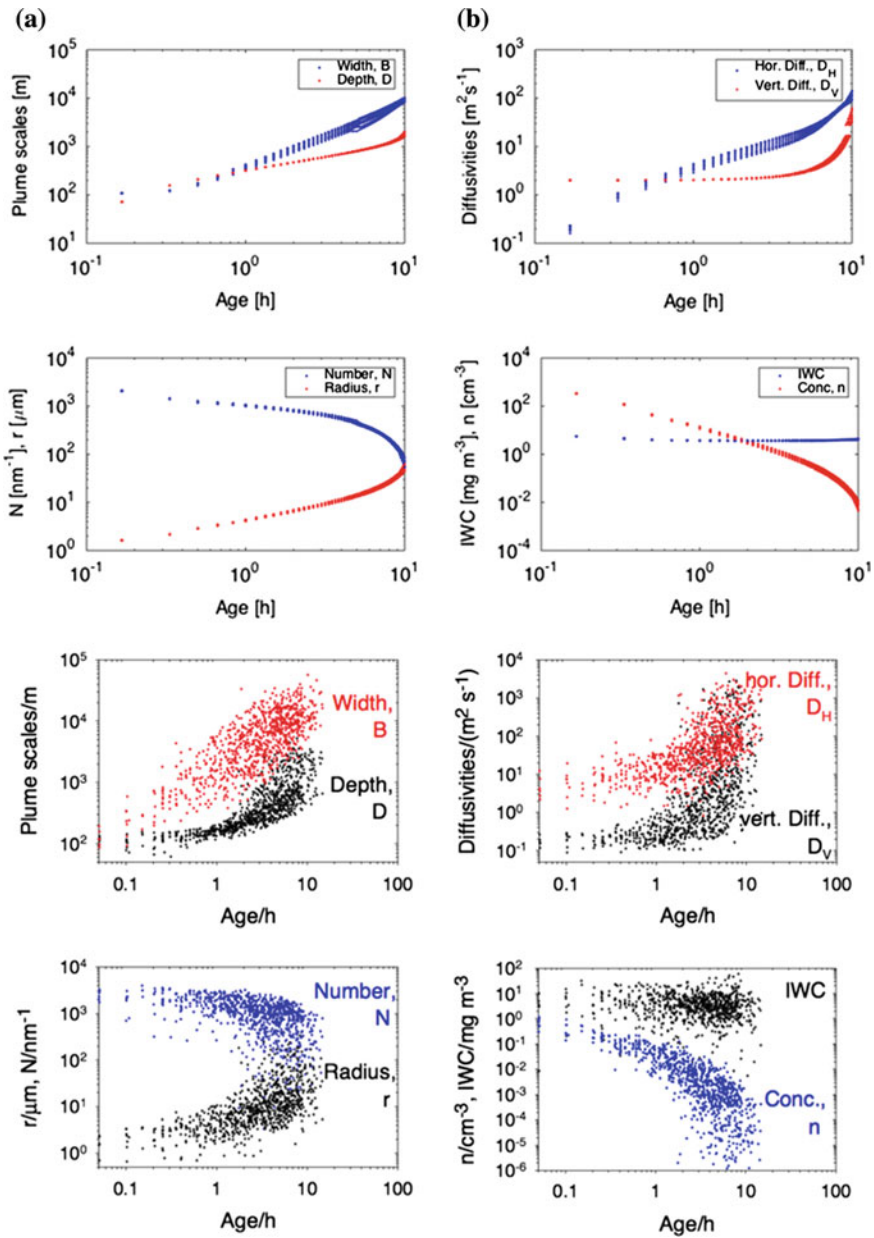
Fig. 21.8 Contrail properties versus age. **a** results from our validation activity. **b** results from Schumann (2012), licensed under CC-BY 3.0. *Top-left panel* Width B and depth D. *Top-right* Horizontal and vertical diffusivities. *Bottom-left* Total number of ice particles per nanometre flight distance N, ice particle volume mean radius r. *Bottom-right* Ice particle number concentration per volume n, ice water content per volume ρI

Fig. 21.9 Flight from Stockholm to Venice (*top left*); iso-persistence regions (*top right*) are mapped along the main flight path (*black line*) using virtual sounding trajectories (*blue lines*) at the initial time, $t = 0$, with the contrail lifetime integrated at a time-step of dt = 2 min. Iso-persistence is closely correlated to ambient temperature (*bottom left*) and RH$_i$ (*bottom right*)

Fig. 21.10 2D contour maps extrapolated from 'odd' trajectories only (*left plot*) and 'even' trajectories only (*right plot*)

trajectories could affect the time-advection of the contrail segments. However, more refined mapping patterns might prove too computationally expensive due to the increased number of trajectories to evaluate, compromising the intended algorithm exploitation in a MOTO framework. Furthermore, it can be noted that a higher resolution at the centre of the radial mapping pattern is desirable for online flight

Fig. 21.11 Zoomed-in plot of the iso-persistence region, obtained by contrail sounding, with lifetimes of (0, 1, 5, 30, 60, 120 and 250) minutes. At increasing distances from the centroid, oscillations or uneven patches arise due to the lower spatial resolutions

trajectory optimisation applications, as fuel/time optimal deviations from the nominal reference trajectory are mainly concerning the central portion, since origin and destination are constrained. In particular, considering constrained initial and final positions, the search domain for more optimal routings takes the form of a rhomboidal region, which is optimally mapped by a radial pattern.

21.4 Simulation Case Studies

21.4.1 Vortex Phase: Survival Factors for Different Size Aircraft

An investigation was conducted for the vortex phase using the linear contrail mapping algorithm. Findings indicate that larger aircraft tend to produce smaller contrail survival factors. This is in essence the fraction of ice particles surviving the vortex phase, given by $0 < f_{surv} < 1$. A higher f_{surv} indicates that a contrail is more likely to survive and persist past the vortex stage. Larger aircraft tend to produce stronger downwash vortices, which will in turn induce greater adiabatic warming, leading to greater sublimation in the plume. The properties of the five different aircraft used in the comparison are presented in Table 21.2.

Table 21.2 Table of aircraft parameters

Aircraft parameters					
Aircraft model	L45	B737	A320	B747	A380
Wingspan S_a (m)	14.6	34.4	34.1	64.4	79.75
Mass M_a (Mg)	8.5	65	64	310	450
TAS in cruise V_a (m s^{-1})	238.9	230	236.8	250	250
Fuel flow m_F (kg s^{-1})	0.17	0.69	0.73	3	3
Soot per fuel mass EI_{soot} (kg^{-1})	2.8e14				
Emission Index for water, EI_{H_2O}	1.23				
Fuel combustion heat Q_{fuel}, MJ kg^{-1}	43.2				
Propulsion efficiency η	0.3				
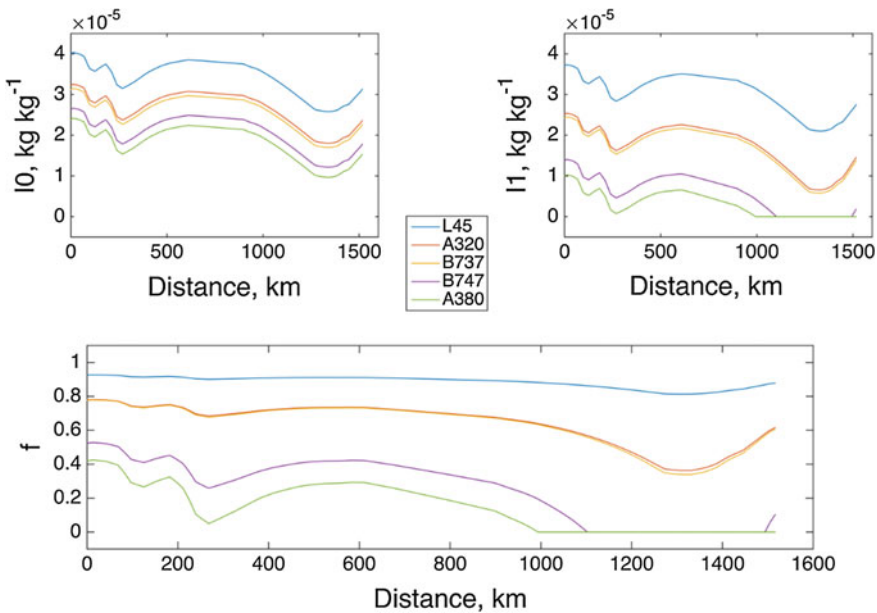
Fig. 21.12 Comparison of initial (*top left*), final (*top right*) ice ratios and survival factors along the vortex phase for different aircraft

The results shown in Fig. 21.12 are based on weather and trajectory data from the Europe case study (Lim et al. 2015). The ice mass ratio at the start of the vortex phase, I_0, measures the water content $\frac{M_{H_2O}}{M_{air}}$ in the plume, which differs between aircraft according to the amount of water emitted and the plume size. The ice mass ratio at the end of the vortex phase, I_1, measures the water content after sublimation due to adiabatic warming. The ratio between the two is the survival factor f_{surv}, given in Eq. (21.19). I_1 and I_0 are not constant along the flight path and depend on ambient temperature and RH$_i$. For small aircraft like the Learjet 45, it can be

observed that f_{surv} is close to 1 and remains relatively constant throughout the flight path, regardless of ambient conditions. This is an indication that vortex effects are small. For larger aircraft, f_{surv} fluctuates according to ambient conditions and the extent of fluctuation depends on the size of the aircraft/wake. Mid-sized aircraft like the Airbus A320 and Boeing 737 show less fluctuation in f_{surv} than the larger Boeing 747 and Airbus A380 aircraft. If wake vortexes are large enough, it is observed that all of the ice particles can sublimate at the end of the vortex phase and f_{surv} goes to zero. In Fig. 21.12, this occurs for the Boeing 747 and the Airbus A380 aircraft at 1100 and 1000 km from the origin, respectively.

21.4.2 Case Study—North America

The 4D contrail mapping algorithm was employed in a case study over North America. The sounding method involved a pulse comprising 12 trajectories radially spaced 30° apart. A fortnight's worth of weather data collected from the GFS showed that a direct flight from Chicago to Quebec City on 1 May, 2015 contained the most favourable conditions for contrail analysis. The full flight details are presented in Table 21.3 and the weather data in Fig. 21.13. In the figure, the temperature decreases with increasing latitude. Additionally, a significantly large region of ice super-saturation can be observed in the north-eastern corner.

21.4.2.1 Contrail Sounding

The temporal evolution of the contrail region is depicted in Fig. 21.14 and is again closely correlated to the ambient RH_i and temperature fields. As these conditions remain fairly constant from 0600 to 0900 h, the contrail region does not show major changes, except for a growth of its core size, as can be seen from the spread of the 160 min isobar. However, all the contrails do not persist beyond the 180 min mark. From 0900 to 1200 h, it is observed that the contrail region shrinks considerably, in line with the receding ice super-saturated region and the progressively warming temperatures. By 1500 h, the contrail region is completely disappeared.

Table 21.3 Details of the flight from Chicago to Quebec

Flight details	
Origin	Chicago O'Hare (42.0°N, 87.9°W)
Destination	Quebec Jean Lesage (46.8°N, 71.4°W)
Aircraft model	Airbus A320
Cruise flight path	KORD—CYQB
Flight time	2 h 25 min
Altitude	FL 340 /FL 300
Date	1 May 2015
Forecast timeframe	0600–1500 h/1800–0300 h (CST)
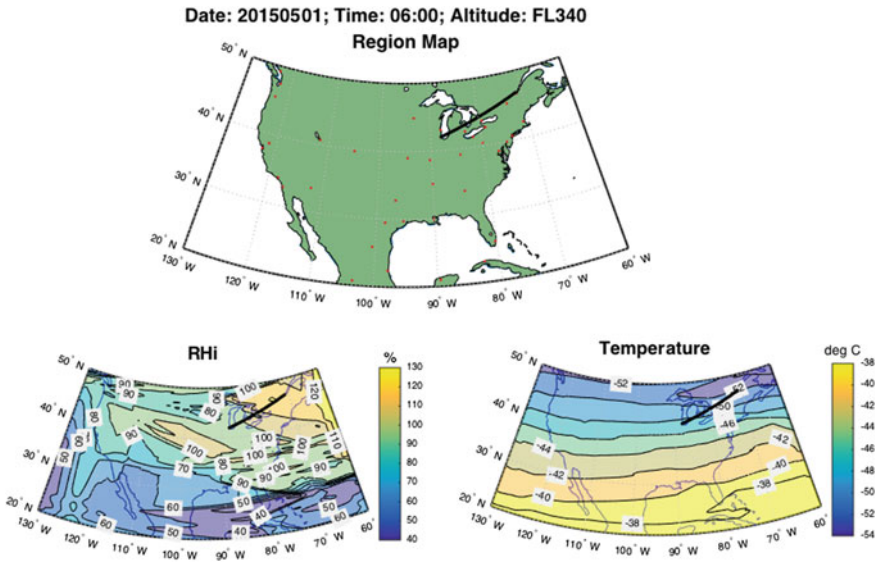
Fig. 21.13 Reference flight trajectory (*top*), RH$_i$ (*bottom left*) and temperature (*bottom right*) plots related to the North America case study
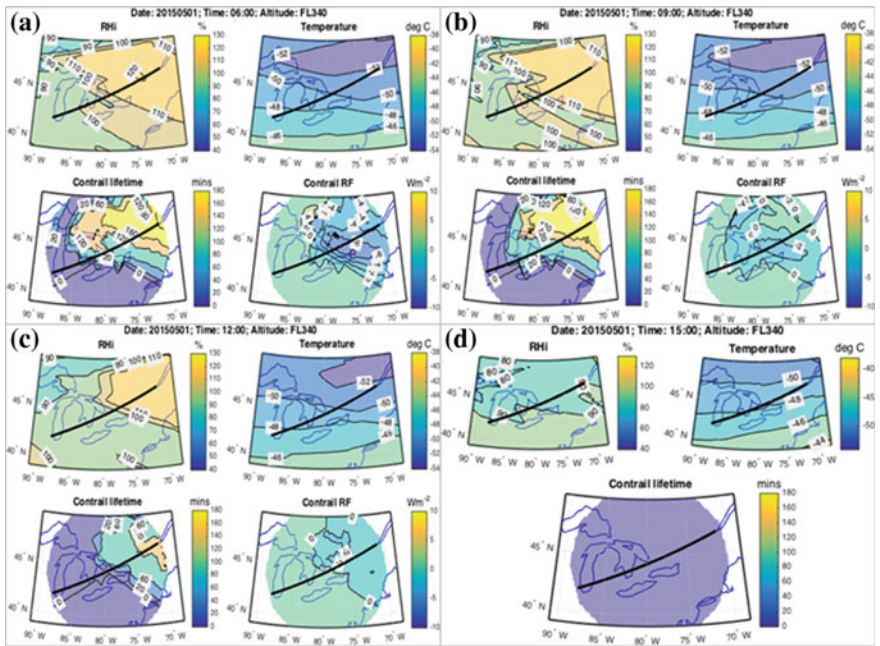
Fig. 21.14 Temporal evolution of contrail regions at 3 hourly intervals (**a** 0600 h; **b** 0900 h; **c** 1200 h; **d** 1500 h), with RH$_i$ (*top left*), temperature (*top right*), lifetime (*bottom left*) and RF (*bottom right*) regions for each timeframe

Notwithstanding the significant contrail persistence regions of up to 2 h, the net contrail-induced RF results negative from 0600 to 1200 h before the contrail region dissipates at 1500 h. Therefore, very different flight paths and schedules could be designated based on the optimisation objective. A minimization of the contrail-induced positive RF could permit paths through the contrail region at certain times of the day (Schumann et al. 2011) while a minimisation of the contrail persistence might produce significant rerouting (Zou et al. 2013; Soler et al. 2014; Sridhar et al. 2011).

21.4.2.2 Altitude Variations

Variations of the original case study were run to investigate, separately: the effects of a decrease in altitude, and the effects of changing the time of day. For the first study, a decrease in cruise altitude, from 34,000 to 30,000 ft, was evaluated. The resulting iso-contrail mappings are shown in Fig. 21.15. Despite the larger regions of ice super-saturation at the lower cruise altitude, the significantly higher temperatures suppress the formation of contrails as per the Schmidt-Appleman criterion, given in Eq. (21.7). This can be seen by comparing Fig. 21.15, which used the Schmidt-Appleman criterion as a restricting factor, with Fig. 21.16, which did not impose the Schmidt-Appleman criterion.
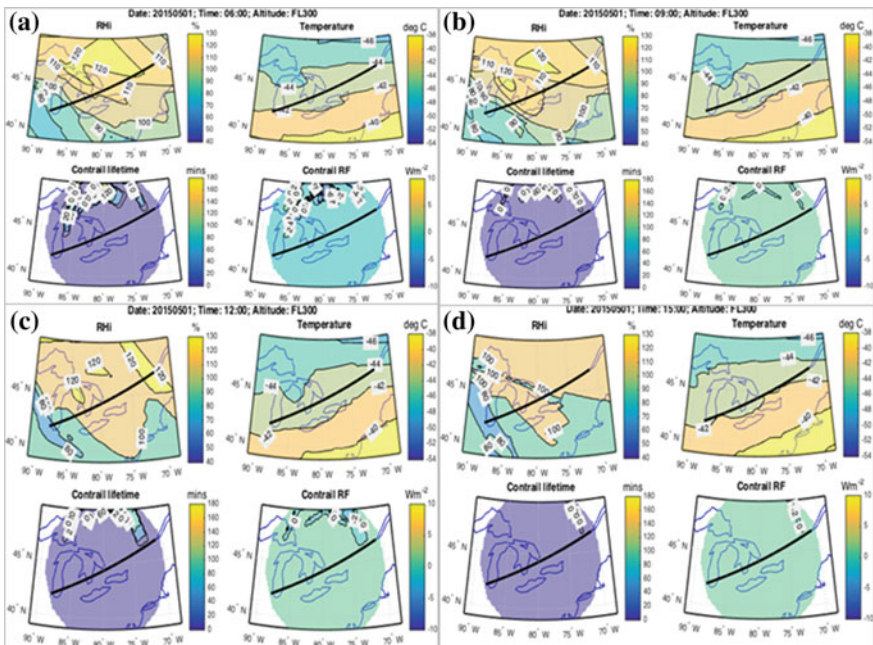
Fig. 21.15 Contrail regions at 30,000 ft, from 0600 to 1500 h. *Panels* show 3 hourly intervals of the contrail region (**a** 0600 h; **b** 0900 h; **c** 1200 h; **d** 1500 h)
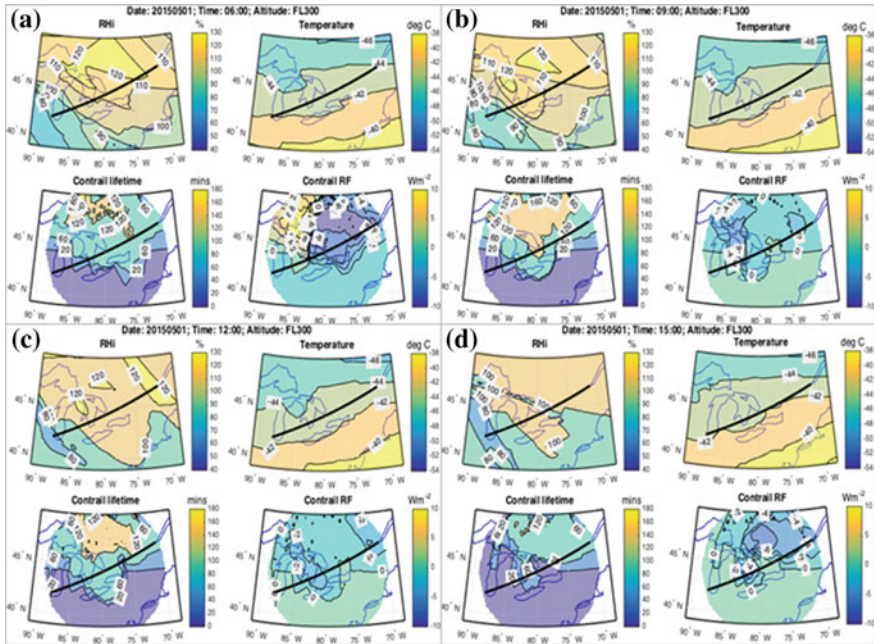
Fig. 21.16 Contrail regions as per Fig. 21.15 but without imposing the Schmidt-Appleman criterion. This assumes direct deposition of water vapour into ice particles without first undergoing a phase-change into water. The contrail regions are significantly larger than those presented in Fig. 21.15

The Schmidt-Appleman criterion determines the formation of contrails from the intersection between the plume mixing line and the water saturation curve. Contrails are catalysed by the moisture in the exhaust plume of the engine, which injects considerable quantities of additional water vapour into an already humid ambient air. In air that is close to water saturation, this causes the condensation of water droplets which quickly freeze and trigger the nucleation of ice in an ice super-saturated region.

The liquid saturation pressure of water vapour in the air increases with temperature and can become considerable at warmer conditions. This implies that at constant RH, increasingly higher water vapour concentrations in the exhaust are required to reach saturation at increasing temperatures. The addition of moisture from the exhaust, while significant enough at low temperatures to trigger the condensation of water droplets, might not be sufficient at higher temperatures (usually above −45 °C), despite ice super-saturated conditions. As it is difficult for water vapour to undergo deposition and transit directly into ice without a phase-change into water, the formation of contrails can be prevented by counter-acting the initial condensation and freezing of the water droplets. Nonetheless, other particulate emissions typically present in aircraft exhausts—such as nitrogen and sulphur oxides (NO_X and SO_X) and soot—act as ice nucleation sites, triggering the

formation of contrails under threshold conditions (Kärcher et al. 1996). The
dependence on the emitted NO_X, SO_X and soot concentrations is, however, not
modelled in the current contrail mapping algorithms.

21.4.2.3 Time-of-Day Variations

To investigate the time-of-day effect, an additional simulation case study was run
for the same weather data, flight trajectory and geographic region as the original
case study, but the time of day was offset by +12 h. This was done by artificially
modifying the local time in the algorithm while keeping all other parameters
unchanged. A different RF field was obtained for the same iso-persistence region
due to the difference in solar zenith angles at different times of the day. The results
are presented in Fig. 21.17. While the original scenario led to a RF of
$-8\,\text{W m}^{-2} < \text{RF} < 2\,\text{W m}^{-2}$, the offset case has a RF of $0\,\text{W m}^{-2} < \text{RF} < 8\,\text{W m}^{-2}$.
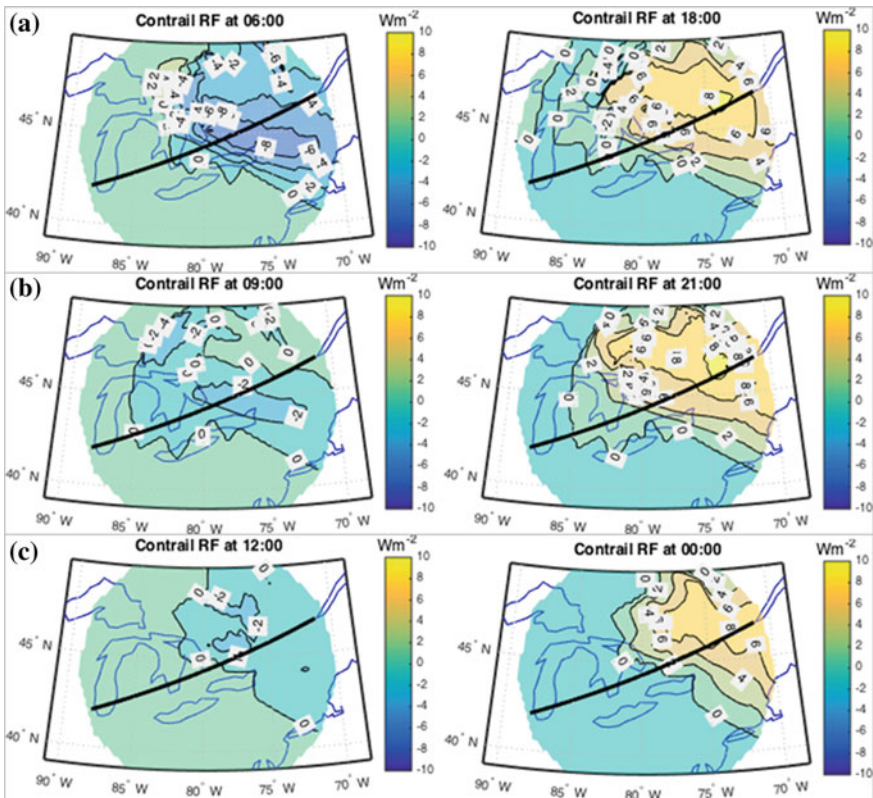
Fig. 21.17 Comparison of the time-of-day effect on contrail-induced RF. The original data is
presented *on the left* and the results with a time offset of 12 h are presented *on the right* for three
timeframes (**a**–**c**)

This is likely because most of the contrails in the case with a time offset were formed close to—and will most likely persist past—sunset, causing the greenhouse effect to dominate over the albedo effect and thus resulting in the positive net RF.

The diurnal variation of contrail RF can be exploited to negate the impact that aviation has on global warming. By shifting the air traffic density in persistent contrail formation regions to specific times of the day, determined with predictive methods using contrail models, the formation of contrails can be triggered such that they have a negligible or even advantageous environmental impact, with negative RF being the main criterion for determining the shift in traffic density (Myhre and Stordal 2001).

21.5 Conclusions

This chapter described in detail the development and preliminary numerical validation of contrail mapping algorithms conceived for integration in a MOTO framework. The theoretical background is reviewed, along with the assumptions and limitations introduced within the model development. Suitable analytical models are identified and implemented, in particular, to determine the formation, persistence and radiative properties of condensation trails (contrails) generated by aircraft. A linear contrail mapping algorithm is developed integrating the contrail formation, persistence and radiative evaluation models, allowing the evaluation of contrail occurrence and properties along an arbitrary aircraft flight trajectory. A 3-dimensional (3D) mapping of the contrail formation, persistence and radiative properties at a specific time instant is also developed, involving the execution of the linear contrail mapping algorithm along an arbitrary number of virtual sounding trajectories within instantaneous *pulses*. The sounding trajectories are constructed radially around a centre position, at individual flight levels. Multiple 3D pulses are combined to determine time variations, ultimately enabling a fully 4-Dimensional (4D) mapping in space and time of contrail formation, persistence and radiative forcing properties. These 4D contrail mappings can be exploited in a MOTO framework to assess and minimise the environmental impacts associated with contrails. The MOTO is the core element of the 4D trajectory planning functionalities in novel avionics and Air Traffic Management (ATM) systems currently being developed (Gardi et al. 2014, 2015; Ramasamy et al. 2014). The optimal flight routing can be updated in real-time during the online stage of the flight by suitable Avionics and ATM Decision Support Systems (DSS) integrating the contrail mapping algorithm. A preliminary numerical validation was performed, evaluating various 2-Dimensional plus Time (2D+T) mappings of the contrail formation regions generated by the 4D contrail mapping algorithm in different geographic locations and times of day. It is shown that while the extent of persistent contrail formation regions largely reflects the conditions of super-saturation responsible for the contrail formation, the net Radiative Forcing (RF) contribution of contrail has a considerable dependency on the time and date. This dependency

promotes the investigation of new air traffic optimisation techniques addressing the temporal distribution of traffic in contrail formation areas, which may prove more environmentally viable than the currently investigated decreases in cruise altitudes or lateral re-routings.

References

Atlas D, Wang Z, Duda DP (2006) Contrails to cirrus—Morphology, microphysics, and radiative properties. J Appl Meteorol Climatol 45:5–19. doi:10.1175/JAM2325.1

Burkhardt U, Kärcher B (2011) Global radiative forcing from contrail cirrus. Nat Clim Change 1:54–58

E Team (2015), ESRL Global Monitoring Division—GRAD Group. Available: http://www.esrl.noaa.gov/gmd/grad/solcalc/sollinks.html, 7 May 2015

European ATM Master Plan—The roadmap for sustainable air traffic management, SESAR JU, Brussels, Belgium, 2012

Flightpath 2050: Europe's vision for aviation—Report of the high level group on aviation research. European Commission—Directorate General for Mobility and Transport, Luxemburg, 2011

Galindo AAS, Candelario K (2011) Next generation air transportation system (NextGen)

Gardi A, Sabatini R, Ramasamy S, Kistan T (2014) Real-time trajectory optimisation models for next generation air traffic management systems. Appl Mech Mater 629:327–332. doi:10.4028/www.scientific.net/AMM.629.327

Gardi A, Sabatini R, Kistan T, Lim Y, Ramasamy S (2015) 4-Dimensional trajectory functionalities for air traffic management systems. In: Proceedings of integrated communication, navigation and surveillance conference (ICNS 2015), Herndon, VA, USA. doi:10.1109/ICNSURV.2015.7121246

Gierens K, Jensen E (1998) A numerical study of the contrail-to-cirrus transition. Geophys Res Lett 25(23):4341–4344. doi:10.1029/1998gl900151

Kärcher B, Peter T, Biermann U, Schumann U (1996) The initial composition of jet condensation trails. J Atmos Sci 53:3066–3083. doi:10.1175/1520-0469(1996)053

Kärcher B, Burkhardt U, Unterstrasser S, Minnis P (2009) Factors controlling contrail cirrus optical depth. Atmos Chem Phys 9:6229–6254. doi:10.5194/acp-9-6229-2009

Lee DS, Fahey DW, Forster PM, Newton PJ, Wit RC, Lim LL et al (2009) Aviation and global climate change in the 21st century. Atmos Environ 43:3520–3537

Lewellen DC, Lewellen WS (2001) The effects of aircraft wake dynamics on contrail development. J Atmos Sci 58:390–406

Lim Y, Gardi A, Sabatini R (2015) Modelling and evaluation of aircraft contrails for 4-dimensional trajectory optimisation. SAE technical paper 2015-01-2538. doi:10.4271/2015-01-2538

Minnis P (2003) Contrails. In: Encyclopedia of atmospheric sciences, pp. 509–520

Myhre G, Stordal F (2001) On the tradeoff of the solar and thermal infrared radiative impact of contrails. Geophys Res Lett 28:3119–3122. doi:10.1029/2001gl013193

NOAA (2015) NOMADS—NOAA Operational Model Archive and Distribution System. Available: http://nomads.ncep.noaa.gov/, 14 May 2015

Oberthür S (2003) Institutional interaction to address greenhouse gas emissions from international transport: ICAO, IMO and the Kyoto Protocol. Clim Policy 3:191–205

Organization for nctoolbox development (2015). Available: https://github.com/nctoolbox, 11 May 2015

Ramasamy S, Sabatini R, Gardi A, Kistan T (2014) Next generation flight management system for real-time trajectory based operations. Appl Mech Mater 629:344–349. doi:10.4028/www.scientific.net/AMM.629.344

Reda I, Andreas A (2008) Solar position algorithm for solar radiation applications. National Renewable Energy Laboratory (NREL), US Dept of Energy NREL/TP-560-34302, Golden, CO, USA

Rogers RR (1976) A short course in cloud physics. A. Wheaton & Co.

Sabatini R, Gardi A, Ramasamy S, Kistan T, Marino M (2015) Modern avionics and ATM systems for green operations. In: Blockley R, Shyy W (eds) Encyclopedia of aerospace engineering, ch. eae1064. Wiley, New York

Schumann U (2012) A contrail cirrus prediction model. Geosci Model Dev 5:543–580. doi:10.5194/gmd-5-543-2012

Schumann U, Graf K, Mannstein H (2011) Potential to reduce the climate impact of aviation by flight level changes. In: 3rd AIAA atmospheric and space environments conference, AIAA paper, vol 3376, pp 1–22. doi:10.2514/6.2011-3376

Schumann U, Mayer B, Graf K, Mannstein H (2012) A parametric radiative forcing model for contrail cirrus. J Appl Meteorol Climatol 51:1391–1406. doi:10.1175/jamc-d-11-0242.1

SESAR and the Environment (2010) SESAR joint undertaking—European Commission, Brussels, Belgium

Soler M, Zou B, Hansen M (2014) Flight trajectory design in the presence of contrails: application of a multiphase mixed-integer optimal control approach. Transp Res Part C Emerg Technol 48:172–194. doi:10.1016/j.trc.2014.08.009

Sonntag D (1994) Advancements in the field of hygrometry. Meteorol Z 3:51–66

Sridhar B, Ng H, Chen N (2011) Aircraft trajectory optimization and contrails avoidance in the presence of winds. J Guid Control Dyn 34:1577–1584. doi:10.2514/1.53378

Sussmann R, Gierens KM (2001) Differences in early contrail evolution of two-engine versus four-engine aircraft: Lidar measurements and numerical simulations. J Geophys Res 106(D5), 4899. doi:10.1029/2000jd900533

Unterstrasser S, Gierens K, Spichtinger P (2008) The evolution of contrail microphysics in the vortex phase. Meteorol Z 17:145–156. doi:10.1127/0941-2948/2008/0273

Veness C (2015) Movable type scripts. Available: http://www.movable-type.co.uk/scripts/latlong.html, 25 March 2015

Zou B, Buxi GS, Hansen M (2013) Optimal 4-D aircraft trajectories in a contrail-sensitive environment. Netw Spat Econ. doi:10.1007/s11067-013-9210-x

Chapter 22
In-Flight Icing Simulations on Airfoils

Nermin Uğur, Serkan Özgen, İlhan Görgülü and Volkan Tatar

Abstract It is crucial to predict the ice mass, shape and regions of the airframe which are prone to icing in order to design and develop de/anti-icing systems for aircraft and airworthiness certification. In the current study, droplet collection efficiency and ice shape predictions are performed using an originally developed computational tool for a wing tip for which experimental and numerical data are available. Ice accretion modeling consists of four steps in the developed computational tool: flow field solution, droplet trajectory and collection efficiency calculations, thermodynamic analyses and ice growth calculations using the Extended Messinger Model. The models used for these steps are implemented in a FORTRAN code, which is used to analyze ice accretion on 2D geometries including airfoils and axisymmetric inlets. The results are compared with numerical and experimental data available in the literature.

Nomenclature

Alphanumerical Symbols

A_p	Droplet cross-sectional area, m^2
b	Span of wing, m
B	Ice thickness, m
C_D	Droplet drag coefficient
C_p	Pressure coefficient
D	Drag force, N

N. Uğur · S. Özgen (✉)
Middle East Technical University, Ankara, Turkey
e-mail: sozgen@metu.edu.tr

N. Uğur
e-mail: nermin.ugur@metu.edu.tr

İ. Görgülü · V. Tatar
TUSAŞ Engine Industries Inc., Eskişehir, Turkey
e-mail: Ilhan.Gorgulu@tei.com.tr

V. Tatar
e-mail: Volkan.Tatar@tei.com.tr

279

g	Gravitational acceleration, ms^{-2}
h	Water layer thickness, m
HTC	Convective heat transfer coefficient, $\text{W/m}^2.\text{K}$
k	Thermal conductivity, W/m.K
LWC	Liquid Water Content, g/m^3
L_F	Latent heat of solidification, J/kg
m	Droplet mass, kg
$\dot{m}_{in}$	Mass flow rate of runback water, $\text{kg/m}^2\text{s}$
$\dot{m}_{e,s}$	Mass flow rate of evaporating (or sublimating) runback water, $\text{kg/m}^2\text{s}$
M	Mach number
MVD	Median Volume Diameter, μm
P	Pressure (N/m^2)
r	Recovery factor
R	Gas constant, J/kg.K
t	Time, s
T	Temperature, K
U_e	Boundary layer edge velocity, m/s
V_x, V_y	Flow velocity components at the droplet location, m/s
V_{rel}	Relative velocity, m/s
V_∞	Freestream velocity, m/s
$\dot{x}, \dot{y}$	Droplet velocity components, m/s
$\ddot{x}, \ddot{y}$	Droplet acceleration components, m/s^2
y	Spanwise distance from root, m

Greek Letters

α   Angle of attack
β   Collection efficiency
γ   Angle between droplet and flow velocity, Ratio of specific heats
ρ   Ambient density (kg/m^3)
θ   Temperature in water layer, K

Subscripts

a	Ambient
f	Freezing
i	Ice
s	Substrate
static	Static freestream conditions
w	Water

22.1 Introduction

In-flight icing on airframes and engines may cause great risk to flight safety due to aerodynamic performance degradation (Mason et al. 2006). Therefore, it is very important to simulate ice accretion to develop anti-icing systems and airworthiness certification purposes (EASA 2015). In this study, icing simulations on a NACA 64A008 wing tip geometry are performed.

In the current approach, the study of Myers (2001) is used as a base for the ice accretion model. Droplet trajectories, collection efficiency calculations and convective heat transfer coefficient calculations are performed with the same approach as in Özgen and Canıbek (2009). NASA Report of Bidwell and Papadakis (2005) is an important reference with numerical and experimental icing analyses data for tail sections, which are used as the reference to compare the results obtained in the current study.

22.2 Methodology

In this section, four modules used in the current approach are briefly explained.

22.2.1 Flow Field Solution

In order to determine the flow velocities required for droplet trajectory calculations, 2D Hess-Smith panel method is used. The external velocity distribution is also provided through this solution, which is used in boundary layer calculations to obtain the convective heat transfer coefficients. In this model, the airfoil is divided into quadrilateral panels, each of which has a constant strength source singularity element plus a vortex singularity that is constant for all panels. Using the flow tangency boundary condition at the collocation points of the surface panels and the Kutta condition at the trailing edge, the singularity strengths are obtained. This provides the velocity potential, in other words, the flow velocity components at any point in the flow field.

22.2.2 Droplet Trajectories and Collection Efficiency Calculations

For droplet trajectories, the following assumptions are employed:

- Droplets are assumed to be spherical.
- The flow field is not affected by the presence of the droplets.
- Gravity and aerodynamic drag are the only forces acting on the droplets.

The governing equations for droplet trajectories are

$$m\ddot{x}_p = -D\cos\gamma, \tag{22.1}$$

$$m\ddot{y}_p = -D\sin\gamma + mg, \tag{22.2}$$

$$\gamma = \tan^{-1}\frac{\dot{y}_p - V_y}{\dot{x}_p - V_x}, \tag{22.3}$$

$$D = \frac{1}{2}\rho V_{rel}^2 C_D A_p, \tag{22.4}$$

$$V_{rel} = \sqrt{(\dot{x}_p - V_x)^2 + (\dot{y}_p - V_y)^2} \tag{22.5}$$

Droplet drag coefficients are calculated using an empirical drag law based on the droplet Reynolds number (Özgen and Canıbek 2009). The droplet trajectories are obtained with the integration of Eqs. 22.1–22.2 over time until the impact of the droplets to the geometry occurs. The particle impact pattern on the section determines the amount of water that impinges on the surface and the region subject to icing. The local collection efficiency (β) is defined as the ratio of the area of impingement to the area through which water passes at some distance upstream of the section.

22.2.3 Thermodynamic Analyses

In order to calculate the convective heat transfer coefficients, a 2D Integral Boundary Layer Method is employed for both laminar and turbulent flows (Özgen and Canıbek 2009).

22.2.4 Extended Messinger Method

Ice accretion analyses are performed with the Extended Messinger Method. The ice shape prediction is based on the standard method of phase change or the Stefan problem. The governing equations for the phase change problem are mainly: energy equations in the ice and water layers, mass conservation equation and a phase change condition at the ice/water interface (Myers 2001).

$$\frac{\partial T}{\partial t} = \frac{k_i}{\rho_i C_{pi}} \frac{\partial^2 T}{\partial y^2}, \tag{22.6}$$

$$\frac{\partial \theta}{\partial t} = \frac{k_w}{\rho_w C_{pw}} \frac{\partial^2 \theta}{\partial y^2}, \tag{22.7}$$

$$\rho_i \frac{\partial B}{\partial t} + \rho_w \frac{\partial h}{\partial t} = \rho_a \beta V_\infty + \dot{m}_{in} - \dot{m}_{e,s} \tag{22.8}$$

$$\rho_i L_F \frac{\partial B}{\partial t} = k_i \frac{\partial T}{\partial y} - k_w \frac{\partial \theta}{\partial y} \tag{22.9}$$

In Eq. (22.8), $\rho_a \beta V_\infty$, $\dot{m}_{in}$ and $\dot{m}_{e,s}$ are impinging, runback and evaporating (or sublimating) water mass flow rates for a control volume, respectively. The coordinate y is normal to the surface. The boundary and initial conditions applicable to Eqs. 22.6–22.9 are as follows (Myers 2001):

- Ice is in perfect contact with the wing surface:

$$T(0,t) = T_s \tag{22.11}$$

The surface temperature is taken to be the recovery temperature (Gent et al. 2000):

$$T_s = T_a + \frac{V_\infty^2 - U_e^2}{2C_p} \frac{1 + 0.2rM^2}{1 + 0.2M^2} \tag{22.12}$$

In the above expression, $M = V_\infty/a_\infty$, while the speed of sound is given by $a_\infty = \sqrt{\gamma R T_a}$. Additionally, r is the adiabatic recovery factor.
- The temperature is continuous at the ice/water boundary and is equal to the freezing temperature:

$$T(B,t) = \theta(B,t) = T_f. \tag{22.13}$$

- At the air/water (glaze ice) or air/ice (rime ice) interface, heat flux is determined by convection, radiation, latent heat release, cooling by incoming droplets, heat brought in by runback water, evaporation or sublimation, aerodynamic heating and kinetic energy of incoming droplets.
- Wing surface is initially clean:

$$B = h = 0, \quad t = 0. \tag{22.14}$$

In the current approach, each panel constituting the geometry is also a control volume. The above equations are written for each panel and ice is assumed to grow perpendicularly to a panel.

22.3   Results and Discussion

A swept, tapered NACA 64A008 wing tip geometry (leading edge sweep angle of 29.1°, a root chord of 116.21 cm, a taper ratio of 0.62 and a cylindrical tip) is studied. The results are compared with numerical (PMARC, a first-order 3D potential flow panel code) and experimental and numerical data presented by Bidwell and Papadakis (2005). It should be noted that 2D results of the current study are compared with 3D experimental and numerical results. Upon investigation of the results given in (Bidwell and Papadakis 2005), the ice shapes at different spanwise locations are similar therefore, three-dimensional effects are not prominent which justifies the 2D analysis of the current study.

Figures 22.1, 22.2, 22.3, 22.4, 22.5, 22.6, 22.7 and 22.8 show C_p distributions and collection efficiencies for $V = 75$ m/s, $T_{static} = 7$ °C and $P_{static} = 95{,}840$ Pa. In

Fig. 22.1 C_p distribution for $\alpha = 0°$
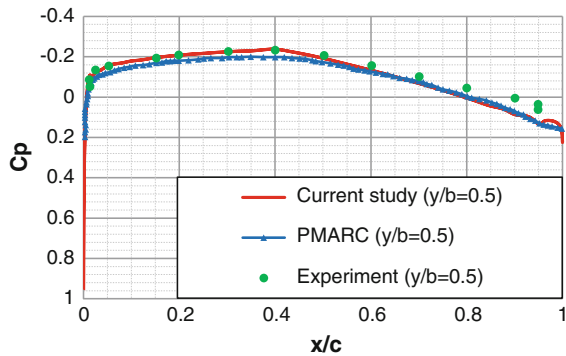
Fig. 22.2 C_p distribution for $\alpha = 6°$
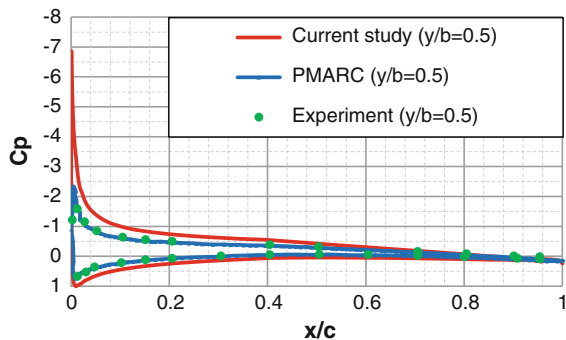
Fig. 22.3 Collection
efficiency distribution for
MVD = 11 μm and α = 0°
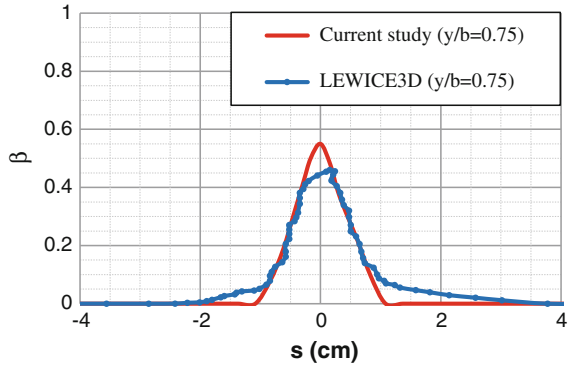
Fig. 22.4 Collection
efficiency distribution for
MVD = 11 μm and α = 6°
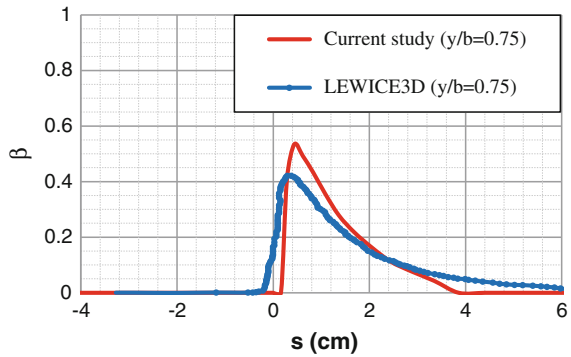
Fig. 22.5 Collection
efficiency distribution for
MVD = 21 μm and α = 0°
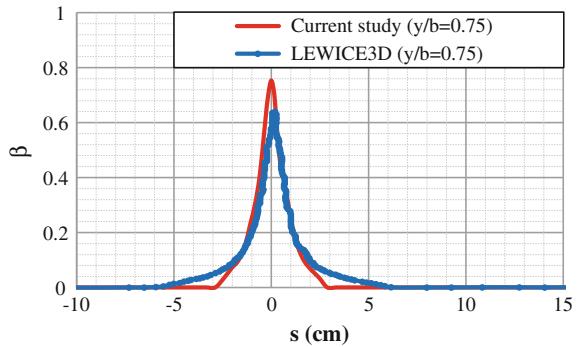
Figs. 22.1 and 22.2, C_p distributions are shown at α = 0° and α = 6°, respectively at the y/b = 0.5 spanwise location of the wing. In both cases, current study results are in good agreement with numerical and experimental data.

Figures 22.3, 22.4, 22.5, 22.6, 22.7 and 22.8 show the collection efficiency results of the current study and their comparison with numerical results obtained

Fig. 22.6 Collection
efficiency distribution for
MVD = 21 μm and α = 6°
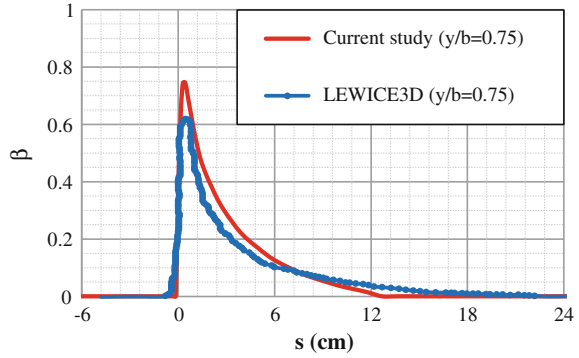
Fig. 22.7 Collection
efficiency distribution for
MVD = 92 μm and α = 0°
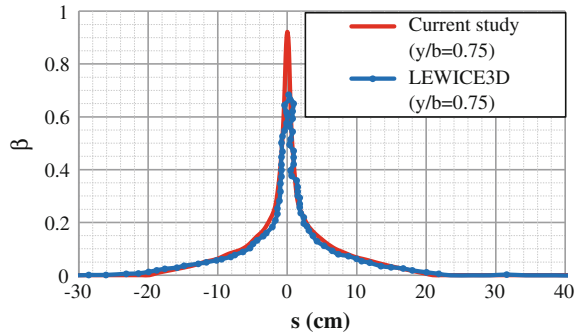
Fig. 22.8 Collection
efficiency for MVD = 92 μm
and α = 6°
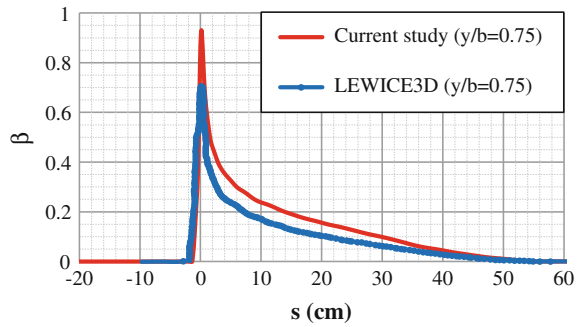
from LEWICE3D. Negative values of the streamwise distance (s) show the upper
surface, while positive values depict the lower surface. In Figs. 22.3, 22.4, 22.5,
22.6, 22.7 and 22.8, collection efficiencies for MVD = 11, 21 and 92 μm and
α = 0° and 6° at y/b = 0.75 spanwise location are shown. It is clearly seen that
current study results match well with LEWICE 3D results. As MVD increases,
maximum β and the impingement zone (region where β > 0) increases as well and
ice is expected to accrete more on the lower surface for α = 6° cases as expected.

In this part of the study, HTC (Heat Transfer Coefficient) and ice shape results are presented for V = 75 m/s, P_{static} = 95,840 Pa, MVD = 21 µm, exposure time of 30 min and varying α, T_{static} and LWC (Liquid Water Content). Such a long exposure is a challenge for the developed tool and requires a multi-layer approach, especially for glaze ice conditions (ambient temperature close to freezing and high LWC). Thus, exposure time is divided into segments, where the flow field solution, droplet trajectories, collection efficiencies and finally ice accretion calculations are repeated for each time interval.

Figures 22.9 and 22.10 show HTC distribution and ice shape predictions for the mentioned conditions. HTC results match well with the numerical data. Ice mass accumulated on the airfoil agrees well with the literature data. The iced region is also well predicted, but the maximum ice thickness is overestimated. The exposure time is divided into 20 sub-intervals, because of glaze ice conditions.

For T_{static} = −29.9 °C, LWC = 0.2 g/m^3 and keeping all other parameters fixed, the ice shape seen in Fig. 22.11 is obtained. The obtained results are in good agreement with numerical data although the maximum ice thickness is slightly overestimated. For this calculation, exposure time is broken down into 10

Fig. 22.9 HTC distribution for α = 0°, T_{static} = −9.3°, LWC = 0.695 g/m^3
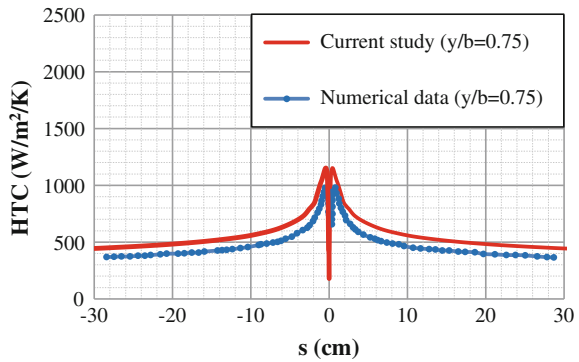
Fig. 22.10 Ice shape for α = 0°, T_{static} = −9.3°, LWC = 0.695 g/m^3
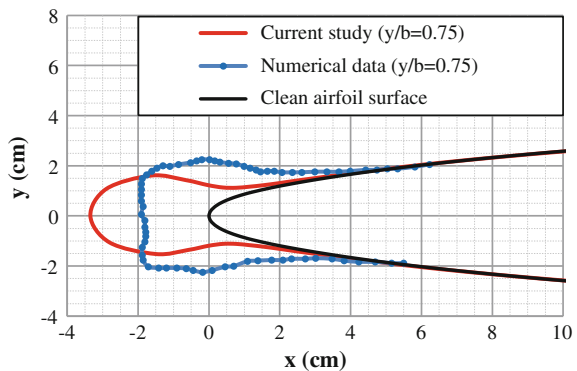
sub-intervals, because the conditions correspond to rime ice conditions and a large number of computational steps are not necessary.

Then, the angle of attack is increased to 6° and the calculations are repeated. HTC and ice shape results are obtained as in Figs. 22.12, 22.13 and 22.14. Smaller values of HTC are calculated on the lower surface when compared with $\alpha = 0°$ case. Ice accumulates more on the lower surface due to positive angle of attack.

Fig. 22.11 Ice shape for $\alpha = 0°$, $T_{static} = -29.9°$, LWC = 0.2 g/m^3
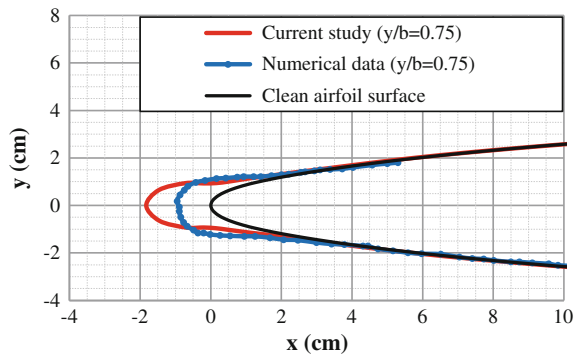
Fig. 22.12 HTC distribution for $\alpha = 6°$, $T_{static} = -9.3°$, LWC = 0.695 g/m^3
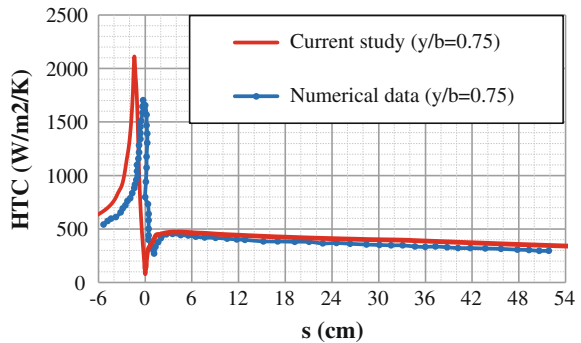
Fig. 22.13 Ice shape for $\alpha = 6°$, $T_{static} = -9.3°$, LWC = 0.695 g/m^3
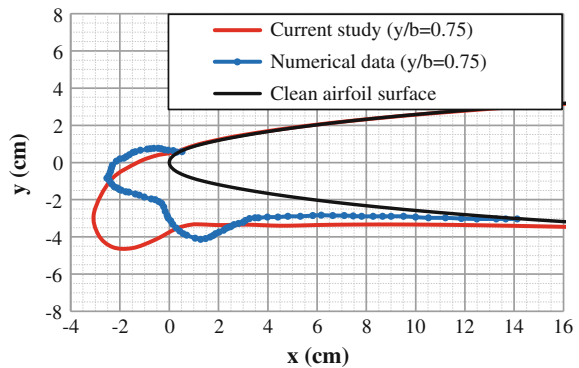
Fig. 22.14 Ice shape for
$\alpha = 6°$, $T_{static} = -29.9°$,
LWC = 0.2 g/m^3
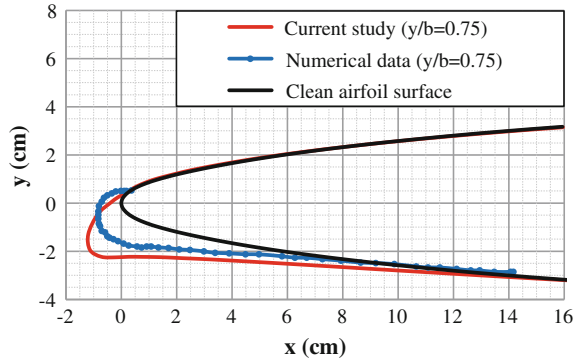
Iced region and ice mass are predicted to be similar to numerical data although the ice thicknesses are overpredicted as in the previous cases.

22.4   Conclusions

HTC, collection efficiency and ice shape predictions are done for NACA 64A008 wing tip. The calculations are performed for different MVD, temperature, α and LWC values. The results are compared with numerical and experimental data. It can be deduced that the current study results are in good agreement with the reference data and the current tool can be used for certification purposes as well as academic purposes.

References

Bidwell CS, Papadakis M (2005) Collection efficiency and ice accretion characteristics of two full scale and one ¼ scale business jet horizontal tails. NASA/TN-2005-213653
European Aviation Safety Agency (EASA) (2015) Certification specifications for large aeroplanes CS-25
Gent RW, Dart NP, Cansdale JT (2000) Aircraft icing. Phil Trans R Soc Lond A 358:2873–2911
Mason JG, Strapp JW, Chow P (2006) The ice particles threat to engines in flight, In: 44th AIAA aerospace sciences meeting and exhibit, Reno, AIAA 2006-206
Myers TG (2001) Extension to the Messinger model for aircraft icing. AIAA J 39:211–218
Özgen S, Canıbek M (2009) Ice accretion simulation on multi-element airfoils using extended Messinger model. Heat Mass Transf 45(3):305–322

Chapter 23
Arrival Traffic Sequence for Converging Runways

Özlem Şahin and Öznur Usanmaz

Abstract Vectoring, automated methods and speed control are available sequencing methods defined by International Civil Aviation Organization (ICAO). Point Merge System (PMS) is an innovative method for merging and sequencing arrival traffic flows. In this study, proposed PMS model for converging runways will be applied to International Istanbul Ataturk Airport. PMS and vectoring will be compared in real-time simulation and the results are assessed in terms of traffic sequence.

23.1 Introduction

The optimum planning and sequencing of arrival traffic flows is a primary task at arrival operations (ICAO-9854 2005). Three different sequencing methods called automated sequencing, speed and vectoring are defined by International Civil Aviation Organization (ICAO). Using traffic management advisory displays, relative position indicators and required time of arrival which are considered as automated sequencing systems explain the first method. Speed control is another method which is applied before executing the procedure. Speed control provides the separation between aircraft and also increases the predictability of performance between different aircraft. The last method is vectoring which is the most flexible way for sequencing arrival flows and the most frequently used; but, in busy conditions controllers should give rapid decision and aircrews should apply these instructions in a critical period (ICAO-9931 2010). In vectoring, traffic flows need to implement numbers of instructions. In this period it is difficult to predict the actual position and sequence of traffic in density terminal areas. Thus, high-frequency occupancy time, the lack of situation awareness and complex dispersion of traffic could be appeared (Favennec et al. 2009). It could be noted that

Ö. Şahin (✉) · Ö. Usanmaz
Faculty of Aeronautics and Astronautics, Anadolu University, Eskişehir, Turkey
e-mail: osahin5@anadolu.edu.tr

291

vectoring provides the least predictability and keeps pilots in uncertainty situation (ICAO-9931 2010).

Point Merge System (PMS) is a new method for merging and sequencing arrival traffic flows (Eurocontrol 2010) added to ICAO sequencing classification and PMS creates the major part of this study. PMS is based on area navigation (RNAV) route structure. Sequencing legs, merge point, and range rings are the elements of PMS. Sequencing legs are defined as an arc of circle and they have equal distance from merge point. These predefined routes are vertically separated and provide spacing between succeeding and preceding traffic. Thus, controllers could easily decide spacing and sequencing between aircraft on the legs. Also, range rings helps controllers calculating distances between aircraft left the legs. After given "direct to" instruction, traffic proceeds to merge point and starts descending (Ivanescu et al. 2009).

Boursier et al. (2007) define a method for merging aircraft flows without heading instructions for landing on a single runway. Boursier et al., from controller and pilot perspectives, investigated benefits of a new method based on the RNAV route structure and called it the PMS compared with vectoring. It was observed that the new method was comfortable, safe, and accurate. Moreover, the results show a decrease in the number of heading and level instructions. Thus, a reduction in frequency occupancy was also obtained.

Another paper published by Ivanescu et al. (2009) modeled a PMS aimed at handling traffic without using radar vectors and merging four arrival traffic flows for landing on a single runway. Vectoring and PMS were compared in fast-time and real-time simulations. Significant reductions were found in term of mean controller task load (20 ± 1 %), the number of instructions to pilot (~ 30 %) and fuel consumptions (170 ± 14 kg).

In this study, prepared PMS model proposal for converging runways will be applied to International Istanbul Ataturk Airport. In real-time simulation, vectoring are compared with PMS method according to sequence of arrival traffic to converging runways and the results are assessed in terms of traffic sequence. Introduction and literature array.

23.2 Methodology

Today, instead of conventional procedures, area navigation terminal procedures, which provide effective and efficient use of terminal maneuvering area (TMA), are beginning to be used for handling and sequencing arrival traffic operations. Although RNAV terminal procedures are effective in busy and congested TMAs, there is a need for vectoring, especially in open standard instrument arrival (STAR) RNAV applications. Therefore, additional caution could help in dealing with increased traffic demand. An innovative method for merging arrival flows from

different directions without using open loop radar vectors is called the PMS. This method is based on the RNAV route structure (Boursier et al. 2007) and could be defined as an RNAV STAR. It is a transitional or initial approach procedure, or a portion thereof, and is defined by a single point called the merge point and pre-defined sequencing legs, iso-distant from the merge point, for path stretching and shortening (Favennec et al. 2010).

PMS is added to ICAO sequencing classification as a new sequencing method. Implementing PMS, traffic maintain the sequencing legs, defined as a circle of arc and limited by flight level, until given to direct to instruction (ICAO 9931 2010). By using predefined sequencing routes, delay is provided without holding and traffic is ordered easily and is allowed flying to merge point.

Traffic could get different sequencing priority for landing. One of them is First Come First Served (FCFS) which is the common and simple way for the assignment of aircraft landing sequencing. Aircraft lands according to Estimated Time Arrival (ETA) to runway. The controller is needed only for maintaining wake turbulence separation between aircraft. FCFS is preferred because it is simple and easy method. So as to limited flexibility or limiting the re-sequencing of traffic, FCFS prevents to increase the workload of controllers. And also aircraft lands in FCFS order according to ETA so FCFS is fair scheduling (Lee 2008). PMS method is similar to FCFS. PMS allows traffic to land according to ETA of merge point besides FCFS let traffic to land according to ETA of runway.

In this study, PMS model is designed for merging and sequencing arrival traffic to converging runways and the design parameters of merge point and sequencing legs are defined. Proposal PMS model is offered as a common method and aims to

Fig. 23.1 A PMS model proposal for converging runways

sequence arrival traffic for converging runways and this general PMS model proposal in simulation environment is given Fig. 23.1.

23.2.1 Sequencing in PMS

Lateral separation minima is a significant factor for airspace design model. In this study, horizontal and longitudinal separation minima are considered as 3 nautical miles (nms) between aircraft. Moreover, while designing procedure, sequencing legs are separated vertically (1000 ft). Traffic could be completed descending and be maintained the defined levels before at least 20 nms to initial fix of PMS procedure. Without holding, traffic could fly on sequencing legs until given direct to instruction to merge point, called MERGE, and after reached MERGE, it could be kept 6000 ft. After leaving merge point, aircraft proceed to runway in use and starts descending according to minimum radar vectoring altitude (MRVA). After reaching final approach point (FAP), traffic intercepts ILS course and lands.

In this study, for comparing PMS and vectoring methods, Istanbul TMA belonged to Istanbul Ataturk International Airport are used in simulation.

In PMS method, arrival traffic to Istanbul TMA could follow the standard arrival routes which connecting with the route structure of PMS procedure. The controller decides the sequence of traffic and gives to instruction to proceed merge point which is located 15 nms from FAP. After passing merge point, traffic proceeds to a defined point on runway course 5 nms to FAP and are prepared to land. Converging runways in use are 17L and 23. The controller decides to runway in use in terms of sequencing. For runway 17L and runway 23, FATIH and BKZ points are used, respectively.

In vectoring method, arrival traffic to Istanbul TMA could maintain FL 170. The controller prepares the approach sequence by giving instructions such as heading, flight level and speed. In case of no intervention of controller, traffic could implement the published conventional standard arrival routes. Traffic could join the holding pattern if needed. The controller is responsible for providing optimum approach and landing sequence. Also, the controller gives a decision about the choice of runway in use.

23.3 Results and Discussion

In simulation, two different controllers (C_A, C_B) are worked for same traffic scenario, 31 arrival traffic, by using different methods, PMS and Vector.

In PMS method, the sum of the difference of traffic sequence value is 14. In vector, it is found 58 (Table 23.1).

Table 23.1 Traffic sequence by using PMS and vectoring

Aircraft ID	PMS		Vector		Difference	
	C_A	C_B	C_A	C_B	PMS difference	Vector difference
ID 24	1	1	1	1	0	0
ID 2	2	2	2	2	0	0
ID 32	3	3	3	5	0	2
ID 5	4	4	4	4	0	0
ID 1	5	5	5	7	0	2
ID 10	6	7	6	6	1	0
ID 23	7	6	7	3	1	4
ID 22	8	8	8	9	0	1
ID 42	9	9	11	10	0	1
ID 37	10	11	10	12	1	2
ID 35	11	10	14	14	1	0
ID 13	12	12	13	13	0	0
ID 39	14	14	12	11	0	1
ID 15	13	13	15	15	0	0
ID 25	15	15	16	16	0	0
ID 48	16	16	17	22	0	5
ID 47	17	19	18	24	2	6
ID 7	19	18	19	18	1	1
ID 20	18	17	21	20	1	1
ID 29	20	21	24	27	1	3
ID 19	21	22	26	32	1	6
ID 38	22	20	23	21	2	2
ID 14	23	24	20	17	1	3
ID 12	25	25	25	23	0	2
ID 45	24	23	22	19	1	3
ID 44	26	26	27	26	0	1
ID 16	27	27	28	28	0	0
ID 33	28	28	31	29	0	2
ID 49	29	29	29	30	0	1
ID 28	30	30	33	25	0	8
ID 41	31	31	32	31	0	1
Total					14	58

23.4   Conclusions

In this study, PMS model proposal for converging runways is presented. In real-time simulation, vectoring is compared with PMS method according to sequence of arrival traffic to converging runways.

Vectoring is flexible and subjective method and also the controller is responsible for traffic sequence. Therefore, it could be possible to see significant difference about traffic sequence between different controllers.

In PMS method, the controller decides traffic sequence according to entry time of sequencing legs. Sequencing legs are increased the situation awareness and the foresight of controllers.

The sum of the difference of traffic sequence value is 14 in PMS method; however, it is found 58 in vectoring. It could be resulted that PMS method allows providing a standard traffic sequence for controllers.

References

Boursier L, Favenne CB, Hoffman E, Trzmiel A, Vergne F, Zeghal K (2007) Merging arrival flows without heading instructions. In: 7th USA/Europe air traffic management R&D seminar, Barcelona

Eurocontrol (2010) Point merge integration of arrival flows enabling extensive RNAV application and CDA—operational services and environment definition. Eurocontrol Experimental Center, Version 2.0

Favennec B, Hoffman E, Trzmiel A, Vergne F, Zeghal K (2009) The point merge arrival flow integration technique: towards more complex environments and advanced continuous descent. In: 9th AIAA aviation technology, integration, and operations conference (ATIO), South Carolina

Favenne B, Vergne F, Zeghal K (2010) Point merge integration of arrival flows enabling extensive RNAV application and CDA—operational services and environmental definition. Eurocontrol Experimental Center, Version 2.0

International Civil Aviation Organization (ICAO) (2005) Document 9854, global air traffic management operational concept

International Civil Aviation Organization (ICAO) (2010) Document 9931-continuous descent operations (CDO) manual, 1st edn

Ivanescu D, Shaw C, Tamvaclis C, Kettunen T (2009) Models of air traffic merging techniques: evaluating performance of point merge. In: 9th AIAA aviation technology, integration, and operations conference (ATIO), South Carolina

Lee H (2008) Tradeoff evaluation of scheduling algorithms for terminal-area air traffic control. Massachusetts Institute of Technology

Chapter 24
Energy Saving via Integrated Passive and Active Morphing During Maneuvers

Tugrul Oktay and Firat Sal

Abstract This paper presents some novel results found using integrated passive and active morphing during different helicopter maneuvers. A nonlinear, rigid blade helicopter model is linearized around three different maneuvering flight conditions. A specific variance constrained controller namely OVC is applied for flight control system. Parameters of autopilot and morphing parameters are simultaneously determined in order to minimize control energy while there are constraints on helicopter and control design parameters. A stochastic optimization method is used for this purpose. Closed loop system response analyses are done in order to see superiority of integrated passive and active morphing with respect to nominal helicopter and existing two morphing approaches.

24.1 Introduction

Control design is significant for safe and performant helicopter operation during maneuvering flights. In particular banked and helical turns are scope of this article. For instance, they allow transitioning between two straight level flight conditions and monitoring an area of interest. Moreover, these maneuvers allow armed helicopters to avoid ground attack and possibly engage in air to air combat, etc. In this paper, design of modern controllers is examined for such maneuvers. Because these maneuvers are highly constrained, any control design should consider constraints on outputs and inputs. Therefore, output variance constrained controllers (i.e., OVCs) are applied for flight control system design.

Throughout the years, several control methods for helicopter flight control system design have been widely examined. In historical order some of these

T. Oktay (✉) · F. Sal
Faculty of Aeronautics and Astronautics, Erciyes University,
Melikgazi, 38039 Kayseri, Turkey
e-mail: tugruloktay52@gmail.com

F. Sal
e-mail: tefaninur@gmail.com

methods are classical pole placement method and simple feedback method (see Fusato et al. 2001; Fusato and Celi 2006; Gong et al. 2013), improved *L*inear *Q*uadratic *R*egulator (LQR) controller and *L*inear *Q*uadratic *G*aussian (LQG) controllers (Zarei et al. 2007; Bo et al. 2011; Park et al. 2013), improved H_∞ control synthesis (Luo et al. 2003; Kureemun et al. 2005; Kung 2008), constrained *M*odel *P*redictive *C*ontrol (MPC) (Bogdanov and Wan 2001; Dalamagkidis et al. 2010; Gibbens and Megagoda 2011), and variance constrained controllers (Oktay 2012, 2015; Oktay and Sultan 2012a, b, 2013a, b, c, d, 2014).

Variance constrained controllers are one of these control techniques. These controllers have many advantages with respect to the other surviving control methods in the literature. First, variance constrained controllers are improved LQG controllers and they apply Kalman filters as state estimators. Second, they benefit second-order information (i.e., state covariance matrix, see (Skelton 1987; Skelton et al. 1998) for more information) and this type of information is very advantageous during multivariable control system design since all stabilizing controllers are parameterized in relation to the physically meaningful state covariance matrix. Finally, for large and strongly coupled multi-input, multi-output systems like the ones encountered helicopter flight control, these controllers give guarantees on the transient behavior of independent variables via enforcing upper limits on the variance of these variables.

Variance constrained controllers have been benefited for several aerospace vehicles (e.g., helicopters: Oktay 2012, 2015; Oktay and Sultan 2012a, b, 2013a, b, c, d, 2014; tiltrotor aircraft: Oktay 2014; Hubble space telescope: Skelton and Lorenzo 1985; and tensegrity structures: Skelton and Sultan 1997; Sultan and Skelton 1997) recently. For example, in Oktay and Sultan (2013a) variance-constrained controllers were used for helicopter flight control system design during maneuvers (i.e., level banked and helical turns). In this article, their performance was also examined when some of the helicopter sensors failed. Satisfactory results (meaning that variance constraints on outputs/inputs were accomplished and also closed loop systems were exponentially stabilized) were obtained for helicopter flight control system. Furthermore, in Oktay and Sultan (2013b) output variance constrained controllers were used for passively morphing helicopters. In this article, the passively morphing parameters were blade chord length, blade flapping spring stiffness, blade linear mass density, blade length, blade twist, and main rotor angular speed. A stochastic optimization method was used to simultaneously design helicopter and flight control system. For the 40 kt straight level flight condition, around 30 % of the control system energy save was accomplished with only 5 % changes on passive design parameters. It is vital to note that for that article the new values of parameters of redesigned helicopter found simultaneous design idea method do not change during flight. In another article of Oktay and Sultan (2014) OVCs were used on control system of actively morphing helicopters. In this article the actively morphing parameters were blade chord length, blade length, blade twist, and main rotor angular speed. For the 40 kt straight level flight, around 85 % of the flight control system energy save was obtained with only 5 % changes on active design parameters. The principal difference between passive and active

morphing approaches is that in the active case the helicopter design parameters except helicopter control system parameters change during flight, but in prescribed interval (±5 %). However, in the passive situation the helicopter design parameters and helicopter flight control system parameters do not change during flight.

Passive morphing and active morphing require variations in some of helicopter parameters (e.g., blade length, blade rotation speed, etc.). The main alteration is that active morphing requires continuous measurements and actuation as well as a feedback control mechanism; however, passive morphing does not. Passive morphing deviations can be applied by engineers and technicians, for example as a one-time change before helicopter initiates the flight mission or even at some point during flight. Once used, these deviations remains fixed for a prolonged period of time during flight. Hence, passive morphing does not necessitate additional actively controlled elements further than the four classical helicopter controls (i.e., blade pitch collective, two cyclics and tail rotor collective). On the contrary, active morphing requires special mechanisms that permit continuous, in flight adjustment of some of the helicopter parameters. These adjustments are computed in response to sensor measurements and applied by feedback control. Hence, active morphing requires extra feedback controlled parameters in addition to the four classical helicopter controls. Clearly passive morphing is simpler to benefit because it does not contain extra feedback driven actuation mechanisms, whereas active morphing requires complex onboard signal processing, multivariable, large dimensional controllers, fast continuous actuation mechanisms, and also computational power. Nonetheless, active morphing is widely expected to produce significant improvement in all features of helicopter flight performance.

In this article, passive morphing and active morphing methods is first time integrated for maneuvering helicopters and integrated morphing maneuvering helicopter is first time simultaneously designed with helicopter flight control system. For this purpose output variance constrained controller is also first time benefited for helicopter flight control system. It is very important to mention that when passive and active morphings are integrated with four classical helicopter controls, the number of controls increases. This causes an important disadvantage. The number of trim unknowns increases with integrated morphing design parameters. Nonetheless, there are no supplemental trim equations. For this reason, in order to solve the resulting nonlinear trim equations, a helpful optimization algorithm is required. For its solution SPSA: simultaneous perturbation stochastic approximation (see Spall 1992; Sultan 2010) for brief description of SPSA) is first time benefited for the simultaneous helicopter and flight control system design problem since it is computationally cheap and effective during solving constrained optimization problems when it is impossible to compute derivatives such as gradients and Hessians, analytically as in the condition herein. It is also important to note that this article is strongly modified and extended version of the conference article presented in 1st International Conference in Sustainable Aviation.

24.2   Helicopter Model, Maneuvers, and Control System

In this article the helicopter models which are derived and mentioned in (Oktay 2012; Oktay and Sultan 2013e) in detail and shortly summarized here are applied. In short, physics principles are applied and this leads to dynamic models consisted of finite set of ordinary differential equations (i.e., ODEs). These models are very beneficial for flight control system design since they simplify the direct use of modern control theory (MCT). MCT depends on state space presentation of any system's dynamics and it is simply derived from ODEs. The main helicopter modeling assumptions are: Firstly, multibody system approach is benefited to get helicopter models and all characteristic helicopter subsystems (e.g., fuselage, empennage: tail rotor hub and shaft, and horizontal tailplane). Secondly, Pitt-Peter's static inflow model is benefited for modeling of the main rotor downwash. Nevertheless, for the modeling of fuselage a formulation using analytical aerodynamics is applied. The modeling methodology summarized above was implemented using MAPLE 16 software and objectively complex nonlinear helicopter models with 29 equations (i.e., nine fuselage equations, 16 blade flapping and lead-lagging equations, three static main rotor downwash equations, one flight path angle equation) are found. After simplifying (it is important to note that a systematic model simplification approach is benefited to truncate these nonlinear equations, see (Oktay 2012; Oktay and Sultan 2013e) for more details) and trimming the nonlinear model using MATLAB 2008 *fsolve* command, continuous *l*inear *t*ime-*i*nvariant (LTI) systems are found.

$$\dot{x}_p = A_p x_p + B_p u_p \tag{24.1}$$

Above x_p and u_p are perturbed state and control vectors, respectively, and matrices of A_p and B_p are of size 25×25 and 25×4. There are 25 perturbed states. These are nine fuselage states (i.e., three linear velocity, three angular velocity states, and three Euler angle states), eight blade flapping states and eight blade lead-lagging states, and four controls (i.e., three main rotor controls: collective, θ_0, lateral cyclic, θ_c, and longitudinal cyclic θ_s, and one tail rotor control: collective, θ_T). It is also important to note that Puma SA 330 helicopter was benefited to validate helicopter models used in this article (see Oktay 2012; Oktay and Sultan 2013e; Padfield 2007 for technical details of this helicopter).

In this article level banked turn without sideslip and helical turn without sideslip are considered (see Chen and Jeske 1981; Celi 1991; Guglieri and Celi 1998; Prouty 2005; Leishman 2006 for more details). For maneuvering flight the helicopter linear velocities are (see Fig. 24.1)

$$\begin{bmatrix} u & v & w \end{bmatrix}^T = \begin{bmatrix} V_A \cos(\alpha_F) \cos(\beta_F) \\ V_A \sin(\beta_F) \\ V_A \sin(\alpha_F) \cos(\beta_F) \end{bmatrix} \tag{24.2}$$

Fig. 24.1 Fuselage angle of attack and sideslip
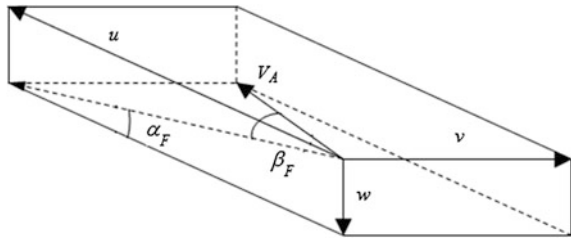
Fig. 24.2 Level banked turn
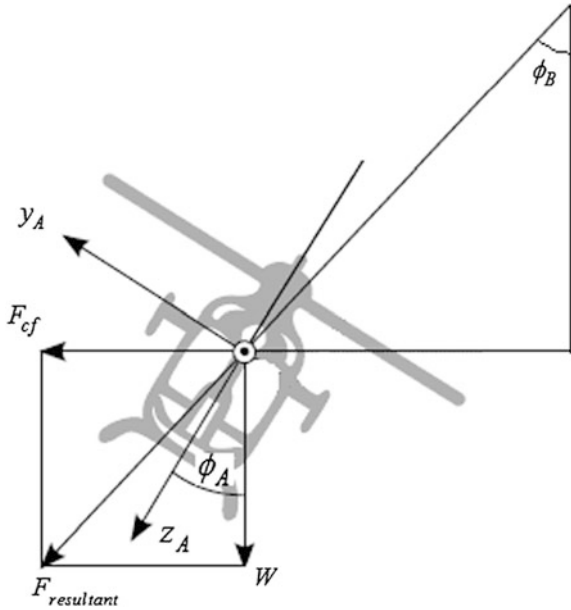
where fuselage angle of attack, α_F, and sideslip, β_F, are given by

$$\alpha_F = \tan^{-1}(w/u), \ \beta_F = \sin^{-1}(v/V_A) \tag{24.3}$$

Level banked turn is a maneuver where the helicopter banks towards the center of the turning circle. For helicopters the fuselage roll angle, ϕ_A, is in general slightly different than the bank angle, ϕ_B. For coordinated banked turn $\phi_A = \phi_B$, but this is not the focus of this work. A picture describing these angles for a particular case ($\theta_A = 0$) is given in Fig. 24.2, where $F_{\text{resultant}}$ is the sum of the gravitational force (W) and the centrifugal force (F_{cf}).

Helical turn is a maneuver where the helicopter moves along a helix with constant speed (see Fig. 24.3). In a helical turn, the flight path angle is different than zero and it is
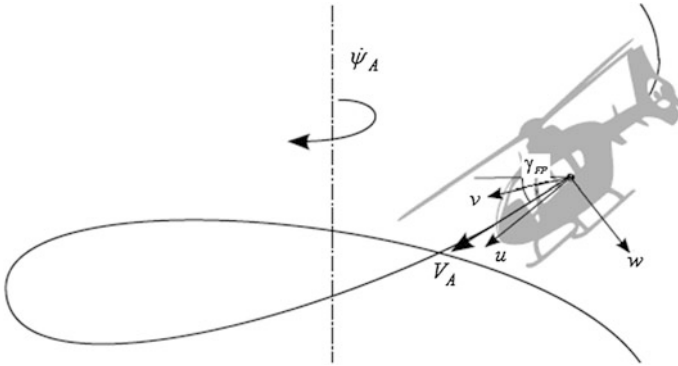
Fig. 24.3 Helical turn
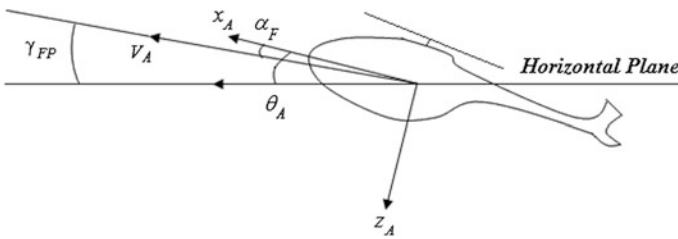
Fig. 24.4 Flight path angle

$$\sin(\gamma_{FP}) = \sin(\theta_A)\cos(\alpha_F)\cos(\beta_F) - \sin(\phi_A)\cos(\theta_A)\sin(\beta_F)$$
$$- \cos(\phi_A)\cos(\theta_A)\sin(\alpha_F)\cos(\beta_F) \tag{24.4}$$

A picture describing the flight path angle for a particular case ($\phi_A = 0$, $\beta_F = 0$) is given in Fig. 24.4.

It is important to note that $\dot{\psi}_A > 0$ is a clockwise turn and $\dot{\psi}_A < 0$ is a counterclockwise turn (viewed from the top) while $\gamma_{FP} > 0$ is referring to the ascending (climbing) flight and $\gamma_{FP} < 0$ is referring to the descending flight.

For helicopter flight control system a specific variance constrained controller namely output variance constrained controller (OVC) is chosen. Its brief description is given next: For a given continuous linear time-invariant (LTI), stabilizable and detectable system

$$\dot{x}_p = A_p x_p + B_p u_p + w_p, \quad y = C_p x_p, \quad z = M_p x_p + v \tag{24.5}$$

and a positive definite input penalty matrix, $R > 0$, find a full order dynamic controller

$$\dot{x}_c = A_c x_c + Fz, \quad u_p = Gx_c \qquad (24.6)$$

to solve the problem

$$\min_{A_c, F, G} \quad J = E_\infty u_p^T R u_p = tr(R \, G \, X_{c_j} G^T) \qquad (24.7)$$

subject to variance constraints on the output or outputs

$$E_\infty y_i^2 \le \sigma_i^2, \quad i = 1, \ldots, n_y \qquad (24.8)$$

Here y and z represent outputs of interest and sensor measurements, respectively, w_p and v are zero-mean uncorrelated Gaussian white noises with intensities of W and V, respectively, F and G are state estimator and controller gain matrices, respectively, x_c is the controller state vector, σ_i^2 is the upper limit imposed on the ith output variance, n_y is the number of outputs, $E_\infty \triangleq \lim_{t \to \infty} E$, and E is the expectation operator. Furthermore, tr and T denote matrix trace and matrix transpose operators, respectively. The quantity of J generally called as flight control system energy or flight control system cost and it is computed using also the state covariance matrix, X_{c_j}.

In reality, OVCs are modified LQGs since they guarantee satisfaction of variance constraints on output/outputs of interest. OVC solution reduces to a LQG problem solution via output penalty matrix $Q > 0$ depending on the inequality constraints. An algorithm for the selection of Q is given in Hsieh et al. (1989) and Zhu and Skelton (1991). After the algorithm converges and the output penalty matrix Q is found, OVC parameters are

$$A_c = A_p + B_p G - FM_p, \, F = XM_p^T V^{-1}, \, G = -R^{-1}B_p^T K \qquad (24.9)$$

Here, X and K are solutions of two algebraic Riccati equations:

$$0 = XA_p^T + A_p X - XM_p^T V^{-1} M_p X + W \qquad (24.10a)$$

$$0 = KA_p + A_p^T K - KB_p R^{-1} B_p^T K + C_p^T QC_p \qquad (24.10b)$$

24.3 Integrated Passive and Active Morphing Problem

The *integrated* passive and active morphing design is explained next.

$$\min_{A_c, F, G, \Psi_p, \Psi_a} \quad J = E_\infty u_p^T R u_p \qquad (24.11)$$

subject to Eqs. (24.5), (24.6) and (24.8) where $\Psi_p = \{\Omega, R, c_b, \theta_{tw}, K_\beta, m\}$ and $\Psi_a = \{\Omega, R, c_b, \theta_{tw}\}$. The elements of Ψ_p and Ψ_a are constrained, i.e., $\Psi_{pi_{min}} \leq \Psi_{pi} \leq \Psi_{pi_{max}}$ and $\Psi_{ai_{min}} \leq \Psi_{ai} \leq \Psi_{ai_{max}}$. It should be clarified that here Ψ_a represents the vector of active morphing controls' *trim* values. Here matrices A_p and B_p are functions of Ψ_p and Ψ_a, and this dependency propagates through control energy computation (Eq. (24.7)) to J and to output variance values (Eq. (24.8)). These dependencies lead to a difficult optimization problem where both the objective, J, and the variance constraints depend on the optimization variables in a sophisticated manner: the expectation operator has to be applied to time varying responses that depend on Ψ_p and Ψ_a as well as on controller parameters (i.e., A_c, F, G), leading to a very complicated optimization problem.

24.4 SPSA

The problem of finding the optimum values of the passive and active morphings is much more complicated than the traditional OVC design due to the introduction of the additional passive and active morphing optimization variables and the related constraints on them. Because there is complex dependency between J and expected values of outputs of interest, computation of their derivatives with respect to these variables is analytically impossible. This advices the use of certain stochastic optimization methods. In order to solve it, a stochastic optimization method namely SPSA is chosen in this article. This method was successfully used in similar complex constrained optimization problems (see Oktay 2012; Oktay and Sultan 2013b, 2014) before. SPSA has many advantages. First, SPSA is inexpensive because it uses only two evaluations of the objective to estimate the gradient (see Spall 1992). It is also successful in solving constrained optimization problems (see Oktay 2012; Oktay and Sultan 2013b, 2014; Sultan 2013). Moreover, under certain conditions (see Sultan 2013) strong convergence of SPSA was theoretically proved. Its short summary is given next.

Let x denote the vector of optimization variables. For the classical SPSA, if $x_{[k]}$ is the estimate of x at kth iteration, then

$$x_{[k+1]} = x_{[k]} - a_k g_{[k]} \tag{24.12a}$$

where

$$g_{[k]} = \left[\frac{\Gamma_+ - \Gamma_-}{2d_k \Delta_{[k]1}} \ldots \ldots \frac{\Gamma_+ - \Gamma_-}{2d_k \Delta_{[k]p}} \right]^T \tag{24.12b}$$

a_k and d_k are gain sequences, $g_{[k]}$ is the estimate of the objective's gradient at $x_{[k]}$, $\Delta_{[k]} \in R^p$ is a vector of p mutually independent mean-zero random variables $\{ \Delta_{[k]1} \ \ldots \ldots \ \Delta_{[k]p} \}$ satisfying certain conditions (see He et al. 2003; Sadegh

and Spall 1998), Γ_+ and Γ_- are estimates of the objective evaluated at $x_{[k]} + d_k\Delta_{[k]}$ and $x_{[k]} - d_k\Delta_{[k]}$, respectively. The adaptation is via the gain sequences, a_k and d_k, and they are

$$a_k = \min\left\{a/(S+k)^\lambda, 0.95 \min_i\{\min(\varphi_{l_i}), \min(\varphi_{u_i})\}\right\}, \qquad (24.13a)$$

$$d_k = \min\left\{d/k^\Theta, 0.95 \min_i\{\min\{\vartheta_{l_i}\}, \min\{\vartheta_{u_i}\}\}\right\}, \qquad (24.13b)$$

where ϑ_l and ϑ_u are vectors whose components are $(x_{[k]i} - x_{\min_i})/\Delta_{[k]i}$ for each positive $\Delta_{[k]i}$ and $(x_{\max_i} - x_{[k]i})/\Delta_{[k]i}$ for each negative $\Delta_{[k]i}$, respectively. In similar, φ_l and φ_u are vectors whose components are $(x_{[k]i} - x_{\min_i})/g_{[k]i}$ for each positive $g_{[k]i}$ and $(x_{[k]i} - x_{\max_i})/g_{[k]i}$ for each negative $g_{[k]i}$, respectively, and d, a, λ, Θ, S are additional SPSA parameters.

In order to solve the integrated passive and active morphing and control design problem for optimal values, the following algorithm is applied in this article.

Step 1: Set $k = 1$ and choose initial values for the optimization parameters, $x = x_{[k]}$, and a specific flight condition (e.g. $V_A = 40$ kts, $\dot{\psi}_A = 0.05$ rad/s, $\gamma_{FP} = -0.05$ rad helical turn maneuver).

Step 2: Compute A_p and B_p, design the corresponding OVC using Eqs. (24.9) and (24.10a, b), and find the present value of the objective, Γ_k applying Eq. (24.11); note that $\Gamma_k = J_k$ for OVC.

Step 3: Perturb $x_{[k]}$ to $x_{[k]} + d_k\Delta_{[k]}$ and $x_{[k]} - d_k\Delta_{[k]}$ and solve the corresponding OVC problems to find Γ_+ and Γ_-, respectively. Then compute the approximate gradient, $g_{[k]}$, applying Eq. (24.12b) with d_k given by Eq. (24.13b).

Step 4: If $\|a_k g_{[k]}\| < \delta x$, where a_k is given by Eq. (24.13a) and δx is the minimum allowed variation of x, or $k + 1$ is greater than the maximum number of iterations allowed, exit, else calculate the next estimate of x, $x_{[k+1]}$, using $x_{[k+1]} = x_{[k]} - a_k g_{[k]}$, set $k = k + 1$ and return to Step 2.

24.5 Closed Loop System Responses

In order to evaluate performance of developed SPSA algorithm, three different maneuvering flight conditions are examined. These are $V_A = 40$ kt, $\dot{\psi}_A = 0.05$ rad/s, $\gamma_{FP} = -0.05$ rad (helical descent turn); $V_A = 40$ kt, $\dot{\psi}_A = 0.05$ rad/s, $\gamma_{FP} = -0.00$ rad (level banked turn) and $V_A = 40$ kt, $\dot{\psi}_A = 0.05$ rad/s, $\gamma_{FP} = -0.05$ rad (descent flight). In Table 24.1 using these three maneuvering flight condition resulting values of active and passive optimization variables using SPSA are given

Table 24.1 Optimization results for different maneuvering flight condition

Parameter	Flight_1 (%)	Flight_2 (%)	Flight_3 (%)
$(\Delta\Omega/\Omega)_a$	−4.9000	−4.9000	−4.9000
$(\Delta R/R)_a$	−4.9000	−4.9000	−4.9000
$(\Delta c/c)_a$	+4.8999	+4.8999	+4.8999
$(\Delta\theta_{tw}/\theta_{tw})_a$	−2.5000	−2.5000	−2.5000
$(\Delta\Omega/\Omega)_p$	−4.9000	−4.9000	−4.9000
$(\Delta R/R)_p$	−4.9000	−4.9000	−4.9000
$(\Delta c/c)_p$	+4.8999	+4.8999	+4.8999
$(\Delta\theta_{tw}/\theta_{tw})_p$	+4.8999	+4.8999	+4.8999
$(\Delta K_\beta/K_\beta)_p$	+4.8999	+4.8999	+4.8999
$(\Delta m/m)_p$	+4.8999	+4.8999	+4.8999

for integrated morphing helicopter. Similar results are found for all 3 maneuvering flight conditions. Therefore, it can be safely said that regardless of maneuver type integrated morphing is very effective *for energy save* (also *fuel save*).

The adaptive SPSA algorithm summarized in previous section was used for solving the integrated passive and active morphing helicopter and helicopter flight control system design problem using the SPSA parameters of $S = 5$, $\lambda = 0.602$, $a = 500$, $d = 20$, $\Theta = 0.101$ via MATLAB software. For this design problem the algorithm was very effective in fast decreasing the helicopter flight control system energy.

The relative energy saving is defined as follows: $\%J = 100(J_n - J_m)/J_n$ where J_n and J_m are costs of OVCs for non-morphing and morphing helicopters, respectively, and J_m is equal to J_p, J_a and J_I for passively morphing, actively morphing and integrated morphing helicopters, respectively. For $V_A = 40$ kt, $\dot{\psi}_A = 0.05$ rad/s, $\gamma_{FP} = -0.05$ rad helical descent turn maneuvering flight condition the relative energy savings for passively morphing, actively morphing and integrated morphing helicopters are 34.4, 94.1, and 94.7 %, respectively. From these results it can be ascertained that integrated morphing approach *is the most advantageous and economical* one over all morphing approaches for maneuvering helicopter, since *it saves more energy* (*also more fuel*) than other two approaches.

In order to better evaluate benefits of integrated passive and active morphing method with respect to the existing two other morphing methods (i.e., passive and active) and also non-morphing (i.e., nominal) situation, closed loop performance of helicopter is examined thoroughly.

In Fig. 24.5, closed loop response of collective main rotor control input is given for all situations. From this figure it can be safely said that since peak values of integrated and active morphing situations are less than passive and nominal situations, these morphing fashions are cheaper than passive and nominal fashions. There exists a strange result here that peak values of integrated morphing are larger than the ones of active morphing. However, in Fig. 24.6, expected result occurs.
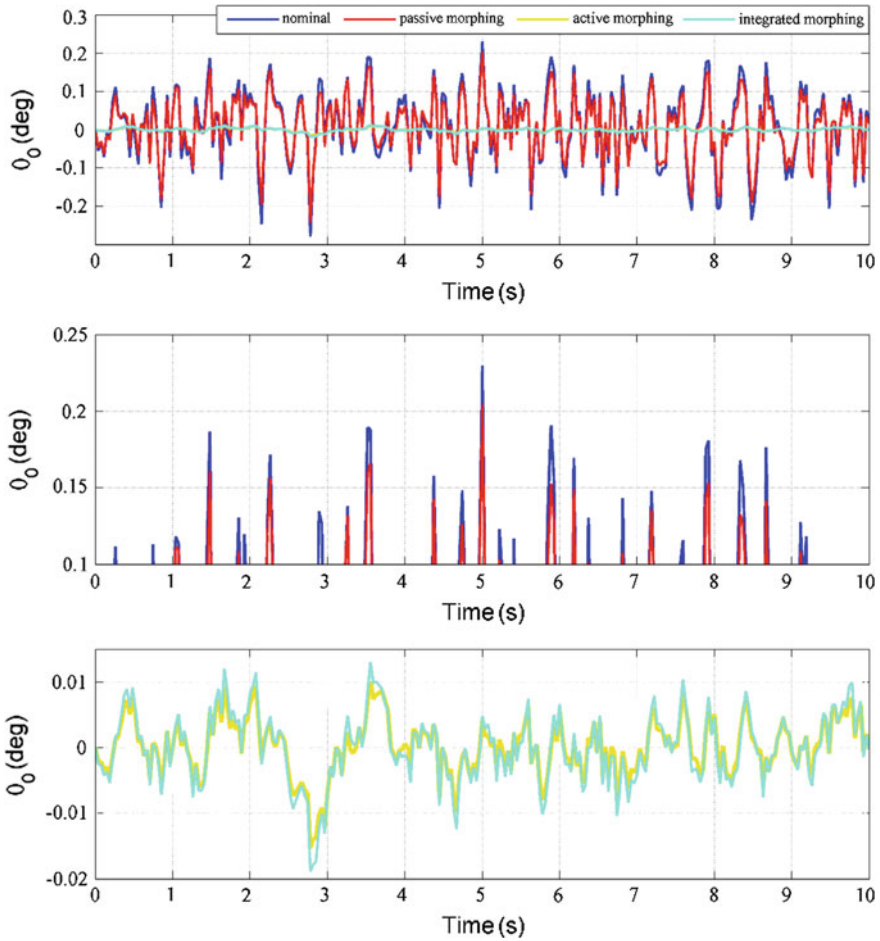
Fig. 24.5 Closed loop response of main rotor collective control for all four cases (zoomed)

In Fig. 24.6 closed loop response of longitudinal cyclic main rotor control input is given for all situations. From this figure it can be safely said that since peak values of integrated and active morphing situations are less than passive and nominal situations, these morphing fashions are cheaper than passive and nominal fashions. Moreover, peak values of integrated morphing are smaller than the ones of active morphing. Our extensive analyses show that for also other two traditional control inputs (i.e., main rotor lateral cyclic pitch and tail rotor collective angle) integrated morphing is cheaper than active, passive morphings and also nominal situation.

In Figs. 24.7 and 24.8, closed loop responses of additional control inputs (i.e., blade radius active morphing control and blade chord active morphing control) are given, respectively. From these figures it can be safely said that for also active
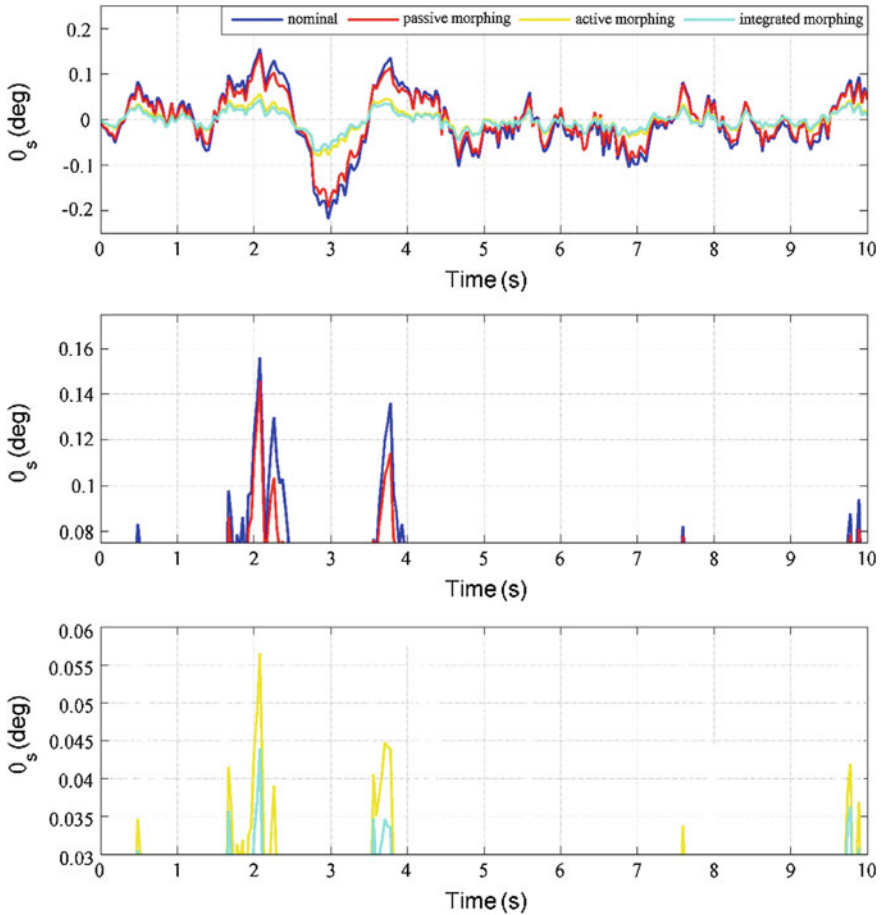
Fig. 24.6 Closed loop response of main rotor longitudinal cyclic control for all four cases (zoomed)

controls integrated morphing is cheaper than active morphing. Our extensive analyses show that for also other two additional control inputs (i.e., main rotor angular velocity active morphing control and blade twist active morphing control) integrated morphing is cheaper than active morphing.

In Fig. 24.9, the closed loop responses of some other outputs (collective blade flapping and lagging angles, in deg.s) are given for integrated morphing case. From this figure it can be easily seen that the other output which are not considered for flight control system design do not experience fast and large behaviors. Our extensive analyses show also other outputs out of collective blade flapping and lagging angles such as fuselage states, longitudinal, lateral and differential blade flapping and lagging angles and velocities do not experience fast and large behaviors during maneuvers for integrated morphing.
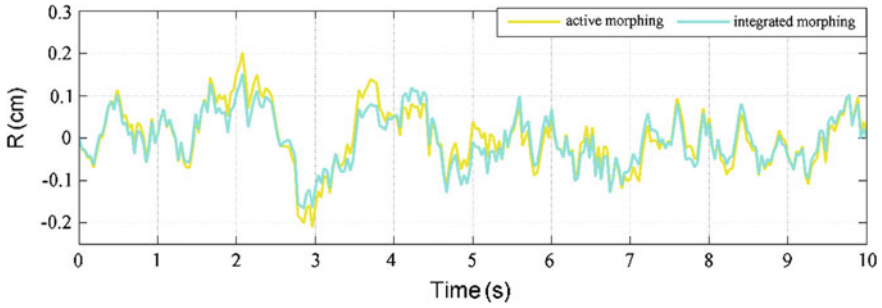
Fig. 24.7 Closed loop response of main rotor blade radius active control for all two cases
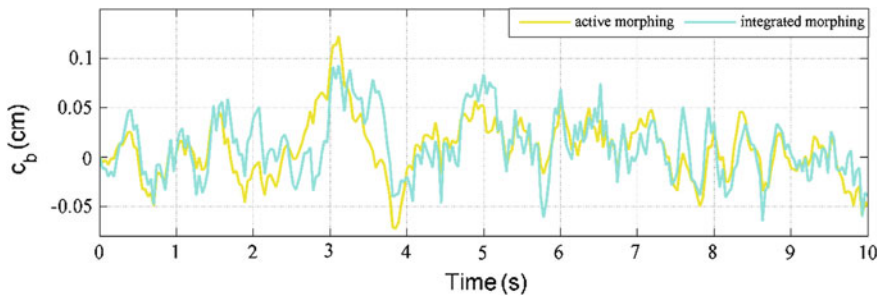
Fig. 24.8 Closed loop response of main rotor blade chord active control for all two cases
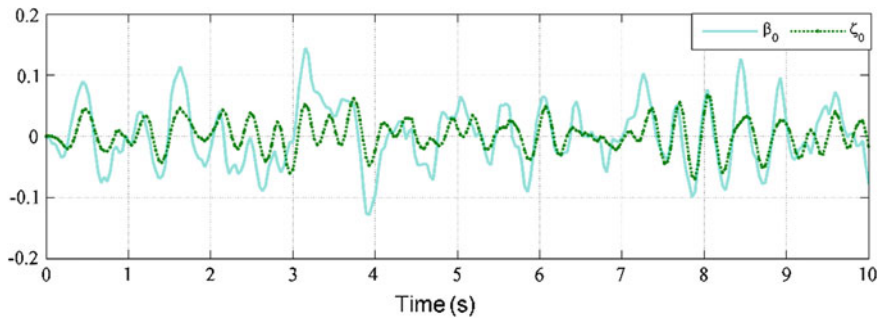
Fig. 24.9 Closed loop response of blade angles for integrated case

24.6   Conclusions

Integrated passive and active morphing idea is investigated in order to save more helicopter flight control system energy during maneuvering flight conditions. Complex, control-oriented, physics-based nonlinear helicopter models are benefited for this intention. *O*utput *V*ariance *C*onstrained (OVC) controller is applied for

helicopter flight control system design. Parameters of helicopter flight control system and integrated morphing helicopter design parameters are simultaneously obtained using a stochastic optimization method named as *s*imultaneous *p*erturbation *s*tochastic *a*pproximation (i.e., SPSA).

Closed loop responses analyses show that for classical controls integrated morphing approach is the cheapest method overall during maneuvers. For also additional controls (i.e., active morphing controls) integrated method is the cheapest overall two methods. Other outputs which are not considered for flight control system design do not experience fast and large behaviors during maneuvers.

From optimization results it can be ascertained that integrated morphing approach *is the most advantageous and economical* one over all morphing approaches for maneuvering helicopter, since *it saves more energy (also more fuel)* than other two approaches. It can be safely said that regardless of maneuver type integrated passive and active morphing is very effective *for energy save* (also *fuel save*).

References

Bo LY, Zhu LW, Qi S (2011) Improved LQG control for small unmanned helicopter based on active model in uncertain environment. In: International conference on electronics, communications and control (ICECC). Ningbo, China

Bogdanov AA, Wan EA (2001) Model predictive neural control of a high-fidelity helicopter model. In: AIAA guidance navigation and control conference. Montreal, Canada

Celi R (1991) Hingeless rotor dynamics in coordinated turns. J Am Helicopter Soc 36(4):39–47

Chen RTN, Jeske JA (1981) Kinematic properties of the helicopter in coordinated turns. NASA technical paper 1773, NASA

Dalamagkidis K, Valavanis KP, Piegl LA (2010) Nonlinear model predictive control with neural network optimization for autonomous autorotation of small unmanned helicopters. IEEE Trans Control Syst Technol 19(4):1–14

Fusato D, Celi R (2006) Multidisciplinary design optimization for helicopter aeromechanics and handling qualities. J Aircr 43(1):241–252

Fusato D, Guglieri G, Celi R (2001) Flight dynamics of an articulated rotor helicopter with an external slung-load. J Am Helicopter Soc 46(1):3–14

Gibbens PW, Megagoda EDB (2011) Efficient model predictive control algorithm for aircraft. J Guid Control Dyn 34(6):1909–1915

Gong H, Zhen Z, Lin X, Jiang J, Wang X (2013) Design of automatic climbing controller for large civil aircraft. J Franklin Inst 350:2442–2454

Guglieri G, Celi R (1998) On some aspects of helicopter flight dynamics in steady turns. J Guidance Control Dyn 21(3):383–390

He Y, Fu MC, Marcus SI (2003) Convergence of simultaneous perturbation stochastic approximation for non-differentiable optimization. IEEE Trans Aerosp Electron Syst 48 (8):1459–1463

Hsieh C, Skelton RE, Damra FM (1989) Minimum energy controllers with inequality constraints on output variances. Optimal Control Appl Methods 10(4):347–366

Kung CC (2008) Nonlinear H_∞ robust control applied to F-16 aircraft with mass uncertainty using control surface inverse algorithm. J Franklin Inst 345:851–876

Kureemun R, Walker DJ, Manimala B, Voskuijl M (2005) Helicopter flight control law design using H_∞ techniques. In: Proceedings of the 44th IEEE conference on decision and control, and the European control conference. Seville, Spain

Leishman JG (2006) Principles of helicopter aerodynamics. Cambridge University Press, Cambridge, pp 263–265

Luo CC, Liu RF, Yang CD, Chang YH (2003) H_∞ control design with robust flying quality. Aerosp Sci Technol 7:159–169

Oktay T (2012) Constrained control of complex helicopter models. Ph.D. Dissertation. Virginia Tech, Blacksburg, VA

Oktay T (2014) Performance of minimum energy controllers on tiltrotor aircraft. Aircr Eng Aerosp Technol 86(5):361–374

Oktay T (2015) Combined output variance constrained and input variance constrained design for flight control. Proc IMechE Part G J Aerosp Eng (to appear)

Oktay T, Sultan C (2012a) Variance constrained control of maneuvering helicopters. In: American helicopter society 68th annual forum. TX, USA

Oktay T, Sultan C (2012b) Integrated maneuvering helicopter model and controller design. In: AIAA guidance, navigation and control conference. MN, USA

Oktay T, Sultan C (2013a) Variance constrained control of maneuvering helicopters with sensor failure. Proc IMechE Part G J Aerosp Eng 227(12):1845–1858

Oktay T, Sultan C (2013b) Simultaneous helicopter and control-system design. AIAA J Aircr 50 (3):911–926

Oktay T, Sultan C (2013c) Modeling and control of a helicopter slung-load system. Aerosp Sci Technol 29(1):206–222

Oktay T, Sultan C (2013d) Robustness of variance constrained controllers for complex helicopter models. American Control Conference, WA, USA

Oktay T, Sultan C (2013e) Constrained predictive control of helicopters. Aircr Eng Aerosp Technol 85(1):32–47

Oktay T, Sultan C (2014) Flight control energy saving via helicopter rotor active morphing. AIAA J Aircr 51(6):1784–1805

Padfield GD (2007) Helicopter flight dynamics. AIAA education series

Park S, Bae J, Kim Y, Kim S (2013) Fault tolerant flight control system for the tilt-rotor UAV. J Franklin Inst 350:2535–2559

Prouty RW (2005) Helicopter performance, stability and control. Robert E. Kreiger Publishing Co., Malabar, FL, pp 340–346

Sadegh P, Spall JC (1998) Optimal random perturbations for multivariable stochastic approximation using a simultaneous perturbation gradient approximation. IEEE Trans Autom Control 43(10):1480–1484

Skelton RE (1987) Dynamic systems control: linear systems analysis and synthesis. Wiley (chapter 8)

Skelton RE, Lorenzo MD (1985) Space structure control design by variance assignment. J Guid Control Dyn 8(4):454–462

Skelton RE, Sultan C (1997) Controllable tensegrity, A new class of smart structures. In: SPIE international symposium on smart structures and materials. San Diego, CA

Skelton RE, Iwasaki T, Grigoriadis K (1998) A unified algebraic approach to linear control design. Taylor & Francis (chapter 40)

Spall JC (1992) Multivariable stochastic approximation using a simultaneous perturbation gradient approximation. IEEE Trans Autom Control 37:332–341

Sultan C (2010) Proportional damping approximation using the energy gain and simultaneous perturbation stochastic approximation. Mech Syst Signal Process 24:2210–2224

Sultan C (2013) Decoupling approximation design using the peak to peak gain. Mech Syst Signal Process 36:582–603

Sultan C, Skelton RE (1997) Integrated design of controllable tensegrity structures. In: ASME international mechanical engineering congress and exposition. Dallas, TX

Zarei J, Montazeri A, Motlagh MRJ, Poshtan J (2007) Design and comparison of LQG/LTR and H_∞ controllers for a VSTOL flight control system. J Franklin Inst 344:577–594

Zhu G, Skelton RE (1991) Mixed L_2 and L_∞ problems by weight selection in quadratic optimal control. Int J Quadratic Optimal Control 63(5):1161–1176

Chapter 25
PMU Deployment in Power System Oscillation Monitoring

Abdelmadjid Recioui, Hamid Bentarzi and Mohamed Tsebia

Abstract Oscillatory events at low frequencies are commonly witnessed in inter-connected power systems. Phasor Measurement Units (PMU) can provide time-synchronized measurements; it can communicate the synchronized local and inter-area information to remote station. In this paper, we have modeled a PMU, and we have tested it in the 14-bus power system. It proposes a real-time monitoring tool that exploits synchronized phasor measurements from PMUs, which allow real-time analysis of higher-frequency events, filling the lack of such monitoring application in the power systems area.

25.1 Introduction

Power system operation and control have for decades been performed with systems built in a centralized architecture, with a SCADA and Energy Management System (EMS) located in a control center. In the control center, operators have been provided with analog measurements and digital indications from the power system via the SCADA system. This has allowed them to monitor and control the power system on a near real-time basis (Phadke 2008; Bentarzi 2010).

A. Recioui (✉) · H. Bentarzi · M. Tsebia
Signals and Systems Laboratory (SiSyLAB),
Institute of Electrical and Electronic Engineering,
University M'hamed Bougara of Boumerdes,
Avenue de l'indépendance, Boumerdes, Algeria
e-mail: recmad2006@yahoo.fr

H. Bentarzi
e-mail: bentarzi_hamid@yahoo.com

M. Tsebia
e-mail: m_tsebia@yahoo.fr

With the advent of new communication and computing technologies, numerous visions for future power system operation and control have been created (Karlsson et al. 2004; Phadke and Thorp 2008; Bakken et al. 2007).[1] Synchronized phasor measurements have started to become available at selected substations in the system. Phasor measurement units (PMU) are devices, which use synchronization signals from the global positioning system (GPS) satellites and provide the positive sequence phasor voltages and currents measured at a given substation (Ouadi et al. 2009). These types of measurements will in turn improve the performance of the state estimators. In these future architectures, the functionality needed for control and protection of the power system can be located at any computing platform within a distributed control system.

There is global interest in the prospects of PMU-based monitoring and control technology (Marinez et al. 2005; Chenine et al. 2009; Zima et al. 2005). These systems promise to offer more accurate and timely data on the state of the power system increasing the possibilities to manage the system at a more efficient and responsive level and apply wide area control and protection schemes. Of the pioneering works in PMU development and utilization, one would state the works done by Phadke et al. (1986), Phadke (1993). Most of the efforts worldwide; e.g., (Chenine et al. 2009; Zima et al. 2005; Phasor Application Classification 2007; Chenine and Zhu 2008),[2] has been on developing monitoring and assessment applications based on PMU measurements in addition to platforms that would support these applications. Monitoring and assessment applications are known as Wide Area Monitoring Systems (WAMS); these new applications were previously impossible with SCADA measurements due to its generally low data sampling rate quality, and lack of exact time synchronization. There has been generally less work on developing protection systems for PMU-based monitoring and assessment application, and even less so for wide area control applications. The latter group of systems which not only monitors the power system states is referred to as Wide Area Monitoring and Control Systems (WAMC).

With the increase of the interconnected power network scale and complexity, the problem of various potential power oscillations has caused a lot of damage to the system stability operation security. The increasing amount of renewable power, which constitutes one kind among different intermittent generation sources, involves numerous new challenges for its integration into existing power systems. Transient, stability issues have already been studied (Wiik et al. 2000). However, it has been only recently that some Transmission System Operators (TSOs) have measured, with PMUs (White and Chisholm 2011), sub-synchronous oscillatory events resulting from interactions between wind farms at frequencies around 13–15 Hz. The oscillations were observed at the consumer level in the form of flickering (White et al. 2012).

---

[1]North American Synchrophasor Initiative, www.naspi.org.

[2]OPNET Modeler, OPNET Inc., www.opnet.com.

This paper is concerned with any oscillatory behaviors occurring at a frequency of the frequency of the power system different from inter-area, or local oscillations will be referred to as sub-synchronous oscillations.

25.2 PMU Modeling

PMU technology provides phasor information (both magnitude and phase angle) in real time. Phasor measurement units (PMUs) are the most accurate and advanced synchronized phasor measurement equipment. Figure 25.1 gives a functional block diagram of a typical PMU. The GPS receiver provides the one pulse-per-second (pps) signal, and a time tag consisting of the year, day, hour, minute, and second.

Effective utilization of this technology is very useful in mitigating blackouts and learning the real-time behavior of the power system. With the advancement in technology, the microprocessor-based instrumentation such as protection Relays and Disturbance Fault Recorders (DFRs) incorporate the PMU module along with other existing functionalities as an extended feature.
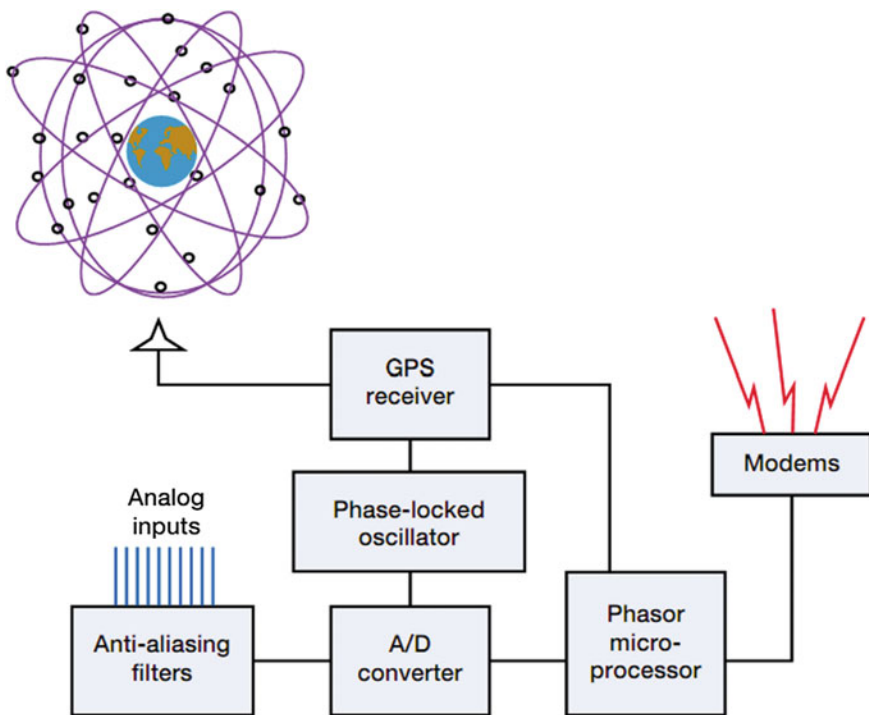
Fig. 25.1 Functional block diagram of a typical PMU

The synchronized phasor measurement technology is relatively new, and consequently, several research groups around the world are actively developing applications of this technology. It seems clear that many of these applications can be conveniently grouped as follows:

- Power System Real-Time Monitoring
- Advanced network protection
- Advanced control schemes

25.2.1 PMU Principle

A pure sinusoidal waveform can be represented by a unique complex number known as a phasor.

Consider a sinusoidal signal

$$X(t) = X_m \cos(\omega t + \Phi) \tag{25.1}$$

X_m the peak value of the sinusoidal voltage,
$\omega = 2\pi f$ the frequency of the voltage in radians per second,
f the frequency in Hz,
Φ the phase angle in radians with respect to the reference value.

The phasor representation of this sinusoidal is given by

$$X(t) = \frac{X_m}{\sqrt{2}} e^{j\Phi} = \frac{X_m}{\sqrt{2}} (\cos \Phi + j \sin \Phi) \tag{25.2}$$

Note that the signal frequency 'ω' is not explicitly stated in the phasor representation. The magnitude of the phasor is the rms value of the sinusoid, and its phase angle is Φ, the phase angle of the signal in Eq. (25.1). The sinusoidal signal and its phasor representation are given by Eqs. (25.1) and (25.2).

25.2.2 Phasor-Data Applications

Although PMU data collected at a few points on the grid can reveal conditions across a wide area and inform a variety of grid applications, PMU placement should support the needs and functionalities of the intended applications and system characteristics. As a result, the discussion on PMU siting is organized according to real-time and off-line applications with sub-categories as shown in Table 25.1.

Table 25.1 PMU real-time and off-line applications

Real-time applications	Off-line applications
Visualization and situational awareness • Situational awareness • Generating stations • Flow gates and regional transmission interfaces • Separation islands	*Analysis and assessment* • Base lining and correlation analysis • Disturbance analysis • Model validation • Frequency response analysis • Renewable generation
Monitoring and alarming • Phasor-data augmented state estimation • Phasor-data only state estimation • Small-signal stability monitoring • Voltage stability • Thermal monitoring and congestion monitoring	*System planning* • Load characteristics • Primary frequency response
Protection and control • Out-of-step protection • Small-signal stability protection • Long-term stability control	

25.3 PMU and Power Systems

Inter-area oscillations result from system events coupled with a poorly damped electric power system. The oscillations are observed in the large system with groups of generators, or generating plants connected by relatively weak tie lines. The low frequency modes (0.1–0.8 Hz) are found to involve groups of generators, or generating plants, on one side of the tie oscillating against groups of generators on the other side of the tie. These oscillations are undesirable as they result in sub-optimal power flows and inefficient operation of the grid. The stability of these oscillations is of vital concern.

To overcome the inter-area oscillation, equipment such as Static Var Compensator (SVC) and various Flexible AC Transmission System (FACTS) devices are being increasingly used. These techniques have become possible due to the recent advancement in power electronic technology. The involvement of SVC and FACTS in a transmission network is through the so-called Variable Series Compensation (VSC). Besides the FACTS devices, the application of Super-Conducting Magnetic Storage (SMES) to enhance the inter-area oscillation damping is also reported.

Although Power System Stabilizers exist on many generators, their effect is only on the local area and does not effectively damp out inter-area oscillations. It can be shown that the inter-area oscillations can be detected through the analysis of PMU located within the system. Oscillations in power systems are classified by the system components that they effect

- Intra plant mode oscillations: Machines on the same power generation site oscillate against each other at 2.0–3.0 Hz.
- Local plant mode oscillations: In local mode, one generator swings against the rest of the system at 1.0–2.0 Hz.
- Inter-area mode oscillations: This phenomenon is observed over a large part of the network. It involves two coherent group groups of generators swinging against each other at 1 Hz or less.

Instability in a power system may be manifested in many different ways. Generally, the stability problem has been one of the maintaining synchronous operations. Instability may also be encountered without loss of synchronism. Since power systems rely on synchronous machines for generation of electrical power, a necessary condition for satisfactory system operation is that all synchronous machines remain in synchronism.

In this paper, we discuss this advanced technology (PMUs) with the help of MATLAB simulation. We design this PMU model in MATLAB SIMULINK, and then we installed this model in the 14-bus power system. Such application is made for the protection, monitoring, and control of a wide power system.

25.4   Simulation of the 14-Bus Power System

We simulated the 14-bus power system associated with the PMUs, and provoked a fault in the line 4 between the time 4 and 5 s as shown in Fig. 25.2. Figures 25.2, 25.3, 25.4, 25.5, 25.6 and 25.7 show the simulation results. Where Fig. 25.4 shows
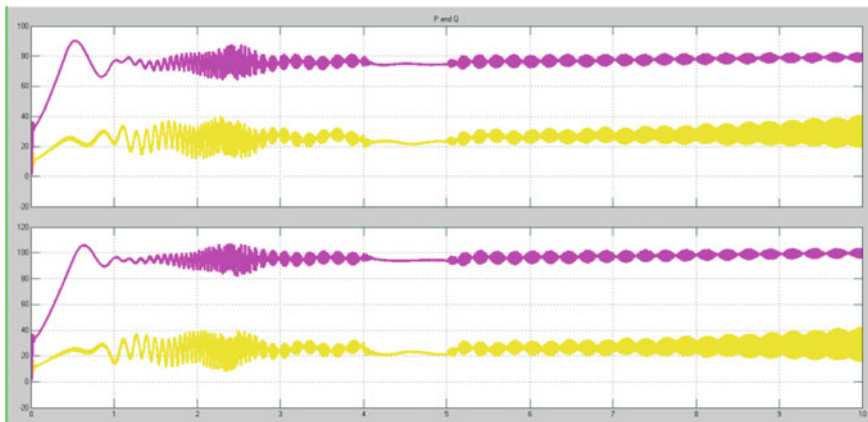
Fig. 25.2 Active power (*pink*) and reactive power (*yellow*) noted by two PMU (G1 and G2)
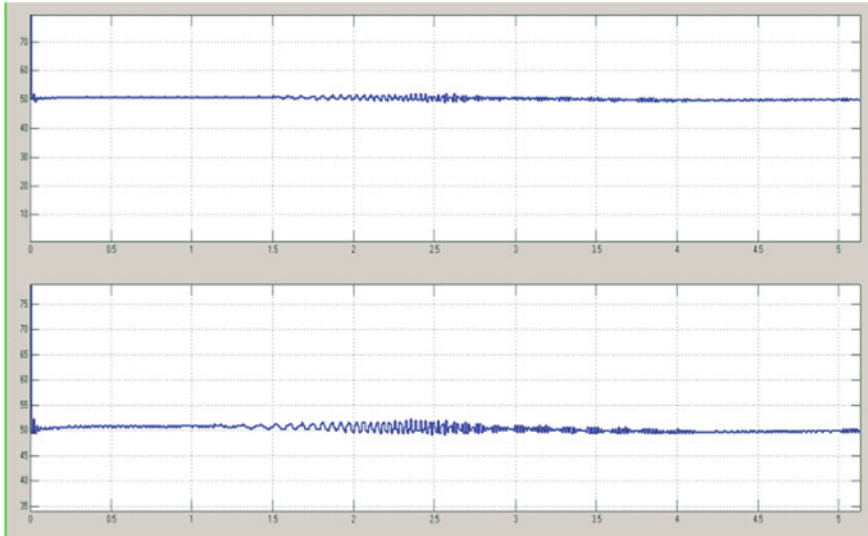
Fig. 25.3 Frequency variations (G1 and G2)
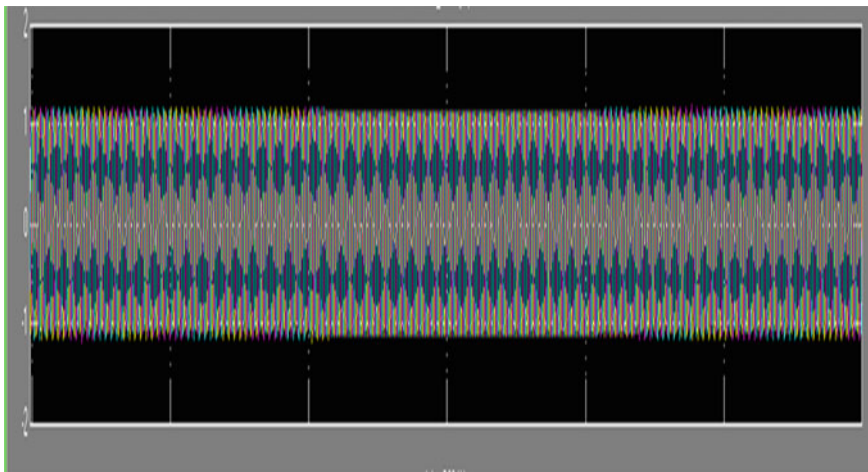
Fig. 25.4 The voltage at the bus 01

the active and reactive power at different generators such as G1 and G2 measured by PMUs. However other curves show frequencies and voltages that can be used for monitoring oscillations in the whole power system and mitigating them by proper switching actions of FACTS. The fault effects may appear at the bus which is near to it. Frequency can significantly be varied at G2 rather than G1 as illustrated in Fig. 25.3.
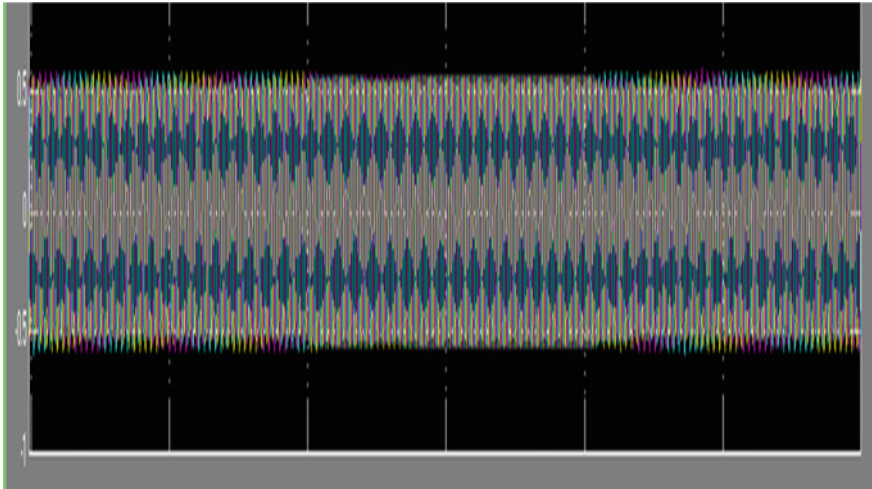
Fig. 25.5 The voltage at the bus 02
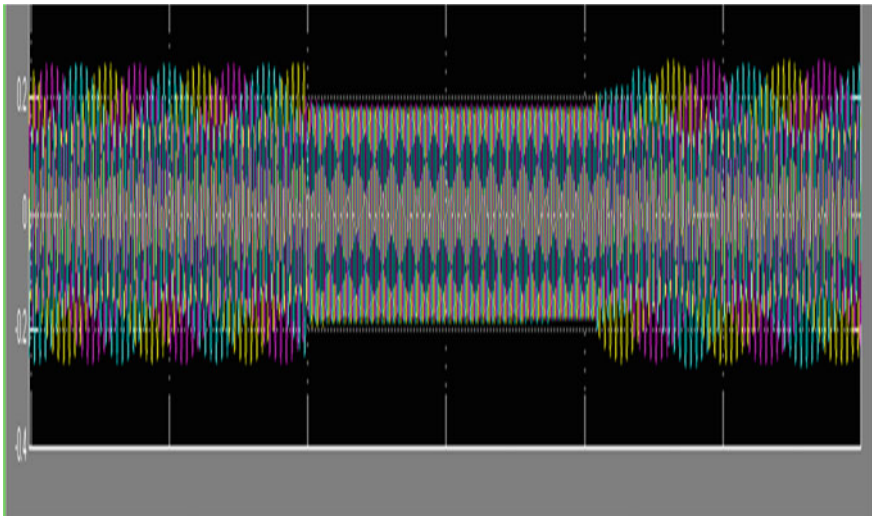
Fig. 25.6 The voltage at the bus 03

The voltages at the bus 4 totally collapse because this bus is too close to the fault (see Fig. 25.7), however, the voltages at the other buses are partially affected or not affected as shown in Figs. 25.4, 25.5, 25.6 and 25.7.
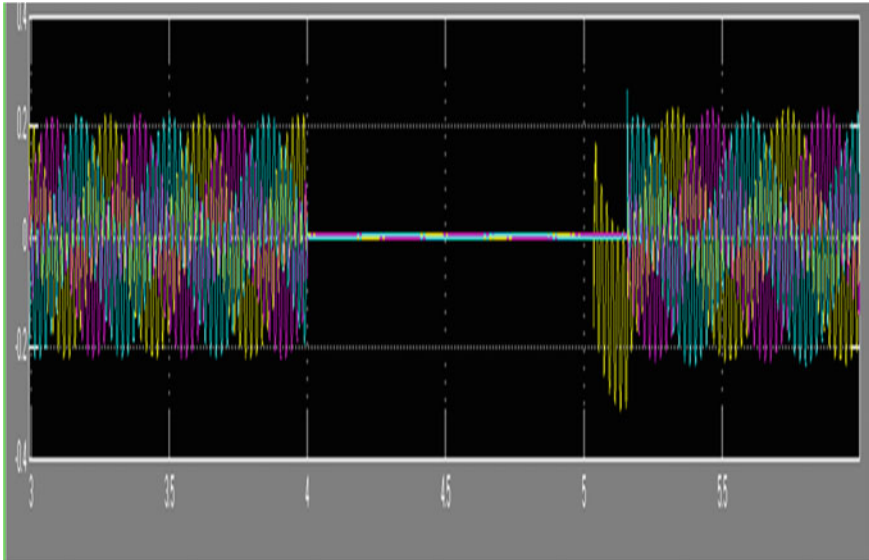
Fig. 25.7 The voltage at the bus 04

25.5   Conclusion

The use of PMU in the electrical network provides good results for monitoring all power system parameters. With the use of GPS for data synchronization, the power system states like voltage magnitude, voltage phase angle, current magnitude, current phase angle, frequency and rate of change of frequency are provided by PMU. All given states are real times. The information supplied by PMU can be used to protect the electric grid. Simulation results show the operation of the PMU for monitoring the power grid.

References

Bakken D, Hauser CH, Gjermundrod H, Bose A (2007) Towards more flexible and robust data delivery for monitoring and control of the electric power grid. Technical Report EECS-GS-009, School of Electrical Engineering and Computer Science, Washington State University

Bentarzi H (2010) Improving monitoring, control and protection of power grid using wide area synchro-phasor measurements (presented in plenary lecture). In: Proceedings of 12th WSEAS international conference on automatic control, modeling and simulation, Catania, Italy, pp 93–98, 29–31 May 2010. ISSN: 1790-5117, ISBN: 978-954-92600-1-4

Chenine M, Zhu K (2008) PMU-based applications requirements: a survey in the Nordic region. Technical Report TRITA-EE 2008:064, Royal Institute of Technology, Stockholm, Sweden

Chenine M, Zhu K, Nordström L (2009) Survey on priorities and communication requirements on PMU-based applications in the Nordic region. In: Proceedings of IEEE power tech 2009

Karlsson D, Hemmingsson M, Lindahl S (2004) Wide area system monitoring and control. IEEE Power Energ Mag 2(5):68–76

Marinez C, Parashar M, Dyer J, Coroas J (2005) Phasor data requirements for real time wide-area monitoring, control and protection applications, CERTS/EPG, EIPP-Real Time Task Team

Ouadi A, Bentarzi H, Maun JC (2009) A new computer based phasor measurement unit framework. In: Proceedings of 6th international conference SSD'09, Djerba, Tunisia, pp 1–6 (IEEE explorer)

Phadke AG (1993) Synchronized phasor measurements in power systems. IEEE Comput Appl Power 6(2):10–15

Phadke A (2008) The wide world of wide-area measurements. IEEE Power Energ Mag 2(4):52–65

Phadke A, Thorp JS (2008) Synchronized phasor measurements and their applications. Springer. ISBN: 978-0-387-76535-8

Phadke AG, Thorp JS, Karimi KJ (1986) State estimation with phasor measurements. IEEE Trans Power Syst 1(1):233–241

Phasor Application Classification (2007) NASPI data and network management task team

White A (OGE), Chisholm S (OGE), Khalilinia H (WSU), Tashman Z (WSU), Venkatasubramanian M (WSU) (2012) Analysis of subsynchronous oscillations at OG&E. NASPI-NREL Synchrophasor technology and renewables integration workshop, Denver, CO

White A, Chisholm S (2011) Relays become problem solvers. Transm Distrib World 63(11):26–33

Wiik J, Gjerde JO, Gjengedal T (2000) Impacts from large scale integration of wind energy farms into weak power systems. In: Proceedings of the international conference on power system technology, pp 49–54

Zima M, Larsson M, Korba P, Rehtanz C, Andersson G (2005) Design aspects for wide-area monitoring and control systems. Proc IEEE 93(5):980–996

Chapter 26
Historical Development of UAV Technologies in the World: The Case of Turkey

Sinem Kahvecioglu and Hakan Oktal

Abstract The new technologies and designs on Unmanned Aerial Vehicles (UAVs) have created a new market which made it possible for many countries to compete by penetrating and dominating the market. The new advances in computer and material science enhanced data link capabilities; developments in sensor technologies and the component miniaturization are the main factors which strengthen the UAV capabilities and accelerate their usage. The UAV applications which become diversified each passing day, have also been leading up to new projects on commercial air transportation in terms of design and areas of usage. In this framework, UAVs become a valuable instrument for development and testing of new fuel and propulsion systems which are one of the concerns of sustainable aviation. The aim of this study is first to explore the historical development of UAVs in the world, second to investigate the main UAV projects proceeded by Turkey and finally to reveal the future targets and the status of Turkey among the countries securing enhanced UAV experience.

26.1 Introduction

Both the technological developments and the usage in military and civilian applications of Unmanned Aerial Vehicles (UAVs) have recently reached unprecedented levels of growth (DeGarmo 2004a). UAVs can be defined as "a powered aerial vehicle that does not carry a human operator, uses aerodynamic forces to provide vehicle lift and can be controlled remotely, autonomously, semi-autonomously or by a combination of these" (Department of Defense 2001).

S. Kahvecioglu · H. Oktal (✉)
Department of Avionics, Faculty of Aeronautics and Astronautics,
Anadolu University, Eskisehir, Turkey
e-mail: hoktal@anadolu.edu.tr

S. Kahvecioglu
e-mail: skahvecioglu@anadolu.edu.tr

The early UAVs used in the First World War were very unreliable and inaccurate, and their overall impact on military applications were not recognized by most military and politicians. None the less, by the beginning of 2000s, the total market for UAVs had reached more than $16 billion. Especially, US Department of Defense (DoD) became a main actor in funding activities, research and development, as well as procurement (Valavanis 2002). The US manufacturers had a market share of over 60 % in 2006. Total UAV market spending across the globe is expected to increase from $5 billion in 2010 to $5.9 billion in 2016 according to the market brief (Lucintel 2011), while the spending increase from 2005 to 2010 was nearly twice ($2.9 billion in 2005 and $5 billion in 2010). This increased attention was arisen from the terrorist attack on World Trade Center in 2001. On the other hand, Northrop Grumman and General Atomics are the dominant manufacturers in this industry, when it comes to the strength of the Global Hawk and Predator/Mariner systems (Unmanned Aerial Vehicles 2015). Israel is one of the most important competitors especially in military UAV market. The Heron which was developed by Israel Aerospace Industries is capable of Medium Altitude Long Endurance (MALE) operations of up to 52 h. It is expected from European countries to spend about €2 billion in research and development and procurement (Valavanis 2002). The other countries undergoing significant UAV development programs are Japan, Australia, South Korea, and China. Incidentally, in terms of numbers of operational UAVs, Japan leads the world with nearly 2000 UAVs being used today for agricultural spraying and planting operations (DeGarmo 2004a). There were more than a hundred UAV developers/manufacturers in China in 2010; that number was increased to over 230, of which over two third of them are private enterprises and the remaining were government owned in 2014. The Chinese UAV market is projected to be $1.6 billion in 2015, and within next two decades, it is expected to increase to $7.5 billion. As the end of 2013, there are over 15,000 UAVs operating in China in the civilian sector alone (Chinese UAV Programs 2015). According to the market brief (Lucintel 2011), the Asia-Pacific region shows the highest growth in UAVs.

It is inevitable to use UAVs in the military and civilian fields because of the missions

- containing the risk of loss of life
- requiring the instantaneous maneuvering
- performed in atmospheric conditions that the humans cannot resist
- requiring the independence from the human physical and mental fatigue.

Furthermore, the other reason to elect UAVs instead of manned aircraft in various missions is the lower costs of production, operation, and maintenance.

In the following sections, primarily historical development of UAV technologies in the world and their usage in both military and civil fields, second major Turkish UAV projects, the future targets and the status of Turkey in the competitive

UAV market are examined. Finally, concerns about the UAV systems purchased from foreign sources in the usage of Turkish border security and the necessity of national UAV projects are emphasized.

26.2 UAV History

When the numerous studies in the literature related to UAVs are examined, it can be seen that the historical development of UAVs may be divided into four phases as mentioned below

Phase I: The early efforts on the mechanism of "flying machine without a human" occurred in Phase I. According to some documents, the idea of UAV initially emerged and was put into practice in the form of mechanical birds in ancient times, and then unmanned balloons were used as unmanned aerial bombers and kites were used for aerial reconnaissance in the second half of 1800s (Valavanis 2002; Barnes 2009; Perley 1863).

Phase II: The presence of today's UAV technology depends on the developments materialized in Phase II. The UAVs in today's context began to develop primarily in the field of military applications during the years of the First World War. Even though ballistic or semi-ballistic vehicles, cruise missiles, and artillery projectiles are not accepted as unmanned aerial vehicles according to the UAV definition, the presence of modern UAV technology is linked to early developmental work on guided bombs and missiles (Department of Defense 2001; Bento 2008). Over the course of the First World War, very similar "guided bombs" research and development programs were administrated by the UK, Germany, and the USA. However, by the end of the First World War, the interest in the research and development of guided bombs decreased and was not resuscitated until the radio-controlled target drones developed during 1930s (Barnes 2009). Though the US and the UK were producing small unmanned systems in volumes, it was the Germans who, during Second World War, made the greatest advances to unmanned aviation technology by means of the vengeance weapons program (DeGarmo 2004a).

Phase III: The requirements of modern UAV concept matured during Phase III. In the early 1950s, the US unmanned researches were solicitous about target drones for air-to-air and surface-to-air gunnery and missile training. In this direction, Teledyne Ryan Q-2 Firebee was developed. Firebee featured adaptability to different missions and being recoverable like the latest modern UAV platforms, hence it can be said that at this point the onset of modern unmanned concept transpired. As the Cold War deepened, the US and NATO became interested in UAVs primarily for reconnaissance, especially after the loss of the U2 spy-plane over the USSR in 1960. During the Vietnam War in 1964, UAVs, so-called Lightning Bug, were used for photo-reconnaissance, electronic intelligence (ELINT), and real-time communications intelligence (COMINT). However, UAV researches cut in the US by the end of the Vietnam War because of financial problems. During the 1970s, Israel secretly purchased twelve Firebees from the USA, and modified these UAVs

to act as surveillance platforms, decoy drones, and also Unmanned Combat Aerial Vehicles (UCAVs). They used these UAVs in the 1973 Yom Kippur War between Israel, Egypt, and Syria. Within a decade after the Vietnam and Yom Kippur Wars, Israel became a world leader especially in small UAV technology for surveillance of the battlespace and urban environment thanks to Scout and Pioneer UAVs (Barnes 2009). After the Operation Desert Storm in 1991 and the conflict in the Balkan Peninsula in the early 1990s, the interest in UAVs gained momentum again (Valavanis 2002). It was also in the 1990s that a more peaceful role for UAV systems was finally conceived. Scientific endeavors, such as persistent environmental monitoring, were seen as an ideal function for UAVs. The solar-powered Pathfinder and Helios, both developed by NASA and the Aerovironment Corporation in the late 1990s, exemplified the development of innovative research UAVs. Other countries also began to develop UAVs for nonmilitary applications. For example, an Australian firm produced a 30 pound UAV, called the Aerosonde Laima, which crossed the Atlantic Ocean for the first time autonomously in 1998 with only 1.5 gallons of automotive gasoline (DeGarmo 2004a). Also, the South American countries such as Argentina and Brazil got in the UAV running at the last half of the 90s. The Lipan M3 was the first surveillance, reconnaissance, and intelligence UAV developed by the Argentine Army in Latin America (Lipan 2015).

Phase IV: Not only the US which is still the dominant in UAV market but also new countries took part in competition in 2000s. The European UAV projects have been performed with the participation of Turkey, France, Germany, Spain, Italy, Greece, Sweden, and Switzerland. At the same time, Asia-Pacific countries such as South Korea, Japan and especially China have great potential for both civilian and military UAV market. Besides, the development of UAV technology was still proceeding especially in the field of the mini/micro UAV category in this final phase. As a consequence of the terrorist attacks on 9/11 and the Afghanistan War and Operation Iraqi Freedom, the conception of UAVs completely changed and these vehicles became a debatable topic not only in the military but also in everyday life thanks to their prominence in the media coverage (Valavanis 2002). Nowadays, the main tasks performed by UAVs in military fields can be mainly listed as Intelligence, Surveillance, Target Acquisition and Reconnaissance (ISTAR), combat and air defense, radar and communication relay, target drone, electronic warfare, antisubmarine warfare and air delivery/resupply (Arjomandi 2006; Haser 2010; Van Blyenburgh 2004). Although UAVs emerged from the military needs, nowadays, civilian intended usage has been increasing day by day. Some of the existing and potential tasks performed by UAVs in civil fields are aerial photography, land survey, weather forecasting, environmental monitoring, emergency operations, mapping, etc. In addition, civil law enforcements in some countries like the US have been using especially rotary wing UAVs in missing person cases and hostage situations. At the beginning of 2000s, as a result of the wide range of UAV usage, the development of air traffic control regulations become a must to enable their safe operation in unsegregated airspace (JPDO 2012; DeGarmo 2004b). The operations of the mini rotary wing UAVs such as mini helicopters and quadrotors
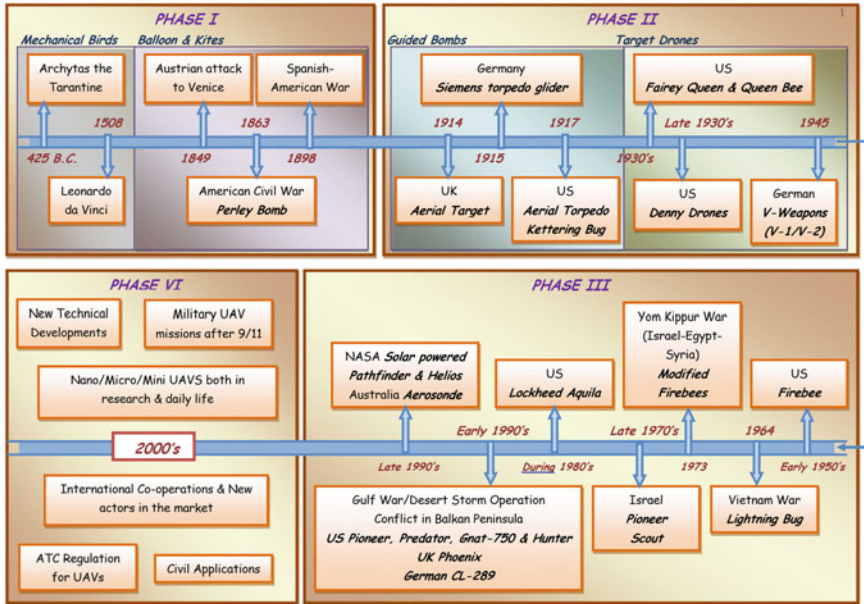
Fig. 26.1 History timeline of UAV development

by the civilians for hobby/recreational flying activities without taking any permission from the aviation authorities can cause an important safety risk for both commercial and military flights.

The summary of these phases are given in Fig. 26.1.

26.3   UAV Studies in Turkey

The UAV needs of Turkish Armed Forces (TAF) were supplied by means of direct procurement from foreign countries until early 2000s. In this period, Banshee target drones, GNAT, and I-GNAT UAVs were purchased from the UK and the USA, respectively.
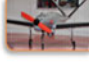
The UAVs and their related systems provided from abroad caused dependency on foreign sources in the matter of maintenance, procurement of spare parts, system and software updating/upgrading. While the direct procurements of TAF continue, the TAF started the firing and the target drones projects with the cooperation of TAI. In this framework, at the beginning of 2000s, the firing target drone *Turna*, the tracking target drones *Keklik, Baykuş, Pelikan, Martı,* and the tactical UAV *Gözcü* were developed as the Turkish indigenous UAVs.

The year 2004 is the milestone for Turkish UAV industry after the Undersecretariat for Defence Industries (UDI) was designated as the authority for

1989	Banshee	Meggitt Defence Systems	→ Direct procurement
March 1990	UAV X-1	TAI	
1994	GNAT	General Atomics	→ Direct procurement
August 1995	Keklik	TAI	
August 1995	Turna	TAI	
May 1998	I-GNAT	General Atomics	→ Direct procurement
2002	Harpy-1	IAI	→ Direct procurement
August 2003	Baykuş	TAI	
August 2003	Pelikan	TAI	
August 2004	Martı	TAI	
December 2004	(MALE) ANKA	TAI	
March 2005	Arı	Vestel Defence	
July 2005	Efe	Vestel Defence	
August 2005	Heron	IUP	→ Direct procurement
October 2006	Bayraktar	Kalekalıp/Baykar Partnership	
2008	Malazgirt	Baykar	
December 2010	Karayel	Vestel Defence	
December 2011	Çaldıran	Kalekalıp/Baykar Partnership	
2012	ANKA/Block-A	TAI	
October 2013	ANKA - S	TAI	
January 2015	ANKA/Block-B	TAI	

Fig. 26.2 The historical development of Turkish UAV industry (Undersecretariat for Defence Industries 2011)

Table 26.1 Technical specifications (UAV Projects—TAI 2015; Efe and Karayel UAV 2015; Baykar UAV Systems 2015)

UAV		MTOW (kg)	MFA (ft)	E (hr)	R (km)	Speed (kts)	UAV		MTOW (kg)	MFA (ft)	E (hr)	R (km)	Speed (kts)
Turna		70	12000	1.5	50+	180 (max.)	R-300		325	10000	4+	200	70 (max)
Keklik		10	10000	0.5	1.5	80 (max.)	Efe		500	22500	20+	150+	60-80 (cruise)
Gözcü		85	10000	2+	50	75 (cruise)	Karayel		4,1	12000	1,5	15	27 (cruise)
ANKA		1600	30000	24	200	110 (cruise)							
Çaldıran		450	22500	14	150	100 (cruise)							
Bayraktar		4.5	3000	1-1.5	15-25	33 (cruise)							
Malazgirt		12	3600	1.5	20	32 (cruise)							

MTOW: Maximum Take-Off Weight   MFA: Maximum Flight Altitude   E: Endurance   R: Range

all research, development, and procurement activities. Mini, Tactical and Medium Altitude Long Endurance (MALE) class UAVs were determined as the primary needs. The MALE class UAV "*ANKA*" developed by TAI, was the most prominent project among all others conducted by private companies and universities. Additionally, *R-300* as a VTOL Intelligence Surveillance Reconnaissance (ISR) UAV by TAI, *Çaldıran* by Kalekalıp/Bayraktar Partnership, *Bayraktar* as a fixed-wing Mini UAV and *Malazgirt* as a rotary wing Mini UAV by Baykar Technologies, *Karayel* as a Tactical UAV and *Efe* as a mini UAV by Vestel Defence are the other indigenous Turkish UAV projects.

The historical development of Turkish UAV industry and the technical specifications of UAVs developed by Turkish companies are given in Fig. 26.2 and Table 26.1, respectively.

26.4 Conclusion

The UAVs are accepted as the revolutionary vehicles in the history of aviation. Although UAVs were designed only for military purposes at the beginning, nowadays, they are also used for civil purposes such as scientific research, emergency operations, cinema, photography, road traffic monitoring, cargo shipping, etc.

It is estimated that the civilian use of UAVs will continue progressively in the future.

As well as the US and Israel are the dominant countries throughout history in UAV market Turkey, France, Germany, China, and Japan are the main countries penetrating the market as the new competitors. Hereafter, the countries are planning to concentrate on the indigenous UAV design and production projects especially for military missions in order to decrease the foreign dependency.

The UAVs have been used as a testing platform in today's commercial air transportation researches, especially in the development of morphing aircraft and new generation propulsion and fuel systems. The use of morphing wings technology in UAVs, the solar or electrically powered UAV systems, the use of biofuel and hydrogen fuel cells in UAVs are the prominent studies which contribute to sustainable aviation.

Today, the UAV studies focus on not only the development of new technologies but also the integration of civil airspace and the reconstruction of air traffic regulations.

References

Arjomandi M (2006) Classification of unmanned aerial vehicles. MECH-ENG 3016, Aeronautical Engineering Handouts

Barnes O (eds) (2009) Air power UAVs: the wider context. Royal Airforce, Directorate of Defence Studies

Baykar UAV Systems (2015). http://baykarmakina.com/sistemler/?lang=en. Accessed 3 Aug 2015

Bento MF (2008) Unmanned aerial vehicles: an overview. Inside GNSS January/February, pp 54–61

Chinese UAV Programs (2015). http://www.wcarn.com/. Accessed 3 Aug 2015

DeGarmo MT (2004a) Issues concerning integration of unmanned aerial vehicles in civil airspace. MITRE Product, McLean, Virginia

DeGarmo MT (2004b) Roadmap for integrating unmanned aerial vehicle (UAV) operations routinely in civil airspace. MITRE Technology Program

Department of Defense (DoD) (2001) Dictionary of military and associated terms. USA

Efe and Karayel UAV (2015). http://www.vestelsavunma.com/?lang=en. Accessed 3 Aug 2015

Haser AB (2010) Bu insansız hava aracı'ndan daha önce yapmamış mıydık? Bilim ve Teknik, Tübitak Yayınları 44(517):32–37

JPDO (USA) (2012) NextGen UAS research, development and demonstration roadmap. Version 1.0

Lipan M3 (2015). http://en.wikipedia.org/wiki/Lip%C3%A1n_M3. Accessed 3 Aug 2015

Lucintel (2011) Growth opportunity in global UAV market

Perley C (1863) Improvement in discharging explosive shells from balloons. US Patent 37771, 24 Feb 1863

UAV Projects—TAI (2015). https://www.tai.com.tr/en/department/uav-systems. Accessed 30 July 2015

Undersecretariat for Defence Industries (UDI) (2011) UAV roadmap (2011–2030) document. Ankara

Unmanned Aerial Vehicles (2015). http://en.wikipedia.org/wiki/Unmanned_aircraft_system. Accessed 10 Aug 2015

Valavanis KP (2002) Advances in unmanned aerial vehicles: state of the art and the road to autonomy. Springer

Van Blyenburgh P (2004) UAVs: a worldwide overview. Paper presented at the Asia-Pacific conference on asian aerospace UAV, 23 Feb 2004

Chapter 27
Additive Manufacturing for Lightweight Aviation Parts

Çağrı Gürbüz

Abstract Environmental performance commitments, complex government requirements and market conditions force aviation industry lead aircraft manufacturers to produce lighter and more efficient products. New concepts and designs are not possible to manufacture with traditional manufacturing methods. Additive manufacturing (AM) methods may answer to the needs of industry.

Environmental performance commitments, complex government requirements and market conditions force aviation industry lead aircraft manufacturers to produce lighter and more efficient products. New concepts and designs are not possible to manufacture with traditional manufacturing methods.

In additive manufacturing (AM) process parts are built up layer-by-layer. 3D CAD model data is sliced into many very thin cross section profiles. These cross section perimeters are traced either by a laser, electron beam, extrusion nozzle or jetting nozzle and the area contained by the perimeters are filled with a hatching pattern. Once a layer has been deposited, the next layer is added. This is repeated until the whole part has been generated. AM is defined by ASTM as "Process of joining materials to make objects from 3D model data, usually layer upon layer, as opposed to subtractive manufacturing methodologies".

Due to this layer manufacturing approach, compared with traditional processes, parts of significantly greater complexity can be produced and it enables the production of parts up to half of its original weight.

This increased complexity generally does not have a significant effect on the cost of the process. This provides the designer with significantly greater design freedom and enables the built part to be closer to the optimum design than is possible with traditional processes.

Ç. Gürbüz (✉)
Sentes-BIR A.S., Kemalpaşa Organize Sanayi Bölgesi Ankara cad.
No: 343, 35730 Kemalpaşa, İzmir, Turkey
e-mail: cagri.gurbuz@sentes-bir.com

333

Todd Rockstroh of GE Aviation claims that AM could save up to 450 kg on a 2700 kg engine. GE is already planned to manufacture 85,000 fuel nozzles for LEAP engines using AM method.[1]

The Airbus Group Innovations conducted a study about an environmental life-cycle comparison of two key production technologies. A generic bracket part is choosen for benchmarking AM process with a conventional casting process as the baseline.

Using AM technologies, the hinge may reduce the weight per plane by 10 kg, a noteworthy saving when overviewed at industry "buy-to-fly" ratios. CO_2 emissions over the whole lifecycle of the nacelle hinges were reduced by nearly 40 % via weight saving that resulted from an optimized geometry, which is enabled by the design freedom offered by the AM process and the use of titanium.

Further analysis focused on the benchmarking of manufacturing process itself. The total energy consumption for creating the initial raw powder metal, then producing the bracket in AM, was slightly smaller than the equivalent cast process steps. The AM process itself used only the material actually needed to make the part—thereby eliminating waste from secondary machining and reducing consumption of titanium by 25 % over the cast application.

Jon Meyer, Additive Layer Manufacturing Research Team Leader stated in his final report "in general, the study revealed that AM has the potential to build light, sustainable parts in regard with the company's CO_2 footprint."

A new research project, entitled Horizon, has begun with the funding of UK Government to boost the aerospace industry. The project will utilise 3D printing to develop the next generation of lighter, greener planes. The UK's Aerospace Technology Institute is backing the project, which hopes to improve processes by taking AM techniques from research and development, through to viable production processes. It is believed the created components could be as much as 50 % lighter than their conventional counterparts with complex geometries that cannot be cost effectively manufactured today.

These new processes will unlock innovations in low drag, high-performance wing designs and lighter, more efficient engine systems, with the potential to dramatically reduce aircraft fuel consumption and emissions.

The following examples show the approach of designers to AM—additional data enhances the structural benefits and savings achieved with the new manufacturing process.

---

[1]Additive Manufacturing, 7/3/2012, Peter Zelinski.

27.1   Engine Bracket

GE challenged the public, with a prize of $7000, to redesign a metal jet engine bracket, making it 30 % lighter while preserving its integrity and mechanical properties like stiffness. Participants from 56 countries submitted 640 designs (Fig. 27.1).

The winning design passed the 30 % weight reduction goal and able to slash its weight by nearly 84 % to just 327 g. The original part weights 2.033 g (Fig. 27.2).[2]

Fig. 27.1 GE engine bracket—original design

Fig. 27.2 GE engine bracket—optimized design

---

[2]http://sffsymposium.engr.utexas.edu/sites/default/files/2014-110-Carter.pdf.

Fig. 27.3 Airbus nacelle
hinge bracket

27.2   Nacelle Hinge Bracket

In the benchmarking study of The Airbus Group Innovations a standard bracket is
choosen as baseline part. The optimized geometry of the hinge may reduce the
weight per plane by 10 kg (Fig. 27.3).[3]

27.3   Fuel Nozzles

Fuel nozzles have complex geometries and 18 different parts are assembled during
manufacturing process. With the use of AM, GE managed to produce all as one
single part. This new design is also almost 25 % lighter compared to old design.

This manufacturing process also offer the chance to include internal cooling
channels which reduces degradation of the nozzle due to the exposure of fuel to the
high temperatures and increase fuel efficiency in time (Fig. 27.4).

Another similar attempt is from a helicopter engine manufacturer. Turbomeca is
adapting AM technology to manufacturing fuel-injector nozzles and combustion
swirlers. With AM these complex parts are manufactured as a single piece and also
it is possible to add advanced injection and cooling functions with new design
(Fig. 27.5).

---

[3]http://www.eos.info/press/customer_case_studies/eads.
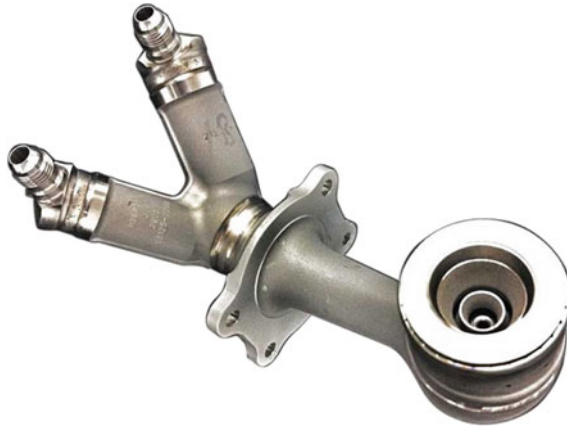
Fig. 27.4 LEAP engine fuel nozzle

Fig. 27.5 Turbomeca's nozzle and combustion swirler

27.4 SAVING Project

The SAVING project (**S**ustainable product development via design optimization and **A**dditi**V**e manufactur**ING**). The project focused on design and process optimisation, applied to AM, with the objective of creating innovative designs that could be manufactured or utilised more efficiently than current practice.

Design optimisation and analysis of hollow and cellular structures would create minimalist geometries.

As an example of these studies, traditionally constructed, airline seat belt buckles weigh between 155 g (Steel) and 120 g (Aluminium) reduced to a Titanium part with 68 g weight made with AM, without compromising strength. An Airbus A380 when configured for economy passengers has 853 seats. Exchanging the traditional steel buckle for an additive manufactured titanium buckle would lead to a total

Fig. 27.6 Lighter seat belt buckle design

weight saving of 74 kg. This could lead to a 3,300,000 l fuel saving over the life of the plane and 0.74 Mt less CO_2 emissions (Fig. 27.6).[4]

AM lends itself to complex internal architectures that could not previously be manufactured using traditional methods, with one such approach being internal lattice structures.
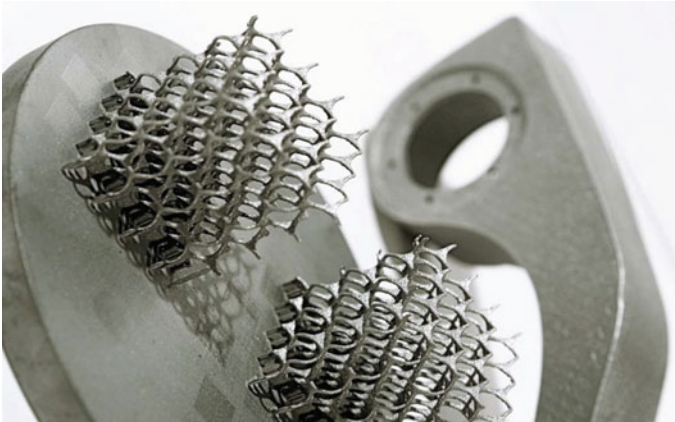
Fig. 27.7 Internal lattices of redesigned monitor arm

---

[4]http://www.3trpd.co.uk/portfolio/saving-project-saving-litres-of-aviation-fuel/.

27.5   Latticed Structures

Re-design of the arm holding the TV monitors in Virgin Atlantic flights' upper class seats. Latticing reduced the arm's weight by 50 %, saving about 500 g per unit, through lifecycle saving of 54.3 t CO_2 emission equivalent to 20,000 l of Jet A1 over lifetime of the aircraft (Fig. 27.7).[5]

27.6   Discussion

These sample components will give us proper feedback about the reliability of this production technology. In near future more parts produced with AM will be seen on airplanes.

AM will be an important tool to keep up with sustainability in aviation.

---

[5]Additive manufacturing: opportunities and constraints, Royal Academy of Engineering November 2013 ISBN: 978-1-909327-05-4.

Part III
Aerodynamics

Chapter 28
Investigation of Airframe in Terms of Aerodynamics

Anil Can Turkmen, Ferit Yildiz, Cenk Celik and Halil Ibrahim Sarac

Abstract In this study, four different types of aircraft body were analyzed according to the aerodynamic flight conditions in the form of cruise. A319, A320, A330, and A340 model aircrafts of the Airbus firm were used. Only the body parts of the plane were drawn and the analysis process has been studied in a scale of 1/1000 for convenience.

28.1 Introduction

In this study, responses across airflow during the cruise of four different models of aircraft offered for commercial use, which are produced by Airbus, were examined. In general, the studies related to the aircraft are on the wing. However, factors such as the stability, fuel consumption, and flight comfort during flight depends on the aerodynamic structure of the airframe. Therefore, only the body of the aircraft was considered.

In 1903, the Wright brothers invented and flew the first airplane (FAI News 2003). After that, airplanes were developed more and they became an important role in all the major battles of World War II. The first jet airliner, the de Havilland Comet, was introduced in 1952 and the Boeing 707 was the first widely successful commercial jet. Now, air transport has become one of today's most widely used transport type. The number of aircrafts in the fleet of airlines around the world has reached to 27047 in 2010. Between the years 2008 and 2009, some airlines returned

A.C. Turkmen (✉) · F. Yildiz · C. Celik · H.I. Sarac
Makine Mühendisliği Bölümü, Kocaeli Üniversitesi, 41380 İzmit, Kocaeli, Turkey
e-mail: anilcan.turkmen@hotmail.com

F. Yildiz
e-mail: ferit.yldz@hotmail.com

C. Celik
e-mail: cenkcelik@kocaeli.edu.tr

H.I. Sarac
e-mail: sarac@kocaeli.edu.tr

their leased aircraft in the fleet and some aircraft were retired because of the effects of the economic crisis and high fuel prices (Simsek 2010).

The design of the fuselage is bounded by a wide range of requirements coming from the manufacturer, from the operator, from the airport, or from the regulator (EASA for Europe or FAA for USA). An airline is interested to carry as much payload as possible, while ensuring enough passenger comfort. In this context, the manufacturer aims to build a flexible, cost efficient, performance-based design.

Today, the aircraft design depends on cabin design. Modern aircraft designs apply a design approach called "from inside out". If in the past, the cabin width was kept constant for all the aircraft family variations, today other factors made the aircraft manufacturers change their approach and allow more design flexibility with this respect. Both views are important at the same time: Passenger comfort challenges environmental requirements for CO_2 reduction and energy savings (Nila et al. 2010).

Developments of aircraft designs still continue and NASA's goals for a 2030-era aircraft are (Sforza 2014)

- Reduction of noise by 71 db below current FAA noise standards to contain objectionable noise within airport boundaries.
- More than a 75 % reduction on the International Civil Aviation Organization's (ICAO) standard for nitrogen oxide emissions for improving air quality around airports.
- More than a 70 % reduction in fuel burn to reduce greenhouse gas emissions and the cost of air travel.

As the analysis results were interpreted, the air flow in the ambiance, the pressure generated around the aircraft, air speed, and turbulence kinetic energy in the ambient are taken into consideration.

28.2 Initial Conditions of the Analysis

For this study, four different aircraft models of Airbus were selected. These are A319, A320, A321, A330. These aircrafts' technical data were shown in Fig. 28.1.

Analysis airframes were drawn in SolidWorks and CFD analyzes were performed with Ansys software. For rapid analysis, drawings were carried out in 1/1000 scale.

Analysis in this study was performed with the given initial conditions and they are the same for all analysis. Analysis was conducted in leading international flight altitude and speed. To simulate this movement, the fuselage was kept constant and the air in the environment was moved. The reduction in the temperature during rising from the ground was taken into account when analysis was performed.

However, another point is being considered in the analysis: the feature of the air in the environment. As known from the other materials, characteristics of the air are depending on various circumstances such as the temperature, movement, and

	A319	A320	A330	A321
Overall length	33.84 m	37.57 m	58.82 m	44.51 m
Cabin length	23.78 m	27.51 m	45.00 m	34.44 m
Fuselage width	3.95 m	3.95 m	5.64 m	3.95 m
Max cabin width	3.70 m	3.70 m	5.28 m	3.70 m
Wing span (geometric)	35.80m	35.80m	60.30m	35.80 m
Height	11.76m	11.76m	17.39m	11.76 m
Track	7.59 m	7.59 m	10.69 m	7.59 m
Wheelbase	11.04 m	12.64 m	22.20 m	16.91 m
Typical seating/Max	124/156	150/180	246/380	185/236
Bulk hold volume	7.20 m³	5.90 m³	19.70 m³	5.90 m³
Total volume (Bulk loading)	27.70 m³	37.40 m³	136.0 m³	51.70 m³
Range	6 850 km	6 100 km	13 400 km	5 950 km
Max ramp weight	64.4 (75.9) tonnes	73.9 (78.4) tonnes	230.9 (242.9) tonnes	89.4 (93.9) tonnes
Max take-off weight	64.0 (75.5) tonnes	73.5 (78.0) tonnes	230.0 (242.0) tonnes	89.0 (93.5) tonnes
Max landing weight	61 (62.5) tonnes	64.5 (66.0) tonnes	180 (182) tonnes	75.5 (77.8) tonnes
Max zero fuel weight	57.0 (58.5) tonnes	61.0 (62.5) tonnes	168.0 (170) tonnes	71.5 (73.8) tonnes
Max fuel capacity	30 190 litres	27 200 litres	139 090 litres	24 050 litres

Fig. 28.1   The aircrafts' technical data (Airbus 2015)

Table 28.1   The initial conditions of the motion of the aircraft (Instrument Flying Handbook 2010)

Altitude	9144 m
Speed	194.44 m/s
Temperature	−34.864 °C
Pressure	30.149 kPa

Table 28.2   The characteristics of the ambient air (U.S. Standard Atmosphere 1976)

Mean molecular weight	28.9644 kg/kmol
Density	0.45904 kg/m^3
Dynamic viscosity	0.000014876 Pa s
Kinematic viscosity	0.000032407 m^2/s
Coefficient of thermal conductivity	0.020522 W/m K

pressure of the ambient. The initial conditions of the analysis are determined considering these variations. The initial conditions of the motion of the aircraft are given in Table 28.1, the air characteristics in the environment are given in Table 28.2. Analysis environment has got a 5 % turbulent and the most suitable environment model for this type of turbulence was Shear Stress Transport (SST) (Ansys 2015).

28.3   Results and Discussion

Looking at the results of the analysis, the longer the body of the A320 series aircraft (A319, A320, A321), the lower is the pressure exerted by the air in the nose. However, the vacuum effect which is created behind the tail increased by the area
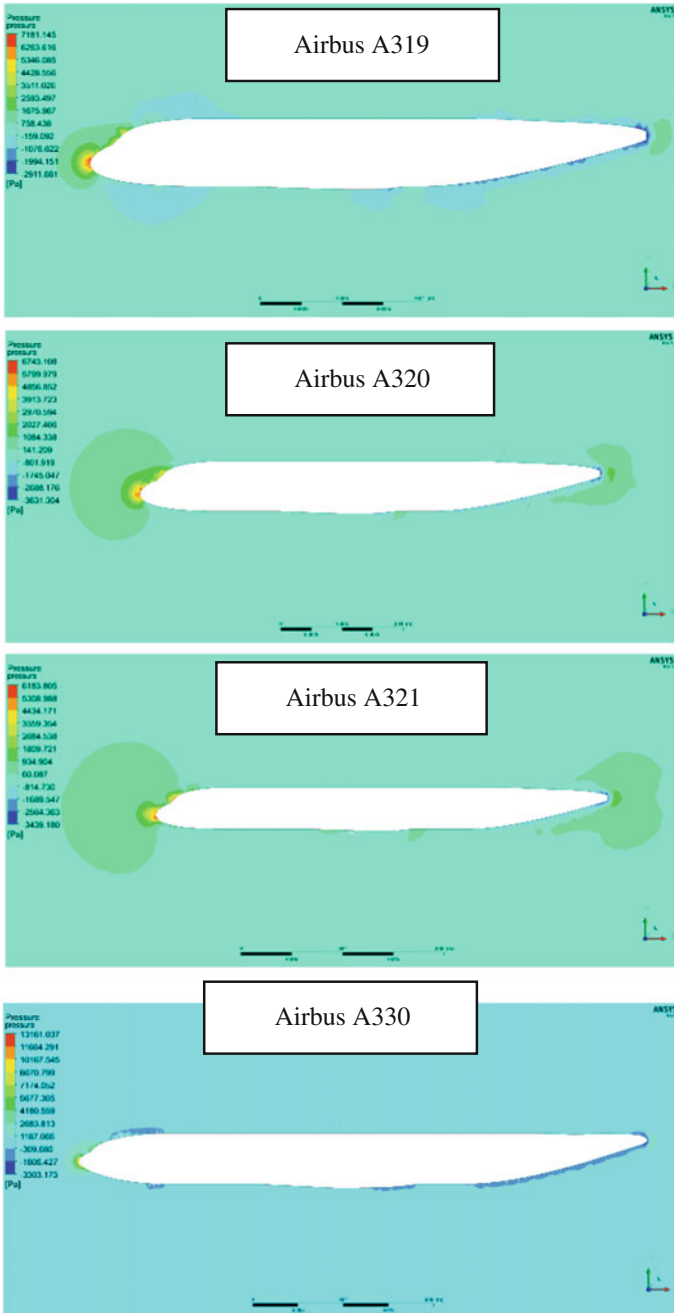
Fig. 28.2 Pressure around fuselage
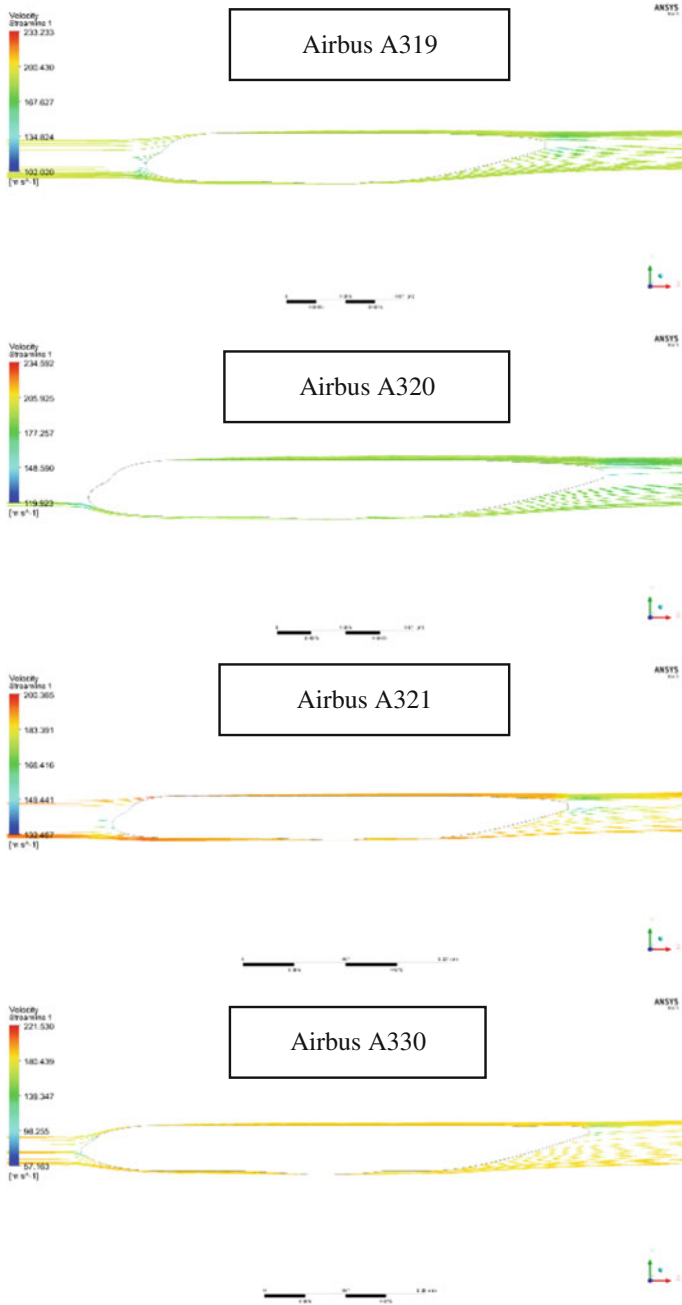
Fig. 28.3 Streamline around fuselage
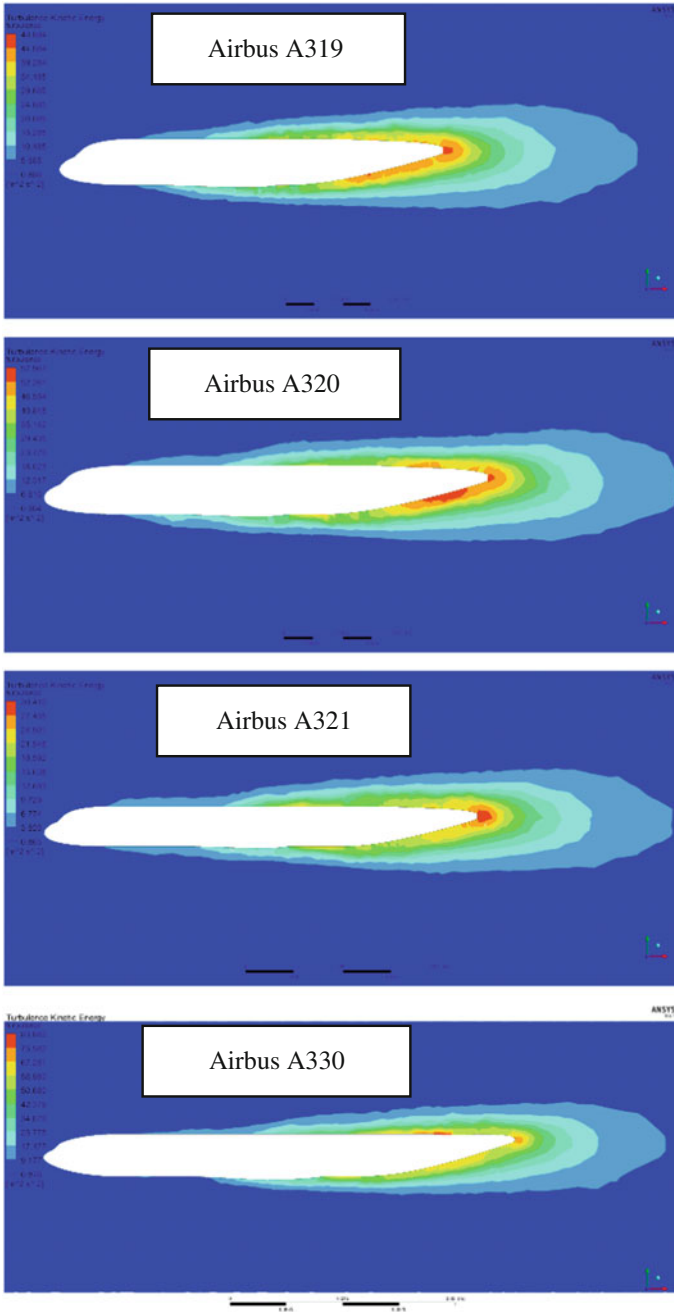
Fig. 28.4 Turbulence kinetic energy around fuselage

Table 28.3 Analysis results

	Pressure (kPa)		Streamline—velocity (m/s)		Turbulence kinetic energy (m^2/s^2)	
	Max	Min	Max	Min	Max	Min
A319	7.181	−2.911	233.233	102.020	48.884	0.886
A320	6.743	−3.631	234.592	119.923	57.967	0.904
A321	6.183	−3.439	200.365	132.467	30.410	0.865
A330	13.161	−3.303	221.530	57.163	83.882	0.876

but decreased by the value. The A330 has about two times the pressure of the other aircraft at the nose area. This is because the end portion is quite sharp compared to other aircraft. Besides this disadvantage, negative pressure formed in the A330s tail is reduced according to the other aircraft (Fig. 28.2).

Looking at the flow lines around the aircraft, analysis which was made of the aircraft model is very close to the surrounding air flow rate, all except the nose and tail sections. But the flow in the tail of the A330 is quite smooth. Because of the larger plane body compared to the others, the speed of the wind at the nose section is very low. Flow lines, which are passing over and under the A320 series aircraft with the same body height as A330 are joined further away (Fig. 28.3).

Turbulent flow is one of the most researched topics of fluid mechanics. The received high-speed path of a fluid in an aircraft must be minimum of turbulence in the ambient. The higher the turbulent kinetic energy is, the higher will be turbulent of the system and of the environment. Analysis results showed that A321 has the lowest turbulence values. If we evaluate the A320 aircraft on its own, then the A321 aircraft has the longest body. In addition, turbulence in the upper part and the lower part of the A330 housing is formed asymmetrically (Fig. 28.4).

Analysis results are shown in the Table 28.3.

28.4   Conclusions

In this study, 194.44 m/s speed in 9144 m altitude for four different fuselage, which was in cruise, CFD analysis was conducted in accordance with the ambient conditions. This analysis shows that the aircraft with the same body height with different length was observed as a result of exposure to less pressure. However, a large amount of body height increases the cross-sectional area of the wind receiving aircraft. The increasing of the cross-sectional area leads to a significant reduction of the wind velocity from the nose of the aircraft. This reduction creates a pressure buildup at the nose of the aircraft.

Analysis carried out under the conditions specified in the model A321 aircraft is forming at least turbulence. Turbulence field created by this model with length/height ratio of approximately 10:30 has a highly symmetrical structure. This is very important for stability during flight status.

If all these conditions are due to the body structure of the 2D analysis only considered, the most suitable aircraft that can be used depending on the initial conditions is A321.

References

Ansys-CFX (2015) User Manual

FAI News (2003) 100 years ago, the dream of Icarus became reality posted 17 December 2003. Retrieved 5 Jan 2007

Instrument Flying Handbook (2008) Instrument flight rules. Federal Aviation Administration, Oklahoma City, OK, p G–9. Retrieved 27 Nov 2010

Nila M, Scholz D (2010) Deutscher Luft- und Raumfahrtkongress. From preliminary aircraft cabin design to cabin optimization

Sforza P (2014) Commercial airplane design principles. In Fuselage design, pp 47–79

Simsek G (2012) 3 thousand aircrafts out of use, Haberturk, 2010

U.S. Standard Atmosphere (1976) U.S. Government Printing Office, Washington, D.C.

www.airbus.com. Accessed on March 2015

Chapter 29
Flow Field Investigation of Rib-Roughened Serpentine Channel

Tolga Yasa, Isa Kavas, Sefa Yilmazturk and D. Funda Kurtulus

Abstract This paper presents numerical flow field and heat transfer analysis of a channel consisting of upstream and downstream channels and a 180° bend. Turbulators (rib) with a square cross-section are placed in the straight part of the channels in order to enhance the heat transfer while flow enters to the model at fully developed conditions at Reynolds numbers of 20000. A constant heat flux boundary condition is provided from the bottom wall of the model. Numerical simulations are performed by a commercial solver using realizable k-ε turbulence model with enhanced wall treatment. The flow field development and evaluation of pressure drop accounted by each rib are analyzed along the channel. The effects of ribs to the flow field are characterized by wall shear distribution. The effect of u-bend on the downstream flow field is investigated.

Nomenclature

D_h	Hydraulic diameter [mm]
De	Dean number
De	$De = Re \cdot \sqrt{(R_{out} - R_{inner})/R_{center}}$
H	Channel height [mm]
P	Pressure [bar]
R	Radius of the curvature [mm]
Re	Reynolds number $Re = (U \cdot \rho \cdot D_h)/\mu$
S	Curvilinear length [mm]
U	Flow velocity [m/s]

Greek

ζ	Kinetic loss coefficient
γ	Heat capacity ratio

T. Yasa (✉) · I. Kavas · S. Yilmazturk
TUSAS Engine Industries, Eskisehir, Turkey
e-mail: tolga.yasa@tei.com.tr

D.F. Kurtulus
Department of Aerospace Engineering, METU, 06800 Ankara, Turkey

ρ   Density [kg/m^3]
μ   Dynamic viscosity [kg/(m s)]
τ   Wall shear stress [Pa]

Subscripts
0   Total quantity
In Inlet plane
st Straight
w   Wall
x   Spanwise coordinate
y   Transverse coordinate
z   Streamwise coordinate (at straight channels)

29.1   Introduction

Serpentine channels with 180° turn are used widely in gas turbine blades, electrical
cooling equipment, and high speed rotating systems. Such channels are usually
equipped with turbulence promoter rib structures on the walls in order to increase
the heat transfer effectiveness. The effect of rib configuration on heat transfer is well
characterized for straight channels in the last decades (Han et al. 1978, 1985, 1989,
1991; Han 1984, 1988; Han and Park 1988; Park et al. 1992; Han and Zhang 1992;
Kukreja et al. 1993; Taslim et al. 1996). Once a compact heat exchanger design is
required, serpentine channels in which such straight pipes are connected to each
other through bends are preferred. In such channels, flow generates a Dean vortex
pair through the u-bend. Dean vortices strongly influence the flow field and heat
transfer characteristics of downstream channel. The characterization of the flow
through a sharp turn is studied by a number of researchers in smooth channels
(Azzola et al. 1986; Schabacker et al. 1998; Liou and Chen 1999; Syuhada et al.
2001). The interaction of the u-bend section and rib-roughened channel is still
under investigation to better understanding of flow physics and their effect on heat
transfer.

The flow field of serpentine rib-roughened channel is numerically analyzed
using Reynolds-averaged Navier–Stokes (RANS), Unsteady Reynolds-averaged
Navier–Stokes (URANS), Large eddy simulation (LES), and Detached eddy sim-
ulation (DES) (Viswanathan and Tafti 2006; Sewall and Tafti 2006; Luo and
Razinsky 2009; Murata and Mochizuki 2004; Egger et al. 2014; Zhao and Tao
1997; Yanase et al. 2005). The modeling of turbulence is one of the key points in
simulations. It is reported by various researchers that SST and realizable k-ε tur-
bulence models give satisfactory results (Luo and Razinsky 2009; Egger et al. 2014;
Zhao and Tao 1997) when such channel flow is simulated.

The relation of geometrical parameters to the aero-thermal performance has also been investigated in the literature. The effect of inner wall on heat transfer characteristics is studied using three different shapes; i.e., straight turn, rounded turn, and circle turn (Wang and Chyu 1994). The maximum heat transfer is observed when the inner wall has a straight turn. Moreover, the influence of inner wall thickness is tested at a $Re = 12000$ and the highest thermal performance is obtained at minimum wall thickness (Liou et al. 2000).

The thermal behavior of serpentine channels is experimentally analyzed by various research groups (Syuhada et al. 2001; Zhao and Tao 1997; Yanase et al. 2005; Wang and Chyu 1994; Liou et al. 2000, 2003, 2007; Ligrani and Hedlund 1998; Mochizuki et al. 1999; Pu et al. 2013; Chanteloup et al. 2002; Egger et al. 2013; Wagner et al. 1992; Mochizuki et al. 1994). Syuhada et al. (2001) perform heat transfer measurements at $Re = 35000$ on a smooth channel. They obtain the maximum heat transfer rate at the outer wall region in the u-bend. A real low pressure blade cooling model, i.e., smooth channel, is investigated using Particle image velocimetry (PIV) technique (Pu et al. 2013). The secondary flows at u-bend outlet and the downstream of the u-bend is characterized at $Re = 44000$. The effect of ribs with 90° and 60° orientation on heat transfer is tested and it is concluded that results with 60° leads to the highest thermal performance (Mochizuki et al. 1999). There are other studies for ribs with 45° orientation where the vortex structures and heat transfer characteristics are correlated (Chanteloup et al. 2002; Egger et al. 2013). In addition to the static experiments, two pass square ducts are tested in a rotation to simulate Coriolis force of turbine blades (Wagner et al. 1992; Mochizuki et al. 1994; Liou et al. 2003, 2007).

In this paper, a rib-roughened channel with a 180° turn is studied numerically to understand the flow field especially downstream of u-turn. The model is equipped with square cross-sectional ribs in upstream and downstream of the channel. The blockage ratio defined as a ratio of rib height to channel height and it is chosen as 0.1. The flow Reynolds number is set to 20000 to simulate real working conditions. The numerical model is validated by a smooth channel case before investigating the flow. The pressure drop of each rib section and u-bend are analyzed.

29.2 Numerical Setup

29.2.1 The Channel Model

The channel model consists of two straight (upstream and downstream) channels which are connected by a 180° bend channel. The tunnel has a square cross-section with a hydraulic diameter of 80 mm which represents a scale up experimental model. Figure 29.1a shows overall dimensions of the model. The straight parts of the model are equipped with six and five ribs, respectively. The ribs have a square cross section and the height is equal to 10 % of the channel height (H) as depicted
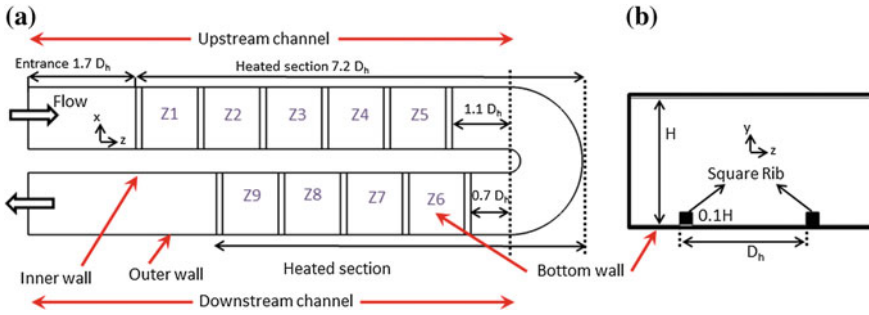
Fig. 29.1 Channel model **a** top view **b** rib-roughened wall

in Fig. 29.1b. Only bottom wall of the model is equipped with the ribs which are perpendicular to the main flow direction. The distance between two consecutive ribs is set to one hydraulic diameter. The first rib in downstream channel is located $0.7\ D_h$ further from the geometrical center of the u-bend.

29.2.2 Numerical Simulations

The flow field of the channel is analyzed based on three-dimensional computations. A commercial finite volume code which solves RANS equations is used with second-order upwind scheme (Barth and Jespersen 1989) for space discretization. Pressure and velocity are solved iteratively. Then, Semi-Implicit Method for Pressure-Linked Equations (SIMPLE) algorithm is selected for pressure and velocity correction scheme instead of simultaneously solving the momentum and continuity equations. Flow assumed fully turbulent and realizable k-ε turbulence model (Shih et al. 1995) is used with enhanced wall function.

The computational domain is generated using structured grid based on multi-domain approach. In order to capture flow structures correctly, high mesh density is used at inter-rib space and u-bend sections as depicted in Fig. 29.2. The final mesh contains about three million elements in whole domain. Y^+ value is kept around 5 at near wall region (Lin et al. 2001).

Mass flow is provided as inlet boundary condition. A fully developed velocity profile is provided together with the turbulence intensity value of 5 % at the inlet. The flow Reynolds number is adjusted to 20000 by varying the inlet mass flow rate. The outlet static pressure is fixed at sea level static pressure. In such configuration, Dean Number (*De*) of the u-bend is equal to 24,121. A constant heat flux of $400\ W/m^2$ is applied to the inter-rib and u-bend surfaces of the bottom wall in order to study cooling effectiveness. Other walls are treated as adiabatic.

All numerical simulations are performed at a workstation computer with 16 Intel Xeon core. The velocity values are monitored at three control points located at u-bend, Z6 and Z7 in order to decide the convergence of the solution. A typical run takes about five CPU hours.
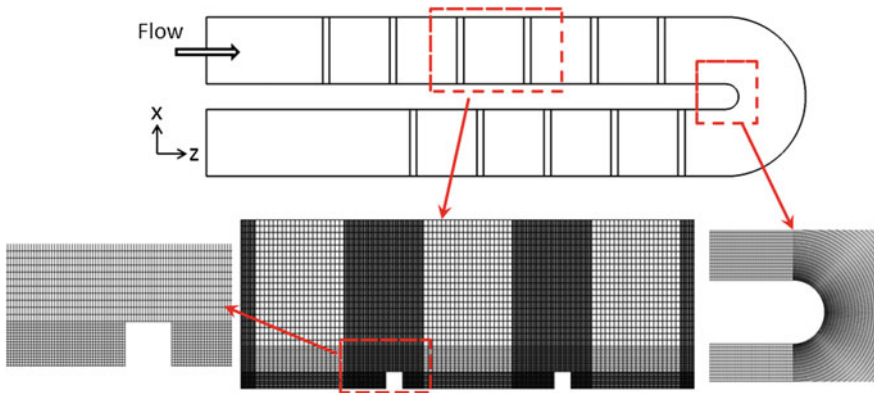
Fig. 29.2 Grid structure at different locations of the domain

29.2.3 Model Validation

In order to verify the numerical setup, a straight channel with a u-bend presented by Cheah et al. (1996) and other studies (Djebedjian et al. 2008; Guden and Yavuz 2014) is used as a validation case. The validation model, operated at *Re* 100000, does not contain any rib. Three turbulence models are tested, namely realizable *k-ε*, RNG and Shear Stress Transport (SST). The spanwise velocity variations at two heights (*y/H* = 0.125 and 0.5) are plotted in Fig. 29.3 at two different locations of the u-bend. The results of RNG and realizable *k-ε* turbulence model compare fairly well with the experiments in the first section (90°). However, the numerical results over predicts the velocities close to the inner wall region at the outlet (180°) of the u-bend.
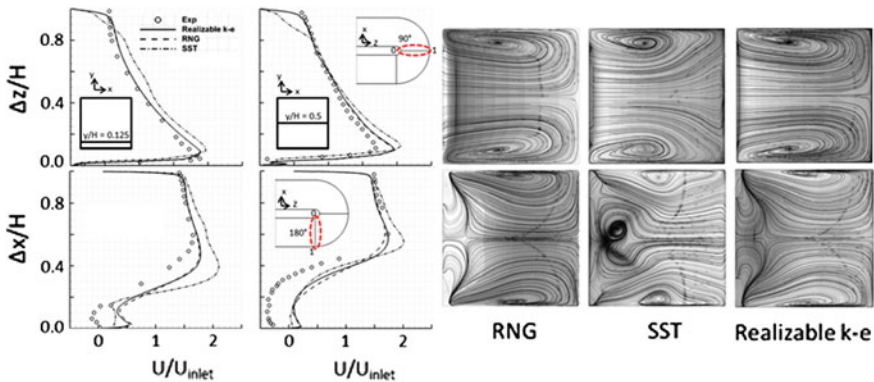
Fig. 29.3 Results of three turbulence models at 90° and 180° sections of u-bend

29.3 Flow Field Investigation

The wall shear stress distribution over the wall is a good indication for the flow field behavior. Therefore it is computed for both straight and u-bend sections (Eq. 29.1). Except Z1 and Z6, all inter-rib regions show similar shear stress distributions. The different results in Z1 and Z6 are addressed to the flow development. Z1 is the first rib space where the flow chances characteristics due to the geometrical modifications. Similar to that, the flow characteristic is affected when it enters the u-bend section and it redevelops in Z6. Once it fully develops, two zero wall shear regions appears in the wall shear stress distributions located just before and after the rib. The flow passes over the rib and forms a large recirculation region just downstream of the rib. This region is usually followed by a re-attachment region (i.e. S/S_{max} of about 0.3 at Z4) which appears with a zero wall shear value. After that, the flow forms a new boundary layer up to the next rib. The potential field of the next rib affects the incoming flow so streamlines rises up to move over the obstacle ahead as shown in Fig. 29.4b

$$\tau_{st} = \mu \frac{\partial U_z}{\partial y} \tau_{bend} = \mu \left(\frac{\partial U_z}{\partial y} \cos \theta - \frac{\partial U_x}{\partial y} \sin \theta \right) \tag{29.1}$$

Figure 29.5 shows the variation of impingement point along the channel. The impingement point is defined as the location where zero wall shear value is achieved. No value is presented for Z1 and Z6 since the wall shear value never goes to zero. The flow develops while passing the first three rib zones (Z1, Z2, Z3). A similar trend is observed also in the downstream channel for Z8, and Z9. The impingement location remains almost unaltered for Z4, and Z5 which is an evidence of the developed flow at upstream channel. U-bend results in an early impingement downstream of the final rib at upstream channel.

Figure 29.6 shows the vortices generated downstream of the rib at different locations namely, Z1: upstream channel developing flow, Z5: upstream channel
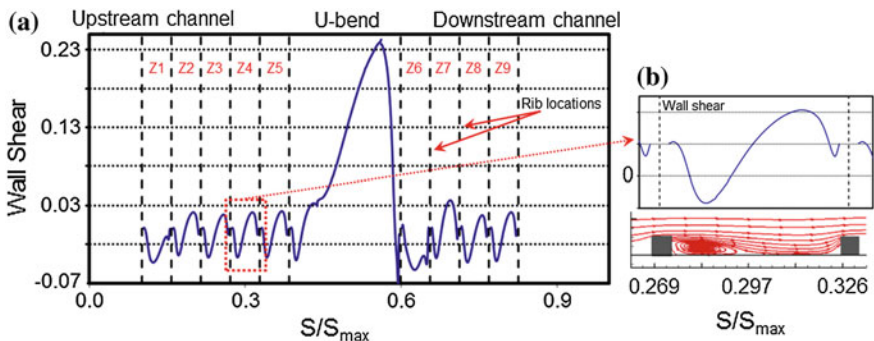
Fig. 29.4 Spanwise averaged wall shear stress distribution **a** along the channel **b** inter-rib space
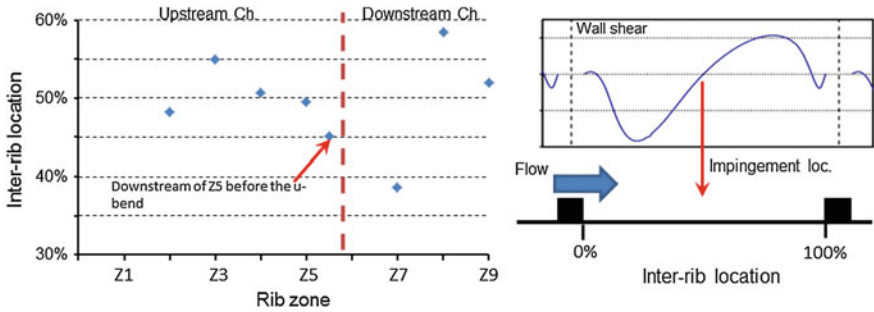
Fig. 29.5 Variation of impingement location along the channel
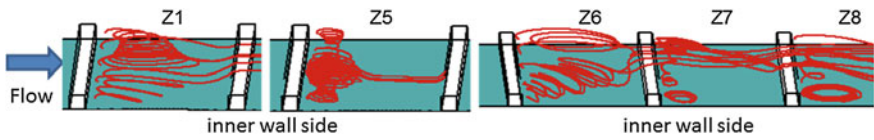
Fig. 29.6 Vortex structures before and after the u-bend

fully developed flow, Z6, Z7, Z8: downstream channel flow. Z6 is characterized mainly by the vortex which is totally different than the upstream channel vortices. However, starting from Z7 the rib downstream vortices become similar to the structures observed at the upstream channel (Z1, Z5).

Z-vorticity distribution is plotted in Fig. 29.7 in order to understand the flow field after u-bend. Two Dean vortices (D1, D2) are captured close to the outer wall region. Additionally, secondary vortices (V1, V2, V3) are generated by the u-bend close to inner wall region. D2, V1 and V2 lift off when it gets close to the rib due to its blockage in Fig. 29.7b. The vortices (V1, V2, V3) diminish right after the rib (plane 3, 10 and 50 % of span in Fig. 29.7). In Z6 new vortex (V4) appears and dominates the inter-rib space. Its effect is extended also to the inner wall region of Z7. Therefore, the unusual shear stress distribution in Z6 shown in Fig. 29.4a, is attributed to the V4.

The pressure drop characteristic is also a critical design consideration when selecting the turbulator configuration. Figure 29.8 demonstrates the kinematic loss distribution along the channel length. The pressure drop is calculated as kinematic loss for each rib zone relative to the inlet (Eq. 29.2). The relevant pressure value is obtained by mass-weighted averaging of the local distribution. In the upstream and downstream channel, except the Z6 and Z7, the kinematic loss increases monotonically. However the loss generated in the upstream channel is almost doubled compared to the one of downstream. The second half of the U-bend generates the maximum pressure drop. Some part of the pressure is recovered in the first half of the u-bend due to flow impingement on lateral and bottom walls (Syuhada et al. 2001).
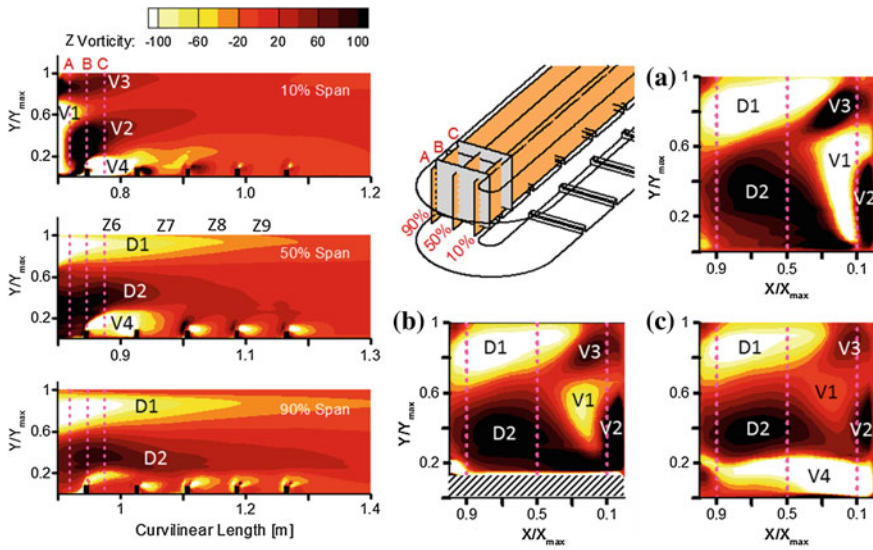
Fig. 29.7 Z-vorticity distribution after u-bend
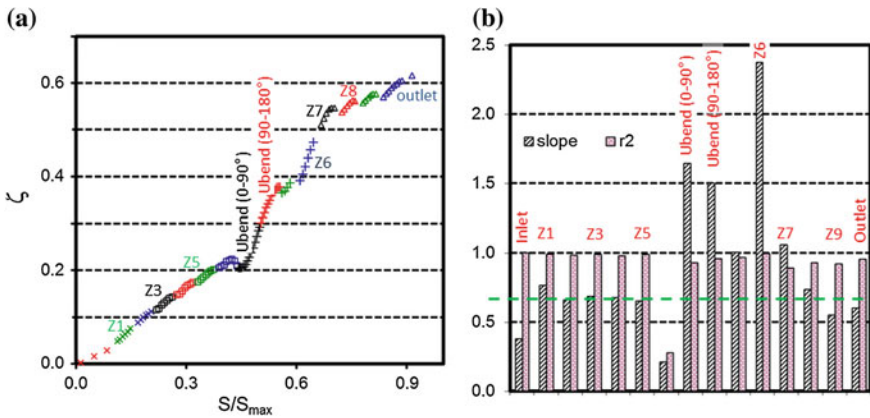
Fig. 29.8 Kinematic loss distribution along the channel

$$\zeta = 1 - \frac{1 - \left(\frac{P}{P_0}\right)^{\frac{\gamma-1}{\gamma}}}{1 - \left(\frac{P}{P_{0,\text{in}}}\right)^{\frac{\gamma-1}{\gamma}}} \tag{29.2}$$

29.4 Conclusions

A scale up model of a serpentine rib-roughened channel analyzed numerically at $Re = 20000$ ($De = 24121$). Upstream channel (from inlet to the bend) has a clear flow stream. Flow develops during the first two rib regions then stays periodic up to the u-bend. Hence, the kinematic loss remains unaltered starting from Z3 whereas the Z1 and Z2 provide higher kinematic loss. The secondary vortices are generated close to inner wall region which dominates the first rib section downstream of the u-bend. Therefore, the aerodynamic performance of Z6 becomes completely different from other zones. Finally, the flow redevelops starting from Z7. Downstream channel performs better compared to the upstream.

References

Azzola J, Humphrey JAC, Iacovides H, Launder BE (1986) Developing turbulent flow in a U-bend of circular cross-section: measurement and computation. J Fluids Engineering 108:214–221

Barth TJ, Jespersen D (1989) The design and application of upwind schemes on unstructured meshes. Technical report AIAA-89-0366, AIAA 27th Aerospace Sciences Meeting. Reno, Nevada

Chanteloup D, Juaneda Y, Bölcs A (2002) Combined 3-D flow and heat transfer measurements in a 2-pass internal coolant passage of gas turbine airfoils. ASME J Turbomach 124:710–718

Cheah SC, Iacovides H, Jackson DC, Ji H, Launder BE (1996) LDA investigation of the flow development through rotating U-ducts. ASME J Turbomach 118:590–596

Dittus PW, Boelter MK (1930) Heat transfer in automobile radiators of the tubular type. Univ Calif Publ Eng 2:443–461

Djebedjian B, Mohamed MS, Elsayed A (2008) Numerical studies of curvature effect on turbulent flows in 180° curved ducts. In: 6th international engineering conference, pp 347–370

Egger C, von Wolfersdorf J, Schnieder M (2013) Heat transfer measurements in an internal cooling system using a transient technique with infrared thermography. ASME J Turbomach 135(041012):1–8

Egger C, von Wolfersdorf J, Schnieder M (2014) Combined experimental/numerical method using infrared thermography and finite element analysis for estimation of local heat transfer distribution in an internal cooling system. ASME J Turbomach 136(061005):1–9

Ekkad SV, Han JC (1997) Detailed heat transfer distributions in two-pass square channels with rib turbulators. Int J Heat Mass Transfer 40(11):2525–2537

Gu X, Wu HW, Schock HJ, Shih TIP (2002) Two-equation versus Reynolds-stress modeling in predicting flow and heat transfer in a smooth U-duct with and without rotation. ASME J GT-2002—30616

Guden Y, Yavuz MM (2014) Analysis and control of complex flows in U-bends using computational fluid dynamics. In: Fluids engineering division summer meeting 2014, FEDSM2014-21557

Han JC (1984) Heat transfer and friction in channels with two opposite rib-roughened walls. ASME J Heat Transfer 106:774–781

Han JC (1988) Heat transfer and friction characteristics in rectangular channels with rib turbulators. ASME J Heat Transf 110:321–328

Han JC, Park JS (1988) Developing heat transfer in rectangular channels with rib turbulators. Int J Heat Mass Transfer 31:183–195

Han JC, Zhang YM (1992) High performance heat transfer ducts with parallel, broken, and V-shaped ribs. Int J Heat and Mass Transfer 35:513–523

Han JC, Glicksman LR, Rohsenow WM (1978) An investigation of heat transfer and friction for rib roughened surfaces. Int J Heat and Mass Transfer 21:1143–1156

Han JC, Park JS, Lei CK (1985) Heat transfer enhancement in channels with turbulence promoters. J Eng Gas Turbines Power 107:629–635

Han JC, Chandra PR, Lau SC (1988) Local heat/mass transfer distributions around sharp 180° turns in two-pass smooth and rib-roughened channels. ASME J Heat Transfer 110(1):91–98

Han JC, Ou Q, Park JS, Lei CK (1989) Augmented heat transfer in rectangular channels of narrow aspect ratios with rib turbulators. Int J Heat Mass Transfer 32:1619–1630

Han JC, Zhang YM, Lee CP (1991) Augmented heat transfer in square channels with parallel, crossed, and V-shaped angled ribs. ASME J Heat Transfer 113:590–596

Kukreja RT, Lau SC, McMillin RD (1993) Local heat/mass transfer distribution in a square channel with full and V-shaped ribs. Int J Heat Mass Transfer 36:2013–2020

Ligrani PM, Hedlund CR (1998) Transition to turbulent flow in curved and straight channels with heat transfer at high Dean numbers. Int J Heat Mass Transfer 41(12):1739–1748

Lin YL, Shih TIP, Stephens MA, Chyu MK (2001) A numerical study of flow and heat transfer in a smooth and ribbed u-duct with and without rotation. ASME J Heat Transfer 123:219–232

Liou TM, Chen CC (1999) LDV study of developing flows through a smooth duct with a 180° straight-corner turn. ASME J Turbomach 121:167–174

Liou TM, Chen CC, Tzeng YY, Tsai TW (2000) Non-intrusive measurements of near-wall fluid flow and surface heat transfer in a serpentine passage. Int J Heat Mass Transfer 43(17):3233–3244

Liou TM, Chen CC, Chen MY (2003) Rotating effect on fluid flow in two smooth ducts connected by a 180-degree bend. J Fluids Eng 125:138–148

Liou TM, Hwang YS, Chen MY (2007) Heat transfer improvement by arranging detached ribs on suction surfaces of rotating internal coolant passages. Int J Heat Mass Transfer 50(11–12):2414–2424

Luo J, Razinsky EH (2009) Analysis of turbulent flow in 180° turning ducts with and without guide vanes. ASME J Turbomach 131(021011):1–10

Mochizuki S, Takamura J, Yamawaki S, Yang WJ (1994) Heat transfer in serpentine flow passages with rotation. ASME J Turbomach 116:133–140

Mochizuki S, Murata A, Shibataa R, Yang WJ (1999) Detailed measurements of local heat transfer coefficients in turbulent flow through smooth and rib-roughened serpentine passages with a 180° sharp bend. Int J Heat Mass Transfer 42:1925–1934

Murata A, Mochizuki S (2004) Large Eddy simulation of turbulent heat transfer in a rotating two-pass smooth square channel with sharp 180° turns. Int J Heat Mass Transfer 47:683–698

Park JS, Han JC, Huang Y, Ou S (1992) Heat transfer performance comparisons of five different rectangular channels with parallel angled ribs. Int J Heat and Mass Transfer 35:2891–2903

Pu J, Ke ZQ, Kaga Y, Wang JH, You HD, Du ZN (2013) An experimental investigation on fluid flow characteristics in a real coolant channel of LP turbine blade with PIV technique. J Exp Therm Fluid Sci 45:43–53

Schabacker J, Bölcs A, Johnson B V, (1998) PIV Investigation of the Flow Characteristics in an Internal Coolant Passage with Two Ducts Connected by a Sharp 180 deg Bend. ASME J 98-GT-544

Sewall EA, Tafti DK (2006) large eddy simulation of flow and heat transfer in the 180-deg bend region of a stationary gas turbine blade ribbed internal cooling duct. ASME J Turbomach 128:763–771

Shih TH, Liou WW, Shabbir A, Yang Z, Zhu J (1995) A new k-e Eddy-viscosity model for high Reynolds number turbulent flows—model development and validation. J Comput Fluids 24 (3):227–238

Syuhada A, Hirota M, Fujita H, Araki S, Yanagida M, Tanaka T (2001) Heat (mass) transfer in serpentine flow passage with rectangular cross-section. J Energy Convers Manage 42(15–17):1867–1885

Taslim ME, Li T, Kercher DM (1996) Experimental heat transfer and friction in channels roughened with angled, V-shaped and discrete ribs on two opposite walls. ASME J Turbomach 118:20–28

Viswanathan AK, Tafti DK (2006) A comparative study of DES and URANS for flow prediction in a two-pass internal cooling duct. ASME J Fluids Engineering 128:1336–1345

Wagner JH, Johnson BV, Graziani RA, Yeh FC (1992) Heat transfer in rotating serpentine passages with trips normal to the flow. ASME J Turbomachinery 114:847–857

Wang T, Chyu MK (1994) Heat convection in a 180-deg. Turning duct with different turn configurations. J Thermophys Heat Transfer 8(3):595–601

Yanase S, Mondal RN, Kaga Y (2005) Numerical study of non-isothermal flow with convective heat transfer in a curved rectangular duct. Int J Thermal Sci 44(11):1047–1060

Zhao CY, Tao WQ (1997) A three dimensional investigation on turbulent flow and heat transfer around sharp 180-deg turns in two-pass rib-roughened channels. Int J Heat Mass Transfer 24:587–596

Chapter 30
Numerical Analysis of Active Control of Flow on a DBD Plasma Actuator Integrated Airfoil

Beycan Ibrahimoglu, M. Zeki Yilmazoglu and Ahmet Cücen

Abstract In recent years, flow control methods on an airfoil have gained interest. Flow control methods can be classified as passive and active control systems. Dielectric barrier discharge (DBD) plasma actuator is an active control method. A DBD plasma actuator can be defined as; a flow control device, without moving parts and same airfoil shape after installation. In this study, numerical analysis of DBD plasma actuator integrated airfoil was performed. Instead of modeling plasma generation, thermal effects, ionization, and momentum forces, a momentum source term was applied to the airfoil in order to observe the effects of plasma actuator integration on airfoil such as drag, lift, etc. ANSYS Fluent was used in the simulations. The cord length was assumed to be 150 mm. The effects of the attack angles were also investigated with 0°, 5°, 10°, and 15° attack angles. Hexahedral mesh structure was selected in order to model boundary layer with lower y^+ values and k-ω SST turbulence model was used. The air velocity was assumed to be 1.9 m/s at the inlet and 200 N/m³ body force was applied to 10 mm after the leading edge for plasma effect analogy.

30.1 Introduction

In recent years, flow control methods on an airfoil have gained interest (Suzen et al. 2005; Sosa et al. 2012; Giorgi et al. 2014; Akansu et al. 2013). Flow control methods can be classified as passive and active control systems. In passive methods, various devices are added to the system and during the operation these devices do not consume any additional auxiliary power. In active methods, an external energy input is required such as blowing and suction from a surface, acoustic excitation, periodic rotation or oscillation, wall motion, and electromagnetic forces. In electrical control of the flow, local ionized air, produced as a result of electrical discharge, drives the bulk motion of neutral molecules which is called Electrohydrodynamic (EHD). EHD

B. Ibrahimoglu · M.Z. Yilmazoglu (✉) · A. Cücen
Department of Mechanical Engineering, Gazi University, Ankara, Turkey
e-mail: zekiyilmazoglu@gazi.edu.tr

is useful as a flow control mechanism, because electrical energy is converted to momentum without any need for moving mechanical parts. It is a promising method for aero-industrial applications because of adequate response time, simple structure, and many features such as controlling the separation, increasing the lift forces, decreasing the drag forces, delaying the stall angle (Klein 2006).

A DBD consists of two electrodes and a dielectric material. In aerodynamic applications, one of the electrodes is embedded into the dielectric material which is located inside the wing, while the other is exposed to the air. Applying AC voltage across the electrodes with enough frequency, the air ionizes in that region and produces a body force. In order to ionize the air, 10–20 kV voltage with a frequency of 1–10 kHz is applied in DBD applications. Large amplifier requirement, costs, and early flow separation due to the larger profile of the electrode on the wing are the main disadvantages of plasma actuators (Stack 2014).

In this study, numerical analysis of DBD plasma actuator integrated airfoil was performed. Instead of modeling plasma generation, thermal effects, ionization, and momentum forces, a momentum source term was applied to the airfoil in numerical analyses. ANSYS Fluent was used in the simulations. The cord length was assumed to be 150 mm. The effects of the angle of attack values were also investigated for 0°, 5°, 10°, and 15°. Hexahedral mesh structure was selected in order to model boundary layer with lower y^+ values and k-ω SST turbulence model was used. The air velocity was assumed to be 1.9 m/s at the inlet and 200 N/m^3 body force was applied in order to model the plasma actuator.

30.2 Method

NACA0015 airfoil (airfoiltools.com 2015) was modeled in ANSYS Design modeler tool. In order to perform a CFD analyses, a 2D computational domain was constituted as shown in Fig. 30.1. The air velocity was set to 1.9 m/s and pressure

Fig. 30.1 2D model of the computational domain
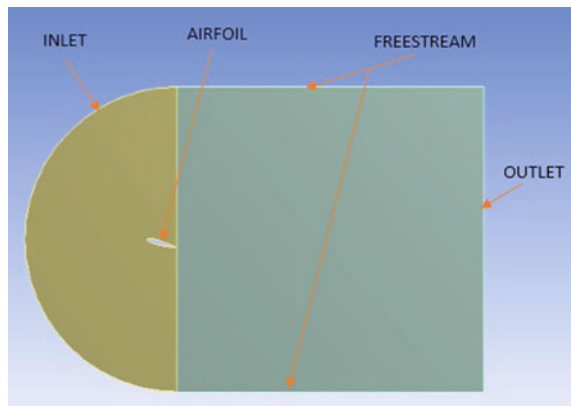
outlet boundary condition was given at the outlet section. Pressure-based solver was chosen for steady state solutions. Air was accepted as incompressible fluid and ideal gas. Viscosity value was calculated by Sutherland model. SIMPLE algorithm was used for pressure-velocity coupling.

In the analyses, initially the airfoil was modeled without a plasma actuator for different attack angles. In the second case, a UDF was coupled to the solution in order to simulate the effect of the plasma actuator as a body force (Font et al. 2009; Mertz and Corke 2008). In the first case, a mesh study was performed to eliminate the effects of the mesh quality. In Table 30.1, Cl, Cd, and y^+ values are given for different mesh types. Fine mesh structure was selected as base case for further calculations. In order to model the boundary layer on the surface of the airfoil, an inflation rate was given. The details of the inflated mesh structure are given in Fig. 30.2. In this area, the value of the y^+ has to be lower than 1.

In the analyses, three different turbulence models were compared: k-ω SST (2 Equations), Spalart Allmaras (1 Equation), and Reynolds stress model (5 Equation). According to the results of the different turbulence models, k-ω SST was selected as base case for turbulence model. The results of different turbulence models on Cl, Cd and y^+ are given in Table 30.2.

Table 30.1 Mesh independency results

	Number of cell	Cl	Cd	y^+
Normal mesh	131,000	0.396	0.1	0.17
Fine mesh	226,000	0.472	0.1	0.116
Very fine mesh	565,000	0.453	0.1	0.059

Fig. 30.2 Inflation layers for boundary layer
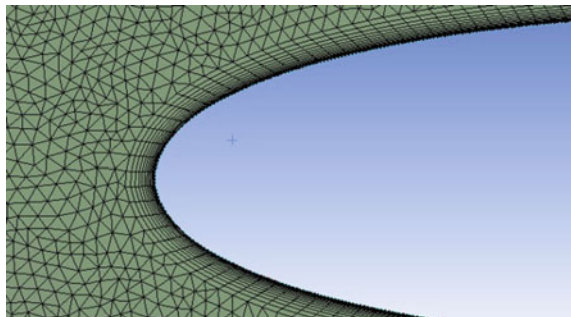
Table 30.2 Comparison of the turbulence models

	Cl	Cd	y^+
k-w SST	0.472	0.1	0.116
Spalart Allmaras	0.708	0.0686	0.11
Reynolds stress model	0.465	0.083	0.114

30.3 Results

30.3.1 Airfoil Without Plasma Actuator

The airfoil was modeled according to the boundary conditions given above. ANSYS Fluent was used in the simulations. In order to show the effects of the plasma actuator on the flow characteristics, the airfoil was modeled for different attack angles. Figure 30.3 shows the results of the simulations performed in 0°, 5°, 10°, and 15° attack angles. As it can be seen from the Fig. 30.3, as the angle of attack increases that the flow was being separated and stall starts. For 15° angle of attack, results show that eddies and wakes were observed according to the Fig. 30.3d. Streamlines and wake profiles are given in Fig. 30.4. For 0° and 5° attack angles streamlines flow over the airfoil. However, for the attack angles greater than 10°, flow separation and wake generation can be easily observed.

30.3.2 Airfoil with Plasma Actuator

Plasma actuator was modeled as a body force on the same direction with flow (Palmerio 2011). According to the literature review given above, the magnitude of the body force was selected as 200 N/m^3. Different approaches can be found on the literature to define the magnitude of the body force (West 2012). Modeling the plasma and ionization can be performed using different commercial codes. However, it should be noted that the body force approach can be an alternative method with rapid solution.

Three different attack angles were selected for the control of flow separation: 5°, 10°, and 15°. Plasma was modeled on the airfoil and located as a source term at x/C dimensionless distances. C stands for the chord length and 0.1, 0.3, 0.5, and 0.9 distances were selected to activate the body force.

In Fig. 30.5, the effects of the plasma actuator for different application distances on the lift coefficient are given. The results show that plasma actuators increase the lift coefficient substantially. Without plasma actuator, the lift coefficient was measured to be around 1.32 for 15° attack angle. However, when plasma actuator was activated the lift coefficient increased as shown in Fig. 30.5, when it is applied to 0.1 dimensionless distance.

Figure 30.6 shows the velocity vectors on the airfoil for different plasma application zones. According to the Fig. 30.6, the flow on the airfoil was slightly attached to the surface again when compared to Fig. 30.3c. It should be noted that plasma actuator was positioned at $x/C = 0.9$ in this case. Because of positioning the plasma actuator at the end of the airfoil, the detached streamlines tends to flow over the airfoil after this location. However, eddies occurred at the end of the airfoil
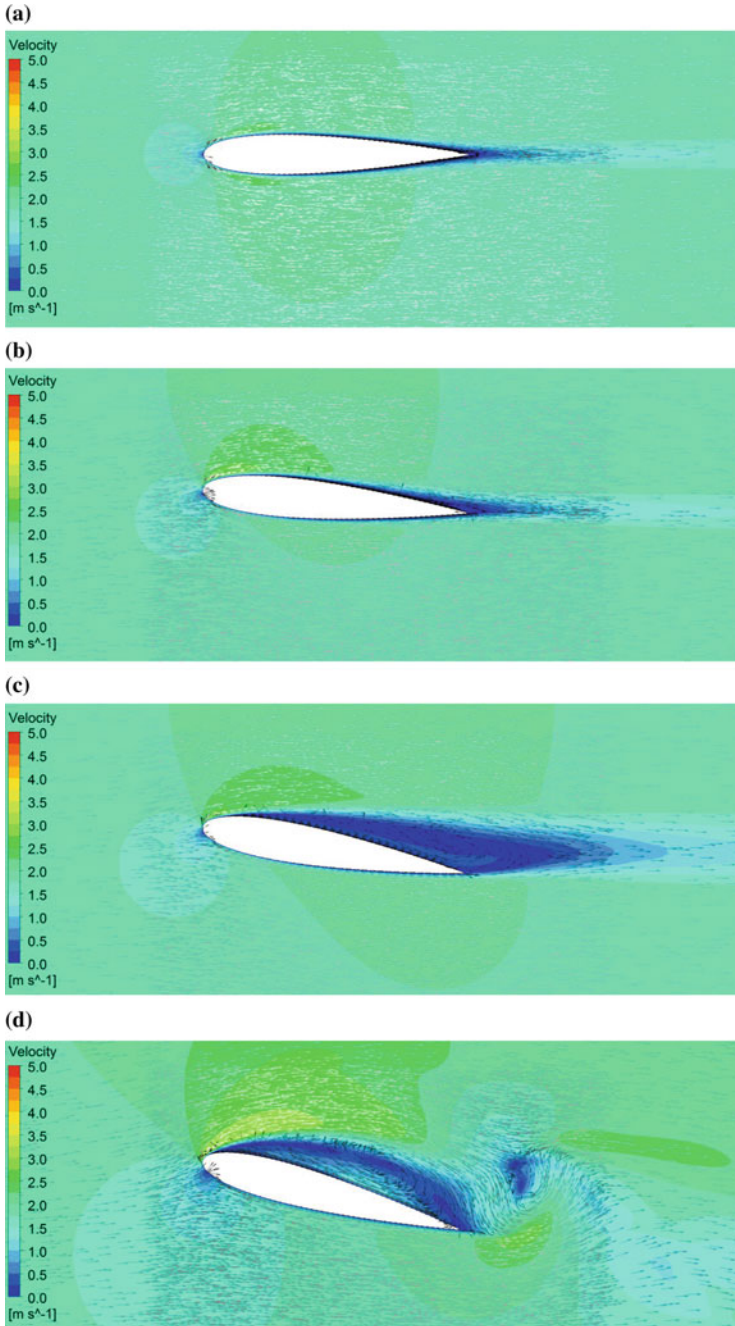
Fig. 30.3 Velocity vectors for different attack angles; **a** 0°, **b** 5°, **c** 10°, and **d** 15°
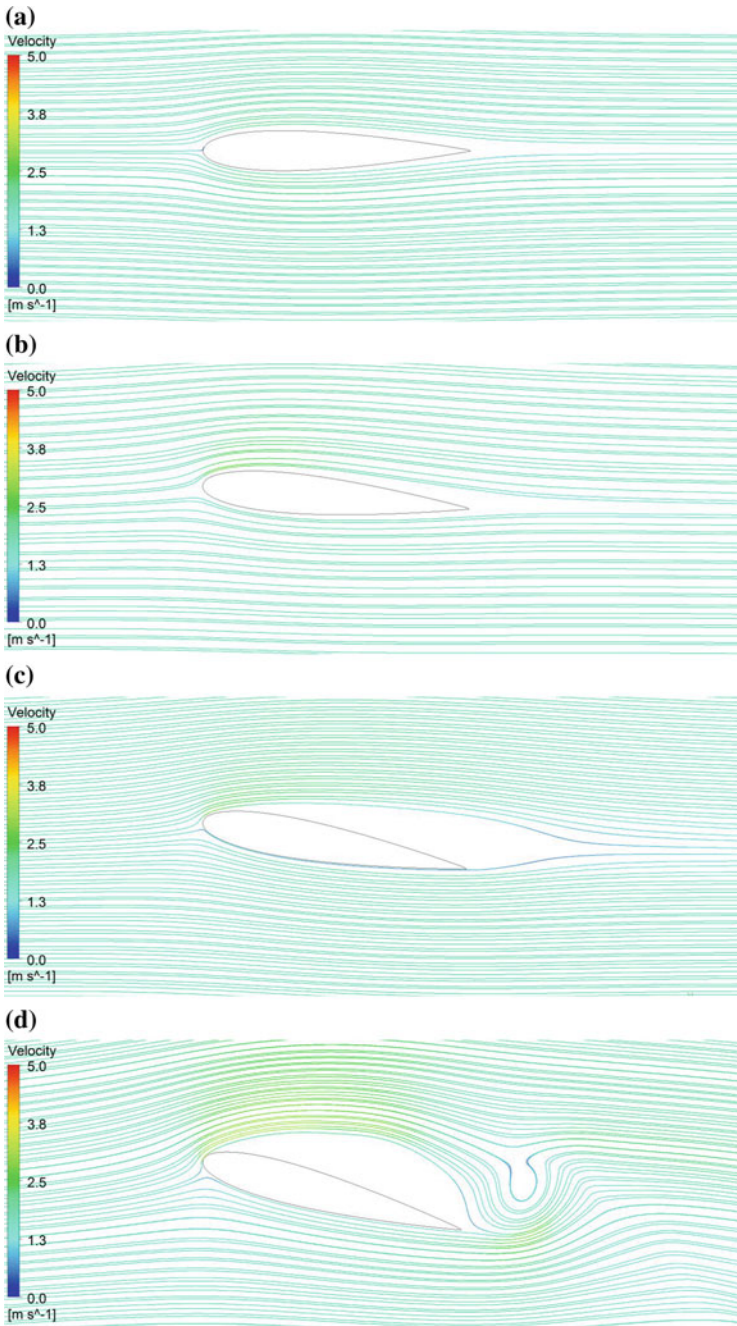
Fig. 30.4 Streamlines for different attack angles; **a** 0°, **b** 5°, **c** 10°, and **d** 15°
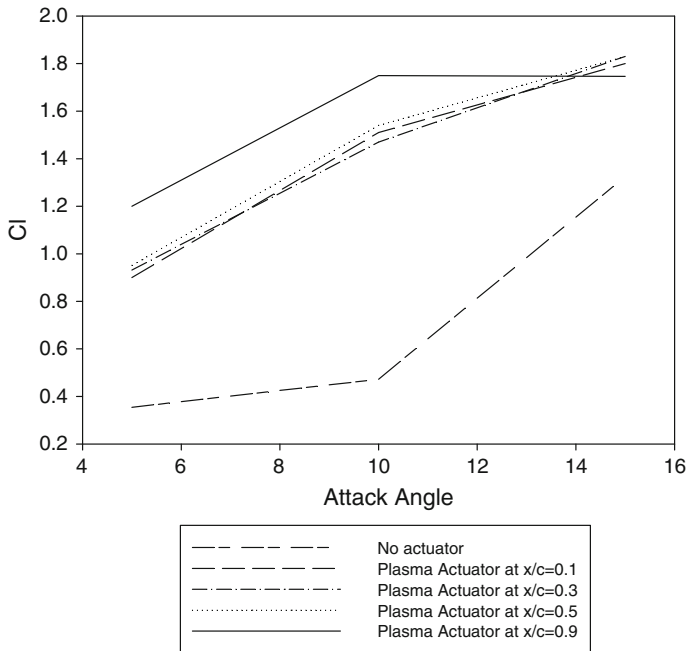
Fig. 30.5 Attack angle lift coefficient relationship

again. Figure 30.8a shows the results for this case on Cl. In Fig. 30.7, plasma actuator is placed to $x/C = 0.9$ for 15° angle of attack. When Figs. 30.3d and 30.7 were compared the effect of plasma, actuator can be observed. The effects of angle of attack and plasma application zone were investigated. Figure 30.8 shows the variation of Cl and Cd values for different angle of attack values with respect to dimensionless plasma application zone.

According to the Fig. 30.8a, the highest Cl value was found when plasma actuator was installed in $x/C = 0.1$ position for 15° angle of attack. For 10° angle of attack, the lift coefficient values slightly increase after the $x/C = 0.3$ position. Similar increment can be found for 5° angle of attack for $x/C = 0.5$ position. However, for 15° angle of attack, Cl decreases rapidly. It should be noted that the position of the plasma actuator has a great importance on Cl. Drag coefficient was also investigated for different angle of attacks. The minimum Cd value is observed when actuator was positioned in $x/C = 0.1$ for 5° and 10° angle of attack. Drag coefficient increases rapidly when the actuator was positioned in $x/C = 0.3$ for 15° angle of attack.

Figure 30.9 shows the comparison of the flow characteristics on the airfoil with and without plasma actuator. In Fig. 30.9a, c, e the plasma actuator was positioned at $x/C = 0.1$. Fig. 30.9b, d, f are 5°, 10°, and 15° angle of attack values, respectively. The results show that the velocity on the airfoil increased with plasma actuator. Flow separation was not observed when compared to Figs. 30.9a, c, e.

(a)

(b)
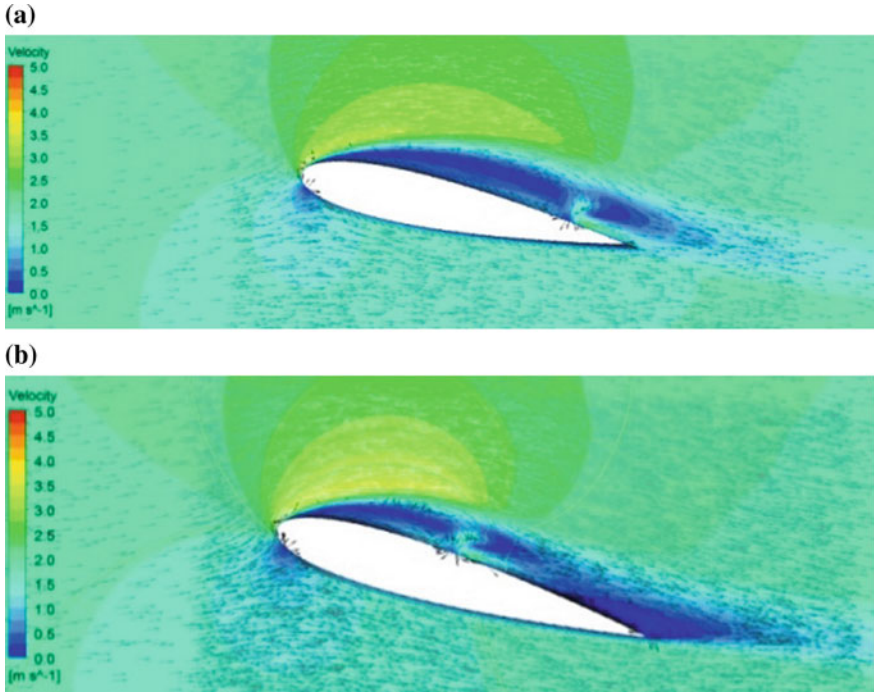
Fig. 30.6 Velocity vectors and contours for different plasma positions on the airfoil
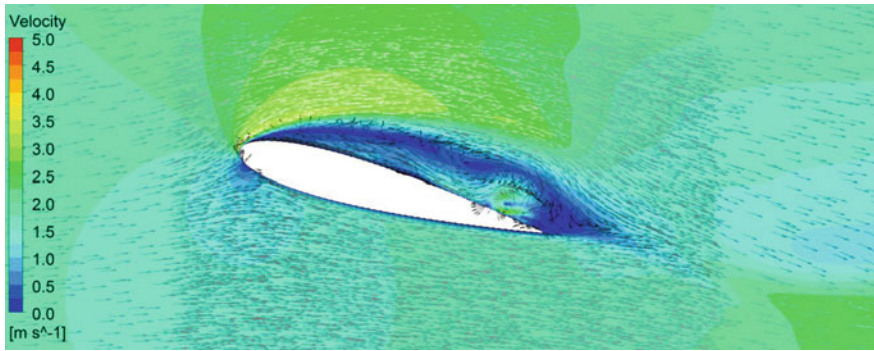
Fig. 30.7 Velocity vectors for 15° angle of attack and $x/C = 0.9$ plasma application zone

(a)

(b)
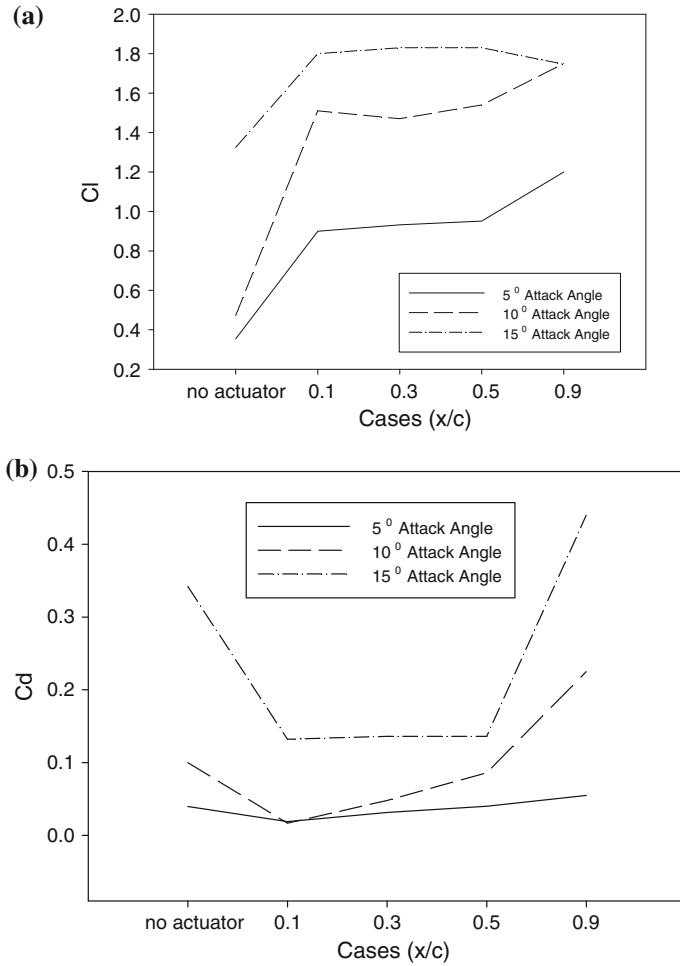
Fig. 30.8 The variation of the Cl and Cd for different plasma application zones for different angle of attack

According to the results, velocity on the airfoil surface increased considerably. Consequently, lift force   and lift coefficient increased. It can be concluded that plasma actuators has a positive effect on the control of the flow on an airfoil. The positions of the plasma actuator on the airfoil and energy consumption of these devices have to be investigated. In addition, the effects of the plasma actuator on Cl and Cd values for higher Ma numbers have to be modeled.

(a)

(b)

(c)
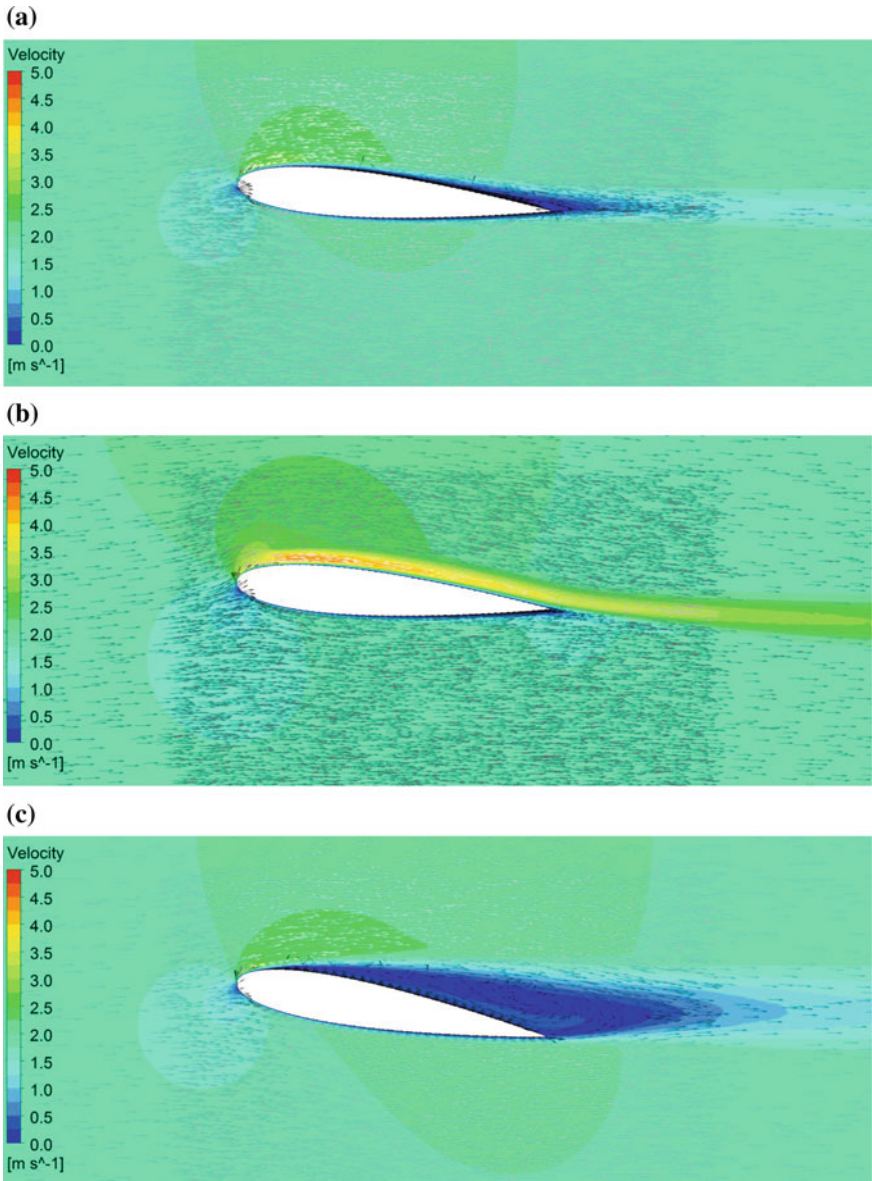
Fig. 30.9 Flow characteristics: without plasma actuator; **a** 5°, **c** 10°, and **e** 15° angle of attack and with plasma actuator; **b** 5°, **d** 10°, and **f** 15° angle of attack
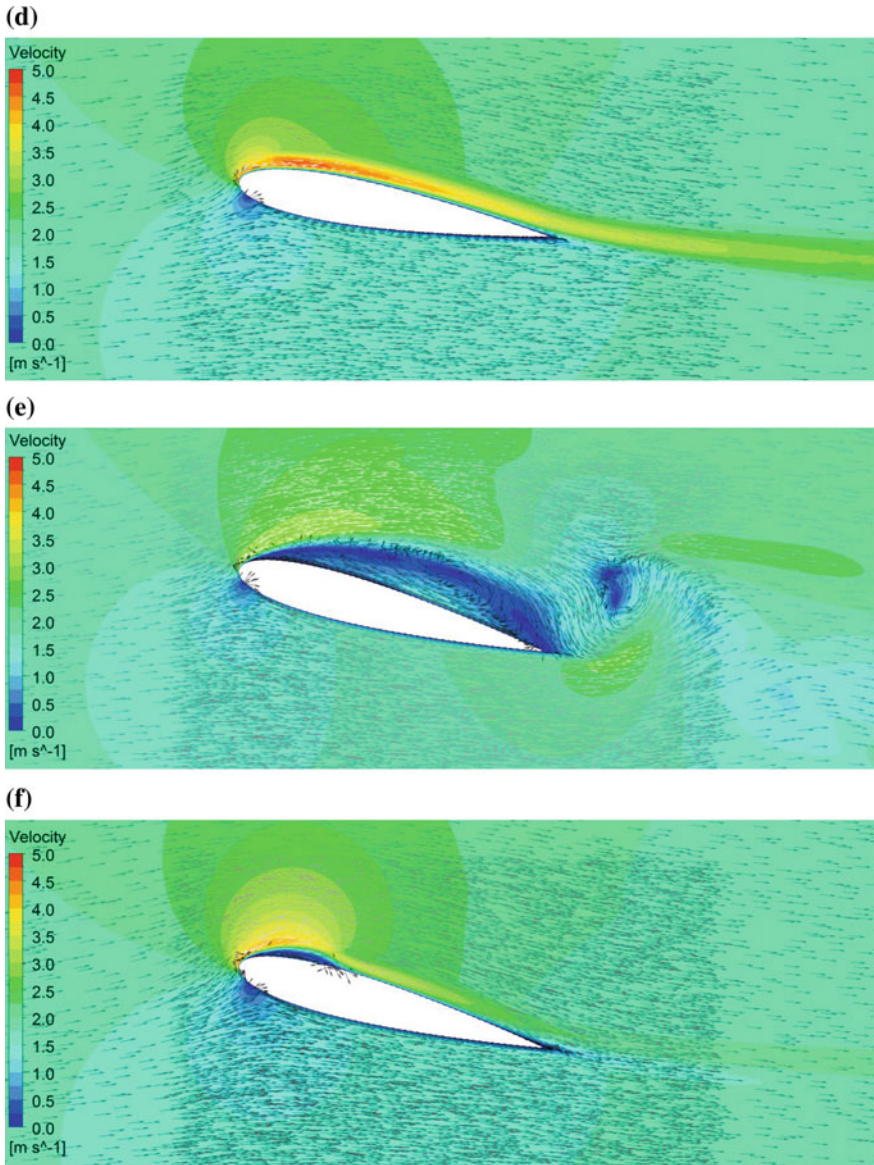
Fig. 30.9 (continued)

30.4   Conclusions

In this study, the effects of the plasma actuator, positioned an airfoil, on flow characteristics were numerically investigated. Velocity profiles and streamlines were compared in order to show the effects of the plasma actuators for different positions. In the numerical study, the effect of the plasma was modeled as a body force. Lift and drag coefficients were calculated for different angle of attack values and dimensionless plasma actuator positions. According to the results, plasma actuator application increases the lift coefficient and decreases the drag coefficient. The position of the plasma actuator has great importance on the performance of these devices. The effects of the plasma actuator on the flow for higher Ma numbers will be carried out in the next step of the study.

References

Akansu YE, Karakaya F, Şanlısoy A (2013) Active control of flow around NACA 0015 airfoil by using DBD plasma actuator. In: EPJ web of conferences 45, 01008

Font GI, Enloe CL, and McLaughlin TE (2009) Effect of volumetric momentum addition on the total force production of a plasma actuator. In: 39th AIAA fluid dynamics conference. San Antonio, Texas, 22–25 June 2009

Giorgi MG, Pescini E, Marra F, Ficarella A (2014) Experimental and numerical analysis of a micro plasma actuator for active flow control in turbomachınery. In: Proceedings of ASME turbo expo 2014: turbine technical conference and exposition

http://airfoiltools.com/airfoiltools/airfoil/index. Accessed 15 Mar 2015

Klein TR (2006) Macroscopic computational model of dielectric barrier discharge plasma actuators, Feb 2006

Mertz BE, Corke TC (2008) Time-dependent dielectric barrier dishcharge plasma actuator modeling. In: 47th AIAA aerospace sciences meeting. Orlando, FL, Jan 2008

Palmeiro D (2011) Modeling of dielectric barrier discharge plasma actuators for flow control simulations

Sosa R, Artana G, Electrostat J (2012) Experimental investigation of the effects of various plasma actuator configurations on lift and drag coefficients of a circular cylinder including the effects of electrodes. Chin J Aeronaut 25(3):311–324

Stack C (2014) Simulating the effect of plasma actuators on the three-dimensionality of the wake of a cylinder in a crossflow

Suzen YB, Huang PG, Jacob JD (2005) Numerical simulations of plasma based flow control applications. In: 35th fluid dynamics conference and exhibit, Toronto, Ontario, 6–9 June 2005

West TK (2012) Numerical investigation of plasma actuator configurations for flow separation control at multiple angles of attack

Chapter 31
Acoustic Control of Flow Over NACA 2415 Aerofoil at Low Reynolds Numbers

M. Serdar Genç, İlyas Karasu, H. Hakan Açıkel, M. Tuğrul Akpolat and Gökhan Özkan

Abstract Within the concept of this study, first low Reynolds number flow phenomena, including laminar separation bubble (LSB) and stall were explained. Then a literature review on the acoustic flow control was presented in three categories: flow control with constant frequency, flow control with constant amplitude, and flow control with variable frequency and amplitude. Aside from the review part, results of a comprehensive experimental study on the effects of acoustic flow control at low Reynolds numbers were presented. Within the scope of this experimental study, the effects of both parallel and perpendicular acoustic flow control were examined by means of pressure measurements, force measurements, hot-wire anemometry, flow visualization, and particle image velocimetry (PIV). In order to establish a baseline data, all of the measurements were first applied for the no control case. The effects of acoustic control were examined especially on the characteristics of LSB and stall. It was found that the acoustic excitation can be employed to decrease the height and length of LSB leading to increased lift coefficient and decreased drag coefficient. Also, acoustic flow control increased the angle of stall. It was also seen that the effective excitation frequency increases also, but the range of Zaman number (St/$Re^{0.5}$) based on effective frequency still is approximately same with increasing Reynolds numbers. Finally, it was shown that the general aerodynamics performance of an aerofoil at low Reynolds numbers can easily be enhanced by employing acoustic flow control, and the parameters of the acoustic flow control can easily be adjusted in order to keep up with the changing conditions of flow.

M.S. Genç (✉) · H.H. Açıkel · G. Özkan
Wind Engineering and Aerodynamics Research (WEAR) Laboratory,
Department of Energy Systems Engineering, Erciyes University,
38039 Kayseri, Turkey
e-mail: musgenc@erciyes.edu.tr

İ. Karasu
Department of Aircraft and Aerospace Engineering, Gaziantep University,
27310 Gaziantep, Turkey

M.T. Akpolat
Department of Airframe and Powerplant, Civil Aviation School, Atilim University,
06836 Ankara, Turkey

31.1 Introduction

The formation and control of the Laminar Separation Bubble (LSB) over the aerofoils have been studied by various researchers and the interest still stands. The control methods employed are classified as active and passive. Some examples are, suction-blowing, vortex generators, gurney flaps, etc. However, the researchers continued to the pursuit of a new means of controlling the flow. It was found out that flow control employing sound waves were easy to adapt to the conditions of the flow, it was effective, and was easy to employ. Various studies were done in 1980s on acoustic control of the flow over flat plates, and in the 1990s the focus was shifted to the acoustic control of the flow over aerofoils.

Acoustic flow control is made by adding pressure energy to the flow region. Most of the civil and military Unmanned Air Vehicles (UAVs) and Micro Air Vehicles (MAVs), wind turbines and gas turbine blades operate at low Reynolds number flow regimes. At the low Reynolds number flow regimes, laminar separation bubble, flow separation, and stall phenomena are commonly encountered. In order to prevent these and their disadvantages, such as low lift and high drag coefficients, various control methods can be employed. An example is vortex generators. By placing vortex generators along a line with constant x/c, vortices can be formed to add energy to the flow, retarding separation. However, this will be convenient to use at few cases, for example when the angle of attack and/or the Reynolds number varied, the position of the vortex generators may not be appropriate. On the other hand, parameters of acoustic flow control methods can easily be adapted to the changing conditions of the flow. This can be done by altering the acoustic excitation frequency and/or amplitude.

The relatively higher energy of high Reynolds number flows leads to a quicker and easier transition because they can vitiate adverse pressure gradients with minimal unsteadiness (Tan and Auld 1992; Burgman et al. 2006). But when it comes to low Reynolds number flows, many experimental studies show separation and reattachment (Tan and Auld 1992; Burgman et al. 2006; Gaster 1967; Hain et al. 2009; Lang et al. 2004; Mayle 1991; Swift 2009; Tani 1964; Ol et al. 2005; Yang et al. 2007; Yarusevych et al. 2007; Ricci and Montelpare 2005; Mohsen 2011).

Transition to turbulence is a phenomenon that occurs through different mechanisms in different applications (Langtry and Menter 2006), and it can be categorized as natural transition, bypass transition, separated flow transition, wake-induced transition, and reverse transition. In order to anticipate the type of transition acceleration parameter (K) may be used. Acceleration parameter represents the effect of free-stream acceleration on the boundary layer, and it is defined as $K = (v/U^2)(dU/dx)$ at the beginning of the transition (Fig. 31.1).

As mentioned before at high Reynolds numbers, the boundary layer on a body may transit to turbulent rapidly due to having the ability to overcome the effects of the adverse pressure gradients (Genç et al. 2012a). Nevertheless, for the low Reynolds number flow regimes, the experimental data indicates the occurrence of

Fig. 31.1 Topology of the different modes of transition in a number-acceleration parameter plane (Mayle 1991)
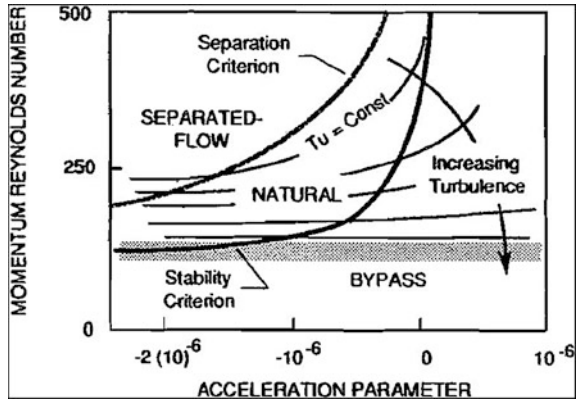
flow separation and reattachment in the transitional region. This occurs because the low Reynolds flows cannot overcome the adverse pressure gradient. Between the separation and the reattachment there is a region of slowly circulating air which is called the LSB (Genç et al. 2012a).

Genç et al. (2012b, c, 2015a, b), Karasu (2011), Karasu et al. (2012, 2013), Açıkel et al. (2012), Açıkel (2013), Açıkel and Genç (2015), carried out experimental investigation of flow and its control over a NACA2415 aerofoil by means of oil flow visualization, hot-wire anemometry, and pressure measurements. In order to gain insight of the concept of separation and reattachment and the phenomena occurs in the boundary layer, these experiments were done in the no control cases. The experiments were conducted at low Reynolds numbers and at various angles of attack. They compared the results of the oil flow visualization experiments with the schematic (Fig. 31.2) of natural transition (Karasu et al. 2013), and modified it to show the separated flow transition phenomena. In Fig. 31.2, the dense area of the colored oil indicates that the flow is decelerated. This deceleration corresponds to the point at which the pressure gradient overcomes the inertial forces of the flow, causing separation. It was resulted that as the angle of attack increased the separation point moved toward the leading edge for all of the Reynolds number cases investigated. At Reynolds number of 100,000, separation occurred at 30 % chord length at $\alpha = 4°$, 20 % chord length at $\alpha = 8°$, 12 % chord length at $\alpha = 12°$, and 5 % chord length at $\alpha = 15°$. The detailed locations of separation, transition, and reattachment points were given in Table 31.1 (Açıkel 2013) along with the laminar separation bubble lengths.

LSB (Fig. 31.3) may cause some adverse effects such as decreased lift, increased drag, vibration, noise, etc. (Ricci and Montelpare 2005; Nakano et al. 2007; Ricci et al. 2007; Zhang et al. 2008). In order to avoid these effects, flow control methods can be employed. But first, the nature of the LSB should be understood. If the pressure plot of an aerofoil with the presence of a LSB is examined, a hump can easily be noticed. This hump indicates the LSB; the region just after the maximum point of the hump indicates the transition (Katz and Plotkin 1991).
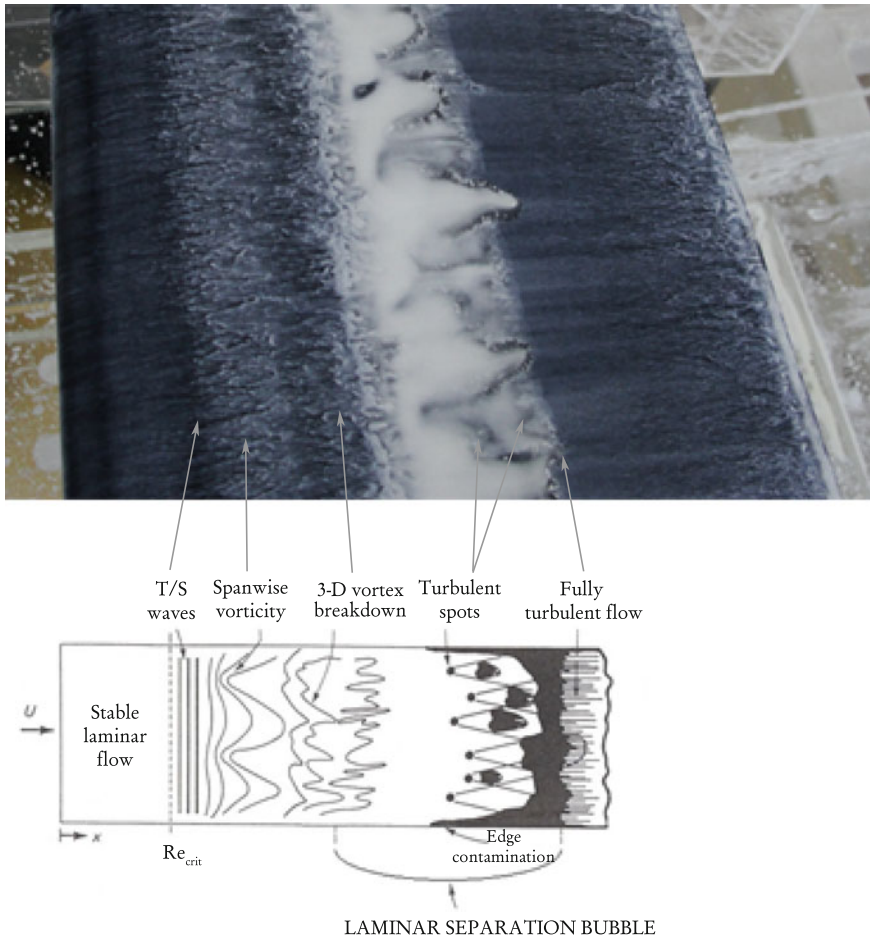
Fig. 31.2 Comparison of schematic of separation-induced transition process with the experimental photograph obtained oil-flow visualization over the NACA2415 aerofoil (Genç et al. 2012b).

Classification of LSBs can be made as short and long. The size and location of a LSB are functions of aerofoil shape, angle of attack, free-stream disturbances, and Reynolds number (Swift 2009; Tani 1964). An increase of the angle of attack causes the LSB to move towards the leading edge, forming a short bubble. With further increasing angle of attack the separation point continues to move toward the leading edge, and at a certain angle of attack the flow can no longer reattach to the surface within a short distance, leading to a phenomenon called the breakdown or the burst of bubble. The burst of a short bubble does not lead to a complete separation, it leads to the formation of a long bubble since the flow reattaches to the surface further downstream. A long bubble has a length of several percent of the chord at lower angles of attack, and it grows rapidly with the increasing angle of

Table 31.1 The locations of separation (Xs), transition (Xt) and reattachment (Xr) points, and bubble length (Lb) (Açıkel 2013)

Re number	α (°)	Xs	Xt	Xr	Lb
50,000	4	0.35	0.62	0.80	0.45
	8	0.22	0.50	0.72	0.50
	12	0.10	0.40	0.90	0.80 (Long bubble)
	15	0.08	–	–	–
75,000	4	0.33	0.62	0.76	0.43
	8	0.20	0.40	0.60	0.40
	12	0.10	0.40	0.70	0.60 (Long bubble)
	15	0.08	–	–	–
100,000	4	0.30	0.62	0.72	0.42
	8	0.20	0.35	0.55	0.35
	12	0.12	0.30	0.42	0.30
	15	0.05	0.15	0.20	0.15
200,000	4	0.35	0.62	0.66	0.31
	8	0.18	0.38	0.48	0.30
	12	0.15	0.25	0.30	0.15
	15	0.04	0.10	0.15	0.11
300,000	4	0.35	0.53	0.60	0.25
	8	0.30	0.35	0.45	0.15
	12	0.15	0.20	0.28	0.13
	15	0.05	0.08	0.15	0.10
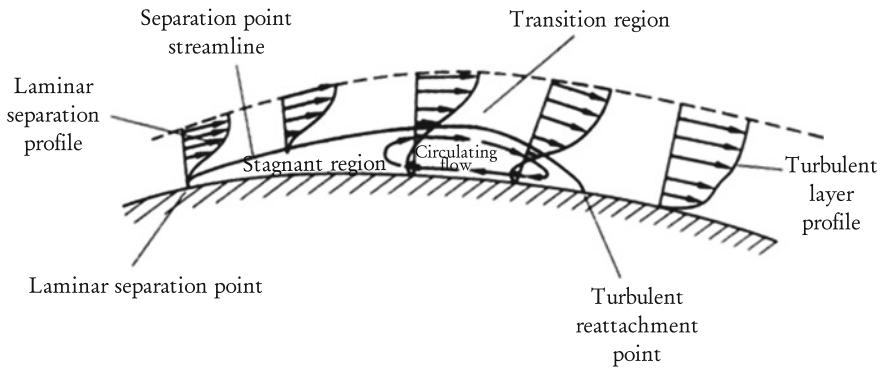
Fig. 31.3 Laminar separation bubble (Lock 2007)
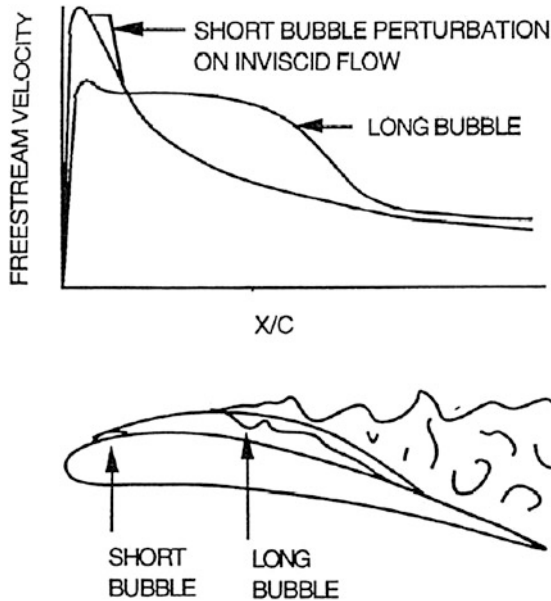
Fig. 31.4 Separation bubble effects on suction side velocity distribution (Mayle 1991)

attack until it covers the entire chord with a maximum thickness about 3 % of the chord (Tani 1964). A short bubble causes a small region of constant pressure in the pressure curve, which causes a plateau in the curve of pressure distribution. In consequence of reattachment the curve of the pressure distribution recovers. But short bubbles do not significantly alter the peak suction. However, long bubbles cause a suction plateau of reduced levels of pressure (Fig. 31.4).

As the angle of attack increases further, the separation point moves toward the leading edge. At a certain angle of attack, lift rapidly falls and drags rapidly increases, indicating trailing edge stall which is encountered on thick aerofoils (McCullough and Gault 1951). Trailing edge stall, which is also named mild stall, begins just after the angle of attack at which the highest lift coefficient is obtained. On the other hand, another type of stall, named leading edge stall, is abrupt. It is caused by the laminar flow separation near the leading edge, mostly without subsequent reattachment, and can be encountered on aerofoils with moderate thickness (McCullough and Gault 1951). Lastly, thin-airfoil stall results from leading edge separation with progressive rearward movement of the point of reattachment. This type of stall occurs on all sharp-edged aerofoils and on some thin rounded leading edged aerofoils (McCullough and Gault 1951).

The effects of different types of stall are shown on the Fig. 31.5 (Bak et al. 1998).
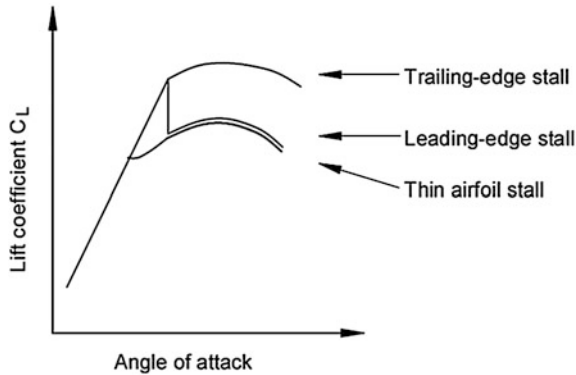
Fig. 31.5 Sketch of the three different stall types (Bak et al. 1998)

31.2 Acoustic Flow Control

Acoustic excitation of the shear layer one of the active flow control methods. In order to prevent the formation of LSB, and prevent/retard the stall phenomena; flow control methods can be employed. Flow control methods can be categorized as passive and active. Passive flow control methods are, as the name itself implies, passive; their elements cannot be moved. For example, in order to 'trip' the flow and retard stall vortex generators may be employed. But, the vortex generators are useful for a limited range of Reynolds numbers and/or angles of attack. So, beyond their effective ranges they are nothing but a source of additional drag. On the other hand, flow control is also doable by employing an active flow control method. One of the many types of active flow control is flow control using suction and blowing. It is simply made by adding energy to the boundary layer by sucking or blowing it. The rate of suction or blowing can be adjusted with the changing conditions of the flow. But still, the holes for suction or blowing are stationary and regardless of being used or not the holes create additional drag.

In order to prevent the additional drag created, acoustic flow control method may be employed. It is simply made by supplying the sound wave with the desired amplitude and frequency to the flow. In a similar manner with active flow control methods, parameters of acoustic flow control method can easily be adjusted with the changing conditions of the flow (Reynolds number and angle of attack) by simply adjusting the amplitude and/or the frequency, and unlike the other active and passive flow control methods there is no need to add any geometries to the surface of the aerofoil, avoiding the unnecessary drag. Even when the acoustic flow control method is not useable, for example at higher Reynolds numbers, it can simply be shut down, and this way the aerofoil can be used as is without any additional components.

An acoustic flow control system simply consists of an amplifier to control the amplitude, a signal generator to generate the sound signal, to control the type of the signal, and to adjust the frequency of the signal, an oscilloscope to monitor the sound signal, and a sound source to supply the signal to the flow in the deserved direction.

The sound waves can be introduced to flow both externally and internally. For the external acoustic excitation, the sound source should be at a distance from the aerofoil. On the other hand, internal acoustic excitation is made by placing the sound source inside the aerofoil, for example the sound waves can be introduced to the boundary layer from a slot on the surface of the aerofoil.

Theoretically, the acoustic excitation energizes the boundary layer by inducing Tollmien–Schlichting waves forcing the transition to begin. There is a useful dimensionless parameter to determine the effective acoustic excitation frequency which was used by Zaman and McKinzie (1991), Zaman (1992) and Yarusevych et al. (2003, 2007). The parameter is $St/Re^{1/2}$, so the effectiveness of the acoustic excitation is a function of frequency, free-stream velocity, characteristic length, and viscosity. This parameter was named Zaman number (Za) for the first time, by the authors Açıkel and Genç (2015), Genç et al. (2015b). In order to adjust the acoustic excitation with the changing conditions of the flow both the frequency and the amplitude of the sound wave can be varied. Various studies investigate the effect of the varying frequency and amplitude.

31.2.1 Flow Control with Constant Frequency

Yarusevych et al. (2007) presented an experimental study on a NACA 0025 aerofoil at low Reynolds numbers. They employed hot-wire anemometry and pressure measurements techniques, and also conducted flow visualization experiments. The results showed that the acoustic excitation with a certain frequency and with sufficient level of amplitude, boundary layer separation delayed. Moreover, the wake of the aerofoil was narrowed owing to the acoustic forcing, so the lift coefficient increased while the drag coefficient decreased. They stated that there were two thresholds for the acoustic excitation amplitude, minimum, and maximum. At the minimum threshold, the effects of the acoustic excitation started to be realized in terms of aerodynamic performance, and at the maximum threshold the effects of the acoustic excitation were started wear off. Collins and Zelenevitz (1975) conducted experiments both with and without acoustic excitation on an aerofoil employing pressure measurements. They integrated the pressure measurement results to obtain the coefficients of lift, drag, and moment. They placed the loudspeaker above the aerofoil introducing the sound wave with constant frequency vertically. They altered the amplitude and stated that when the amplitude value of the acoustic excitation increased, the effects of the acoustic excitation increased as well.

31.2.2 Flow Control with Constant Amplitude

Ricci and Montelpare (2005), Ricci et al. (2007) carried out a study of the effects of acoustic excitation on LSB over an RR3823HL aerofoil by means of IR

thermography. They introduced a sinusoidal sound wave with a frequency range of 200–800 Hz with a step of 100 Hz to the aerofoil at the angles of attack of 2° to 8°. As a result, the acoustic forcing successfully reduced the length of the LSB by retarding the separation. Zaman and McKinzie (1991) investigated the effects of acoustic excitation over two dimensional aerofoils at low angles of attack by means of hot-wire anemometry and smoke-wire flow visualization. They kept the amplitude constant but varied the frequency. The results showed that the adverse effects are reduced due to the acoustic excitation of the flow; the lift coefficient increased significantly. Yarusevych et al. (2003) investigated the effects of acoustic excitation on a NACA 0025 aerofoil at Reynolds numbers of 57,000, 100,000, and 150,000, and at the angles of attack of 0°, 5°, and 10°. The experiments were conducted employing hot-wire anemometry, and they attached nylon tufts to the surface in order to have an insight on the behavior of the boundary layer. They concluded that external acoustic excitation having appropriate amplitude could reduce or suppress the separated region of the flow. They stated that the effectiveness of the acoustic control also depended on the Reynolds number and angle of attack.

31.2.3 Flow Control with Variable Frequency and Amplitude

Ahuja et al. (1983) investigated the effects of acoustic excitation on the turbulent boundary layers. They carried out experiments in order to obtain lift coefficients, mean velocities and turbulence intensities, and they also carried out flow visualization experiments over a GA (W)-1 aerofoil. The effects of acoustic excitation were examined as a function of the excitation frequency and amplitude. The results showed that the separation of turbulent boundary layer can be controlled at both pre-stall and post-stall conditions. In addition, they stated that acoustic excitation was more effective with a higher amplitude. Ahuja and Burrin (1984) conducted experiments over the NACA 65(1)-213 aerofoil having various chord lengths. They used both internal and external acoustic excitation. They proved that with a longer chord a higher excitation frequency is needed. In addition, they found out that the frequencies that increased the lift coefficient had an effect on the fluctuating pressures on the surface of the aerofoil. As another result, they stated that the acoustic excitation was found to be more effective just before and just after the stall. Nishioka et al. (1990) studied on the control of leading edge separation employing acoustic forcing over a flat plate at a chord Reynolds number of 40,000, and they presented that the separated shear layer flow was extremely unstable to small amplitude disturbances and rolled up to form discrete vortices. Also it was shown that these growing discrete vortices with certain scales and frequencies are efficient in reattaching the flow as long as their scale was matched to that of the bubble. But after a certain angle of attack they became inefficient.

   This chapter explains the effects of parallel and perpendicular acoustic excitation on the flow over a NACA 2415 aerofoil at low Reynolds numbers, and is a presentation of the results of a project (Genç et al. 2012a, b, 2015a, b; Karasu 2011; Karasu et al. 2012, 2013; Açıkel et al. 2012; Açıkel 2013; Açıkel and Genç 2015). In the authors' previous study, first the flow characteristics of the NACA2415 aerofoil without acoustic forcing were examined in different angles of attack, at various Reynolds employing force measurements, pressure measurements; hot-wire anemometry, and smoke-wire flow visualization technique (Genç et al. 2012b; Karasu 2011; Karasu et al. 2012, 2013). Then, the acoustic excitation was applied for the same cases of Reynolds numbers and angles of attack (Açıkel et al. 2012; Genç et al. 2012c, 2015a, b; Açıkel 2013; Açıkel and Genç 2015). Moreover, the optimum range of the Za number for the flow control was found to be 0.02–0.03 by Zaman and McKinzie (1991), Zaman (1992) and Yarusevych et al. (2003, 2007), in this study a different range of optimum Za number was determined, distinguishing from the other studies' results.

31.3   Experimental Methods

The experiments were carried out in Wind Engineering and Aerodynamic Research (WEAR) Laboratory at the Department of Energy Systems Engineering, Erciyes University. The laboratory consists of a low-speed suction type wind tunnel with a square test section of 500 mm × 500 mm (Fig. 31.6). The free-stream turbulence intensity of the wind tunnel at the maximum speed (40 m/s) is about 0.3 %, and at the lowest speed (5 m/s) the turbulence intensity is about (0.7 %) (Genç et al. 2012b; Karasu 2011). The aerofoil used was a NACA 2415 having a chord of 180 mm. The experiments were done at chord Reynolds numbers of 50,000, 75,000, 100,000, and 150,000, and at a range of angle of attack of 0° to 25°. Pressure measurements via pressure transducers, velocity measurements via
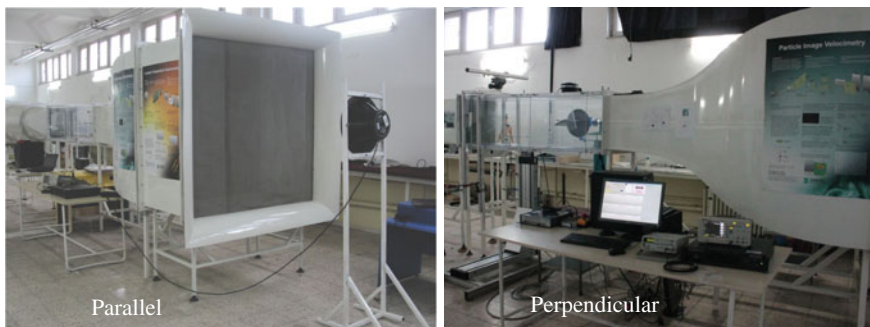
Fig. 31.6 Photographs of the experimental setup including the acoustic apparatus

hot-wire anemometry, smoke-wire flow visualization, and PIV experiments were used for the experimental study.

Pressure measurements were conducted by using a NACA 2415 aerofoil with 24 pressure tappings of 0.8 mm diameter distributed on both suction and pressure sides of the aerofoil. A pressure transducer was connected to each pressure tapping to acquire data. The pressure transducers were calibrated by using a pressure chamber with known pressure values. The pressure data were collected at a sampling frequency of 1000 Hz over 60 s. Pressure coefficients were calculated using a MATLAB code for each case, and the pressure distributions were plotted based on the data collected.

Force measurements were done by employing an external three-component load-cell system, and lift force and drag force were measured to calculate the force coefficients, C_L and C_D. Known weights were used to calibrate the system, and the force data were collected at a sampling frequency of 1000 Hz over 120 s. Mean forces and force coefficients were calculated using a MATLAB code.

The smoke-wire flow visualization experiments were carried out by using a wire of high resistance. The wire, or for some cases a coil of wires, was stretched between the upper and lower walls of the wind tunnel test section, and then coated with oil. When the voltage is applied to the wire, the wire gets hot and the oil starts evaporate to create short bursts of smoke filaments, marking the streak lines. The filaments can show the behavior of the flow, separation and reattachment points, laminar separation bubble, and fully separated flow. As the Reynolds number gets higher, it gets challenging to get a proper image of the streak lines since the smoke filaments are easily dispersed through the flow. Therefore, in this study the smoke-wire flow visualization experiments were only done for Reynolds number of 50,000. The photographs were taken by using a CANON EOS 1100D camera.

Particle image velocimetry was employed in order to examine the flow over the aerofoil and the laminar separation bubble. Instantaneous data measurements were done for the streamlines, vorticity, and turbulence intensity. In order to enlighten the plane, a pair of pulsed mini Nd: YAG Laser with a maximum energy output of 120 mJ per pulse was used. The lens of the laser shutter was placed below the wind tunnel, and the aerofoil was placed upside-down, since the laminar separation bubble occurs on the suction side of the aerofoil. 60 mm lens was employed for the camera. The camera of the PIV system is a 1.3 Megapixel Hi-Sense Mk-II model which has a quantum efficiency of 70 %. The images taken by the system was processed using Dynamic Studio. The lenses used for the laser are modified for wind tunnels. Then the images were processed employing Dynamic Studio with various correlations and the scaler and vectorial maps of the flow field were obtained. In order to generate the fog particles, 10T20 Blitz fog fluid was used in Safex fog generator. Double frame images were acquired 8 images per second. Sequences of 240 velocity fields (total time was 30 s) were produced for each measurement. Post-process was performed by means of Dantec Dynamic Studio software, average filter and Gaussian smoothing were applied. A x B pixel images were acquired which corresponding $83 \times 56 = 4248$ vectors per image. The uncertainty of the velocity measurements is estimated to be 3 % of the free-stream

velocity. In the PIV experiments, PIV equipment and their placement in the test section of the wind tunnel do not allow the experiments of perpendicular acoustic control to be conducted, thus in this chapter only the results of parallel acoustic control experiments are presented. In addition, the camera was defected because of the reflection of the laser to the camera and some pixels of the camera were broken during the PIV experiments, therefore the velocity values are incorrect in the free-stream in some points.

The velocity measurements were done by employing Dantec Dynamics Multichannel Constant Temperature Anemometer by using single and boundary layer hot-wire probes. The single wire probe was used for the velocity measurements at the wake of the aerofoil. The probe was located at two chord lengths from the trailing edge, and traversed across the wake vertically per 0.05 mm using Dantec Dynamics 2D Traverse System, and the mean velocity and velocity spectrum were calculated at each measurement location. The probes were calibrated by using a Dantec reference velocity probe with fourth order polynomial curve fitting having linearization errors between −1.0 and 0.9 % from the calibration data. At each velocity measurement point, 4096 velocity values were acquired at a sampling rate of 1 kHz with a low-pass filter setting of 1 kHz.

The acoustic system (Açıkel 2013) consists of a loudspeaker, an amplifier, a signal generator, and an oscilloscope. The loudspeaker was placed in front of the wind tunnel with a distance of 1.5 meters for the parallel acoustic excitation experiments as shown in left photograph in Fig. 31.6, and it was placed above the aerofoil to the top of the wind tunnel test section for perpendicular acoustic excitation experiments as seen in right photograph in Fig. 31.6. The distances for both types of acoustic excitation were selected in order not to make the excitation system interfere with the flow.

The effect of wind tunnel resonance characteristics is an important issue in the experimental studies on the acoustic excitation of the flow in order not to conflict with the wind tunnel resonance frequencies. Wind tunnel resonance characteristics were examined by employing a ½ inch Brüel and Kjær microphone with 2671 preamplifier. The microphone was placed at $x/c = 0.5$ and $y/c = 0.15$ (Yarusevych et al. 2007), above the upper surface and sound pressure levels (SPL) for 0 to 3000 Hz were measured. The SPL measurements were done with no free-stream velocity. Figure 31.7 shows the SPL values of each frequency for parallel acoustic excitation. The first peak, which is believed to be associated with the resonance frequency of the wind tunnel's test section, was seen at the frequency of 430 Hz, and the peaks at the frequencies of 860, 1300 and 1750 Hz are believed to be the first, second, and third harmonics of 430 Hz, respectively. The peak frequencies indicate the resonance frequencies (360, 611 and 870 Hz) of the wind tunnel's test section in Fig. 31.8 for perpendicular acoustic control. These figures suggest that the frequencies used for acoustic control are not equal to the peak frequencies of the wind tunnel test section.

Fig. 31.7 Resonance characteristics of the wind tunnel test section for parallel acoustic excitation
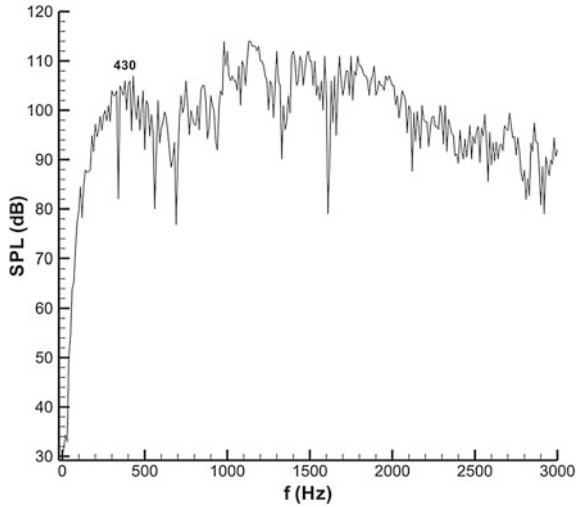
Fig. 31.8 Resonance characteristics of the wind tunnel test section for perpendicular acoustic excitation
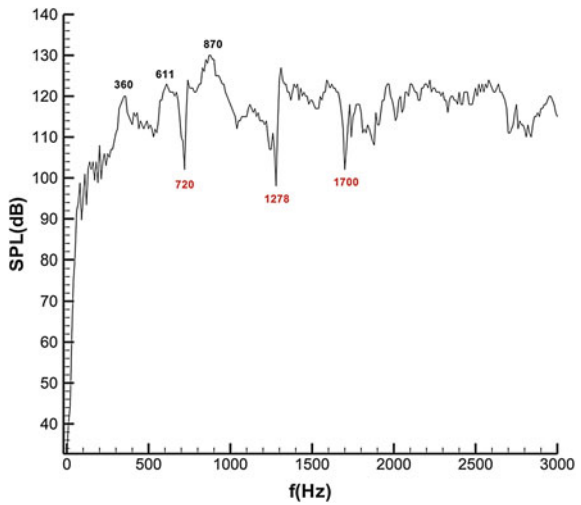
31.4 Experimental Results

31.4.1 Pressure Distribution Results

Pressure measurements were carried out to obtain the pressure distributions of both pressure and suction sides of the aerofoil to determine the locations to determine the locations of separation, transition and reattachment points and consequently the length of the LSB for no control and controlled cases, and the acoustic control was made both parallel to the flow and perpendicular to the flow. Initially experiments

Fig. 31.9 Pressure
distribution over the
NACA2415 aerofoil
without/with parallel acoustic
forcing at $Re = 50,000$ and
$\alpha = 15°$
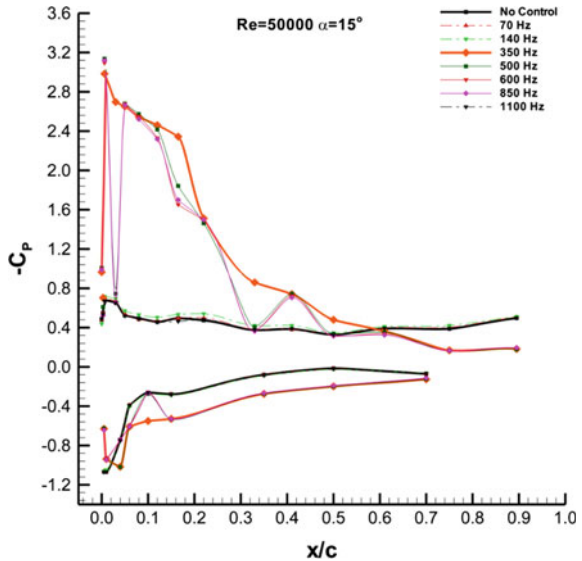
were done at $Re = 50,000$ and $\alpha = 15°$ in order to determine the optimum range of acoustic excitation frequencies (Fig. 31.9). In no control case, the aerofoil was stalled. With parallel acoustic excitations of 70 and 140 Hz, the flow could not be forced to reattach to the surface of the aerofoil. The stall was retarded using the frequency range of 200–850 Hz. Frequencies higher than 850 Hz did not affect the flow. Figure 31.9 shows instantaneous effects of different excitation frequencies, the effect can be seen for one frequency and then the effect vanishes for the other. This is because the stall is associated with stream-wise fluctuation frequencies and the frequencies that suppress these stream-wise fluctuation frequencies are effective. In order to gain insight of the effect of acoustic excitation, the time-dependent pressure for various points of measurements was plotted in Fig. 31.10. These plots indicate an increased pressure difference with acoustic excitation.

The curves of the pressure coefficient distribution show the development of the boundary layer from the leading edge to the trailing edge, and the pressure difference slowly decreases after peak suction. In the curve of the pressure coefficients, a slight increase or constant pressure and then decrease over suction surface point out the separation of flow due to the adverse pressure gradient and reattachment, respectively. For the perpendicular acoustic control case, the acoustic frequency of 50 Hz did not affect the flow in Fig. 31.11. With the frequency of 100 Hz, the flow separated from the point of $x/c = 0.08$ and reattached at $x/c = 0.25$, which points out LSB formation. With acoustic forcing of 300 and 500 Hz, the flow attached and small laminar separation bubble occurred. With the acoustic excitation of 700 Hz, the separated flow could not be controlled completely. The frequency range of 100–500 Hz was found to be effective for forcing the flow reattach to the surface of the aerofoil.
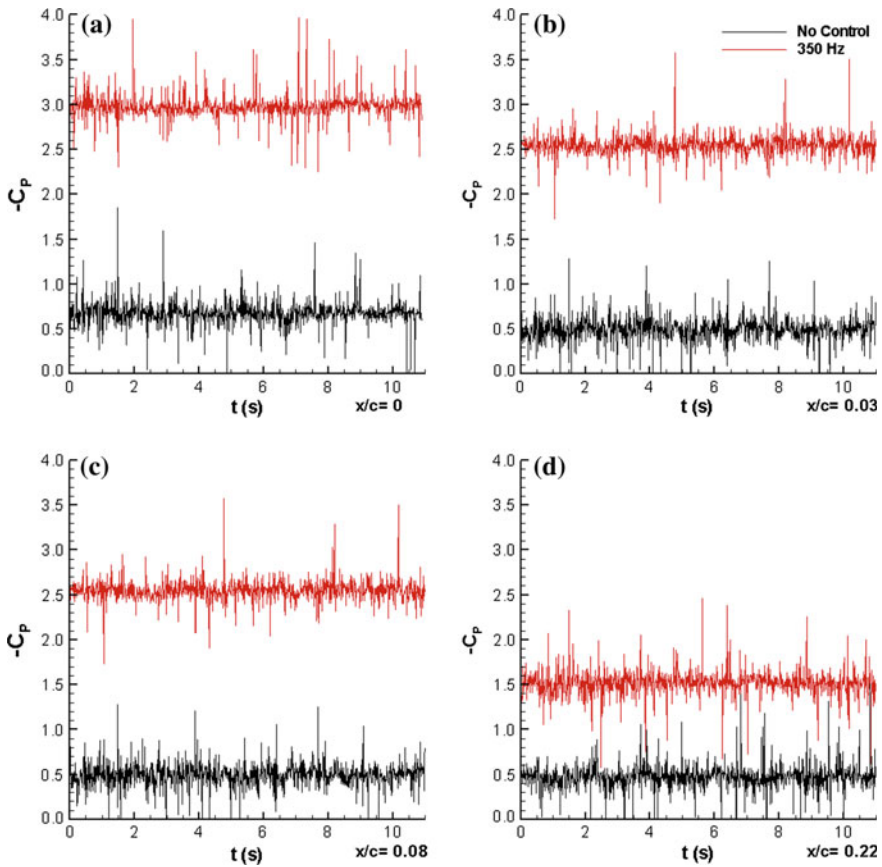
Fig. 31.10 Time histories of C_p measured at different points over the NACA2415 aerofoil without/with parallel acoustic forcing with 350 Hz at $Re = 50{,}000$ and $\alpha = 15°$

The pressure measurements at $Re = 50{,}000$ and $\alpha = 8°$ for no control case were resulted in a LSB having a length of 0.5 c, with a separation point at $x/c = 0.22$, and a reattachment point at $x/c = 0.72$ as shown in Fig. 31.12. With a parallel acoustic excitation of 70 Hz, the separation point was at the same location but the reattachment point moved to $x/c = 0.65$, shortening the LSB. In the parallel acoustic excitation having a frequency of 140 Hz, the separation point was also at the same location but the reattachment point was at $x/c = 0.61$. At the parallel acoustic control frequency of 200 Hz, the separation point was at $x/c = 0.33$, and the reattachment point was at x/c = 0.5. With parallel acoustic excitation having a frequency of 350 Hz, the separation point was at $x/c = 0.33$, and the reattachment point was at $x/c = 0.5$.

As seen from Fig. 31.13, the pressure measurements at $Re = 50{,}000$ and $\alpha = 8°$ with perpendicular acoustic excitation having a frequency of 50 Hz did not affect

Fig. 31.11 Pressure
distribution over NACA2415
without/with perpendicular
acoustic forcing at
Re = 50,000 and α = 15°
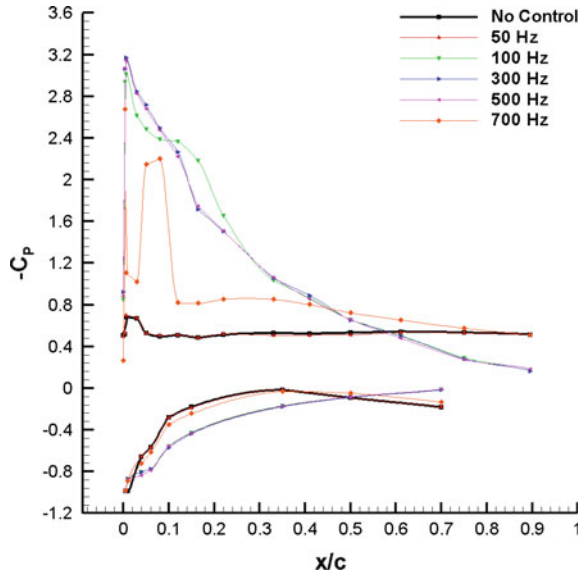
Fig. 31.12 Pressure
distribution over NACA2415
without/with parallel acoustic
forcing at *Re* = 50,000 and
α = 8°
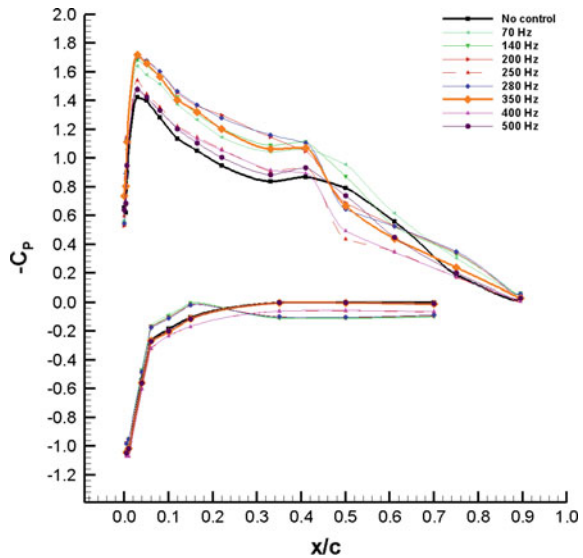
the flow; separation and reattachment points were at the same locations. In perpendicular acoustic excitation of 100 Hz, the separation point was again at the same *x/c*, but the reattachment point moved to *x/c* = 0.55, shortening the length of the LSB 33 % compared to the no control case. For perpendicular acoustic excitation with a frequency of 300 Hz, the reattachment point moved further toward the leading edge to *x/c* = 0.45, shortening the LSB 54 %. The location of the separation

Fig. 31.13 Pressure distribution over NACA2415 without/with perpendicular acoustic forcing at $Re = 50{,}000$ and $\alpha = 8°$
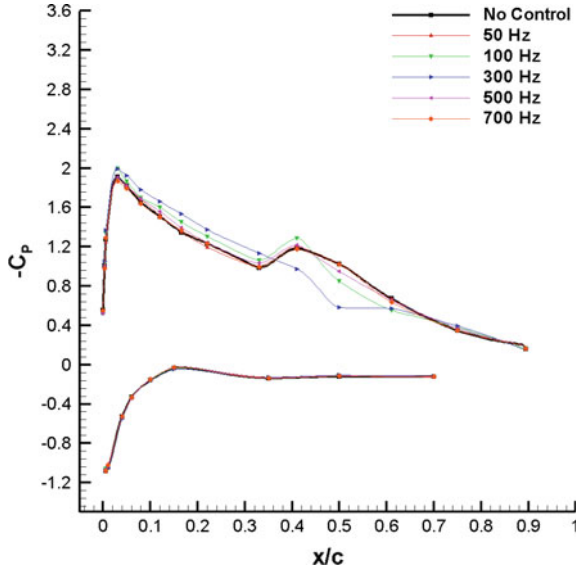
Fig. 31.14 Pressure distribution over NACA2415 without/with parallel acoustic forcing at $Re = 75{,}000$ and $\alpha = 8°$
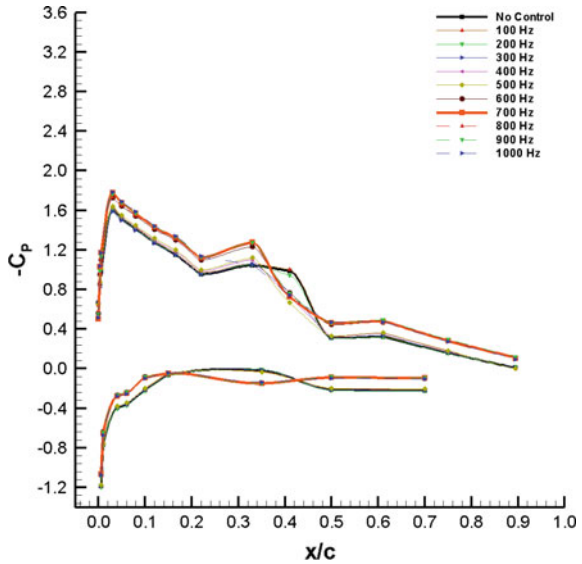
point also stayed the same. Perpendicular acoustic excitation frequencies of 500 and 700 Hz did not affect the flow.

At $Re = 75{,}000$ and $\alpha = 8°$, the pressure measurements results showed the separation point was at $x/c = 0.20$, and the reattachment point was at $x/c = 0.60$ with no acoustic control (Fig. 31.14). The parallel acoustic excitation did not affect the flow up to 500 Hz (Fig. 31.14). The parallel acoustic excitations of 600 Hz and

Fig. 31.15 Pressure
distribution over NACA2415
without/with perpendicular
acoustic forcing at
$Re = 75{,}000$ and $\alpha = 8°$
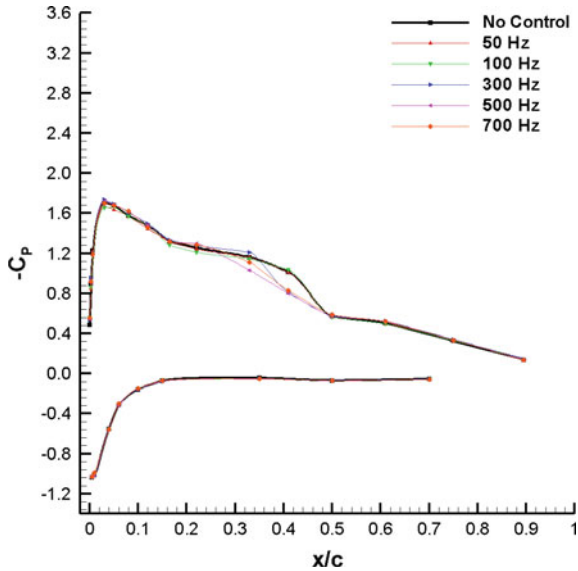
higher affected the flow. Comparing with the $Re = 50{,}000$ case, the lower threshold
of effective frequency range was increased.

With perpendicular acoustic excitation of 300 Hz, the location of the separation
point was the same but the reattachment point moved toward the leading edge,
shortening the LSB as shown in Fig. 31.15. The vertical acoustic excitation with a
frequency of 500 Hz shortened the LSB further, with a reattachment point at
$x/c = 0.32$. The separation point location was the same but still the LSB was
shortened 70 %.

At $Re = 75{,}000$ and $\alpha = 15°$, the flow was fully separated with no control in
Fig. 31.16. Parallel acoustic excitation range of 100 Hz to 400 Hz could not sup-
press the flow to reattach. But with the parallel acoustic excitation frequency of
700 Hz, the flow was successfully suppressed to reattach to the surface of the
aerofoil. All of the perpendicular acoustic excitation frequencies (50–700 Hz)
forced the flow to reattach with small laminar separation bubbles for some cases
(Fig. 31.17).

At $Re = 100{,}000$ and $\alpha = 18°$, the pressure distributions indicated stalled flow at
no acoustic control case (Fig. 31.18). For the parallel acoustic excitation, the range
of excitation frequency was selected as 600–1500 Hz. While in the parallel case
acoustic flow control cannot reattach the flow, the separated flow was forced to
reattach with acoustic forcing in the perpendicular case. As given in Fig. 31.19, the
excitation frequency was applied from 600 to 2100 Hz. The acoustic excitation
having the frequencies of 600, 700, 800, 900, 1000, 1100, 1200, 1350, and
1550 Hz forced the flow to reattach, but a laminar separation bubble having the
length of 0.1 x/c formed. However, the cases of 1750 and 2100 Hz were not

Fig. 31.16 Pressure
distribution over NACA2415
without/with parallel acoustic
forcing at $Re = 75,000$ and
$\alpha = 15°$
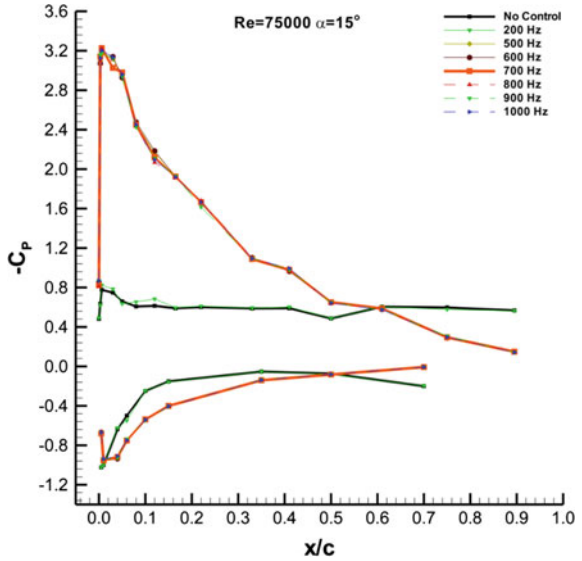
Fig. 31.17 Pressure
distribution over NACA2415
without/with perpendicular
acoustic forcing at
$Re = 75,000$ and $\alpha = 15°$
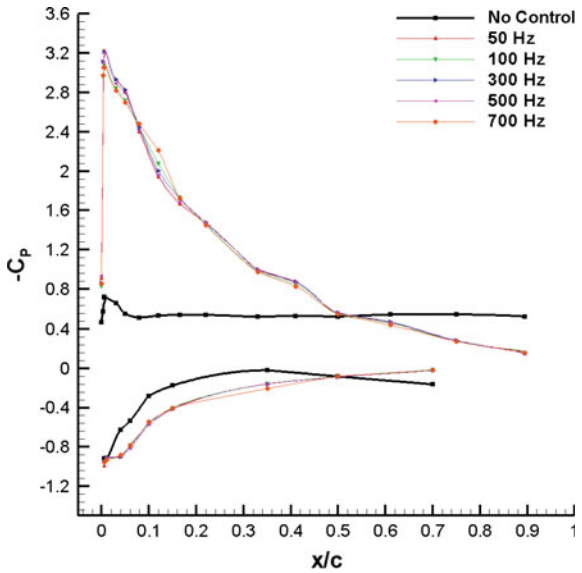
Fig. 31.18 Pressure
distribution over NACA2415
without/with parallel acoustic
forcing at $Re = 100,000$ and
$\alpha = 18°$
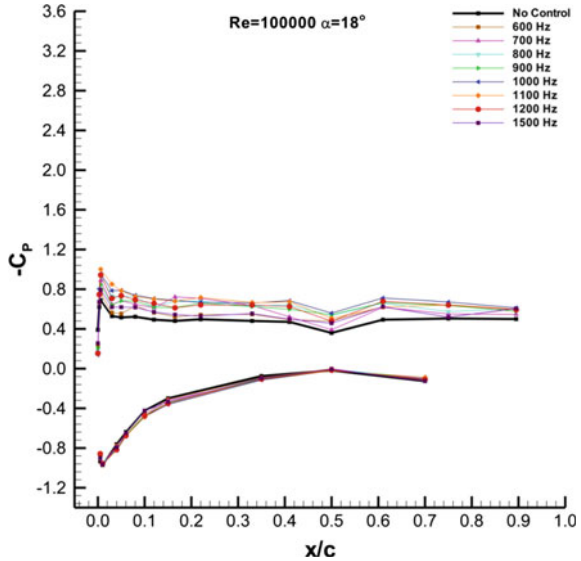
Fig. 31.19 Pressure
distribution over NACA2415
without/with perpendicular
acoustic forcing at
$Re = 100,000$ and $\alpha = 18°$
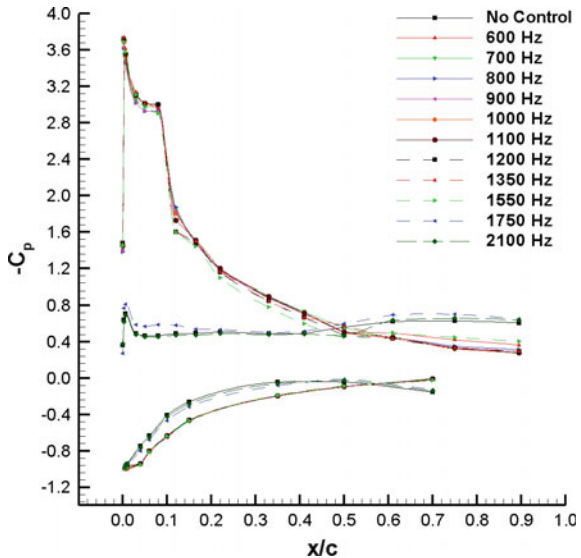
successful to force the flow to reattach, and the stall observed for these cases. It was
obtained that as Reynolds number increased, the applied frequency and effective
frequency range of the acoustic excitation increased in both acoustic control cases.
Moreover, it was shown that the effective frequency range of the acoustic forcing
was large in perpendicular acoustic forcing.

Consequently, as the Reynolds number increases, the effective excitation frequency increases, but the range of Za number based on effective frequency still is approximately same, for all Re number the effective range of Za number was obtained approximately between 0.03 and 0.07 (Genç et al. 2015b).

31.4.2 Force Measurement Results

The effective frequency ranges of different Reynolds numbers for both parallel and perpendicular acoustic excitations were determined from the results of pressure measurement experiments. These effective frequency ranges were used in the force measurement experiments. The experiments were conducted at a range of angles of attack of 0°–25°, and at Reynolds numbers of 50,000, 75,000, 100,000 and 150,000. The experiments consisted of lift and drag force measurements, and C_L and C_D coefficients were calculated to be a comparison for different cases of acoustic flow control.

As can be seen from Fig. 31.20a, b, at $Re = 50,000$ the angle of stall was 12° with a maximum C_L of 1.20 for no acoustic control case. Parallel acoustic excitation was applied in the range of 200–400 Hz. With 200 Hz acoustic excitation, the angle of stall was increased to 13° and C_{Lmax} was increased to 1.44. For the 250 Hz case, the stall angle was not affected, but C_{Lmax} was increased to 1.34. The angles of stall with acoustic excitation frequencies of 280, 350, and 400 Hz was 15°, 16°, and 13°, respectively. With 350 Hz of acoustic excitation, C_{Lmax} was increased by 30 % up to 1.56. Cd was not affected for non-stall angles of attack. But because of the increased angle of stall, C_D was decreased by the parallel acoustic excitation by 40 % at post-stall angles of the normal case.
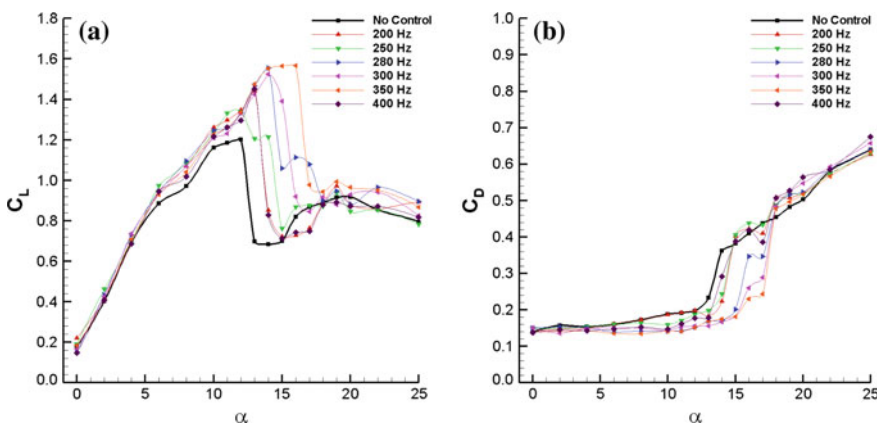
Fig. 31.20 Aerodynamic force coefficients versus the angle of attack over NACA2415 without/with parallel acoustic forcing at $Re = 50,000$

The perpendicular acoustic excitation frequencies of 50, 100, 300, 500, and 700 Hz increased the angle of stall to 14°, 15°, 18°, 17°, and 17°, respectively (Fig. 31.21a, b). The maximum C_L values were also increased slightly with the perpendicular acoustic control. Also, the flow was stalled abruptly in the no control case, but the acoustic excitation transformed the abrupt stall to mild stall by suppressing the flow. The values of C_D were decreased by the acoustic excitation.

At $Re = 75,000$, the stall angle was 13° with a C_{Lmax} of about 1.2. Parallel acoustic excitation range of 300 Hz to 900 Hz with a step of 100 Hz was applied in order to control the flow (Fig. 31.22a, b). Parallel acoustic excitation with a frequency of 700 Hz was found to be the most effective frequency, since it increased the angle of stall to 17° with a C_{Lmax} of 1.39, and at this angle of attack C_{Dmax} decreased from about 0.4 to 0.2 by 50 %.
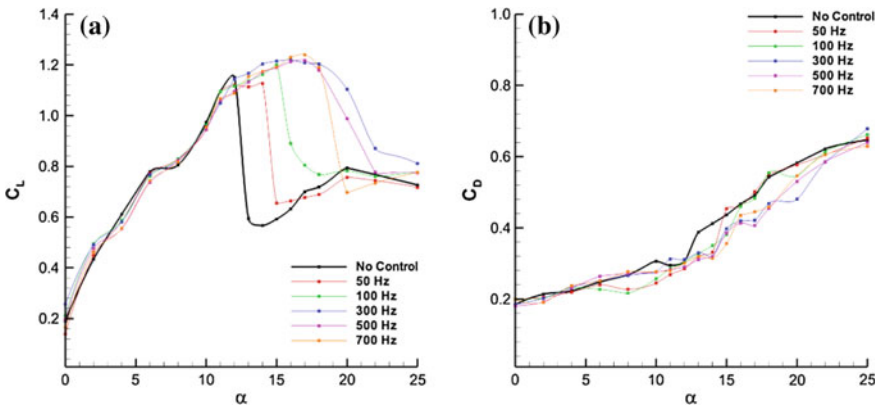
Fig. 31.21 Aerodynamic force coefficients versus the angle of attack over NACA2415 without/with perpendicular acoustic forcing at $Re = 50,000$
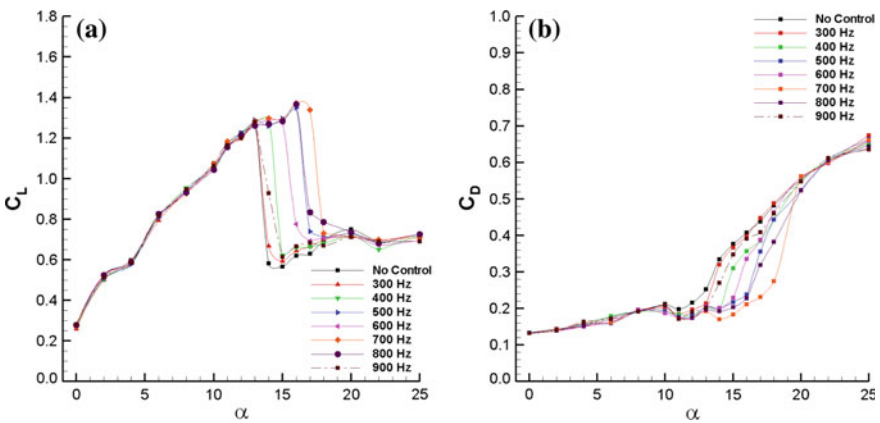
Fig. 31.22 Aerodynamic force coefficients versus the angle of attack over NACA2415 without/with parallel acoustic forcing at $Re = 75,000$
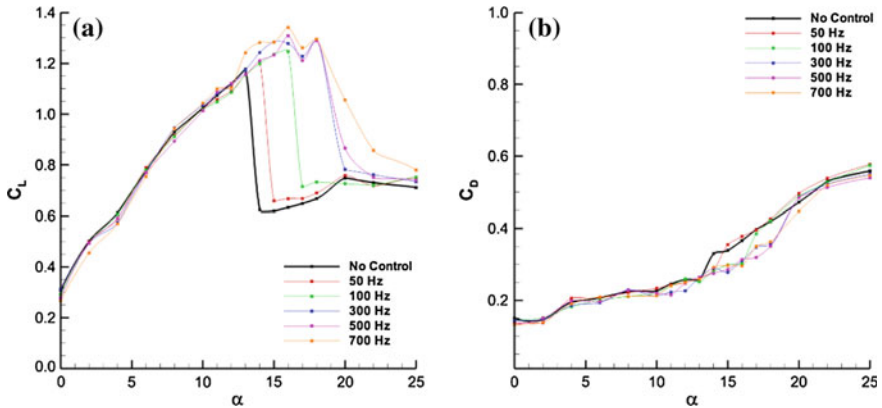
Fig. 31.23 Aerodynamic force coefficients versus the angle of attack over NACA2415 without/with perpendicular acoustic forcing at $Re = 75{,}000$
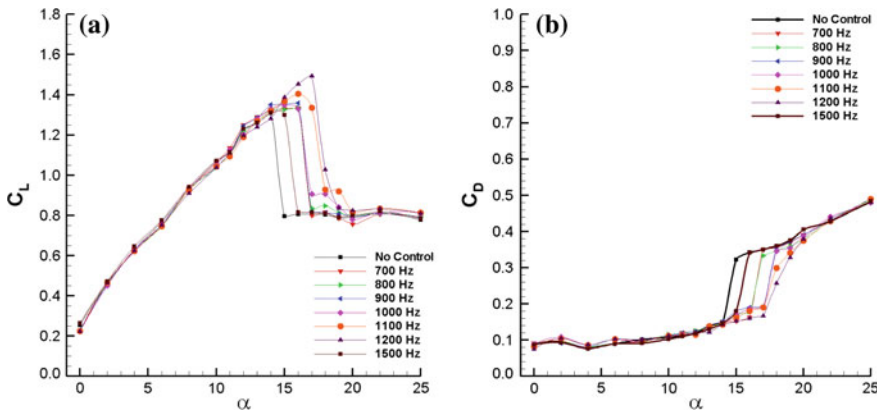
Fig. 31.24 Aerodynamic force coefficients versus the angle of attack over NACA2415 without/with parallel acoustic forcing at $Re = 100{,}000$

For $Re = 75{,}000$, the perpendicular acoustic excitation of 50 and 100 Hz increased the angle of stall to 14° and 15°, respectively (Fig. 31.23a, b). The acoustic excitations with the frequency of 300, 500, and 700 Hz forced the flow to reattach and increased the stall angle to 17°, with a maximum lift coefficient of 1.28, 1.30, and 1.32, respectively. The most effective frequency was found to be 700 Hz with a C_{Lmax} of 1.32. As can be seen from the figure, C_D values of pre-stall and post-stall angles of attack are decreased by the perpendicular acoustic excitation.

At $Re = 100{,}000$ the angle of stall was 14° with a C_{Lmax} of 1.30, with no acoustic control (Fig. 31.24a, b). A parallel acoustic excitation frequency range of
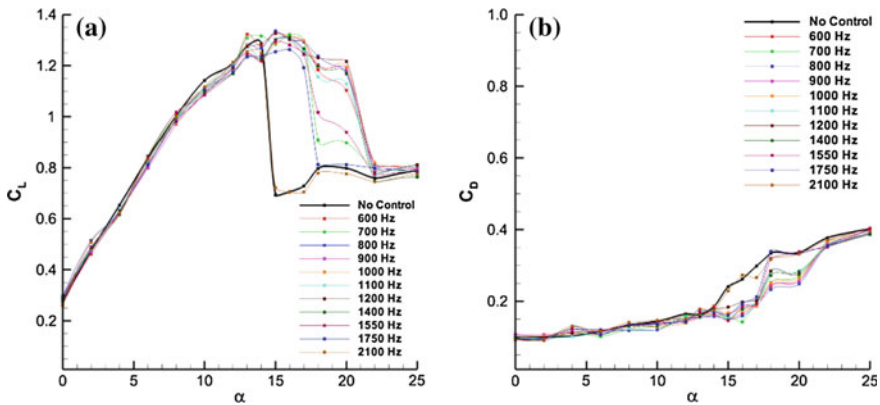
Fig. 31.25 Aerodynamic force coefficients versus the angle of attack over NACA2415 without/with perpendicular acoustic forcing at $Re = 100,000$

700–1500 Hz was applied. The frequencies of 700–1000 Hz did not affect the flow. With 1100 Hz, the angle of stall was increased to 17°, but there was no significant change in C_{Lmax}. The most effective frequency was determined as 1200 Hz with an angle of stall of 17° and a C_{Lmax} of 1.55.

The effect of perpendicular acoustic excitation on aerodynamic coefficients is shown in Fig. 31.25a, b. For this case, various frequencies of the perpendicular acoustic excitations did not affect the flow significantly. However, the stall was retarded and the abrupt stall was converted to mild stall. In addition, the plots of drag coefficients show a decrease in the values of C_D at limited pre-stall and post-stall angles of attack.

At $Re = 150,000$, the angle of stall was 15° with a C_{Lmax} of 1.32 in no control case. A parallel excitation frequency range of 900–2400 Hz with a step of 300 Hz was applied (Fig. 31.26a, b). Frequency range of 900–2100 Hz had a slight effect on the aerodynamic force coefficients. There was no significant enhancement in the C_D values. The perpendicular acoustic excitation for this case did not have a significant effect on C_L (Fig. 31.27a, b). On the other hand, C_D was slightly decreased. For parallel and perpendicular acoustic flow control, acoustic disturbance forced the flow to reattach but the flow could not reattach fully at $Re = 100,000$ and $Re = 150,000$.

31.4.3 Velocity Measurement Results

31.4.3.1 Velocity Measurement Results in Wake Region

In order to understand the effect of acoustic excitation on the velocity fluctuations and vortex shedding phenomenon, the measurements via hot-wire anemometry were conducted. Experiments were done at Reynolds numbers of 50,000, 75,000,
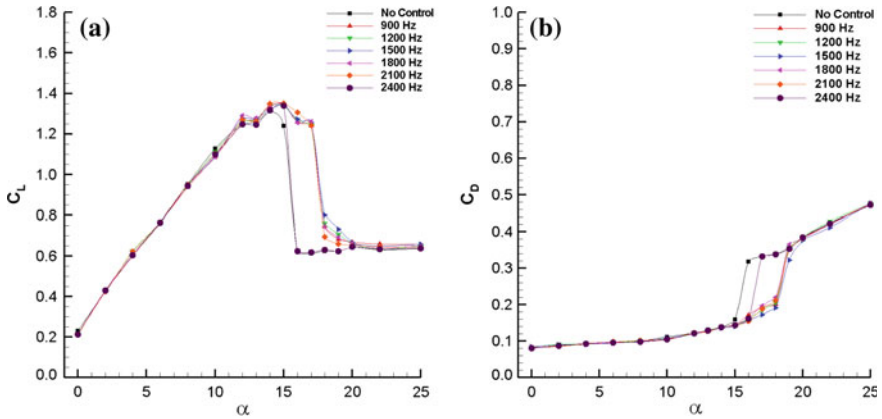
Fig. 31.26 Aerodynamic force coefficients versus the angle of attack over NACA2415 without/with parallel acoustic forcing at $Re = 150,000$
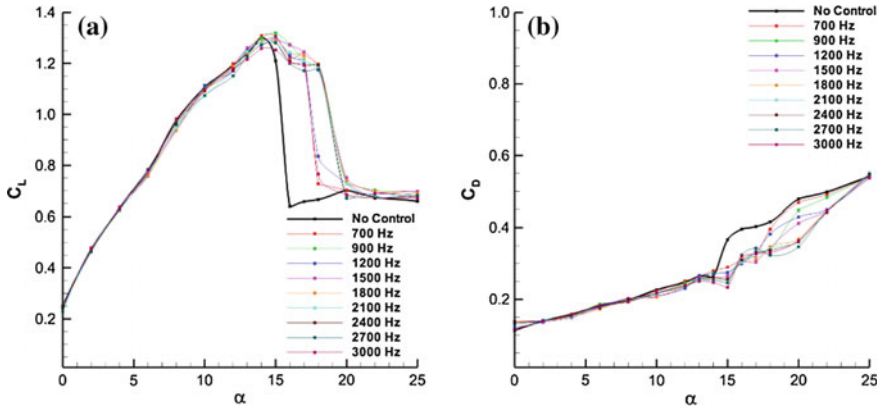
Fig. 31.27 Aerodynamic force coefficients versus the angle of attack over NACA2415 without/with perpendicular acoustic forcing at $Re = 150,000$

100,000, and 150,000, and at angles of attack between 0° and 20° for parallel acoustic control cases. The probe was located at two chords distance from the trailing edge and traversed vertically.

Figure 31.28 shows the plots of dimensionless velocity (u/U_∞) in the wake of the aerofoil at Reynolds number of 50,000, and at the angles of attack of 0°, 6°, 10°, 13°, 16°, and 20°. The plots indicate that with parallel acoustic excitation, the boundary layer was narrowed. As can be seen from the aerodynamic force coefficients plots, and pressure distributions with an acoustic excitation with a frequency of 350 Hz successfully controlled the flow at a range of angles of attack from 10° to 16°. Figure 31.29 illustrates the spectral analysis results of both no control case and flow control with acoustic excitation of 350 Hz case. In the no control case, there is
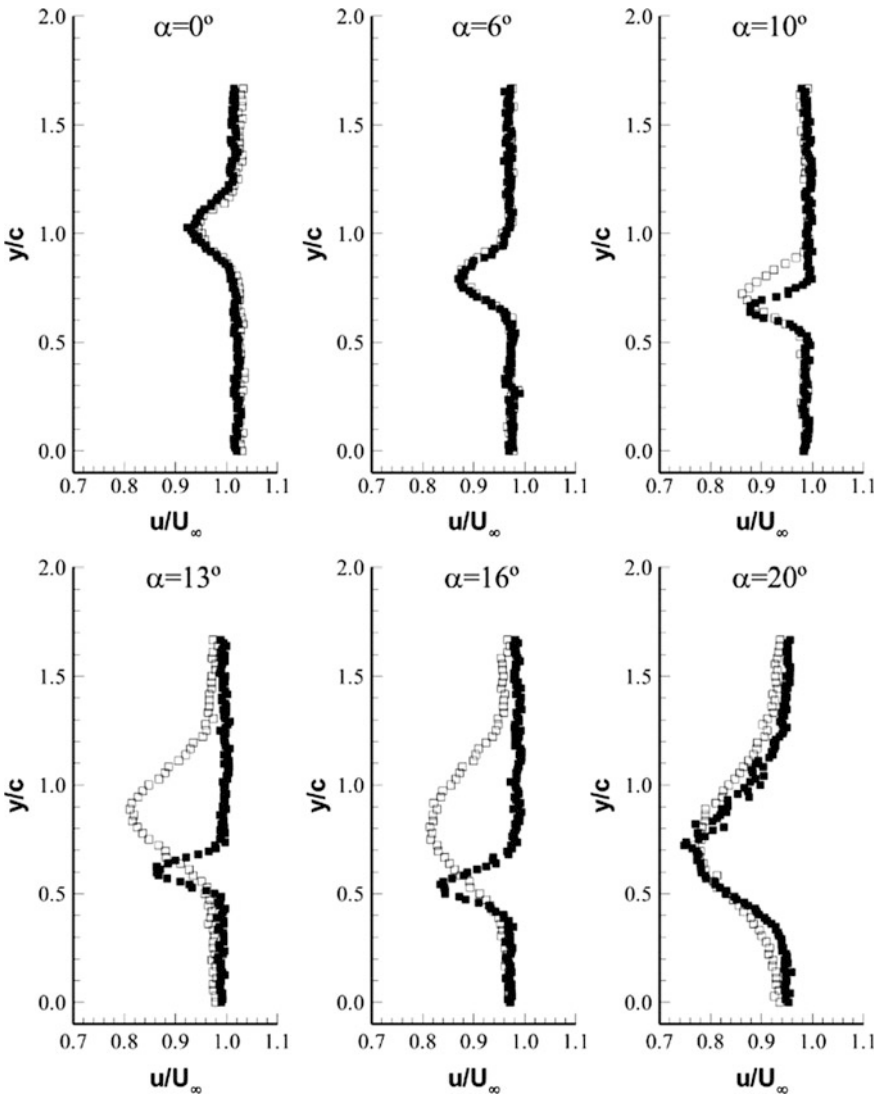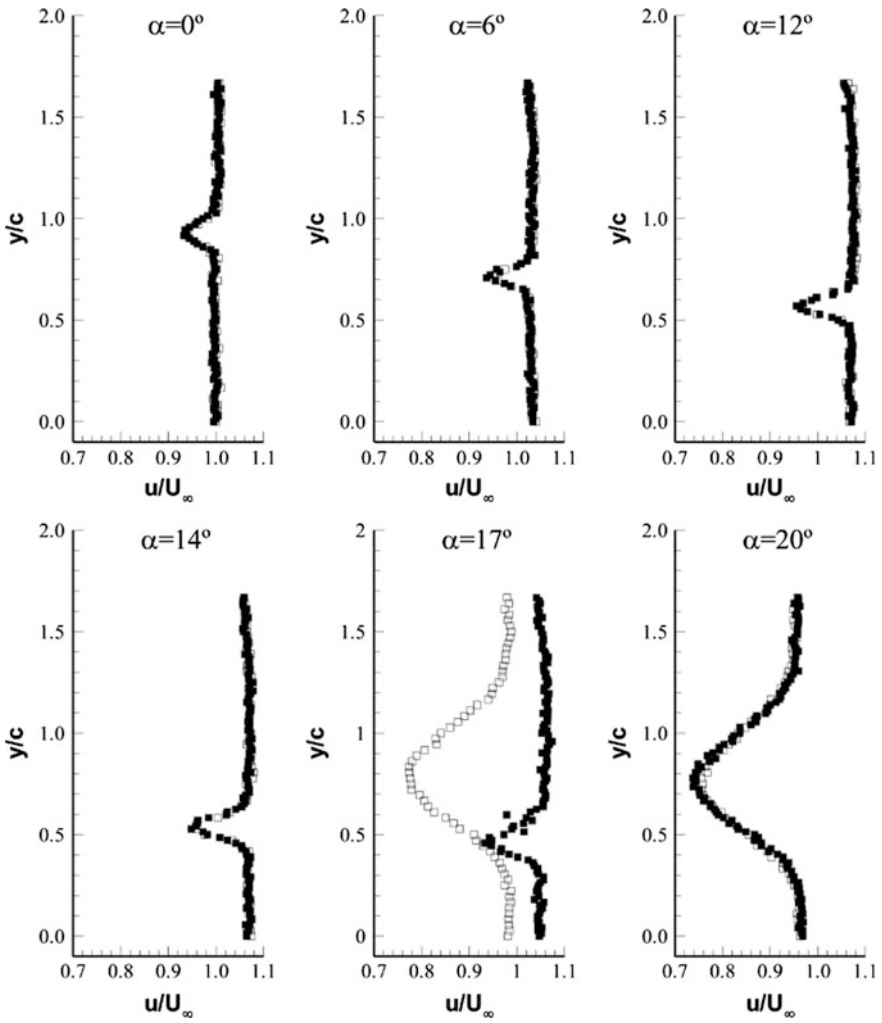
Fig. 31.28 Velocity distribution in the wake of the NACA2415 aerofoil without/with parallel acoustic forcing with the frequency of 350 Hz at $Re = 50{,}000$ at various angles of attack (*square* No control, *filled square* 350 Hz)

Fig. 31.29 Spectra of
velocity fluctuations in the
wake of the NACA2415
aerofoil without/with parallel
acoustic forcing with certain
frequencies at $Re = 50,000$
and $\alpha = 16°$
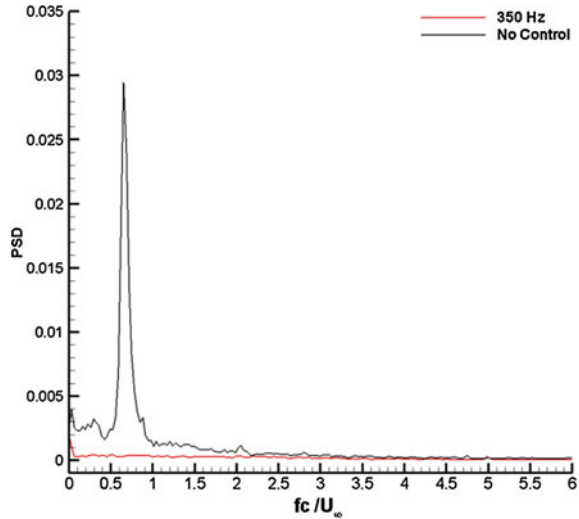
a peak frequency at St = 0.7, this peak is vortex shedding frequency, and with acoustic forcing large vortex shed from the surface of the aerofoil was given placed to eddies. It can easily be seen that the acoustic excitation forced to flow to reattach to the surface of the aerofoil, and it also narrowed the boundary layer which lead to decreased vortex formation and lowered power spectrum densities of vortex.

Figures 31.30, 31.32, and 31.34 indicate the plots of dimensionless velocity (u/U_∞) in the wake of the aerofoil at Reynolds number of 75,000, 100,000, and 150,000, respectively. The certain frequencies of parallel acoustic excitation controlled the flow and forced to flow to reattach. In addition, it was concluded that there was a peak point of St number values in all of the cases this points out that larger vortices formed from the spectral analysis graphics in Figs. 31.31, 31.33 and 31.35. When the acoustic excitation was applied, no peak was observed and there was no any further formation of large vortices. With the acoustic excitation of certain frequency, there were only little eddies having much more less power spectrum density values formed. At pre-stall angles and post-stall angles, the acoustic excitation suppressed the stream-wise fluctuations, which led to the reduction of the forming of vortices and consequently forcing the flow to reattach.

31.4.3.2 Velocity Measurement Results Over the Aerofoil

Velocity measurements via hot-wire anemometry over the surface of the aerofoil were conducted at Reynolds number of 50,000 at $\alpha = 15°$. At the angle of attack of 15° and the Reynolds number of 50,000, the flow was separated from near the
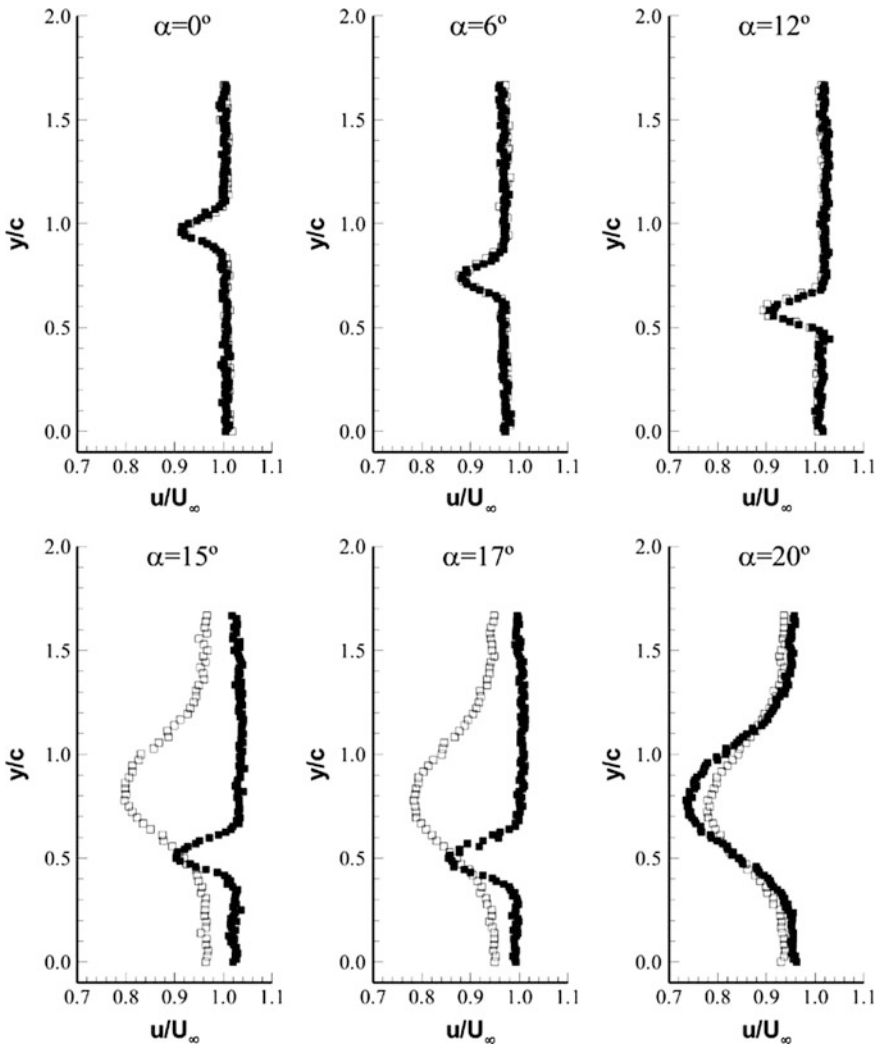
Fig. 31.30 Velocity distribution in the wake of the NACA2415 aerofoil without/with parallel acoustic forcing with the frequency of 700 Hz at $Re = 75{,}000$ at various angles of attack (*square* No control, *filled square* 700 Hz)
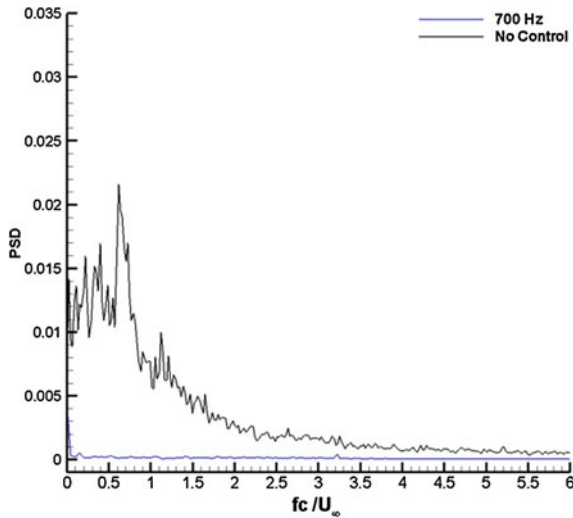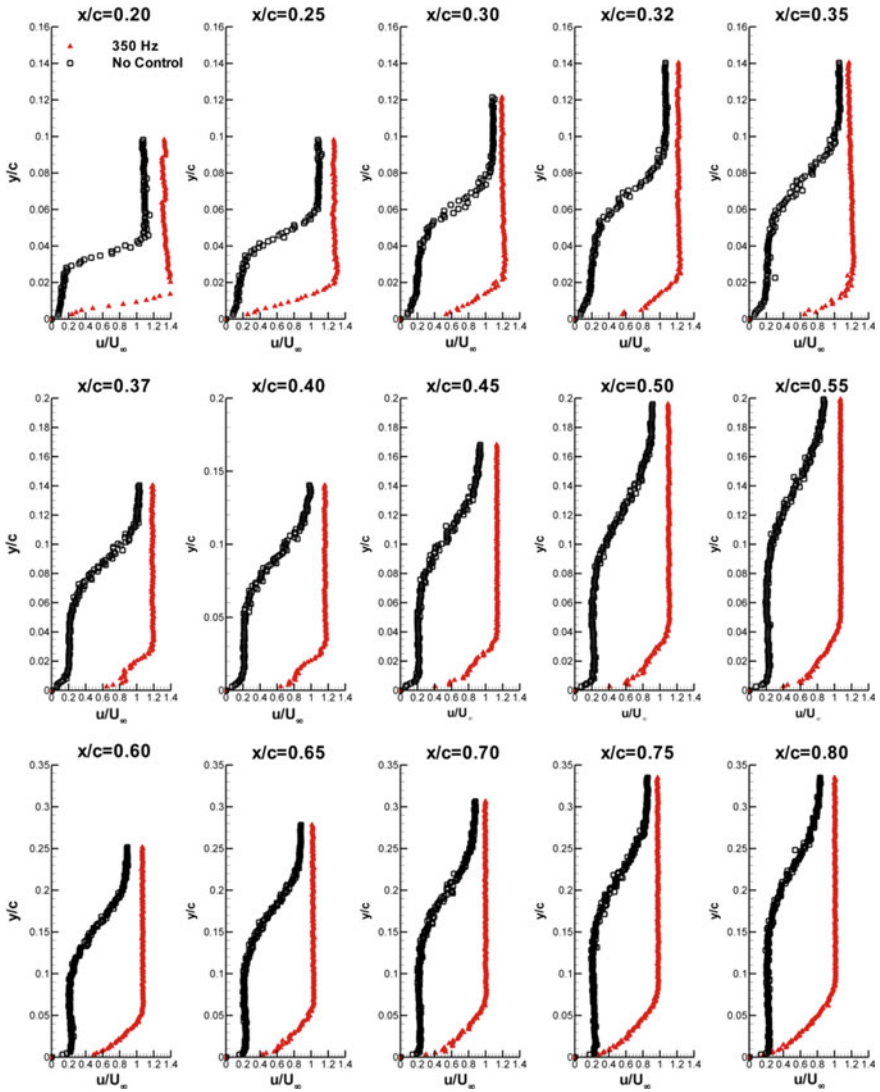
Fig. 31.31 Spectra of velocity fluctuations in the wake of the NACA2415 aerofoil without/with parallel acoustic forcing with certain frequencies at $Re = 75,000$ and $\alpha = 16°$

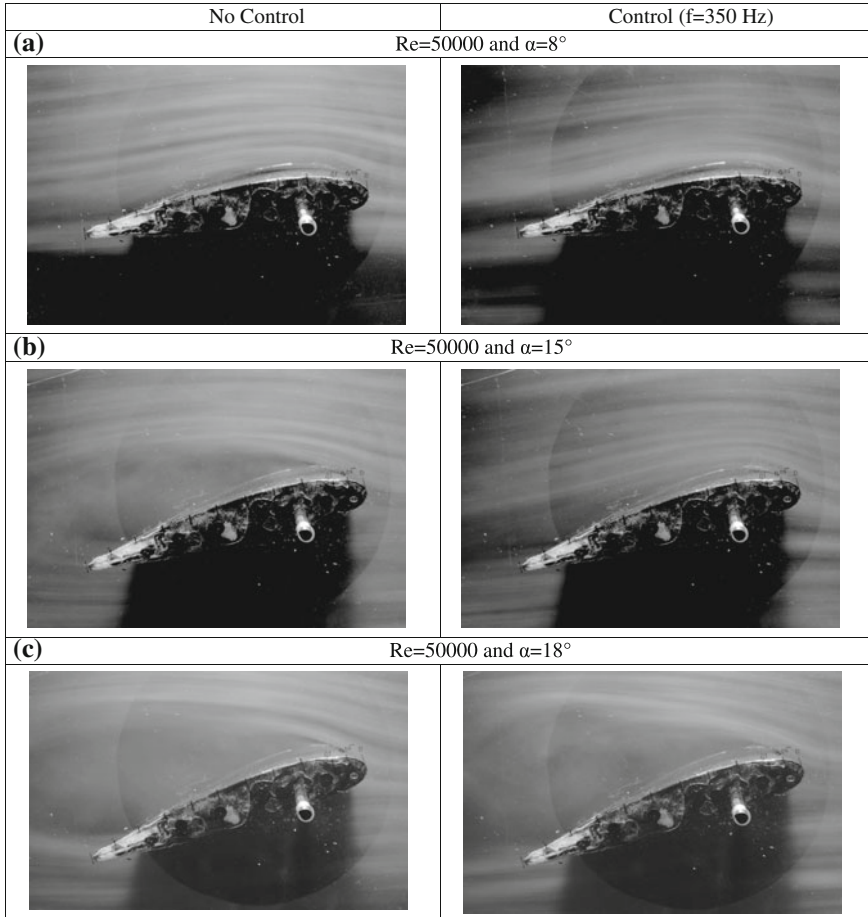leading edge in the no control case (Fig. 31.36). With a parallel acoustic excitation of 350 Hz, the reattachment of the separated flow is seen in Fig. 31.36.

The velocity measurements over the aerofoil via hot-wire anemometry experiments were conducted at Reynolds number of 50,000, and at the angles of attack of 15° with perpendicular acoustic excitation too. Figure 31.37 shows the effect of perpendicular acoustic excitation with 500 Hz of frequency at $Re = 50,000$ and $\alpha = 15°$. The flow was fully separated for the no control condition, but with perpendicular acoustic excitation of 500 Hz, the flow was reattached to the surface of the aerofoil.

31.4.4 Smoke-Wire Flow Visualization Experiment Results

The flow was visualized employing the smoke-wire flow visualization technique in order to see the effect of the acoustic excitation via the streak lines. The effect of parallel acoustic excitation was examined with the frequencies of 350 Hz at $Re = 50,000$ for the angles of attack of 8°, 15°, and 18° (Fig. 31.38). At $\alpha = 8°$, it can be seen that the flow separated nearby $x/c = 0.2$ and reattached nearby $x/c = 0.7$ (not seen clearly) with no acoustic control. The effect of parallel acoustic excitation with 350 Hz shrunk the LSB, and moved the separation point to $x/c = 0.3$, and the reattachment point to nearby $x/c = 0.6$. Besides, the results clearly indicate that the parallel acoustic excitation caused the flow to reattach ($\alpha = 15°$) and thus increased the stall angle. This effect wears off at relatively higher angles of attack ($\alpha = 18°$).
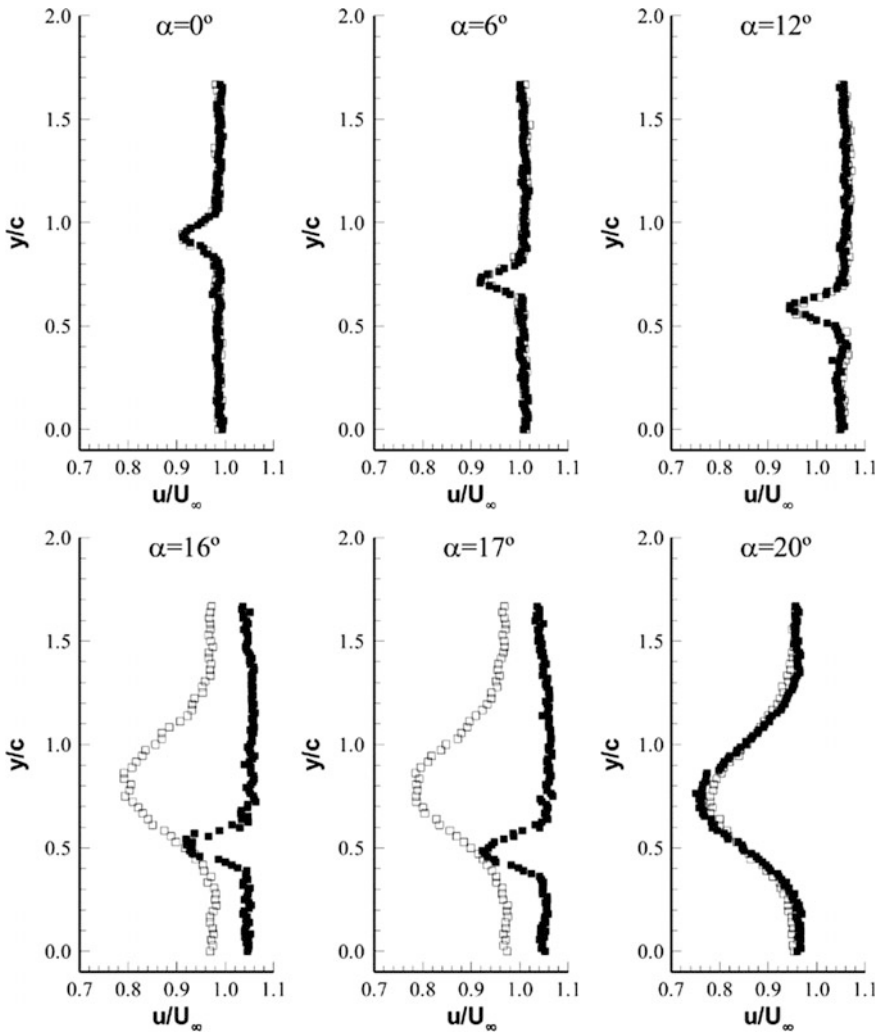
Fig. 31.32 Velocity distribution in the wake of the NACA2415 aerofoil without/with parallel acoustic forcing with the frequency of 900 Hz at $Re = 100,000$ at various angles of attack (*square* No control, *filled square* 900 Hz)
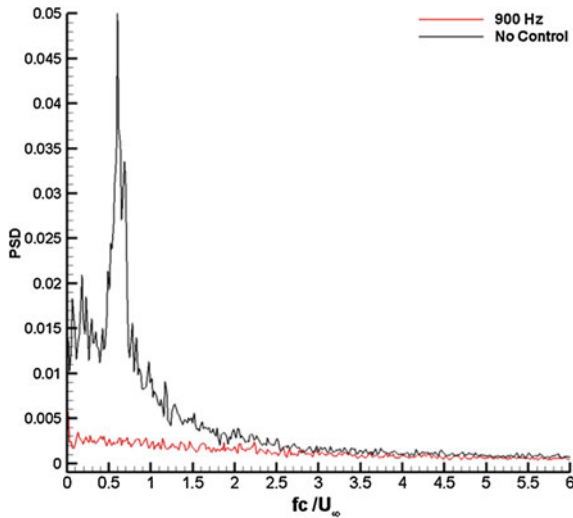
Fig. 31.33 Spectra of velocity fluctuations in the wake of the NACA2415 aerofoil without/with parallel acoustic forcing with certain frequencies at $Re = 100{,}000$ and $\alpha = 17°$

Figure 31.39 shows results of flow visualization experiments at Reynolds number of 50,000 at different angles of attack (8°, 15° and 20°) with perpendicular acoustic excitation with the frequencies of 300 Hz. At the angle of attack of 8°, the perpendicular acoustic excitation decreased the length and the height of the LSB. At angles of attack of 15°, the visualization photographs showed that acoustic disturbance is effective at controlling the flow. In addition, acoustic flow control effect reduces at the angle of attack of 20°.

At $Re = 75{,}000$ and $\alpha = 8°$ (Fig. 31.40), the effect of the parallel acoustic excitation having frequency of 700 Hz can be seen from the results of flow visualization experiments, as a decreasing in the length and the height of the LSB. At $\alpha = 15°$, it can be clearly seen from the results that parallel acoustic excitation forced the separated flow to reattach. This effect wears off at relatively higher angles of attack ($\alpha = 18°$).
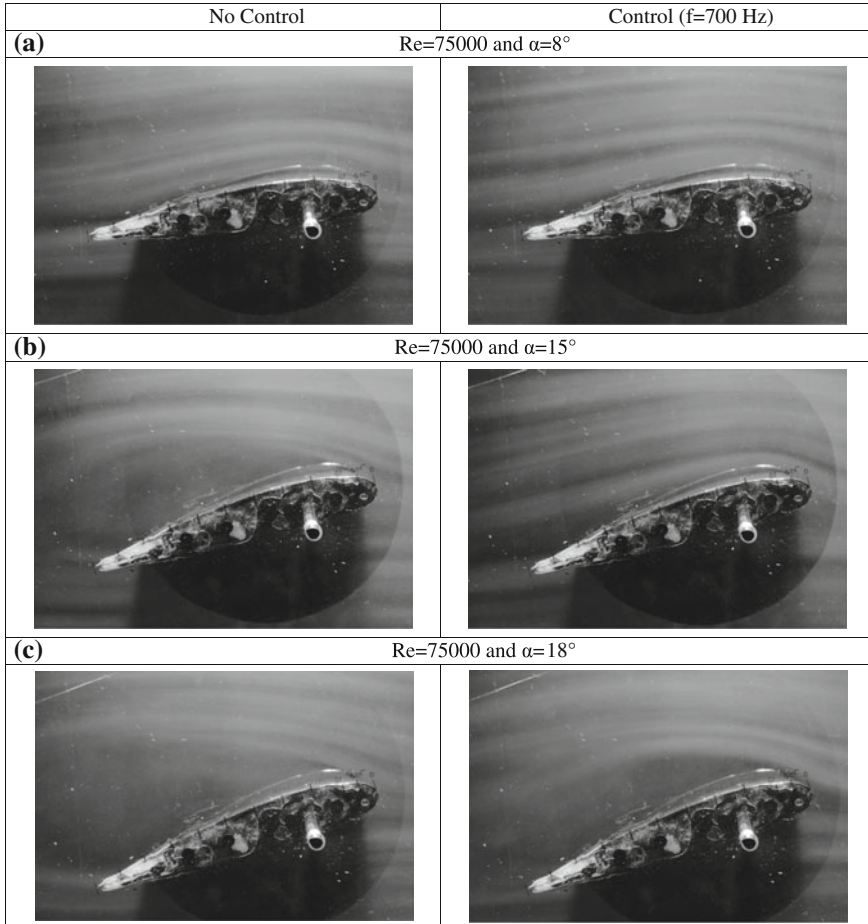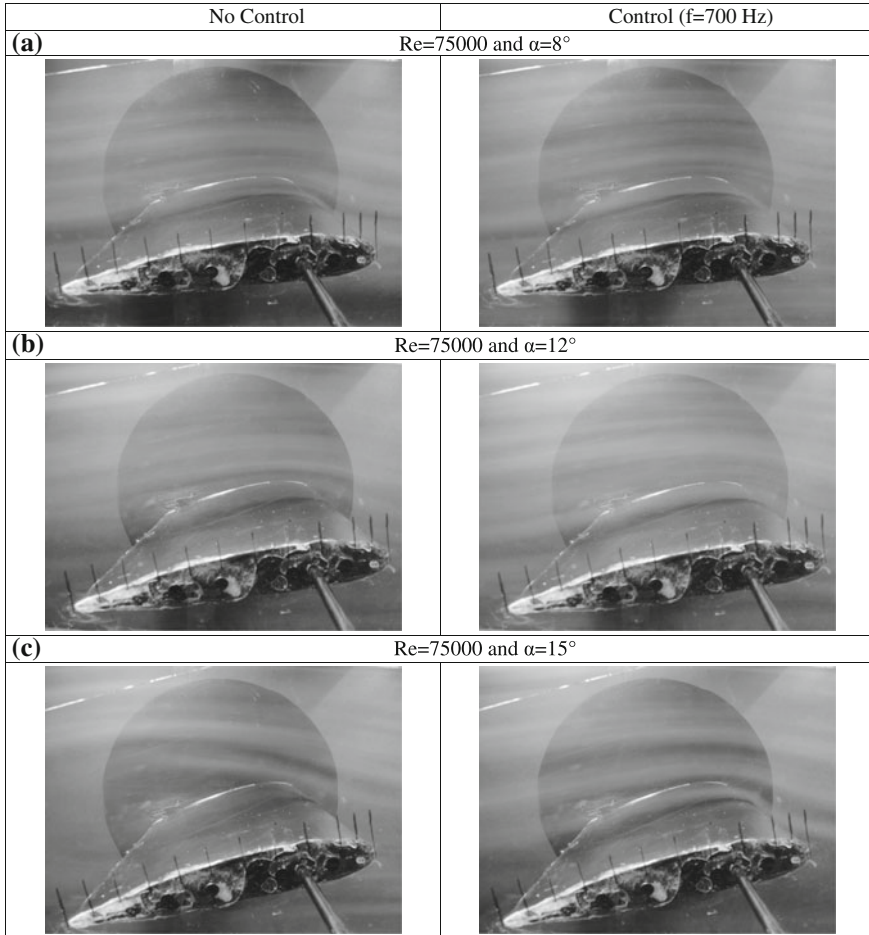
Figure 31.41 shows smoke-wire visualization results without/with perpendicular acoustic forcing with 700 Hz at $Re = 75{,}000$ and various angle of attack. At $\alpha = 8°$, the effect of the perpendicular acoustic excitation having frequency of 700 Hz was decreased the length and the height of the LSB. Moreover, the same effect for the case of 12° angle of attack can be seen in Fig. 31.41. With perpendicular acoustic excitation, the long LSBs are successfully transformed to short LSB. At $\alpha = 15°$, the perpendicular acoustic forcing forced the separated flow to reattach to the aerofoil surface.

Fig. 31.34 Velocity distribution in the wake of the NACA2415 aerofoil without/with parallel acoustic forcing with the frequency of 1800 Hz at $Re = 150{,}000$ at various angles of attack (*square* No control, *filled square* 1800 Hz

Fig. 31.35 Spectra of velocity fluctuations in the wake of the NACA2415 aerofoil without/with parallel acoustic forcing with certain frequencies at $Re = 150,000$ and $\alpha = 18°$
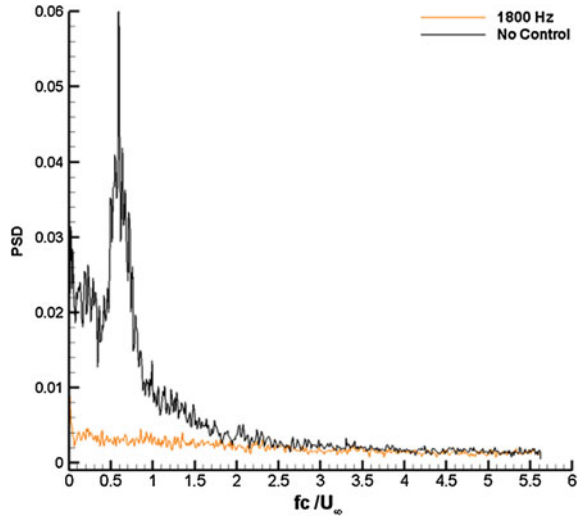
31.4.5 Particle Image Velocimetry Results

The results of PIV validated the results of other experiments conducted. However, for example, the results of PIV experiment at Reynolds number of 50,000 and the angles of attack of 8°, 15°, and 17° for the no control and parallel acoustic control cases can be seen in Fig. 31.42, and it is exactly the same with the pressure measurements and smoke-wire flow visualization results. At $\alpha = 8°$, because the result of PIV experiment does not demonstrate clearly the separation bubble in the case of fully flow over the NACA 2415 aerofoil, it was focused on specified region of $x/c = 0.25$ and $x/c = 0.80$ of the aerofoil from leading edge to trailing edge in Fig. 31.42 a and b. As can be seen from Fig. 31.42a, the separation point occurred at $x/c = 0.22$ and the reattachment point occurred at $x/c = 0.72$. With a 350 Hz of parallel acoustic excitation, the separation and reattachment point shifted to $x/c = 0.28$ and $x/c = 0.56$, respectively. This was also seen from the results of pressure measurements and flow visualizations. Figure 31.42 also shows the results of PIV experiments with a parallel acoustic excitation with a frequency of 350 Hz at the angles of attack of 15° and 17° at $Re = 50,000$. As can be seen from the results of force measurements the stall angle was increased from 12° to 16°, and this situation is seen from PIV experiments and the parallel acoustic control prevented the leading edge separation, but the flow was separated from the trailing edge at $\alpha = 17°$.

Fig. 31.36 Velocity profile over the NACA2415 aerofoil without/with parallel acoustic forcing with certain frequencies at $Re = 50{,}000$ and $\alpha = 15°$
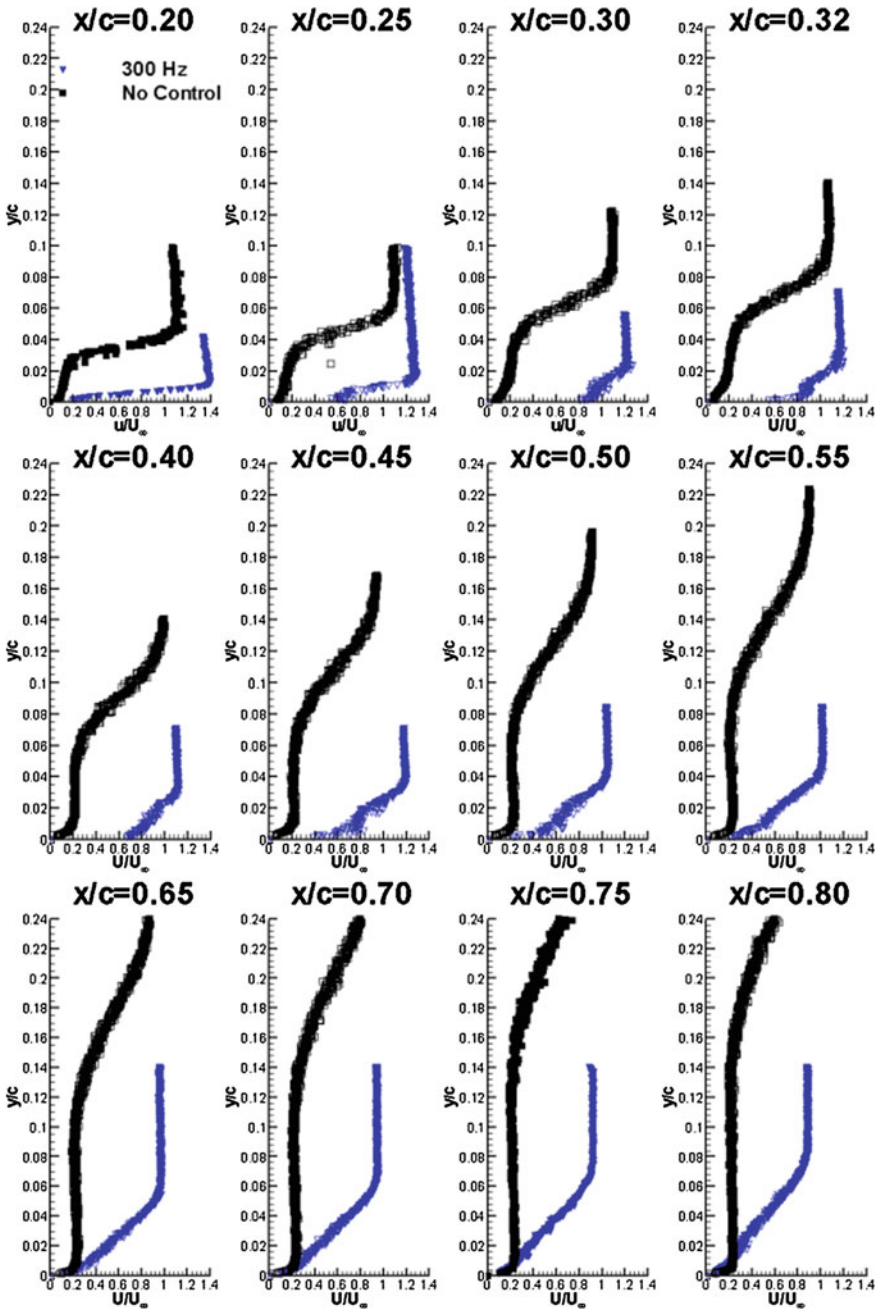
Fig. 31.37 Velocity profile over the NACA2415 aerofoil without/with perpendicular acoustic forcing with certain frequencies at $Re = 50,000$ and $\alpha = 15°$

No Control	Control (f=350 Hz)
(a) Re=50000 and α=8°	

| **(b)** Re=50000 and α=15° | |

| **(c)** Re=50000 and α=18° | |

Fig. 31.38 Smoke-wire visualization results without/with parallel acoustic forcing with 350 Hz at *Re* = 50,000 and various angles of attack

The effect of perpendicular acoustic excitation on the flow over the aerofoil for *Re* = 75,000 at the angles of attack of 8°, 15°, and 17° by using PIV experiments is indicated in Fig. 31.43. For the angle of attack of 8°, the LSB is seen and shortened with a 700 Hz of parallel acoustic excitation. As seen from Fig. 31.43c and Fig. 31.43d, at α = 15° the flow separates from the leading edge, which is characterized as trailing edge separation, while the separated region is reattached with parallel acoustic excitation of 700 Hz. The acoustic control provides that the flow reattaches, and the LSB occurs between *x*/*c* = 0.3 and *x*/*c* = 0.8 as seen in pressure distribution graphs. Also, the results show that the stall was retarded at the angles of attack from 15° to 17°, and trailing edge stall was present instead of leading edge stall.

No Control	Control (f=300 Hz)
(a) Re=50000 and α=8°	
(b) Re=50000 and α=15°	
(c) Re=50000 and α=20°	
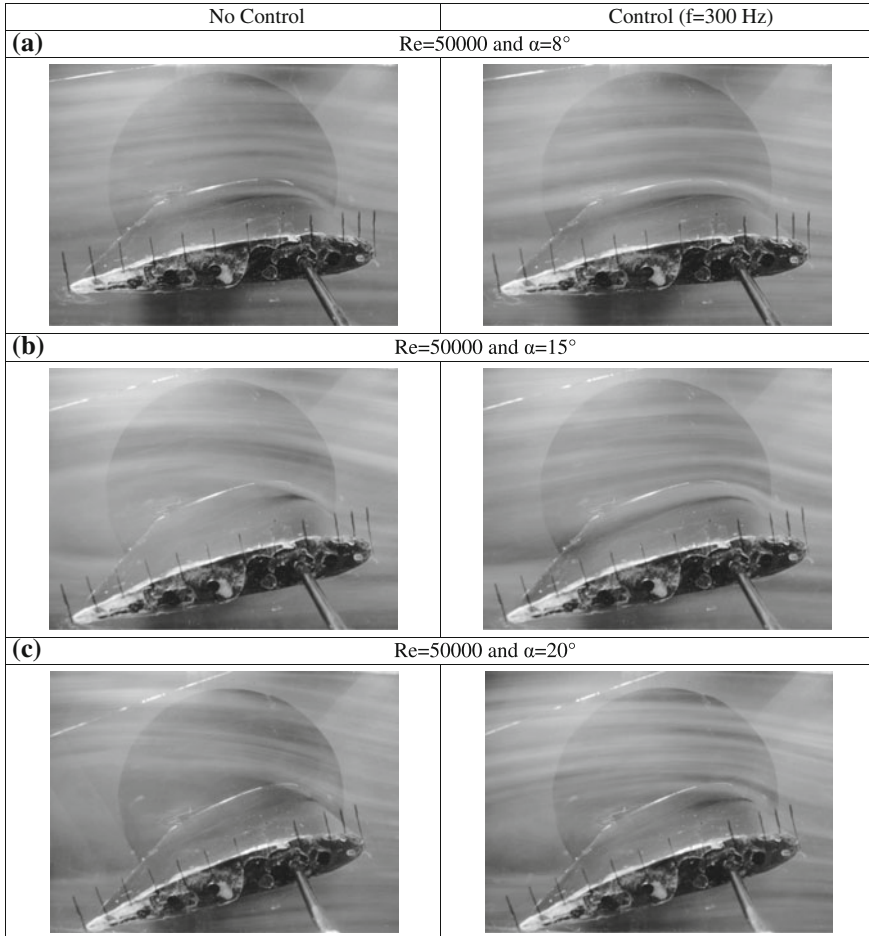
Fig. 31.39 Smoke-wire visualization results without/with perpendicular acoustic forcing with 300 Hz at *Re* = 50,000 and various angles of attack

In the results of pressure coefficient distributions, the reattachment is not obtained clearly because the pressure taps were inadequate near the trailing edge. The separated flow at low Reynolds numbers reattaches over the aerofoil after the transition; which can be seen from the turbulence kinetic energy results in Fig. 31.44. The turbulence kinetic energy increased since transition from laminar to turbulence occurs at approximately $x/c = 0.65$ over the aerofoil, and the flow reattached over the surface of aerofoil with increasing its energy. The vorticity contours (Fig. 31.44) illustrate that vortices at the beginning of LSB are strong while that near the surface of the aerofoil are weaker. High levels of vorticity indicate the shear layer, which point out that the shear layers shed from the upper surface.

No Control	Control (f=700 Hz)
(a) Re=75000 and α=8°	

| **(b)** Re=75000 and α=15° | |

| **(c)** Re=75000 and α=18° | |

Fig. 31.40 Smoke-wire visualization results without/with parallel acoustic forcing with 700 Hz at *Re* = 75,000 and various angles of attack

31.4.6 *Flow Physics and the Effect of Acoustic Excitation on the Flow*

This study showed that the flow was controlled with the acoustic disturbance. In order to understand the effect of the acoustic forcing, more experimental work had been done, especially on the stream-wise fluctuations. By using the hot-wire measurements over the aerofoil at a range of Reynolds numbers of 50,000–150,000, spectral analysis of the data at every measurement point were investigated. For example, the results of the spectral analysis at $x/c = 0.25$ and $\alpha = 12°$ at every Reynolds number are given in Fig. 31.45. It can be seen that the frequency values of 427, 455, 735, and 1500 Hz are repetitive for every *Re* number. If these values

No Control	Control (f=700 Hz)

(a) Re=75000 and α=8°

(b) Re=75000 and α=12°

(c) Re=75000 and α=15°

Fig. 31.41 Smoke-wire visualization results without/with perpendicular acoustic forcing with 700 Hz at *Re* = 75,000 and various angles of attack

are not taken into account, for *Re* numbers of 50,000, 75,000, 100,000 and 150,000 the frequencies of 340, 744, 1145, and 1816 Hz are the nearly coinciding values with respect to the effective acoustic excitation frequencies, respectively. As a result, the effective frequencies were found to be effective because they resonate with the stream-wise fluctuations, thus giving energy to the flow. In addition, it was concluded that when *Re* number increased, the power spectrum density and frequency of velocity fluctuation increased, and a higher acoustic excitation was needed. This condition was also seen in the hot-wire experiments done in the wake of the flow. When the acoustic excitation was off, the vortices formed over the aerofoil showed an increase with the increasing Reynolds number.
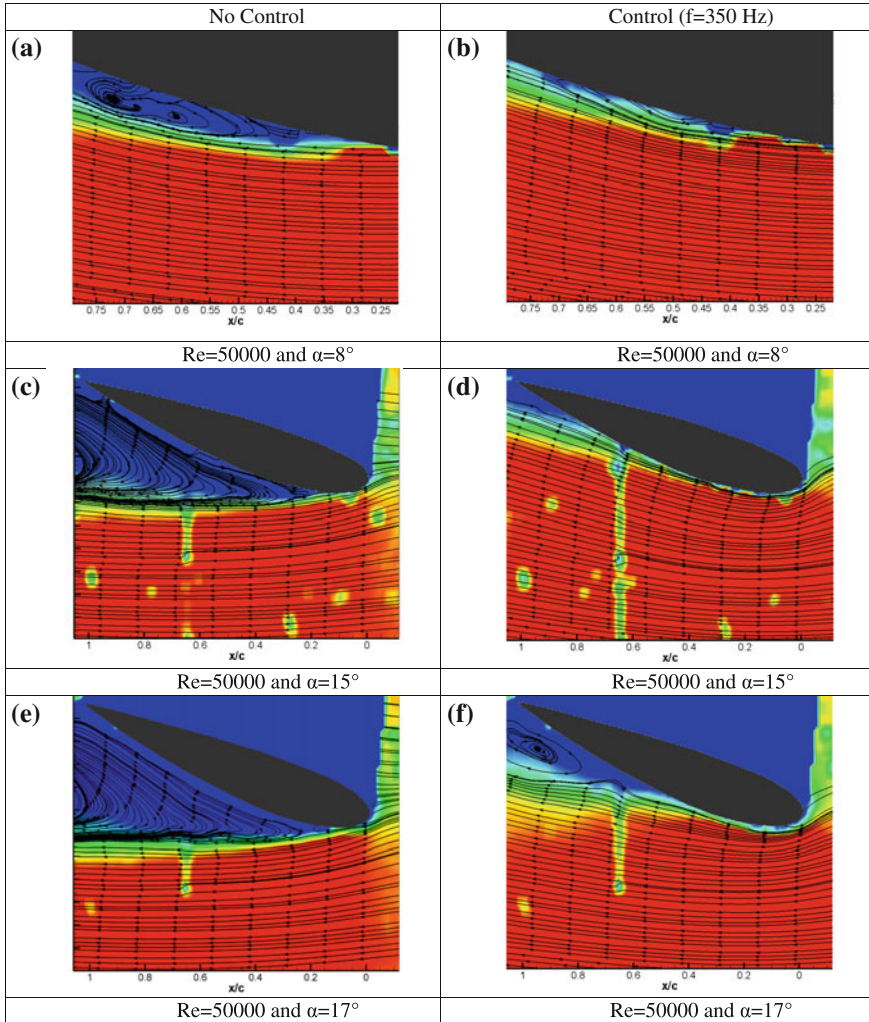
Fig. 31.42 PIV results at *Re* = 50,000 and various angles of attack without/with parallel acoustic control

31.5 Conclusion

LSB degrades the aerodynamic performance of an aerofoil by decreasing lift coefficient and increasing drag coefficient. Also, LSB causes vibration, noise, and stability problems. By forcing the flow to transition from laminar regime to turbulent regime with no LSB present, these adverse effects of the LSB may be avoided. Besides, with a relatively smaller LSB these adverse effects may be enhanced. Terminating or shrinking LSB, and increasing the stall angle are possible

No Control	Control (f=700 Hz)
(a)	(b)
Re=75000 and α=8°	Re=75000 and α=8°
(c)	(d)
Re=75000 and α=15°	Re=75000 and α=15°
(e)	(f)
Re=75000 and α=17°	Re=75000 and α=17°
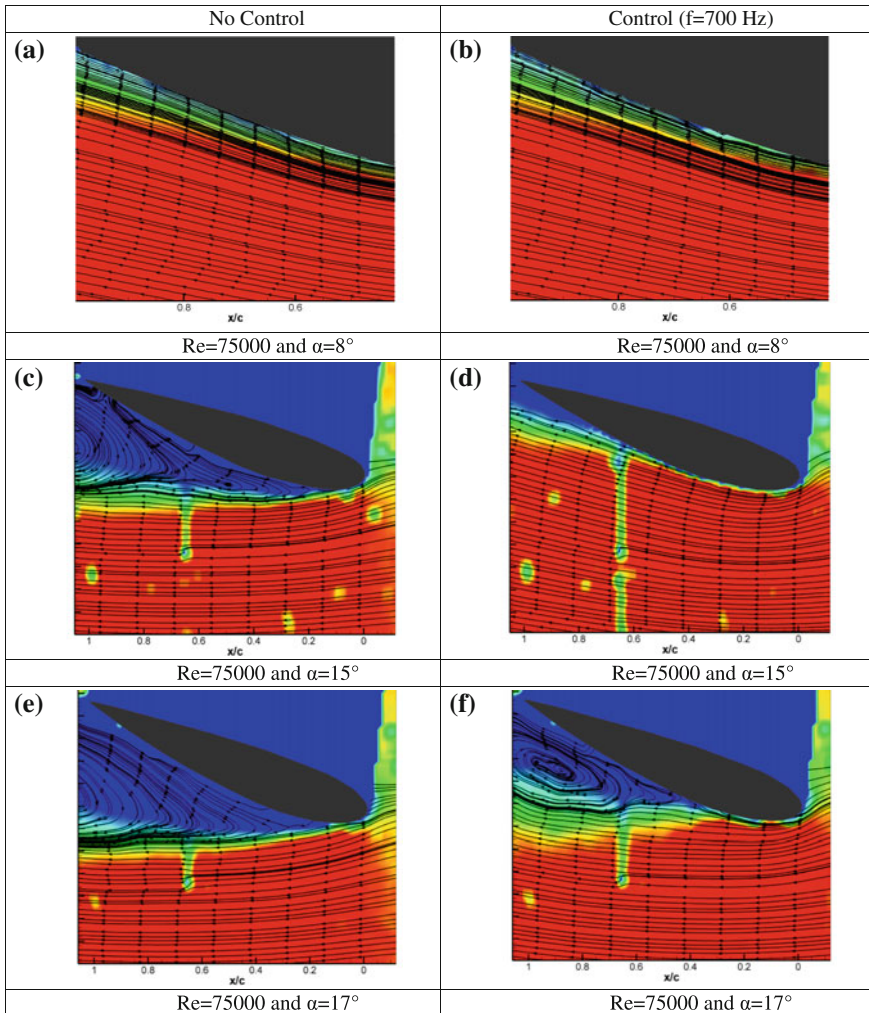
Fig. 31.43 PIV results at *Re* = 75,000 and various angles of attack without/with parallel acoustic control

by employing flow control methods. One of these methods is acoustic flow control. Its advantages are explained in the introduction section of this paper. By employing acoustic flow control, more energy efficient utilization of an aerofoil at low Reynolds numbers is possible. Consequently, this study shows that;

- For the condition with no acoustic control at Reynolds numbers of 50,000 and 75,000, the separated flow at high pre-stall angles of attack could not reattached at a short distance. This caused burst of bubble and long LSB was formed with a reattachment in the vicinity of the trailing edge.
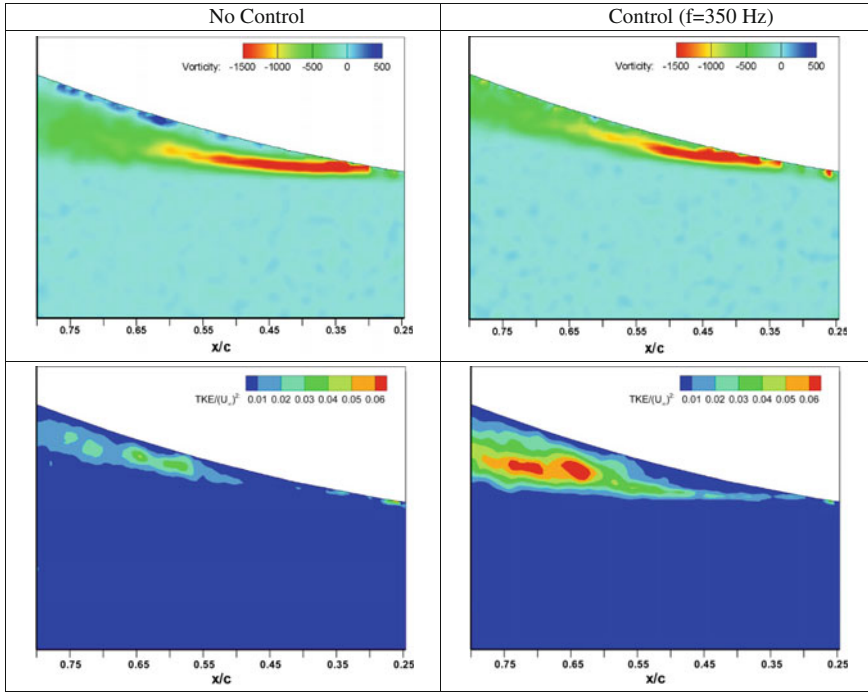
Fig. 31.44 PIV results at $Re = 50,000$ and $\alpha = 8°$ without/with parallel acoustic control

- It was seen that short LSB did not affect the pressure distribution that much. However, the formation of the long LSB caused unfavorable pressure distributions and abrupt stall with increasing angle of attack. With increasing Reynolds number shorter LSBs started to form and the stall was transformed to be mild.

- The results indicate that with acoustic flow control, the height and length of LSB are decreased at relatively small angles of attack such as $8°$. Control of the LSB leaded to increased C_L and decreased C_D. Besides, the acoustic control of certain frequencies increased the stall angle, resulting with an increased C_{Lmax}. With parallel acoustic control the angles of stall for Reynolds numbers of 50,000 and 75,000 are increased from $12°$ and $13°$ to $16°$ and $17°$, respectively. At $Re = 100,000$, the parallel acoustic control increased the angle of stall from $14°$ to $17°$. With a perpendicular acoustic excitation at Reynolds numbers of 50,000 an 75,000 the angle of stall was increased from $12°$ and $13°$ to $18°$ and $18°$, respectively.

- The results indicate that the effective acoustic excitation frequency is increased with an increasing Reynolds number. It was also seen that, with an increasing Reynolds number the effect of acoustic excitation started to wear off.
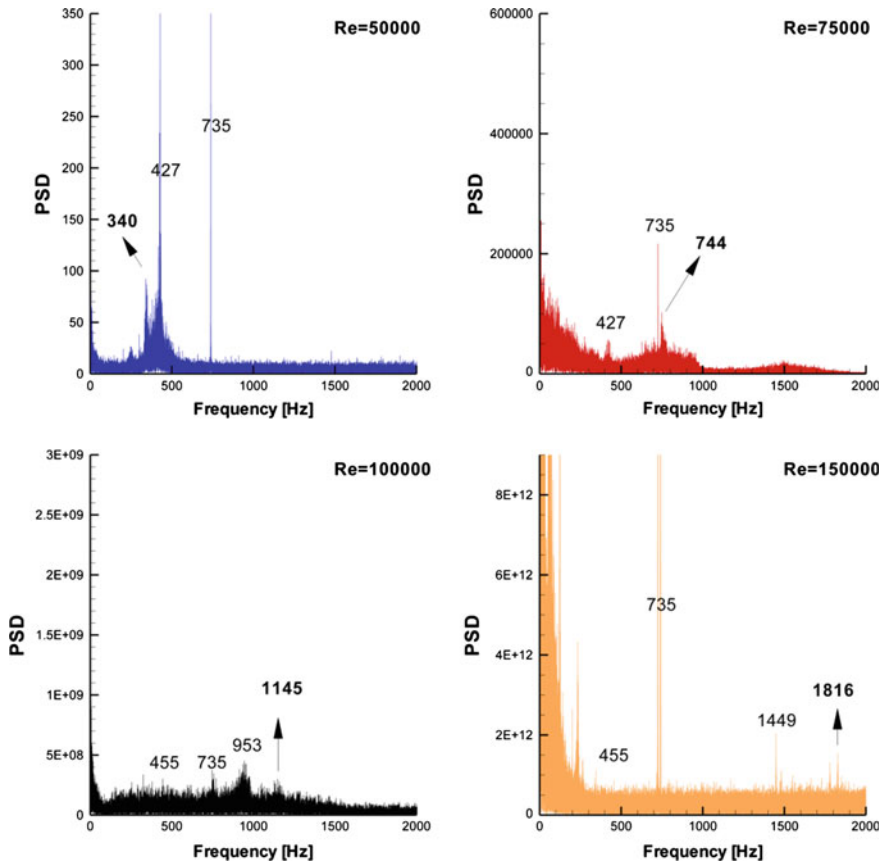
Fig. 31.45 Spectral results of velocity fluctuations over the aerofoil without acoustic forcing for different Reynolds numbers

- Moreover, it was easily seen from the pressure and velocity histories that the fluctuations on the suction side of the aerofoil were reduced and as a result of the reduction of the fluctuations on the suction side of the aerofoil resulted in a narrowed wake, increased lift, and decreased drag.
- It was clearly seen from the results of the experiments that there were a minimum and a maximum threshold for the effective acoustic excitation frequencies.
- As the Reynolds number increases, the effective excitation frequency increases also, but the range of Za number based on effective frequency still is approximately same.
- It was seen that as *Re* number increased, a higher acoustic excitation frequency was needed since the power spectrum density and frequency of velocity fluctuation increased. Acoustic excitation suppressed the stream-wise fluctuations, which reduced the forming of vortices, and forced the flow to reattach.

- Finally, it was seen that the aerodynamic performance of an aerofoil at low Reynolds numbers can be enhanced via acoustic flow control, and the parameters of acoustic flow control can easily be changed with varying conditions of the flow.

References

Açıkel HH (2013) Experimental investigation of effect of acoustic forcing to flow over an aerofoil at low reynolds number flows (in Turkish). M.Sc. Thesis, Graduate School of Natural and Applied Sciences, Erciyes University, Kayseri, Turkey

Açıkel HH, Genç MS (2015) Flow control with perpendicular acoustic forcing on NACA 2415 aerofoil at low Reynolds numbers. Proc IMechE Part G J Aerosp Eng. doi:10.1177/0954410015625672 (in press)

Açıkel HH, Genç MS, Akpolat MT, Karasu I (2012) An experimental study of acoustic disturbances effect on laminar separation bubble and transition on an aerofoil at low Reynolds number. In: AIAA-2012-2684, 6th AIAA flow control conference. New Orleans, Louisiana, USA, 25–28 June 2012

Ahuja KK, Burrin RH (1984) Control of flow separation by sound. AIAA paper no. 84-2298, New York

Ahuja KK, Whipkey RR, Jones GS (1983) Control of turbulent boundary layer flows by sound. AIAA Paper No. 83-0726, New York

Bak C, Madsen HA, Fuglsang P, Rasmussen F (1998) Double stall, riso national laboratory technical report riso-R-1043(EN). Riso National Laboratory, Roskilde, Denmark

Burgman S, Brücker C, Shröder W (2006) Scanning PIV measurements of a laminer separation bubble. Exp Fluids 41:319–326

Collins FG, Zelenevitz J (1975) Influence of sound upon separated flow over wings. AIAA J 13:408–410

Gaster M (1967) The structure and behaviour of separation bubbles. Aeronautical Research Council Reports and Memoranda, No 3595, London

Genç MS, Karasu İ, Açıkel HH, Akpolat MT (2012a) Low Reynolds number flows and transition. In: Genç MS (ed) Low Reynolds number aerodynamics and transition. Intech-Sciyo. ISBN 978-953-51-0492-6

Genç MS, Karasu İ, Açıkel HH (2012b) An experimental study on aerodynamics of NACA2415 aerofoil at low Re numbers. Exp Thermal Fluid Sci 39:252–264

Genç MS, Akpolat MT, Açıkel HH, Karasu I (2012c) An experimental study of perpendicular acoustic disturbances effect on flow over an aerofoil at low Reynolds numbers. In: ASME 2012 ınternational mechanical engineering congress & exposition IMECE2012. Houston, Texas, USA, 9–15 Nov 2012

Genç MS, Açıkel HH, Akpolat MT, Özkan G (2015a) Acoustic control of separated flow over NACA2415 aerofoil at low Re numbers. In: International symposium on sustainable aviation. Istanbul, Turkey, May 31–June 3, 2015

Genç MS, Açıkel HH, Akpolat MT, Özkan G, Karasu İ (2015b) Acoustic control of flow over NACA2415 aerofoil at low Renolds numbers. J Aerosp Eng ASCE. doi:10.1061/(ASCE)AS.1943-5525.0000639 (in press)

Hain R, Kahler C, Radespiel J (2009) Dynamics of laminer separation bubbles at low Reynolds number aerofoils. J Fluid Mech 630:129–153

Karasu I (2011) Experimental and numerical investigations of transition to turbulence and laminar separation bubble over aerofoil at low Reynolds number flows (In Turkish), M.Sc. Thesis, Graduate School of Natural and Applied Sciences, Erciyes University, Kayseri, Turkey

Karasu I, Genç MS, Açıkel HH, Akpolat MT (2012) An experimental study on laminar separation bubble and transition on an aerofoil at low Reynolds number, AIAA-2012-3030. In: 30th AIAA applied aerodynamics conference. New Orleans, Louisiana, USA, 25–28 June 2012

Karasu I, Genç MS, Açıkel HH (2013) Numerical study on low Reynolds number flows over an Aerofoil. J. Appl. Mech. Eng. 2:131

Katz J, Plotkin A (1991) Low-speed aerodynamics from wing theory to panel methods. McGraw-Hill, Inc.

Lang M, Rist U, Wagner S (2004) Investigations on controlled transition development in a laminar separation bubble by means of LDA and PIV. Exp Fluids 36:43–52

Langtry R, Menter F (2006) Overview of industrial transition modelling in CFX. ANSYS Germany GmbH, ANSYS CFX

Lock GD (2007) Lecture notes: thermofluids 4-fluid mechanics with historical perspective. University of Bath, UK

Mayle RE (1991) The role of laminar-turbulent transition in gas turbine engines. J Turbomach 113:509–537

McCullough GB, Gault DE (1951) Examples of three representative types of airfoil-section stall at low speed. NACA technical note 2502, AMES Aeronautical Laboratory Moffet Field. California, USA

Mohsen J (2011) Laminar separation bubble: ıts structure, dynamics and control. Chalmers University of Technology. Research Report 2011:06

Nakano T, Fujisawa N, Oguma Y, Takagi Y, Lee S (2007) Experimental study on flow and noise characteristics of NACA0018 airfoil. J Wind Eng Ind Aerodyn 95:511–531

Nishioka M, Asai M, Yoshida S (1990) Control of flow separation by acoustic excitation. AIAA J 28:1909–1915

Ol MV, McAuliffe BR, Hanff ES, Scholz U, Kahler C (2005) Comparison of laminar separation bubble measurements on a low Reynolds number airfoil in three facilities. In: 35th AIAA fluid dynamics conference and exhibit

Ricci R, Montelpare SA (2005) Quantative IR thermographic method to study the laminar separation bubble phenomenon. Int J Therm Sci 44:709–719

Ricci R, Montelpare S, Silvi E (2007) Study of acoustic disturbances effect on laminar separation bubble by IR thermography. Exp Thermal Fluid Sci 31:349–359

Swift KM (2009) An experimental analysis of the laminar separation bubble at low Reynolds numbers. University of Tennesee Space Institute, Ms.c. Thesis

Tan ACN, Auld JD (1992) Study of laminar separation bubbles at low Reynolds number under various conditions. In: 11th Australasian fluids mechanics conference. Universiy of Tasmania, Hobart, Australia

Tani I (1964) Low speed flows involving bubble separations. Prog Aerosp Sci 5:70–103

Yang Z, Haan LF, Hui H (2007) An experimental investigation on the flow separation on a low-Reynolds number airfoil. In: 45th AIAA aerospace sciences meeting and exhibit. Reno Nevada

Yarusevych S, Kawall JG, Sullivan PE (2003) Effect of acoustic excitation on airfoil performance at low Reynolds numbers. AIAA J 41(8):1599–1601

Yarusevych S, Kawall JG, Sullivan PE (2007) Separated shear layer transition at low Reynolds numbers: experiments and stability analysis. In: 37th AIAA fluid dynamics conference and exhibit. Miami, Florida, USA, 25–28 June

Yarusevych S, Sullivan PE, Kawall JG (2007b) Effect of acoustic excitation amplitude on airfoil boundary layer and wake development. AIAA J 45(4):760–771

Zaman KBMQ (1992) Acoustic excitation on stalled flows. AIAA Journal 30:1492–1498

Zaman KBMQ, McKinzie DJ (1991) Control of laminar separation over airfoils by acoustic excitation. AIAA Journal 29:1075–1083

Zhang W, Hain R, Kahler CJ (2008) Scanning PIV investigation of the laminar separation bubble on a SD7003 airfoil. Exp Fluids 45:725–743

Index